Volatile Geochemistry and Eruption Dynamics at Kīlauea Volcano, Hawai`i

Isobel Ruth Sides
Trinity Hall College
University of Cambridge

A dissertation submitted for the degree of
Doctor of Philosophy

December 2012

Volatile Geochemistry and Eruption Dynamics at Kīlauea Volcano, Hawai`i

Isobel Sides

Kīlauea volcano is one of the most extensively studied and closely monitored volcanoes on Earth and as such, is a type locality for basaltic volcanism. Eruptions are typically associated with large-volume, effusive outpourings of pahoehoe lava flows or occasional spectacular lava fountains. However, the eruptive history of the volcano is surprisingly varied and dramatic changes in behaviour have occurred over intervals of days to centuries, from periods of quiescent lava lake activity, to transient subplinian explosions and phreatomagmatic episodes. We know from previous studies at Kīlauea that like many ocean islands, melting beneath Hawaii taps a heterogeneous mantle source region, giving rise to significant changes in the chemical composition of melts supplied to the volcano over time scales of years to centuries. It is therefore expected that the source region will be heterogeneous with respect to volatile concentrations, which may lead to some parental magmas being inherently enriched/depleted in volatiles relative to others, directly influencing magmatic properties and eruptive style. Alternatively eruptive activity may be largely determined by shallow magmatic processes operating at magma reservoir depths. This thesis investigates the long and short-term controls on eruptive behaviour at Kīlauea volcano, through geochemical analysis of 374 olivine-hosted melt inclusions and matrix glasses. The data are used to explore the relationships between parental melt heterogeneity, fractionation, magma mixing, degassing and eruption style.

Prehistoric and historical melt inclusions preserve a record of progressive changes in pre-eruptive melt chemistry over the past five centuries, reflecting temporal changes in the mantle source composition and extent of partial melting. Significant differences exist between the compositions of melts supplying different eruption styles at Kīlauea. High-Hawaiian fountains and fissure eruption melts are inherently more primitive, and enriched in incompatible trace and volatile elements, than effusive and transient explosive events, which are consistently more evolved and volatile-poor. The dataset also reveal that melts supplying different eruption types undergo shallow pre-eruptive processes to different extents, such that effusive and subplinian melts are stored for longer periods within the summit reservoir prior to eruption, where they experience extensive fractionation, homogenisation by mixing, degassing and gas flushing with a CO_2-rich vapour. High-fountaining and fissure eruption melts undergo more rapid ascent through the plumbing system. Early exsolution of CO_2-rich bubbles enable these melts to become buoyant enough to overcome density stratification within the convecting reservoir, facilitating rapid passage to the surface with less extensive pre-eruptive degassing, homogenisation and fractionation. The results indicate that eruption behaviour at Kīlauea and other basaltic volcanoes, is strongly influenced by the composition of the melts supplied from depth. Whether a primary melt is inherently volatile-enriched or -depleted, determines the extent to which the ascending melts are subjected to shallow magmatic processes within the summit reservoir, which in turn exert controls on eruption dynamics, in addition to large-scale structural features within the plumbing system.

This dissertation also explores short-term controls on eruption dynamics during a single Hawaiian eruption. High-fountaining eruption dynamics at Kīlauea and other basaltic volcanoes are complex and often display large variations in fountain geometry and height over time. Study of a detailed time-series of melt inclusion compositions from the 1959 Kīlauea Iki eruption, demonstrates the importance of olivine fractionation, magma mixing, lava drainback and CO_2 gas flushing during a high-fountaining eruption. Progressive decreases in melt H_2O and S concentrations throughout the eruption are effectively explained by a model of lava drainback and the mixing of degassed lavas with increasingly limited volumes of undegassed melt supplied throughout the eruption. Melt inclusion CO_2 concentrations reflect volumes of new magma and CO_2-rich vapour input into the reservoir. The results suggest that CO_2 gas is important for triggering lava fountaining, whilst H_2O remains the dominant control on driving fountains. Melt inclusion CO_2 correlates inversely with fountain height and it is proposed that melt CO_2 decreases mass flow rates and exit velocities, caused by the higher density of CO_2 than H_2O at a fixed pressure and temperature. The results provide new constraints on the controls of fountain dynamics and support previous models of Kīlauea plumbing and degassing.

Declaration

I declare that the work in this dissertation was carried out in accordance with the requirements of the Universities Regulations and Code of Practice for Research Degree Programmes and that it has not been submitted for any other academic award. Except where indicated by specific reference in the text, the work is the candidate's own work. Work done in collaboration with, or with the assistance of others, is indicated as such. The total length does not exceed the 225 page limit for text, illustrations and references, as stipulated by the Degree Committee of Earth Sciences.

Isobel Sides
December 2012

Acknowledgements

I would like to thank my supervisors, Marie Edmonds and John Maclennan, for their encouragement, advice and persistent patience throughout this project. This research has been made possible by funding from the Natural Environment Research Council of the U.K. In addition to this, field work was supported by a U.S. Geological Survey Kleinman Grant for Volcano Research, and numerous travel grants awarded by Trinity Hall College, the Cambridge Philosophical Society and the Volcanic and Magmatic Studies Group.

This research has only been possible as a result of individuals who have given their time, guidance and expertise over the past four years. In Cambridge thanks go to Martin Walker for advice on sample preparation, Chiara Petrone and Jason Day for their help with the electron microprobe and LA-ICP-MS respectively, and Ming Zhang for assisting with experimental FTIR and Raman spectroscopy. SIMS analyses were all performed with support from staff at the NERC Ion Probe Facility at the University of Edinburgh and special mention must go to Cees-Jan De Hoog, Richard Hinton and John Craven for their incredible dedication throughout and for their helpful discussions on data processing and standards.

Many thanks go to the U.S.G.S Hawaiian Volcano Observatory staff for their hospitality and assistance during field work. The first field trip in 2009 was a group effort with members of the Cambridge Volcanology Group, and thanks go to Rob Martin, Georgina Sawyer, Vitchko Tsanev, Marie Edmonds and Ricky Herd for teaching me some of the tricks of the gas sampling trade and helping to ship 120 kg of tephra samples. Warmest thanks especially go to Don Swanson and Bruce Houghton for giving their time so generously to guide me in the field. Their knowledge about Kīlauea and all things volcanological is truly awe inspiring and time spent in the field with them was both an absolute joy and a great privilege. Thanks are also owed to Wendy Stovall for discussions about Kīlauea Iki and to Sam Weaver for providing a ballistic sample for use in this study. I am also extremely grateful to Mike Poland for helping out with so many of the field work logistics, and for his support over the past few years. Finally, thanks must also go to the U.S. National Park Service for granting permission for the sampling and to Pele, for letting me take away some of her rocks. An additional sample was very kindly supplied by Dave Clague of the Monteray Bay Research Institute in California, which, along with some interesting discussions and reviews, were extremely helpful.

Finally I would like to thank my friends and last but by no means least, my family, for their unwaivering love and support, and for the many midnight cups of tea.

Contents

List of Figures

List of Tables

Chapter 1

Introduction

Volatile components make up only a minor mass fraction of basaltic melts, but play a fundamental role in melt generation and eruption. At mantle depths, the major volatile species, water and carbon dioxide (H_2O and CO_2), influence the extent of mantle melting, as well as the composition and physical segregation of melts from residual mantle minerals (*Hauri et al.*, 2006). At upper lithospheric–crustal depths, H_2O and CO_2 have important effects on magma crystallisation, ascent rates and the explosivity of eruptions (e.g *Woods and Huppert*, 2003; *Sparks*, 2003). Volatiles have relatively low solubilities in silicate melts and will exsolve into a separate vapour phase as melts ascend to shallower depths (e.g. *Gerlach*, 1986; *Dixon et al.*, 1995). The differing pressure-dependent solubility of volatile species ($CO_2 < H_2O < S < Cl < F$) leads to progressive compositional changes of the gas and melt phase as a function of the depth and dynamics of degassing (e.g. *Spilliaert et al.*, 2006). Understanding the volatile geochemistry of basaltic melts can therefore provide important information about a magmatic system from source to surface.

Ocean island volcanoes, which form above upwelling mantle plumes, are associated with significant fluxes of volatiles to the atmosphere (*Gerlach et al.*, 2002; *Halmer et al.*, 2002). They are sites of prolific basaltic volcanism and produce eruptions that exhibit a broad range of eruptive styles from lava flows to high-Hawaiian fountains (up to 600 m), strombolian and occasional subplinian explosions (*Houghton and Gonnerman*, 2008). These changes in activity may be abrupt and can occur over time scales of hours to decades. Temporal and geographical variations in major element geochemistry and isotopic ratios of lavas are observed at many oceanic islands including Iceland (e.g. *Maclennan*, 2008a), the Galapagos (e.g. *Geist*, 1992) and Hawaiian islands (e.g. *Pietruszka and Garcia*, 1999a; *Garcia et al.*, 2003), and a number of studies have found evidence for greater variation in the volatile content of the magmas, than can be accounted for by fractionation and/or degassing (*Workman et al.*, 2006; *Aubaud et al.*, 2005). However to date, few studies have examined the relationship between temporal variations in parental melt volatile concentrations and eruption style at an oceanic volcano.

Investigation of melt volatile heterogeneity is challenging. This is in part, due to the low solubility of volatiles in magmas, such that subaerial eruption products do not preserve undegassed concentrations. Submarine lavas are erupted under pressures sufficient to preserve H_2O concentrations but not CO_2, and are difficult and expensive to sample. Relatively recent advances in high-precision analytical techniques (*Hauri*, 2002; *Humphreys et al.*, 2006; *Kent*, 2008), enable information about the pre-eruptive melt volatile concentrations to be retrieved from melt inclusions; parcels of melt trapped within early crystallising phases (typically olivine phenocrysts in basaltic systems), which are preserved in rapidly quenched eruption products. These tiny glass inclusions ($\sim$10–300 μm) preserve a detailed record of the pre-eruptive evolution and degassing history of the bulk magma, provided they are not extensively compromised by post-entrapment processes (*Metrich and Wallace*, 2008; *Kent*, 2008).

This thesis is based on geochemical analyses of nearly 400 olivine-hosted melt inclusions from Kīlauea volcano, Hawai`i. Kīlauea is used here as a case study for exploring the roles of mantle source and parental melt compositions, fractionation, magma mixing and degassing, on basaltic eruption dynamics. Eruptions from Kīlauea are frequent, easily accessible and extremely well documented, making it an ideal natural laboratory for such a study.

1.0.1 Introduction to Kīlauea Volcano

Kīlauea is one of five volcanic centres that make up the Big Island of Hawai`i, located on the southeast front of a linear chain of volcanic islands and seamounts that extends 6000 km across the Pacific Ocean (Figure 1.1a and b). The Hawaiian Ridge-Emperor volcanic chain formed over the past 80–75 Ma as the Pacific plate moved over a pseudo-stationary mantle melting anomaly referred to as a mantle plume or hotspot (*Clague and Dalrymple*, 1987). Seismic tomography images from beneath Hawai`i indicate the presence of a slow velocity anomaly extending towards the lowermost mantle supporting a deep origin for the upwelling manle material feeding the Hawaiian hotspot (*Montelli et al.*, 2004). The volcanic chain originates as the Pacific plate gradually moves (at $9\,\mathrm{cm\,yr^{-1}}$) each growing volcano off the hotspot, leading to formation of a new volcano at the front of the chain and leaving a trail of volcanoes and seamounts which become progressively older towards the northwest (*Clague and Dalrymple*, 1987; Figure 1.1a).

Kīlauea is the youngest subaerial volcano of the Hawaiian chain; it is a broad tholeiitic shield that abuts the southeastern flank of Mauna Loa, the largest volcanic centre on Big Island (Figure 1.1b). The summit region of Kīlauea is characterised by the presence of a fault-bounded caldera 4 km long, 3.2 km wide and 120 m deep at its western edge (Figure 1.1c and d). The southwest region of the caldera contains a circular collapse pit ~ 1 km in diameter known as Halema`uma`u crater, which has been the principal site of summit eruptive activity for the past two centuries (*Holcomb*, 1987). Radiating from the summit caldera are the East and Southwest rift zones (ERZ and SWRZ respectively; Figure 1.1c). These are two volcanically active zones 4–6 km wide that are dominated by en-echelon eruptive fissures, pit craters, open fissures, grabens aligned along the axis of the rifts, small monogenetic shields and cones. Both the ERZ and SWRZ extend from the summit caldera to the shore with the ERZ continuing offshore for a further 75 km. Submarine volcanism in the ERZ has formed the Puna Ridge, which extends to depths of 5400 m (Figure 1.1b). In contrast to the northern slopes of Kīlauea, the south flank is unbuttressed and is characterised by southward-dipping normal faults (the Koae and Hilina fault systems) that respond to inflation within the summit and rift zones and record cumulative displacements of more than 300 m (*Swanson et al.*, 1976).

1.0.2 The magmatic system

Proposed more than 50 years ago, the basic model for the Kīlauea magma transport system is still largely valid (*Eaton and Murata*, 1960) but has been extended and synthesized by *Ryan et al.* (1981) and others (e.g. *Dzurisin et al.*, 1984; *Tilling and Dvorak*, 1993; *Okubo et al.*,

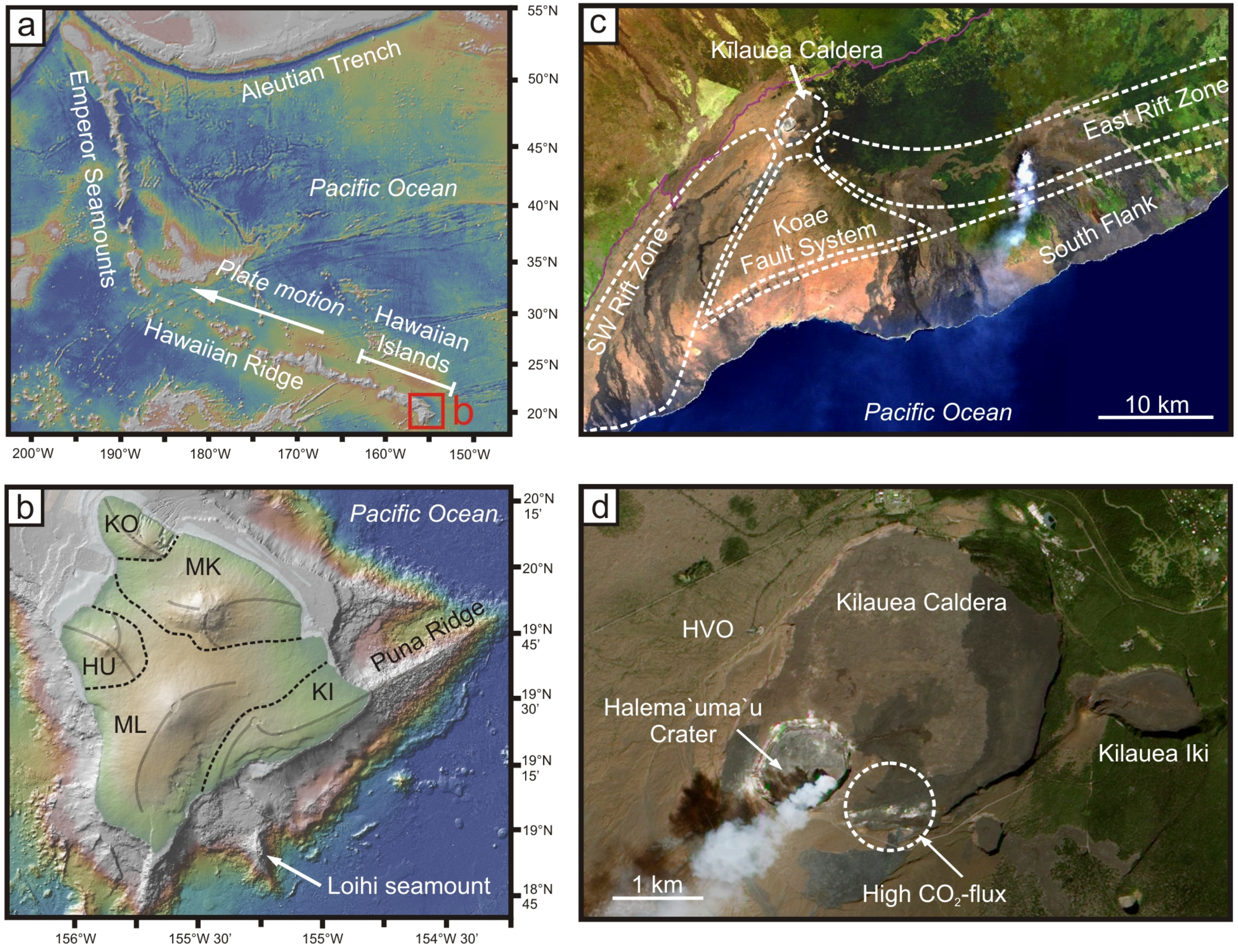

Figure 1.1: (a) Map of the Hawaiian Ridge-Emperor seamount chain in the Pacific Ocean; (b) the Big Island of Hawai`i showing the five volcanic centres: KO = Kohala, HU = Hualalai, MK = Mauna Kea, ML = Mauna Loa and KI = Kīlauea volcano. Pale grey lines trace the line of rift zones at each volcano; (c) Aerial photograph of Kīlauea volcano showing the extent of the caldera, rift and fault zones; (d) A natural-colour NASA EO-1 satellite image of Kilauea Caldera, Halema`uma`u crater and the Hawaiian Volcano Observatory (HVO). The circled area labelled high-CO_2-flux marks the sub-surface location of the shallow magma reservoir (*Gerlach et al.*, 2002).

1997; *Pietruszka and Garcia*, 1999b). Geochemical studies of mantle xenoliths in Hawaiian lavas suggest that partial melting beneath Hawaii begins at depths > 80 km (*Sen and Jones*, 1990). These melts ascend through the upper mantle and lithosphere in channels within a pipe-like feature defined by earthquake foci beneath the summit region (*Tilling and Dvorak*, 1993). Between 20–40km depth, this pipe-like region is ~ 10 km wide, and is associated with long-period seismic deep volcanic tremor, resulting from magma ascent (*Tilling and Dvorak*, 1993). Parental melts are delivered to a summit magma reservoir region between 7 and 1 km depth beneath the summit caldera (Figure 1.2; *Koyanagi et al.*, 1976; *Dzurisin et al.*, 1984; *Tilling and Dvorak*, 1993). The lower part of the reservoir extends to within 6 km of the surface. It is defined as an aseismic zone with a high fluid-to-rock ratio and pathways for magmatic transport both vertically and laterally into the rift zones. The upper sections of the reservoir from 1–2 km depth is dominated by intense seismicity as a result of pervasive fracturing and intrusion (*Tilling and Dvorak*, 1993). Persistent high CO_2-gas flux measurements from a ~ 1 km^2 area on the caldera floor immediately east of Halema`uma`u crater, indicate the approximate subsurface location of the shallow upper reservoir (*Gerlach et al.*, 2002) (Figure 1.1d). Apparent shifts in the location of pressure centres during and between eruptions, as well as systematic changes in the direction of daily summit tilt measurements suggest that the reservoir is a plexus of dike and sill intrusions (*Fiske and Kinoshita*, 1969; *Tilling and Dvorak*, 1993). The exact structure and volume of the reservoir has been the subject of much debate over the past thirty years. Volume estimates range from 2–3 km^3 based on Pb, Sr, and Nd isotopic studies (*Pietruszka and Garcia*, 1999b), 2–13 km^3 from geodetic measurements of summit tilt, to 40 km^3 estimated from the size of the aseismic zone. Estimates based on geochemical data most likely reflects the hotter, molten core of the reservoir region, whereas geophysical volumes may include portions of the outer crystal-mush zones and hotter ductile regions surrounding the reservoir, leading to the large discrepencies (*Pietruszka and Garcia*, 1999b). Primary magma is supplied to the reservoir region at a relatively steady rate (average 0.1 km^{3}yr^{-1}; *Dzurisin et al.* 1984), although there is evidence that this has recently increased (*Poland et al.*, 2012). Storage within the summit is transitory as magma is either supplied to the surface or into the rift zones.

Flank eruptions within the ERZ at Kīlauea are common and prior to many eruptions, patterns of migrating seismicity indicate lateral transport of magma from the base of the

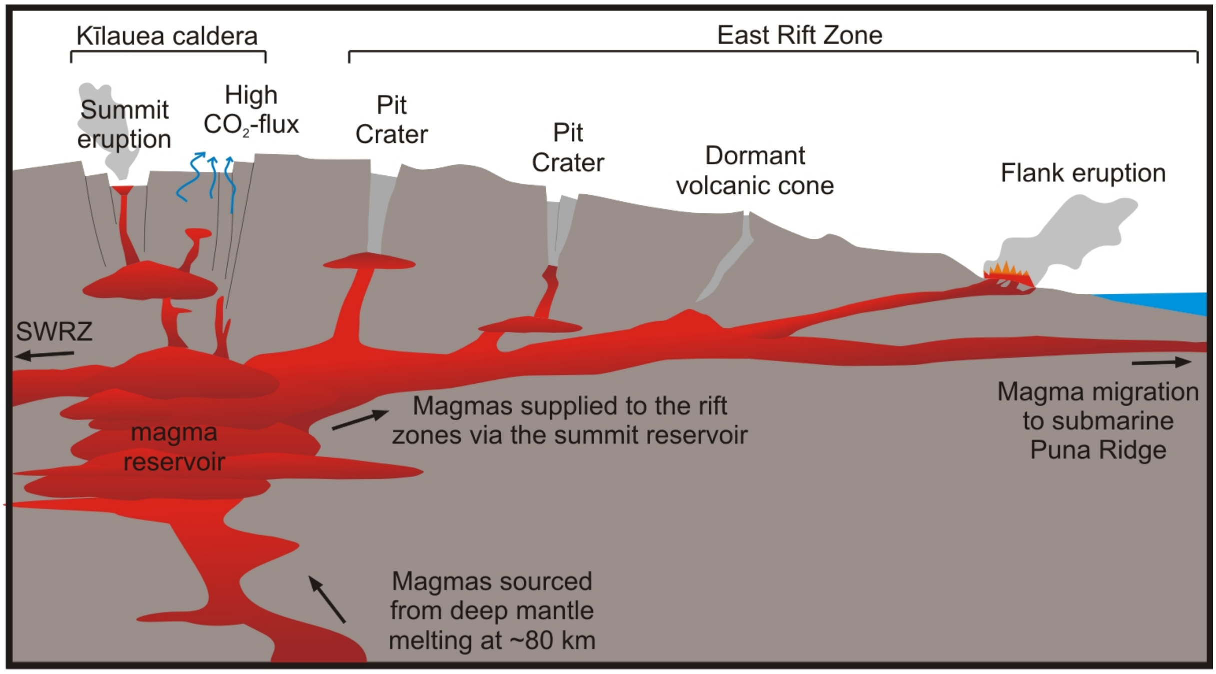

Figure 1.2: Schematic cross section of the shallow magmatic system at Kīlauea volcano.

summit reservoir to the eruption sites via shallow rift zone conduits (Figure 1.2; *Duffield et al.*, 1982; *Dvorak*, 1990). The concept of a lateral magma transport system at Kīlauea is not recent. According to William Ellis, an early Christian missionary to the Hawaiian islands in 1820, Hawaiian guides reported that flank eruptions occurred "on which occassions they supposed (the goddess) Pele went by road underground from her house in the crater to the shore" (*Ellis*, 1826). The existence of this sub-horizontal transport within the ERZ has since been determined from ground deformation studies (*Fiske and Jackson*, 1972; *Swanson et al.*, 1976), which recorded summit inflation during magma injection into the reservoir, and pronounced summit deflation during rift zone eruptions. The petrology of rift zone lavas that are typically more differentiated than summit lavas and represent the products of magma mixing with rift-stored melt (*Wright*, 1971), together with extensive seismic studies (*Ryan et al.*, 1981; *Tilling and Dvorak*, 1993) further identified the presence of secondary magma reservoirs within the rift zone (Figure 1.2). In contrast to the ERZ, eruptions within the SWRZ are less frequent and there is little evidence of established magma transport pathways from the summit; instead they are fed intermittently by drainage of the upper reservoir (*Duffield et al.*, 1982). These differences between the rift zones are thought to be due to the proximity of the SWRZ to the southern flank of Mauna Loa volcano. While the two volcanoes have independent plumbing systems, periods of inflation at Mauna Loa coincide with periods of dormancy within the SWRZ implying compressive stresses exerted on the rift zone may impede magma transport and eruption (*Lockwood et al.*, 1999).

1.1 Thesis aims and organisation

This thesis is broadly divided into two separate investigations. The first study aims to explore the relationship between compositional heterogeneities in the parental melts supplied to Kilauea volcano and the variations in eruption styles occurring at the surface. The major, trace and volatile compositions of 374 olivine-hosted melt inclusions, and 165 carrier glasses erupted over 500 years, are used to track the heterogeneous melt evolution through shallow reservoir processes of fractionation, magma mixing and degassing, to determine the long-term controls on eruptive behaviour at an ocean island volcano.

In addition to the investigation of large-scale, inter-eruption variations in magma chemistry, a second study explores variations within a single high-fountaining eruption. Observations of individual eruptions suggest that the short-term controls on eruption dynamics are complex. High-fountaining eruptions at Kīlauea and other basaltic volcanoes often display large variations in fountain geometry and height over time (*Houghton and Gonnerman*, 2008). This project examines a detailed time-series of melt inclusion compositions from the 1959 Kīlauea Iki eruption to determine the influence of syn-eruptive magma mixing, gas flushing and lava drainback on fountain height and eruption dynamics over timescales of hours to days.

The dissertation is organised into the following chapters:

- **Chapter 2** contains a summary of the sample preparation methods used and a detailed description of the instrumentation and analytical techniques used for this project.
- **Chapters 3 and 4** are part I and II respectively, of the investigation into the magmatic controls on eruptive behaviour at Kīlauea volcano through geochemical analyses of Kīlauea's prehistoric and historical melt inclusions. **Chapter 3** introduces the motivation and background to this study with a description of Kīlauea's eruptive history

and basaltic eruption styles. Previous work on this subject is also reviewed in detail. **Chapter 4** documents fieldwork sampling methods and describes the classification of the stratigraphy and sample suite. Geochemical analyses are presented and used to examine the effects of mantle source heterogeneity, variations in primary melt volatile concentrations, and the roles of degassing, mixing and fractionation in determining the compositions of melts supplying different eruption styles.

- **Chapter 5** examines the short-term degassing history of melts produced during the 1959 Kīlauea Iki eruption, which produced the highest lava fountains ever observed in Hawaii. A detailed review of the eruption history and previous work is provided. Geochemical data from a suite of tephra samples produced at progressive stages of the eruption are presented and combined with estimates of magma volume flux recorded throughout the 36 day event, to generate a model for the effects of lava drainback on melt volatile compositions and to assess the influence of melt H_2O-CO_2 concentrations on Hawaiian fountain heights.
- **Chapter 6** summarises the conclusions of this dissertation, examining the findings in the broader context and suggesting possible avenues for further research.

Chapter 2

Analytical Techniques

This chapter describes the procedures of sample preparation and geochemical analyses performed on all samples in this study. Furthermore, details on instrument calibration, technical set-up, data quality and processing are explained in full.

2.1 Sample Preparation

Lava and tephra samples were thoroughly dried after collection using a series of heating lamps in a laboratory at HVO (Figure 2.1a). Once transported back to Cambridge, selected samples were crushed coarsely using a pestle and mortar (Figure 2.1b) and sieved to size fractions of > 2.0 mm, 2.0–1.0 mm, 1.0–0.5 mm and < 0.5 mm. Sieved fractions were inspected using a binocular microscope and olivine crystals were hand-picked from each group. Intact olivines with visible glassy melt inclusions were carefully selected. Pristine, crystal-free matrix glass fragments from each of the samples were also hand-picked. Both glass and olivine grains were mounted in a 25 mm diameter disk of epoxy resin (Buehler EpoThin) (Figure 2.1c). Once set, each sample disk was ground with silicon carbide paper to expose the olivine and glass grains at the surface which was then polished to a high standard using diamond and alumina solutions of 6–0.3 µm grade. Every disk was then mapped in detail: the disks were scanned in high resolution and individual grains were numbered and photographed under reflected and transmitted light microscopes to facilitate identification during analysis (Figure 2.1d). Detailed mapping also allowed close inspection of melt inclusions exposed at the surface.

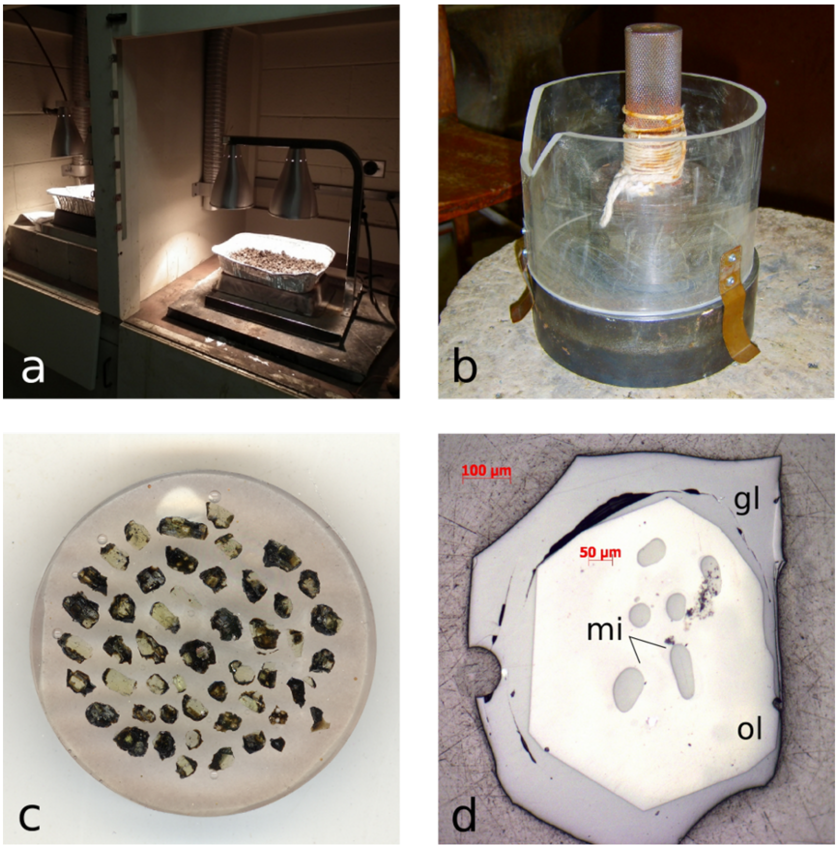

Figure 2.1: Photographs illustrating stages of sample preparation: (a) heating lamps used for sample drying prior to transport; (b) hand-held crushing equipment; (c) olivines and glass grains mounted in a 25 mm diameter epoxy disk, polished and scanned; (d) reflected light image of an individual olivine crystal (ol) with surrounding matrix glass (gl). Olivines containing melt inclusions (mi) exposed at the surface were suitable for analysis.

Only those inclusions which were considered to be of primary origin, which were glassy, $>35\,\mu m$ and not breached by cracks within the host olivine were selected for analysis.

Many of the Kīlauean melt inclusions contained vapour bubbles. The volume of each inclusion and any bubbles they contained was estimated by measurement of their long and short axes and diameters, under transmitted light. The volumes of the inclusions were calculated as standard ellipsoids with equal semi-axes; bubble volumes were calculated as spheres. Where bubbles were present in the measured inclusions, they typically occupied <7 vol% of the inclusion.

After polishing, and prior to analyses the disks were cleaned with pure ethanol and by sonification in deionised water. Final preparation prior to placement within the SIMS and EPMA instruments was application of a gold and carbon coat respectively. These were removed after analysis by polishing with an ultra-fine Al_2O_3 solution.

2.2 Secondary Ion Mass Spectrometry (SIMS)

Secondary Ion Mass Spectrometry is a microbeam technique employed in the measurement of elements from H to U (*Hinton*, 1990). Advances and improvements to the technique over the past decade has seen a rise in the popularity of SIMS as a tool for melt inclusion studies owing to the low detection limits (at concentrations of ppm and ppb), the excellent spatial resolution (beam size <25 µm) and the ease of sample preparation (*Blundy and Cashman* 2008; *Hauri et al.* 2002a).

SIMS analysis involves bombardment (sputtering) of a sample surface under vacuum, with a highly focused beam of primary ions, typically Cs^+ or O^+ (*Shimizu et al.*, 1978). Sputtering damages the sample surface, creating a small crater ~2 µm deep (*Blundy and Cashman*, 2008), and results in the generation of charged particles (secondary ions) which are ejected from the sample surface. A high voltage of $\sim\pm 4500\,V$ is placed on the sample to accelerate the secondary ions, which are extracted by an immersion lens and transferred into the mass spectrometer where they are discriminated as a function of their energy and mass/charge ratio by electrostatic and magnetic analysers respectively (*Hervig et al.*, 2006). The 'double focusing' accomplished by this process creates conditions of high mass resolution (*Craven*, 2007). The secondary ions are then detected by either an electron multiplier or faraday cup.

SIMS relies on the element being analysed to generate favourable yields of high energy secondary ions (*Hinton*, 1990). The ion yield of an element can vary enormously depending on the analytical conditions used and on the mass of the element. One of the major advantages of SIMS is the extremely low detection limits for analysis of light elements (e.g. Li, B, REE etc) which have higher ion yields.

A complication of the technique is that sputtering of the sample can produce molecular secondary ions as well as monatomic species (*Hinton*, 1990). Under conditions of low mass resolution, the secondary molecular ions cannot easily be distinguished from monatonic species on the basis of their mass differences, leading to interferences in detection and false concentrations being measured. An example of this is the interference of $^{24}Mg^{2+}$ on $^{12}C^{+}$ peaks. This creates a significant problem in the measurement of ^{12}C in basaltic glasses owing to the high Mg content of the glass. The problem is partly overcome by using kinetic energy filtering. This relies on the principle that molecular ions have a narrower and typically lower energy distribution than monatomic species. Reducing the sample extraction voltage by 50 to 100 eV, effectively reduces transmission of the molecular ions by sampling only the higher energy distributions (*Blundy and Cashman* 2008; *Hinton* 1995, 1990). Careful peak selection is also required prior to each analysis.

In this study, the concentrations of Li, B, H_2O and CO_2 were measured in melt inclusions and matrix glasses at the NERC Microanalytical Facility at the University of Edinburgh using a Camerca IMS 4f. Two substantial grants were received over the course of study for analyses to be carried out in one week periods between May 2009 and January 2011, over which time the procedure remained consistent.

2.2.1 Instrumentation

Sample mounts were gold coated to reduce surface charging during analysis. Relatively high vacuum conditions were achieved by allowing the mounts to outgas in the machine airlock at $< 5 \times 10^{-8}$ torr for a minimum of 24 hours. Sample chamber pressures during analysis were $< 2 \times 10^{-9}$ torr. Positive secondary ions were generated using a 15 kV primary beam of O^{-} ions. An O^{-} beam was preferred as it prevents charge build up on the sample. The secondary ions were then accelerated to 4500 eV, with an offset of -75 eV for ^{1}H, ^{7}Li and ^{11}B and -50 eV for ^{12}C, to reduce the transfer of molecular ions into the secondary column. The primary beam was rastered over a 50×50 µm area for 3 minutes prior to the start of each analysis in order to effectively remove any surface contamination. A primary beam current of 5–6 nA was used during acquisition, with a non-rastered, oval-shaped beam covering a 20 µm area on single spots within the boundaries of the inclusion.

Peak positions were verified before each analysis. ^{1}H, ^{7}Li, ^{11}B, $^{25}Mg^{2+}$, and ^{30}Si were analysed at low mass resolution with a 25 µm image field used, and counting for 3 s in each of a 10 cycle run. ^{12}C was measured independently of ^{1}H, using the same beam conditions but with a 50 µm image field (achieved by combined use of the 25 µm and 250 µm transfer lenses) to improve transmission at moderate mass resolution. A mass resolution of ~ 1600 was sufficient to resolve $^{24}Mg^{2+}$ at the ^{12}C peak position for all measurements. ^{12}C was analysed for 3 s in each 20 cycle run, in which $^{24}Mg^{2+}$, $^{28}Si^{2+}$ and ^{30}Si were also measured.

2.2.2 Calibration and Data Processing

SIMS analyses of volatile elements are highly sensitive to variations in the instrument background concentrations. High background counts can be caused by excessive outgassing of epoxy resins under vacuum, or by surface contamination of the samples, and can strongly affect the detection limits during each analytical session. The problem is most significant for CO_2 owing to its low positive ion yield and typically low concentration in natural samples (*Blundy and Cashman*, 2008). Background was minimised by using a low volatility epoxy resin (*Engwell and Hall*, 2008) and working under high vacuum conditions, achieved with a liquid nitrogen cold trap in the source. In addition, the first 10 cycles of each ^{12}C analyis and the first 5 cycles of a ^{1}H run, were discarded to avoid the effects of any surface contamination.

Background counts were monitored regularly by analysing materials known to contain little or no volatiles. For H_2O, background checks were performed on the olivine hosts. Though not completely anhydrous, olivines contain water on the ppm level only (e.g.*Aubaud et al.* 2004) and the concentrations analysed were typically < 0.03 wt%. Olivine could not be used for carbon backgrounds owing to its high MgO content and the $^{24}Mg^{2+}$ interference on ^{12}C measurements. Backgrounds were instead measured on synthetic basaltic glass standards (bcr-2g and gsa-1g) and also on matrix glasses. Although these glasses may contain some residual CO_2, the low count rates achieved during analysis (typically as low as 2 cps under good vacuum conditions) demonstrated that they were CO_2-free and could provide a good estimate of the instrument background. These extremely low counts on basaltic glasses also demonstrated that the methods used to reduce $^{24}Mg^{2+}$ interference were effective. Background counts were averaged over each day and the mean counts were subtracted from the raw data.

For SIMS analysis, conversion of counts per second into concentration requires that secondary ion counts are referenced to those of a species whose concentration is known (*Blundy and Cashman* 2008; *Craven* 2007). In this study, background-subtracted raw counts were normalised to ^{30}Si. Calculation of concentrations is dependent on the use of well-characterised standards that bracket the range of the unknown compositions. A suite of natural, experimental and synthetic glasses were analysed regularly throughout each day and are listed in Tables 2.1 and 2.2. Basaltic glasses were used for H, Li and B, and standards of a wide range of compositions from rhyolitic to basaltic glasses were used for carbon.

The reference species is used to calculate the relative ion yield (RIY) of an element:

$$RIY_{element} = (cps/conc)_{element}/(cps/conc)_{Si} \tag{2.1}$$

If the RIY of a standard material is known, as well as the concentration of the reference species (SiO_2) in the unknown sample, the element concentration in a sample can be calculated from the raw counts per second. This is done by generating a working curve and plotting for example, ^{7}Li/^{30}Si versus Li ppm/SiO_2 ppm for the standard glasses bcr-2g and gsa-1g from which the Li (and B) concentrations in this study were calculated. However, for H concentrations, it has been found that variation in the relative ion yield for H is correlated with SiO_2 content, such that plotting ^{1}H/^{30}Si versus H_2O yields a single working curve for glasses of variable SiO_2 content (Figure 2.2a) (*Blundy and Cashman* 2008; Hinton, pers. comm). Blundy and Cashman (2008) suggest this is also true for CO_2 however, in the initial stages of this study, CO_2 concentrations were calculated from working curves (of ^{12}C/^{30}Si vs CO_2) that were dominated by CO_2-rich rhyolite standards. When a greater number of basaltic standards were acquired and analysed, concentrations calculated without a correction for SiO_2 were greater than their reference values by a factor of $\sim$1.4. A correction for SiO_2 was therefore applied for all carbon measurements (Figure 2.2b) and concentrations produced from standard repeats were then accurate to within error of their original characterisation.

2.2.3 Data Quality

The instrument detection limit (IDL) is the minimum concentration of an analyte which is detectable above the background noise level. For each analytical session, the IDL was calculated as:

Table 2.1: CO_2 abundances of SIMS silicate glass standards and estimation of accuracy and precision from repeat analyses between May 2009 - January 2011.

Standard	Material	Reference*	SiO_2 wt%	Reference CO_2, ppm	Mean observed, ppm	Accuracy, %	Precision, %
rb480	rhyolite	1	73.6	10380 (±500)	9717	6	8
rb497	rhyolite	1	80.4	10270 (±500)	10055	2	6
ST-2	basalt	2	48.1	1136 (±74)	1261	11	5
ST-6	basalt	2	48.7	871 (±16)	914	5	7
ST-1	basalt	2	48.0	691 (±11)	629	9	8
siss51	rhyolite	3	75.6	558	424	24	7
2678-6	basalt	4,5,6	50.0	183 (±12)	229	25	11
2390-5	basalt	4,5,6	48.6	144 (±10)	176	22	10

---

*

(1) *Brooker et al.* (1999)
(2) *Shishkina et al.* (2010)
(3) *Mangan and Sisson* (2000)
(4) *Le Roux et al.* (2006)
(5) *Sims et al.* (2002)
(6) *Sims et al.* (2003)

Table 2.2: H_2O abundances of SIMS silicate glass standards and estimation of accuracy and precision from repeat analyses between May 2009 - January 2011.

Standard	Material	Reference*	SiO_2 wt%	Reference H_2O, wt%	Mean observed, wt%	Accuracy, %	Precision, %
TPF	basalt	1	46.1	6.21	6.16	1	5
ST-1	basalt	2	48.0	2.96 (±0.09)	2.70	9	6
ST-2	basalt	2	48.1	2.84 (±0.05)	2.79	2	5
ST-6	basalt	2	48.7	1.58 (±0.09)	1.46	8	3
CFD	basalt	1	48.0	1.391	1.51	6	9
ST-3	basalt	2	48.8	1.33 (±0.04)	1.42	6	9
2390-5	basalt	3,4,5	48.6	0.68 (±0.05)	0.73	7	6
TPA	basalt	1	48.2	0.403	0.41	2	4
2678-6	basalt	3,4,5	50.0	0.21 (±0.02)	0.21	0	6

---

*
(1) *Hall* (1999)
(2) *Shishkina et al.* (2010)
(3) *Le Roux et al.* (2006)
(4) *Sims et al.* (2002)
(5) *Sims et al.* (2003)

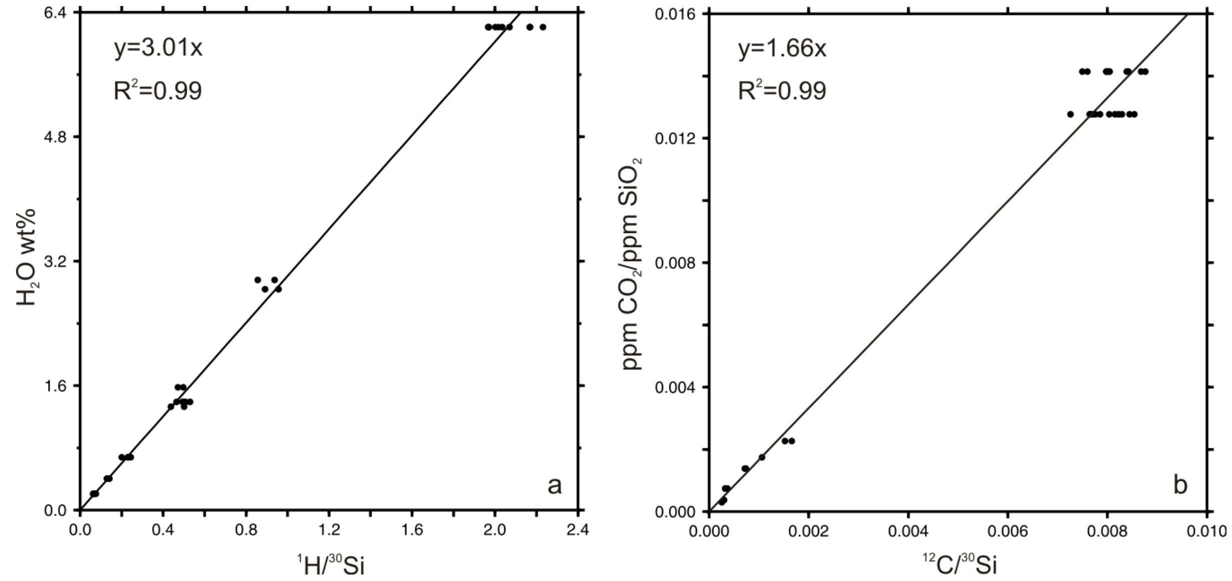

Figure 2.2: Example working curves for SIMS analyses of: (a) H_2O, derived from basaltic glass standards; (b) CO_2, derived from rhyolite and basaltic glasses of known composition. CO_2 concentration of the standard is normalised to SiO_2 to account for the variations in the SiO_2 content of the standards. The solid black line is the linear regression fit to the standard measurements. Both curves were produced during an analytical session in January 2011.

$$IDL = 3\sigma_{bkg} \tag{2.2}$$

where σ_{bkg} is the standard deviation of the background concentrations (*Reed*, 2005). All analyses were filtered to eliminate those below detection limits, which varied from session to session. The average CO_2 and H_2O backgrounds over seven sessions were 56 ppm and 0.03 wt% respectively. The precision and accuracy were monitored throughout each session by repeat analyses on the standards and are shown in Tables 2.1 and 2.2. Accuracy was calculated as:

$$Accuracy(\%) = 100 \times \frac{(\overline{x}_{obs} - x_{ref})}{(x_{ref})} \tag{2.3}$$

where $\overline{x}_{obs}$ is the mean of the observed concentrations and x_{ref} was the reference concentration. Precision was calculated as:

$$Precision(\%) = 100 \times \frac{\sigma}{\overline{x}_{obs}} \tag{2.4}$$

where σ is the standard deviation on repeat measurements of concentration. Accuracy and precision for CO_2, on standards of similar composition to the samples of this study (ST-1,2 and 6) were $< 11\,\%$ and $< 8\,\%$ respectively; H_2O values on the same standards were $< 9\,\%$ and $< 6\,\%$ respectively.

2.3 Electron Microprobe Analysis (EMPA)

Electron microprobe analysis (EMPA) is a technique used for analysing the chemical composition of a sample by bombarding its surface with a 1–20 µm beam of electrons. Bombardment causes electron excitation and transfer between the inner orbitals of target atoms, resulting in the emission of X-rays. The X-ray lines produced are characteristic of the specific elements and their intensities are a function of concentration (*Reed*, 2005). Quantitative analysis requires accurate calibration of each X-ray line, such that intensities of each line must be compared to those produced from a standard of known composition. X-rays can be selected and counted by either energy dispersive (ED) or wavelength dispersive (WD) spectroscopy. EDS uses a semiconductor detector to record the entire energy spectrum of the X-rays produced simultaneously; WDS methods use diffraction from crystals to select specific wavelength at any one time and direct them to detectors. WDS requires several crystals of different interplanar spacings in order to cover the range of compositional wavelengths, and although more time consuming than EDS, results in higher resolution spectra and superior signal-to-noise ratios.

In principal, the full range of elements with atomic numbers 4 to 92 are available using WDS but in practice, elements are generally restricted to those with higher concentrations (i.e. the major elements) owing to errors and uncertainties in background corrections at low concentrations. ‘Light’ elements are also more difficult to analyse using EMPA than SIMS. H and He do not produce characteristic X-rays and C, B and Li are at the limit of detectable wavelengths. However EMPA is a widely used tool for analysis of glasses and melt inclusions owing to the spatial resolution and the ability to measure not only all major (Si, Al, Mg etc) and minor (Cr, Mn, P) elements, but volatiles (S, Cl and F) as well.

In this study, EMPA was always performed following SIMS analysis. Samples must be carbon coated prior to EMPA and any residual coating would pose a potential contamination risk during ^{12}C SIMS analyses. A more significant problem is damage to hydrous silicate glasses by irradiation with an electron beam. Alkali (especially Na, K and Li) X-ray lines decrease in intensity during EMP analysis, as alkali ions migrate away from electrons implanted by the beam; an effect which increases with increasing beam current and exposure time (*Reed* 2005; *Humphreys et al.* 2006). Alkali migration can lead to abnormally low totals and an increase in major elements such as Si and Al. H-bearing species are also affected by migration and become enriched near the sample surface as OH^- species diffuse towards the embedded electrons. Local heating of the sample during analysis can also cause loss of CO_2 and H_2O from the sample.

2.3.1 Instrumentation

Major, minor and volatile (S, Cl, F) elements were analysed in all matrix glasses and melt inclusions, together with the composition of their olivine host crystals. Analyses were performed between June 2009 and February 2011 at the University of Cambridge using a Cameca SX100 EMP.

Samples were carbon coated to a uniform thickness of 15 nm prior to being placed in the instrument chamber under vacuum conditions. Analyses were performed in WDS mode on 4 spectrometers with LTAP, TAP, LPET and LIF crystals. All analyses were conducted using a defocussed 10 µm beam and an accelerating volatage of 15 kV. Beam currents and counting times were varied according to the material analysed, with 4 and 60 nA used for glasses; 10 and 100 nA used for olivine analyses. During glass measurements, Na peaks were counted first to avoid significant migration during the run. On peak counting times for most major elements were 20 s, with 60 s for minor elements (Mn, Cr, Ni), 120 s for S, Cl and P, and 500 s on F. Fluorine is a 'light' element (atomic number 9) and consequently a long counting time and high beam current was required to optimise detection limits. Each element was calibrated using a mineral standard at the beginning of every analytical session. Tables 2.3 and 2.4 document the analytical conditions and calibration standards used for each element.

In WD analysis, X-ray intensities are measured by counting output pulses in a given period of time. The instrument software converts the count rate into concentrations by performing a series of linear background corrections and calibrating against the input standard

Table 2.3: EMP analytical conditions for glass measurements. All analyses were run with a 10 µm beam at 15 kV. Pk(s) is the on-peak counting time in seconds.

Element	Pk(s)	Crystal	Current (nA)	Detection Limit (ppm)	Standard
Na	20	LTAP	4	463	Jadeite
Si	20	TAP	4	651	Diopside
Al	20	TAP	4	483	Corundum
Mg	20	LPET	4	561	Periclase
K	20	LPET	4	411	K-felspar
Ca	20	LPET	4	661	Diopside
Ti	20	LPET	4	459	Rutile
Fe	20	LIF	4	2124	Fayalite
F	500	LTAP	60	175	Fluorite
Cl	120	LPET	60	40	Halite
S	120	LPET	60	39	Pyrite
P	120	LPET	60	45	Apatite
Mn	60	LIF	60	202	Manganese
Cr	60	LIF	60	200	Chromium
Ni	60	LIF	60	296	Nickel

Table 2.4: EMP analytical conditions for olivine measurements. All analyses were run with a 10 µm beam at 15 kV. Pk(s) is the on-peak counting time in seconds.

Element	Pk(s)	Crystal	Current (nA)	Detection Limit (ppm)	Standard
Si	20	TAP	10	397	Diopside
Mg	30	TAP	10	586	Periclase
Fe	20	LIF	10	1363	Fayalite
Na	30	LTAP	100	54	Jadeite
Al	30	TAP	100	61	Corundum
Ca	30	LPET	100	303	Diopside
Ni	30	LIF	100	210	Nickel
Mn	30	LIF	100	303	Manganese
Cr	30	LIF	100	210	Chromium

compositions. The software calculates oxygen concentrations obtained by stoichiometry and final oxide concentrations are presented in weight per cent.

2.3.2 Data Quality

Detection limits were calulated as in Eq. (2.2). Average detection limits for each element are shown in Tables 2.3 and 2.4. Data were filtered and any values below detection removed. Analyses with totals of < 98 wt% or > 102 wt% were also removed.

In addition to calibration of each X-ray line, a series of secondary reference standards (olivines, pyroxenes, feldspars and glasses) were measured daily to check accuracy, precision and totals. The precision and accuracy of repeats on a natural basaltic glass 2390-5 are shown in Table 2.5. Precision estimates on the 2390-5 glass for S, Cl and F are < 21 %. The accuracy of F and S were 4 and 2 % but much greater for Cl at 61 %. This discrepency is most likely the result of 2390-5 being a natural submarine glass, rather than error. Natural heterogeneity or sea water contamination could result in the large difference between the Cl reference and measured values. The lack of synthetic or experimental basaltic glass standards for S, F, and Cl makes testing the accuracy of EMPA values for these elements difficult. However, in addition to repeat analyses on standard materials, a minimum of two repeats were made, where possible, on inclusions and glass samples. The standard errors on 444 melt inclusion repeats were calculated, and reveal that errors in repeatability for S, F and Cl, are no greater than 81, 50 and 19 ppm respectively.

2.4 Laser-Ablation Inductively-Coupled-Plasma Mass-Spectrometry (LA-ICP-MS)

Laser-ablation inductively-coupled-plasma mass-spectrometry (LA-ICP-MS) is a micro-analytical technique for the in-situ determination of trace element abundances in small sample volumes. LA-ICP-MS can provide a similar suite of trace elements as SIMS, but has the advantage of greater sensitivities to transition metals and platinum group elements, as well as more rapid acquisition times (*Kent*, 2008).

Table 2.5: Composition of EMPA secondary standard 2390-5 (basaltic EPR glass, *Le Roux et al.* (2006) and *Sims et al.* (2003)). Accuracy and precision calculated for each element are based on 77 repeat analyses made between June 2009 - February 2011. Obs. is the average composition measured and σ the standard deviation of the repeats.

Element, wt%	Ref.	Obs.	σ	Acc. %	Prec. %
SiO_2	48.60	49.42	0.60	2	1
TiO_2	2.01	2.55	0.07	27	3
Al_2O_3	16.00	15.39	0.31	4	2
FeO	10.40	10.69	0.35	3	3
MnO	0.17	0.18	0.03	6	16
MgO	7.01	6.48	0.19	8	3
CaO	9.80	10.33	0.24	5	2
Na_2O	3.16	3.20	0.23	1	7
K_2O	0.63	0.88	0.13	39	15
P_2O_5	0.31	0.44	0.01	41	2
S ppm	1421	1386	128	2	5
F ppm	630	604	127	4	21
Cl ppm	241	388	49	61	13

The LA-ICP-MS system consists of a laser source with a modified petrographic microscope for sample observation and a vacuum sample cell beneath the laser, which is connected to an inductively-coupled plasma and mass spectrometer (*Heinrich et al.*, 2003). Samples are placed in a vacuum cell and a pulsed laser beam of 30–100 µm size, is focussed on the selected surface. Each laser pulse causes destruction of chemical bonds in the sample spot and ejection of material as particulates from the flat-bottomed, circular crater created by the ablation process. A stream of carrier gas transports the ejecta into the Ar plasma of the ICP-MS instrument where the particulates are rapidly atomised and ionised prior to entering the high vacuum mass spectrometer. The mass spectrometer records transient signals sequentially, cycling through the mass of elements selected for measurement and analysing each for a short period or ‘dwell time’. Dwell times must be carefully selected, as multi-element analysis of small samples requires a trade-off between signal intensity and signal duration. This can be particularly problematic for melt inclusion analyses where signal duration may be very short if the laser ablates through the inclusion.

As with SIMS, errors in concentrations measured can arise due to interferences of polyatomic ions created from elements in the sample matrix. The intensity of such interferences can co-vary with the intensity of the ablation signal. Alhough problematic, the effect can be minimised by selecting different isotopes of the analyte, for example ^{65}Cu instead of ^{63}Cu which suffers interference by $^{40}Ar^{23}Na^{+}$, an ion cluster generated by interaction of the sample matrix with the plasma (*Heinrich et al.*, 2003).

Another potential source of error is elemental fractionation, which can occur during ablation by the laser or incomplete vapourisation in the plasma. Fractionation is detectable as variations in the element intensity ratios during analysis of homogeneous samples, and is effectively reduced by using a deep UV wavelength laser with a homogeneous energy distribution and He as a carrier gas (*Kent*, 2008).

A further similarity between the LA-ICP-MS technique and that of SIMS is the need for both external (reference material of known composition) and internal (a reference element of known concentration in the sample) standards. External standards are used to calculate the sensitivity for each element, expressed as counts per second and concentration (cps/ µg/g). Sensitivities are strongly dependent on ablation and ionisation efficiency, and the ratio between sensitivities of various elements is identical between measurements of standards and unknowns, such that there is no change in elemental ratios related to ablation (*Fryer et al.* 1995; *Halter et al.* 2002). The ratio of the sensitivities of various elements (RSF) is effectively the same as the relative ion yield (Eq. 2.1) for SIMS analysis, and can therefore be used to determine elemental concentrations in the unknown:

$$C_i{}^{SAMP} = \frac{C_i{}^{STD} \cdot I_i{}^{SAMP}}{I_i{}^{STD} \cdot RSF} \tag{2.5}$$

where $C_i{}^{SAMP}$ is the concentration of the element i in the unknown and $C_i{}^{STD}$ is the concentration in the external standard; $I_i{}^{SAMP}$ is the intensity of the element in the unknown and $I_i{}^{STD}$ is the intensity in the standard (*Halter et al.*, 2002).

The RSF is identical for all elements in any one analysis but in order to establish the RSF for each analysis and hence calculate absolute abundances, a reference element is, is used whose concentration has been independently determined is used with a rearrangement of Eq. (2.5):

$$RSF = \frac{C_{is}{}^{STD} \cdot I_{is}{}^{SAMP}}{I_{is}{}^{STD} \cdot C_{is}{}^{SAMP}} \tag{2.6}$$

Once the RSF is known, the concentration of all other elements in the sample can be obtained from Eq. (2.5) (*Halter et al.*, 2002).

LA-ICP-MS is a destructive technique and for this reason, could only be performed once all SIMS and EPMA measurements had been completed.

2.4.1 Instrumentation

Trace element compositions of matrix glasses, melt inclusions and selected olivines were measured using a New Wave UP213 Nd:YAG laser ablation system interfaced to a Perkin-Elmer Elan DRC II ICP-MS in the Department of Earth Sciences at the University of Cambridge. Helium was used as the carrier gas and was delivered to the sample ablation cell via a mass controller system (MKS Instruments, Cheshire, UK). The helium flow rate was precisely controlled at $0.70 \pm 1\,\mathrm{L\,min^{-1}}$. The helium flow carrying the ablated sample material was joined by a y-piece to the argon from the ICP-MS at $0.85\,\mathrm{L\,min^{-1}}$ before entering the plasma.

The elements analysed are listed in Table 2.6. A 60 µm diameter laser beam, with a repetition rate of 10 Hz and laser power of $\sim 1\,\mathrm{mJ}\,(12\,\mathrm{J\,cm^{-1}})$ was used for most analyses. The spot size was chosen as a compromise between signal intensity and the size of the material for analysis. Signal intensity is greater with larger beam sizes, but where melt inclusions were less than 60 µm in diameter, the laser beam size was reduced to 30 or 40 µm. For small inclusions, tests were performed on adjacent olivine to certify that the correct laser size was selected and to ensure that wherever possible, the beam was within the melt inclusion boundaries or clear of microlite patches in glass samples. Analysis of incompatible elements by LA-ICP-MS is insensitive to incorporation of the host mineral, in the unlikely event of mixed ablation, (*Kent*, 2008). However, olivine-compatible elements such as Ni are affected, and care was taken to identify samples in which any contamination had occurred.

The ICP-MS data acquisition conditions were set to 1 sweep per reading, for 55 readings, with 1 replicate, and total data acquisition lasted for 1 minute and 22 seconds. The first 20 seconds was a gas blank for each spot, followed by the laser analysis. There was a 60 second gas rinse out time after each spot to allow the element signals to return to baseline levels before moving to the next analysis. The data was acquired at a rate of approximately

Table 2.6: Laser Ablation ICP-MS acquisition data for all analyses between November 2009 - January 2012

Element	Mass	Dwell Time ($\times 10^{-3}$ s)	Integration Time ($\times 10^{-3}$ s)
Mg	24	1	55
Si	30	1	55
Ca	44	1	55
Sc	45	10	550
Ti	47	1	55
V	51	10	550
Fe	57	1	55
Ni	60	10	550
Cu	65	5	275
Zn	66	10	550
Rb	85	10	550
Sr	88	1	55
Y	89	10	550
Zr	90	1	55
Nb	93	20	1100
Ba	137	10	550
La	139	10	550
Ce	140	10	550
Pr	141	20	1100
Nd	143	20	1100
Sm	147	40	2200
Eu	153	40	2200
Gd	157	40	2200
Tb	159	40	2200
Dy	163	40	2200
Ho	165	40	2200
Er	166	40	2200
Tm	169	40	2200
Yb	172	40	2200
Lu	175	40	2200
Hf	178	20	1100
Ta	181	20	1100
Pb	208	10	550
U	238	20	1100

one point per second. The dwell time for each mass was dependent on the isotope and concentration of the element in the samples and is listed in Table 2.6.

2.4.2 Data processing and calibration

Raw data files containing the signal intensity data versus acquisition time (the output from the Elan software) were processed, and concentrations calculated using Glitter software (GEMOC, Australia). Examples of the raw data output for two different inclusion analyses are shown in Figure 2.3(a) and (b). In both analyses the first 20 seconds (segment 1) recorded background concentrations during the gas blank prior to laser firing. Segment 2 of the output shows the intensities recorded during ablation of the inclusion. If the inclusion was small and completely ablated the signal intensities changed dramatically with the introduction of olivine into the analysis (segment 3 in Figure 2.3(b)). Processing of these raw files in the Glitter software enabled careful selection of the gas blank background and the signals specific to the inclusion such that any contamination could be removed. Signal selection for the two inclusions is shown in Figures 2.3(c) and (d). The software used the selected gas blank signals as background and any counts recorded during that interval were then subtracted from the raw counts prior to calculation of concentrations. The 1σ errors, and theoretical detection limits were also calculated by the software and were exported to a spreadsheet program for further data evaluation and processing.

For all data, NIST 610 (trace elements in a glass matrix 3 mm wafer (National Institute of Standards and Technology, Gaithersburg, Maryland, USA) was used for calibration of element sensitivity. The certificate values of 50 ppm nominal for each element are not accurate, so instead the published and widely agreed values from a compilation of more accurate data from *Pearce et al.* (1997) were used. The CaO content of each glass and inclusion sample was used for internal standard normalization of the trace element signals and MgO was used for olivine measurements. Calibration accuracy was verified by repeat analysis of the USGS standards BCR-2G, BHVO-2G and KL2-G (MPI-DING, Mainz) during each analytical run. Preparation of the BHVO-2G glass from powder was performed by J. Day in the Department of Earth Sciences in Cambridge and was similar to the method of *Campbell* (2003). ICP-MS drift during the analytical session was less than 10 % each day and was compensated for by

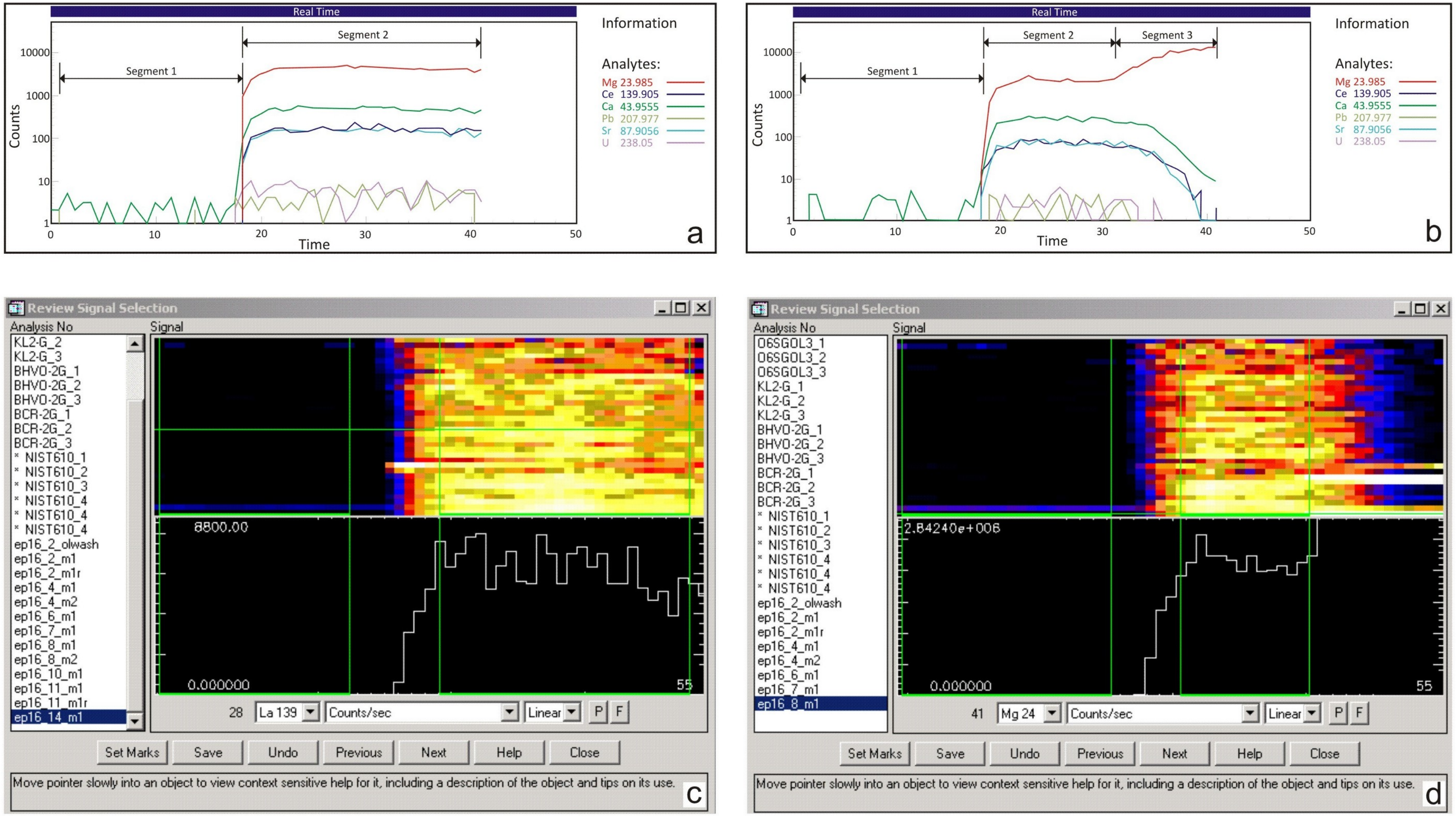

Move pointer slowly into an object to view context sensitive help for it, including a description of the object and tips on its use.

Figure 2.3: Typical raw data output and signal processing for LA-ICP-MS analyses of two different melt inclusions:(a) and (b) are the transient signal outputs from the Elan software and obtained during ablation of a large and small melt inclusion (ep16_14_m1 and ep16_8_m1 respectively). Segment 1 is the gas background, segment 2, the interval during which the melt inclusion is ablated and segment 3 (in fig. 2.3b), the interval in which host olivine is analysed after complete ablation of the small inclusion. (c) and (d) demonstrate the data processing of the two analyses (ep16_14_m1 and ep16_8_m1 respectively) in the Glitter software. Glitter allows careful signal selection, by element, for each analysis. ^{24}Mg and ^{60}Ni signals were monitored closely as dramatic increases in intensity for these isotopes was indicative of olivine contamination and was selected against.

the internal standard calculations.

2.4.3 Data quality

Data were automatically filtered and any values below detection limits removed. As with all instruments in this study, detection limits were 3σ of the background concentrations. Accuracy and precision of the method were calculated from repeat analyses of standards. The spots were chosen carefully to avoid contamination and ensure laser sampling from the target material only. Accuracy and precision were calculated as in Eq. (2.3) and (2.4) respectively. The accuracy and precision from repeats on the KL2-G glass standard are shown in Table 2.7. KL2-G is the standard closest in composition to the samples in this study. Wherever possible during sample analysis, repeats of two or three spots were also performed to assess sample heterogeneity.

2.5 Modeling post-entrapment processes

Melt inclusions are invaluable in petrologic studies, having the potential to preserve pre-eruptive melt compositions and remain isolated during magma evolution and eruption. However, significant modification of their compositions can occur after entrapment, due to crystallisation and diffusive re-equilibration of elements between the inclusion and the host and/or external melt.

Post-entrapment crystallisation (PEC) is inevitable in all inclusions (*Kent*, 2008). After entrapment of the melt, a decrease in temperature results in crystallisation of the host mineral phase on the margins of the inclusion (*Roedder* 1984; *Sobolev and Chaussidon* 1996). In the absence of re-equilibration, crystallisation is almost purely fractional. In olivine hosted inclusions, PEC leads to crystallisation of an olivine rim that is more magnesian than the trapped melt, following Fe^{2+}/Mg partitioning relationships (*Roedder and Emslie* 1970; *Ford et al.* 1983; *Putirka et al.* 2007), where:

$$K_D = \frac{[X_{Fe}/X_{Mg}]^{ol}}{[X_{Fe}/X_{Mg}]^{liq}} \tag{2.7}$$

Table 2.7: Estimation of accuracy and precision of trace elements analysed by LA-ICP-MS in glass standard KL2-G, based on 70 repeat measurements from November 2009 – January 2012. Reference values (Ref. value) are the compiled and preferred concentrations as presented on the Max Planck Institute database for reference materials: GeoRem. σ is the standard deviation of the repeats.

Isotope	Ref. value[1], ppm	Observed value, ppm	σ, ppm	Accuracy. %	Precision %
^{45}Sc	32.30	29.08	1.52	-10.0	5.2
^{51}V	370.00	311.01	9.54	-15.9	3.1
^{60}Ni	112.00	105.64	6.58	-5.7	6.2
^{65}Cu	87.90	88.50	5.87	0.7	6.6
^{66}Zn	110.00	105.11	6.76	-4.4	6.4
^{85}Rb	8.70	8.80	0.36	1.1	4.1
^{88}Sr	356.00	354.84	16.27	-0.3	4.6
^{89}Y	25.40	23.12	1.68	-9.0	7.2
^{90}Zr	152.00	145.89	14.27	-4.0	9.8
^{93}Nb	15.00	14.33	1.82	-4.5	12.7
^{137}Ba	123.00	119.49	6.91	-2.9	5.8
^{139}La	13.10	13.38	0.75	2.1	5.6
^{140}Ce	32.40	32.56	1.32	0.5	4.1
^{141}Pr	4.60	4.67	0.32	1.6	6.8
^{143}Nd	21.70	21.96	1.35	1.2	6.2
^{147}Sm	5.55	5.56	0.38	0.3	6.8
^{153}Eu	1.95	2.00	0.12	2.6	6.0
^{157}Gd	5.92	5.35	0.53	-9.6	9.8
^{159}Tb	0.93	0.85	0.07	-8.7	7.9
^{163}Dy	5.22	4.91	0.45	-5.9	9.1
^{165}Ho	0.96	0.95	0.08	-1.0	8.9
^{166}Er	2.54	2.32	0.19	-8.6	8.3
^{169}Tm	0.33	0.31	0.03	-6.4	9.6
^{172}Yb	2.10	2.00	0.18	-4.8	8.9
^{175}Lu	0.29	0.27	0.03	-4.2	10.7
^{178}Hf	3.93	3.83	0.37	-2.7	9.8
^{181}Ta	0.96	0.85	0.13	-11.9	14.8
^{208}Pb	2.07	2.13	0.86	2.8	40.4
^{238}U	0.55	0.56	0.04	1.1	7.8

K_D is the distribution coefficient relating the partitioning of Fe and Mg between olivine (ol) and liquid (liq). X_{Fe} and X_{Mg} refer to the mole fractions of Fe and Mg respectively. K_D is independent of temperature, bulk composition and oxygen fugacity and remains constant at 0.30 ± 0.04 (*Roedder and Emslie* 1970; *Putirka et al.* 2007). PEC results in the trapped melt composition becoming increasingly depleted in Mg relative to Fe^{2+} and the increments of olivine crystallised become progressively less Mg-rich. Extensive PEC causes the formation of an Fe-rich olivine zone surrounding the inclusion (*Sobolev and Shimizu*, 1993) (Figures 2.4B), a decrease in the melt inclusion Mg content (and other compatible elements) and an increase in the concentration of incompatible elements and volatiles. Correction for this process can be made by either experimental reheating of the inclusion or by numerical calculation (*Kent*, 2008). The principal of the correction calculation is reconstruction of the melt composition at the time of entrapment, by modelling reverse fractional crystallisation. Olivine of a composition in equilibrium with the trapped melt is iteratively added back into the measured melt composition until the melt is in equilibrium with that of the host olivine according to Eq. (2.7) (*Sobolev and Chaussidon*, 1996).

PEC corrections are complicated if diffusive re-equilibration has occurred between the inclusion and the host crystal and/or the external melt, which can result in fractionation of elements with different diffusion rates, and thus induce chemical signatures in the inclusions which do not reflect magmatic variations (*Danyushevsky et al.* 2000; *Gaetani and Watson* 2000, 2002). The rate of re-equilibration is dependent on the diffusivity of the individual species within the host olivine and the degree of disequilibrium between the host and inclusion. Re-equilibration is also more rapid in inclusions which are smaller and which cooled more slowly (*Cottrell et al.*, 2002).

Re-equilibration of Fe is the largest source of error in standard PEC correction calculations. At slow cooling rates, the Fe-rich olivine rim that crystallises in the inclusion, equilibrates with the more magnesian host olivine. As Fe diffuses from the rim to the host, so the inclusion also begins to equilibrate with the rim by ‘adding’ Fe, to maintain the Fe/Mg equilibrium (Eq. 2.4) (*Danyushevsky et al.*, 2000) (Figures 2.4). This process is known as ‘Fe-loss’ since the result is a population of inclusions with Fe contents far below those of the external matrix glasses (Figures 2.5). Fe-loss cannot be corrected for experimentally, and results in lower than normal Fe/Mg ratios which if used in the standard PEC reversal calculations generates an overestimation of the inclusion Mg# (*Danyushevsky et al.*, 2000).

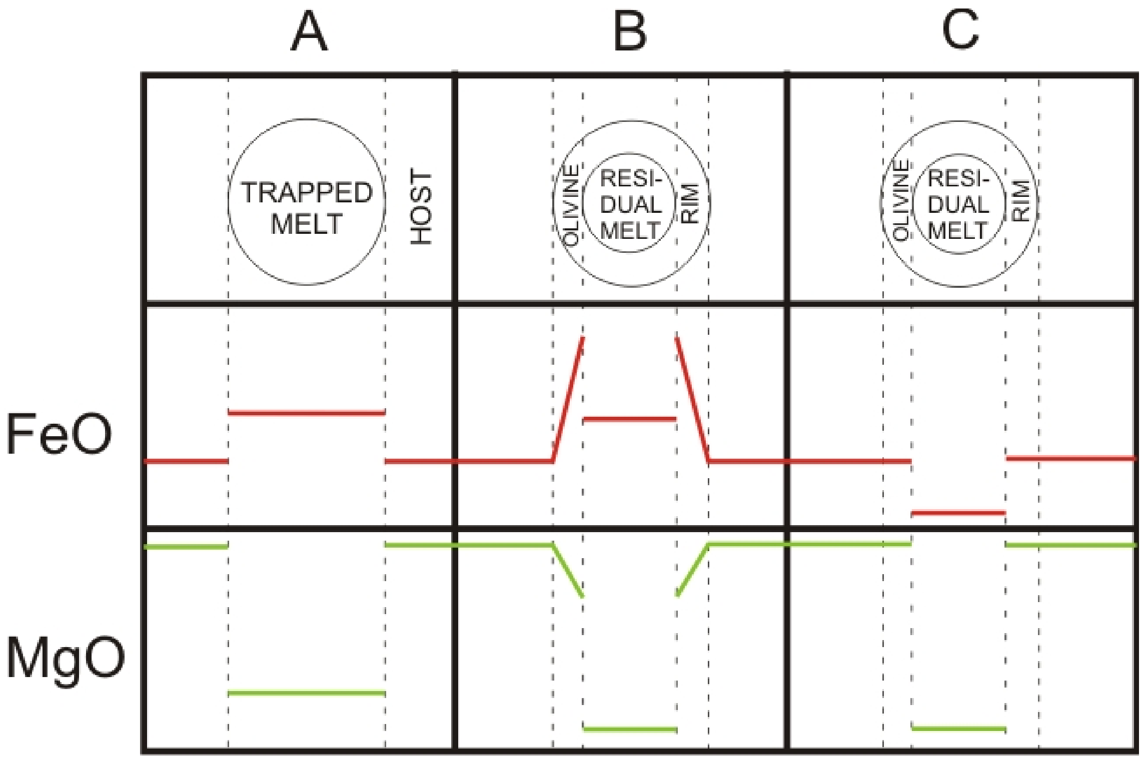

Figure 2.4: Schematic representation of inclusions and their Fe and Mg compositional cross-section profiles at the time of formation (A), after post-entrapment crystallisation (B) and re-equilibration (C).

2.5.1 Petrolog Procedure

In order to correct the melt inclusion compositions in this study for variable amounts of PEC and Fe-loss, Petrolog3, a software developed by *Danyushevsky and Plechov* (2011) was used to reconstruct the initial entrapment compositions. The software is based on the procedures outlined in *Danyushevsky et al.* (2000) and applies an iterative correction scheme. The program requires specification of the measured major and minor element compositions of each inclusion, the Fo content of the host olivines, the H_2O content of the inclusion and the oxidation state of the melt. The oxygen fugacity (fO_2) selected was the magnetite-wüstite buffer, found to be the closest fO_2 conditions for Kīlauean melts (*Rhodes and Vollinger*, 2005). The program was run for each of the 374 melt inclusions from this study.

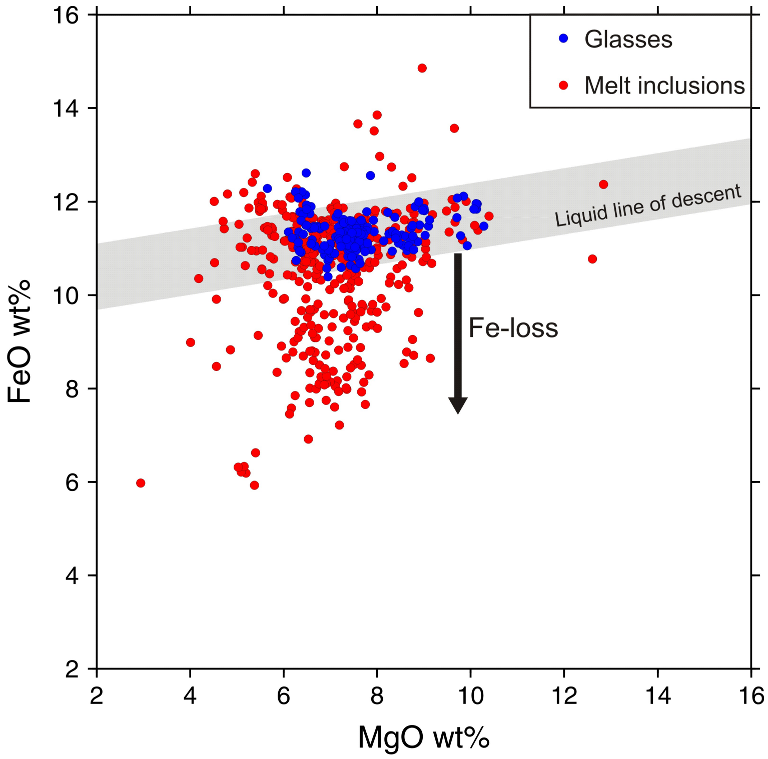

Figure 2.5: Indications of Fe-loss in Kīlauean melt inclusions. Anomalously low FeO contents in olivine-hosted melt inclusions measured in this study. Matrix glasses, also from this study, define an olivine-control line with near constant FeO values. The inclusions with very low FeO concentrations have lost Fe during post-entrapment diffusive re-equilibration when Fe diffused away from the inclusion in order to maintain Fe/Mg equilibrium with the host olivine.

In order to correct for Fe-loss, the initial FeO content of the inclusion at the time of entrapment (FeO*) must be specified. Primitive MgO contents can be difficult to estimate, but the FeO content of primitive melts is little affected by olivine crystallisation (*Putirka*, 2005), and is nearly constant along the olivine control line, Figure 2.5. The input FeO* value specified for the model calculations was 11.33 wt%. This was the average of the matrix glass FeO concentrations and agrees well with the estimate of primitive melt FeO for Hawai‘i determined by *Putirka* (2005) (11.4 wt% ± 0.03). The assumption of a constant FeO* value may carry with it significant error if the olivines analysed are mantle-derived xenocrysts. A recent study by *Keiding et al.* (2011) highlights the problems associated with assuming that all Mg-rich olivines are derived from crystallisation of Mg-rich melts with near constant FeO concentrations. High-Fo olivines can crystallise from melts produced by protracted, dynamic melt extraction from the mantle which leads to strong variation and depletion of FeO in the source region. It is therefore possible that the FeO* may be more variable than the 11.33 wt% value used in the PEC calculations. However, all of the olivines analysed in this study have moderate CaO contents (0.18–0.35 wt%) (discussed in detail in Chapter 4) which strongly suggests that they are not entrained crystals of mantle olivine but derived from melt compositions defining an olivine liquid line of descent (blue symbols: Figure 2.5) (e.g *Jurewicz and Watson* (1988)).

Essentially the Petrolog3 algorithm corrects for PEC by simulating homogenisation of the inclusion, via step-by-step addition of PEC olivine back into the melt composition. The olivine host is then kept at a given temperature until the inclusion is in complete equilibrium with the host. In the algorithm, this temperature corresponds to the olivine liquidus temperature of the measured melt inclusion composition. The program then simulates Fe and Mg exchange between the melt and olivine during the re-equilibration process. Once equilibrium is reached, the algorithm compares the FeO content of the melt to the specified FeO* content at entrapment. If the FeO* content is higher than the melt inclusion FeO, the program simulates an increase in the experimental temperature whilst simultaneously maintaining the inclusion-host equilibrium. The process is continued until the FeO content in the melt matches the FeO* value specified.

PEC corrections typically required $< 15\,\%$ olivine addition, although a small number of inclusions required up to 20 %. Calculation of errors introduced into the elemental concentrations from PEC and re-equilibration corrections are difficult to constrain. Olivine-compatible elements, notably MgO and FeO, are the most sensitive to the corrections. However *Kent* (2008) suggests that corrections applied to basaltic melt inclusions have little effect on the incompatible element concentrations beyond the errors in measurement, and therefore these elements and their ratios are considered robust.

It should be noted that diffusive re-equilibration can also lead to significant H_2O loss from olivine-hosted melt inclusions, as H^+ and H_2O may diffuse rapidly through olivines (*Mackwell and Kohlstedt* 1990; *Portnyagin et al.* 2008). The process cannot be corrected for by numerical calculation, although an attempt to minimise the effect for inclusions in this study was made by carefully selecting rapidly cooled samples. The effects of H_2O loss are discussed in more detail in the following chapters.

Chapter 3

Magmatic controls on eruption behaviour at Kīlauea volcano: Part I

3.1 Introduction

Basaltic volcanoes, unlike their silicic counterparts, produce low viscosity lavas and frequent eruptions, which are easily accessible to scientists and tourists alike. As a result, eruptions from basaltic volcanoes are often overlooked as natural hazards with potentially profound economic and societal consequences. However basaltic eruptions span a range of six orders of magnitude in mass discharge rate (10^2–$10^8\,\mathrm{kg\,s^{-1}}$; *Houghton and Gonnerman* 2008) and exhibit a broad variety of eruptive activity, from quiescent lava flows to violent Plinian explosions.

Controls on eruptive behaviour at basaltic volcanoes are complex, although it has long been recognised that the transition between effusive and explosive styles depends on the regime of gas-melt segregation, magma supply and ascent rates (e.g. *Pioli et al.*, 2008; *Houghton and Gonnerman*, 2008; *Namiki and Manga*, 2008). Over the last 25 years, efforts to understand the mechanics of these processes at active volcanoes, including Etna and Stromboli in Italy, have focussed largely on analogue and numerical models of vesiculation (e.g. *Wilson and Head*, 1981; *Head and Wilson*, 1987; *Parfitt and Wilson*, 1995; *Parfitt*, 2004; *Slezin*, 2003; *Vergniolle and Jaupart*, 1986, 1990; *Jaupart and Vergniolle*, 1988, 1989; *Vergniolle and Mangan*, 2000; *Namiki and Manga*, 2008) or detailed study of quantifiable morphological properties of eruption products such as vesicle abundance and size distribution (e.g. *Mangan et al.*, 1993; *Cashman et al.*, 1994; *Mangan and Cashman*, 1996; *Polacci et al.*, 2006; *Lautze and Houghton*, 2007; *Polacci et al.*, 2008).

While these studies have dramatically advanced our understanding of eruption dynamics, fewer studies have explored the role of geochemical controls, specifically those relating to magmatic volatiles, in initiating these dramatic changes in activity at a single volcano. Investigation of melt volatile compositions is of particular importance owing to their fundamental impact on the physical properties of the host magma and their influence on the degree of source mantle melting, crystallisation, melt buoyancy, viscosity and ascent rates (e.g. *Metrich and Wallace*, 2008; *Sisson and Layne*, 1993; *Giordano and Dingwell*, 2003; *Pichavant and Macdonald*, 2007).

Kīlauea volcano is one of the most extensively studied and closely monitored volcanoes on Earth and as such, is a type locality for varied basaltic volcanism. Eruptions are typically associated with large-volume, effusive outpourings of pahoehoe lava flows or occasional spectacular lava fountains. However, the eruptive history of the volcano is surprisingly diverse and dramatic changes in behaviour have occurred over intervals of days to centuries, from periods of quiescent lava lake activity, to transient subplinian explosions and phreatomagmatic episodes, some of which have caused significant loss of life. The causes of eruptive variation at Kīlauea remain largely undetermined, though geophysical studies of deformation and volcanological studies of eruption products indicate that shifts within the shallow plumbing structures of the volcano exert some control on behaviour (e.g. *Holcomb* 1987).

We know from previous studies at Kīlauea that melting beneath Hawai`i taps a heterogeneous mantle source region, giving rise to significant changes in the chemical composition of melts supplied to the volcano over time scales of decades to millenia (e.g. *Garcia et al.*, 2000, 2003; *Pietruszka and Garcia*, 1999b,a). It is therefore expected that the source region will be heterogeneous with respect to volatile concentrations, which may lead to some parental magmas being inherently enriched/depleted in CO_2 and H_2O relative to others; directly influencing magmatic properties and eruptive style. Alternatively, eruptive activity may be largely determined by shallow magmatic processes, such as the separation of bubbles and melt (e.g. *Houghton and Gonnerman*, 2008), operating at magma reservoir depths.

The following two chapters examine the controls on eruptive behaviour at Kīlauea through the first detailed study of the geochemistry of Kīlauea's prehistoric and historical melt inclusions. Forty three tephra and lava samples erupted from the summit and upper rift zones of the volcano were collected and 374 olivine-hosted melt inclusions analysed. The samples document a 500 year record of the changes in pre-eruptive melt chemistry at a single basaltic volcano and are used to determine the effects of parental melt composition, crystallisation, degassing, magma mixing and gas flushing on eruptive activity and to understand why some melts erupt explosively while others do not.

Kīlauea is an ideal natural laboratory for studying magmatic processes and basaltic eruption dynamics. It has a history of frequent eruptions and has been scientifically monitored since the founding of the US Geological Survey's Hawaiian Volcano Observatory in 1912. Eruption products at Kīlauea are exceptionally well preserved and reveal a long history of varied behaviour.

Owing to the large scope of this investigation it has been divided into two parts. This chapter sets the premise for the study by detailing the eruptive history of Kīlauea and the documented changes in volcanic behaviour, together with a summary of previous work on the subject and a more thorough explanation of how the dataset acquired will be used to answer questions on the relationship between source and surface processes. Part II of this work is presented in Chapter 4 and details the field sampling methods, results and discussion of the findings.

3.1.1 Overview of the eruptive history of Kīlauea volcano

Although Kīlauea is one of the most intensely monitored volcanoes in the world, relatively little is known about much of its early eruptive history. Growth of the volcano is thought to have initiated between 200–300 ka ago, with the onset of subaerial volcanism ~ 100 ka BP (*Easton and Garcia*, 1980; *Holcomb*, 1987). Information about its early eruptive behaviour has largely been determined from study of incomplete, altered or reworked exposures of eruption products. Detailed mapping of Kīlauea's surface by *Holcomb* (1987) revealed that ~ 90 percent of the volcano's surface consists of rocks younger than 1100 years, highlighting the bias of the stratigraphic record towards more recent events. Written records of eruptions from Kīlauea only began with the arrival of Christian missionaries at the beginning of the nineteenth century, with Rev. William Ellis documenting the first descriptions of Kīlauea's summit caldera in 1823. Prior to this, the only records of volcanic activity were eyewitness observations incorporated into Hawaiian oral traditions and legends about Pele, the Polynesian goddess of fire, who was believed to have lived within Halema`uma`u Crater. Despite the mythical element of these accounts, there is widespread consistency in genealogies (*Holcomb*, 1987) and they have provided useful descriptions of some eruptions prior to 1823, which have been corroborated and incorporated by volcanologists in studies of previous activity (e.g. *Swanson and Christiansen*, 1973; *Swanson*, 2008). In this study, the term 'historical eruptions' refers to those documented in written accounts of activity and is typically the term used for eruptions from 1823 onwards (e.g. *Garcia et al.* (2003)). A complete listing of historical eruptions at Kīlauea, including eruption volumes and durations are presented in Appendix Data Table 1. 'Prehistoric eruptions' refers to volcanic activity prior to 1823 for which dates have been obtained by palaeomagnetic or radiocarbon dating or by estimation of relative age from stratigraphic sections. Eruptive behaviour of the volcano is summarised in Table 3.1, and described more fully below.

3.1.1.1 Prehistoric Eruptions

The stratigraphy of Kīlauea volcano is broadly divided into three major formations according to *Easton* (1987): The Hilina Basalt (100–25 ka BP), the Pahala Ash (25–10 ka BP) and the Puna Basalt (10 ka–present) (Figure 3.1). Study of these deposits indicates that the earliest stages of subaerial volcanism at Kīlauea were dominated by sustained eruptions from vents at or near to the present volcano summit (*Easton and Garcia*, 1980; *Easton*, 1987; *Holcomb*, 1987). These prolonged eruptions were significant in the early shield-building stage of the volcano, producing extensive tube-fed pahoehoe lava flows, occasionally interspersed with pyroclastic ash fall and surge deposits. These pyroclastic episodes in the stratigraphy indicate explosive events were also occurring throughout the early stages of Kīlauea's growth, possibly associated with successive early caldera collapse at the summit (*Holcomb*, 1987).

Despite the fact that many prehistoric deposits can be traced back to vent localities at or close to the modern summit position, the structure of Kīlauea's summit has changed

Table 3.1: Summary of Kīlauea's summit geological history

Date	Event
$\sim$200–300 ka BP	Initiation of Kīlauea volcanism
$\sim$100 ka BP	Onset of subaerial volcanism
$\sim$100–10 ka BP	Subaerial shield growth Effusive pahoehoe flows with intermittent explosive eruptions
$\sim$200 BC	$>$130 m summit collapse and formation of Powers caldera
$\sim$200 BC –1000 AD	Hawaiian fountains and violent episodic explosions within caldera Formation of the Uwekahuna Ash
$\sim$1000–1470 AD	Effusive eruptions overfill caldera Observatory and `Ailā`au shield growth
$\sim$1470–1510 AD	Collapse of shields, formation of present caldera
$\sim$1510–1800 AD	Hawaiian fountains, circumferential fissure eruptions, phreatomagmatic and phreatic explosions within caldera Formation of the Keanakakoi Ash
1800-1823(?) AD	Hawaiian fountain eruption within caldera
1823–1924 AD	Nearly continuous lava lake activity
1832 AD	$>$100 m caldera collapse and caldera rim eruption
1840 AD	$\sim$100 m caldera collapse and large ERZ eruption
1868 AD	$M_{7.8}$ earthquake and 90–130 m caldera collapse
1924 AD	Drainage of lava lake, $\sim$400 m collapse, violent phreatic explosions
1924–1982 AD	Infrequent, short-lived fissure and effusive lava eruptions ($<$1 day to few months). Most within caldera and Halema`uma`u crater
1983–present	Partial draining of summit magma reservoir during ongoing (1983–2012) ERZ eruption at Pu`u `Ō`ō
2008–present	Explosions from vent in Halema`uma`u exposure of convecting and degassing magma column in crater transient, non-magmatic (externally triggered) explosions

Table modified from *Garcia et al.* (2003). Sources: *Brigham* (1909); *MacDonald et al.* (1983); *Holcomb* (1987); *Easton* (1987); D. Swanson (pers. comm. 2010).

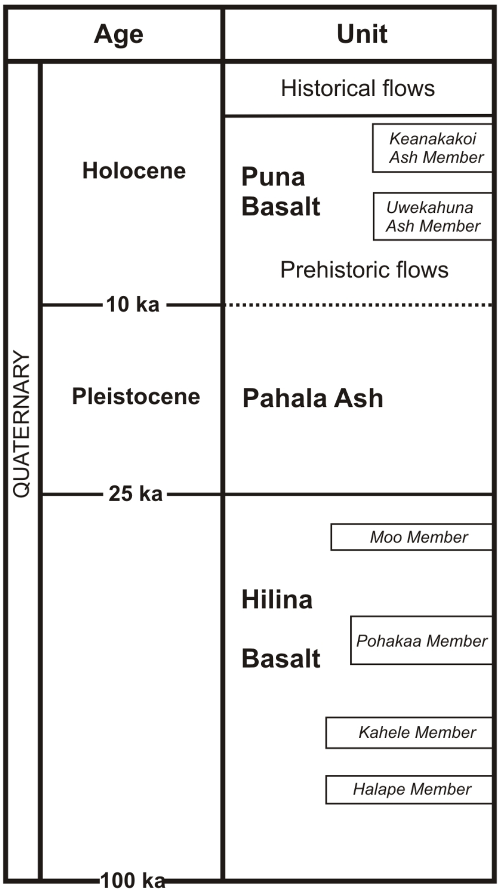

Figure 3.1: Generalised subaerial stratigraphy of Kīlauea volcano. Nomenclature follows that of *Easton* (1987). Dashed line between the Puna Basalt and Pahala Ash formations indicates that locally lowermost Puna flows are intercalated with Pahala Ash.

repeatedly throughout the volcano's history. In approximately 200 BC, summit collapse resulted in formation of the Powers caldera (*Powers*, 1948; *Holcomb*, 1987; *Swanson et al.*, 2012a). A forerunner of the modern caldera, it was at least 130 m deep, inferred from large vertical displacements in the stratigraphy dated from this period (*Powers*, 1948; *Holcomb*, 1987; *Swanson et al.*, 2012a).

Formation of the Powers caldera was succeeded by a period of summit eruptions lasting 1000–1200 years (*Fiske et al.*, 2009). The sequence initiated with high Hawaiian fountaining followed by energetic explosions from vents within the caldera, producing abundant pyroclastic tephra falls around the summit. The eruptions that ended around 900–1000 AD produced the stratigraphic sequence known as the Uwekahuna Ash Member of the Puna Basalt (more recently termed a formation in its own right; *Fiske et al.* 2009), so named after its type section locality beneath Uwekahuna Bluff in the present summit caldera.

Following this period of violent episodic explosions, summit activity stabilised into sustained quiescent eruption of large volumes of lava, over a ∼150–200 year period. The Uwekahuna Ash was overlain by lava flows which subsequently overfilled the Powers caldera and built the Observatory and \`Ailā\`au shields that occupied the summit from between 1000–1400 AD (*Clague et al.*, 1999; *Swanson et al.*, 2012a). The Observatory shield developed over the northwestern edge of the present caldera, close to the Hawaiian Volcano Observatory (HVO) (Figure 3.2), while the \`Ailā\`au shield was located over the eastern edge of Kīlauea Iki crater (*Swanson et al.*, 2012a; *Clague et al.*, 1999). The eruption from the \`Ailā\`au vent alone continued for at least 50 years and produced flows which covered 30 percent of Kīlauea's surface from the summit to the east rift zone (ERZ) coast (*Clague et al.*, 1999), in one of the longest and most prolific eruptions identified from Kīlauea. After cessation of this summit eruption in around 1470 AD (*Clague et al.*, 1999), collapse of the Observatory and part of the \`Ailā\`au shield around arcuate faults (seen in Figure 3.2), formed the current summit caldera between 1470–1510 AD (*Swanson et al.*, 2012a). It has been suggested that the caldera formed sequentially, in response to emptying of the summit magma reservoir either during the prolonged \`Ailā\`au eruption, or following intrusion from the reservoir into the rift zone, until the roof of the reservoir complex could no longer be supported (*Swanson et al.*, 2012a).

The first eruptive activity (preserved in the stratigraphy) after caldera formation was the start of a 300 year period of eruptions between 1500–1800 AD. These produced the Keanakakoi Tephra Member of the Puna Basalt. Like the Uwekahuna Ash, the Keanakakoi Tephra record that the post-caldera eruptions began with high and intense Hawaiian fountaining from vents within the caldera, followed by a period of phreatomagmatic and explosive eruptions which produced ash-rich plumes and base surges (a form of pyroclastic density current; *Decker and Christiansen*, 1984; *McPhie et al.*, 1990; *Swanson and Christiansen*, 1973; *Swanson et al.*, 2012a). One such surge produced during the mid–late stages of this period resulted in the deaths of ∼80 Hawaiian people travelling south of the caldera at the time (*Swanson and Christiansen*, 1973; *Ellis*, 1826; *Dibble*, 1843). The eruptive period culminated with a series of large lithic block falls thought to have been produced by a final phreatic stage of activity (*McPhie et al.*, 1990; *Swanson et al.*, 2012a).

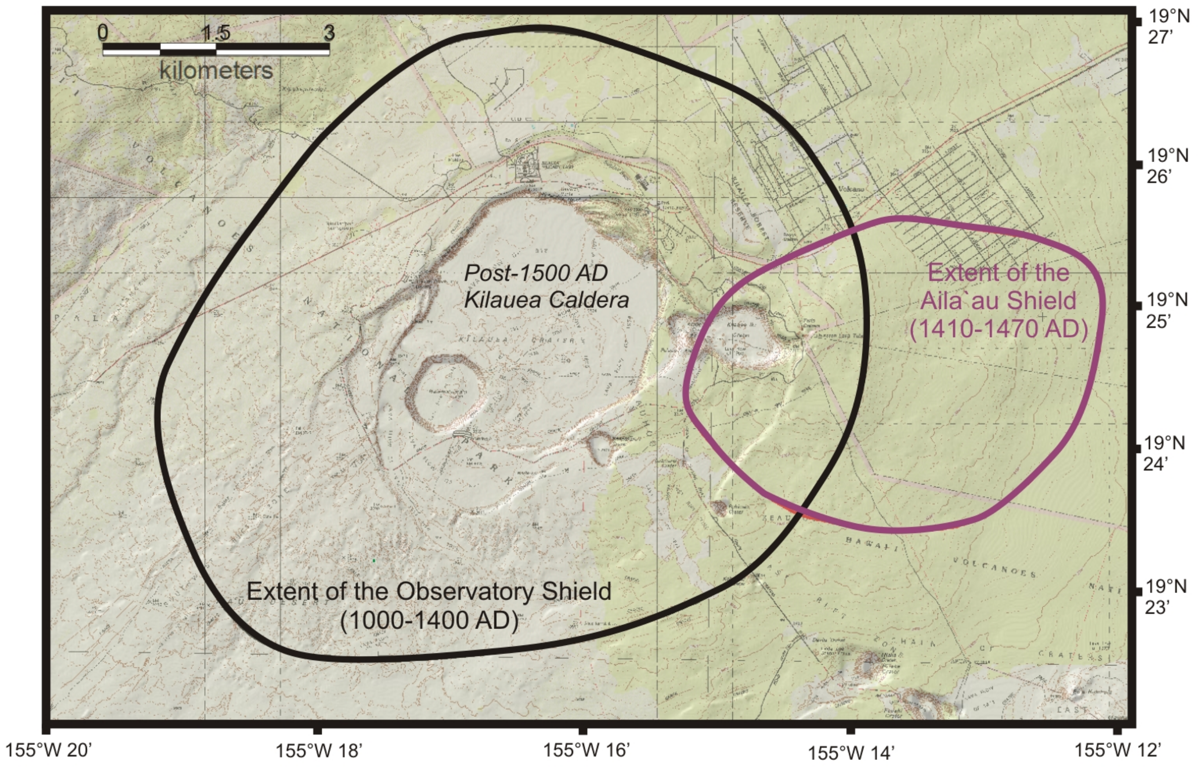

Figure 3.2: Summit map for Kīlauea, showing the approximate extents of both the Observatory and `Ailā`au shields produced during prolonged periods of large-colume effusive eruptions between 1000–1470 AD. Lava flows erupted from each shield went far beyond the boundaries of the shields themselves, but the outline of each structure is delineated by the topographic highs produced by flows piled upon flows closest to the eruptive vents (D. Swanson, pers. comm.).

The preservation of the basal reticulite deposit in the Keanakakoi Tephra has been used to provide constraint on the initial depth of the caldera after formation (*Swanson et al.*, 2012a). Reticulite is a basaltic foam with vesicularity up to 99 vol%, and is produced only in Hawaiian fountains that reach heights of > 300 m (*Mangan and Cashman*, 1996). The basal reticulite of the Keanakakoi Tephra is preserved in exposures around almost all of the caldera rim and up to 5.3 km away from the caldera's outer edge. Isopach studies have suggested the vent localities were within the caldera or along the bounding arcuate faults (*May*, 2008). The presence of reticulite suggests that the initial depth of the caldera must have been least 300 m and may have been as great as 600 m (*Swanson et al.*, 2012a). Hawaiian chants record that the sister of Pele dug the caldera so deeply after the `Ailā`au eruption ended, that there were warnings about water coming in and drowning the fires of Pele (*Emerson*, 1915; *Swanson*, 2008). This, together with the largely phreatomagmatic component of the subsequent Keanakakoi Tephra, suggests that the caldera may have collapsed to depths below that of the regional water table (which is, at the present day, at a depth of 515 m below the 120 m deep caldera floor), resulting in the formation of a shallow lake above the active vent and causing phreatomagmatic explosions. The early basal reticulite was most likely produced in fountains that formed rapidly after the initial caldera collapse, before the groundwater system could recharge and stabilise itself at its former level (*May*, 2008).

Following the explosive episode of the Keanakakoi eruptions, activity returned to high Hawaiian fountaining within the caldera between 1820–1823, producing another distinctive 'golden pumice' deposit preserved around the southern rim of the caldera (*Sharp et al.*, 1987).

3.1.1.2 Historical Eruptions – 1823 to 1923

In 1823, the Rev. William Ellis documented his first expedition to the summit of Kīlauea Volcano (*Ellis*, 1826), with the following description:

> We at length came to the edge of a great crater, where a spectacle, sublime and even appalling, presented itself before us– "We stopped and trembled". Astonishment and awe for some moments rendered us mute, and, like statues, we stood fixed to the spot, with our eyes riveted on the abyss below.
>
> Immediately before us yawned an immense gulf, in the form of a crescent, about two miles in length...nearly a mile in width, and apparently 800 feet deep.
>
> The bottom was covered with lava...one vast flood of burning matter, in a state of terrific ebullition, rolling to and fro its "fiery surge" and flaming billows.
>
> Fifty-one conical islands, of varied form and size, containing so many craters, rose either around the edge or from the surface of the lake...
>
> The sides of the lake before us...were perpendicular for about 400 feet, and rose from a wide horizontal ledge of solid black lava of irregular breadth, but extending completely round. Beneath this ledge the sides were sloped gradually towards the burning lake, which was, as nearly as we could judge 300 or 400 feet lower. It was evident that the large crater had been recently filled with liquid lava up

> to this black ledge, and had, by some subterranean canal, emptied itself into the sea, or upon the low land on the shore.

The lava lake activity witnessed by Ellis on his first visit persisted and dominated eruptive behaviour at the summit of Kīlauea for the following century, with patterns of lake filling, drainage, collapse and refilling (*Brigham*, 1909; *MacDonald et al.*, 1983; *Holcomb*, 1987). By 1832 the lake described by Ellis had filled the central basin such that a new floor stretched across the crater. At this time, a small eruption on Byron Ledge (the bounding platform between the caldera and Kīlauea Iki crater) marked an opening of the ERZ allowing magma to drain from the summit and resulting in a >100 m collapse of the caldera floor, and a reversion back to the existence of an inner basin and black ledge as described by Ellis (1823). Lake activity resumed shortly after and by 1840 had led to the development of a broad dome 30 m high over the southwestern corner of the caldera. The central vent of the dome was filled with a lake and was referred to as Halema`uma`u. Once again, the structure collapsed by ~ 100 m, accompanying major eruptions in the ERZ (*MacDonald et al.*, 1983) followed shortly after by a rapid resumption of summit activity (Figure 3.3)

Subsequent summit eruptive activity was centered on Halema`uma`u vent, where dome growth and a languid-lake persisted until 1868, when the largest historical earthquake recorded in Hawai`i ($M_{7.9}$; *Wyss and Koyanagi* 2006) resulted in two thirds of the caldera floor subsiding by 90–180 m and an eruption of lava from the caldera rim into Kīlauea Iki crater. Once again, lake activity within Halema`uma`u resumed, with the pattern of changes repeated for several decades until 1894 (Figure 3.4a and b) when the lake drained completely and summit activity ceased for a 13 year period; the first break in the otherwise continuous activity since before 1823.

From 1907 to 1924, eruption of lava from Halema`uma`u crater resumed (Figure 3.4c) with repeated minor collapses, major lava overflows and fissure eruptions which, from 1918–1921, covered large portions of the caldera floor. Episodes of lake subsidence were often accompanied by eruptions in the ERZ or SWRZ. One such eruption in 1919–20, which occurred 9 km from the caldera in the SWRZ, was substantial enough to form Mauna Iki, a new shield fed directly by lavas that had initially been erupted into Halema`uma`u.

Figure 3.3: Kīlauea summit caldera circa 1840–41, by Titian Ramsey Pearle, chief naturalist for the United States Exploring Expedition. The image shows the main features of the re-established central lake following the collapse of 1840, viewed looking south from western end of Steaming Bluff. The inner pit with numerous cones is surrounded by a broad ledge, features similar to those described by Ellis on his first expedition to the summit in 1823 (*Ellis*, 1826). The constricted part of the inner pit at the far end is the present location of Halema`uma`u. Image courtesy of The Bishop Museum, Hawai`i.

3.1.1.3 Historical Eruptions – 1924 to 2012

In 1924, drainage of the lava lake within Halema`uma`u occurred over a number of weeks and was accompanied by substantial subsidence of the whole summit region and the onset of numerous violent explosions from the vent (Figure 3.4d). The explosions initially occurred at irregular intervals lasting up to a few hours and producing cauliflower-like ash clouds which reached heights of up to 4 km above the caldera floor. Explosions were accompanied by frequent lightning flashes and ejection of large blocks (some more than a metre in diameter), lithic lapilli and ash (*Jaggar and Finch*, 1924). At the end of the eruption, the diameter of Halema`uma`u had increased to >1 km and was ~ 400 m deep. No juvenile lava was erupted during the explosions and *Jaggar and Finch* (1924) noted that only white steam

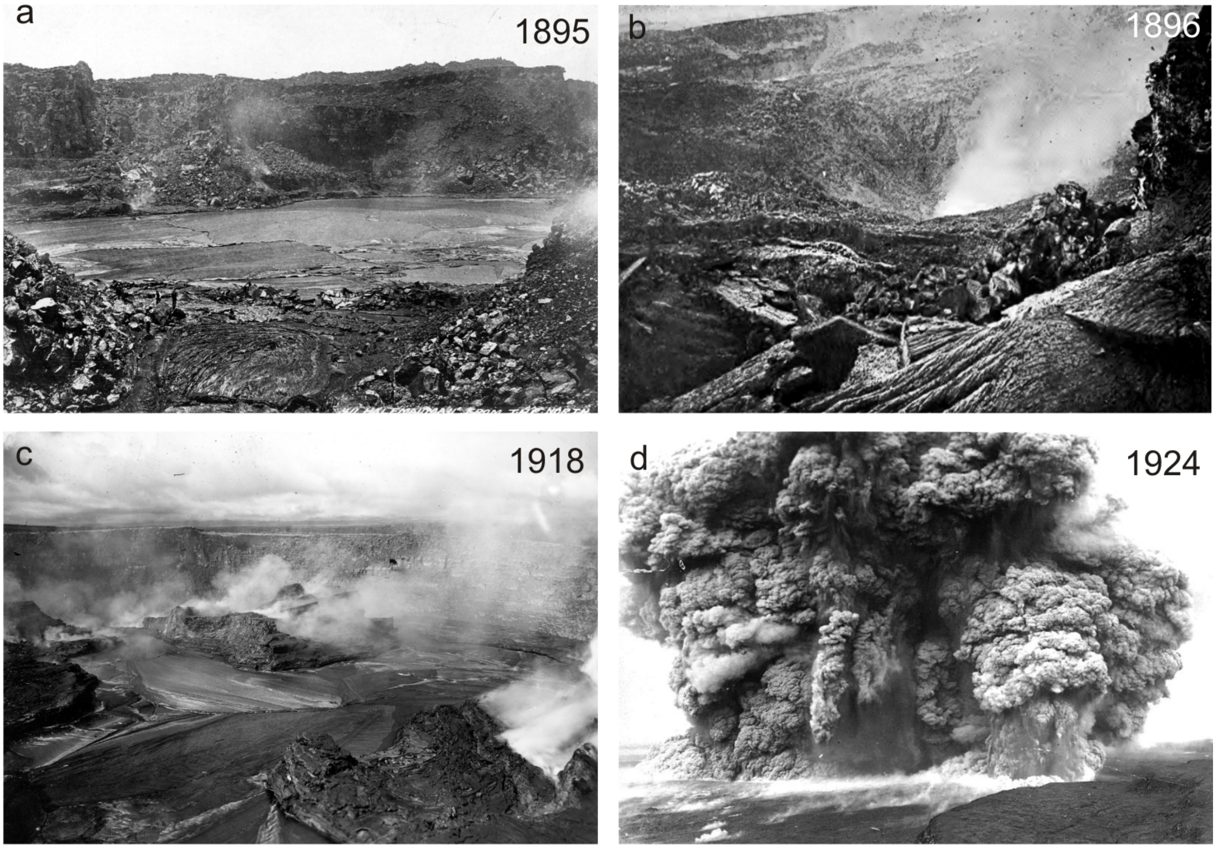

Figure 3.4: Photographs of Kīlauea's summit activity from 1885–1924. (a) Halema`uma`u lava lake in 1885 (photograph by J.S. Diller, USGS); (b) Halema`uma`u after withdrawal of lava from the lake and a subsequent collapse event in 1886 ((*Hitchcock*, 1911)); (c) View of extended Halema`uma`u crater and lake in 1918 (photograph by T.A. Jaggar); (d) Explosive phreatic eruption within Halema`uma`u crater in May 1924 (photography by H.T. Stearns).

clouds were emitted from the vent following cessation of activity, with a distinct lack of volcanic gases. These observations suggest that the explosions were entirely phreatic (*Jaggar and Finch*, 1924; *Dvorak*, 1992). As described above, the sequence of repeated lake drainage from the summit of Kīlauea had occurred many times during the previous century but had not produced the same phreatic response. It is suggested that the conditions for the 1924 eruption were produced through a combination of a decrease in the magma column by a few hundred metres together with the withdrawal of at least a few hundred million cubic metres of magma from the reservoir, facilitated by ERZ activity at low elevations or below sea level (*Epp et al.*, 1983) and leading to a decrease in hydrostatic pressure within the summit magma reservoir (*Dvorak*, 1992). This led to an influx of groundwater which, in contact with exposed superheated conduit rocks, caused violent steam explosions.

1924 marked a change in the eruptive behaviour of Kīlauea from the continuous quiescent activity of the previous century. Subsequent summit eruptions were more sporadic, with seven eruptions occurring within Halema`uma`u lasting a few days to 1 month between 1924 and 1934 (*Finch*, 1940; *Jaggar*, 1947; *MacDonald et al.*, 1983). All activity at the volcano ceased in 1934 and remained quiet for 18 years during the longest dormant period in Kīlauea's recent history.

However, in early 1950 deformation at the summit indicated that inflation of the volcano had once again resumed and countered the increasingly popular belief that the volcano was 'dead' (*MacDonald et al.*, 1983). In June 1952 the long-awaited eruption within Halema`uma`u began with a 'curtain of fire' between 15 and 50 m tall along the length of a fissure on Halema`uma`u floor. The rate of outpouring was tremendous, close to 5.5×10^6 m^3 per hour and lava filled the crater floor to 10 m depth within the first hour. A lava lake quickly established covering the fissure vent in the crater and activity persisted until the beginning of November. Despite the eruption, inflation of the volcano continued through 1953-54, and in May 1954 another fissure and lake eruption ensued (Figure 3.5). The eruption closely resembled that of 1952 but for the extension of the fissure from Halema`uma`u up the northeastern wall of the crater and onto the caldera floor. Subsequent eruptions within the summit caldera occurred in 1961, 1967-68, 1971, 1975 and 1982 (Figure 3.5). These were largely short-lived events, similar to the 1952 eruption, and produced from fissures and vents in and around Halema`uma`u crater (*MacDonald et al.*, 1983). Short-lived summit eruptions also occurred outside the caldera in 1959, 1971, 1974 and 1982. Of these, the November 1959 eruption which occurred within Kīlauea Iki crater is of particular interest (Figure 3.5). The eruption, which lasted 36 days, produced the highest fountains ever observed in Hawai`i (580 m, *MacDonald*, 1962; *Richter*, 1970). Cessation of the 1959 eruption was followed, in January 1960, by another high fountaining eruption (up to 427 m) in Kapoho village, in the lowermost ERZ. The 1959–60 eruptions are examined in detail in chapter 5.

Summit activity ceased in 1982 and entered yet another quiescent phase for 26 years, during which time activity was restricted to the ERZ. An explosion from a vent within Halema`uma`u in March 2008 marked the onset of a new phase of summit activity and an end to the short-lived effusive/fissure eruptions of the previous century. The 2008 summit eruption is thought to have been initiated by withdrawal of magma from the summit reser-

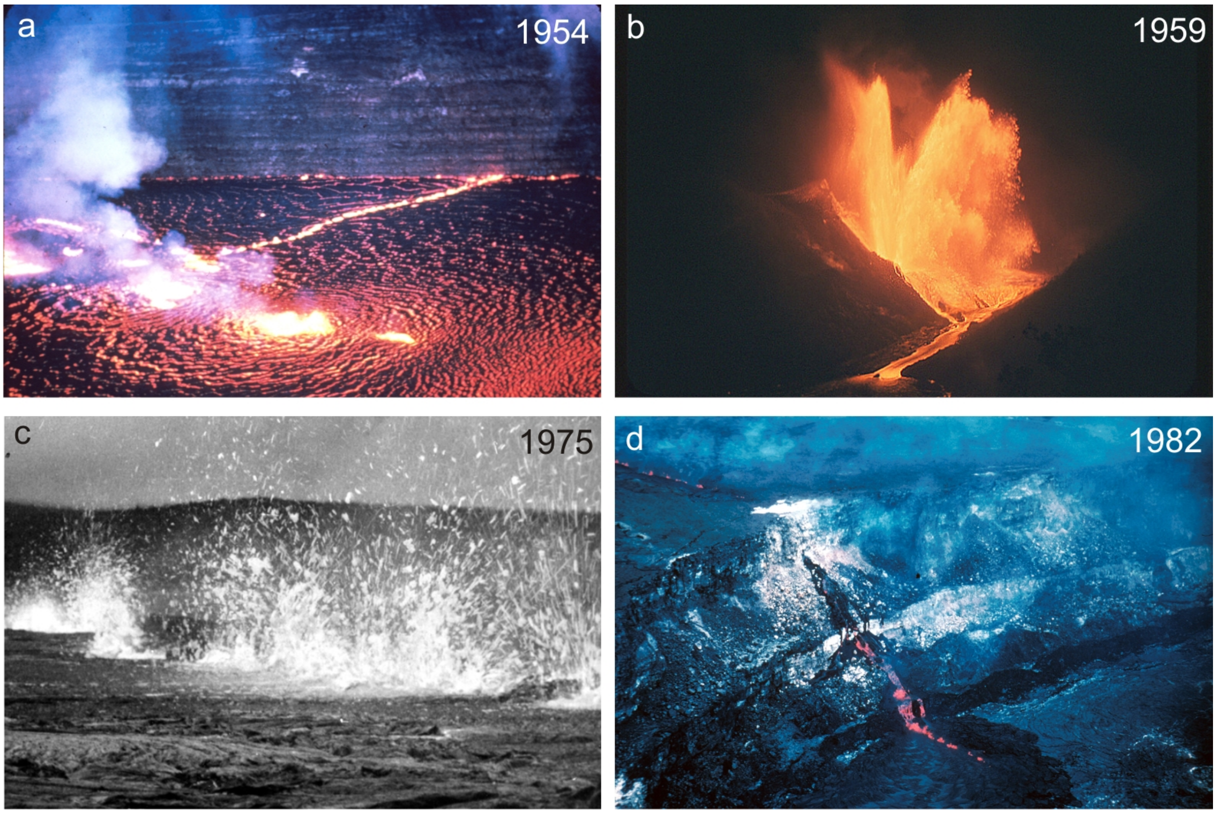

Figure 3.5: Photographs of Kīlauea's summit activity from 1924–1982. (a) May 1954 summit eruption of Kīlauea. A fissure extending from Halema`uma`u crater floor, up the northeast wall onto the caldera floor, fed a deepening lava lake within Halema`uma`u (photograph by J.P. Eaton, USGS); (b) November 1959 High-fountaining summit eruption within Kīlauea Iki crater (photograph by J.P. Eaton, USGS); (c) 1975 fissure eruption within Kīlauea caldera (photograph by R.I. Tilling); (d) 1982 fissure summit eruption within Kīlauea caldera. Lava from the fissure, on the caldera floor is ponding within Halema`uma`u crater. (Photograph by J.P. Lockwood, USGS).

voir causing static decompression and degassing of the magma column (*Poland et al.*, 2009). The comparatively minor explosion cleared a vent within Halema`uma`u which has been gradually increasing in diameter (to >160 m in September 2012), at the base of which is a convecting column of magma (Figure 3.6a and b). Unlike many previous summit eruptions, the current vent is not a standard lava lake but rather, the convecting upper surface of the magma column (pers. comm. Swanson, 2009). The eruption has been characterised by transient explosions which are believed to be the result of disturbance of subsurface gas accumulation by external triggers, usually collapse of vent wall rocks into the conduit (*Houghton et al.*, 2011). The short-lived nature of these events and the production of convecting ash-rich eruption columns has lead to them being termed 'transient subplinian' explosions in this study (pers. comm. Houghton, 2011). They have recently been acknowledged as a previously under-recognized class of eruption, a variant of decoupled flow of magmatic volatiles through a basaltic shallow conduit, and it seems likely that a significant number of earlier explosive eruptions from Kīlauea occurred under similar conditions (*Houghton et al.*, 2011). Between the explosive events of the current summit eruption, activity is restricted to quiescent degassing from the convecting lava surface, the level of which typically varies between 60 m and 150 m depth below the rim of the vent. These fluctuations in height of the column correlate with cycles of deflation and inflation recorded at the summit of the volcano (pers. comm. Poland, 2010).

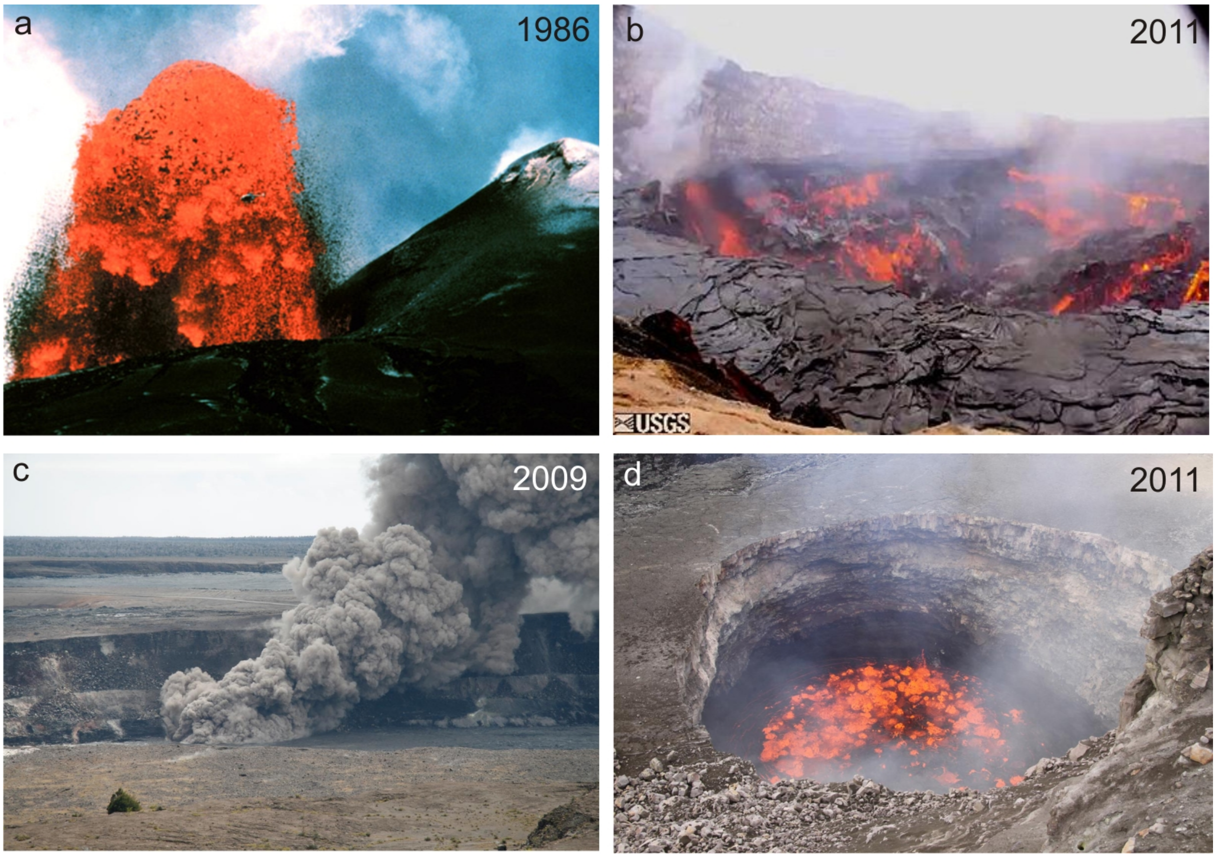

Figure 3.6: Photographs of the current summit and ERZ eruptions at Kīlauea. (a) A lava fountain produced during the early stages (1986) of the ongoing Pu`u `Ō`ō eruption in the ERZ; (b) A collapse within Pu`u `Ō`ō vent in March 2011. The vent at Pu`u `Ō`ō has undergone many repeat cycles of lava lake development, drainage and collapse in recent years, similar to the eruption behaviour at the summit during the nineteenth century. Withdrawal of shallow magma beneath the vent in 2011 resulted in rapid susidence and collapse within minutes. The image is captured from a webcam video of the event which can be seen at http://hvo.wr.usgs.gov/multimedia; (c) A transient explosive event (January 2009) from the current eruption vent within Halema`uma`u crater; (d) View of the same vent as shown in (c) during quiescent degassing of the magma column. The image shows the magma column during a high-stand event. Photographs from the USGS Hawaiian Volcano Observatory.

While the above description of eruptive activity has focussed predominantly on summit eruptions it is worth noting that major eruptions have also occurred along the subaerial portions of both rift zones in prehistoric and historic times. The ERZ had major fissure eruptions in 1790, 1840, 1955, 1960 and 1969-74 (*MacDonald et al.*, 1983; *Holcomb*, 1987). The 1969–74 ERZ eruption produced the Mauna Ulu shield and similarly to the 1959 eruption at Kīlauea Iki, the magmas were MgO-rich and produced very high fountains, up to 540 m high (*Swanson et al.*, 1979). Since 1955, the ERZ has become a more frequent site of eruptions and intrusions, including the ongoing Pu`u `Ō`ō eruption (Figure 3.6c and d) which is in its 29th year at the time of writing (e.g. *Heliker and Mattox*, 2003; *Garcia et al.*, 1996). The eruption which began in 1983 has produced an array of eruption styles, but initiated with a phase of high Hawaiian fountaining which dominated the early years of activity. The sustained and continuous eruption has become more effusive in character, having developed the Pu`u `Ō`ō cone in the middle ERZ and inundated large coastal sections with tube-fed pahoehoe flows. Eruptions in the SWRZ have been far less frequent in historical times, with only two major (1823 and 1919-20) and three minor eruptions in 1868, 1971, and 1974 (*MacDonald et al.*, 1983). It is worth noting that the current eruptive conditions at Kīlauea with a sustained summit eruption occurring simultaneously with a very long-lived rift zone eruption (Pu`u `Ō`ō) are unprecedented in historical times.

3.1.2 Previous Work

There are few comprehensive studies of eruptive behaviour at Kīlauea but perhaps the most extensive review is that of *Holcomb* (1987), which assessed the long term variations in Kīlauea's eruptive activity through detailed mapping, palaeomagnetic dating and morphological analysis of surficial lava flows. *Holcomb* (1987) recognised that different intervals of Kīlauea's history had been dominated by different eruptive behaviours and that changes included variations in both frequency and type of eruption. Indeed the patterns can be recognised from the above review of activity in which caldera-forming events are followed first by production of high lava fountains and subsequently by violently explosive (largely phreatomagmatic) eruptions. Once the explosive episodes have passed, prolonged periods of large-volume, effusive lava flow production and fissure eruptions occur, followed once again by summit caldera collapse. *Holcomb* (1987) also noted that different parts of Kīlauea have differed in eruptive behaviour, with most sustained eruptions having occurred at summit vents, while unstable and pyroclastic events have been more numerous along the rift zones. The author acknowledged that the major controls on eruptive behaviour remained undetermined by the study but proposed a number of possible evolutionary, cyclic and stochastic behavioural models (Figure 3.7), all of which involved shifts in the sites of principal magma storage as a likely cause of the variations.

Studies of short-term changes in eruptive activity at Kīlauea have concentrated largely on individual eruptions or eruption styles, such as the onset of Hawaiian fountain production or the structural causes of phreatomagmatic events (*McPhie et al.*, 1990; *Mastin*, 1997). The mechanics of Hawaiian fountains in particular, have been investigated in detail through analogue and numerical models of bubble-melt fluid flow through shallow conduits (e.g. *Wilson and Head*, 1981; *Head and Wilson*, 1987; *Parfitt and Wilson*, 1995; *Parfitt*, 2004; *Slezin*, 2003; *Vergniolle and Jaupart*, 1986, 1990; *Jaupart and Vergniolle*, 1988, 1989; *Vergniolle and Mangan*, 2000; *Namiki and Manga*, 2008) (see Chapter 5 for a review of these models). However, these focussed investigations provide no comparison between eruption styles and make no reference to magma compositions or their control on the eruption dynamics.

Geochemical analyses of whole rock samples from Kīlauea have been extensively studied over the past sixty years for their major, trace and isotope compositions (e.g. *Powers*, 1948; *MacDonald and Katsura*, 1961; *Murata and Richter*, 1966a; *Wright*, 1971; *Wright and Fiske*, 1971; *Wright*, 1973; *Wright et al.*, 1975; *Tilling et al.*, 1987; *Garcia et al.*, 1998; *Pietruszka and Garcia*, 1999b,a; *Garcia et al.*, 2000; *Pietruszka et al.*, 2001; *Garcia et al.*, 2000, 2003; *Marske et al.*, 2007, 2008). The fundamental processes operating within the plumbing system of the volcano have been delineated in detail, including crystal fractionation (dominantly olivine-controlled) and mixing of summit magmas between eruptions and between melts stored within the rift zones (e.g. *Murata and Richter*, 1966a; *Wright*, 1971). With the development of new analytical tools over the past twenty years, more recent studies have illustrated that the effects of fractionation and mixing are superimposed upon the changes in the composition of parental magmas supplied to the volcano from mantle depths (e.g. *Tilling et al.*, 1987; *Garcia et al.*, 1998; *Pietruszka and Garcia*, 1999b,a; *Garcia et al.*, 2000; *Pietruszka et al.*, 2001; *Garcia et al.*, 2000, 2003; *Marske et al.*, 2007, 2008), although it

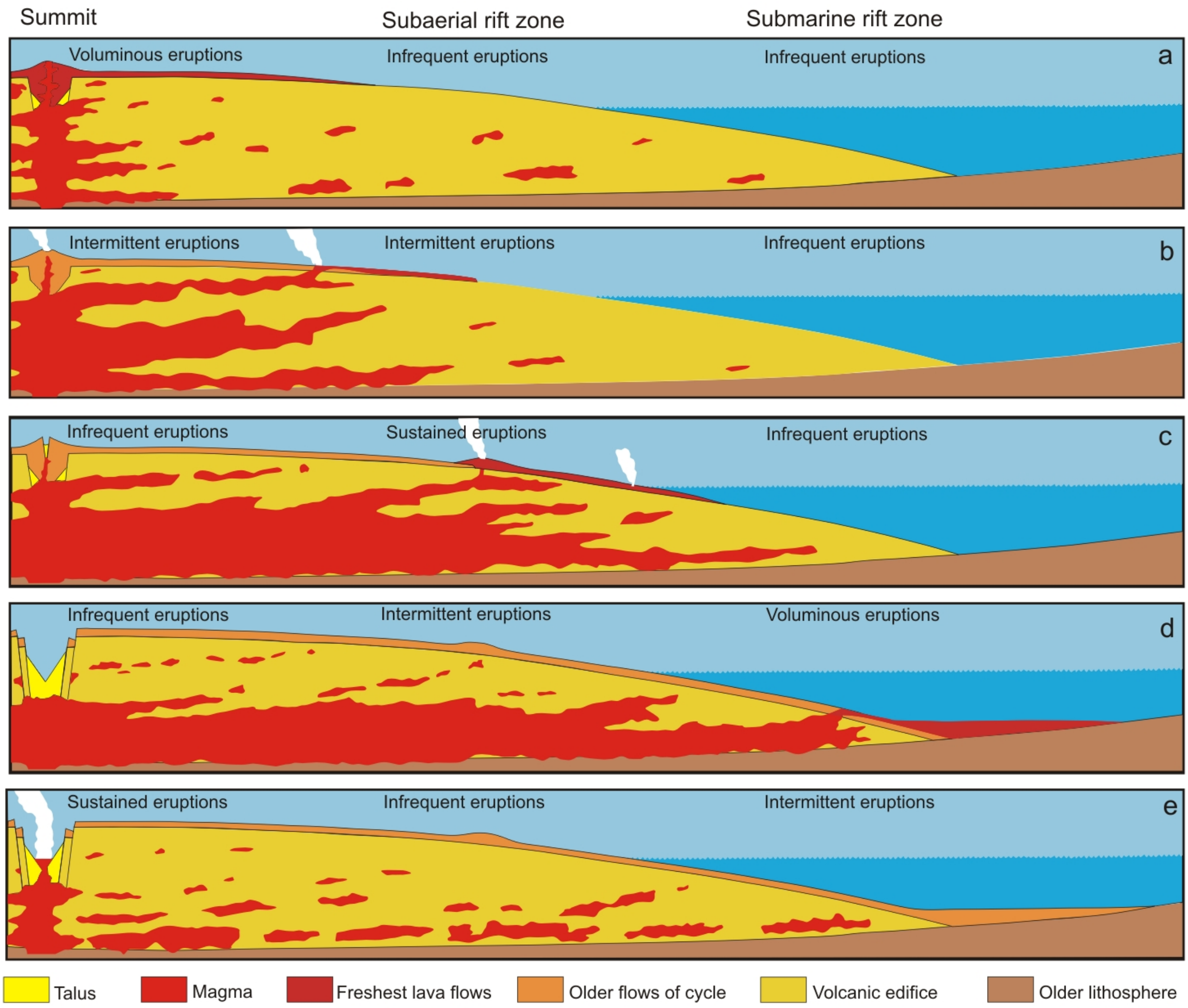

Figure 3.7: Cyclical model of *Holcomb* (1987) for long-term behaviour at Kīlauea, based on repeated episodes of caldera collapse and filling. Schematic profiles of the east rift zone show five stages of the cycle representing dynamic equilibrium between hydrostatic, thermal and frictional factors. (a) Eruptions are long-sustained and restricted to caldera, filling it so that most magma is stored beneath the summit. As magma column rises, dikes are injected laterally under increasing pressure and magma begins to migrate into the rift zones. (b) Summit eruptions are less sustained and rift zones more frequent as more magma is diverted into the rift zones. (c) As continuity is developed in the rift zone plumbing, longer eruptions occur further from the summit. As lava is erupted at lower elevations, the magma column subsides beneath the summit and caldera-filling lava slowly cools. (d) Voluminous eruptions from the rift zones drain magma from the upper parts of the edifice, and collapse ensues. Collapse at the summit rejuvenates the caldera, and collapse along the rift zones reduces continuity of their plumbing systems. (e) Magma rising from deep beneath the summit now finds its easiest escape into the newly deepened caldera; activity is once again sustained and voluminous within the caldera and continuity is further reduced in the rift plumbing system as dikes solidify. Figure reproduced and modified from *Holcomb* (1987).

is worth noting that the concept of compositionally different magma batches had been recognised as early as 1948 by *Powers* (1948). Further investigation of the 'magma batch' concept by *Pietruszka and Garcia* (1999a) and *Garcia et al.* (2003) using isotopic and trace element analyses of summit lavas erupted between 1790–1982 AD has revealed that lava compositions vary systematically over time (Figure 3.8). Prior to the 1924 phreatic explosions and summit collapse, a trend of increasing incompatible elements and CaO concentrations, and decreasing SiO_2 abundance prevailed in MgO-normalised lava compositions (*Garcia et al.*, 2003). Thereafter, the trend reversed and persisted for the remainder of the 20th century eruptions. The distinct temporal changes in the parental magma compositions delivered to the summit in historical times have been interpreted as indicating a source region that is chemically and isotopically heterogeneous. The authors propose that the degree of partial melting (dictated by differing fusibilities of the small-scale heterogeneities within the mantle plume) decreased from the early 19th century until the mid-20th century correlating with a lower eruption rate between 1840 to 1959. Temporal changes in lava chemistry have also been identified on individual eruption timescales. Analysis of lavas from the 1983–present Pu`u `Ō`ō eruptions in the ERZ were used to suggest that at least three distinct mantle source components were required to explain the overall isotopic and chemical variability of the eruption lavas over a 25 year period (*Marske et al.*, 2008).

Unfortunately whole rock geochemical studies do not reveal anything about composition of volatiles dissolved in the melts which, owing to their low solubility at shallow crustal depths extensively degas from the lavas on eruption. However, the degassing budget of Kīlauea is broadly well understood from numerous studies of surface gas measurements (e.g. *Gerlach and Graeber*, 1985; *Gerlach*, 1986; *Dixon et al.*, 1991; *Clague et al.*, 1995; *Wallace*, 1998; *Elias et al.*, 1998; *Sutton et al.*, 2001; *Gerlach et al.*, 2002; *Sutton and Kauahikaua*, 2003; *Edmonds and Gerlach*, 2006; *Elias and Sutton*, 2007; *Edmonds et al.*, 2009; *Hager et al.*, 2008; *Poland et al.*, 2009). Owing to the low solubility of CO_2, magmas become saturated at high pressures (up to 1 GPa or $\sim$40 km depth; *Gerlach and Graeber*, 1985), such that CO_2 exists as a separate fluid phase throughout the magmas' ascent through the crust, with only a small fraction remaining in the melt at 3-5 km depth (*Gerlach et al.*, 2002). Numerous authors have proposed that CO_2-rich vapour segregates from magma at summit reservoir depths (7–1 km) and escapes through fractures from a $\sim 1\,\text{km}^2$ area on the caldera

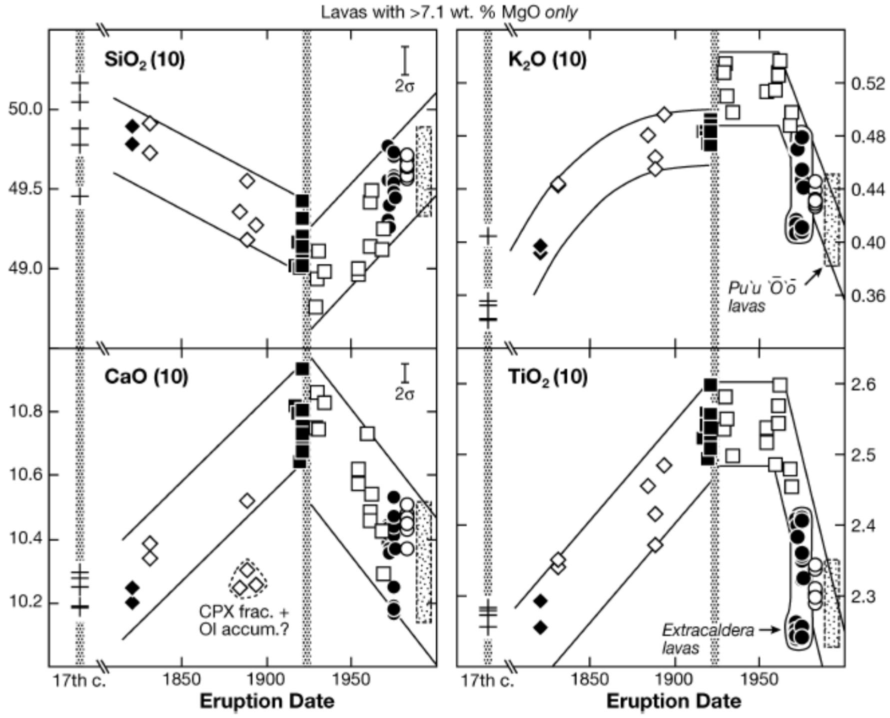

Figure 3.8: Temporal major element variation for whole-rock samples of Kīlauea historical summit eruptions and Pu`u `Ō`ō (stippled block), presented in a study by *Garcia et al.* (2003). Only samples with MgO contents > 7.1 wt% were used to minimize the effects of fractionation beyond olivine-control. Compositions were normalised to 10 wt% MgO by addition or subtraction of olivine. The stippled bars are periods of explosive eruptions during the 17th century and in 1924. *Garcia et al.* (2003) interpreted these temporal variations as indicative of changes in the degree of melting of a heterogeneous mantle source region. Figure reproduced from *Garcia et al.* (2003).

floor immediately east of Halema`uma`u crater (*Gerlach and Graeber*, 1985; *Gerlach*, 1986; *Gerlach et al.*, 2002; *Hager et al.*, 2008), via a process of bubble rise and foam formation (*Vergniolle and Jaupart*, 1990). While CO_2 degassing is occurring continuously from the magma reservoir, only small fluxes of H_2O and SO_2 are degassed from the summit during periods of no summit eruption (*Gerlach and Graeber*, 1985). A second stage of degassing occurs during rift zone eruptions when magmas equilibrated at reservoir depths migrate down-rift to the eruption site, where they degas SO_2 and H_2O at low pressures (< 5 MPa).

Petrological constraints on pre-eruptive volatile concentrations in Kīlauea melts are limited: few measurements of volatiles in melt or fluid inclusions from Kīlauea exist (*Harris and Anderson*, 1983; *Anderson and Brown*, 1993; *Wallace*, 1998; *Hauri*, 2002) and those analysed have invariably lost a significant proportion of their CO_2 by degassing prior to melt entrapment. Melt inclusion studies have typically focussed on specific eruptions such as the high fountain-producing 1959 Kīlauea Iki eruption (*Anderson and Brown*, 1993; *Wallace*, 1998; *Loewen*, 2011), while other workers have concentrated on variably degassed submarine glasses erupted along the east rift zone (e.g. *Dixon et al.* 1991). These geochemical studies have provided insight into the degassing processes at Kīlauea and have constrained estimates of primary melt volatile concentrations, suggesting that typical melts contain 0.4–0.8 wt% H_2O (*Dixon et al.*, 1991; *Wallace*, 1998; *Dixon et al.*, 2002) and 1500–2000 ppm of S (*Wallace and Carmichael*, 1992). Parental melt CO_2 contents have been estimated at ~ 0.7 wt% based on surface gas flux measurements and magma supply rates (*Gerlach et al.*, 2002), rather than petrological estimates. Recent statistical analysis of CO_2–H_2O distributions in existing melt inclusion datasets from Kīlauea indicate that parental melt CO_2 concentrations may in fact be significantly higher and more variable than the gas estimates, with CO_2 contents of between 2–6 wt% (*Barsanti et al.*, 2009).

Very few volatile studies have attempted to link melt CO_2 and H_2O concentrations to eruption behaviour at Kīlauea and no comprehensive volatile datasets exist for temporal eruption series. The most detailed investigation was that of *Anderson and Brown* (1993) for the high-fountaining 1959 eruption in which the authors suggest that pre-eruptive concentrations of CO_2 in the melt may play a crucial role in achieving surface eruption of lavas from the summit. They argue that exsolution of CO_2 at great depths leads to increased buoyancy of primitive melts which would otherwise pond beneath the compositionally more evolved summit reservoir magmas owing to the higher density of the new melt input. This would indicate that enrichment or depletion of volatiles (particularly CO_2) inherited from the mantle source may determine whether an eruption occurs at all.

Kīlauea has been described as the ‘best understood basaltic volcano in the world’ (*Tilling and Dvorak*, 1993), and while there is an extremely extensive and comprehensive volume of literature (far more than can be effectively summarised above) to attest to this statement, a number of questions still remain, including the following:

1) Are parental melts supplied to Kīlauea inherently heterogeneous?

2) Is there a relationship between pre-eruptive melt composition and eruptive style at Kīlauea?

3) What role do the processes of degassing, magma mixing and fractionation play in

influencing eruption style?

This following Chapter attempts to answer these questions through the analysis of the major, trace and volatile compositions of olivine-hosted melt inclusions and matrix glasses from tephras and lavas produced from a broad variety of eruptive activity which occurred between ∼1400 AD to 2010. This is the most comprehensive dataset ever amassed for Kīlauean melt inclusions and, in combination with existing observational, geochemical and geophysical datsets, is used here to explore the relationships between source compositions, magma storage, transport and eruption processes.

Chapter 4

Magmatic controls on eruption behaviour at Kīlauea volcano: Part II

4.1 Methods

4.1.1 Sampling

Samples for this study were collected during two field seasons at Kīlauea in May 2009 and June–July 2010. The main objective of the fieldwork was to sample rapidly-quenched, glassy eruption products from a broad range of prehistoric and historic eruptions in order to cover the greatest variation in eruption styles and temporal range. Fieldwork was largely concentrated at the summit of Kīlauea, within and around the caldera, but a number of sampling sites in both rift zones were also included owing to their particular eruption features. Sampling was carried out with the assistance of D. Swanson, and reference to the geologic map of *Neal and Lockwood* (2003), with additional assistance from B. Houghton and M. Edmonds.

Over the two field seasons 79 samples were collected but only 43 were selected for analysis. These 43 samples included material from 25 eruptions over a 500 year period, with representatives of four of the five classes of eruption style. All samples analysed are listed in Table 4.1, with sample localities shown in Figure 4.1.

The majority of tephra and lava samples were collected by hand from surface exposures although collection methods varied depending on the age and type of material, as some older

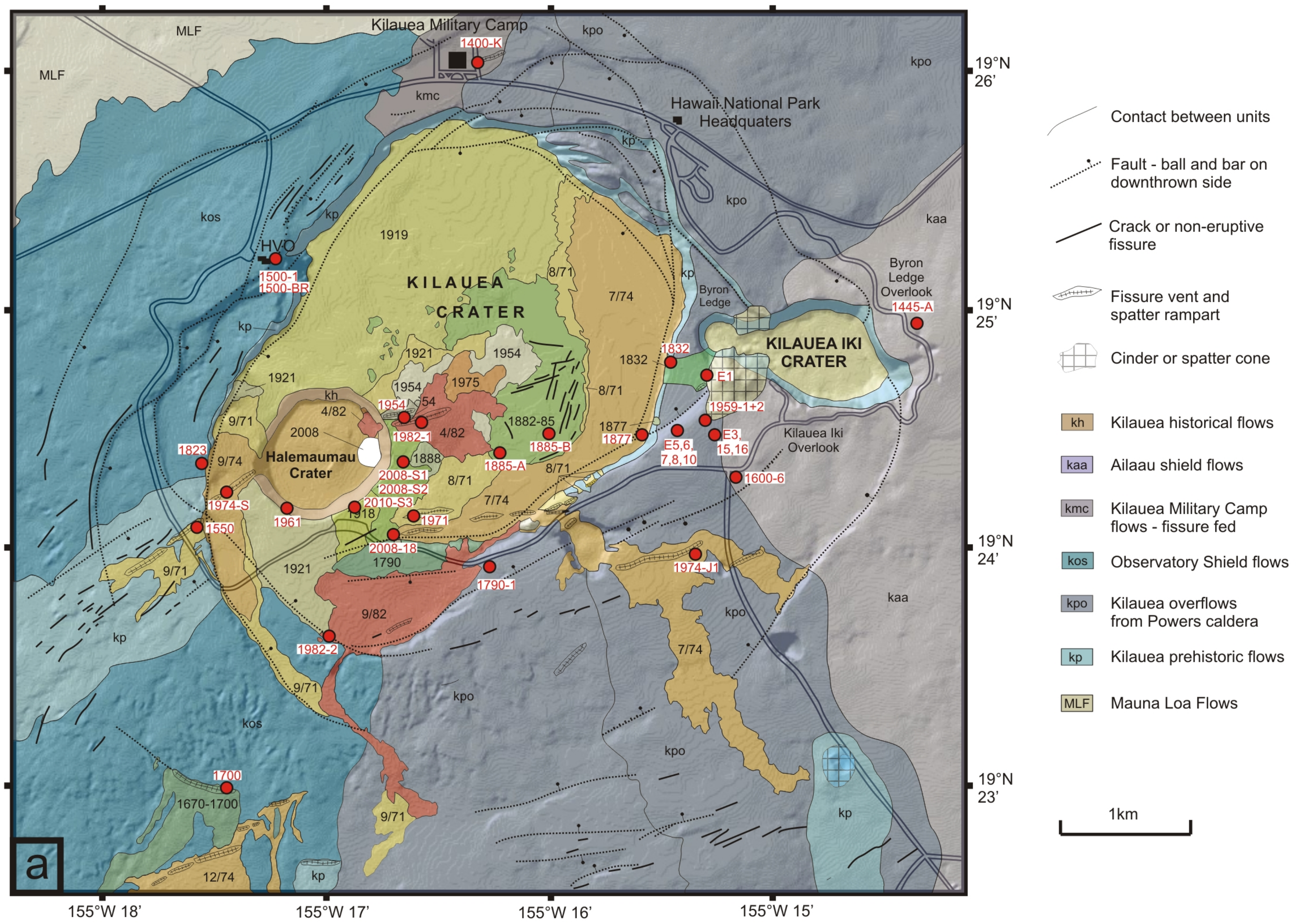

Figure 4.1: (a) Summary geological map of the prehistoric and historical eruption deposits within the summit area of Kīlauea volcano (after *Neal and Lockwood* 2003). The colours indicate the relative ages of the flows (blue and purple for older flows, green, yellow and red for progressively younger eruptions). Locations of samples studied are shown by black and red circles. HVO marks the location of the Hawaiian Volcano Observatory.

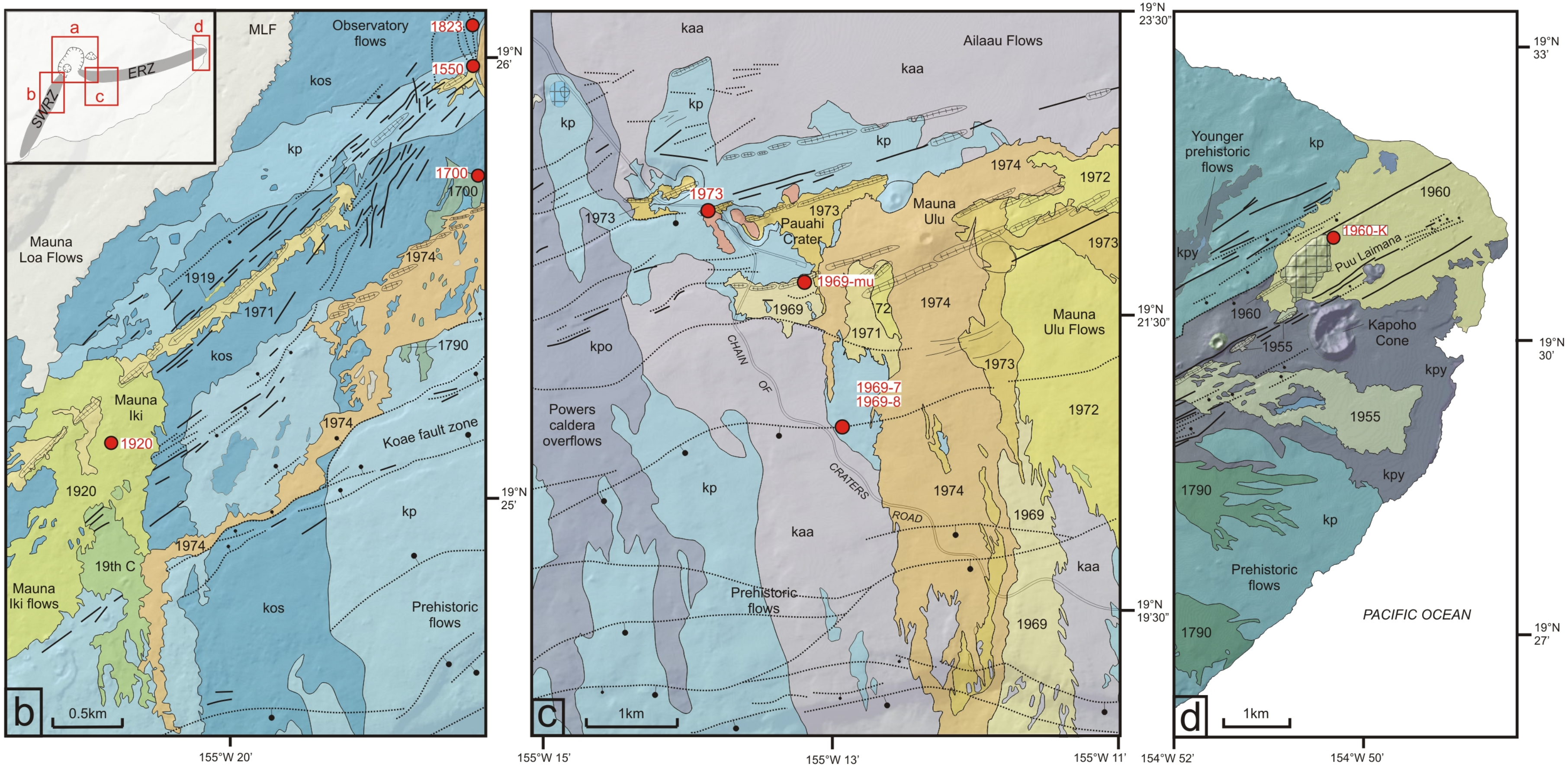

Figure 4.1: Summary geological maps of the prehistoric and historical eruption deposits within (b) the upper southwest rift zone (SWRZ), (c) the upper east rift zone (ERZ) and (d) the lowermost ERZ). Schematic map inset in (b) shows the relative locations of maps (a)–(d) on Kīlauea Volcano. Symbols and stratigraphies as shown in the key to (a) on the previous page. Maps are adapted from *Holcomb* (1987) and *Neal and Lockwood* (2003).

Table 4.1: Summary of the tephra and lava samples collected and analysed in this study.

Eruption Date	Sample	Eruption style	Locality	Deposit Type	Map^{*1} & Lit. Reference^{*1}
~ 1400	1400-K	Fissure	Summit	Pumiceous spatter	A; *Neal and Lockwood* (2003)
~ 1445	1445-A	Effusive	Summit	Pahoehoe flow top	A; *Clague et al.* (1999)
~ 1500	1500-1	Hawaiian fountain	Summit	Pure reticulite	A; *Swanson et al.* (2012a)
~ 1500	1500-BR	Hawaiian fountain	Summit	Pure reticulite	A; *Swanson et al.* (2012a)
~ 1550	1550	Phreatomagmatic	Summit	Scoria, lithics, ash & accretionary lapilli	A; *Swanson et al.* (2012a)
~ 1600	1600-6	Transient explosive	Summit	Scoria lapilli	A; *McPhie et al.* (1990)
~ 1700	1700	Fissure	SWRZ	Dense spatter	A/B; *Swanson et al.* (2012a)
~ 1790	1790-1	Transient explosive	Summit	Dense, bomb-crust	A; *Swanson et al.* (2012b)
~ 1790	1790-w	Transient explosive	Summit	Dense, rounded juvenile bombs	A; *Weaver et al.* (2010)
1820-1823	1823	Hawaiian fountain	Summit	Golden pumice	A; *Sharp et al.* (1987)
Jan. 1832	1832	Fissure	Summit	Vesicular spatter	A; *Brigham* (1909)
May 05, 1877	1877	Fissure	Summit	Vesicular spatter	A; *Brigham* (1909)
1882-1885	1885-A	Effusive	Summit	Tumulus flow top	A; *Brigham* (1909)
1882-1885	1885-B	Effusive	Summit	Pahoehoe flow top	A; *Brigham* (1909)
1919-1920	1920	Effusive	SWRZ	Pahoehoe flow top	A; *Holcomb* (1987)
May 31, 1954	1954	Fissure	Summit	Vesicular spatter	A; *MacDonald and Eaton* (1954)
Nov.14, 1959	(1959)-E1	Hawaiian fountain	Summit	Pumice lapilli, achneliths & Pele's hair	A; *Richter* (1970)
Nov.26, 1959	(1959)-E2	Hawaiian fountain	Summit	Pumice & Pele's hair	A; *Richter* (1970)
Nov.28, 1959	(1959)-E3	Hawaiian fountain	Summit	Pumice	A; *Richter* (1970)
Dec.06, 1959	(1959)-E5	Hawaiian fountain	Summit	Fluidal pumice lapilli	A; *Richter* (1970)
Dec.07, 1959	(1959)-E6	Hawaiian fountain	Summit	Fluidal pumice lapilli	A; *Richter* (1970)
Dec.08, 1959	(1959)-E7	Hawaiian fountain	Summit	Fluidal pumice lapilli	A; *Richter* (1970)
Dec.10, 1959	(1959)-E8	Hawaiian fountain	Summit	Fluidal pumice lapilli	A; *Richter* (1970)
Dec.14, 1959	(1959)-E10	Hawaiian fountain	Summit	Pumice lapilli & achneliths	A; *Richter* (1970)

Table 4.1: Summary of the tephra and lava samples collected and analysed in this study (cont'd)

Eruption Date	Sample	Eruption style	Locality	Deposit Type	Map^{*1} & Lit. Reference^{*2}
Dec.17, 1959	(1959)-E15	Hawaiian fountain	Summit	Golden pumice	A; *Richter* (1970)
Dec.19, 1959	(1959)-E16	Hawaiian fountain	Summit	Golden pumice	A; *Richter* (1970)
Jan.17, 1960	1960-KO	Hawaiian fountain	ERZ	Golden pumice	D; *Richter* (1970)
Feb. 1961	1961	Hawaiian fountain	Summit	Pumice lapilli	A; *Richter et al.* (1964)
May 24, 1969	1969-mu	Fissure	ERZ	Vesicular spatter	C; *Swanson et al.* (1979)
Sep.06, 1969	1969-7	Hawaiian fountain	ERZ	Golden pumice/reticulite	C; *Swanson et al.* (1979)
Dec.30, 1969	1969-8	Hawaiian fountain	ERZ	Pumice lapilli & achneliths	C *Swanson et al.* (1979)
Aug.14, 1971	1971	Fissure	Summit	Vesicular spatter	A; *Duffield et al.* (1982)
Nov.10, 1973	1973	Fissure	ERZ	Pumiceous spatter	C; *Holcomb* (1987)
Jul.19, 1974	1974-J1	Fissure	ERZ	Vesicular spatter	A; *Lockwood et al.* (1999)
Jul.19, 1974	1974-J2	Fissure	Summit	Vesicular spatter	A; *Lockwood et al.* (1999)
Sep.19, 1974	1974-S	Fissure	Summit	Vesicular spatter	A; *Lockwood et al.* (1999)
Apr.30, 1982	1982-1	Fissure	Summit	Vesicular spatter	A; *Neal and Lockwood* (2003)
Sep. 1982	1982-2	Fissure	Summit	Vesicular spatter	A; *Neal and Lockwood* (2003)
Apr.09, 2008	2008-S1	Transient explosive	Summit	Pumiceous bombs/lapilli & lithics	A; *Houghton et al.* (2011)
Aug.27, 2008	2008-S2	Transient explosive	Summit	Pumiceous bombs/lapilli & lithics	A; *Houghton et al.* (2011)
Sep.2, 2008	2008-18	Transient explosive	Summit	Pumiceous bombs/lapilli & lithics	A; *Houghton et al.* (2011)
Apr.26, 2010	2010-S3	Transient explosive	Summit	Pumiceous bombs/lapilli & lithics	A; *Houghton et al.* (2011)

---

*

(1) Reference to Map a, b, c or d in Figure 4.1
(2) Example literature reference for eruption

deposits were buried beneath vegetation or had to be sampled from sections within man-made and natural collapse pits. The nature of the deposits varied greatly depending on the eruptive behaviour which produced them, and ranged from ash and lapilli beds to scoria/pumice pyroclasts and lava flow surfaces. Despite the variation, the common feature of all samples collected was the presence of a significant juvenile magmatic component which was glass-rich. Olivine hosted melt inclusions are highly susceptible to diffusive re-equilibration between the inclusion and carrier melts via exchange of ions with, and through, the host olivine crystal (e.g. *Danyushevsky et al.*, 2000; *Gaetani and Watson*, 2000; *Hauri*, 2002; *Gaetani et al.*, 2012; *Lloyd et al.*, 2012). The diffusion is rapid at high temperatures and both major elements (Fe and Mg) and H_2O concentrations within the melt inclusions may be strongly affected if the samples undergo slow cooling. To minimise diffusive re-equilibration and preserve the pre-eruptive concentrations, care was taken to ensure that all samples had undergone rapid cooling on eruption. However this limited the number of eruptions which could be sampled as many products were crystalline and had not cooled sufficiently quickly to form even glassy selvages.

4.1.1.1 General description and classification of the Kīlauea sample suite

The deposit types collected for this study can be broadly divided into groups according to the eruption styles which produced them.

The effusive eruption endmember was sampled from summit overflows of pahoehoe lavas (Figure 4.2), where the upper 1–1.5 cm of the glass-rich rope-texture on small sections of the flow surfaces were removed. While glass could be obtained from these effusive products, it is recognised that they may not be immune to the effects of diffusive re-equilibration if flows were fed with lavas which had remained at high temperatures for long periods within a convecting lava lake. However, samples were pristine and the upper selvages were typically vesicular suggesting that the melts had not been stagnant at atmospheric pressures for long periods prior to eruption.

Fissure or weak fountain deposits were a spectrum of highly vesicular to dense scoria clasts picked by hand from spatter ramparts that developed along the lengths of the eruption fissure. The scoria or 'cinder' clasts were typically fragments 2–3 cm in diameter with either

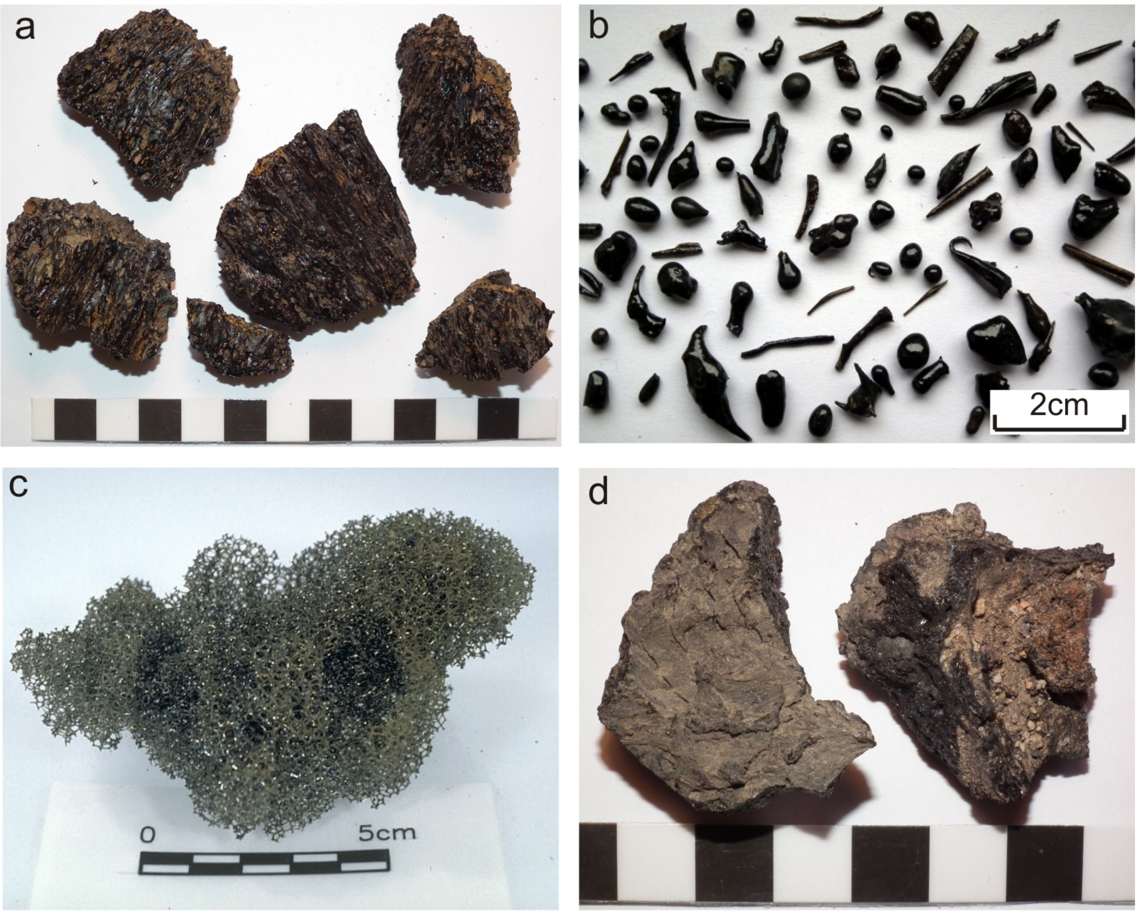

Figure 4.2: Examples of the Kīlauea sample suite: (a) Effusive eruption samples collected from the upper glass-rich surfaces of the `Ailā`au flow (sample 1445-A); (b) achnelith lapilli, glass spheres, shards and droplets or 'Pele's Tears' produced during the high-Hawaiian eruptions (sample 1959-E1); (c) reticulite clast with >98 vol% vesicles, produced in Hawaiian fountains >300 m high; (d) clasts of angular scoria produced during a discrete subplinian explosions in 2008 (sample 2008-S2). The clast interiors are vesicular with relatively thick bubble-walls, the exteriors are 'skinned' with a breadcrusted texture and appear dusty due to the lithic ash-cloud produced during the event. The right-hand clast shows small fragments of conduit wall-rock and ash stuck to the exterior surface.

a fluidal, smooth exterior of dense glass or irregular broken faces revealing an inner vesicular core of $\sim$70–85% vesicularity. Scoria vesicles were generally spherical and up to 0.5 cm diameter, with relatively thick bubble walls. Vesiculation is not restricted to the conduit and occurs post-fragmentation within all types of fountains (*Stovall et al.*, 2011). As a result, pyroclasts from low fissure fountains undergo less vesiculation and are more dense than the pumice clasts produced in high fountains where post-fragmentation vesiculation and clast expansion can continue for longer in the thermally insulated fountain core.

The high Hawaiian fountain products were variable in character. Some were dominated by black, glassy achnelith-rich (*Walker*, 1973) lapilli including Pele's tears, glass spheres and pumice clasts with fluidal surfaces and highly vesicular interiors (Figure 4.2b), while other units contained ragged, highly vesicular golden to light brown pumice and reticulite with up to 98–99% vesicularity, produced in fountains > 300 m (*Mangan and Cashman*, 1996) (Figure 4.2c). The higher fountains also produced units with large (up to 25 cm diameter) spatter bombs. High fountain deposits were usually sampled at localities downwind of the eruption vent, in beds up to several metres thick. Clasts were collected from sections exposed in existing collapse pit structures and from 1–2 m deep pits dug by hand.

The involvement of significant quantities of external water during phreatomagmatic eruptions results in deposits which are much finer grained than the pyroclasts produced from fissures and high fountains. These 'wet' pyroclastic deposits were characteristically well-bedded as a result of their deposition by fall, or displayed low-angle cross stratification as a result of base surge formation. The deposits were often a mixture of juvenile and lithic components with grain sizes ranging from well-sorted fine ash, loose crystals and lapilli to scattered large blocks which measured up to 1 m and produced clear impact structures or 'bomb-sags' in the underlying stratigraphy. Unlike fissure and high fountain products, fluidal clasts were absent from the phreatomagmatic ashes and most lapilli-sized particles were microcrystalline and bounded by fractured surfaces; consequently locating pristine glasses within the deposits could be challenging.

Phreatic eruptions, which constitute another endmember of activity at Kīlauea, are purely steam explosions and involve direct interaction of juvenile magmas with external water. As such, the resulting deposits consist of large lithic block falls of conduit wall rock with no juvenile component, and therefore phreatic samples are not represented in this study.

Eruptions classified as transient subplinian explosions produce a broad range of products. Similarly to phreatomagmatic explosions, the deposits contained a mixture of lithic and juvenile material including lithic blocks, lapilli and ash from the conduit walls. However, they also include Pele's hair and tears, and juvenile bombs up to 20 cm diameter. The bombs may be discrete globules of vesicle-rich spatter and pumice, angular chunks of fresh and oxidised scoria (Figure 4.2d) and glass-coated bombs and lapilli. The material is scattered downwind of the vent as discrete clasts and despite the broad range of clast morphology, the volumes of ejecta are too small to form well-sorted beds. These gas-rich, melt-poor explosions have only recently been identified as an endmember of activity at Kīlauea (*Houghton* *et al.*, 2011) and the low volume output from such eruptions are likely to result in under representation in the stratigraphy of the volcano. However, a number of prehistoric and historic eruptions sampled in this study are now thought to have been produced during such events, and belong to this category of samples.

Classification of the samples by eruption style is problematic owing to the range of behaviour within individual eruptions. For example, the 1969-74 Mauna Ulu eruption began as a series of low fountaining fissures which evolved into a point source vent producing high fountains as the eruption proceded, and ended with large-volume effusive lava flows (e.g. *Swanson et al.* 1979). Many of the eruptions sampled were not witnessed in historic times, consequently it is not possible to know how each event began, evolved and ended. While there are undoubtedly uncertainities associated with ascribing the samples to specific categories, it has been done by careful study of the deposit characteristics and where observational accounts of the eruptions exist, by the character of the eruption which produced them, such that lava flows are classified as effusive regardless of whether the eruption began with weak spattering or low fountains, because at the point at which the sample was was produced, the eruptive conditions were effusive.

4.1.1.2 Summary of the stratigraphy sampled

The oldest samples analysed in this study were erupted prior to formation of the current caldera. These included a fissure eruption within what is now the Kīlauea Military Camp on the northern margin of caldera, which is thought to have erupted during the summit overflow period during growth of the Observatory shield, or possibly earlier (circa 1400 AD; D. Swanson, pers. comm; *Neal and Lockwood*, 2003). Another pre-caldera sample was the pristine glassy upper surfaces of the \`Ailā\`au effusive flow ∼ 1445 AD (*Clague et al.*, 1999), preserved beneath thick forest soils to the east of Kīlauea Iki crater (Figure 4.1).

Other prehistoric products collected were from units within the Keanakāko\`i Tephra Member, the deposit produced during the 300 year period following caldera collapse (*McPhie et al.*, 1990). These deposits were widespread around the caldera rim, with the thickest and best preserved sections exposed within 1–2 m wide rifted gullies within a 1 km distance of the southern caldera boundary fault (Figure 4.1). A summary of the Keanakāko\`i stratigraphy

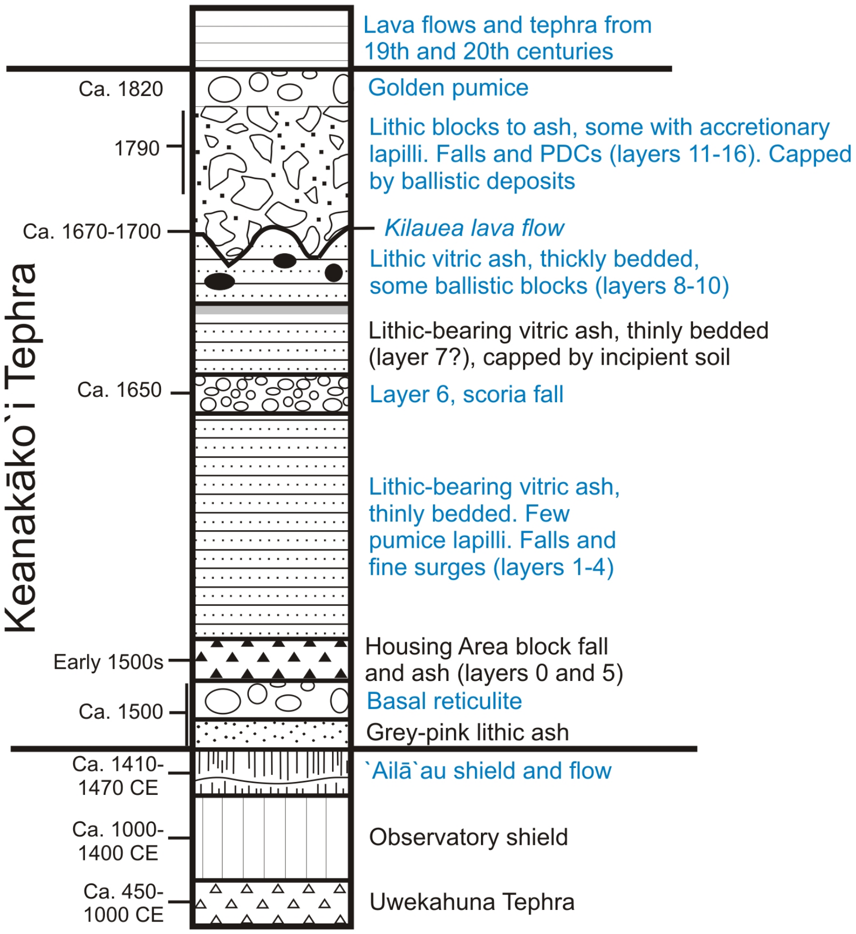

Figure 4.3: Generalised stratigraphy of the Keanakāko`i Tephra Member erupted during ~ 1500–1800 AD from vents within the summit caldera of Kīlauea. Units sampled in this study are highlighted in blue text. Stratigraphic section modified from *Swanson et al.* (2012a)).

and the beds sampled is shown in Figure 4.3. Seven samples were analysed from within the Keanakāko`i, including two from the basal reticulite produced during high Hawaiian fountains immediately after the summit collapse (Figure 4.4); lapilli and ash falls produced during the phreatomagmatic events (Figure 4.4c); dense scoria and ash from the 'Layer 6' unit of *McPhie et al.* (1990); spatter from circumferential fissures on the SW margin of the caldera and dense, non-vesicular juvenile lava blocks and lava-coated bombs from block falls attributed to transients subplinian explosions (Figure 4.4d and e). Also sampled was the 1–3 m thick golden pumice deposit of *Sharp et al.* (1987) which directly overlies the Keanakāko`i Tephra and was produced during vigorous high-fountaining within the caldera.

Historical eruptions between 1823 and 1924 were dominated by lava lake activity which

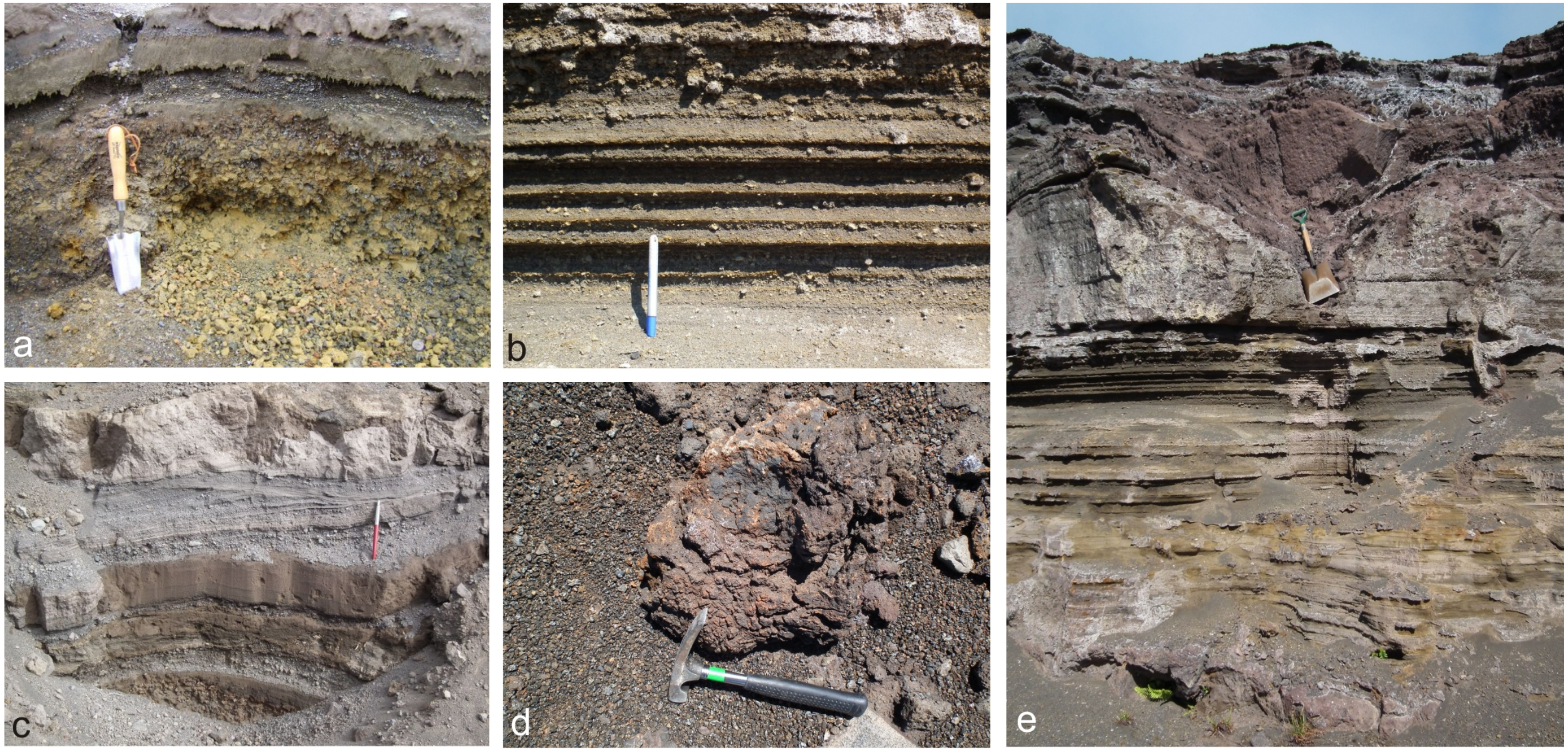

Figure 4.4: Photographs of units within the Keanakāko`i Tephra which were sampled for this study: (a) The basal unit of the Keanakāko`i, consisting of pristine golden reticulite produced during Hawaiian fountaining (1500-1 and 1500-BR); (b) Fine-bedded juvenile ash and lapilli fall deposits produced during phreatomagmatic explosions (1550); (c) cross-bedded lithic ash deposits produced by base surge events during phreatomagmatic explosions; (d) Ballistic blocks ejected during the later stages of the Keanakāko`i are scattered across much of the SW caldera floor. Many of these large bombs are 'cored', containing a lithic center with an outer coating of pasty, juvenile lava with rare glassy selvages (1790-1); (e) Photograph showing a condensed section of the upper Keanakāko`i Tephra stratigraphy, exposed within a non-eruptive fissure. The bulk of the exposed unit consists of the finely-bedded juvenile ash and lapilli shown in (b), which is overlain by poorly sorted lithic blocks and ash falls. The largest lithic block has created a 'bomb-sag' in the underlying ash deposits which were unconsolidated at the time of the violent phreatic explosions.

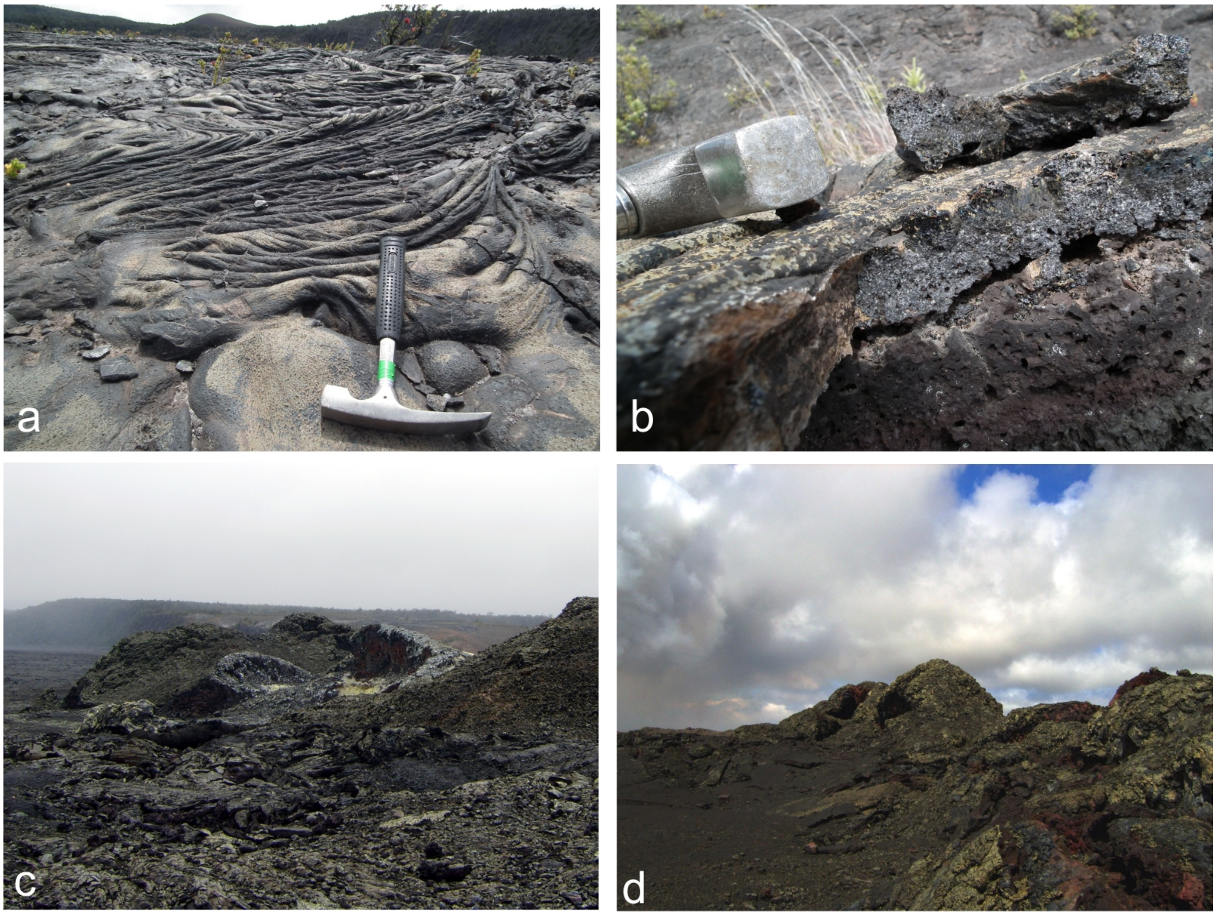

Figure 4.5: Photographs of the *in situ* lava and tephra samples collected in during fieldwork in 2009 and 2010: (a) One of the 1882–1885 pahoehoe lava flows exposed on the caldera floor (1885-B); (b) Photograph demonstrating sampling of glass from the same effusive flow; the outer ∼ 1–2 cm of the flow consisted of pristine glass; (c) and (d) are fissure ramparts within the caldera, produced during the August 14, 1971 and April 30, 1982 summit eruptions respectively (samples 1971 and 1982-1)

.

produced numerous pahoehoe flows across the caldera floor. Repeated eruptions of this nature however, resulted in the burial of many earlier flows and thus limited the sampling potential of this period. However, spatter from the 1832 fissure eruption on Byron Ledge and from a fissure on the east caldera wall in 1877 (*Brigham*, 1909) were examined. In addition to these, two samples from an overflow from the 1882–1885 Halema`uma`u lake were picked from the caldera floor (Figure 4.5a and b), along with a sample of effusive material from the 1919–20 Mauna Iki eruption in the SWRZ which was fed by summit lavas (Figures 4.1A and 4.1B).

No juvenile material was produced during the phreatic summit explosions in 1924 and

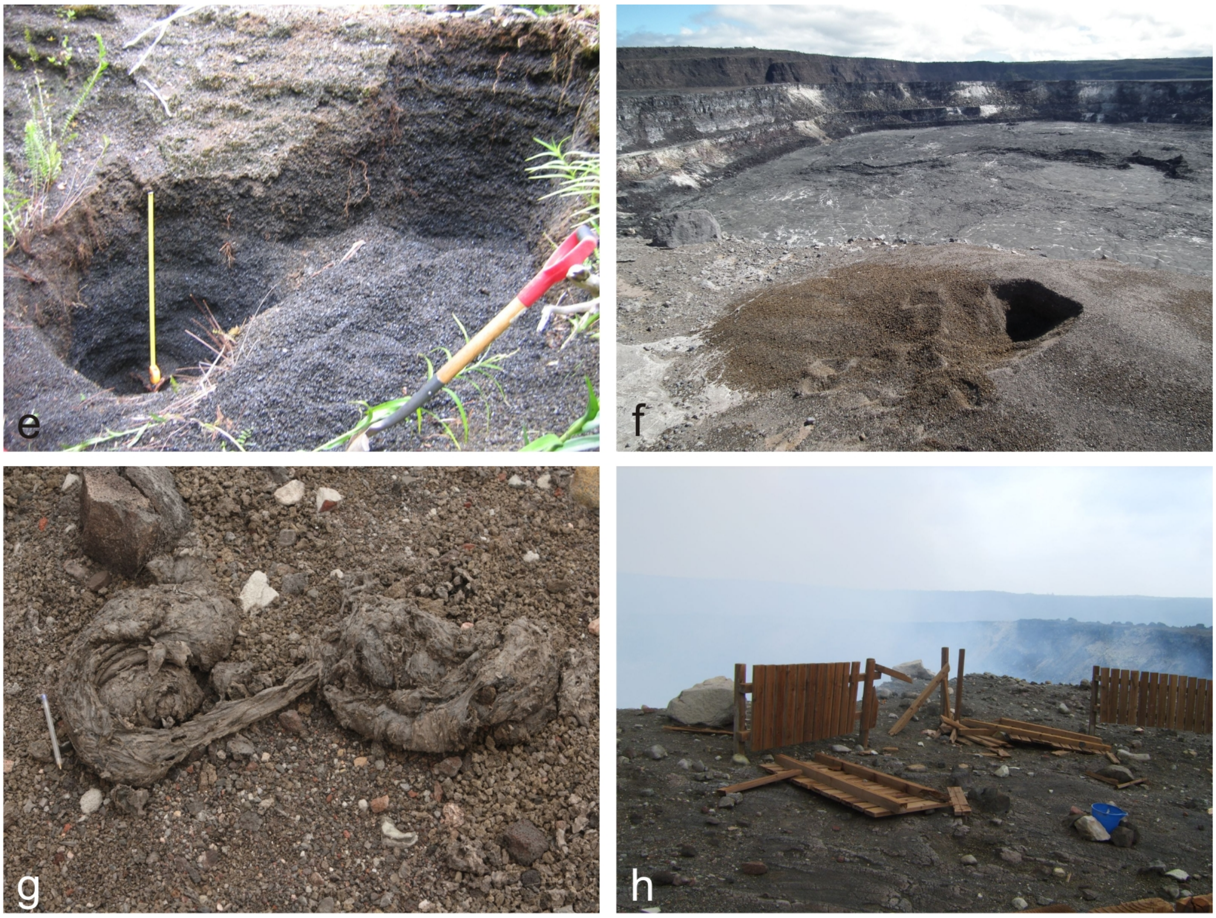

Figure 4.5: Photographs of lava and tephra samples cont'd: (e) sampling pit for collection of pumice tephra produced during the 1959 Kīlauea Iki Hawaiian fountaining; (f) pumice from the 1961 high fountains within Halema`uma`u crater (background) is still pristine and remains exposed at the eruption site. The pit dug for sampling is 30 cm wide (sample 1961); (g) a 'cow-pat' bomb produced during the September 2, 2008 transient subplinian explosion within Halema`uma`u (sample 2008-18). The scoracious bombs are scattered over the floor of the caldera adjacent to Halema`uma`u; (h) buckets placed on Halema`uma`u crater rim, adjacent to the current eruption vent are checked daily by USGS staff to accurately record the volume of material produced (samples 2008-S1, 2008-S2 and 2010-S3 were collected using this method). The wooden structure is the old visitor overview which was destroyed by explosions from the Halema`uma`u vent in March 2008.

unfortunately none of the products from the seven brief eruptions which followed the event are still exposed within the caldera. However, resumption of eruptive activity from 1952 onwards produced many fissure ramparts, flows and pyroclastic deposits which are preserved and easily accessible. As a result, vesicular, scoriacious spatter produced during the summit fissures eruptions in 1954, 1971, 1974 and 1982 were sampled from ramparts on the caldera floor (Figure 4.1 and Figures 4.5c and d). Most of these fissures lie above the location of the summit magma reservoir, east of Halema`uma`u crater and as a result they are sites of well-developed gas fumaroles which has lead to significant alteration and sulphide coating of the spatter and scoria clasts. Care was therefore taken to select samples which were as pristine as possible.

Tephras produced during the high-fountaining eruption in Kīlauea Iki crater during the 1959 eruption were sampled extensively from multiple pits (Figure 4.1 and 4.5e). These samples are examined in detail in Chapter 5 where further details of their sampling can be found. Lapilli-sized pumice clasts from a smaller point source fountain within Halema`uma`u crater in 1961 were also collected from a surface-exposed deposit within the caldera (Figure 4.5f).

The most recent Kīlauea summit samples analysed were vesicular scoria and scoracious 'cow-pat' bombs produced during the 2008–current eruption from the open vent within Halema`uma`u crater (Figure 4.1 and 4.5g). The bombs, though juvenile, were coated in lithic ash and contained many wall-rock fragments. They were ejected during four transient explosive events on 9 April 2008, 27 August 2008, 2 September 2008 and 26 April 2010. The September 2008 cow-pat bombs were scattered across a $\sim 500\,\mathrm{m}^2$ area south of the eruption vent and material was picked from the caldera floor during fieldwork. All other scoria clasts were collected by D. Swanson as part of ongoing USGS monitoring of the current eruption. Tephra output from the Halema`uma`u vent is measured daily using 'tear catcher' sampling boxes and buckets placed at specific localities downwind of the vent (Figure 4.5h).

Rift zone sampling was largely restricted to the upper rift zone portions (Figure 4.1) and included material from the 1969–74 Mauna Ulu eruption. Both spatter produced during the initial fissure stage and reticulite samples from the later high-fountain were collected. The majority of the other rift zone samples were produced during fissure activity, and these included the 1973 fissure near Pauahi crater and the 1974 fissure in the ERZ (Figures 4.1 and 4.1).

In addition to the subaerial samples from Kīlauea, a submarine tephra deposit from Lō`ihi volcano, a seamount rising 950 m below sea level and located 30 km off the south coast of Kīlauea, was also analysed in this study. The sample (deposit D, P5-401-Sc3) was a tholeiitic olivine-rich clastic sand or hyaloclastite, comprised of angular, flat, glass fragments produced during submarine strombolian explosions. The material was collected from a spatter cone on the northeast rim of Lō`ihi by Hawai‘i Underseas Research Laboratory's Pisces-V submersible and was supplied D. Clague. Full details of the sample and methods of collection can be found in *Clague et al.* (2003). Contrary to many subaerial eruption products which have undergone significant degassing prior-to and during eruption, submarine basaltic glasses and melt inclusions generally preserve the bulk of their initial volatile contents through rapid quenching at the higher pressures of their eruption depths. This material may provide a record of undersaturated volatile concentrations within the olivine-hosted melt inclusions, which might otherwise not be recorded in the subaerial products. If undersaturated, the submarine melt inclusions would provide a useful comparative estimate of parental CO_2 and H_2O concentrations in Hawaiian melts.

4.1.2 Analytical Techniques

Splits of each sample were crushed and sieved. Olivine phenocrysts and fresh, crystal-free glass were handpicked, mounted in epoxy resin and polished to expose the melt inclusions. Glasses and melt inclusions were analysed for major elements, S, Cl, and F on a CAMECA SX100 electron microprobe at the University of Cambridge. H_2O, CO_2, Li and B were analysed by secondary ion mass spectrometry (SIMS) at the University of Edinburgh. Trace element compositions were also determined for all samples by LA-ICP-MS at the University of Cambridge. All melt inclusions required compositional correction for post-entrapment crystallisation (PEC) of the host olivine on the walls of the inclusions. The correction procedure followed the methods of *Danyushevsky et al.* (2000) and involved the incremental addition of between 0.39 – 35% olivine, although the majority of inclusions required less than 20% olivine addition. For full details of sample preparation, analytical conditions, data quality and PEC correction see Chapter 2. Full melt inclusion and glass datasets are presented in the Appendix.

4.2 Results

4.2.1 Petrography

The fragile and fragmented nature of the majority of samples precluded the making of thin sections and therefore detailed modal or vesicle density analysis was not possible beyond estimation by eye. However inspection of the samples with transmitted and reflected light microscopy revealed the majority of glasses to be pristine, with vesicularities varying in the range 20–98 vol % (Figure 4.6a). All tephras and lavas sampled were olivine-phyric with the abundance and size of the phenocryst population appearing to increase with increasing eruption rate such that many of the intra-caldera lava flows and fissures were notably phenocryst-poor (< 5 vol%) in stark contrast with all high-fountaining products and the 1973 Pauahi fissure eruption in the ERZ which contained abundant olivine ($\sim$ 10–20 vol% in some samples), often with a diverse range of morphologies (Figure 4.6b).

Olivine is by far the most abundant phenocryst present in all samples and usually occurs as equant, euhedral grains between 0.5–2.0 mm size, although skeletal, elongate, rounded and aggregate forms up to 8 mm were also observed in some fountain tephras (Figure 4.6b). Clinopyroxene and plagioclase phenocrysts were rare or absent in the tephras and glassy selvages collected although some rare microcrysts of plagioclase were observed within several effusive and transient explosive glass samples.

Inclusions of translucent, pristine pale brown glass (melt) up to 300 µm, euhedral chromite or Cr-rich spinel and clusters of small CO_2 fluid inclusions are common throughout most olivine phenocrysts (Figure 4.6c). The glass melt inclusions have elliptical or subrounded to irregular subangular forms and those which were fractured, necked or contained oxides > 5 vol% were discarded from analysis. Rare spherical sulphides up to 10 µm diameter were also identified in a number of melt inclusions from a variety of eruption products (Figure 4.6d).

Vapour bubbles can form within melt inclusions after entrapment, due to differential contraction between the melt and host olivine during cooling (*Anderson and Brown*, 1993; *Metrich and Wallace*, 2008; *Shaw et al.*, 2010) (Figure 4.6c). A large proportion of Kīlauea inclusions (116 of 374) contain small bubbles, most occupying > 7 vol%, but some bubbles

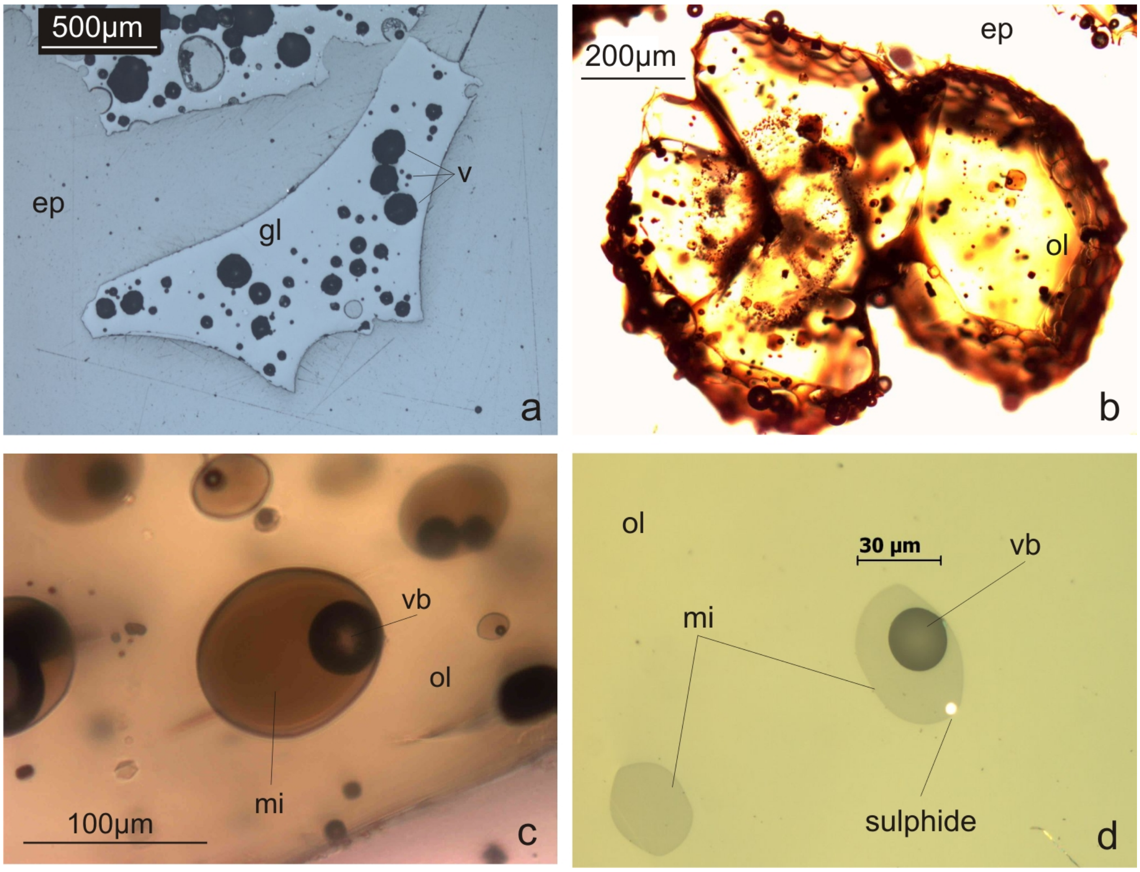

Figure 4.6: (a) Reflected light image of a pristine matrix glass (gl=glass; ep=epoxy); (b) Transmitted light image of an olivine (ol) phenocryst from the high-fountaining eruption of Mauna Ulu in 1969. The image shows an aggregate morphology, with a concentric zone of small glass and fluid inclusions, and oxides. The preferential core alignment of inclusions indicates entrapment during a period of rapid crystal growth. The occurance of this core within what appears to be an aggregate of multiple grains provides intriguing support for recent studies suggesting that such olivines may not be aggregates but are in fact a form of growth morphology of individual liquid-suspended grains (*Welsch et al.*); (c) Transmitted light photograph of a typical olivine-hosted (ol) glassy melt inclusion (mi) analysed in this study, containing an unruptured vapour bubble (vb); (d) Reflected light image of a similar inclusion containing a large exposed bubble and rounded sulphide.

occupy up to 73 vol%. The prevalence of the vapour bubbles within samples meant that it was not possible to conduct this study without analysing bubble-containing inclusions. Despite this, the inclusions were not homogenised to remove the bubble prior to analysis. Homogenisation requires heating the inclusions to ~1200° C and can lead to diffusive loss of H_2O and other mobile elements. Heating can also result in melt expansion, overpressure and rupture of the inclusions, and does not always succeed in dissolution of the vapour bubble. It is possible to calculate a compositional correction to account for bubble formation (*Shaw et al.*, 2010), but the large range of bubble volumes within the Kīlauea inclusions implies that not all bubbles (particularly those up to 73 vol%) could have formed by differential contraction alone, and some may represent exsolved vapour bubbles which were trapped with melt during crystallisation. For this reason, no additional correction was applied to the samples, and therefore all CO_2 and H_2O analyses of inclusion glasses are interpreted as minimum estimates of the original volatile composition of the melt.

4.2.2 Olivine Chemistry

Compositions were determined for 264 olivine phenocrysts from the Kīlauea sample set and a further 10 olivines from the submarine Lō`ihi sands. The olivine core compositions in the Kīlauea tephras range from $Fo_{77.5}$ to $Fo_{89.2}$, and from $Fo_{85.5}$ to $Fo_{89.1}$ in the Lō`ihi sample, where:

$$Fo = Mg\#_{ol} = 100 \times \frac{X_{Mg}}{X_{Mg} + X_{Fe^{2+}}} \tag{4.1}$$

This range is in close agreement with previous examinations of Kīlauea and Hawaiian olivines (*Garcia et al.*, 2003; *Dixon and Clague*, 2001). The range of olivine core compositions as a function of the carrier glass Mg# is shown in Figure 4.7. The crystal population for each sample show a very broad range in Fo compositions and in general, a poor positive correlation with the average Mg# of the host glass. The majority of olivine compositions lie above the line of Kd=0.3 indicating that the crystals were not in equilibrium with their host melts at the time of eruption. The sample furthest from equilibrium is that of 1790-1, a transient subplinian tephra not shown in Figure 4.7 owing to the extremely low Mg# of the glass, 36 (4 wt% MgO), with anomalously high Fo olivines ranging from Fo_{86}–Fo_{88}.

The olivine compositions in Figure 4.7 are coloured-coded for eruption style and labelled according to eruption date. Figure 4.7 demonstrates that all eruption types produce olivines and matrix glasses with a wide range of compositions although the highest Fo and Mg# values were produced in high-fountaining eruptions ($Fo_{89.5}$ in 1500) and the lowest Fo and Mg# glass by effusive lava flows (1885A and B). Figure 4.7 also shows that in general the effusive and transient subplinian eruptions lie closest to the Kd line of equilibrium. There is no progressive change in phenocryst composition with eruption date.

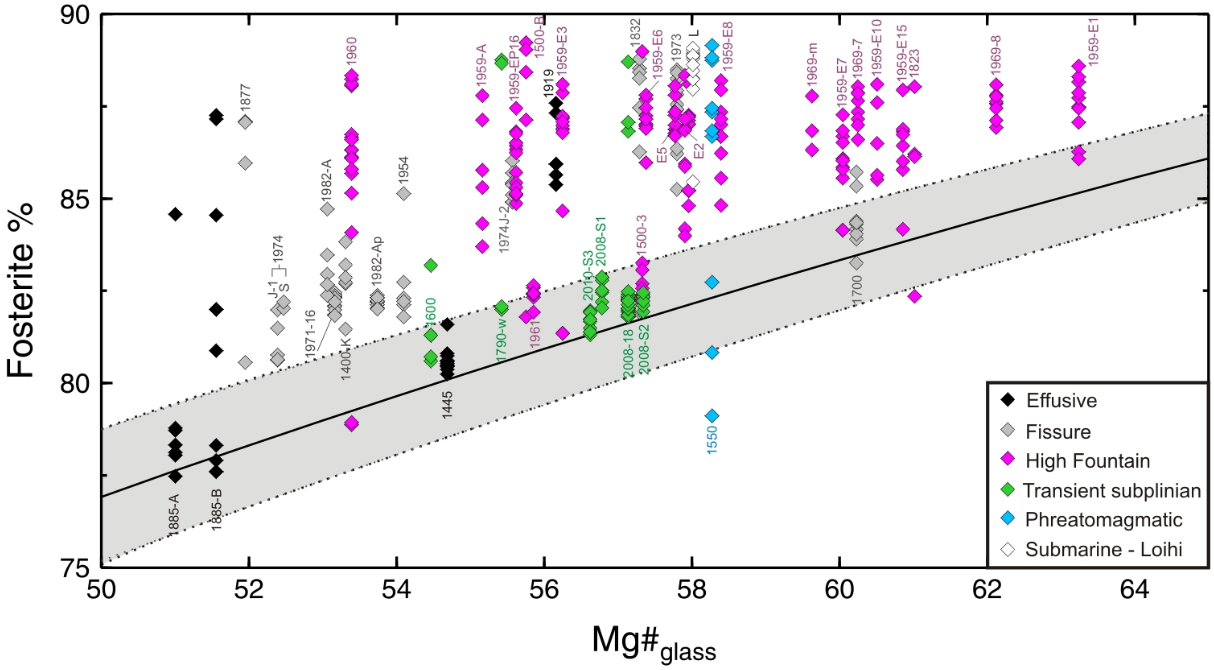

Figure 4.7: Olivine core compositions (fosterite %) compared with matrix glass Mg# [where Mg# = ((XMg/XFe^{2+} + XMg) × 100), with the Fe^{2+} set to 90 % of total iron (*Garcia et al.*, 2003)] in Kīlauea prehistoric and historical tephras. Data points are labelled by sample name and symbols coloured according to eruption style (see key and text for explanation). The gray band shows the range of equilibrium olivine compositions for a given Mg number when Kd=0.3 ±10%, according to *Roedder and Emslie* (1970). The 2σ errors are smaller than the symbol size.

Minor elements such as NiO vary systematically within the olivine populations such that an increase in Fo content from Fo 77.5 to 89.2 mol% correlates positively with a linear increase in NiO concentrations from 0.18 to 0.48 wt% (Figure 4.8a). CaO compositions for the Kīlauea and Lō`ihi olivines range from 0.18 to 0.35 wt%. Olivines produced during effusive, fissure and transient explosive eruptions define a negative linear correlation between CaO and Fo compositions, while high-fountain erupted olivines display greater variation in CaO at constant Fo composition (Figure 4.8b).

Investigation of olivine zoning in the prehistoric and historical samples was beyond the scope of this study. However, a subset of 79 olivine crystal rims (outer 10-20 µm) were analysed in addition to their cores, to determine possible heterogeneity within each of the phenocrysts. In accordance with the findings of *Garcia et al.* (2003) and *Clague et al.* (1995), the majority of Kīlauea's olivines appear to be in equilibrium with their carrier melts and are normally zoned or unzoned, with the maximum normal zoning observed between Fo 88.6 to 88.2 mol%. Only two olivines were found to exhibit reversely zoned rims thought to be

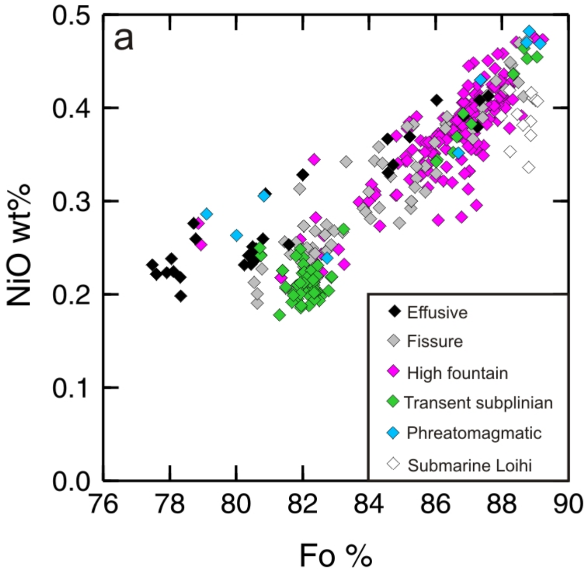

Figure 4.8: Plots of minor elements (a) NiO and (b) CaO, versus Fo composition of olivines from prehistoric and historical Kīlauea and Lō`ihi tephras.

indicative of pre- or syn-eruptive magma mixing (*Garcia et al.*, 2003), with the maximum zoning only Fo 86.7 to 87.8 mol%.

4.2.3 Major Elements

All of the Kīlauea and Lō`ihi glasses and melt inclusions analysed have total alkali (Na_2O + K_2O wt%) concentrations between 1.8–3.8 wt% and fall into the tholeiitic basalt compositional field in Figure 4.9 with the exception of one melt inclusion from sample 1550-26 (a phreatomagmatic ash) and one matrix glass sample (1445-AA; an effusive flow sample from the `Ailā`au eruption).

The major element compositions of the prehistoric–historical Kīlauea, and Lō`ihi eruptions are shown, together with the previously published whole rock data of *Garcia et al.* (2003), in MgO variation diagrams in Figure 4.10. In addition to Figure 4.10, in which the data is coded by eruption style, Figures 4.11 and 4.12 show the same dataset as a function of eruption date and vent locality (intra- versus extra-caldera) respectively.

The post-entrapment corrected Kīlauea inclusions display a wide range of MgO concentrations from 6.41 to 14.73 wt%, in contrast with the more evolved concentrations of the matrix glasses which range from 4.27 to 10.28 wt%. The inclusion compositions lie within

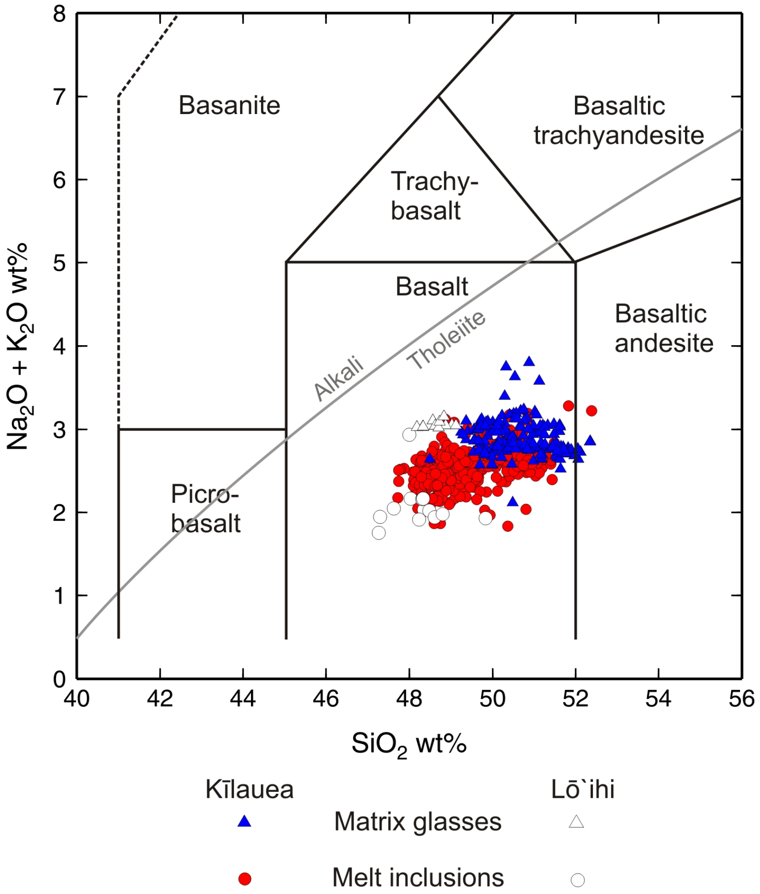

Figure 4.9: Total Alkali-Silica diagram for the pre-historic and historical Kīlauea tephras and submarine Lō`ihi sample. The grey line represents the alkali-tholeiite divide (*MacDonald and Katsura*, 1964).

the concentration ranges reported previously for the Hilina Basalts, the oldest subaerial lavas exposed at Kīlauea (5.8–18 wt%; *Easton and Garcia* 1980) and the historical summit lavas analysed by *Garcia et al.* (2003) (6.0–17.8 wt%; Figure 4.10).

The high-MgO content of many of the inclusions relative to the significantly more evolved compositions of the matrix glasses suggests that the inclusions are representative of more primitive compositions trapped prior to eruption. Melt inclusions from Lō`ihi seamount are on the whole more primitive than the Kīlauea melts, with MgO values between 10.92 to 15.28 wt%.

The major elements in Figure 4.10 define negative correlations indicative of dominantly olivine-controlled liquid lines of descent (LLD) such that as MgO decreases, the concentrations of SiO_2, CaO and Al_2O_3 increase. The lack of a discernible inflection in the melt

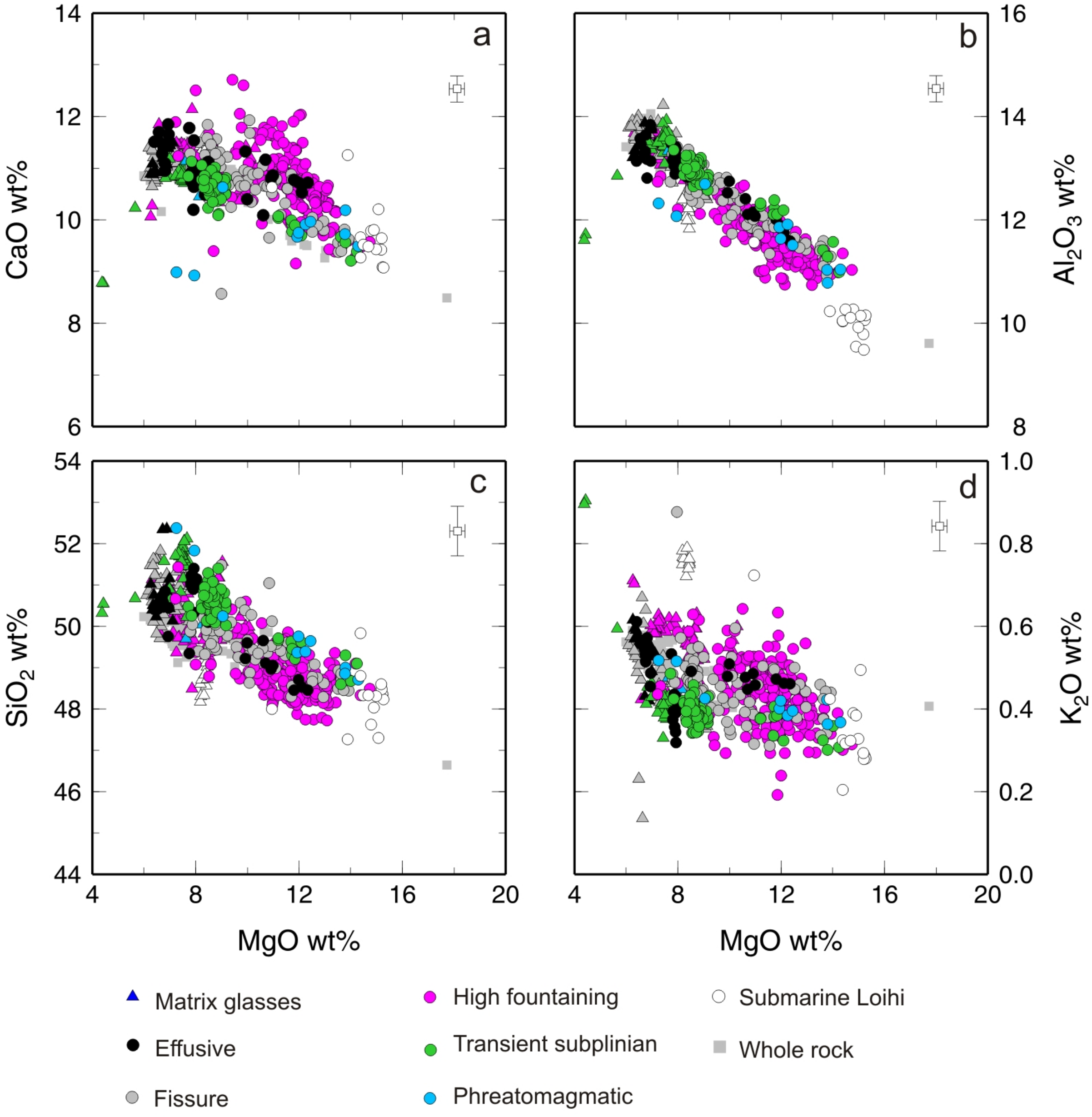

Figure 4.10: Harker MgO-variation plots of major element abundances for matrix glasses (triangles) and melt inclusions (circles coloured by eruption style). Melt inclusion compositions from Lō`ihi are shown in white. Published whole rock data for historical summit lavas (grey squares) are from *Garcia et al.* (2003). Representative error bars based on 1σ precision on standard repeats are shown for each element.

inclusion CaO contents and the relatively tight negative trend in the Al_2O_3 compositions suggest that pre-eruptive melts did not undergo significant clinopyroxene (cpx) or plagioclase crystallisation prior to entrapment. Low CaO and CaO/Al_2O_3 (<0.8; Figure 4.10g) in the matrix glasses however, particularly at MgO <7.0 wt% suggests the appearance of

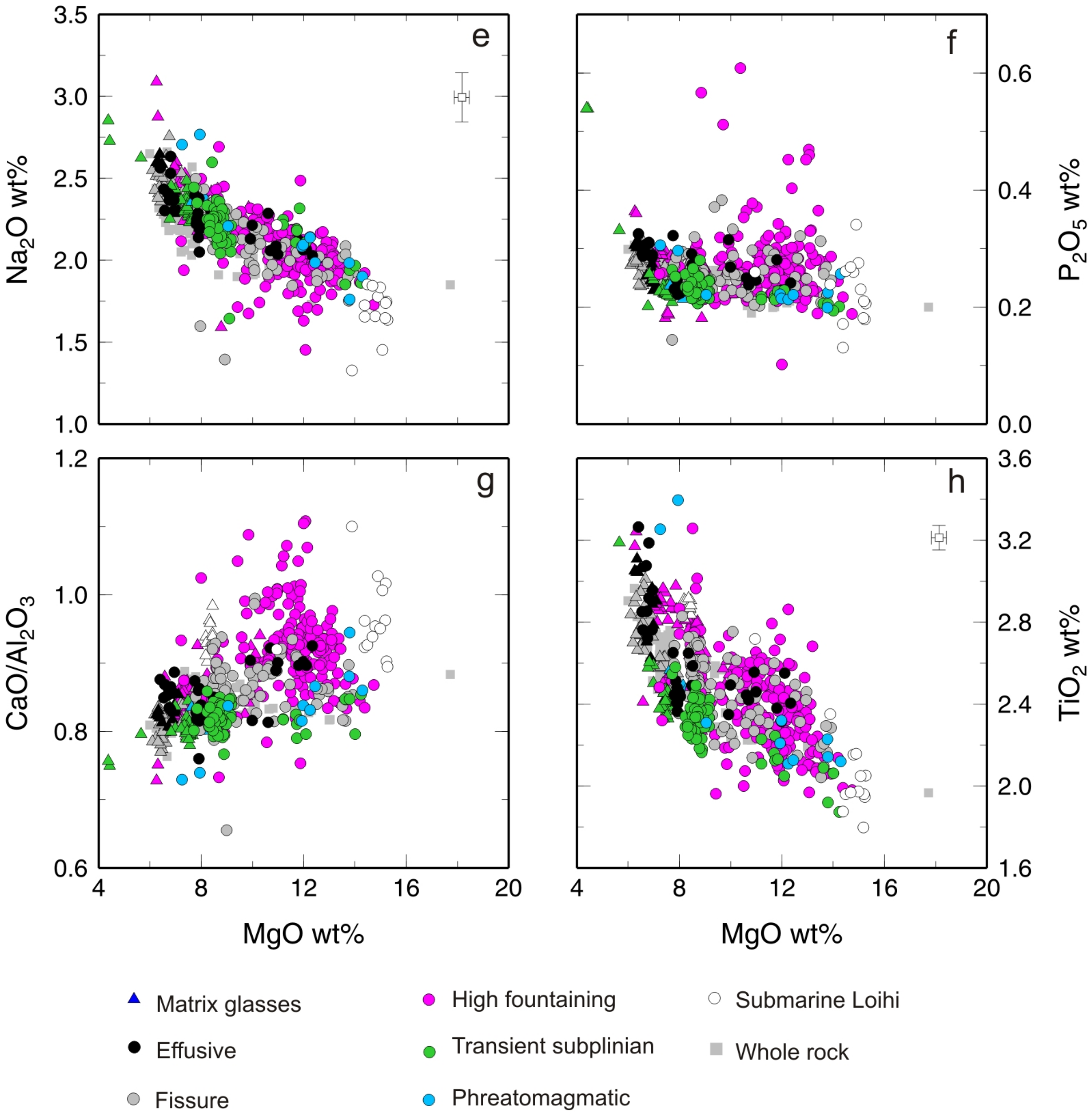

Figure 4.10: Harker MgO-variation plots of major element abundances (cont'd). Error bars for P_2O_5 and CaO/Al_2O_3 concentrations are smaller than the symbol size.

cpx on the liquidus, despite the absence of a visible cpx phenocryst population in the tephra samples, indicating that differentiation beyond olivine-only control has occurred in a number of the carrier melts.

There is significant variation in both glass and inclusion CaO/Al_2O_3 at constant values of MgO, with scatter beyond that expected from analytical error (Figure 4.10). In Al_2O_3–CaO space, this scatter can be seen more clearly (Figure 4.13), and those inclusions which

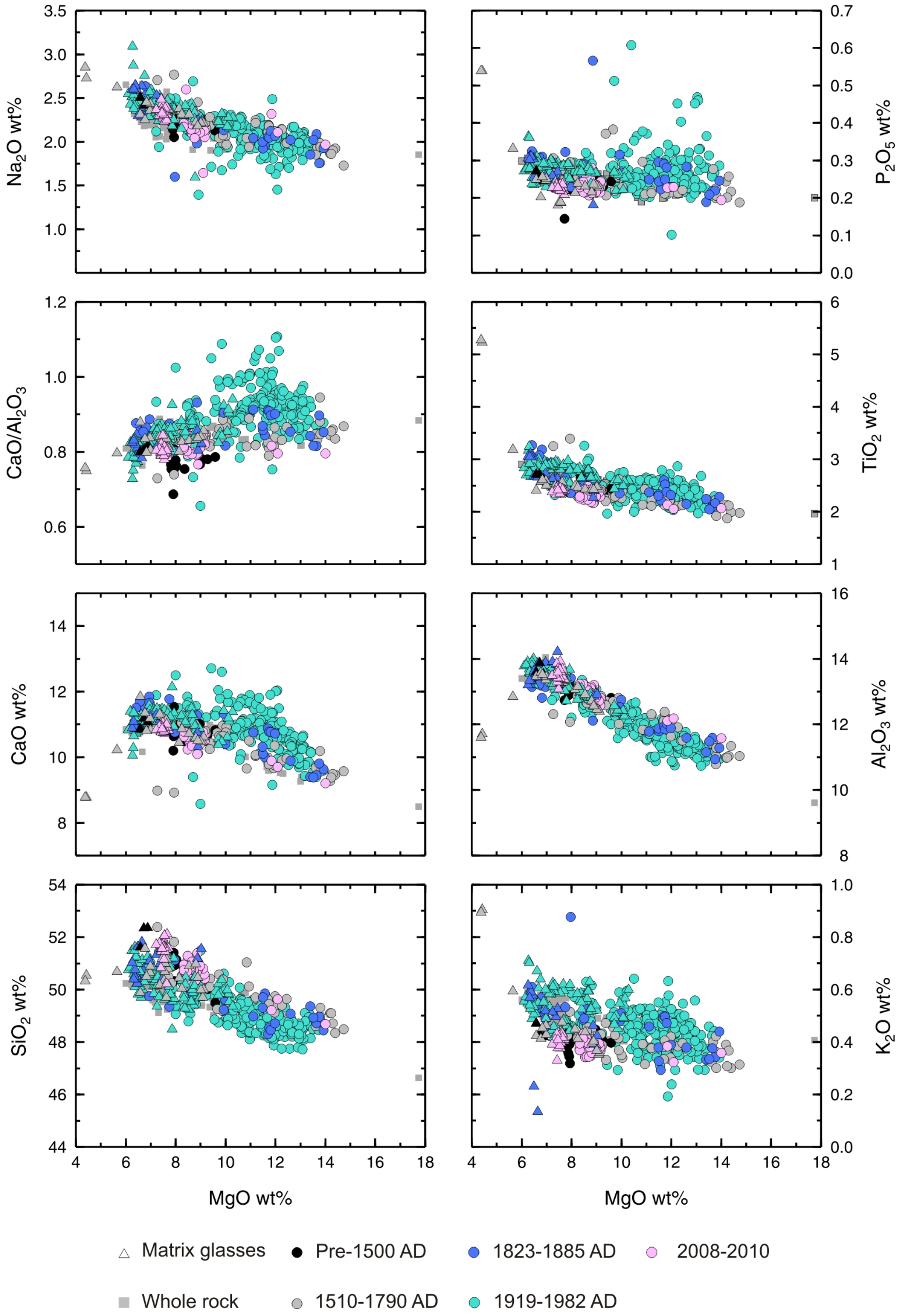

Figure 4.11: MgO-variation plots of major element abundances as a function of eruption date.

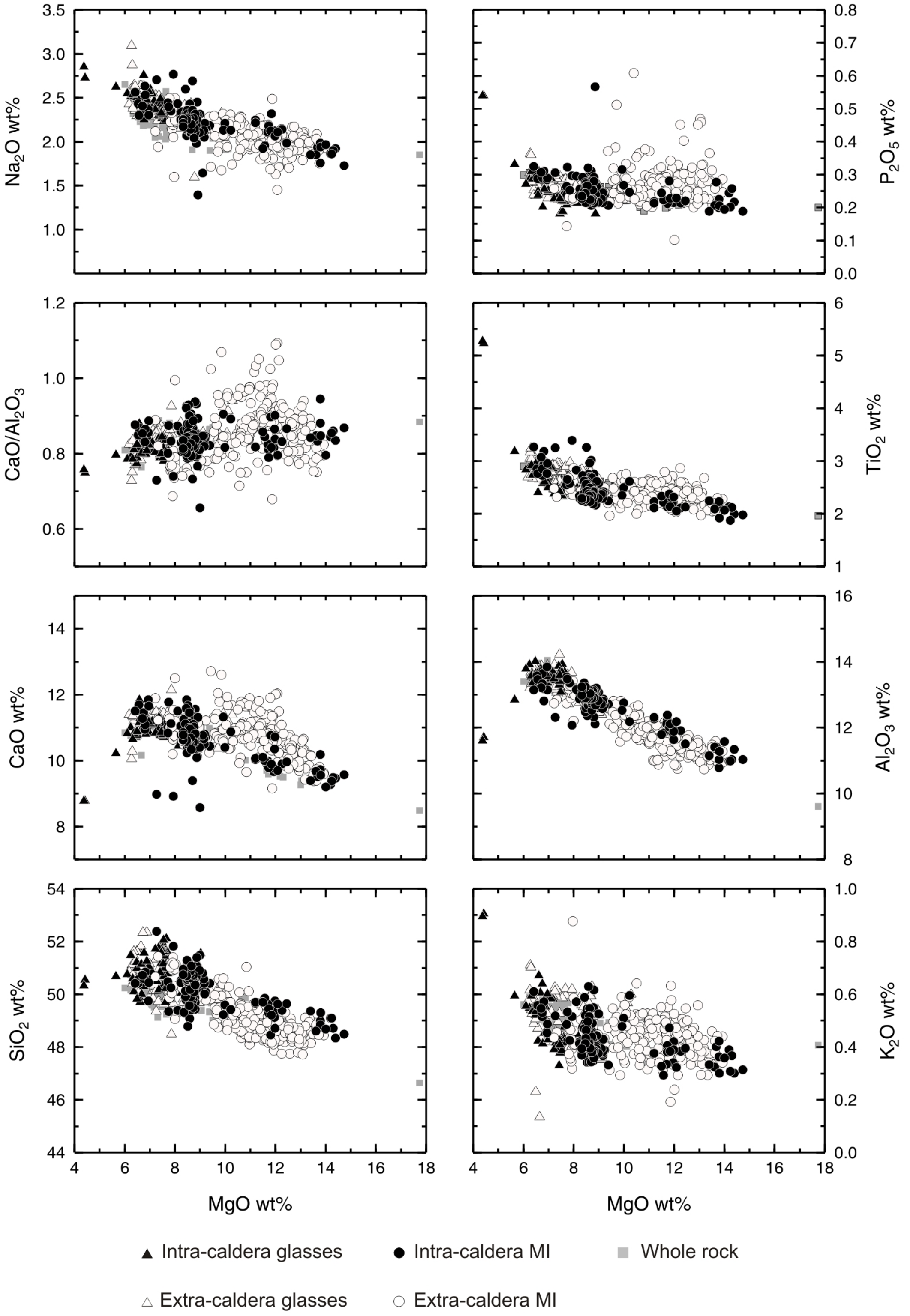

Figure 4.12: MgO-variation plots of major element abundances as a function of eruption vent positions: inside or outside the margins of the present caldera.

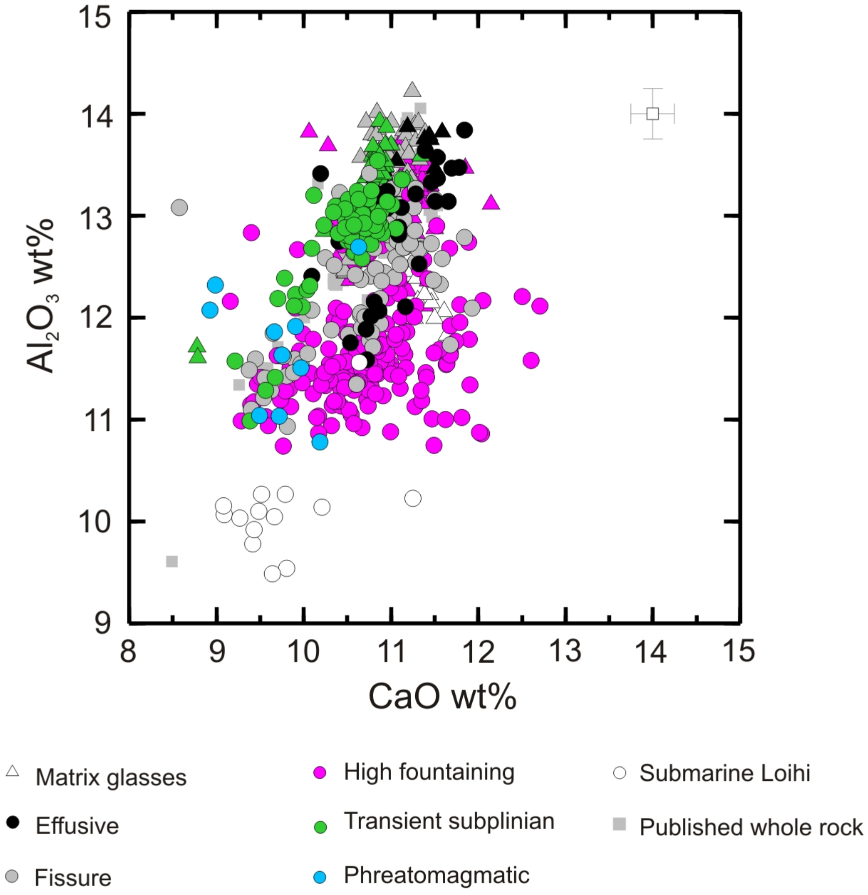

Figure 4.13: Al_2O_3 versus CaO contents of the prehistoric and historical Kīlauea and Lō`ihi melt inclusions and matrix glasses. Representative errors shown with the white square symbol are the 1σ precision on standard repeats. Published whole rock data from *Garcia et al.* (2003).

do not lie along the compositional trend defined by the majority of glasses, inclusions and whole rock values, are typically enriched in CaO relative to Al_2O_3.

K_2O, TiO_2, Na_2O and P_2O_5 are all incompatible in Kīlauea and Lō`ihi melts and all form broadly negative correlations when plotted against MgO. All of these oxides display significant variation at fixed MgO values. Inclusions with anomalous compositions have extremely high P, high and low K, and low Na concentrations. These anomalous values are in excess of their analytical errors and are not correlated with each other. For example, high P inclusions do not lie along the liquid line of descent in Ti and Na space (Figure 4.14) and are found over the entire range of K concentrations.

Melt inclusions from samples produced during different styles of activity at Kīlauea span the full range of MgO concentrations (Figure 4.10), although there appears to be a general

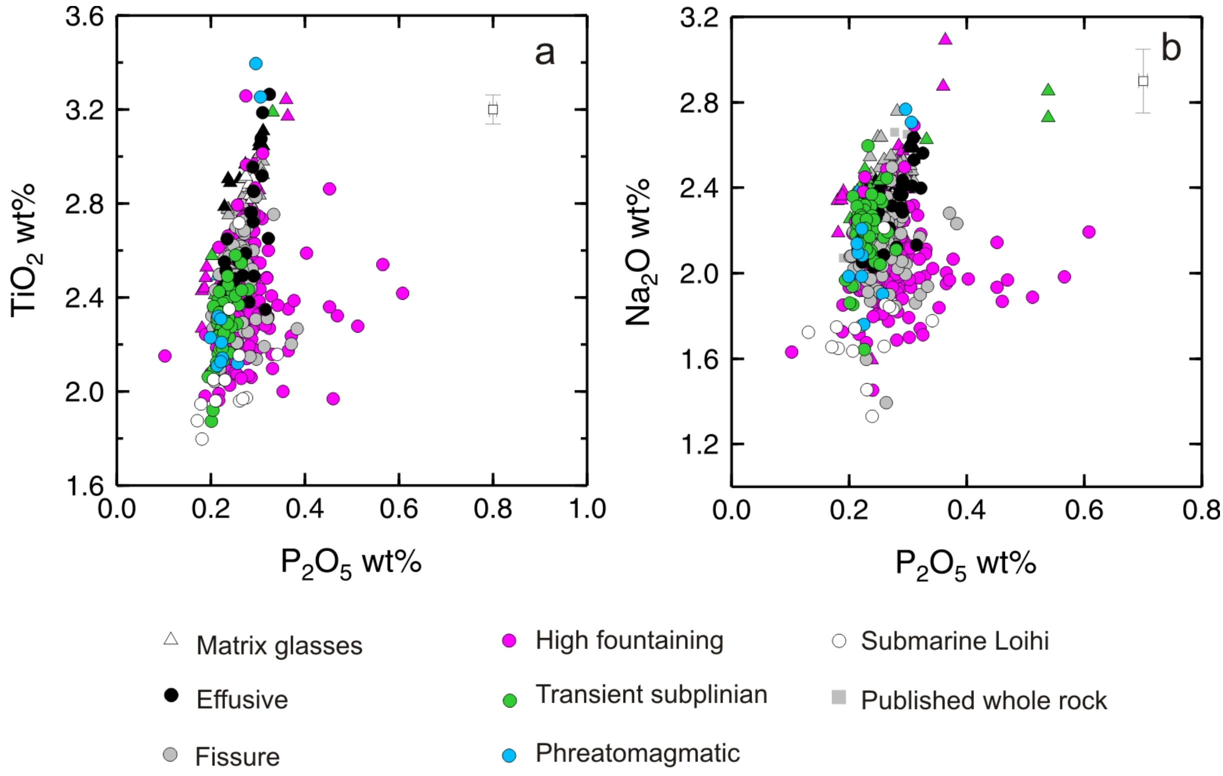

Figure 4.14: Minor element compositions of Kīlauea and Lō`ihi melt inclusions and matrix glasses; (a) TiO_2 versus P_2O_5 and (b) Na_2O versus P_2O_5. Representative errors shown with the white square symbol are the 1σ precision on standard repeats. Whole rock data from *Garcia et al.* (2003).

concentration of effusive and subplinian inclusions at lower MgO values, with a greater proportion of high-fountaining samples lying at higher MgO concentrations. In Al_2O_3–CaO space, the high-fountains and fissures display the greatest range of CaO contents, with the fountain products exhibiting the highest CaO values observed. The high-fountaining inclusions also display a broader range in minor element compositions than the other eruptive groups (Figures 4.10 and 4.14). However it is important to note that while it is possible to describe generalised trends in the major and minor element data based on eruption styles, it is also acknowledged that a potential bias exists in the data due to the greater number of samples analysed in some of the eruption groups. The significance of this will be discussed in detail below.

Figure 4.11 indicates that the oldest eruptions analysed, those prior to caldera formation (pre-1500 AD) and those of the 21st century (2008–2010 AD) are more MgO-poor and SiO_2-rich than those of the other sampled periods. The 20th century melt inclusions display the greatest variation at constant MgO content. This variation is also observed in the group of samples which erupted outside of the current caldera (Figure 4.12). On average intra-caldera eruptions have higher concentrations of SiO_2 and lower CaO compositions than extra-caldera events.

Similar to the findings of previous whole rock studies at Kīlauea (e.g. *Pietruszka and Garcia*, 1999a; *Garcia et al.*, 2003; *Marske et al.*, 2008), the matrix glass and inclusion compositions appear to vary significantly with age (Figures 4.15 and 4.16). The glass and inclusion compositions in Figures 4.15 and 4.16 are shown normalised to 10 wt% MgO in order to remove the effects of crystal fractionation. Normalisation is achieved by addition or subtraction of equilibrium olivine in small steps (0.5 mol%) and only melts with > 7.0 wt% MgO were used, as those with lower MgO are likely affected by fractionation beyond olivine control.

Matrix glass compositions appear relatively uniform between 1500 to the early 19th century, after which the incompatible elements and CaO abundance increase and SiO_2 decreases until the 1959 Kīlauea Iki eruption. Subsequent eruptions (1961–2010) have significantly lower incompatible element and CaO contents and higher SiO_2, indicating a reversal in compositional variation. These trends appear to follow those observed in the whole rock compositions of *Garcia et al.* (2003), also shown in Figure 4.15, although it is noted that the glass compositions display a greater degree of compositional variation for each eruption sample than those of the whole rock equivalents.

The melt inclusion compositions shown in Figure 4.16 seem to mimic the glass and whole rock temporal variations with a noticeable increase in incompatible element abundance from the early 19th century to mid 20th century and a decrease in TiO_2 and K_2O concentrations from 1961–2010. However the temporal trends are far less distinct than those in Figure 4.15 owing to the large range of inclusion compositions within each eruption population. For example, the 1959 samples contain inclusions with the most enriched CaO and K_2O concentrations observed in the total prehistoric and historical dataset, but compositions within the population also span almost the entire range of Kīlauea values.

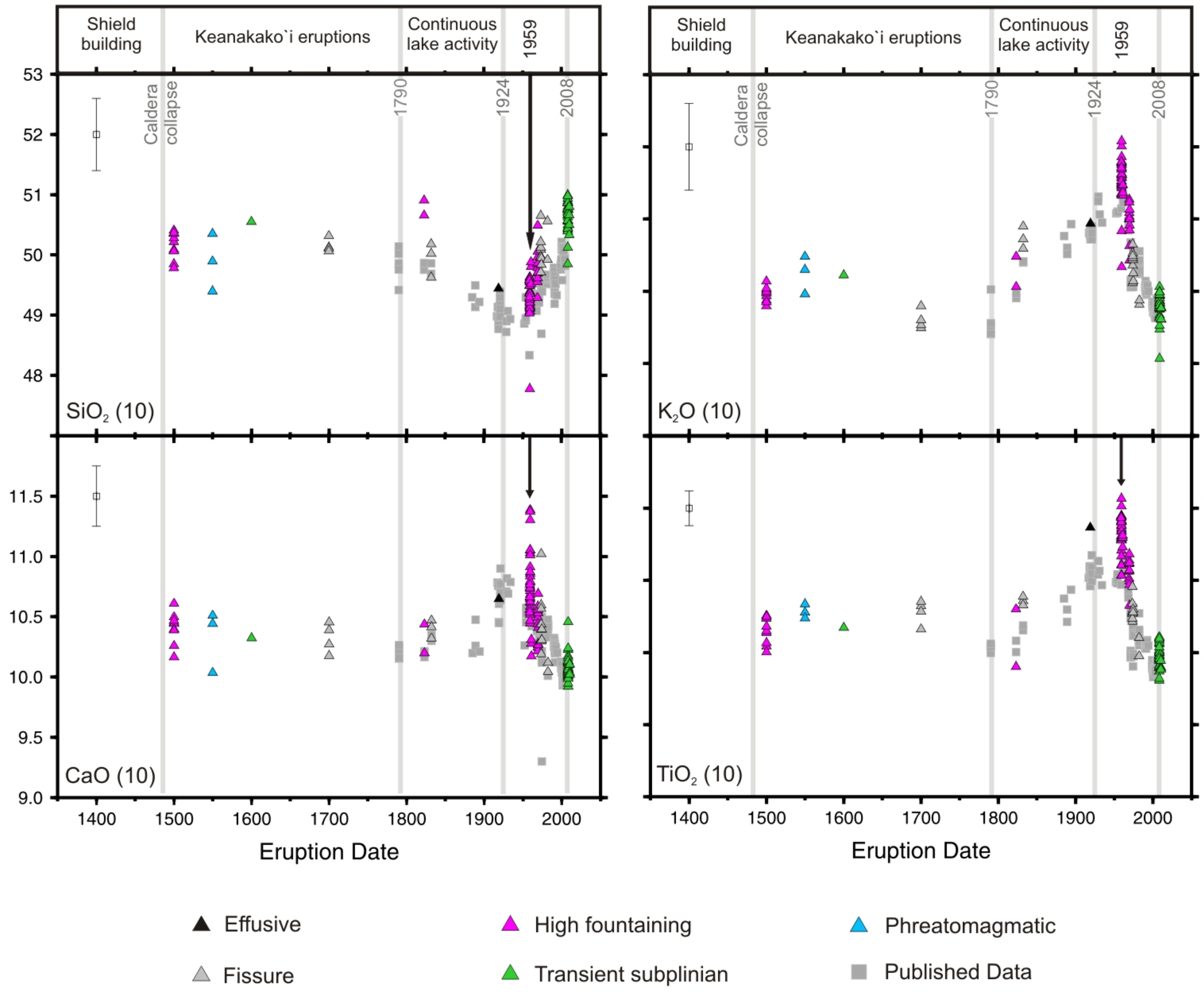

Figure 4.15: Temporal major element variation for matrix glass samples from Kīlauea prehistoric and historical eruptions. Only glasses with MgO contents of > 7.0 wt% were used above, to minimise the effects of fractionation beyond olivine control. Compositions were normalised to 10 wt% MgO by incremental (0.5 mol%) addition or subtraction of equilibrium olivine. Gray squares represent whole rock data for historical summit lavas (*Garcia et al.*, 2003) and samples from the 1983–present Pu`u `Ō`ō eruption (*Garcia et al.*, 1996; *Marske et al.*, 2008). Labels describe eruptive periods and vertical grey lines indicate specific events during the volcano's recent history, including caldera collapse ~1480 AD, the 1790 explosions marking the end of the Keanakako‘i eruptions, the 1924 phreatic event and the 2008 explosive onset of the current summit eruption. Error bars represent 1 σ precision on standard repeats analysed in this study.

4.2.4 Trace Elements

Trace element concentrations within the prehistoric and historical glasses and melt inclusions from Kīlauea exhibit substantial variations both within and between individual eruptions. Figures 4.17 and 4.18 are plots of trace element concentrations versus an independent index of fractionation, in this case, MgO concentration. Similar to Figure 4.10 the trace element

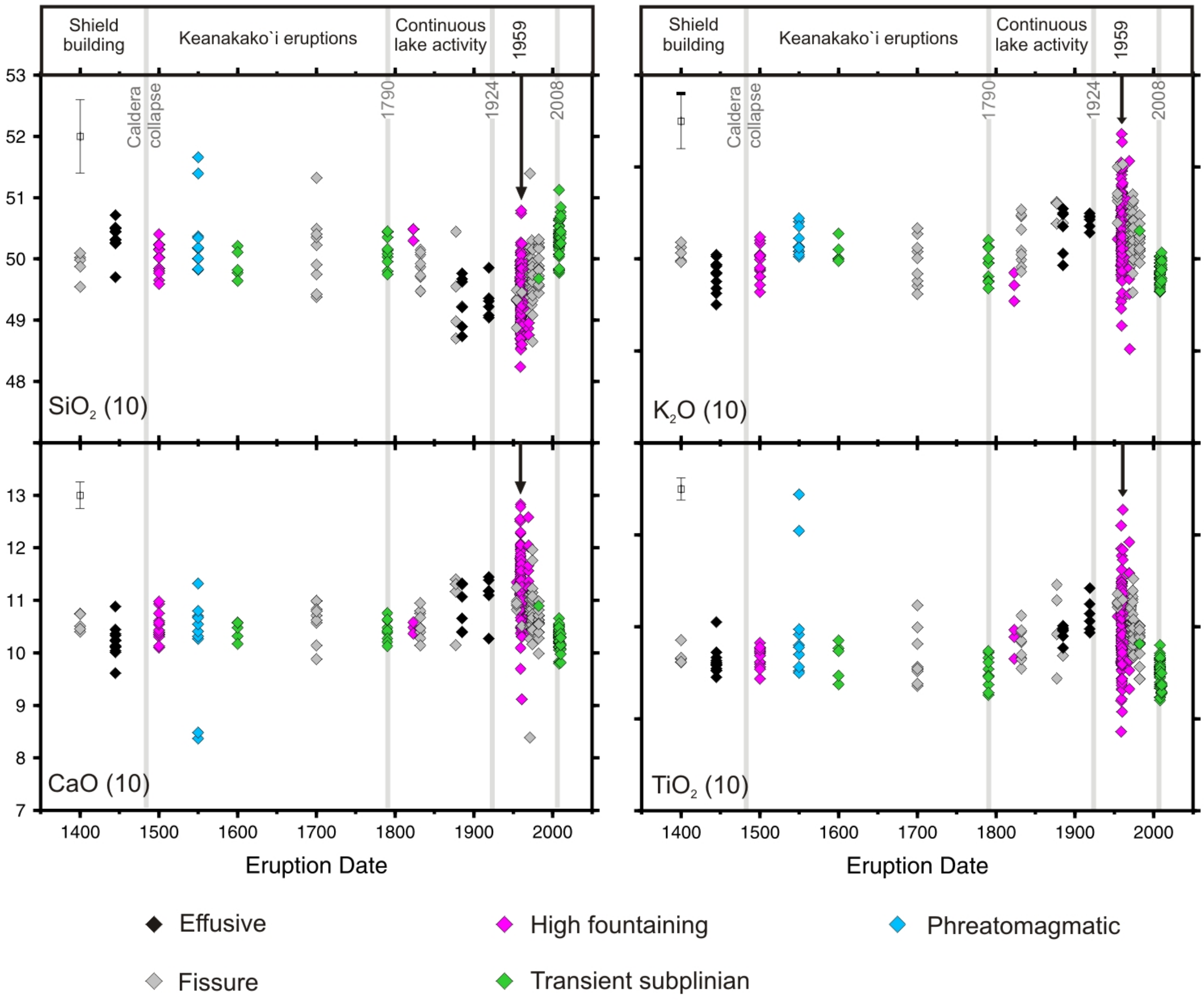

Figure 4.16: Temporal major element variation for melt inclusions from Kīlauea prehistoric and historical eruptions. As in Figure 4.15, inclusion values were normalised to 10 wt% MgO by addition and subtraction of equilibrium olivine in order to remove the effects of fractionation on melt composition. Error bars represent 1 σ precision on standard repeat measurements. Labels are as in Figure 4.15

data is shown as a function of eruption style. Decreases in MgO concentration correlate with increases in highly incompatible large ion lithophile elements (LILE), high field strength elements (HFSE), rare earth elements (REE), Y and U abundances. Matrix glasses have consistently more enriched trace element compositions relative to the melt inclusion populations and at concentrations < 7.0 wt% MgO, many of the glass LILE and light REE (LREE) appear to increase further. When cpx joins the liquidus as a crystallising phase, the MgO content of the remaining melt decreases at a lower rate, and a larger amount of fractionation is required to produce the same decrease in MgO that results from olivine crystallisation

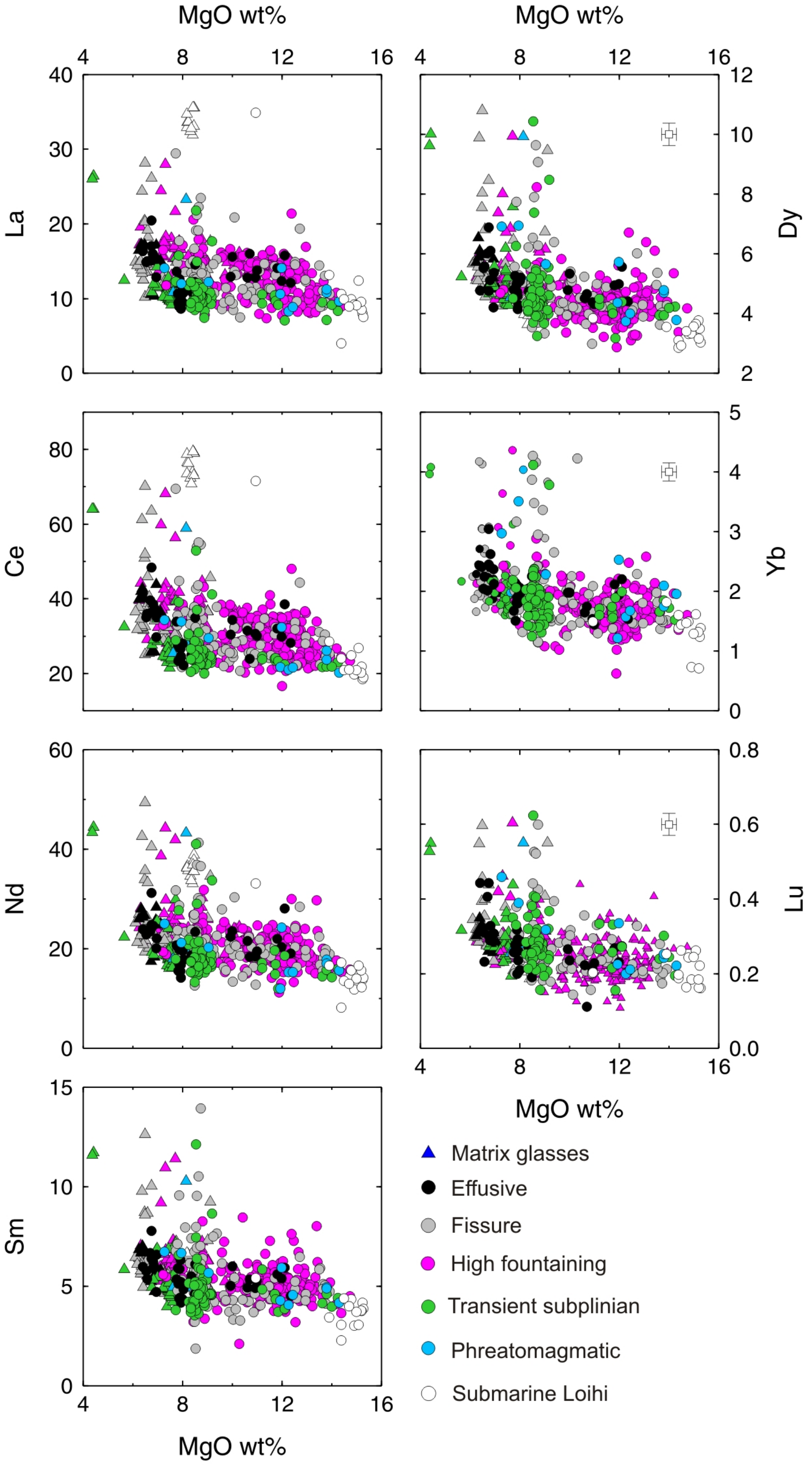

Figure 4.17: MgO wt% versus selected rare earth element concentrations of melt inclusions and matrix glasses of Kīlauea and Lō`ihi, plotted as a function of eruption syle. Representative errors are 1σ precision on standard repeats. These are absent where errors are smaller than the data symbol sizes.

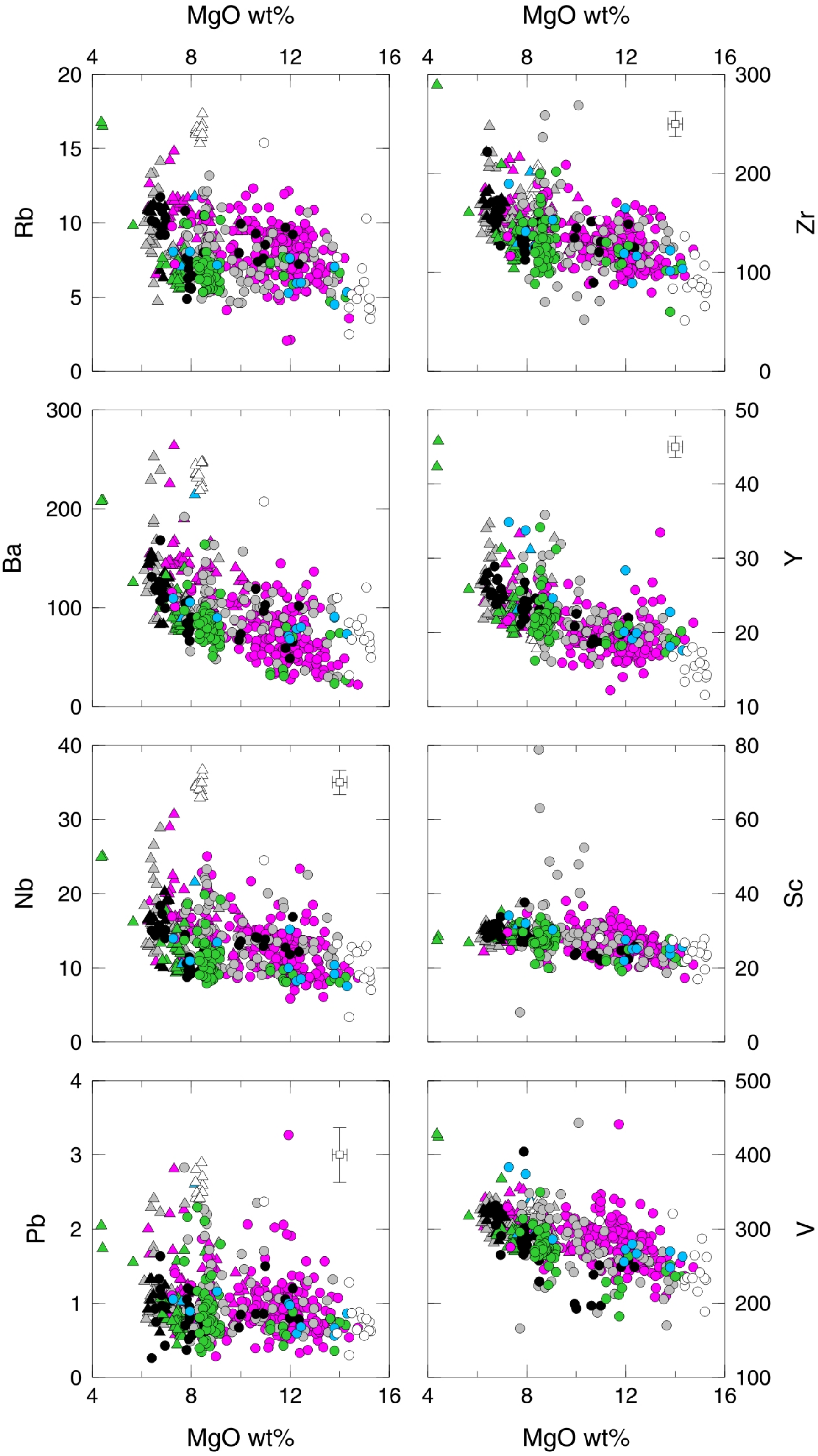

Figure 4.18: MgO wt% versus trace element concentrations of melt inclusions and matrix glasses of Kīlauea and Lō`ihi, plotted as a function of eruption style. Symbols, colours and errors are identical to those in Figure 4.17.

alone. The decrease in the rate of MgO reduction with fractionation results in an increase in the slope of highly incompatible elements against MgO. These increases are not observed in the same glasses for less incompatible elements such as Sc and V; Sc in particular is compatible in cpx, while LILE and LREE are highly incompatible in both cpx and olivine. The consistent increase in highly incompatible trace elements throughout the Kīlauea inclusions and glasses is in accordance with the progressive fractionation trends observed in Figure 4.10.

Kīlauea tephras and lavas show substantial trace element variations at constant MgO concentrations in Figures 4.17 and 4.18, with scatter far exceeding analytical error. These large variations are seen for all elements and throughout all eruption style categories. Enrichment factors (total compositional variation) for incompatible elements in the Kīlauea melt inclusions span a broad range from 10.1 and 4.3 for Rb and Nb, to 3.7 and 5.1 for Sr and Zr and 3.0 and 2.6 for Y and V. These factors are significantly greater than those observed in both the matrix glasses (3.6 to 1.6, Rb and V respectively) and in other whole rock studies of Kīlauea lavas (1.9 to 1.3, Rb and V respectively; (*Garcia et al.*, 2003)).

Primitive mantle-normalised multi-element and REE diagrams for the Kīlauea and Lō`ihi melt inclusion compositions are shown in Figures 4.19 and 4.20. Despite the broad range of the Kīlauea inclusion compositions, all profiles exhibit very similar patterns with enrichment of highly incompatible LILE and LREE relative to HFSE and HREE, consistent with melts being produced from a garnet-bearing mantle source.

The multi-element diagrams in Figure 4.19 show the data grouped by eruption style. All samples display depletions in Pb and Sc relative to primitive mantle compositions and have average matrix glass compositions which mirror the melt inclusion profiles but lie at higher concentrations for all elements. Melt inclusions within the high Hawaiian fountain group have the greatest compositional range and more enriched HFSE ratios with variations in Nb/Y ratios up to 70%. Effusive and phreatomagmatic inclusions display the most restricted compositional range, with Nb/Y ratios which vary by 51 and 43% respectively (Figure 4.21a).

REE profiles in Figure 4.20 are grouped by eruption date. As in Figure 4.19, the REE profile patterns of enrichment between groups are similar. The compositions of the pre-1500 AD and majority of 2008–2010 inclusions display a more limited compositional range

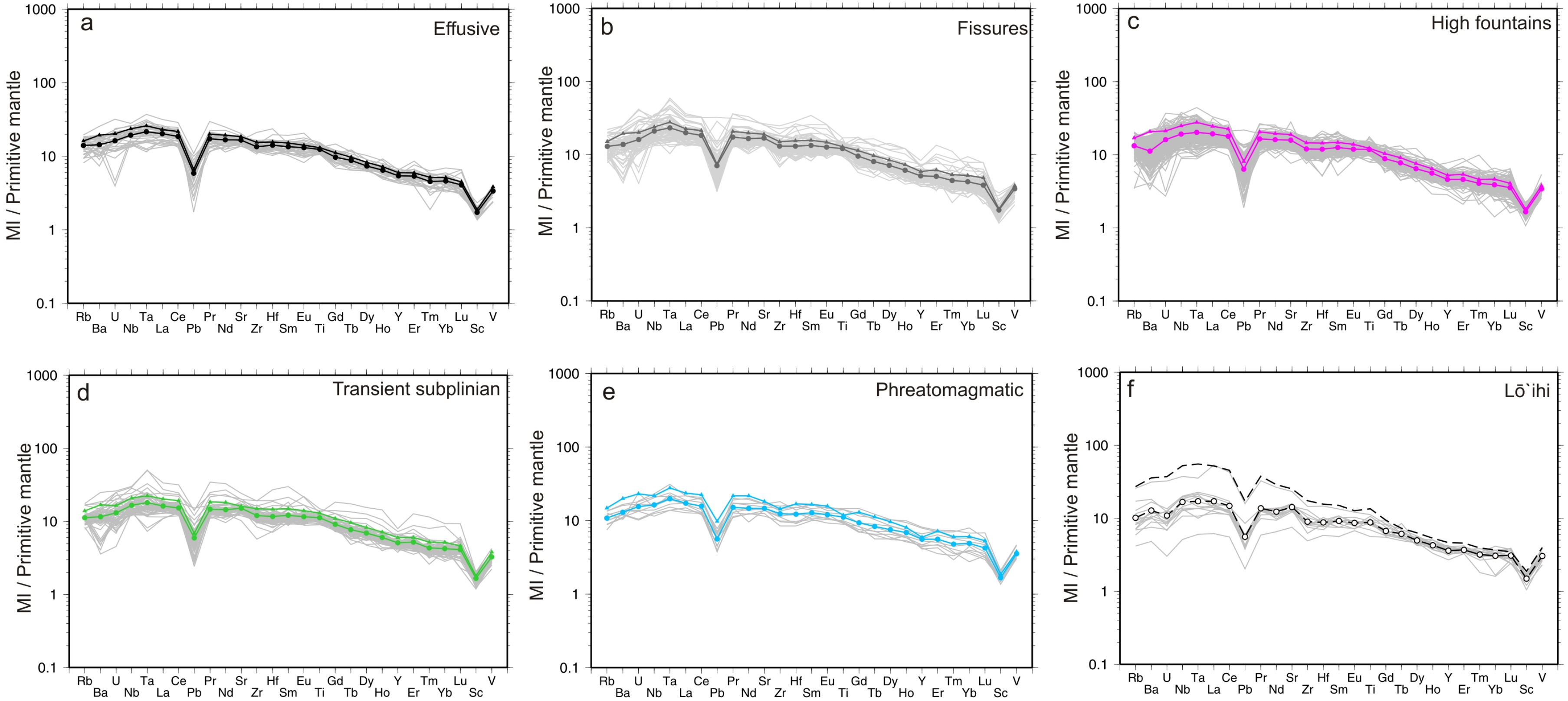

Figure 4.19: Primitive mantle-normalised (*McDonough and Sun*, 1995) multi-element diagrams (a)–(f) for melt inclusion and glass compositions for each eruption style group. Grey lines represent the profiles for the total melt inclusion dataset of each category and coloured circled profiles are the average melt inclusion compositions. The average glass compositions for each group are represented by the coloured triangle symbols and profile.

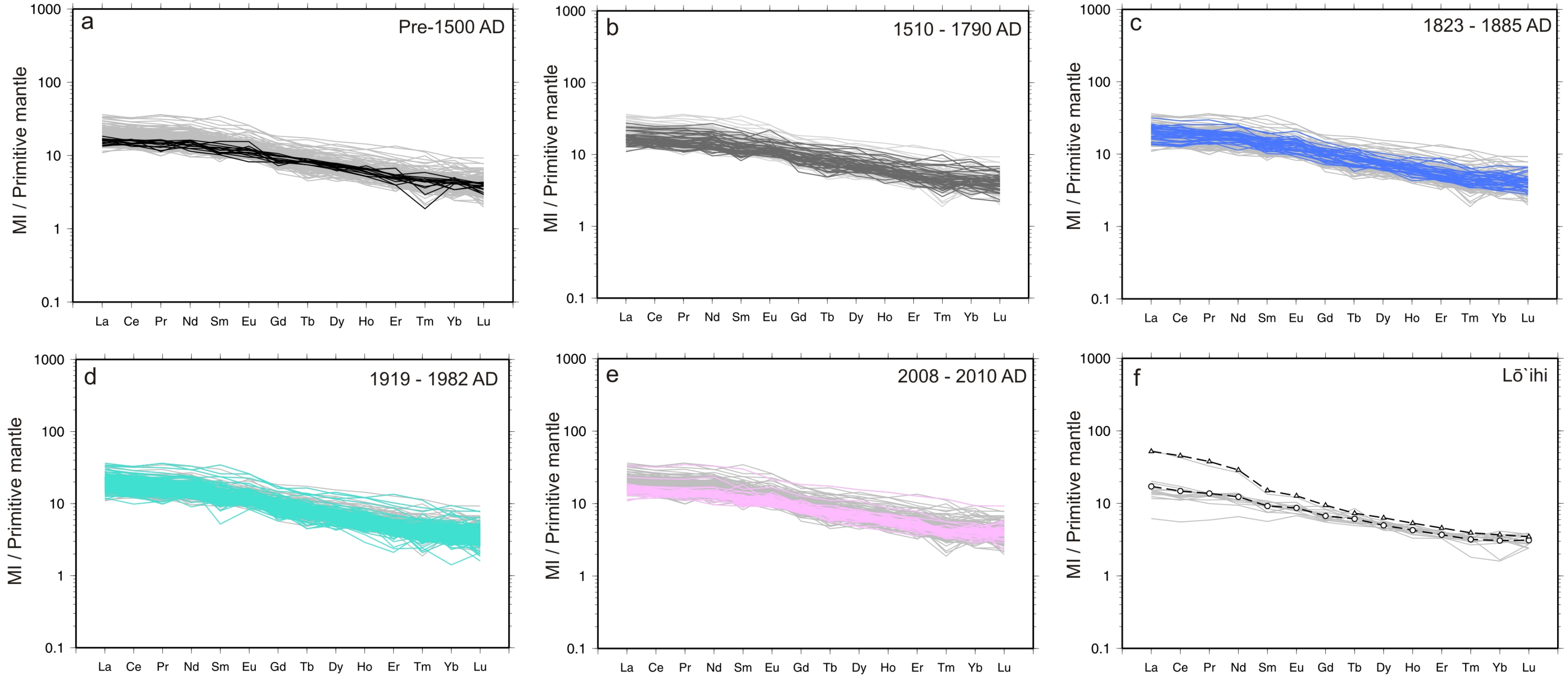

Figure 4.20: Primitive mantle-normalised (*McDonough and Sun*, 1995) Rare Earth (REE) diagrams (a)–(f) for melt inclusions compositions for Kīlauea and Lō`ihi eruption products. Kīlauea data is grouped by eruption date. Grey lines represent the profiles for the entire Kīlauea melt inclusion dataset and coloured profiles are those specific to each time period.

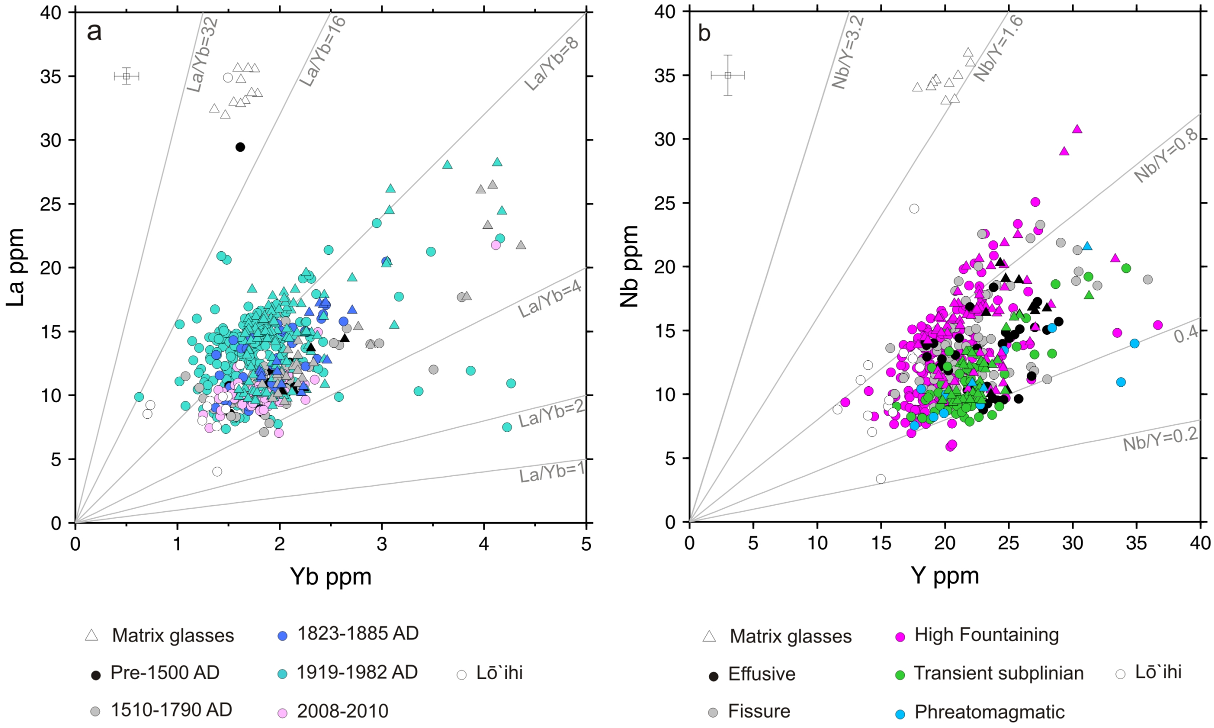

Figure 4.21: (a) Nb versus Yb for the Kīlauea and Lō`ihi melt inclusions and matrix glasses as a function of eruption style; (b) La versus Yb concentrations for the same data as in (a) but grouped by date of eruption. Grey lines define constant ratios of Nb/Y and La/Yb respectively.

at lower overall concentrations, with La/Yb ratios varying by only 35%. Melt inclusions produced during 1919–1982 eruptions have the largest range in trace element abundance and La/Yb (LREE/HREE) varying up to 89% (Figure 4.21b).

Figure 4.22 shows the La/Yb and Nb/Y ratios of the glasses, whole rocks and inclusions as a function of sample age. Similar to the MgO-normalised major element compositions in Figures 4.15 and 4.16 the melt compositions display a systematic variation with time, whereby melts erupted between 1400–1790 AD are relatively uniform in composition but become progressively more enriched between 1790–1959. As with the incompatible major elements, melts from subsequent eruptions between 1961–2010 show a reversal in this compositional trend, with a systematic decrease in La/Yb and Nb/Y to the present day. Once again, the trends are more conspicuous in the glass and whole rock samples (Figure 4.22a and c) than the inclusions which display greater compositional variation within each sample population.

The Lō`ihi multi-element and REE profiles are similar to those of Kīlauea in their overall

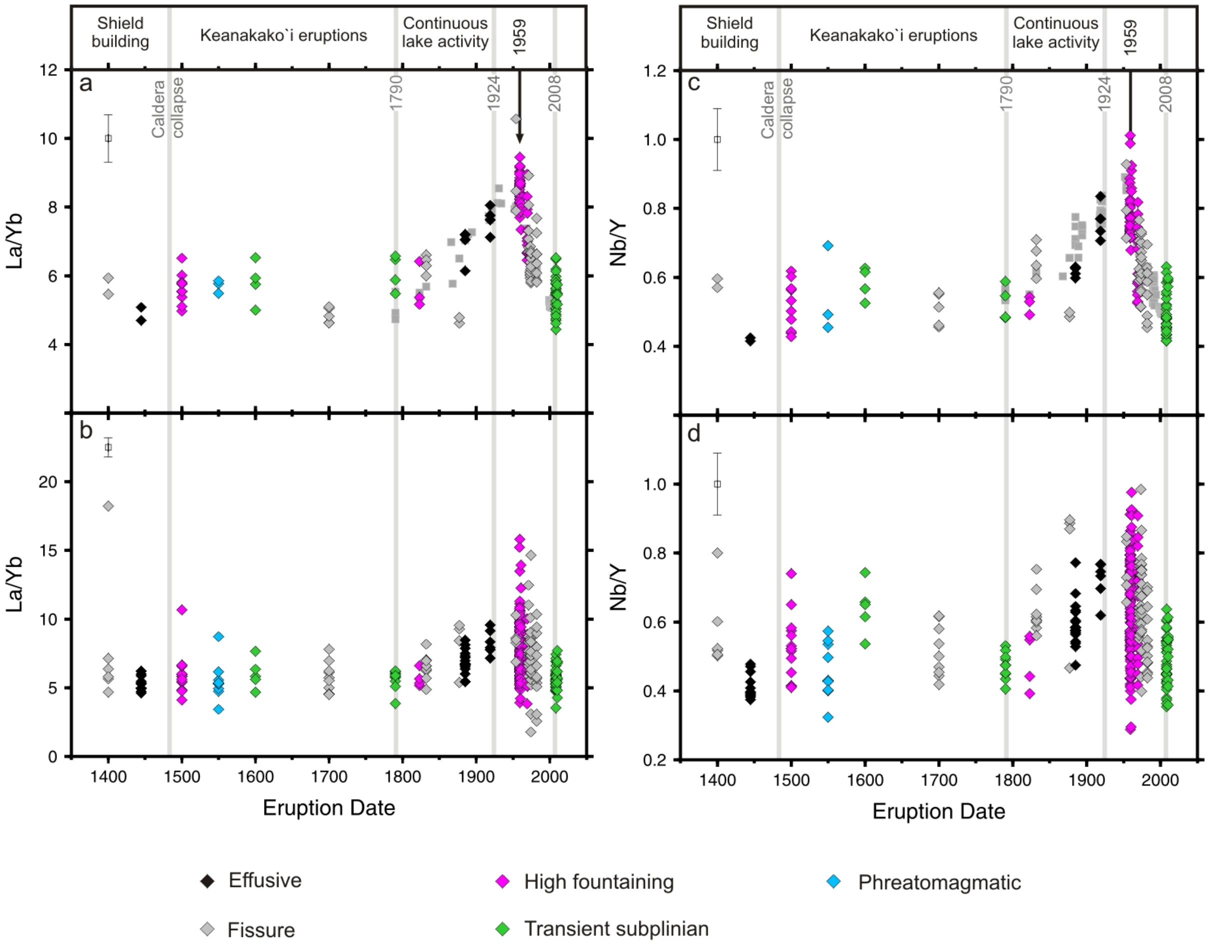

Figure 4.22: Highly to moderately incompatible element ratios for Kīlauea's glass, whole rock and melt inclusion compositions, versus sample eruption date. (a) and (b) are La/Yb ratios of glass, with whole rock data, and melt inclusions respectively. (c) and (d) are the same but for Nb/Y compositions. Whole rock data is reproduced from *Garcia et al.* (1996), *Pietruszka and Garcia* (1999a), *Garcia et al.* (2003) and *Marske et al.* (2008).

patterns of enrichment in LILE and LREE, and depletions in Pb and Sc (Figures 4.19 and 4.20). However the Lō`ihi inclusions display a far greater range in highly incompatible elements and more restricted range of HFSE and HREE concentrations than the Kīlauea samples. In Nb–Y and La–Yb space, the Lō`ihi inclusion compositions lie within the same range as the Kīlauea inclusions but the submarine matrix glasses are highly enriched relative to all other analysed material.

4.2.5 Volatile elements

The H_2O and CO_2 concentrations of all the melt inclusions and matrix glasses analysed are shown in Figure 4.23. Concentrations in the Kīlauea inclusions are highly variable and range from 0.07–0.91 wt% H_2O and from below detection limits to 839 ppm CO_2. These values are in accordance with those of previous studies for Kīlauea and other Hawaiian volcanoes (*Harris and Anderson*, 1983; *Anderson and Brown*, 1993; *Wallace*, 1998; *Hauri*, 2002), although the maximum H_2O concentrations measured in this study exceed the estimate for undegassed Kīlauea melts of *Wallace* (1998). Matrix glass H_2O concentrations vary between 0.02–0.52 wt% and all CO_2 concentrations were below detection limits. If melts are saturated with respect to H_2O and CO_2 concentrations at the time of inclusion entrapment, their melt concentrations can be used to calculate the pressure of inclusion formation (*Dixon*, 1997). Isobars, lines of H_2O–CO_2 compositions at constant pressure were calculated using VolatileCalc (*Newman and Lowenstern*, 2002) and the model of *Dixon* (1997), and are shown in Figure 4.23. The data suggest that all Kīlauea inclusions form at relatively shallow pressures (< 1.5 kbar) during melt storage and crystallisation within the plumbing system of the volcano. However, estimation of formation pressures relies on the assumption that the pre-eruptive melts were saturated at the time of entrapment, which may not be true for all inclusions. Pressure calculations also do not account for the presence of vapour bubbles within the inclusions and consequently the values are treated as minimum pressure estimates only.

The data in Figure 4.23 demonstrate significant differences in the volatile concentrations of pre-eruptive melts from different eruption styles, with the largest range in concentrations within high fountaining and fissure products. Effusive and transient subplinian inclusions generally lie at lower concentations of both H_2O and CO_2 than the majority of other eruption types. The effusive category have a very narrow range of H_2O contents < 0.15 wt% but contain two inclusions with very high CO_2. The few phreatomagmatic inclusions are broadly scattered throughout H_2O–CO_2 space.

The H_2O concentrations of the Lō`ihi melts are more uniform and generally greater than most Kīlauea inclusions, ranging from 0.62–0.77 wt% H_2O. CO_2 varies from below detection to 479 ppm CO_2. The submarine matrix glasses contain between 0.64–0.71 wt%

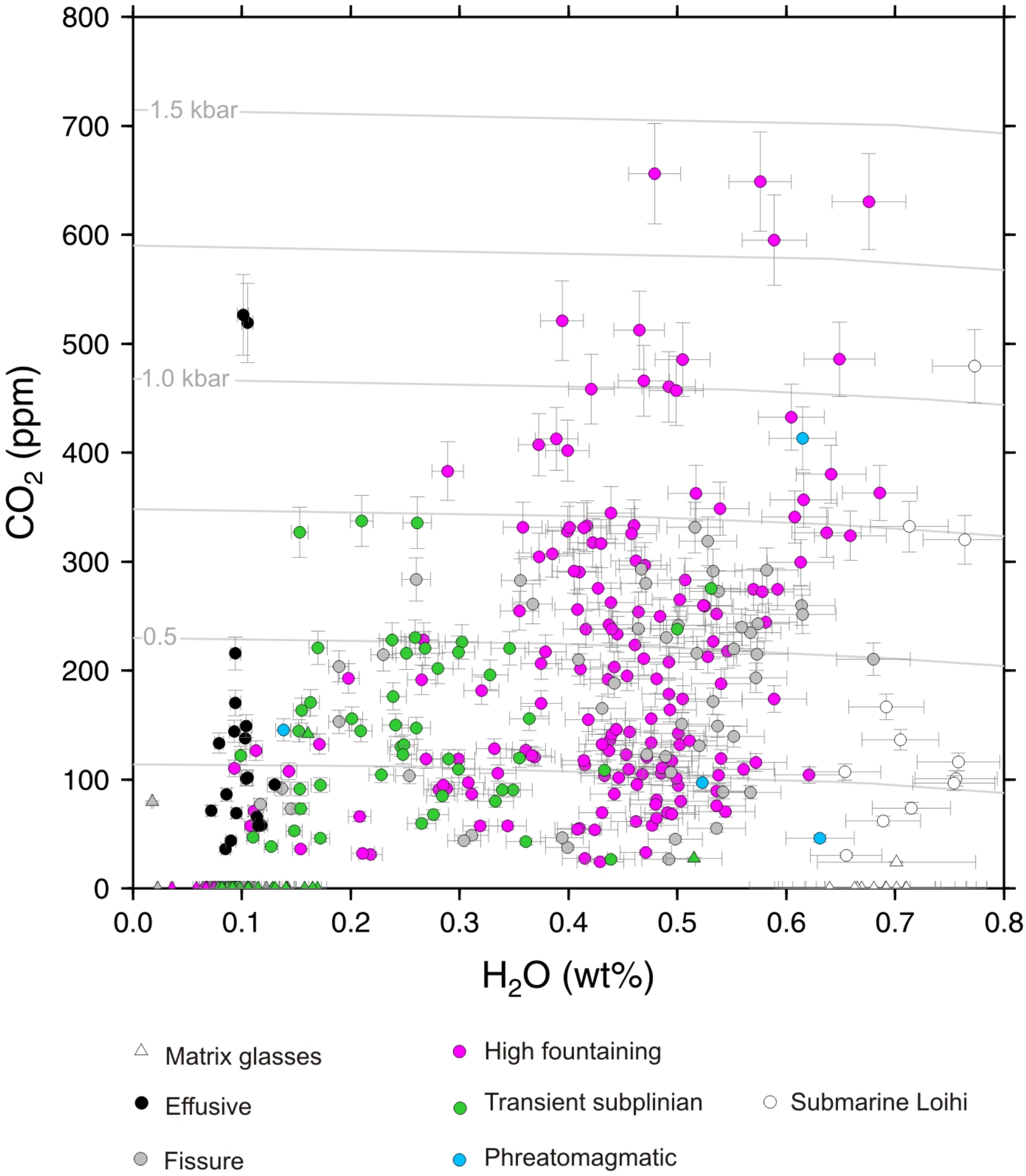

Figure 4.23: Dissolved H_2O and CO_2 concentrations in prehistoric and historical Kīlauea and Lō`ihi melts. Data are presented as a function of eruption style. Grey lines are isobars calculated using the VolatileCalc (*Newman and Lowenstern*, 2002) and the H_2O-CO_2 saturation model of *Dixon* (1997). Calculations performed for melts with 49 wt% SiO_2, at 1100° C. Errors shown are 1σ precision on standard repeats. Note that the maximum H_2O and CO_2 concentrations referred to in the text are not shown in the figure as the corresponding element for each maximum value was not determined.

H_2O, far greater than any of the subaerially erupted Kīlauea glasses although all CO_2 values for Lō`ihi glasses were similarly below detection limits.

Sulphur (S) concentrations within the Kīlauea dataset range between 107–1791 ppm within the inclusions (Figure 4.24), and from 35 ppm to 1459 ppm in the matrix glasses, although the majority of glasses have < 400 ppm S. These S values are similar to those previously reported for subaerial and submarine Kīlauea glasses (e.g. *Swanson and Christiansen*, 1973; *Gerlach and Graeber*, 1985; *Garcia et al.*, 1989; *Dixon et al.*, 1991; *Wallace*, 1998) and those observed in other ocean island basalts (e.g. *Workman et al.* (2006)). Contrary to submarine Kīlauea glasses however, the tephra data show no correlation between S concentrations and other volatile or non-volatile elements (Figure 4.24). While the distribution of data in S–CO_2 space may resemble that in Figure 4.23, there appear to be few significant differences in the S concentrations of melts produced during different eruption behaviours. This implies that the controls on S degassing and S-melt systematics are significantly different to those influencing H_2O and CO_2 concentrations.

Unlike the more enriched H_2O content of the Lō`ihi melt inclusions, S values in the submarine seamount material are comparable to the subaerial Kīlauea samples with melt inclusions concentrations between 789–1329 ppm and a more restricted range of 833–928 ppm in the matrix glasses.

Chlorine (Cl) and fluorine (F) concentrations in the Kīlauea melt inclusions vary from 62–1108 ppm and 176–807 ppm respectively, and from 51–301 ppm Cl and 97–1012 ppm F in the subaerial matrix glasses. The concentration range observed in both the glasses and inclusions exceeds that of halogen concentrations previously recorded in both subaerial and submarine Kīlauea material (*Gerlach and Graeber*, 1985; *Hauri*, 2002; *Edmonds et al.*, 2009) but is comparable with Cl and F concentrations observed in melt inclusions at other Hawaiian volcanoes (*Hauri*, 2002).

The highly variable Cl and F concentrations of the Kīlauea dataset do not demonstrate any significant correlations with non-volatile incompatible elements such as La (Figures 4.25a and b), or with other volatile elements (e.g. H_2O; Figure 4.25c and d). High-fountaining products have the greatest range of Cl and F concentrations, while transient subplinian inclusions tend to cluster at lower values for both elements. However Figure 4.25 demonstrates that the behaviour of Cl and F differs within the melts, as a subset of high-fountaining inclusions are significantly more enriched in Cl relative to F.

MgO-normalised concentrations of F and Cl (Figure 4.26) display similar temporal variations as the incompatible major and trace elements in Figures 4.15, 4.16 and 4.22, although

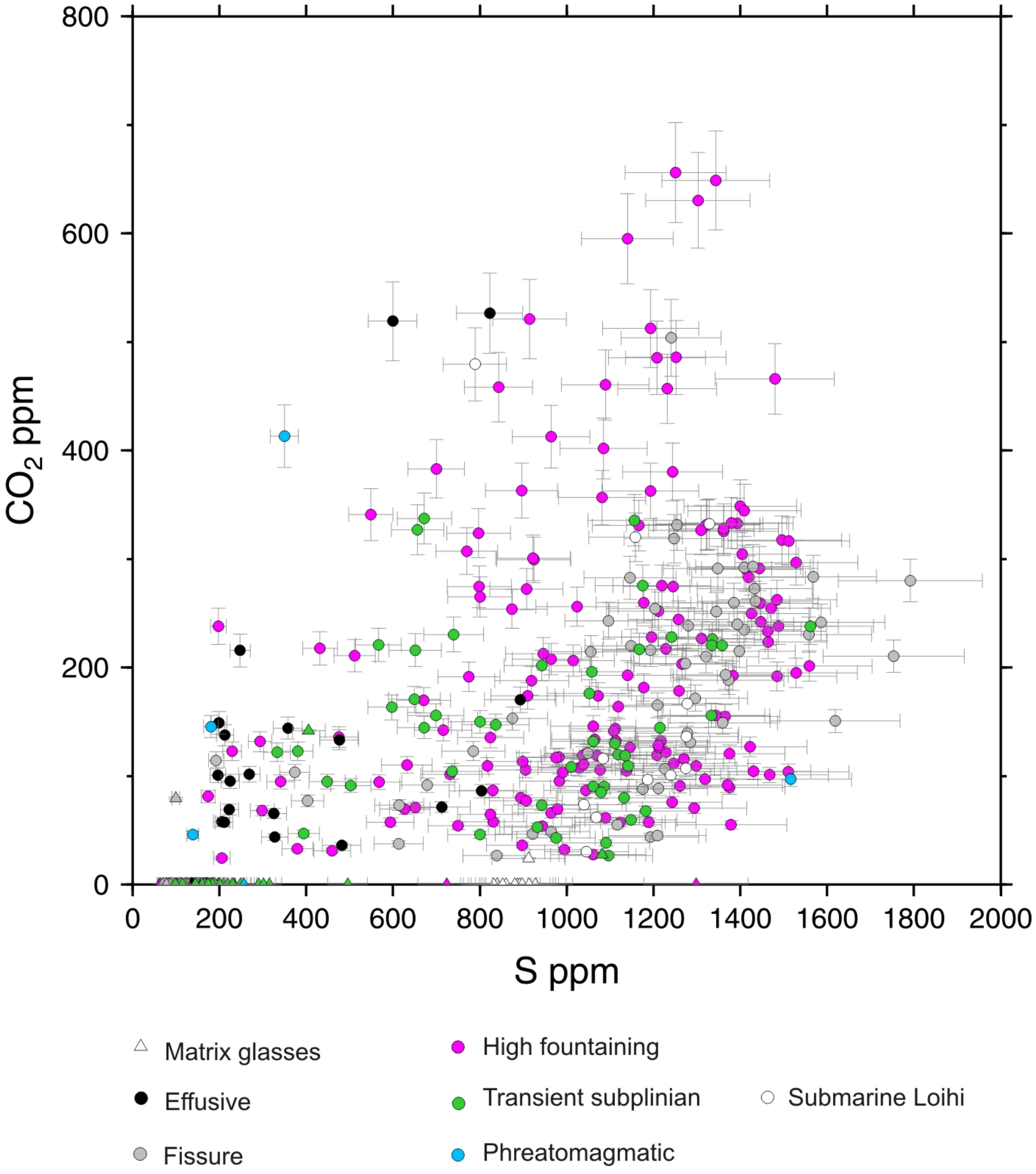

Figure 4.24: S versus CO$_2$ concentrations in Kīlauea and Lō`ihi melt inclusions and glasses as a function of eruption behaviour. Errors shown are 1σ precision on standard repeats.

the trends are less easily distinguished beyond analytical error for many of the eruptive periods. However, the most F- and Cl-enriched melts observed were produced during the mid-20th century and the highest recorded are within the 1959 eruption samples. In contrast to the halogens, MgO-normalised H$_2$O, CO$_2$ and S concentrations display no significant, systematic variations with sample eruption age.

Lō`ihi halogen data is comparable with the Kīlauea material for both inclusions and glasses, with Cl values ranging from 443–480 ppm and 53–533 ppm. The absence of anoma-

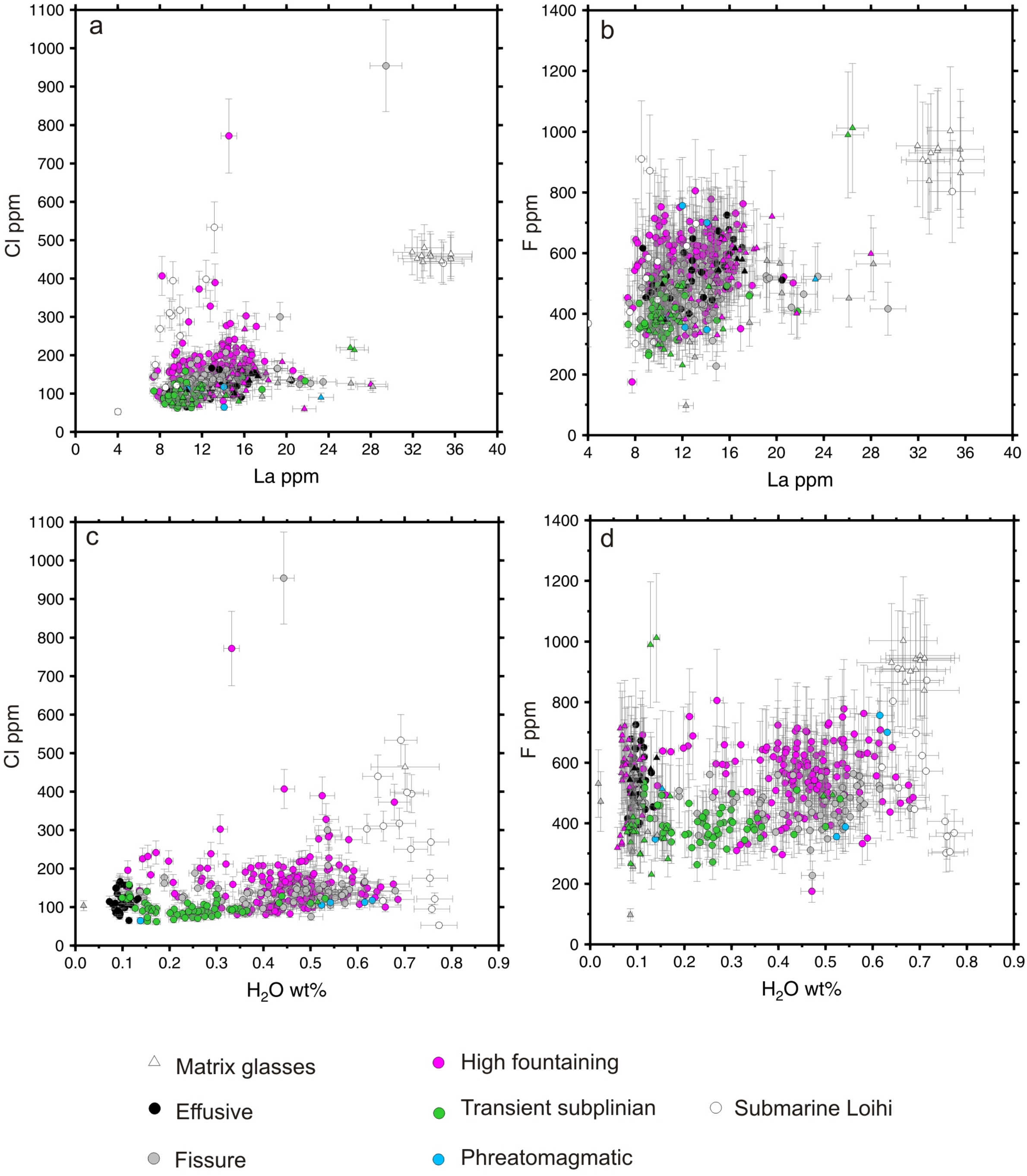

Figure 4.25: Halogen concentrations versus non-volatile and volatile elements in Kīlauea and Lō`ihi melts. (a) Cl versus La; (b) F versus La; (c) Cl versus H_2O; (d) F versus H_2O.

lously high Cl values in the Lō`ihi material confirms that these data are representative of melt compositions and have not been affected by sea water assimilation or alteration pre- or post-eruption. F concentrations vary from 839–1003 ppm in the glasses and 302–910 ppm in the melt inclusions.

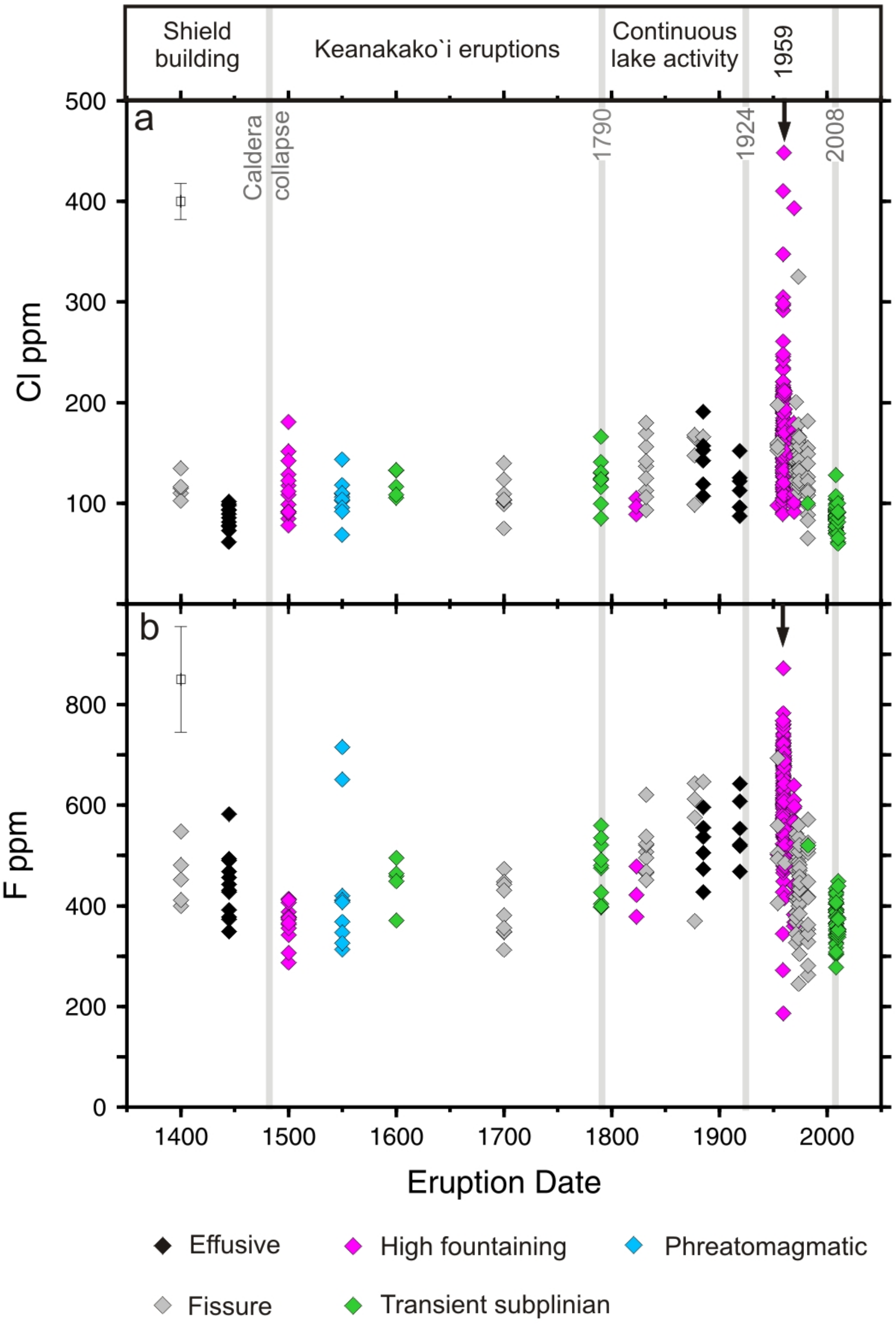

Figure 4.26: Temporal variations in Cl and F concentrations of Kīlauea's prehistoric and historical melt inclusions. Compositions have been normalised to 10 wt% MgO in order to remove the effects of crystal fractionation. Samples are coloured by eruption style. Error bars are representative of 1σ precision on standard repeats.

4.3 Discussion

This discussion will be divided into sections which address first the provenance of the inclusions, followed by examination of the roles of fractionation, melt mixing, and heterogeneity on the chemistry of eruption products. The relationship between melt chemistry, time, eruption style and location will then be considered in detail.

4.3.1 Relationship between melt inclusions and host magmas

As this study relies on melt inclusion data to investigate pre-eruptive processes, it is important to assess the extent to which the inclusions analysed are representative of the volcanic system and melt compositions at the time of the eruptions from which they were sampled. Using melt inclusion compositions to study host magmas requires extrapolation across spatial scales of up to $\sim 10^{10}$ m and may be erroneous if the host crystals are genetically unrelated to the carrier melts, or if processes leading to inclusion entrapment do not produce populations that reflect the melt compositions within the reservoir (*Kent*, 2008). Visual examination of the crystals and inclusions however, do not reveal these potential sources of error.

The poor correlation between the host olivines and their average carrier melt compositions in Figure 4.7 indicates a high degree of crystal-melt disequilibrium for the majority of eruption samples. Disequilibrium between high-Fo olivines and carrier melts can occur if the olivines are xenocrysts formed at deep crustal or mantle depths which have been accidentally transported to the shallow reservoir. However, disequilibrium is not restricted to high-Fo olivines only, but is almost ubiquitous throughout the dataset and a xenocryst explanation is not consistent with the moderate CaO contents (0.18–0.35 wt%) of all Kīlauea and Lō`ihi olivines analysed (Figure 4.8) which suggests they were not formed within the mantle (e.g. *Garcia et al.*, 2003; *Jurewicz and Watson*, 1988). The olivines are therefore interpreted to be antecrysts: crystals formed within the volcanic plumbing system but which are not in chemical equilibrium with their carrier melts at the time of eruption (*Davidson et al.*, 2007; *Maclennan*, 2008b). Disequilibrium is most likely the result of olivine crystallisation occuring concurrently with extensive mixing of variously fractionated melts. However, preservation of chemical disequilibrium requires that the olivines were held in the final carrier melt for a timescale that was short compared with that required for diffusional equilibration (*Maclennan*, 2008b).

While the olivine compositions reveal that they are genetically related to the system in which they were carried, they cannot be used to determine provenance of the melt inclusions. The inclusions analysed display a wider diversity of melt compositions than are represented by the matrix glasses for each eruption (Figure 4.19). Inclusion-bearing magmas represent mixtures of smaller volumes of melt with variable compositions that are present within the melt generation and transport systems (*Kent*, 2008; *Maclennan*, 2008b). Mixing of these melts within the reservoir produces the erupted bulk lava and glass compositions and reduces compositional heterogeneity. If inclusions form prior to or during mixing in the reservoir they therefore are preserving a greater range of compositions, but are these populations reflecting the pre-eruptive variability of melts supplying the specific eruptions from which they were sampled? If each inclusion represents a sample of an equal volume of melt, the mixing of these volumes should produce a bulk (glass) composition equal to the average of the inclusions. This is crudely exemplified in the multi-element profiles for the eruption groups in Figure 4.19, in which the average melt inclusion profiles are very similar to the glass profiles for each group, but this is better tested using the average melt inclusion La/Yb ratios for each eruption versus the La/Yb of the matrix glasses (Figure 4.27). The majority of eruption samples in Figure 4.27 lie within error of the 1:1 correspondence line between glass and melt inclusion concentrations implying that most inclusion populations do reflect the pre-eruptive melt compositions within the magma reservoir and plumbing system prior to each event.

However there are a smaller number of samples which do not fall close to the 1:1 correlation and of these, most belong to high fountaining and fissure eruptions. These may well represent populations which contain unrelated or residual olivine-hosted inclusions from other eruptions, however Figure 4.27 assumes that the carrier melts are the result of complete mixing of melts supplied from depth, all of which should be represented in the inclusion population. While this appears true for many eruptions, it is possible that those melts may have encountered stored magmas of different La/Yb compositions at shallow reservoir depths and incomplete mixing, perhaps during rapid ascent of these fountain-producing melts, could result in heterogeneous carrier glasses or the over/undersampling of magma batches by the inclusion populations. Despite these variations between the glass and inclusion populations,

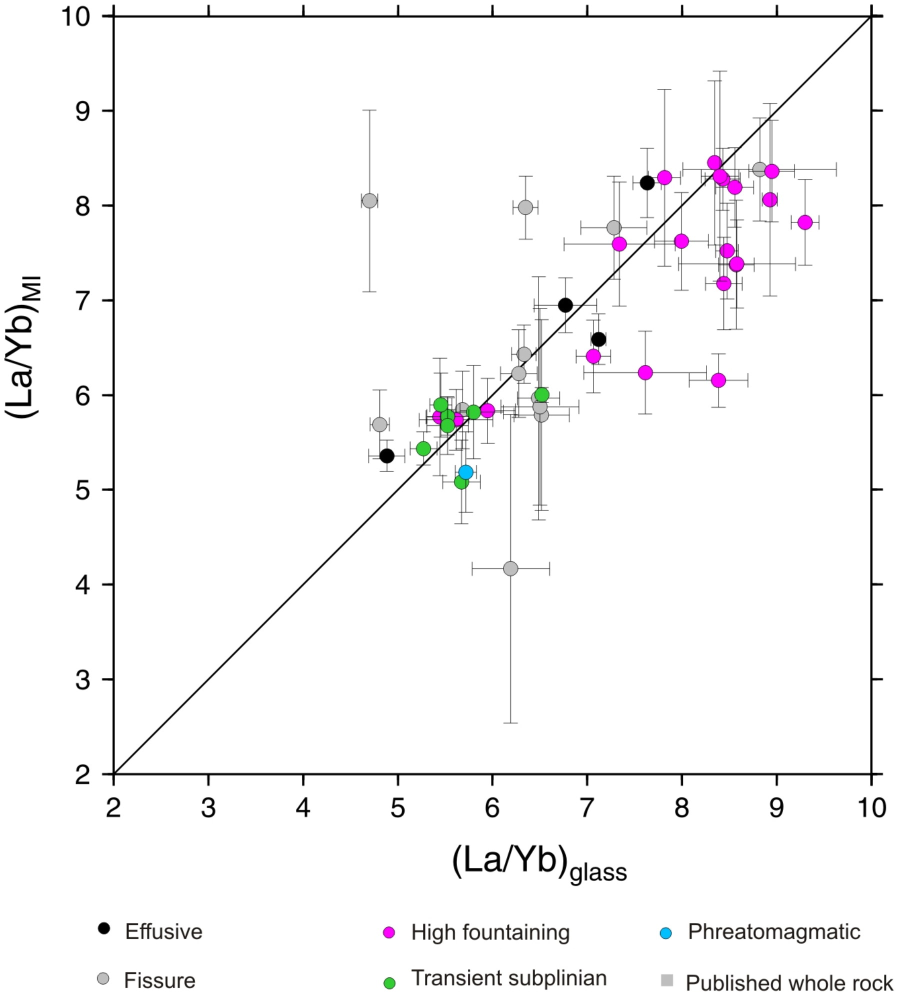

Figure 4.27: Compositional relationship between melt inclusions and host glasses for each prehistoric and historical eruption sampled. Mean La/Yb for melt inclusions (mi) versus mean La/Yb of the host matrix glass (mg). Ratios are calculated as $\sum$La/$\sum$Yb for each eruption population and, because all samples were analysed for La and Yb this average is equivalent to $\overline{La}/\overline{Yb}$. Ratios are calculated in this way because if each inclusion represents a sample of equal volume, mixing should produce a melt with La/Yb equal to $\overline{La}/\overline{Yb}$ of the inclusions (*Maclennan*, 2008b). Error bars represent the 1σ standard error of estimate of the means.

the clustering of all the data close to the 1:1 correlation is a strong indication that the data is largely representative of the eruptions from which they originated. The exception is the Lō`ihi sample which is not shown in Figure 4.27 owing to the extreme disequilibrium between the glass (La/Yb=20.8) and inclusion (La/Yb=8.2) values. The Lō`ihi material was submarine pyroclastic sand which may have mixed after deposition with products produced during different events resulting in the significant difference.

It is possible for melt inclusion compositions to be extensively modified by the post-entrapment process of diffusive re-equilibration of elements between the inclusion, host olivine and carrier melts. Re-equilibration is dependent on the existence of a gradient in concentration between the entrapped melt and the carrier matrix, as well as the temperature, size of the inclusion and olivine, and the diffusivity of the individual element species. Re-equilibration of Fe is discussed in detail in Chapter 2 along with correction procedures employed in this study, but re-equilibration of incompatible element species including CO_2, S, Cl and F are not considered significant post-entrapment processes for these Kīlauea inclusions. Experimental determination of trace element diffusion rates in 1 mm radius natural olivines containing $50\,\mu$ melt inclusions at 1300° C indicate that timescales of REE diffusion range from 10^4 to 10^7 years (*Cherniak*, 2010), much longer than the estimates of transit times for basalt from the mantle source through the crust, and longer than the repose period between the sampled historical eruptions (see Appendix Data Table 1). To date, there is no experimental evidence for diffusive loss of CO_2, Cl, F or S from melt inclusions (*Portnyagin et al.*, 2008; *Metrich and Wallace*, 2008).

One final consideration is whether individual, anomalous inclusion compositions which lie far from the liquid lines of descent (Figure 4.10 and 4.14) represent heterogeneous reservoir melts or are the result of incorporation of boundary layers which form at growing crystal-melt interfaces. Olivine growth rates in basaltic melts are highly variable and dependent on cooling and eruptive history, but melt entrapment typically occurs during periods of significant undercooling and rapid crystallisation at rates of between 10^{-6} to $10^{-9}\,\mathrm{m\,s^{-1}}$ (e.g. *Baker*, 2008; *Welsch et al.*). Olivines growing rapidly with respect to element diffusion in a silicate melt deplete the adjacent melt in compatible elements and enriches in incompatible elements forming a boundary layer (*Kent*, 2008; *Baker*, 2008; *Faure and Schiano*, 2005). Inclusions which trap this boundary layer would be expected to have enrichments in slow diffusing elements such as P_2O_5 (with diffusivity of $10^{-13}\,\mathrm{m\,s^{-1}}$; *Baker*, 2008), which can be seen in the anomalous Kīlauea inclusions (Figure 4.10). However, boundary layer entrapment would also predict enrichment of Al_2O_3 relative to CaO due to the slower diffusion rate of Al_2O_3 in silcate melts (*Liang et al.*, 1996). There is little evidence for large deviations in Al/Ca in the Kīlauea or Lō`ihi inclusions and while large deviations in CaO/Al_2O_3 are observed (Figure 4.10 and 4.13) these are in fact the result of relative CaO enrichment indicative of petrological source variations, such as differences in the degree of mantle melting and the amount of cpx present within the mantle source.

4.3.2 Major and trace element constraints on magmatic processes

Unlike whole rock analyses of lavas, melt inclusion compositions are unaffected by contamination from crystal accumulation and their chemistry records the variety of magmatic processes occuring in the magma reservoir prior to eruption. The high-MgO concentrations of the most primitive PEC-corrected inclusions analysed (up to 14.73 wt%) exceed the typical values for basaltic inclusions, but are comparable with the most MgO-rich glasses recorded from Kīlauea, sampled from submarine sections of the ERZ (15 wt% MgO; *Clague et al.* 1995). As a result, high-MgO inclusions most likely represent compositions closest to that of parental melts supplied from depth.

The broadly negative correlations between MgO concentrations and incompatible major and trace elements in Figures 4.10, 4.17 and 4.18 corroborate the findings of numerous whole rock studies suggesting that fractionation within the summit reservoir is dominantly olivine-controlled (e.g. *Murata and Richter*, 1966a; *Wright*, 1971), with evidence of minor cpx crystallisation occurring within only a few matrix glasses.

These fractionation signatures however overprint significant compositional variations preserved within the melt inclusion populations. The large range of incompatible major and trace element abundances at constant MgO values, as shown in Figures 4.10, 4.18 and within the MgO-normalised temporal plots (4.15 and 4.16) reveal that, while fractionation is an important process within the summit reservoir, batch fractionation of parental melts with a uniform composition cannot account for the variation, which may only be explained if melts entering the reservoir from depth are chemically heterogeneous as a result of variable source composition or changes in the degree of partial melting.

Magma mixing is another inevitable process occurring within the summit reservoirs of all basaltic volcanoes as new melts are continuously supplied from depth. The reduced variability of the matrix glasses compared with the melt inclusion populations for each sample (Figure 4.27) is evidence of melt mixing in the reservoir prior to and during each eruption, but further evidence can be found within the inclusion dataset alone.

Figure 4.28 shows the change in melt inclusion La/Yb variability (ϕ) versus the fosterite content of the olivine hosts. The parameter ϕ is calculated as:

$$\phi = X_{mi} - \bar{X}_e \tag{4.2}$$

where X_{mi} is the La/Yb of the melt inclusion and $\bar{X}_e$ is the average La/Yb for the carrier melt. The ϕ parameter gives the difference between a sample concentration and the average of the eruption that it comes from, therefore enabling comparision between the evolution of compositional variation for a number of different eruptions which all have different average La/Yb ratios. Figure 4.28 shows a decline in the variation of La/Yb (ϕ) over the interval of Fo_{89}–Fo_{78}. The decrease in Fo content of the olivines records progressive cooling and crystallisation of magma batches, while the decrease in the range of ϕ values tracks the degree of compositional homogenisation by mixing. The declining variability at lower Fo values is consistent with concurrent cooling and mixing of melts within the Kīlauea plumbing system. Similar behaviour has been observed in Icelandic melts from multiple localities (*Maclennan*, 2008b) and likely reflects the action of continuous convection within the reservoir both during and between eruptive events.

4.3.3 Parental melt volatile compositions at Kīlauea

One of the primary aims of this study was to investigate the pre-eruptive volatile composition of the melts supplied to Kīlauea over time and to determine whether the parental melts are heterogeneous with respect to their CO_2 and H_2O concentrations. Volatile heterogeneity across the Hawaiian plume has been explored previously by *Dixon and Clague* (2001) in a study of undegassed submarine glasses but to date volatile heterogeneity at a single Hawaiian volcano has not been investigated. Determining parental melt concentrations from subaerial eruption products is particularly challenging owing to the high diffusivity and low solubility of volatiles, especially CO_2, in basaltic magmas. Melts become saturated with respect to CO_2 at great depths (up to ∼40 km; *Gerlach* (1986)), and are thought to enter the summit reservoir at Kīlauea with CO_2 existing as a separate vapour phase (*Gerlach and Graeber*, 1985). H_2O, S, Cl and F have higher solubilities and are lost to a gas phase at shallower

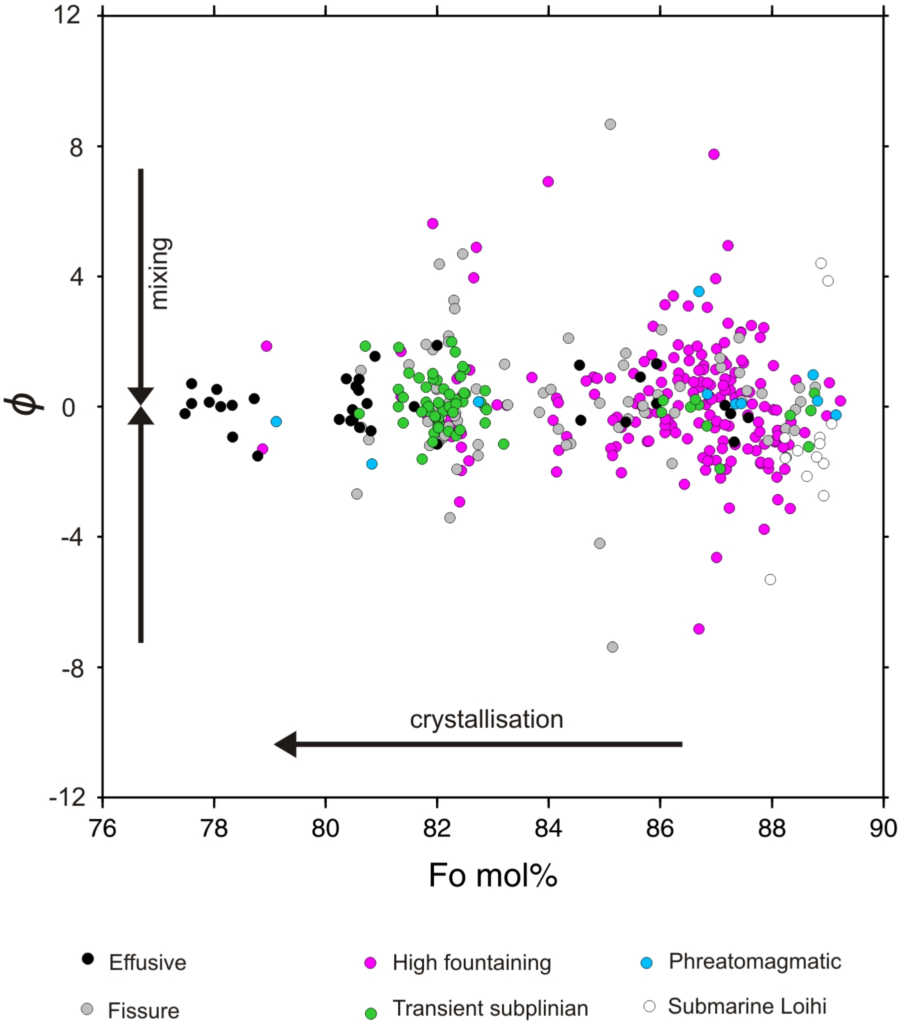

Figure 4.28: Variability of melt inclusion La/Yb ratios (ϕ; see text for details) versus Fo mol% of the host olivines. The decrease in La/Yb variation with decreasing Fo content is evidence for concurrent mixing and homogenisation of melt batches with cooling and crystallisation within the reservoir. Melts supplying effusive and transient subplinian eruptions appear to have undergone greater extents of mixing and fractionation than the pre-eruptive fissure and fountain melts.

depths within the plumbing system and on eruption (*Gerlach and Graeber*, 1985; *Gerlach*, 1986; *Edmonds et al.*, 2009).

In subaerial eruption products, melt inclusions present the only means of preserving primitive undegassed compositions, but the range of inclusion concentrations observed, and the low entrapment pressures calculated from the H_2O-CO_2 data (Figure 4.23) suggest that at the time of entrapment, the melts had already undergone variable amounts of degassing. However, the primitive melt concentrations and the extent of pre-eruptive degassing may be examined with the use of non-volatile trace elements. Volatile elements are highly incompatible during melting/crystallisation and as such, fractionation of an undersaturated melt, prior to volatile loss or enrichment should result in a constant ratio between the volatile element and a non-volatile trace element with a similar partition coefficient. This has been observed in numerous submarine melt inclusion studies, for example undersaturated inclusions from the Siqueiros mid-ocean ridge were found to have a constant CO_2/Nb ratio of 239 ±46 (*Saal et al.*, 2002) and H_2O/Ce ratios of 168 (±8). By comparison, the CO_2/Nb ratios of the Kīlauea melt inclusions range from 2 to only 68 (Figure 4.29a). The range of the ratios and the low maximum of this study indicate that all of the analysed inclusions are saturated with respect to CO_2 and have undergone significant depletion from extensive CO_2-degassing prior to melt entrapment.

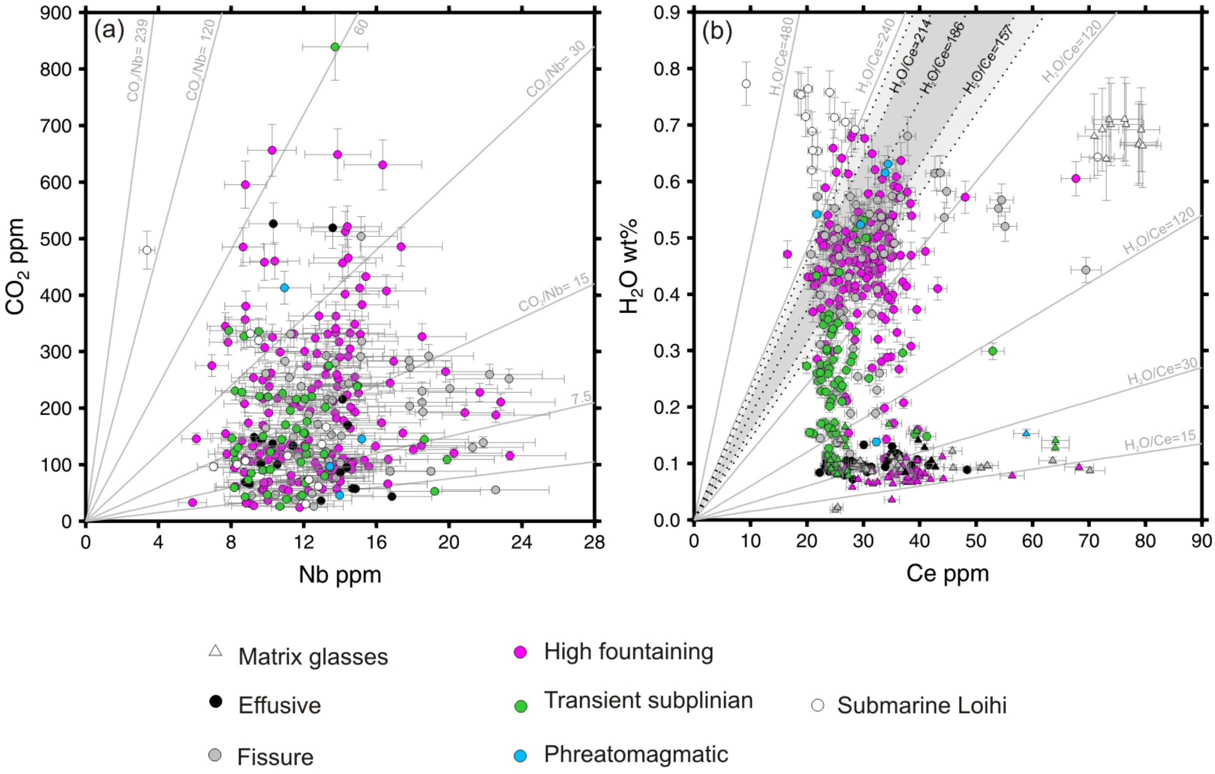

Figure 4.29: (a) CO_2 versus Nb concentrations in Kīlauea and Lō`ihi melt inclusions. Grey lines represent constant ratios of CO_2/Nb; the value of 239 is that of undersaturated MORB glasses of the EPR (*Saal et al.*, 2002). All inclusions lie at low CO_2/Nb ratios owing to significant loss of CO_2 from the melt; (b) H_2O versus Ce concentrations in the Kīlauea and Lō`ihi inclusions, with grey lines of constant $H_2O$/Ce ratios. The dark grey shaded region within black dotted lines represents ratios previously determined for undegassed submarine Hawaiian glasses from *Dixon and Clague* (2001). Ratios of 214, 186 and 157 were determined from analysis of Lō`ihi, Kīlauea and North Arch Volcanics glasses. Light grey envelopes denote the errors on the previously published ratios (8%).

H_2O/Ce ratios range from 18–315, the upper end of which range is far in excess of the MORB inclusion ratios of Siquerios. Previous studies of submarine Hawaiian glasses from Lō`ihi, Kīlauea and the North Arch volcanics have found that H_2O/Ce ratios vary across the Hawaiian plume and range from 157–214, with MgO-rich tholeiitic glasses from the ERZ of Kīlauea containing H_2O/Ce ratios from 182–196. A large proportion (mostly fountain and fissure samples) of the subaerially erupted inclusions have ratios which far exceed those previously recorded (Figure 4.29b) for Kīlauea and Hawaiian basalts, and both the range and higher values of these ratios at > 150 indicate that some of the trapped pre-eruptive melts are both undersaturated with respect to H_2O and may be inherently enriched in H_2O to variable extents. Figure 4.29b also shows that the majority of subplinian transient inclusions appear to show variable depletion of H_2O at relatively constant Ce values and all effusive samples have low and near-constant H_2O/Ce ratios of $\sim$20–30 indicating that the pre-eruptive melts supplying both types of activity have undergone significant H_2O-loss by degassing or diffusive H-loss.

The concept of constant volatile/non-volatile element ratios in undersaturated melts can be used to estimate the volatile concentrations of primitive melts. The ratio of 239 (±46) from the Siqueiros inclusions has been used previously by *Workman et al.* (2006) to estimate concentrations of CO_2 in primitive melts from Vailuluu, Samoa and by *Collins et al.* (2009) for melts from Piton de la Fournaise, Reunion. However, more recent studies have revealed that the CO_2/Nb ratio may vary according to geological setting and mantle source compositions and are likely to extend to much greater values for ocean island basalts (*Cartigny et al.*, 2007; *Hauri*, 2010). No values for CO_2/Nb ratios in undersaturated Hawaiian melts have been reported to date. The submarine Lō`ihi melts, which may have equilibrated in a deeper magma reservoir and were erupted under the increased pressure of $\sim$1 km water depth, might be expected to be undersaturated with respect to $CO_2$, resulting in higher $CO_2$/Nb ratios. However, the Lō`ihi inclusion CO_2/Nb ratios range from 2.5 to 142 (Figure 4.21a) suggesting that like the Kīlauea samples, they have all undergone significant CO_2-loss prior to entrapment. In order to calculate a possible primary CO_2 concentration for these melts, we use a CO_2/Nb ratio of 314 (±125), reported in undersaturated Icelandic melt inclusions (*Hauri et al.*, 2002b). The ratio is a suitable estimate for ocean island basalts as the maximum CO_2/Nb ratio reported for inclusions from the Galapagos islands are 350

(*Koleszar et al.*, 2009), within error of the Icelandic ratio.

Before calculating the primitive volatile concentrations, the melt inclusion compositions were normalised to 15 wt% MgO using the reverse fractional crystallisation simulation of PETROLOG 3.1 (*Danyushevsky and Plechov*, 2011) by incremental addition of olivine to the melt compositions. Normalisation removes the effects of fractionation on the trace element concentrations within the melts such that any remaining variation reflects differences inherited from the mantle source or degree of melting. The calculations indicate that primitive Kīlauea melt CO_2 concentrations have varied between 0.17 (±0.07) to 0.68 (±0.27) wt% over the past five hundred years. Despite the errors associated with using an Icelandic CO_2/Nb ratio, the maximum estimates of CO_2 concentrations from the inclusion compositions are remarkably similar to estimates for primary Kīlauea melts produced by other methods, including those calculated from magma supply rate and surface gas flux measurements (0.7 wt%; *Gerlach et al.* 2002).

Primitive melt H_2O concentrations are calculated using a similar method. Ce concentrations are normalised to 15 wt% MgO, but rather than using a literature value for H_2O/Ce ratios, an average of H_2O/Ce ratios from this study which are > 150 (average $= 186 \pm 30$; Figure 4.29b) may be used instead as these are the least affected by degassing and H_2O-loss. Calculations suggest that H_2O concentrations in melts supplying Kīlauea over the eruptive period have varied from 0.28 (±0.05) to 0.87 (±0.15) wt%, which is far more variable than the uniform 0.39 wt% H_2O estimated previously for primary Kīlauea melts with 15 wt% MgO (*Clague et al.*, 1995; *Wallace*, 1998).

Calculating primary melt concentrations of other volatile species such as S is complicated as S solubility is strongly dependent on melt temperature, oxygen fugacity, S fugacity, bulk composition (particularly the FeO content of the melts) and pressure. The presence of immiscible sulphide globules in several samples (Figure 4.6) suggests that a number of the melts are sulphide-saturated which, in addition to degassing, may act to decouple the S concentrations from a similarly incompatible non-volatile element. Formation of immiscible sulphides can decrease the S concentration of the melts, and at low pressures, breakdown of sulphide globules may also buffer melt concentrations during degassing. Undersaturated Siqueiros ratios of S/Dy observed by *Saal et al.* (2002) were 225 (±49), and those analysed from Fernandina and Santiago islands above the Galapagos plume, are 250 and 200 respectively (*Workman et al.*, 2006). However, S/Dy ratios for the Kīlauea inclusions range from 40–869 and average 420 (±183), a factor of 2 greater than observed at other locations. If the ratio of 225 (±49) is used, the primary melt S concentrations for Kīlauea range from 596 (±129) to 2003 (±436) ppm. This is consistent with estimates for other ocean island basalts (*Wallace and Carmichael*, 1992; *Dixon and Clague*, 2001).

Cl and F have significantly higher solubilities than other volatile elements and the overlap between melt inclusion and matrix glass concentrations in both elements shows that there is little obvious loss prior to or during eruption, consistent with inefficient halogen degassing from H_2O-poor basaltic melts (*Edmonds et al.*, 2009). Cl and F concentrations in the Kīlauea melts are estimated using Cl/K and F/Nd ratios. Average Cl/K ratios for OIBs are reported at 0.04 (*Stroncik and Haase*, 2004; *Koleszar et al.*, 2009) and 21 for F/Nd (*Workman et al.*, 2006). The average ratios from this study and used in the calculations are 0.03 ±0.02 Cl/K and 26 ±7 F/Nd and produce primary melt estimates of 62 (±29)–290 (±132) ppm and 291 (±75)–1075 (±277) respectively. The lack of significant halogen degassing, together with the preservation of temporal variation in F and Cl concentrations (Figure 4.26) which mimic the trends observed for other non-volatile trace elements, is strong evidence that the heterogeneity in the primary melt volatile concentrations is genuine and inherited from changes in the mantle source composition or degree of melting, over time.

4.3.4 Volatile geochemistry, degassing and eruption styles

Whilst it has been demonstrated that pre-eruptive melts supplying Kīlauea are heterogeneous with respect to their major, trace and volatile compositions, the question remains as to whether these chemical differences impact on eruption dynamics observed at the surface. This is investigated by dividing the inclusion and glass chemistry into groups according to eruption type, determined from the observation of the eruption behaviour and/or from the morphology of the eruption products. Collection of material and characterisation of samples inevitably introduces error through subjective selection but every care was taken to be consistent in assignment methods, and decisions on eruption classes for each sample were made in discussion and agreement with others (D. Swanson, B. Houghton and M. Edmonds). Although binning the compositional data into eruption categories is a gross oversimplification of processes operating during each individual event which may be very variable in behaviour from start to finish, it is clear from the results that significant differences do exist between the pre-eruptive chemistry of melts supplying different eruption types.

The data plots in the results section of this chapter illustrate that inclusions from all eruption styles span a broad range of compositions, but the distribution of data appears to differ for each group. The pre-eruptive melts of high Hawaiian fountaining and fissure eruptions have the greatest variation in major, trace and volatile element concentrations and also have most enriched concentrations of LREE/HREE, LILE/HFSE (Figure 4.21), MgO (Figure 4.10), CO_2, H_2O (Figure 4.23), S (Figure 4.24), Cl and F (Figure 4.25). Conversely, effusive and transient subplinian explosive inclusion compositions appear to cluster at low MgO and volatile concentrations; they are least enriched in incompatible elements and also display more restricted compositional variation. The phreatomagmatic inclusions are highly variable and do not apear to follow any consistent compositional trends. This may be due to the limited number of inclusions in this group which are all from a single eruption sample (sample 1550). The material was collected from an ash and lapilli bed and olivine crystals were loose within the deposit. While the deposit appeared undisturbed it is possible that some of the crystals may have originated from other events.

Owing to the broad range of volatile concentrations and the non-normal distribution of melt compositions within each eruption category, determining whether the apparent differences between eruption groups are significant is challenging. The Kolmogorov-Smirnov (KS) test is a non-parametric (distribution-independent) statistical test which provides a means of examining the difference between the melt inclusion populations. The analyses in each eruption group are plotted together as cumulative histograms (Figure 4.30),where the number of analyses are scaled so their cumulative sums are 100 and each step in the plots corresponds to a data point. Plotting the data in this way removes any bias resulting from different numbers of analyses in each group and allows comparison of the distribution of data in each population. For example, in Figure 4.30a, the histogram for CO_2 concentrations shows that 85% of the effusive inclusion population have CO_2 concentrations < 200 ppm, whereas only 55% of the high-Hawaiian fountain population have < 200 ppm CO_2. The KS test uses the maximum offset in cumulative % at a given concentration in order to ascertain if sets of melt inclusions are drawn from the same underlying population. The greatest absolute difference between the plotted samples is the KS statistic. This is demonstrated in Figure 4.31 (a simplified version of Figure 4.30a) in which the only the distributions of CO_2 in the effusive and high-Hawaiian fountain melt inclusions are shown. The KS statistic, D is equal to 0.355 or 35.5%, which is the maximum difference between the two groups. The P-value for the this KS statistic is 0.021. P-values report how significant the difference is, and when P is small (by convention, < 0.05) as it is in this example, the null hypothesis (that there is no difference between the populations) can be rejected at the $> 95\%$ confidence level.

The resulting cumulative histograms (Figure 4.30) allow visual comparison between all of the groups and KS statistics confirm that different eruption styles at Kīlauea are associated with significantly different pre-eruptive melt volatile signatures, with more than 95% certainty that each group is sampling different underlying populations. While the spread of melt inclusion concentrations are comparable between eruption groups, the histograms highlight the shifts between the distributions. Hawaiian high-fountain and to a lesser extent fissure eruption populations, have distributions with higher preserved concentrations of CO_2 and H_2O (Figure 4.30) than those inclusions from either effusive activity or transient subplinian explosions. High-fountain and fissure eruption melts at Kīlauea are also significantly and inherently more enriched in highly incompatible LREE and LILE abundances than melts supplying any other eruption types. This greater Nb/Y and La/Y abundance implies that the primary melts supplying fountain and fissure eruptions from depth would also be more volatile-rich. Melt inclusions in the Hawaiian high-fountain category, which includes products from earliest Keanakakoʻi eruption ca. 1500, the 1820-1823 Golden Pumice, Kīlauea Iki eruption in 1959, Kapoho in 1960 and Mauna Ulu in 1969, are hosted in the most Fo-rich olivine populations at Kīlauea, indicating that their pre-eruptive melts are more primitive than those of other styles including the fissure events.

4.3.4.1 Volatile systematics and shallow magmatic processes

Although it has already been established that the measured volatile concentrations represent melts which have undergone variable extents of degassing, the distribution of inclusion compositions in H_2O-CO_2 space (Figure 4.23) reveals that melts supplying the different groups are not only compositionally different but undergo different processes at shallow depths

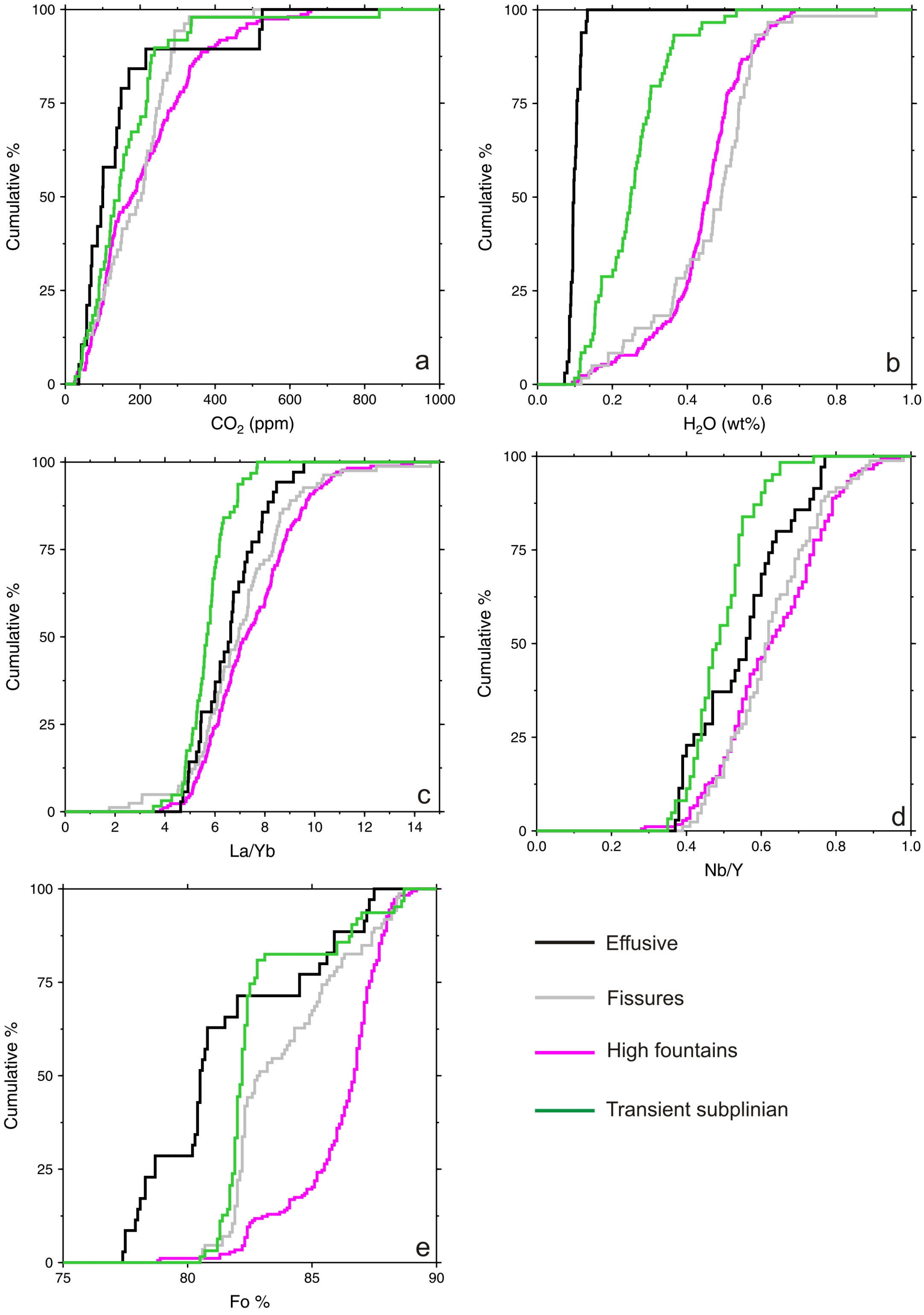

Figure 4.30: Cumulative histograms to show the comparison between melt inclusion populations produced during different eruption styles using the Kolmogorov-Smirnov test. The cumulative % refers to the number of inclusions analysed for (a) CO_2, (b) H_2O, (c) La/Yb, (d) Nb/Y and (e) Fo mol% of the host olivines.

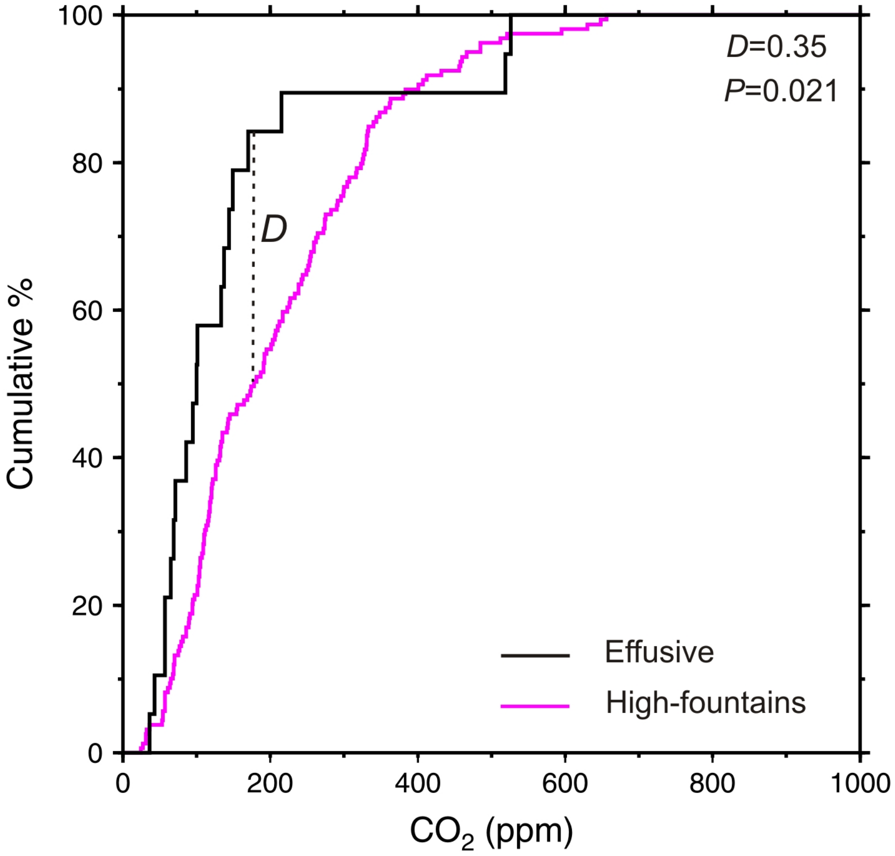

Figure 4.31: Cumulative histogram for CO_2 concentrations in the effusive and high-Hawaiian fountain inclusion populations. The maximum difference between the two distributions at a fixed CO_2 concentration is the KS statistic, *D*. Here *D* is equal to 0.355 or 35.5% with a *P*-value of 0.021. The closer the *p*-value to zero, the more significant the difference between the two populations.

within the plumbing system of the volcano. Saturation pressures for the melt inclusions cover a broad range between < 0.1–1.5 kbar and inclusions from the high fountaining eruptions indicate that crystallisation and melt entrapment occurred at higher pressures (up to ca. 1.5 kbar) than most of the effusive, transient or fissure eruptions (mostly < 0.7 kbar).

H_2O concentrations in the inclusions are expected to be highly influenced by diffusive re-equilibration during magma storage and the low H_2O contents of the effusive and subplinian eruption samples may to some extent reflect diffusive H-loss through the olivine crystal during equilibration with the host melt at low pressures, during eruption within the lava flows or within the convecting magma column (2008-10 eruption; Figure 3.6). However, there is no evidence that S and CO_2 are affected by diffusion out of the host crystal in the same way (*Portnyagin et al.*, 2008). S in particular has been shown to exolve at shallow pressures in tandem with H_2O exsolution (e.g. *Gerlach*, 1986; *Wallace and Carmichael*, 1992; *Dixon and Clague*, 2001) and many of the low-H_2O effusive and subplinian inclusions also demonstrate low S concentrations (Figure 4.24), suggesting that degassing, rather than diffusive H-loss is responsible for many of the low H_2O concentrations.

Variable extents of magma mixing within the summit reservoir and degassing of melts with heterogeneous primary volatile concentrations may explain the spread of melt inclusion compositions in H_2O-CO_2 space, however many of the H_2O- and S-poor inclusions have CO_2 concentrations greater than predicted by CO_2 solubility models (*Dixon and Stolper*, 1995). Mixing between degassed and volatile-rich primitive undegassed magmas would result in sub-populations of high CO_2/H_2O inclusions trapped in high Fo-olivines which are not observed in these samples. Instead, the greater than expected CO_2 concentrations may be explained if melts stored at shallow depths within the reservoir are subjected to pre-eruptive CO_2-rich gas flushing. Gas-flushing is a predominant process at many basaltic volcanoes (e.g. Etna; *Spilliaert et al.*, 2006; *Collins et al.*, 2009, and Jorullo; *Johnson et al.*, 2008) in which excess CO_2-rich vapour segregates from ascending melts at depth to interact with magmas stored within the reservoir, resulting in isobaric dehydration of these melts (*Blundy and Cashman*, 2008).

The greater saturation pressures observed for the high-fountain inclusions, together with the preservation of higher volatile concentrations records the evolution of melts undergoing rapid ascent from depth and indicates that prior to eruption, most of these magmas equilibrated at greater pressures within the summit magma reservoir. The more primitive, enriched and heterogeneous compositions of these melts suggests they experienced a shorter storage time with limited fractionation and mixing with more evolved melts (e.g. Figure 4.28). Their inherently enriched trace and volatile compositions would result in saturation of the melt at greater depths and the early onset of vapour exsolution may provide the buoyancy needed to overcome any density stratification present in the magma reservoir (*Anderson and Brown*, 1993; *Anderson*, 1995), facilitating rapid ascent and the production of high fountains at the surface. The majority of high-fountaining events have occurred outside of the current caldera suggesting that these rapidly ascending melts may by-pass the main summit reservoir, thus avoiding significant pre-eruptive mixing and degassing.

Low-fountaining fissure eruptions, many of which have frequently taken place within the caldera, close to the magma reservoir footprint, represent an intermediate eruption type: they are generated from inherently volatile-rich melts that have been stored for slightly longer times at shallow depths, undergoing greater fractionation with hybrid magmas in the summit, but still have enough vapour associated with them to be more buoyant and erupt in pyroclastic fashion.

In contrast, melts supplying both the subplinian explosive eruptions and the effusive lavas have been gas-flushed to a much greater extent and under open system conditions. The pre-eruptive loss of volatiles from the melts decreases magma buoyancy and prevents extensive magma fragmentation through bubble development and growth on ascent. The evolved compositions of these melts indicate prolonged storage and mixing at shallow levels (< 0.5 kbar) within the summit reservoir. These results are consistent with observations of continuous high fluxes of CO_2 gas at the summit (>8000 t/d; *Gerlach et al.*, 2002), which requires sustained percolation of CO_2-rich bubbles through melts stored at shallow depths beneath the summit, resulting in extensive dehydration and crystallisation. The degassed nature of the melts supplying the transient explosive eruptions is consistent with observations that these events are most likely triggered by external influences such as conduit wall-rock collapse (*Houghton et al.*, 2011) or decompression degassing (*Poland et al.*, 2009). These shallow magmatic processes are summarised in Figure 4.32.

4.3.5 Temporal variations in pre-eruptive melt compositions

That primary melts supplying different eruption styles at Kīlauea are compositionally heterogeneous and undergo different shallow magmatic processes is already clear. However, the results section of this chapter also reveal that when grouped by eruption date, the melt inclusions and glasses record distinctive temporal variations. Grouping of the data by eruption age was more challenging and a more subjective process than for eruption styles, but divisions were decided on the basis of cessations in long periods of continuous activity (e.g. the end of the `Ailā`au eruption prior to caldera formation, and the end of the Keanakakoʻi eruptive period). In addition to these categories, divisions were also made based on those defined by previous workers (*Pietruszka and Garcia*, 1999a; *Garcia et al.*, 2003).

In MgO-normalised temporal plots, melt compositions throughout the early 19th to mid-20th Centuries appear to become progressively more varied and enriched in highly incompatible elements (Figures 4.22 and 4.26), but the trends reverse during the mid-20th Century and subsequent melts display a progressive decrease in LREE/HREE and LILE/HFSE ratios back to compositions reminicient of pre-caldera erupted melts in the late 15th Century. However, as with the plots coded for eruption style, the MgO-normalised figures expose the large compositional variations within each group and consequently the same statistical approach is used here for examining the differences between the groups.

Figure 4.33 shows the cumulative histograms for each of the date categories. It is clear that the 20th Century melts erupted between 1919–1982 have compositional distributions that are more primitive, far more enriched in highly incompatible elements and preserve much higher volatile concentrations than eruptions during any other period. The pre-1500 AD and 21st century melts are compositionally more alike with no statistical difference in their La/Yb ratios. These eruptions are volatile poor and significantly more evolved than those produced during the intermediate periods. The Keanakakoʻi melts erupted between 1510–1790 AD preserve greater H_2O concentrations, than the majority of eruptive episodes but are compositionally similar to the pre-1500 and 21st century with respect to their trace element ratios. The 19th century melts have an intermediate La/Yb and Nb/Y signature but are volatile-poor.

Temporal fluctuations in Kīlauea melts have previously been explored in detail through whole rock studies by *Tilling et al.* (1987), *Pietruszka and Garcia* (1999a), and *Garcia et al.* (2003). The temporal data observed in Figure 4.33 and in the MgO-normalised plots of this study are comparable with the trends observed in these earlier studies. In addition to major and trace element analyses *Pietruszka and Garcia* (1999a) measured Pb, Sr and Nd isotopes and observed similar systematic changes in composition over time. The co-ordinated isotopic and trace element ratio changes have been used to suggest that the source region for Kīlauea is isotopically and chemically heterogeneous, with source variations explained by melting of small-scale heterogeneities within the Hawaiian plume. The isotopic data was further used to model variations in the degree of partial melting for a heterogeneous source, and calculations suggest the degree of melting decreased by a factor of 2, from the early 19th–mid-20th century, correlating with a period of lower eruption and magma supply rate. Subsequently, the degree of partial melting and eruption rate were shown to have increased between the mid to late-20th century. The pre-eruptive inclusion compositions shown here correlate extremely well with the whole rock trends, suggesting that parental melts supplying the volcano do reflect source and melting variations.

It is interesting to note, that the distributions of melt inclusion compositions in Figure 4.33 are very similar to those shown in the eruption style histograms of Figure 4.30 such that most of the enriched high-fountaining events sampled, occurred during the 20th century, many of the intermediate-enriched fissure products collected were formed during the 19th and 20th century and all of the 21st century eruptions were volatile-poor, compositionally more evolved transient subplinian events. However it is important to consider that not all high-fountaining eruptions occurred within the 20th century, and others such as the reticulite-producing (sample 1500) fountains which occurred immediately after caldera formation in ~1510 AD may not be as compositionally enriched as a fissure produced during the 20th century. It has not been possible to investigate compositional differences between all of the individual eruptions sampled here and while each sample most likely records a complex history of process and source variations on short time-scales, the overall populations define distinct chemical trends which suggest that eruptive styles at Kīlauea are dictated not only by tectonic structures and shallow magmatic processes but also by changes in the composition and degree of melting of the mantle source on the time-scales of years to decades.

At the beginning of this chapter, the structural control on eruptive behaviour at Kīlauea was discussed in relation to the model of *Holcomb* (1987) (Figure 3.7) which described the long-term changes in activity in relation to cycles of caldera formation. The formation of the current caldera in 1500 AD was preceded by the `Ailā`au eruption, a large-volume, effusive event which continued for at least 50 years. A recent study of the Keanakakoʻi tephra and the caldera formation in 1500 AD suggests that understanding the causes of caldera formation may be of greater relevance than might first appear, given that the ongoing Pu`u `Ō`ō eruption at Kīlauea is currently in its 30th year, already half the duration of the `Ailā`au eruption, and summit subsidence recorded during the first 20 years of activity produced a 2 m drop in the caldera floor by 2004 (*Swanson et al.*, 2012a). This could be interpreted as sagging above an emptying reservoir. While it appears that the controls on such activty are structural and determined by factors such as magma supply rate, the results of this study indicate that the most recent 21st century melts erupted from Kīlauea are in fact identical statistically in trace element compositions to those erupted just prior to caldera formation. This raises an intriguing question of whether the chemistry of parental melts at Kīlauea influences cycles of caldera formation or may be used in conjunction with geophysical data to forecast such events.

4.3.6 Summary

This chapter presents the first detailed study of major, trace and volatile element compositions of pre- and syn-eruptive melts from Kīlauea volcano. The results have been used to examine the roles of fractionation, melt mixing and heterogeneity on the chemistry of eruption products and to investigate the relationship between melt composition, time and eruption style.

- Melt inclusions from prehistoric and historical eruptions record evidence of concurrent cooling, fractionation and magma mixing within the summit reservoir during and between eruptive events. These fractionation and mixing signatures overprint existing compositional variation which may only be explained as chemical heterogeneity inherited from a compositionally variable mantle source region and/or changes in the degree of melting.

- Parental melts supplying Kīlauea over time are heterogeneous with respect to their volatile contents. Estimates of primary melt CO_2, H_2O and S concentrations suggest they have varied between 0.17–0.68 wt%, 0.28–0.87 wt% and 596–2003 ppm repectively, over a 500 year period. These values are consistent with previous estimates for Kīlauea and other OIBs. Cl and F primary melt concentrations have varied between 62–290 and 291–1075 ppm respectively.

- Significant differences exist between the pre-eruptive chemistry of melts supplying different eruption styles at Kīlauea. Pre-eruptive melts supplying high-Hawaiian fountains and fissures are inherently more primitive and enriched in LREEs, LILEs and volatiles, whereas effusive and transient subplinian melts are more evolved and volatile-depleted.

- Melts supplying different eruption types also undergo shallow pre-eruptive processes to different extents. Effusive and subplinian melts appear to have been stored for greater periods within the summit reservoir prior to eruption, experiencing more extensive fractionation, homogenisation by mixing, degassing and gas flushing with a CO_2-rich vapour originating from greater depths within the plumbing system. High-fountaining and to a lesser extent fissure melts, generally equilibrate at greater depths within the magma reservoir or are stored within the system, for much shorter periods, therefore undergoing less extensive pre-eruptive degassing and fractionation. Their inherently more volatile-enriched compositions likely enables the melts to become buoyant enough to overcome density stratification within the convecting reservoir, facilitating rapid ascent to the surface and pyroclastic eruption.
- The Kīlauea inclusion compositions preserve a record of progressive changes in pre-eruptive melt chemistry over time. The changes correlate with temporal trends in trace and isotopic whole rock data of previous studies and reflect changes in the source composition and degree of melting over the past 500 years, with a decrease in the extent of partial melting of the source region between the 19th–mid-20th century with an abrupt reversal of the trend after 1959.

The results of this chapter illustrate that eruption styles at Kīlauea are strongly related to and perhaps even dictated by, the chemistry of melts supplied from depth. These in turn are subject to the temporal changes in mantle source composition and degree of partial melting. Shallow magmatic processes such as fractionation, magma mixing degassing and gas flushing, as well as structural features of the plumbing system are nonetheless crucial in determining how eruptions proceed when the parental melts reach shallow crustal depths. Investigation of pre-eruptive historical melt chemistry provides useful insight into both long and short-term controls on eruptive behaviour and further study of melt chemistry at Kīlauea and other basaltic volcanic centres may be invaluable for predicting major changes in eruptive behaviour when used in conjunction with geophysical and surface gas geochemical data.

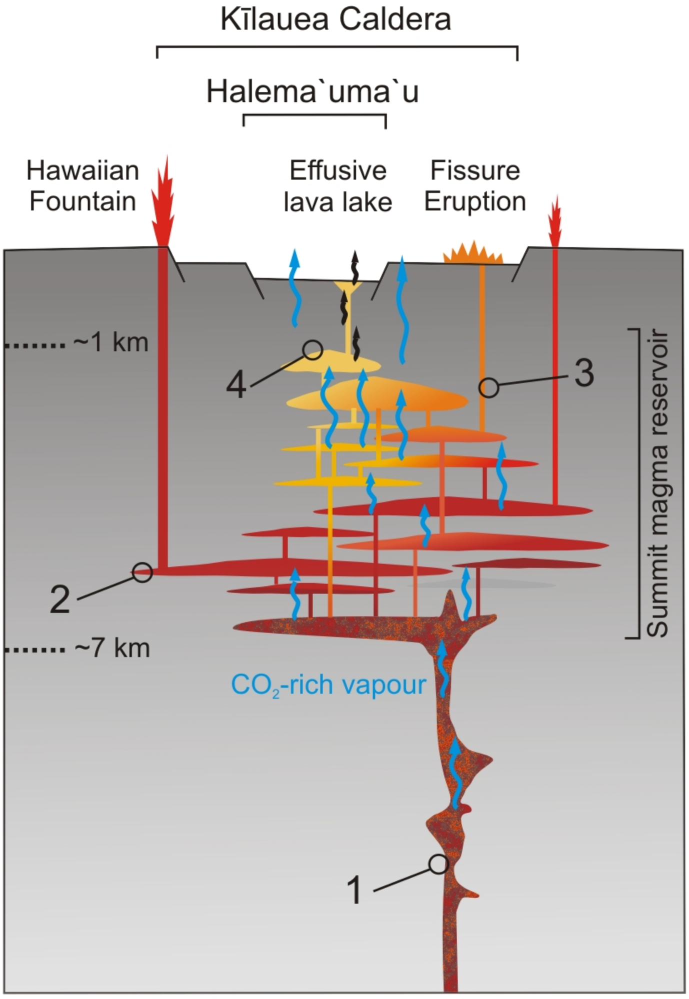

Figure 4.32: Schematic view of the magmatic plumbing system beneath the summit of Kīlauea and the influence of magma storage depths and gas flushing on producing different styles of eruption. (1) Primitive, heterogeneous melts (dark red + orange) arrive at the base of the summit storage region at ~7 km depth (*Tilling and Dvorak*, 1993), and is saturated with respect to CO_2, which exists as a separate vapour phase (blue) (*Gerlach and Graeber*, 1985); (2) volatile-enriched melts (red) undergo relatively rapid crystallization and exsolution at greater pressures, preserving higher melt CO_2-H_2O concentrations and more primitive melt compositions. At these higher pressures the melts may be able to retain a greater proportion of their associated exsolved vapour, undergoing rapid ascent towards the surface, under closed system degassing conditions, and producing high-fountain eruptions. (3) Fissure eruptions are fed by volatile-rich magmas (orange) which have undergone storage at shallower depths within the summit reservoir, undergoing greater fractionation and gas flushing but still retaining enough vapour to remain buoyant and as low-fountains. (4) Volatile-depleted melts (yellow) stored at shallow depths undergo open system degassing (black arrows), extensive CO_2-gas flushing (blue arrows) and dehydration. Mixing of melts at shallow depths, as well as pervasive percolation of CO_2 vapour from depth, promote crystallization and generation of more evolved melt compositions (pale gray). This favors effusive eruption or short-lived, externally-triggered explosions. The structure of the shallow magmatic system is inferred from the geochemical data presented in this study, together with geophysical constraints on the plumbing system as described in Chapter 1.

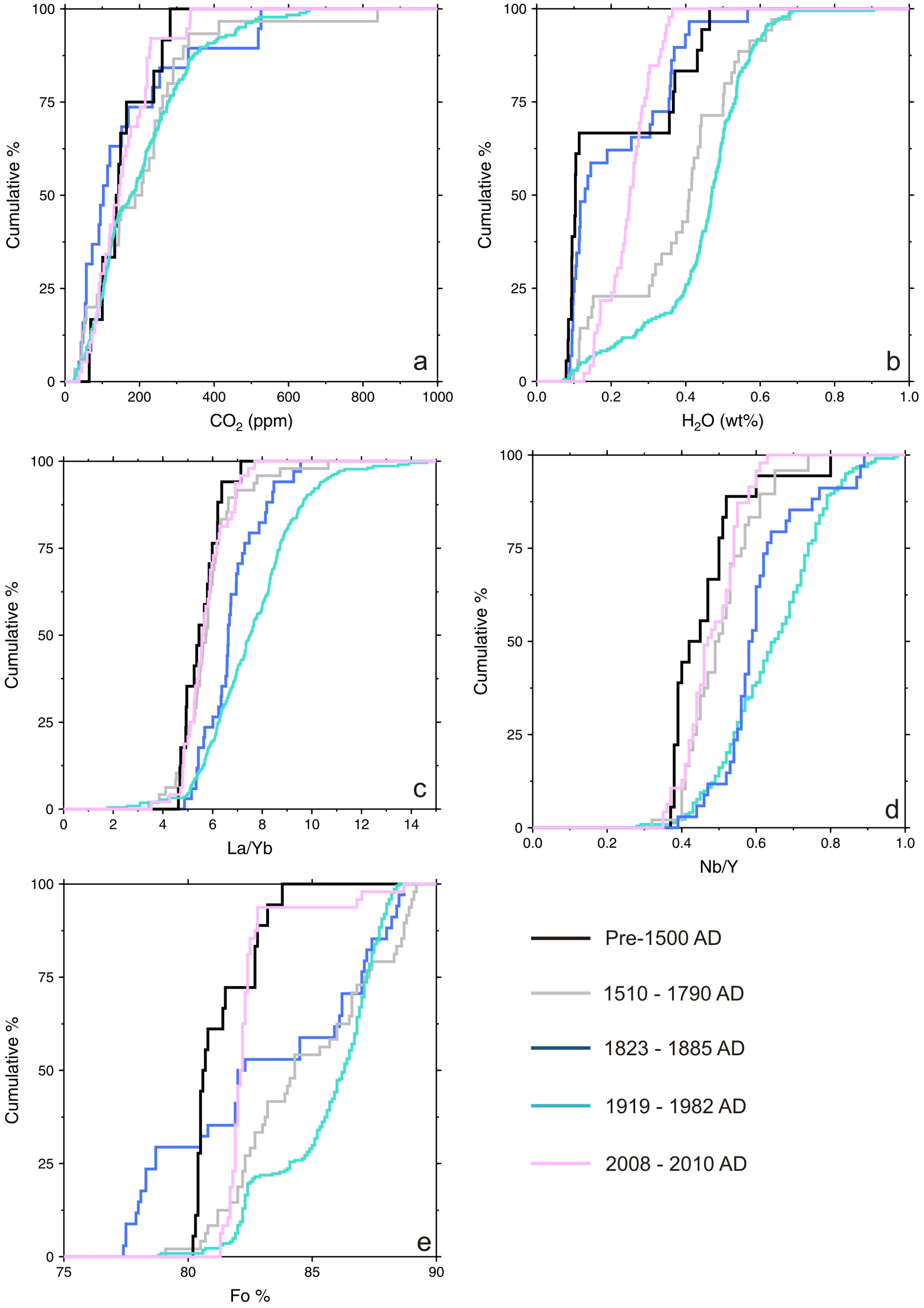

Figure 4.33: Cumulative histograms to show the comparison between melt inclusion populations produced during different time periods using the Kolmogorov-Smirnov test. The cumulative % refers to the number of inclusions analysed for (a) CO_2, (b) H_2O, (c) La/Yb, (d) Nb/Y and (e) Fo mol% of the host olivines.

Chapter 5

Degassing and eruption dynamics during the 1959 eruption of Kīlauea

Hawaiian fountain eruptions are characterised by jets of gas and fragmented tephra, which can reach tens to hundreds of metres in height and may be sustained for hours to days (e.g. *Houghton and Gonnerman*, 2008; *Parfitt*, 2004). Fountaining is an endmember of eruptive behaviour at Kīlauea and has commonly been observed at many other basaltic volcanoes, including Etna in Italy (e.g. *Bertagnini et al.*, 1990; *Allard et al.*, 2005), Plosky Tolbachik volcano in Kamchatka, (e.g. *Fedotov et al.*, 1980), Miyakejima (*Aramaki et al.*, 1986) and Laki in Iceland (e.g. *Thordarson et al.*, 1996). The previous chapter explored the effects of parental magma composition, volatile degassing and magma storage on influencing the type of eruptive activity at Kīlauea. The results suggested that relative to other eruption types, fountaining events are characterised by melts that equilibrated at greater depths within the summit magma reservoir and which underwent rapid ascent to the surface. These more primitive melts followed closed-system degassing pathways, with the melt retaining greater concentrations of H_2O and CO_2 to shallow magma reservoir depths prior to eruption. The results of the previous chapter revealed geochemical differences between eruptions in different categories of eruption styles. However, individual eruptions may be complex in their dynamics, degassing behaviour and melt geochemistry as the eruption proceeds. This chapter examines the degassing history of melts produced in a single, high-fountaining Hawaiian eruption, using the 1959 summit eruption of Kīlauea as a case study. Geochemical data from a suite of tephra samples produced during progressive episodes throughout the eruption are used to determine the effects of syn-eruptive melt mixing, gas-flushing and crystallisation in a single eruption and to understand why some fountains reach exceptional heights and others do not.

5.1 Introduction

High-fountaining Hawaiian eruptions usually commence as fissure-fed discharges which rapidly evolve into concentrations of ejecta from one or more point-source vents, frequently reaching heights >300 m. The behaviour is characterised by repeated episodes of rapid and continuous magma discharge separated by pauses or repose periods that are typically longer in duration than the episodes of activity (*Houghton and Gonnerman*, 2008). Depending on the topography surrounding the vent prior to, or during eruption, erupted lavas may be allowed to pond close to the open conduit. If these ponded lavas reach sufficent depths to cover the vent, fountaining may cease as lavas drain back into the vent during the repose periods. When activity resumes, sustained fountains are often pulsatory with intensity and discharge rate increasing with time and reaching maximum fountain heights later in the eruption (*Stovall et al.*, 2012). Episodes usually cease abruptly, with little or no waning activity.

Hawai`i is the type locality for fountains and this eruptive pattern has been observed during all of the historical high-fountaining eruptions at Kīlauea, including those of Kīlauea Iki (1959) (*MacDonald*, 1962; *Richter*, 1970), Kapoho (1960) (*Richter*, 1970), Mauna Ulu (1969-74) (*Swanson et al.*, 1979) and Pu'u 'Ō'ō (1983-2012) (*Heliker and Mattox*, 2003) (Figure 5.1), all of which produced fountains >400 m high.

The 1959 summit eruption of Kīlauea volcano is one of the most extensively studied examples of Hawaiian-style activity and produced the highest fountains ever observed in Hawai'i (580 m; *Richter* (1970)). The eruption occurred in Kīlauea Iki, a pit crater approximately 1500 m in length, adjacent to the eastern wall of Kīlauea Caldera (Figure 5.1). It lasted for 36 days and consisted of 17 discrete episodes of activity. Each episode typically began as low fountaining, with activity increasing in power and height later in the episode. As the eruption proceeded, episodes became shorter and more frequent (Figure 5.2). The

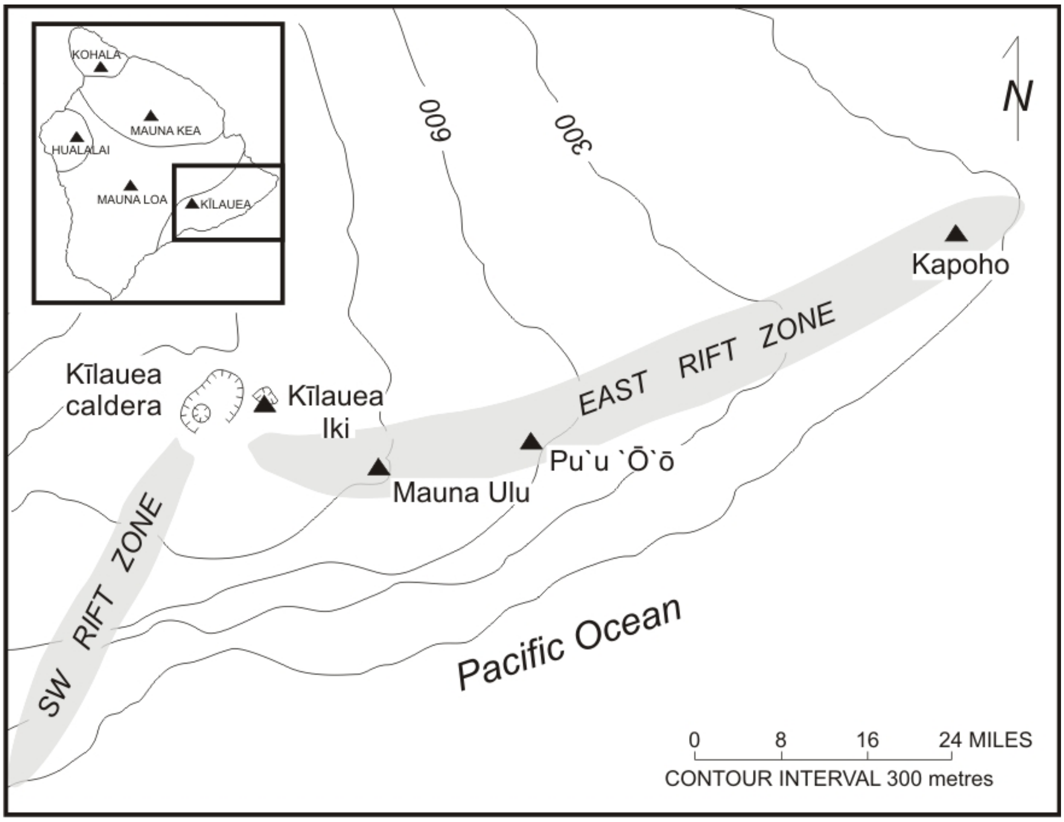

Figure 5.1: Map showing the localities of the four most recent, high-fountain-producing (>400 m) eruptions at Kīlauea. Eruption sites are marked by black triangles.

final significant episodes, 15 and 16, produced two of the three highest fountains of the entire eruption (*Richter*, 1970). Similar activity was observed during the first 6 months of the 1969 Mauna Ulu eruption which took place in the east rift zone (ERZ) (Figure 5.1). Initial fountain heights were low, but gradually increased as the eruption continued, reaching heights of up to 540 m by the 9th episode (*Swanson et al.*, 1979). The early stages of the 1983–present Pu‘u ‘Ō‘ō eruption were dominated by fountains averaging 170 m in height. After the 23rd episode, the heights increased and consistently reached >400 m until the 39th episode (*Heliker and Mattox*, 2003). The maximum and average fountain heights, and the average erupted volumes for the 1959, 1969 and 1983 eruptions are all similar (*Houghton and Gonnerman*, 2008). High fountains are prevalent at many basaltic volcanoes and are a particularly frequent occurrence at Mt. Etna in Italy, with some fountains reaching >800 m in height. More than 150 fountaining episodes have been recorded since 1990 (*Coltelli et al.*,

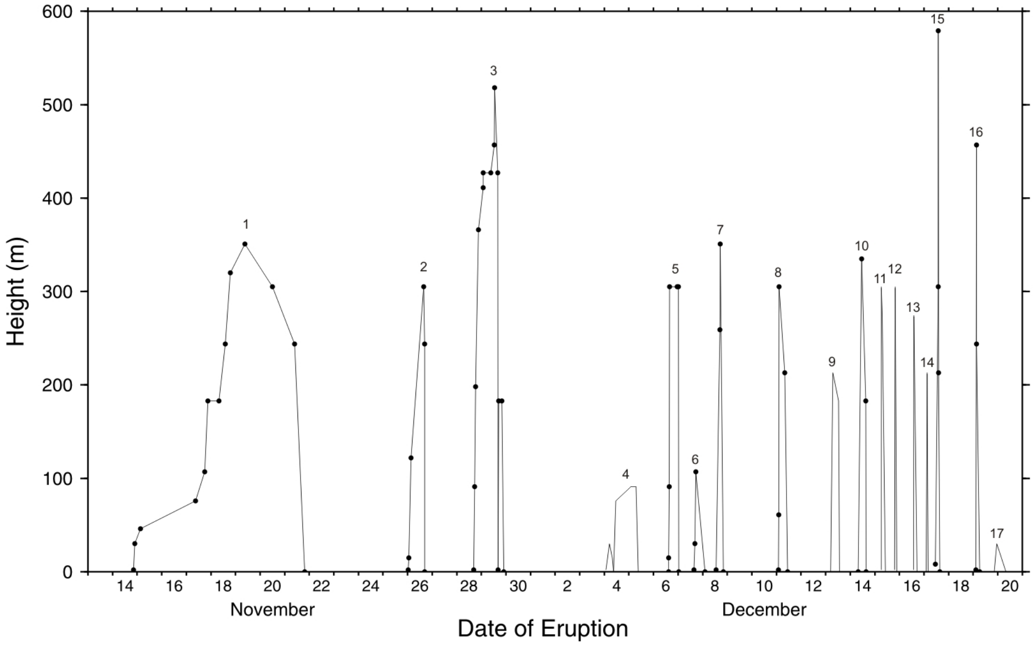

Figure 5.2: Fountain heights during the 1959 Kīlauea Iki eruption. Data from *Richter* (1970).

2000), with the most recent event in April 2012. Although the fountains at Etna are sustained, they are typically less powerful than those produced at Kīlauea and often exhibit more complex changes in behaviour, alternating between episodes of Strombolian (impulsive, short-lived explosions) to Hawaiian fountain activity (*Houghton and Gonnerman*, 2008).

Understanding the mechanisms of fountain production has been the focus of many studies over the past 30 years, and from these, two conceptual models have developed which differ in their treatment of the flow dynamics. The first model proposed was that of *Wilson* (1980) and *Wilson and Head* (1981), the basic premise of which was the concept that explosivity is dependent on the rise speed of the magmas. This has been developed through numerous subsequent studies (*Head and Wilson*, 1987; *Wilson and Head*, 1988; *Fagents and Wilson*, 1993; *Parfitt and Wilson*, 1994, 1995; *Parfitt et al.*, 1995; *Parfitt*, 1998; *Parfitt and Wilson*, 1999; *Parfitt*, 2004; *Slezin*, 2003): Rising magma exolves gas into existing and freshly nucleating bubbles as it reaches progressively lower pressure environments. Bubbles are buoyant relative to the melt, but if the ascent rate of the magma is sufficiently fast, the exsolved bubbles essentially become coupled with the magma to become a homogeneous two-phase flow. As the magma ascends, bubbles continue to grow and expand through diffusion and decompression (*Sparks*, 1978) until the bubble volume fraction reaches a critical value (∼ 60–

95%; *Parfitt* 2004). The bubble volume fraction eventually exceeds the tensile strength of the magma and leads to fragmentation, enabling the mixture of gas and magma pyroclasts to then accelerate rapidly in the conduit due to decompression and expansion of the gas phase, producing a continuous fountain at the vent. The alternative model suggests that fountains originate as a result of complete collapse of a highly vesicular foam layer at the roof of a sub-vent reservoir (*Vergniolle and Jaupart*, 1986, 1990; *Jaupart and Vergniolle*, 1988, 1989; *Vergniolle and Mangan*, 2000; *Vergniolle*, 2008). *Vergniolle and Jaupart* (1986) challenged the assumption of a gas-coupled homogeneous flow regime, and used numerical and experimental models to propose that when magmas are stored prior to eruption, exsolved bubbles are able to separate and rise through the melt. The decoupled bubbles accumulate as a foam layer at the contact between the conduit and upper reservoir. On attaining a critical thickness, the foam undergoes a complete, near-instantaneous collapse, leading to an annular, separated two-phase flow upwards through the conduit, resulting in production of a sustained high fountain until the foam layer and gas supply is depleted.

One of the many fundamental differences between the two proposed models is that the first assumes the 'driving' gas species is H_2O owing to its exsolution at shallow depths within the conduit during magma ascent (*Wilson*, 1980; *Wilson and Head*, 1981; *Parfitt*, 2004), whereas the alternative model assumes that CO_2 is the dominant volatile species because at magma reservoir depths, H_2O solubility is too high to allow significant exsolution and therefore only a CO_2-rich gas phase may form the foam layer. Neither model uses petrological volatile data to test assumptions about the composition of the vapour species driving the events. Adaptations of the *Wilson* (1980) and *Wilson and Head* (1981) model have been used to interpret the causes of variations in fountain height during an eruption (*Parfitt and Wilson*, 1995). It has been suggested that fountain heights are controlled primarily by magma gas content, volume flux and the amount of lava re-entrainment or drainback (*Parfitt et al.*, 1995; *Head and Wilson*, 1987), with heights decreasing as the proportion of re-entrained magma increases. However the relationship between eruption dynamics, fountain height and melt volatile content remains unclear: during most Hawaiian high-fountaining eruptions the extent of drainback increases as the eruption continues, and consequently the proportion of degassed melt mixing with undegassed reservoir melts must also increase. This should act to decrease the observed eruption rates and fountain heights with time, and does not explain the increased heights and volume fluxes observed in later episodes of the 1959, 1969 and 1983–86 eruptions at Kīlauea. The composition of the gas phase employed in both of the previously proposed models is a gross simplification, and more recent studies have demonstrated the importance of considering natural systems with a two-component gas phase ($H_2O + CO_2$) (*Papale and Polacci*, 1999; *Papale*, 1997, 2005; *Papale et al.*, 2006). Changing the proportions of these two volatile components, or the total volatile content of the melt can have significant effects on the eruption dynamics, in particular, even small changes (ppm level) in the amount of CO_2 within the system can alter the gas volume fractions, mass flow rates, and magma fragmentation depths, all of which may strongly influence eruptive behaviour and fountain heights.

This chapter is not an attempt to distinguish which of the previously proposed fountain models is 'correct', but to investigate the temporal variations in the volatile, trace and major element compositions of melts erupted throughout a single eruption in order to elucidate the role of pre-eruptive melt H_2O and CO_2 compositions on eruption dynamics. The 1959 summit eruption of Kīlauea provides an ideal case study for furthering our understanding of magma degassing and dynamics during high-fountaining eruptions. The event was documented in meticulous detail by scientists at the Hawaiian Volcano Observatory with exceptional field observations and extensive geophysical measurements. Tephra samples produced during the eruption remain in pristine condition and are easily accessible in situ.

5.1.1 Background and previous work on the 1959 Eruption of Kīlauea

5.1.1.1 Chronology of the 1959-60 Kīlauea Eruption

In 1924, an explosive eruption within Halema'uma'u Crater in Kīlauea Caldera (Figure 5.3) heralded the end of a near-continuous period of lava lake activity at the summit of the volcano. The phreatomagmatic eruption occurred in response to draining of the summit magma reservoir into the East Rift Zone (ERZ), which subsequently allowed groundwater to enter the conduit and upper storage regions, thus driving the explosions (*Decker and Christiansen*, 1984; *Dvorak*, 1992; *Hurwitz et al.*, 2003). No further eruptions occurred at the summit for 28 years, until the onset of new fissure and lake activity in and around Halema'uma'u in 1952 and 1954. Geophysical and geochemical studies of activity throughout

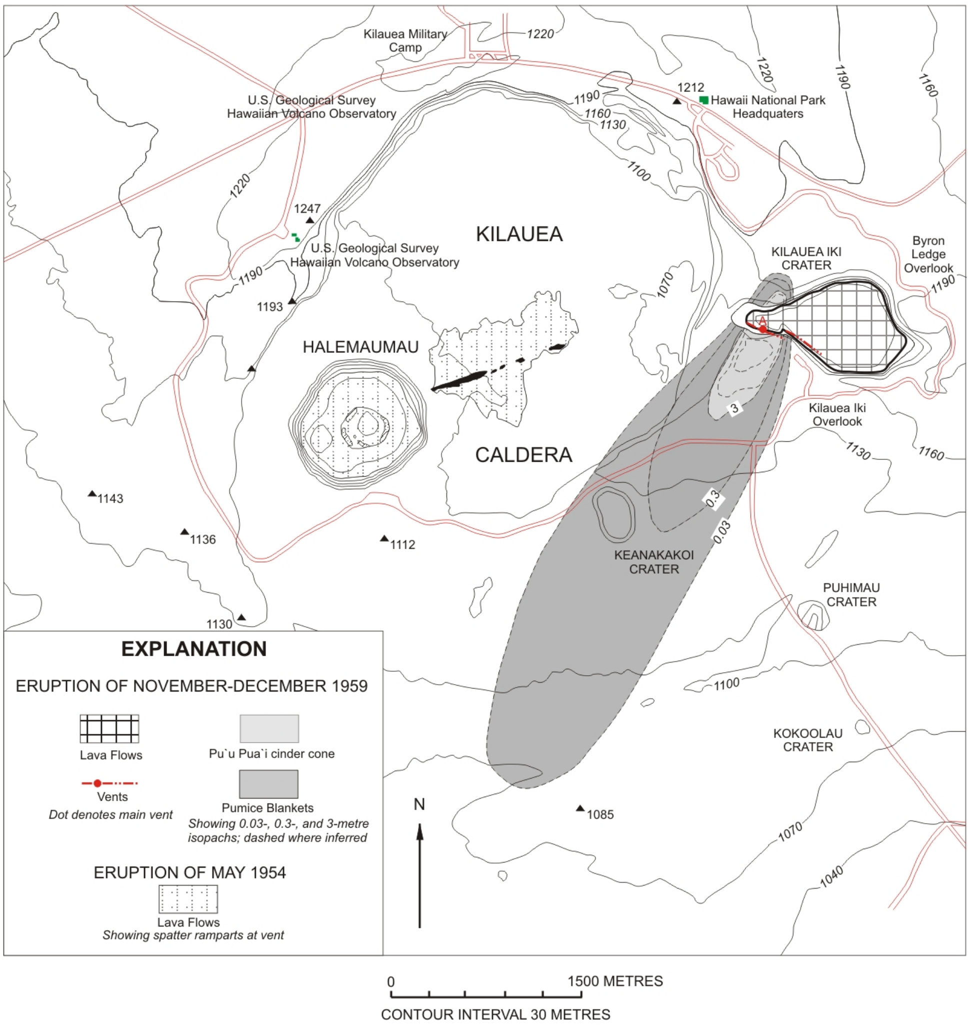

Figure 5.3: Map of the Kīlauea summit area, showing the features of the 1959 eruption in and around Kīlauea Iki crater. Modified from *Richter* (1970).

the 1950s and 60s suggest the summit reservoir at that time consisted of separate inflation centres occupied by compositionally distinct batches of magma (*Fiske and Kinoshita*, 1969; *Wright et al.*, 1975; *Anderson and Brown*, 1993).

From November 1957 to May 1959 the summit of Kīlauea underwent slow and steady inflation (*Eaton et al.*, 1987). In mid-August 1959, 3 months before the onset of the 1959 eruption, a deep swarm of seismicity was recorded several kilometres north of Kīlauea caldera at a depth of 50–55 km, suggesting new magma was rising from the mantle (*Eaton et al.*, 1987; *Helz*, 1987). Within six weeks of the start of the eruption, swarms of shallow intra-caldera earthquakes from a source near the northeast rim of Halemaʻumaʻu crater (close to the outbreak of the 1954 fissures, Figure 5.3) were recorded and summit inflation increased to three times faster than in previous months as new magma was supplied to the reservoir (*Richter and Eaton*, 1960; *MacDonald*, 1962; *Eaton et al.*, 1987).

The course of the eruption was described in detail by *Richter and Eaton* (1960), *MacDonald* (1962) and *Richter* (1970) and their observations are the basis for the following summary. The eruption was concentrated in Kīlauea Iki pit crater, separated from the main caldera by a low ridge known as Byron Ledge (Figure 5.4). Previous eruptive activity within the pit crater had occurred in 1868 from a fissure on the southwest wall, and prior to that event, a small fissure eruption had occurred on Byron Ledge in 1832 (*MacDonald*, 1959). The initial phase of the 1959 eruption began at 20:08 (Hawaiian Standard Time) on 14 November, when ten fissure segments opened to form a 900 m long ‘curtain of fire’ about halfway up the south wall of Kīlauea Iki crater (Figures 5.4 and 5.5a), close to the line of outbreak of the 1868 eruption (*MacDonald*, 1959, 1962). The initial fountains were 30 m in height and fed a lava pond at the eastern base of the pit (Figure 5.5b). By the nightfall on 15 November, eruption at the outermost vents along the fissure had ceased and activity became centered on a single fountain 35–40 m high from vent A, at the western edge of the fissure (Figure 5.5c). The development of a point source vent resulted in an increase in magma flux and fountain height until it reached it’s maximum level on November 18, when the fountain exceeded 300 m and the lake depth reached 45 m. Fountain deposits were concentrated downwind of the vent, and resulted in growth of the Pu`u Pua`i (‘gushing hill’) cinder cone to the southwest of the pit crater (Figure 5.4b). At the peak of the eruptive episode the accumulation rate of scoria and spatter forming Puʻu Puaʻi was ~ 7 m per hour (Houghton, pers. comm.). Occasionally, bursts of hot gas, without liquid lava, could be seen between the cone and the fountain, revealing there were periods when outgassing of accumulated vapour without any significant magma flux occurred (*Richter*, 1970). Fountaining continued unabated until November 20 when the level of the 98 m deep lava lake surpassed that of the vent and began to disrupt the fountain. On 21 November episode 1 ended abruptly with the sudden cessation of the fountain which had produced 30×10^6 m^3 of lava and formed a lake 102 m deep (*Eaton et al.*, 1987). Episode 1 stands apart in character from the subsequent eruptive phases as it was the longest episode, lasting 167 hours, and produced the greatest volume of extruded lava (Figure 5.2) (*Richter*, 1970; *Eaton et al.*, 1987). Subsequent phases

Table 5.1: Summary of physical properties recorded throughout the 1959 Kīlauea Iki eruption. Data collated from both *MacDonald* (1962) and *Richter* (1970). Maximum fountain heights are those presented in *MacDonald* (1962). Lake depths reported are values recorded at the end of each episode, after both fountaining and drainback.

Eruption Episode	Duration (hrs)	Repose (hrs)	Maximum Height (m)	Lake Depth (m)	Lake depth after drainback (m)	Eruption Rate (m^3/s)
1	167	101	380	102	100	83
2	15	48	305	107	97	102
3	29	101	520	104	100	53
4	32	26	200	120	109	130
5	9	15	380	123	114	324
6	11	11	245	126	118	215
7	7	42	425	125	114	198
8	19	17	335	126	115	124
9	8	14	213	126	113	278
10	8	9	335	125	115	313
11	4	16	365	123	116	417
12	2	604	335	120	114	417
13	4	9	350	120	115	313
14	2	8	350	119	117	417
15	4	35	580	121	115	243
16	3	-	455	123	116	556

lasted 2–32.5 hours and produced a range of fountain heights from 30–580 m (*MacDonald*, 1962; *Richter*, 1970) (Figure 5.2). The characteristics of each episode, including fountain heights and calculated eruption rates are summarised in Table 5.1.

Episode 3 produced fountains up to 519 m high (Figure 5.5d) and despite its relatively short duration, this phase produced more spatter and pumice than any other episode, and led to the formation of a secondary cone adjacent to and overlying Pu`u Pua`i. At the end of the eruptive phase, the pumice cone behind the main vent became unstable, causing a large section to dislodge and slide into the lake, exposing an incandescent core (Figure 5.5e). The continued collapse of cone sections following episode 3 caused a shift in the position of the main eruptive vent. At the onset of episode 4, extrusion began from 2 vents ∼40 m above the surface of the lake within the steep face of the cone. One vent produced large quantities of gas with minor spatter; the second, 10 m to the west, produced a stream of lava into the lake simultaneously. Phase 4 of the eruption was the second longest episode (32.5 hours) and

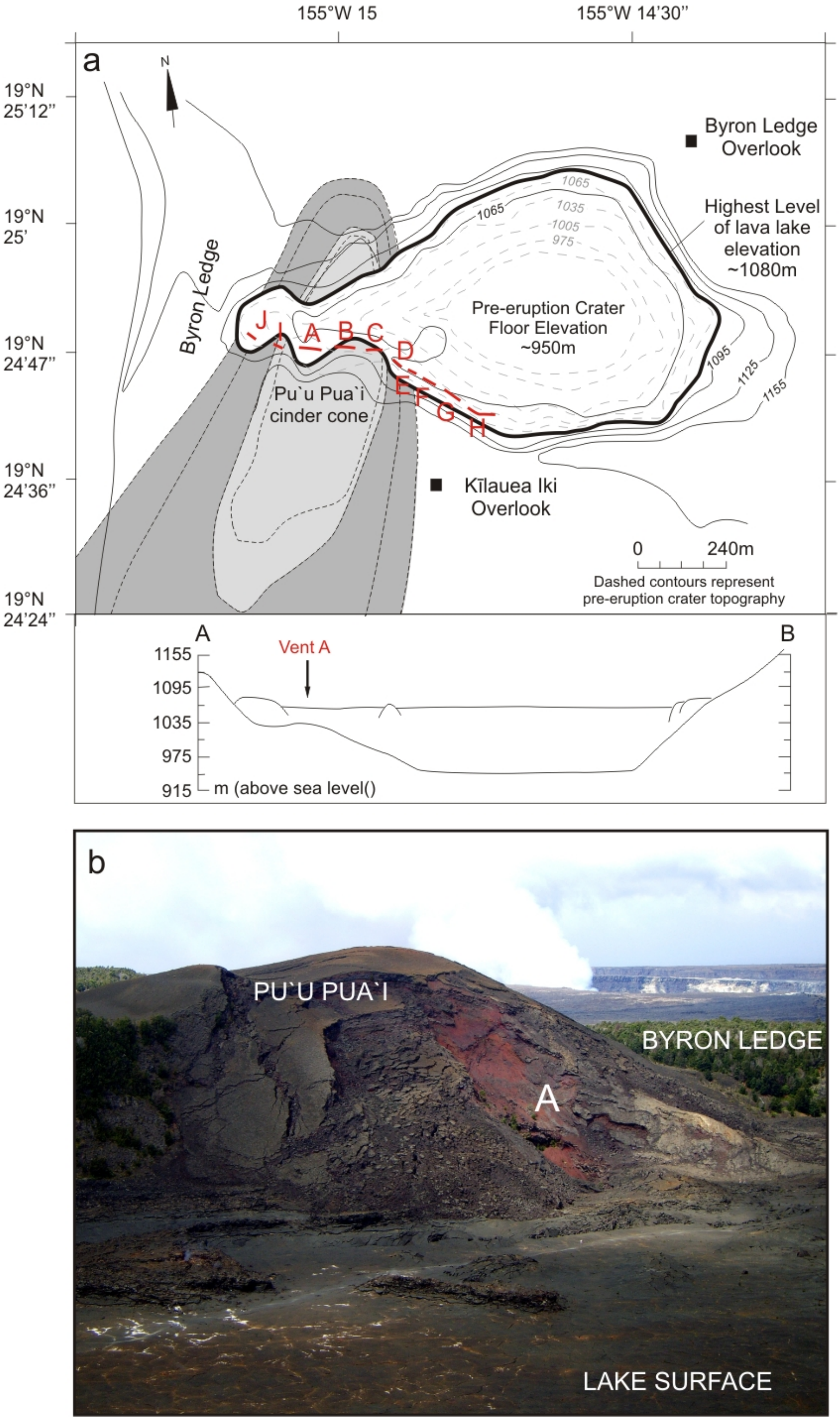

Figure 5.4: (a) Map and cross section of Kīlauea Iki Crater showing the pre- and post-eruption topography.Red lines mark the location of the initial outbreak of fissures and the letters correspond to ther individual segments as described in the text. (b) Photograph of the remains of the eruptive vent 'A', taken in 2010, with a view to southwest from Byron Ledge overlook. The image illustrates the relative height of the post-eruptive lake surface and the partially collapsed Pu'u Pua'i cinder cone which developed behind the vent. Kīlauea Caldera can be seen in the background beyond Byron Ledge, with the current summit eruption plume rising from Halema'uma'u Crater.

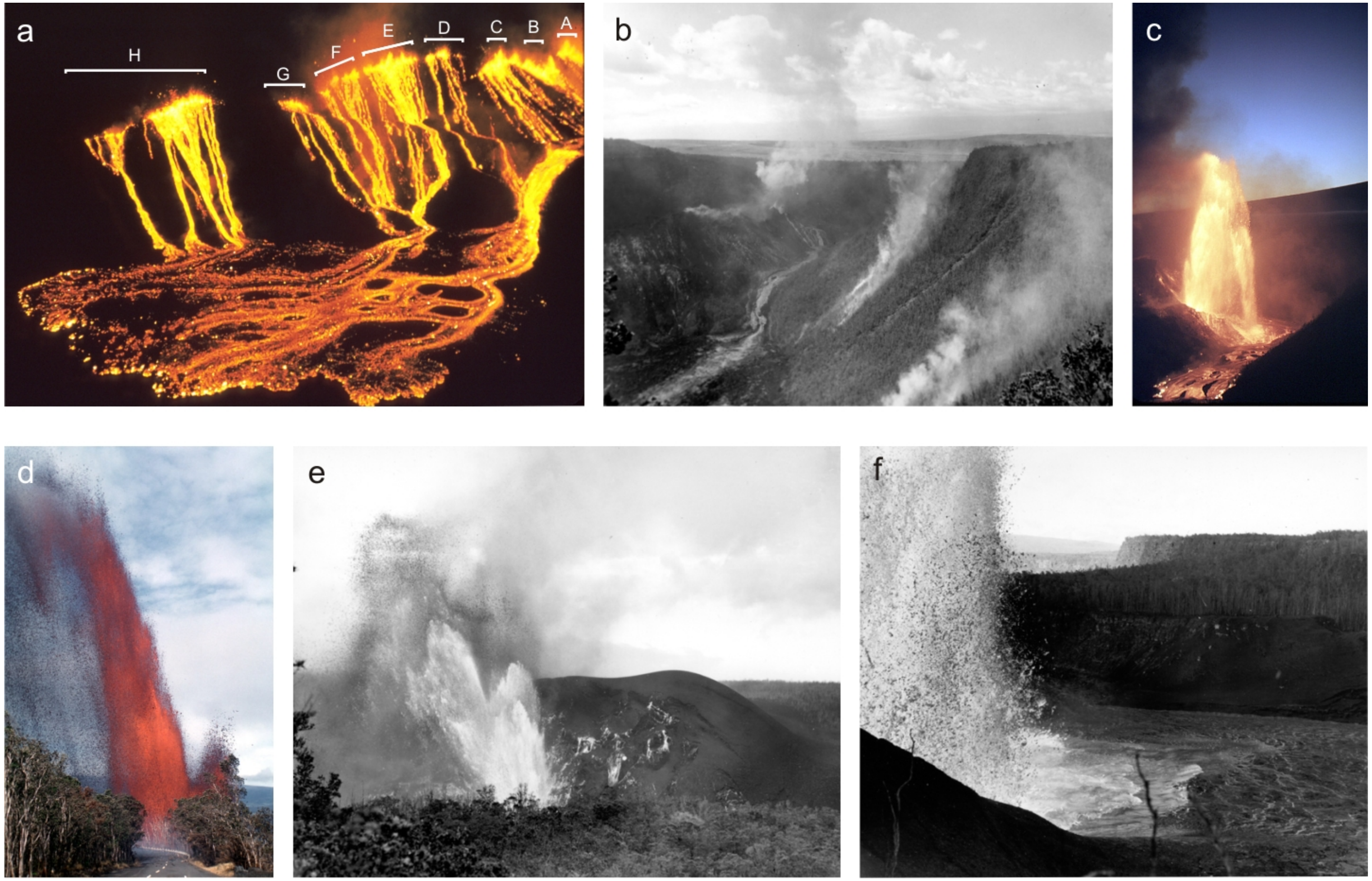

Figure 5.5: Photographs of the 1959 eruption: (a) 14 November, 1959, approximately 90 mins after the start of the eruption in Kīlauea Iki showing the initial line of fissures. Active fissures are labelled A-H. (b) 15 November, 1959. View from Byron Ledge over-look showing the fountain at vent A and the developing lava pond at the base of the crater. (c) 18 November, 1959. Fountain approximately 250 m high from a point source at the former vent 'A'. (d) 29 November, 1959. Inclined fountain jets at 427 m high during episode 3 of the eruption; a dark curtain of pumice and spatter is wafted to greater heights. (e) 29 November, 1959. View from the NW rim of Kīlauea Iki crater showing the episode 3 fountain deflected by flank collapse of Pu`u Pua`i cone over part of the vent. (f) 14 December, 1959. Image of the episode 10 fountain from Kīlauea Iki overlook. Interference of the high lake level with the base of the fountain generates huge lava waves. Photographs by D.H. Richter and J. Eaton (U.S. Geological Survey).

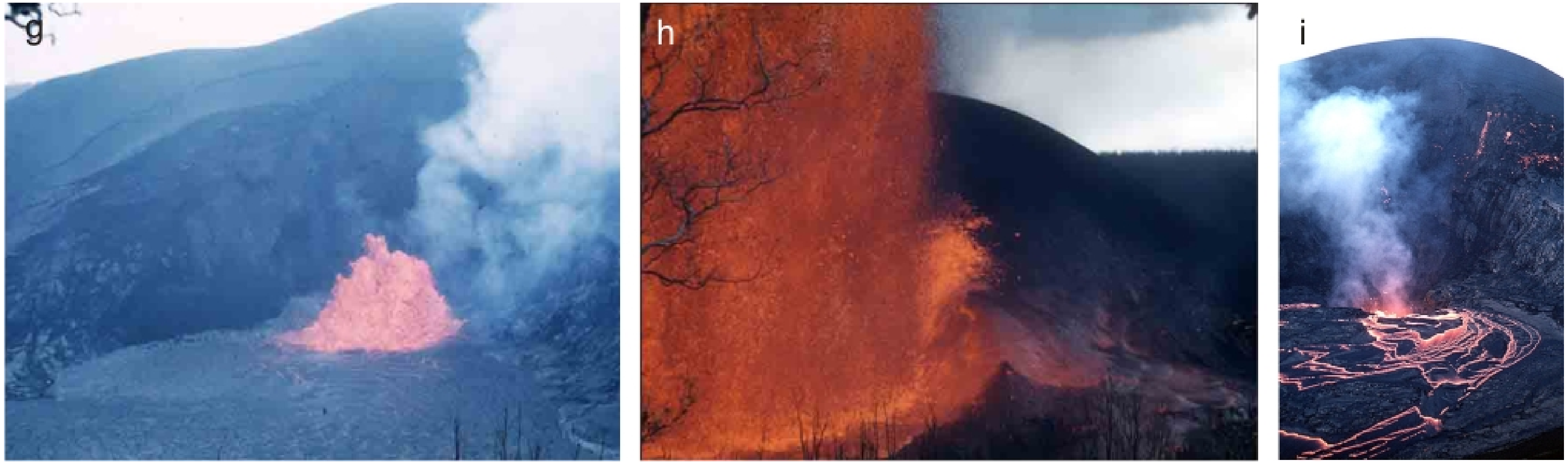

Figure 5.5: Photographs of the 1959 eruption (cont'd): (g) 17 November, 1959. The first few hours of episode 15 began with lava boiling in the vent to approximately 30 m height. (h) 17 December, 1959, about 10 minutes after (g) was taken, during episode 15, activity increased to a produce a colossal fountain 580 m high. (i) 19 December, 1959. Drainback of the lava lake into the vent at the end of episode 17. Photographs by D.H. Richter and J. Eaton (U.S. Geological Survey)

was characterised by unusually low fountains and the hottest lavas observed throughout the entire eruption — 1192 °C (*Ault et al.*, 1961; *Richter*, 1970). Similar to episode 1, backflow of lavas into the vent did not occur immediately following the cessation of activity.

With the exception of episode 1, all subsequent eruptive phases were preceded by significant amounts of lava drainback from the lake into the vent, and as a result each episode would start with a clearing of the conduit of residual outgassed lavas (*Stovall et al.*, 2012). Episodes typically began with boiling lava at the vent, and production of gas and spatter. Once the new fountain became established, the voluminous outpouring of lavas would refill the lake until it flooded the mouth of the vent and interfered with fountain production (Figure 5.5f), after which the lavas would begin to drain back into the conduit (Figure 5.5i). Drainback, which after episode 1 had been slow and inconspicuous, was visible and rapid at the end of subsequent episodes, with the rate of lava withdrawal in the early stages of each repose period often exceeding the rate of effusion during the previous eruptive stage (*Richter and Eaton*, 1960; *MacDonald*, 1962; *Eaton et al.*, 1987).

As the eruption proceeded the pattern of activity changed, with phases becoming shorter in duration and much more frequent (Figure 5.2). Drainback could be observed, at times occurring simultaneously with fountaining from the same vent. Changes in fountain behaviour were also observed: in earlier episodes, the highest fountain heights had been reached following a gradual increase throughout the phase of activity (Figure 5.6a). After episode 10, maximum fountain heights were reached rapidly at the beginning of each eruptive phase (Figure 5.6b). In later episodes such as episode 15, following only a few hours of low (15 m high) spattering and syn-fountain drainback (Figure 5.5 g), a sudden burst of activity produced a fountain 580 metres high in a matter of minutes (Figure 5.5 h).

The summit eruption ended on 19 December 1959, with a quiescent effusion of relatively viscous lavas during the final episode (Figure 5.5 (i)). The final lake depth was 111 m deep and contained 38×10^6 m^3 of lava.

Shortly after the end of the Kīlauea Iki eruption on 20 December 1959, tiltmeters at the summit continued to record inflation of the magma reservoir. Earthquakes recorded along the ERZ in late December indicated that magma was being injected along the rift zone and moving out of the summit. By mid-January 1960, a new fountaining eruption began in the

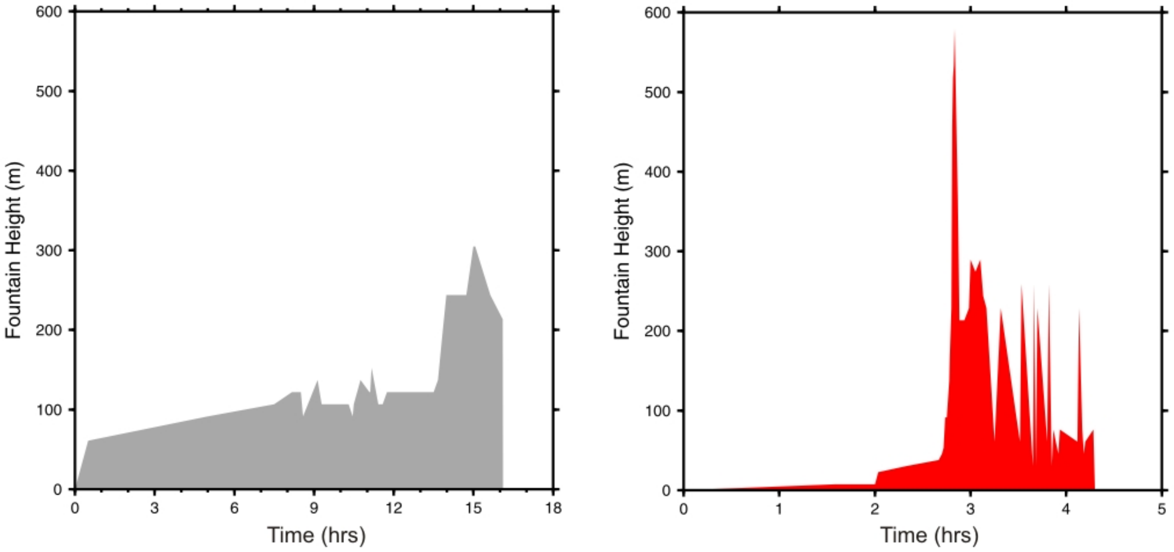

Figure 5.6: Variations in fountain heights with time for episodes 2 (gray) and 15 (red). Time is reported as cumulate hours since the beginning of the eruptive episode.

village of Kapoho at the eastern end of the rift zone (Figure 5.1), some 20 km from the volcano's summit. The flank eruption began on 13 January 1960, lasted 38 days, produced fountains up to 427 m in height and led to deflation of the summit reservoir and subsequent collapse of the Halema`uma`u Crater floor.

5.1.1.2 Previous studies

One of the most comprehensive studies of the Kīlauea Iki eruption to date is that by *Eaton et al.* (1987) in which the authors combined geophysical observations of deformation at the summit with the detailed log of lava eruption and drainback volumes, in order to establish a record of magma movement through the summit magma reservoir during the eruption. Seismic and geodetic data suggest that the lake lavas that drained back into the vent were recycled via the magma reservoir where they mixed turbulently with new magmas being supplied from depth. The $30 \times 10^6\,\mathrm{m}^3$ of lava originally withdrawn from the reservoir during episode 1 was, over the course of the eruption, more than replaced by $60 \times 10^6\,\mathrm{m}^3$ of lava rising from depth. Of this $60 \times 10^6\,\mathrm{m}^3$, $40 \times 10^6\,\mathrm{m}^3$ was retained in the reservoir, $8 \times 10^6\,\mathrm{m}^3$ was added to the lake and $12 \times 10^6\,\mathrm{m}^3$ was driven out of the reservoir into the upper ERZ due to excessive overpressure during late drainback episodes. Reservoir volumes, together

Table 5.2: Volumes of lava erupted into and withdrawn from Kīlauea Iki lava lake during the 16 principal phases of the 1959 eruption. Column 2 data are the reservoir volumes at the start of each episode, relative to the reservoir volume at the end of episode 1. Volumes in columns 7 and 8 are calculated by subtraction of column 3 from 5, and 4 from 6 respectively. Data from *Eaton et al.* (1987).

		Lava volume (10^6 m^3)				Volume gain or loss (10^6 m^3)		
Eruption Episode	Reservoir relative end ep 1	Deflation episode	Inflation episode	Erupted	Drain -back	First stage of phase ($5-3$)	Second stage of phase ($6-4$)	Entire phase
1	2	3	4	5	6	7	8	9
1	30.6	-	-	30.6	1.1	-	-	(-1.1)
2	10.4	2.8	13.1	3.6	4.5	+0.8	+8.6	+9.5
3	22.0	8.6	2.8	3.2	2.0	-5.4	+0.8	-4.5
4	30.6	6.3	6.3	11.5	6.3	+5.2	0.0	+5.2
5	33.6	6.0	4.7	6.5	4.7	+0.5	0.0	+0.5
6	33.6	5.7	4.6	6.6	3.8	+0.8	+0.8	+1.6
7	36.1	4.4	2.1	3.7	5.6	-0.7	-3.5	-4.2
8	40.4	6.2	3.7	6.7	6.0	0.0	-2.3	-2.3
9	38.5	5.7	4.0	5.7	6.9	0.0	-2.9	-2.9
10	41.0	5.0	6.0	6.3	4.9	+1.3	+1.1	+2.4
11	39.8	5.2	4.1	4.7	4.1	-0.5	0.0	-0.5
12	42.8	2.1	4.7	2.2	3.1	+0.1	+1.6	+1.8
13	42.8	3.9	1.8	3.2	2.4	-0.7	-0.6	-1.3
14	41.6	1.8	1.0	1.8	1.0	0.0	0.0	0.0
15	38.5	1.9	0.7	1.7	3.2	-0.2	-2.5	-2.8
16	39.1	3.9	3.4	4.1	4.1	+0.2	-0.7	-0.5

with the magma volume budgets for each episode calculated by *Eaton et al.* (1987) are shown in Table 5.2 and will be discussed later in this chapter.

Many of the previous studies of the Kīlauea Iki eruption have focused on the geochemistry (e.g., *Richter and Moore*, 1966; *Murata and Richter*, 1966a; *Stone*, 1991), petrography (*Richter and Murata*, 1966; *Helz*, 1987, 2009) and geothermometry (*Ault et al.*, 1961; *Helz and Thornber*, 1987) of the Kīlauea Iki lake lavas. Slow crystallisation of the lake over the past 53 years has provided an accessible analogue for real-time magma chamber processes (e.g., *Jellinek and Kerr*, 2001; *Helz*, 2009; *Vinet and Higgins*, 2011).

Initial geochemical studies of the 1959 summit lavas revealed the significant role of olivine crystallisation in controlling the compositional trends of the erupted lavas. MgO concentrations of whole rock samples were 7–20 wt% and could be explained by the addition or removal of Fo_{87} olivine (*Murata and Richter*, 1966a). The high MgO composition of the whole rock lavas defined the Kīlauea Iki eruption as unique, being the only historical Kīlauea eruption known to have produced picritic lavas. Eruption of lavas with the highest MgO content correlated with the highest recorded discharge rates and measured eruption temperatures (1060–1190 °C; *Ault et al.* 1961) (*Murata and Richter*, 1966a). *Murata and Richter* (1966a) also recognised the presence of two compositionally distinct endmembers within the suite of lavas analysed from the first phase of the eruption, termed S1 and S2. S1 is a CaO-rich composition which deviates from the olivine-liquid line of descent, whereas S2 lies at the more evolved, Mg-poor end of the compositional range. Both the strong variation in the olivine contents and proportion of the S1 endmember in later episodes of the 1959 summit lavas was originally considered to have been achieved by the tapping of different levels of a stratified summit magma reservoir and the erosion of a basal cumulate pile during episodes of rapid extrusion (*Murata and Richter*, 1966a,b).

These initial observations of *Murata and Richter* (1966a) were further developed by *Wright* (1973) who generated models of S1 and S2 endmember mixing. They observed that the pure S1 and S2 components were only erupted during the initial stage of episode 1, with each endmember produced from the westernmost and easternmost segments of the fissure on November 14. Throughout the subsequent episodes of the eruption, the proportions of the two mixed components changed. The S1 and S2 endmembers are suggested to be the result of varying inputs from two separate, stratified magma bodies within the summit reservoir region. Alternatively, the S1 magma may have been derived from the same parental batch as S2, and later enriched with clinopyroxene through either gravitational settling of phenocrysts or flow segregation (*Wright*, 1973).

Textural and compositional studies of olivines from the 1959 tephras (*Schwindinger and Anderson Jr* 1989; *Helz* 1987; *Vinet and Higgins* 2011) have advanced the mixing models of *Wright* (1973) and *Murata* (1966). These studies have described several distinct varieties of crystal: (1) rounded, large olivines with deformation textures, reversely zoned and Mg-rich rims, (2) variably zoned euhedral and skeletal crystals and (3) dunitic clusters and aggregates of olivines with other textural features. The largest crystals with deformation features were most common in early S1 erupted lavas and are largely interpreted as being carried from conduit and reservoir margins from depth (*Murata*, 1966; *Helz*, 1987; *Vinet and Higgins*, 2011). *Helz* (1987) rejects the earlier suggestions that the S1 magmas may have evolved by dissolving augite whilst crystallising olivine, since this would require both endmember melts to have been stored for a prolonged period prior to eruption, which is inconsistent with the geophysical data of *Eaton et al.* (1987). Instead, a revised model is proposed in which the hotter, more Mg-rich S1 is thought to have been released from mantle depths during the August earthquake swarms, arriving at the base of the summit reservoir by late September 1959 (*Helz*, 1987; *Eaton et al.*, 1987). The magma followed a seldom-used pathway and encountered a separate body of older stored S2 magma (*Wright*, 1973; *Helz*, 1987). The S1 melts broke through this older chamber to the north-east of Halema`uma`u, whilst mingling with and entraining some of the more evolved magma en route to the surface.

Despite the large number of petrologic and major element studies carried out on the 1959 lavas, few systematic trace element investigations have been published. A study by *Gunn* (1971) analysed a suite of Kīlauea Iki lavas for their trace element compositions in order to determine trace element partition coefficients during fractionation of olivine. The trace element composition of ten summit samples (from episodes 1, 4 and 17) were analysed by *Tilling et al.* (1987) in a comparative study of historical Kīlauea and Mauna Loa lavas. They report that the mean composition of the 1959 lavas are distinct from other historical olivine-controlled summit lavas in their high concentrations of K_2O, TiO_2, P_2O_5, Ba, Hf, U and REE. The unique trace and major element composition of the 1959 lavas is suggested by *Tilling et al.* (1987) and *Wright* (1973) to be the result of the lavas being fed from a different source to those summit eruptions in the 1952–62 period. A more comprehensive study of trace elements and trace metal behaviour throughout the 1959 eruption has recently been completed by *Loewen* (2011) in which additional constraints on the fractionation and mixing of melts have been investigated, in order to better understand the potential volatility of trace metals.

A suite of five samples from the 1960 flank eruption in Kapoho was analysed for major and trace element concentrations by *Murata and Richter* (1966a), *Wright* (1971) and *Tilling et al.* (1987). Compositional variations in the Kapoho lavas are not solely related to olivine fractionation but are proposed to be the result of complex mixing between undifferentiated and differentiated magmas (*Wright*, 1971). Temporal changes in the composition of the lavas throughout the flank eruption have been observed, with the composition of the early erupted magmas resembling those of the previous 1955 ERZ eruption (*Murata and Richter*, 1966a). As the eruption proceeded, the lavas became progressively more MgO-rich and contained a significantly increased abundance and variety of olivine phenocrysts. These late-stage magmas (1–19 February) are interpreted by *Murata and Richter* (1966a) as residual magmas from the 1959 summit eruption which, having been intruded into the ERZ at the end of the summit eruption, migrated down-rift, mixed with the residual 1955 melts and erupted at Kapoho. To date, no published melt inclusion or volatile analyses exist for the Kapoho lavas.

Degassing during the Kīlauea Iki eruption is not well constrained. A study by Anderson and Brown (1993) investigated H_2O and CO_2 concentrations in ~ 50 melt inclusions from 4 eruptive episodes. Volatile contents measured in the melt inclusions include 0.24–1.12 wt% H_2O, < 20–758 ppm CO_2 and 0–0.19 wt% S. The estimated formation pressures of the inclusions, calculated from H_2O-CO_2 solubility models, indicated that the majority of the inclusions (41 of 50) were trapped at shallow depths within the summit magma reservoir prior to eruption ($<$ 100–200 MPa). Only two of the analysed inclusions were formed at pressures > 2 kb. They suggest that the primitive parental melts must have been sufficiently CO_2-rich and buoyant for the picritic material to pass through the summit reservoir and erupt. The initial dataset and interpretations of *Anderson and Brown* (1993) were later revised and expanded by *Wallace* (1998). Examination of precision estimates on the original FTIR dataset revealed that the maximum H_2O concentrations for the 1959 melt inclusions was 0.84 wt%. The data were used to investigate the effects of repeated drainback of magmas into the summit reservoir, on the H_2O concentrations of the melts. The data show a decrease in H_2O content of the melt inclusions through the (limited) number of episodes, which the authors interpret as being due to progressive mixing of greater volumes of degassed melt with the undegassed reservoir supply.

Although there are significant differences between many of the geochemical studies, the importance of extensive olivine fractionation, mixing of at least two different endmember magma compositions and lava drainback is commonly recognised. However, a number of significant questions about the geochemistry and dynamics of the 1959 eruption remain unanswered:

(1) What are the contrasting roles of CO_2 and H_2O in fountain dynamics through a single eruption? Observations of the of the 1959 eruption, together with numerical models of fountaining (e.g., *Wilson and Head* 1981) suggest that abundant gas is one of the most important factors influencing fountain height. Do temporal variations in the volatile geochemistry of the eruption products enable determination of the driving gas composition?

(2) What are the relative effects of crystal fractionation, magma mixing and lava drainback on the volatile concentrations of the 1959 melts? If the *Wilson and Head* (1981) model for fountaining is correct, a decrease in the pre-eruptive melt H_2O concentration with time due to drainback, as recorded by *Wallace* (1998), is not consistent with the observation that some of the highest fountains occurred during the later episodes.

(3) Are the melts supplied from depth throughout the eruption chemically uniform? Might some have been inherently more volatile- or vapour-rich than others?

(4) Do the volatile concentrations of the flank eruption lavas compare with those of the summit eruption, and if so, what are the broader implications for melt transport and high-fountain production during eruptions in the lower east rift zone?

This chapter attempts to answer these questions through the analysis of the major, trace and volatile compositions of olivine-hosted melt inclusions and matrix glasses from tephras produced throughout the different episodes of the 1959-60 eruption. Variations in major elements and incompatible trace element ratios are used to explore the roles of magma mixing and melt heterogeneity. Volatile and trace element data are combined with observational, geochemical and geophysical datasets to develop a comprehensive model for the plumbing system and degassing behaviour throughout a high fountain-producing Hawaiian eruption.

5.2 Methods

5.2.1 Sampling

Tephra samples from 10 episodes of the Kīlauea Iki eruption were collected in June 2010 from stratigraphy exposed in three pits downwind of the eruption vent (Figure 5.7). Sampling was directed and assisted by B. Houghton and D. Swanson. The stratigraphy corresponding to specific episodes has been determined through work by Houghton and W. Stovall (pers. comm.). Episode deposits have been identified by comparing data to that collected by HVO scientists who probed the depth of tephra along a cross wind traverse after episodes 1, 3, 11 and 17 in 1959.

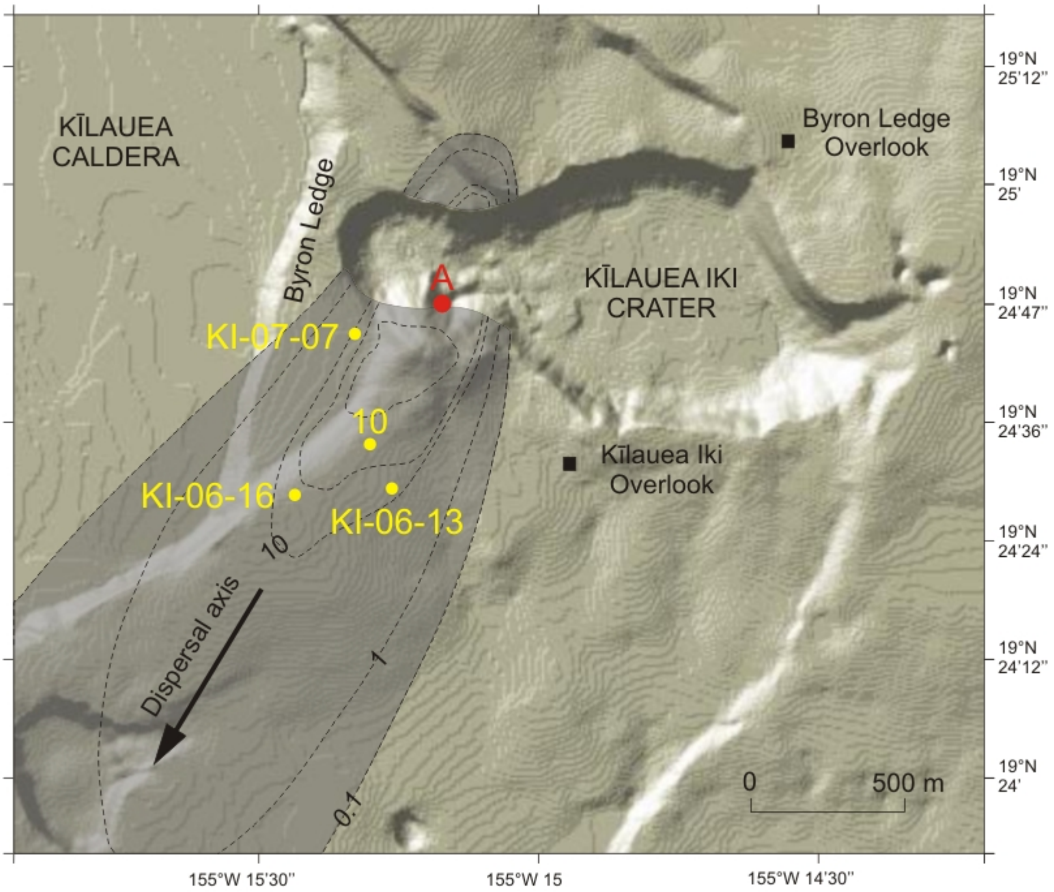

Figure 5.7: Map of sampling localities for the 1959 Kīlauea Iki tephra. Samples were collected downwind of the main eruption vent (marked in red) from pits KI-07-07, KI-06-13 and KI-06-16 marked in yellow. Site 10 marks the locality of sampling in April 2009. Isopachs denoting tephra deposit thickness with distance from the vent are in shown in grey; thickness values are in feet as adapted from *Richter* (1970). Basemap modified from GeoMapApp (*MGDS*, 2012).

The sample sites were mostly existing collapse pits that provided sections through the upper ~ 1–2 m of the stratigraphy (Figure 5.8), and were chosen on the basis of their position within the main dispersal axis of the eruption. At the sampled distances from the vent, the tephra was relatively proximal but not welded. The stratigraphy is biased towards episodes of longer duration and higher fountain heights. Material from low fountain episodes, such as phase 4, did not reach sufficient heights to exit the crater and are therefore under-represented in the stratigraphy. For those episodes which were preserved, many of the deposits are zoned, consisting of a basal layer of denser, fluidal clasts overlain by an upper pumice-rich layer.

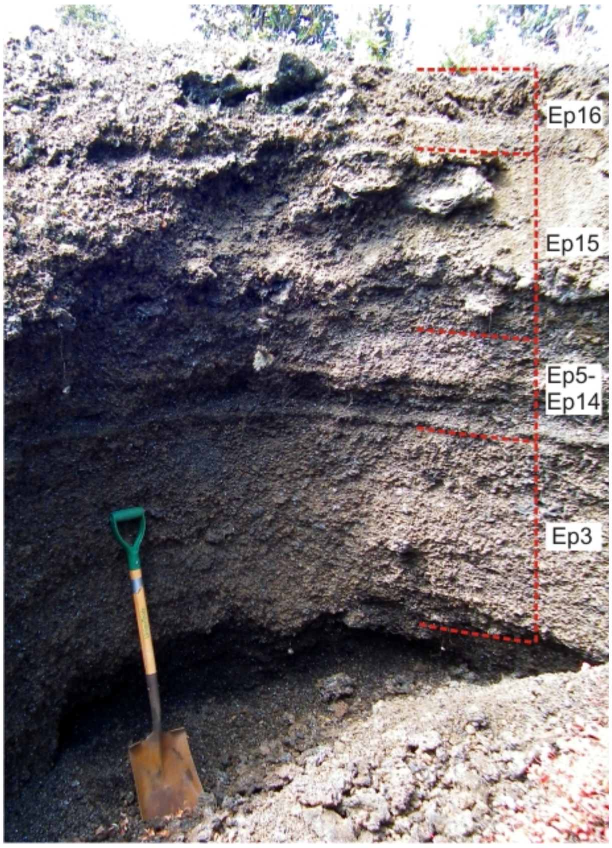

Figure 5.8: Photograph of the excavated collapse pit KI-06-13. Samples from episode 3, 15 and 16 were obtained from the labelled units. Episodes 4–14 have not been clearly identified in this section and appear as a condensed unit.

Samples of juvenile lapilli and small bombs produced during episodes 1, 2, 3, 5, 6, 7, 8, 10, 15 and 16 were collected from pits KI-07-14, KI-06-16 and KI-06-13 (*Stovall et al.*, 2011, 2012). Material was carefully selected from the middle–upper sections of each episode bed to avoid sampling recycled lavas. Stratigraphic logs, sampling positions and photographs of tephra collected from pits KI-06-16 and KI-06-13, are shown in figures 5.9 and 5.10. The deposits varied significantly in character: episode 1 tephra (Figure 5.9) is dominated by black, glassy achnelith lapilli (*Walker and Croasdale*, 1972) including Pele's Tears, small glass spheres, shards and rods and fluidal clasts, with shiny external surfaces which show flow lines and vesicular interiors with mm- to cm-sized bubbles. Deposits produced by the highest fountains (3, 15 and 16) are characterised by a larger average grain size of several cm, with spatter bombs up to 25 cm in length. The units consist of ragged, highly vesicular, golden to light brown pumice. Episodes of intermediate height produced tephra with varying proportions of pumice, fluidal clasts and achneliths. Detailed textural and density analyses of clasts were beyond the scope of this study and have been documented elsewhere for episodes 1, 15 and 16 (*Stovall et al.*, 2011, 2012), but the dominant characteristics of each sample are shown in Figures 5.9 and 5.10. Episodes 9 and 11–14 were not clearly represented in the stratigraphy, and appear only as highly condensed beds within pits KI-06-16 and KI-06-13. Sampling was not possible owing to the need for further work in cross-correlating the units with reconcilable beds in other locations (Houghton, pers. comm.). In addition to the June 2010 collection, two samples: KL0911 and KL0912 were included in the total Kīlauea Iki dataset. These samples were collected during the first field season in April 2009 from a collapse pit at Site number 10 on Figure 5.7. The samples were pumice-rich and obtained from within 50 cm of the exposed ground surface. They are most likely to be from episode 15 or 16 but due to the uncertainty in their dating, the data from these samples have not been assigned episode numbers.

Tephra from the 1960 flank eruption at Kapoho was also sampled for comparison with the summit episodes. Dating of the golden to light–brown pumice near to the Kapoho vents is problematic owing to the the remobilisation of tephra during the eruption and the subsequent development of the area as quarry. However the sample was collected from a section of the ‘pumice loaf’ described by *Richter* (1970) which formed during rigorous fountaining. The ‘loaf’ developed on 27 January 1960 and was broken up by \`a\`a flows on 29 January, as chunks of it ‘floated’ on the flows and passed further from the vent. Maximum fountain heights for this period were 427 m.

5.2.2 Analyses

Samples were dried, crushed, seived and prepared for analysis using the methods outlined in Chapter 2. Matrix glasses, olivines and their melt inclusions were analysed for major, volatile and trace element compositions using EMPA, SIMS and LA-ICP-MS respectively. Precision and accuracy data for the analyses is presented and discussed in Chapter 2. All melt inclusion compositions were corrected for variable extents of post-entrapment crystallisation

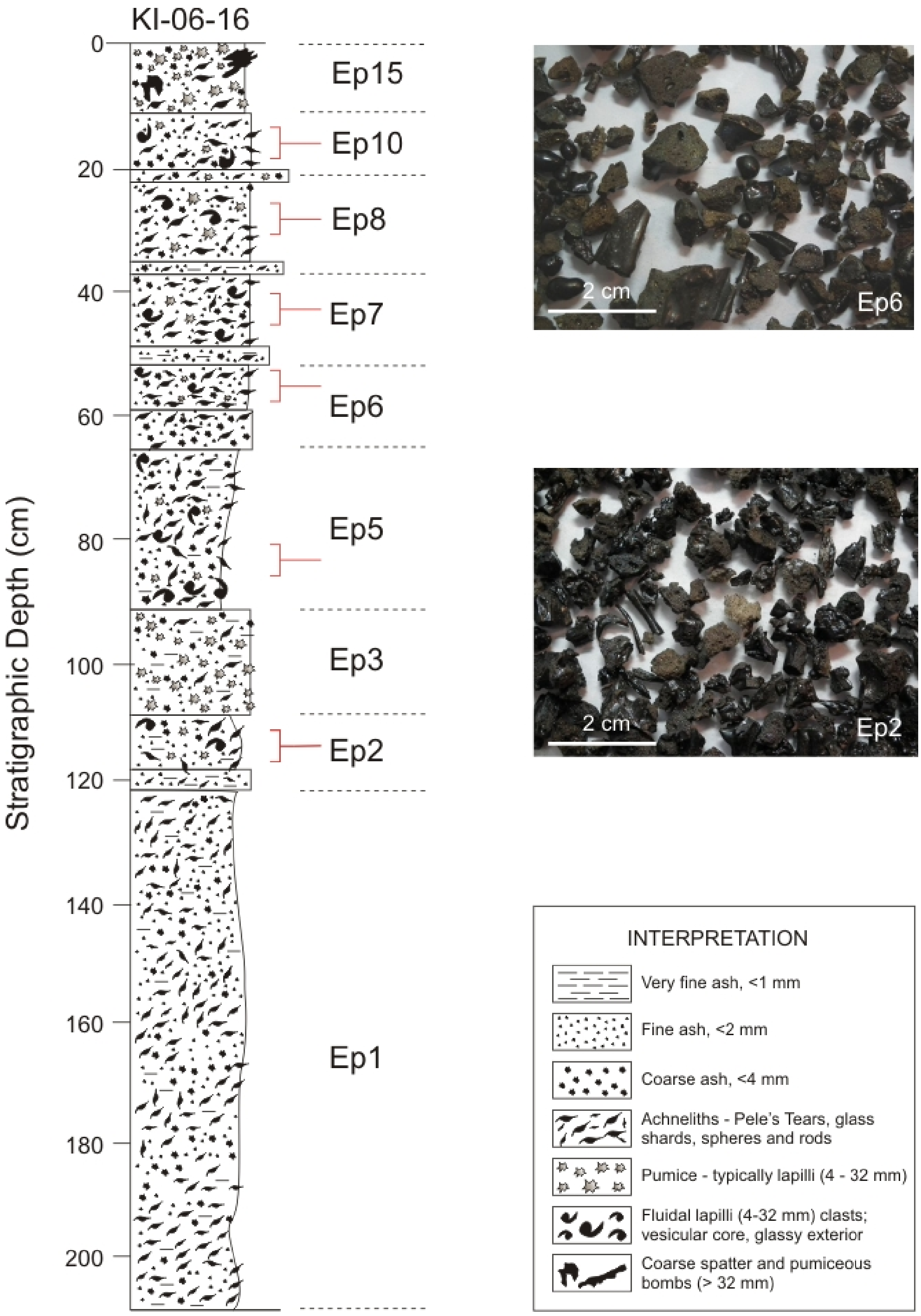

Figure 5.9: Stratigraphy and sample positions in pit KI-06-16. Beds are attributed to specific episodes, identified by reconciling characteristics of cross correlation with hundreds of other similar pits (B. Houghton; pers. comm.). Red markers indicate the position of sampling within each unit. Photographs of episode 2 and episode 6 tephras indicate typical deposit characteristics within the section.

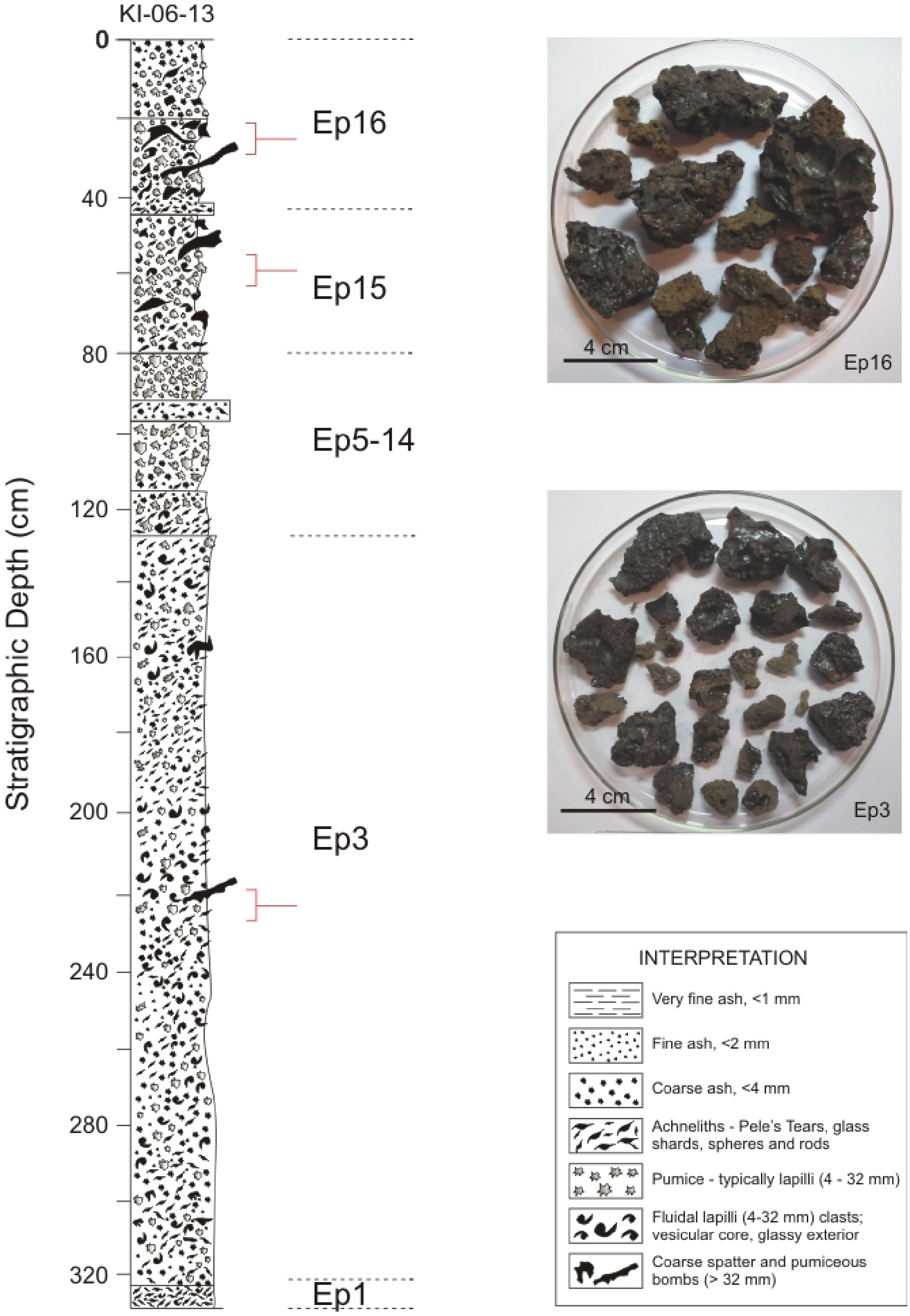

Figure 5.10: Stratigraphy and sample positions in pit KI-06-13. Red markers indicate the position of sampling within each unit. The section is dominated by deposits from high-fountaining episodes (3, 15 and 16), which is strongly reflected in both the thickness of the deposit and dominance of highly-vesicular pumice and large bombs. Photographs of episode 3 and episode 15 tephras are also shown.

and required on average 13 % olivine addition. The complete dataset can be found in Tables 2, 4 and 10 of the Appendix.

5.3 Results

5.3.1 Petrography and olivine chemistry

By comparison with many historical Kīlauea eruption tephras, the Kīlauea Iki samples are overwhelmingly olivine-phyric, with large (between 0.5–5.0 mm) unaltered olivines ubiquitous throughout every episode sampled; loose individual crystals were especially abundant in the episode 1 tephra. Clinopyroxene and plagioclase phenocrysts are extremely rare or absent within these samples. The olivine crystals occur as isolated euhedral to subhedral phenocrysts and as aggregates of two or more grains. All of the morphology groups identified by Helz (1987) have been observed in the tephra samples, with most of the morphology groups appearing in tephras from all of the sampled episodes.

The olivines contain translucent, pale brown glass inclusions up to 300 μm in diameter (Figure 5.11a). Care was taken to analyse melt inclusions hosted within a range of different olivine morphologies but also to avoid over-sampling inclusions from the largest grains that showed obvious resorption textures, which may be representative of older, pre-1959 magmas. Many of the inclusions contain single, euhedral crystals of Cr-rich spinel and some rare spherical sulphides (10–50 μm) (Figure 5.11). Inclusions that contained oxides occupying > 5 % of the total volume were excluded from analysis. Many of the olivines also contained abundant CO_2-rich fluid inclusions. Of the 116 melt inclusions analysed, 48 contained a vapour bubble, typically occupying < 7 vol%. A number of vapour bubbles were observed at > 73 vol% of the inclusion. Where some MIs contain bubbles, invariably all of the inclusions within the same olivine crystals were observed to also be bubble-bearing, whereas in some crystals, from the same episode or tephra clast, all melt inclusions were bubble-free. The organisation of bubble-bearing and bubble-free inclusions, and the presence of some bubbles occupying > 73 vol% is unlikely to result solely from volume-dependent nucleation during cooling (*Anderson and Brown*, 1993) and it is important to note that the presence of bubbles within > 40 % of the MIs, implies that the CO_2 and H_2O values measured in the MI glass

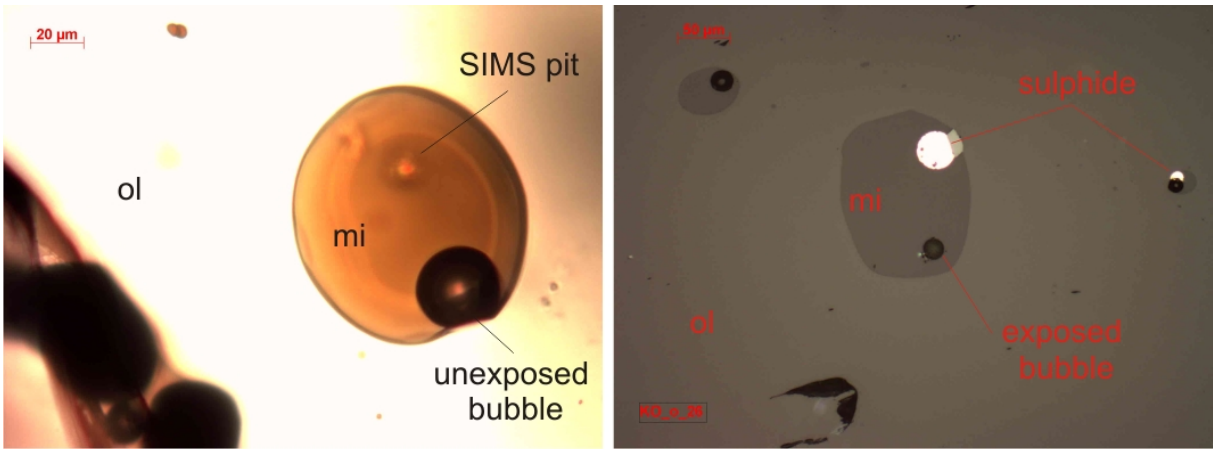

Figure 5.11: Melt inclusions from the 1959-60 eruption (a) transmitted light photomicrograph of a Kīlauea Iki melt inclusion containing a spherical vapour bubble; (b) a reflected-light micrograph of a rare olivine grain with two immiscible sulphides exposed within two glass inclusions. This was the largest sulphide observed in any of the historical Kīlauea samples analysed. This example was found within a grain erupted in the 1960 flank eruption; other smaller sulphides were also found in a number of other inclusions analysed in this study, from the 1959 summit eruption.

represent a minimum estimate of pre-eruptive melt volatile concentrations.

Forsterite (Fo) contents of the olivine phenocryst cores range from $Fo_{78.9}$ to $Fo_{88.6}$ where:

$$Fo = Mg\#_{ol} = 100 \times \frac{X_{Mg}}{X_{Mg} + X_{Fe^{2+}}} \tag{5.1}$$

Figure 5.12 shows the range in composition of the olivine phenocrysts as a function of the matrix glass composition, $Mg\#_{glass}$. The crystal populations for each episode show a broad range of Fo compositions, and a poor positive correlation with the average matrix glass compositions, with all olivine compositions lying above the line of Kd=0.3, indicating that the olivine cores were not in equilibrium with their carrier melts at the time of eruption. The range of olivine compositions may represent crystals produced at varying stages of fractional crystallisation which have accumulated prior to eruption. This is in line with the whole rock studies of *Murata* (1966).

Figure 5.13 shows the average olivine composition for each episode population as a function of eruption date. When comparing the averages of compositions between episodes, it is important to consider the quality of these estimates of the means. The error in estimating the mean of a population is dictated by the natural variation within the group (*Maclennan*, 2008b) and is quantified using:

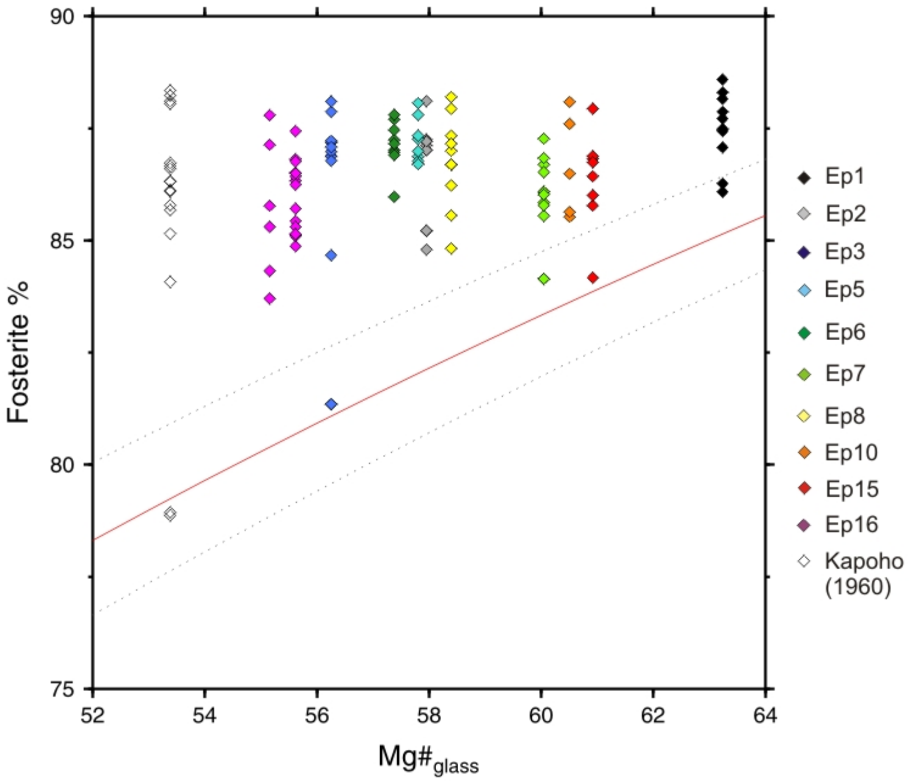

Figure 5.12: Olivine core composition (fosterite %) compared with averaged matrix glass Mg number for each eruptive episode [where Mg# = ((XMg/XFe+2+ + XMg) × 100), with the Fe+2+ set to 90 % of total iron (*Garcia et al.*, 2003)] produced during the Kīlauea Iki 1959 eruption. The solid red line is the equilibrium olivine composition for a given Mg# at Kd=0.3. The dotted grey lines are calculated equilibrium compositions at Kd=0.27 and 0.33.

$$SE = \frac{\sigma}{\sqrt{N}} \tag{5.2}$$

where SE is the standard error of estimate of the mean, σ ist the standard deviation of the population and N is the number of samples (olivines) within each population.

Temporal variations in the average Fo composition of olivines from each episodes are shown in figure 5.13. The data show that there is a weak correlation between olivine compositions and eruption date, such that the earliest erupted olivines produced during episode 1 had a more primitive, Fo-rich composition than the later episodes.

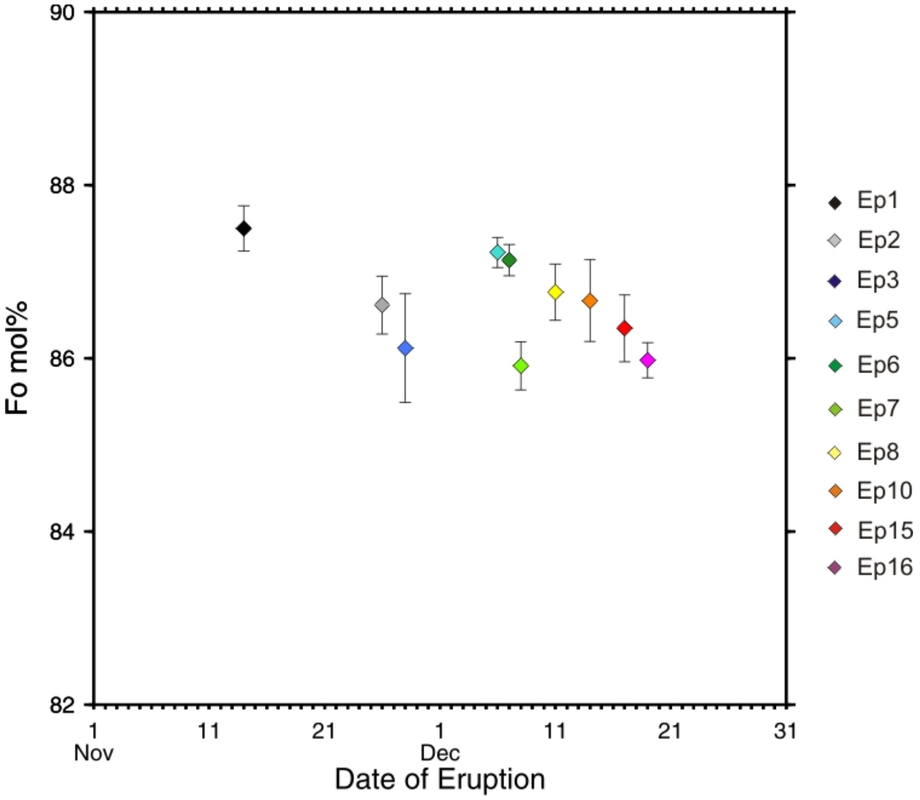

Figure 5.13: Temporal variations in the average olivine composition for each eruptive episode. Error bars represent the standard error of the estimate of the mean for each population (see text for exlanation)

5.3.2 Major element chemistry

The major element compositions of melt inclusions and matrix glasses from the 1959 and 1960 eruptions are shown, together with the previously published whole-rock data of *Murata and Richter* (1966a), in MgO-variation diagrams in Figure 5.14. The corrected melt inclusion compositions span a broad compositional range from 7.2–13.9 wt% MgO, compared with the significantly more evolved compositions of the matrix glasses at 6.3–10.3 wt% and are consistent with pre-eruptive entrapment of more primitive melt compositions. The whole-rock data defines a tight fractionation trend and shows the effect of olivine accumulation, with lavas containing up to nearly 20 wt% MgO.

The data in Figure 5.14 show clear fractionation trends: as the MgO decreases, the concentrations of SiO_2, Al_2O_3, CaO, K_2O, TiO_2 and P_2O_5 increase in both the MIs and glasses. The negative correlations are consistent with fractionation dominated by olivine crystallisation. The decrease in CaO/Al_2O_3 ratios of the glasses, suggests some degree of clinopyroxene (cpx) fractionation, although this contradicts the apparent absence of cpx crystals within the tephra samples, and the absence of a strong inflection in the whole rock CaO and CaO/Al_2O_3 which indicates that clinopyroxene fractionation may only be at the level of groundmass crystallisation. The incompatible behaviour of Al_2O_3 in the whole rock compositions suggests that there was no extensive crystallisation of plagioclase.

There is considerable scatter in the minor element (P_2O_5, TiO_2 and K_2O) concentrations at a given MgO value, with a number of inclusions at unusually high P, low Ti and low K concentrations, which deviate significantly from the olivine-liquid line of descent defined by the whole rock and glass compositions. Minor element concentrations are tightly correlated in the glass, whole rock and majority of melt inclusions, however inclusions with anomalous compositions beyond analytical error do not correlate in their trace element concentrations, such that samples with high P concentrations are not also Ti-rich (Figure 5.15a). They are therefore not considered to be artifacts of instrument error.

The S1 and S2 endmember compositions of *Murata and Richter* (1966a) and *Wright* (1973) are shown for comparison in Figures 5.14 and 5.15b. The S2 composition appears to be more closely related to the fractionation trend determined by the glass and whole rock compositions, and the S1 endmember resembles the melt inclusions in their deviation from this trend at higher CaO values (Figure 5.15b).

Melt inclusions from the first episode of the eruption have the greatest range in MgO concentrations of any subsequent phases. Episodes 2, 7 and 16 display the greatest range in minor element compositions (Figure 5.14). Due to the range of inclusion compositions within each episode population, distinguishing clear temporal trends from Figure 5.14 is challenging. The average MgO concentrations of glasses, inclusions and whole rock data for each episode are shown in Figure 5.16. The average glass compositions show a general trend from the more primitive first episode, at greater MgO concentrations, to more evolved melts produced during the final episodes, 15 and 16. However, MgO changes in the glasses and inclusions are slight and not systematic between episodes.

Melt inclusions from the 1960 flank eruption span a similar range in MgO concentrations as those of episode 1 (from 7.21–13.63 wt%). Despite the 'hybrid' character of the 1960 lavas determined by *Murata and Richter* (1966a) and *Wright* (1973), the melt inclusions

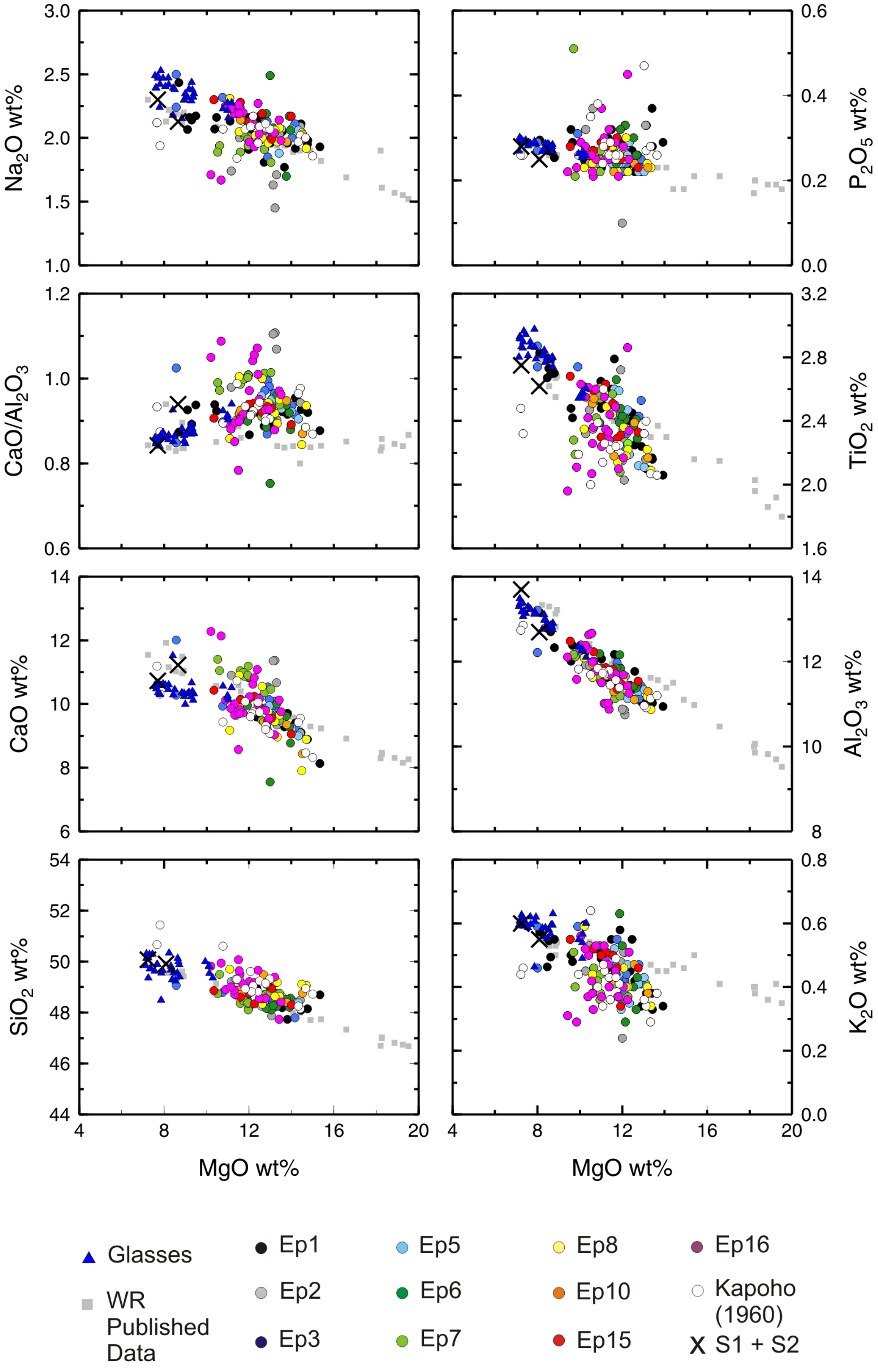

Figure 5.14: MgO variation plots of major element abundances for matrix glasses (triangles) and melt inclusions (circles coloured by eruption episode). Published whole-rock data (grey squares) are from *Murata and Richter* (1966a). The S1 and S2 mixing endmember compositions of *Murata and Richter* (1966a) and *Wright* (1973) are shown for reference.

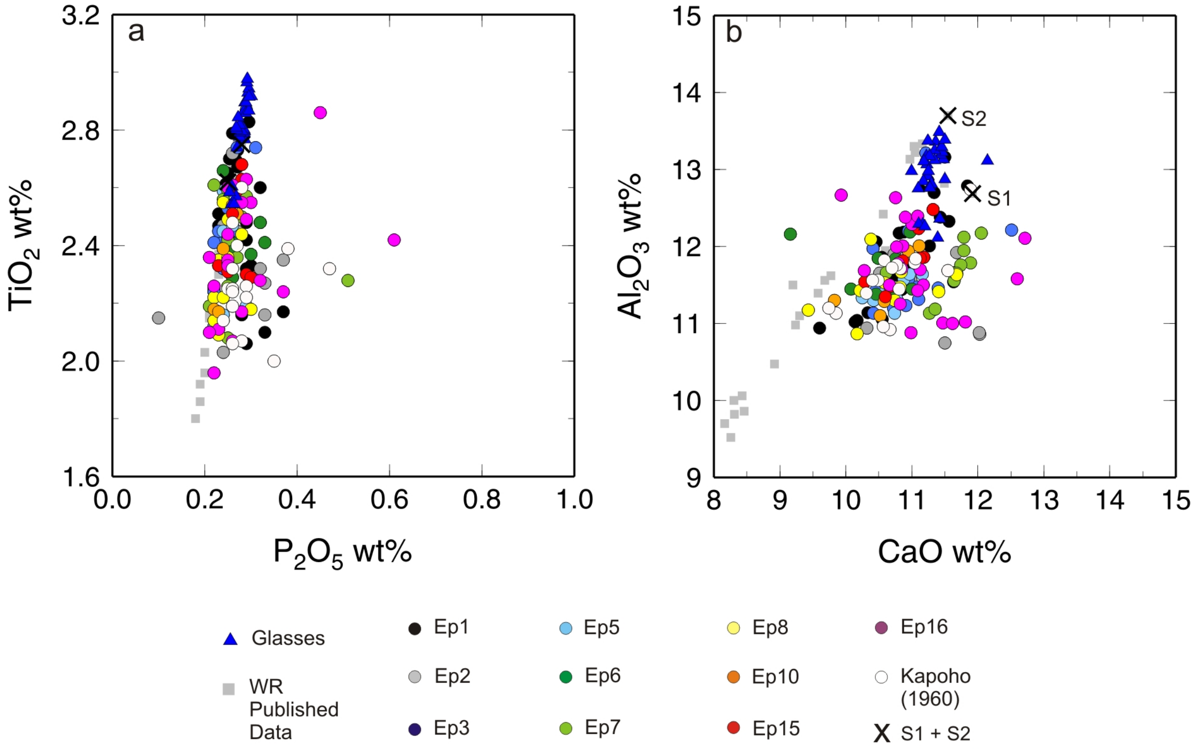

Figure 5.15: (a) TiO_2 against P_2O_5 concentrations and (b) Al_2O_3 versus CaO contents of the 1959 and 1960 melt inclusions and matrix glasses. Published whole rock data from *Murata and Richter* (1966a) and S1-S2 compositions from *Wright* (1973).

compositions in Figure 5.14 generally follow the liquid line of descent characterised by the 1959 lavas and inclusions. The Kapoho samples show no evidence of extensive clinopyroxene or plagioclase crystallisation, although it should be noted that the 1960 samples collected represent only a snapshot of the mid-late eruption melts. However, the samples which were produced on 27 January 1960 show a broad range of minor element concentrations comparable with that of all 1959 episodes combined.

5.3.3 Trace element variation

The trace element concentrations in the Kīlauea Iki and Kapoho eruption samples mirror the widespread variability of the major element dataset. Figures 5.17 and 5.18 show plots of MgO (as an index of fractionation independent of the trace element dataset) versus the trace element data. Decreasing concentrations of MgO are accompanied by increases in highly incompatible large ion lithophile elements (LILE), high field strength elements (HFSE),

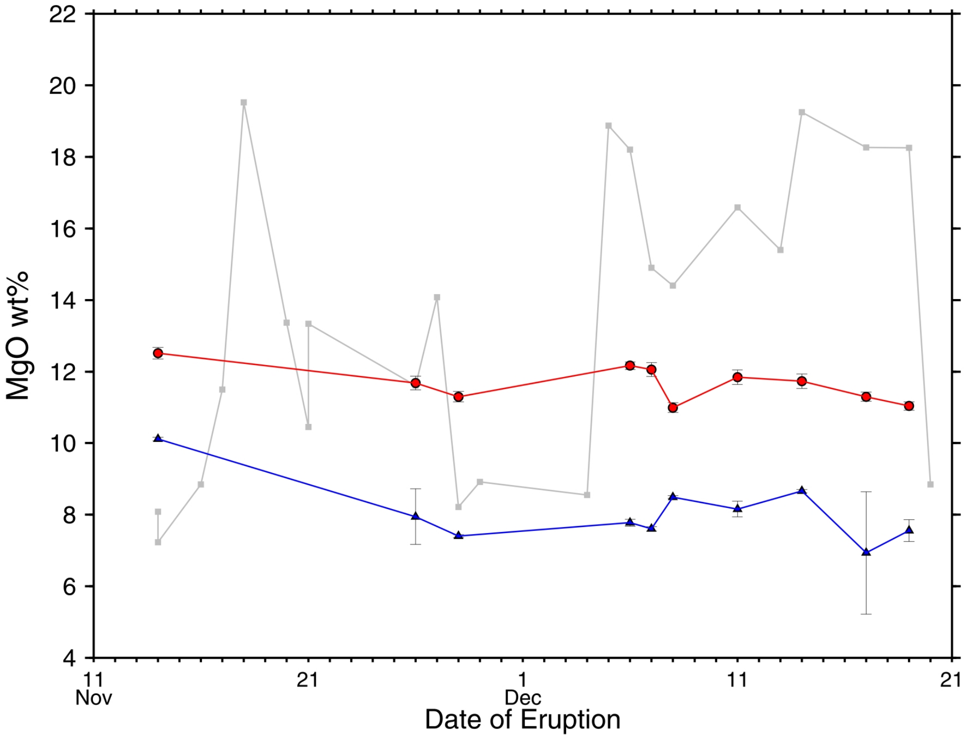

Figure 5.16: Temporal variations in MgO contents of melt inclusions, glasses and whole rock values in the 1959 eruption. Melt inclusions and matrix glasses from this study are shown in red and blue respectively. Whole-rock data from *Murata and Richter* (1966a) are shown wth gray line and squares.

and rare earth elements (REE) between the melt inclusion and glass compositions. These relationships are similar to the major element fractionation trends in Figure 5.14, with matrix glasses lying at higher concentrations of trace elements than the melt inclusions. Sc is the only element which does not show a fractionation trend between the inclusions and glass compositions. It is compatible during clinopyroxene (cpx) removal from the melt and the slight Sc decrease in the matrix glass concentrations at low MgO values may be consistent with some degree of cpx fractionation. Where available, whole rock trace element and REE data published by *Tilling et al.* (1987) are in agreement with the glass and inclusion trends, although the melt inclusions display a much greater variation in the trace element contents within restricted MgO values, than the matrix glasses. This variation is considered to be real and not the result of analytical error or post-entrapment processes such as diffusion. Unlike many major elements, incompatible trace elements diffuse much more slowly through olivine and can remain at pre-eruptive magmatic temperatures for tens to hundreds of years without any diffusive loss or gain (*Spandler et al.*, 2007).

Figures 5.17 and 5.18 also demonstrate the large degree of trace element variation within the inclusion populations from each individual episode, with no distinctive temporal trends identifiable in the data.

Primitive mantle-normalised multi-element diagrams for each of the Kīlauea Iki episodes and the Kapoho eruption are shown in Figure 5.19. The inclusion compositions for each episode exhibit a broad range of concentrations, but the average melt inclusion compositions between the different episodes are very similar in their patterns of LILE and HFSE enrichments and depletions. All elemental patterns exhibit the strong negative Pb anomaly relative to primitive mantle, characteristic of Kīlauea melts (Chapter 4; Figure 4.19), and a minor negative Sc anomaly. Of the different populations, melt inclusions within episode 2 olivines, and those from the Kapoho flank eruption display the greatest variation in LILE/HFSE, with variations in Rb/Y ratios of up to 84% and 68% respectively.

Primitive mantle-normalised REE patterns are smooth profiles, showing LREE enrichment relative to HREE, consistent with melts being produced from a garnet-bearing source. Cross-cutting REE patterns reflect differing LREE/HREE ratios across the dataset and show that the LREE enrichment is variable between episodes, albeit within a narrow range. Melt inclusions from episode 2 show the greatest LREE enrichment, with an average La/Yb ratio of 9.19, and the Kapoho eruption samples are the most LREE depleted; a La/Yb ratio of 6.18. There are no Eu anomalies observed in any of the inclusion or glass average compositions, confirming major element evidence that plagioclase is not a significant crystallising phase. The 1959 inclusions compositions span a broad range within the compositions of all pre-historic and historical melt inclusion profiles analysed for Kīlauea in this thesis, but unlike the whole rock data analysed by *Tilling et al.* (1987) the 1959-60 inclusions in this study do not exhibit profiles significantly more enriched than the average Kīlauea composition (Figure 5.20).

The variation in LREE/HREE and HFSEs of the glasses and melt inclusions are shown in Figure 5.21. The matrix glasses define almost linear trends in the La–Y and Nb–Y space, however the melt inclusion compositions are much more variable and span a broad range of ratios. There are no distinctive or progressive temporal variations in LREE/HREE or HFSE

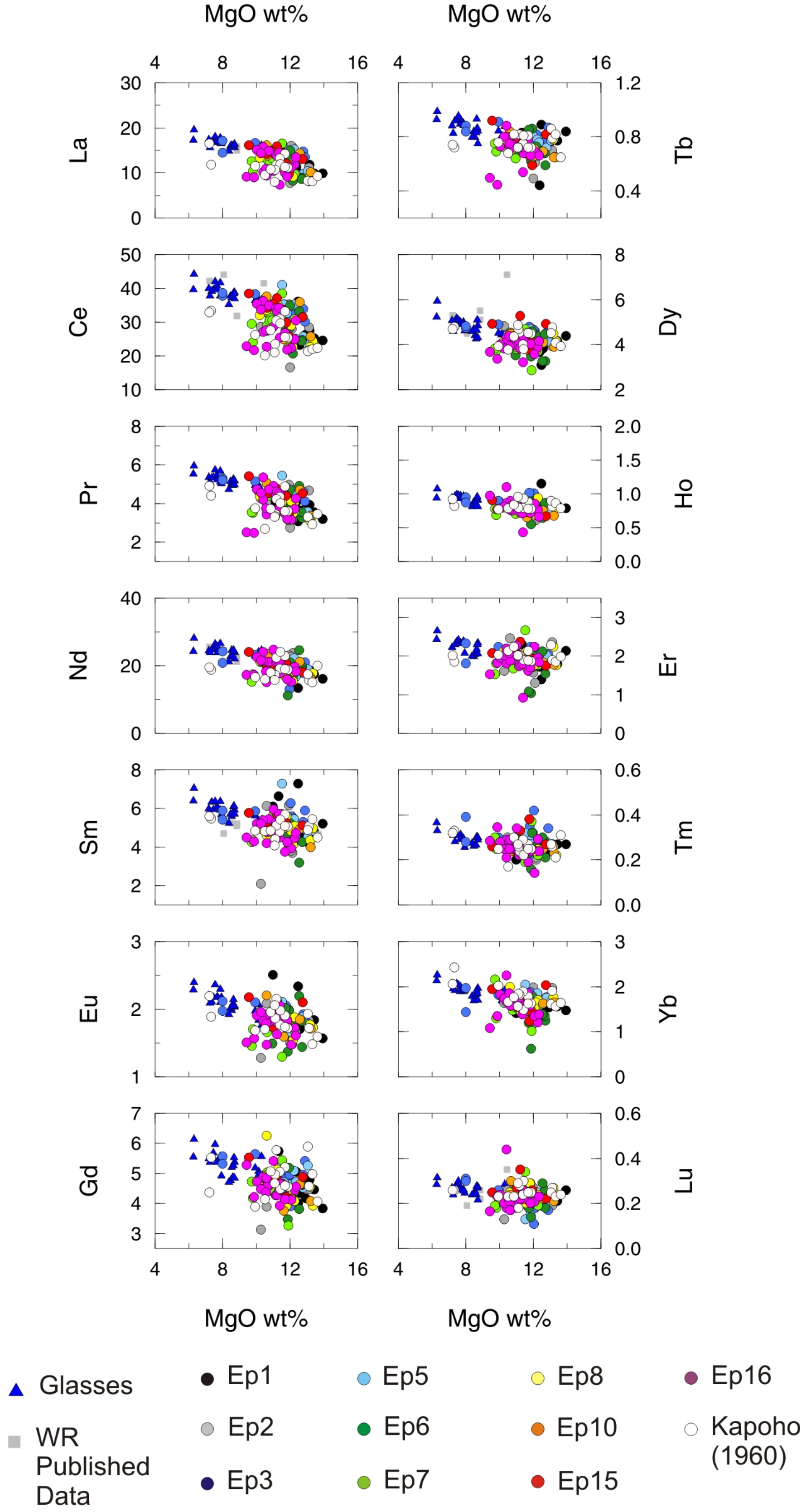

Figure 5.17: MgO wt% versus rare earth element concentrations of melt inclusions and matrix glasses of the 1959 and 1960 eruption. Where available, published whole rock data are from *Tilling et al.* (1987).

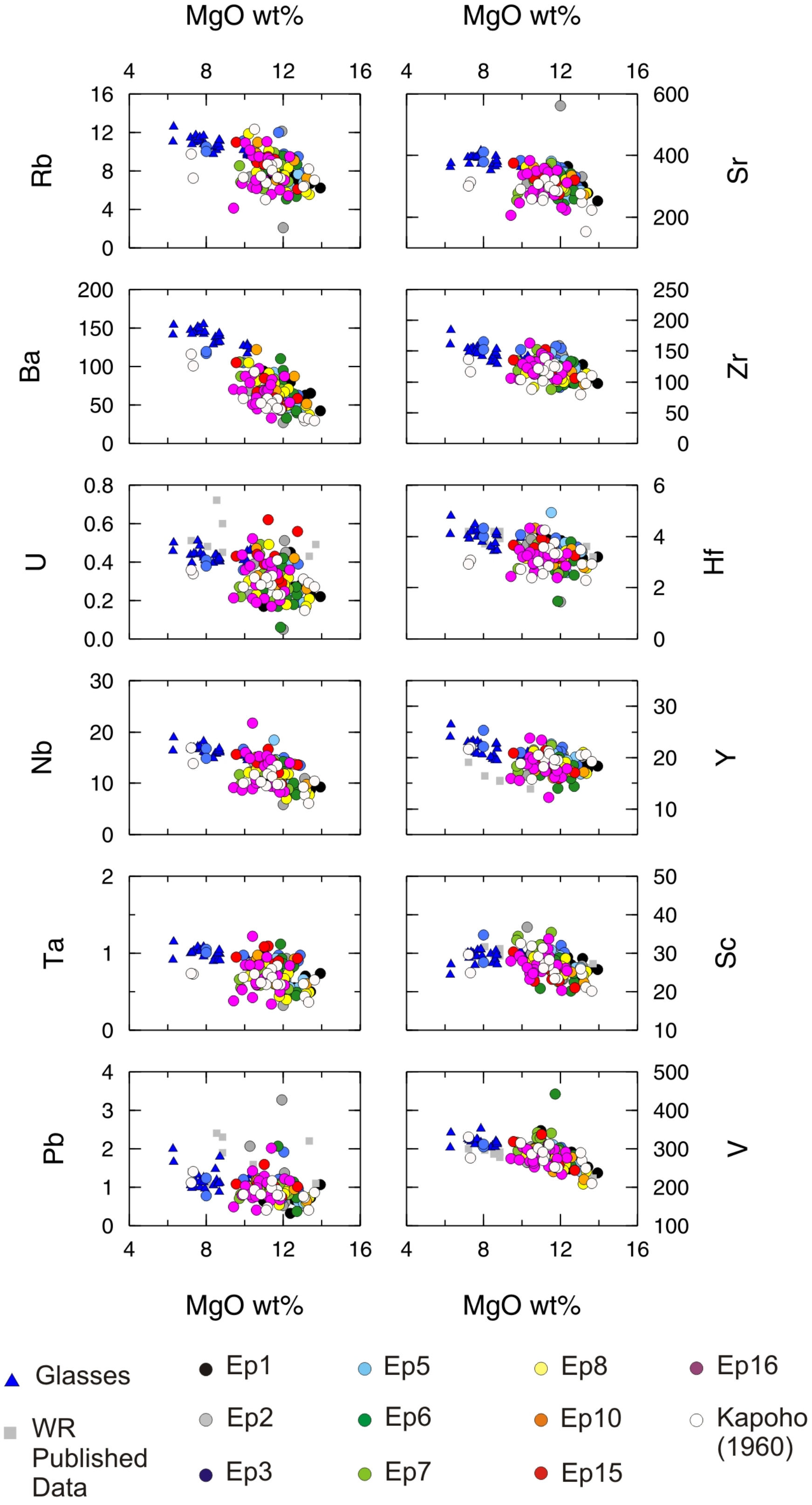

Figure 5.18: MgO wt% versus trace element concentrations of melt inclusions and matrix glasses of the 1959 and 1960 eruption. Published whole rock data are from *Tilling et al.* (1987).

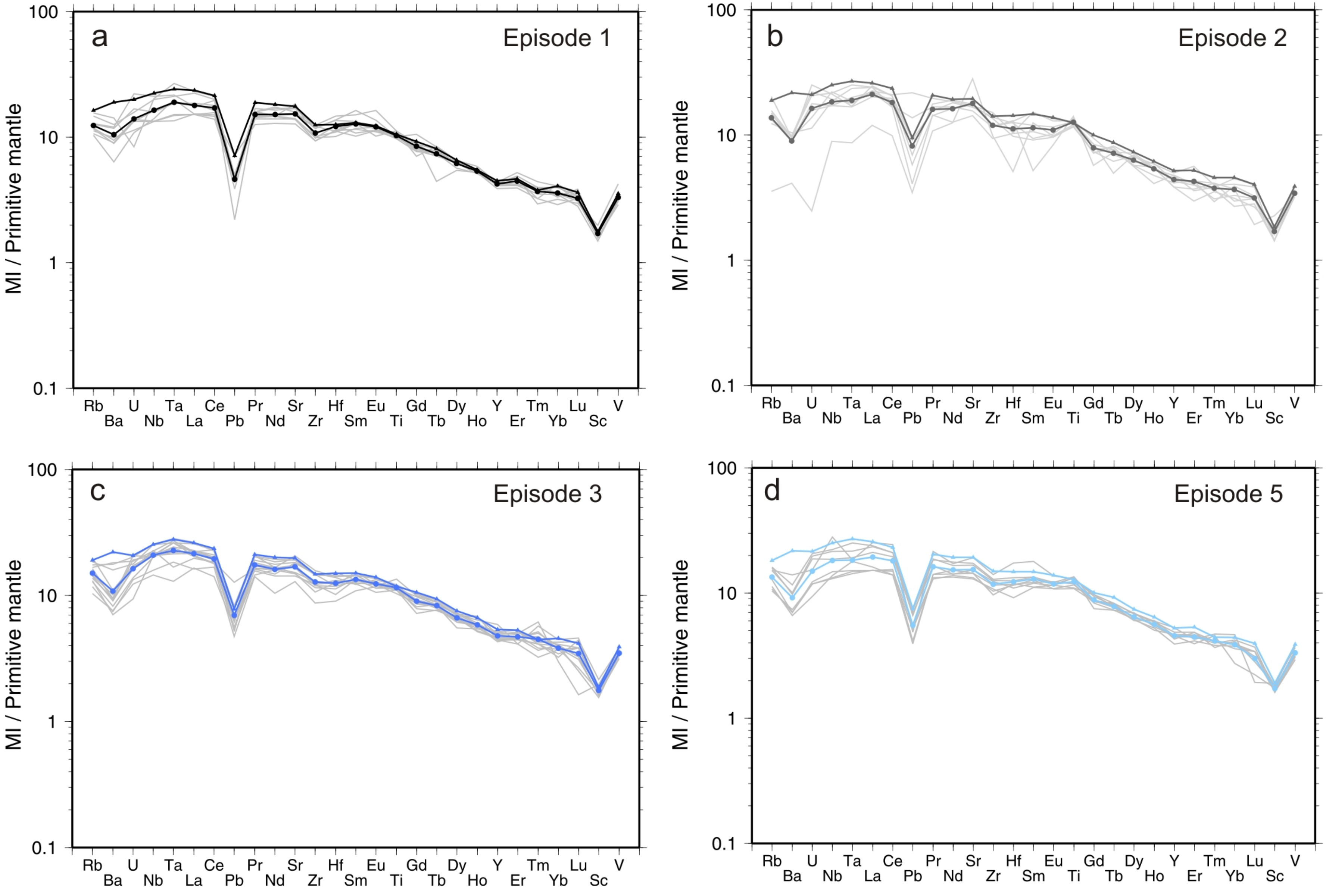

Figure 5.19: Primitive mantle-normalised (*McDonough and Sun*, 1995) multi-element diagrams (a–k) for each episode of the 1959 Kīlauea Iki eruption and 1960 Kapoho eruption. Grey lines represent all melt inclusion analyses for the episode and circled profiles show the average inclusion composition. The average normalised matrix glass profiles are also shown (triangle symbols).

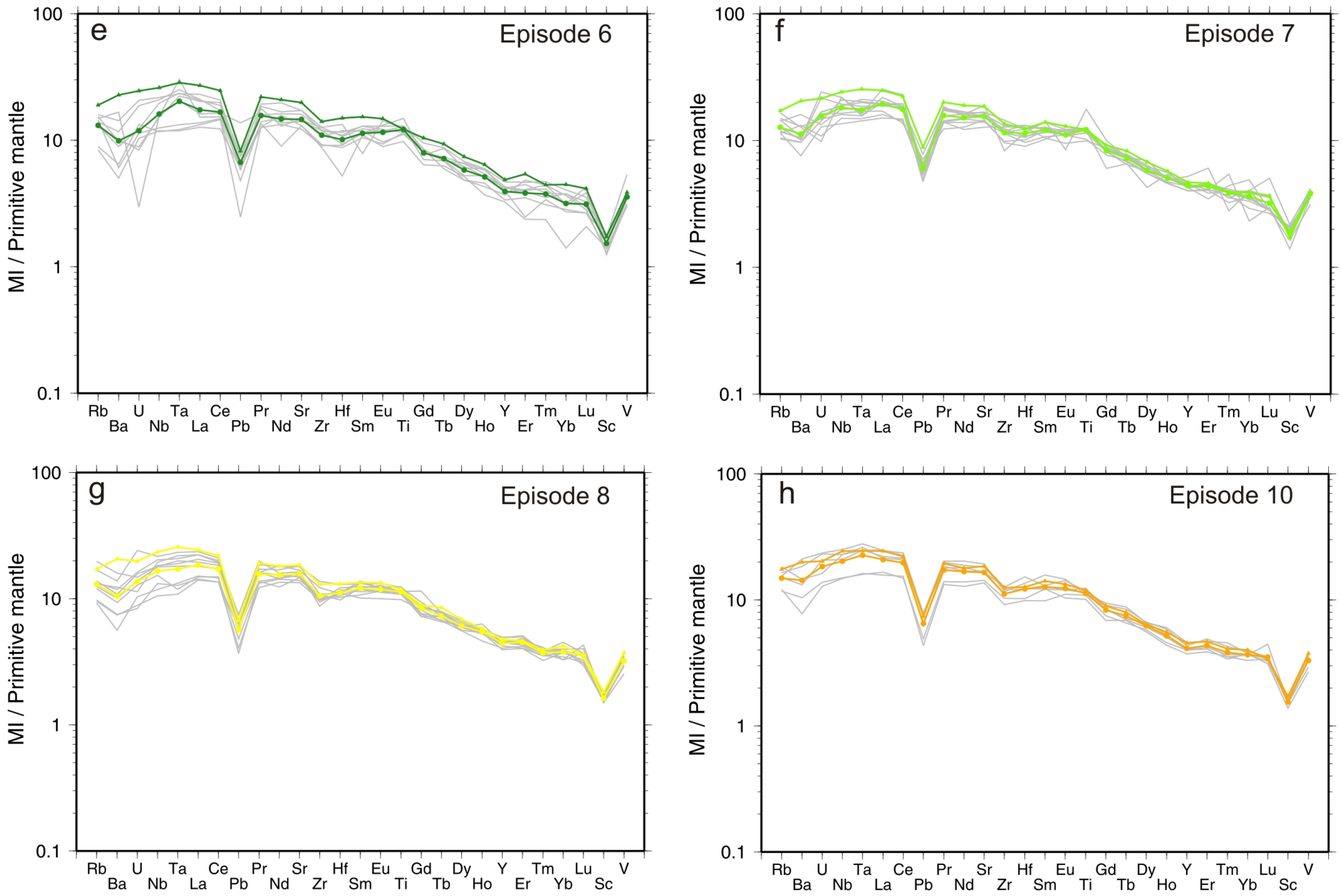

Figure 5.19: Primitive mantle-normalised (*McDonough and Sun*, 1995) multi-element diagrams (cont'd).

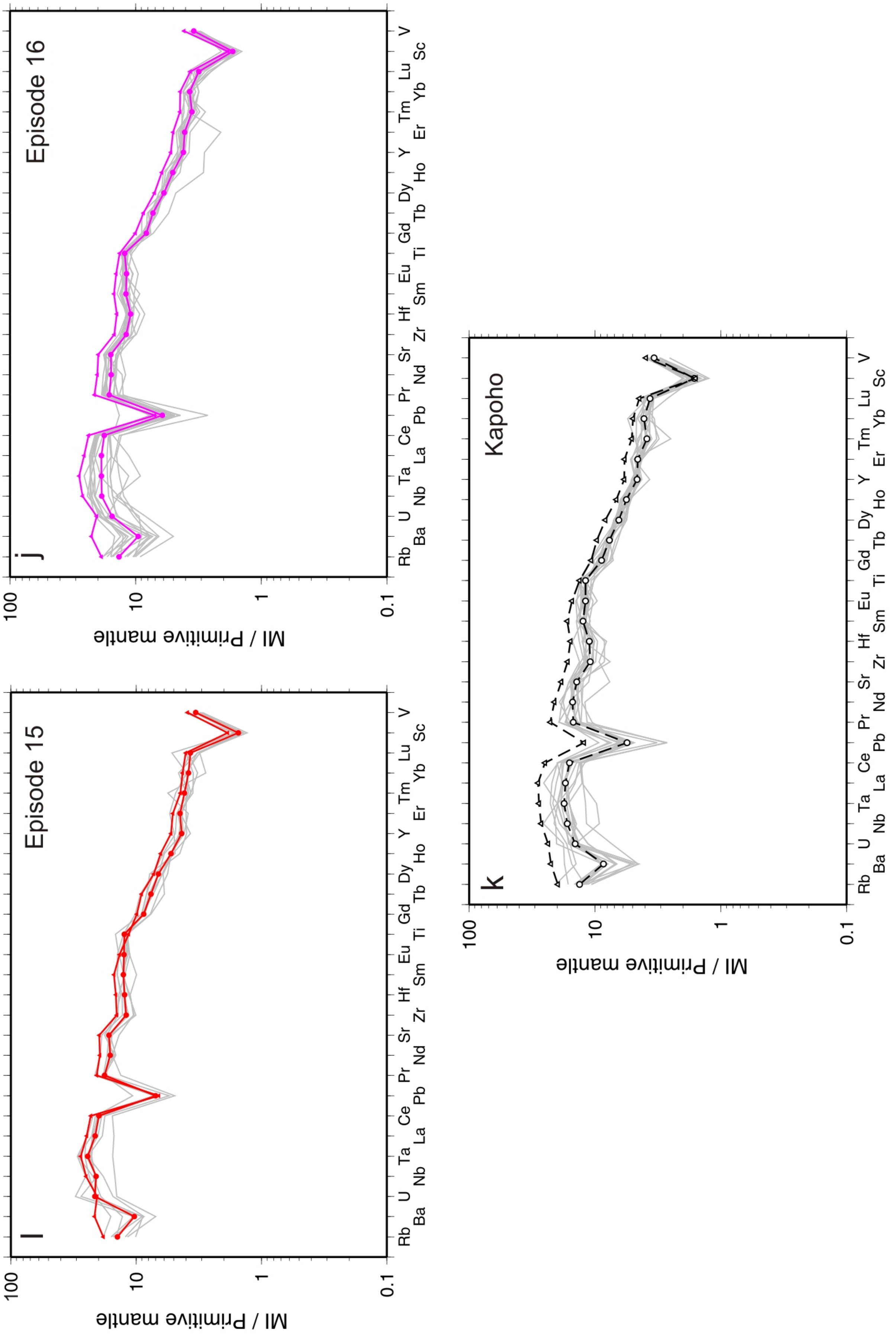

Figure 5.19: Primitive mantle-normalised (*McDonough and Sun*, 1995) multi-element diagrams (cont'd).

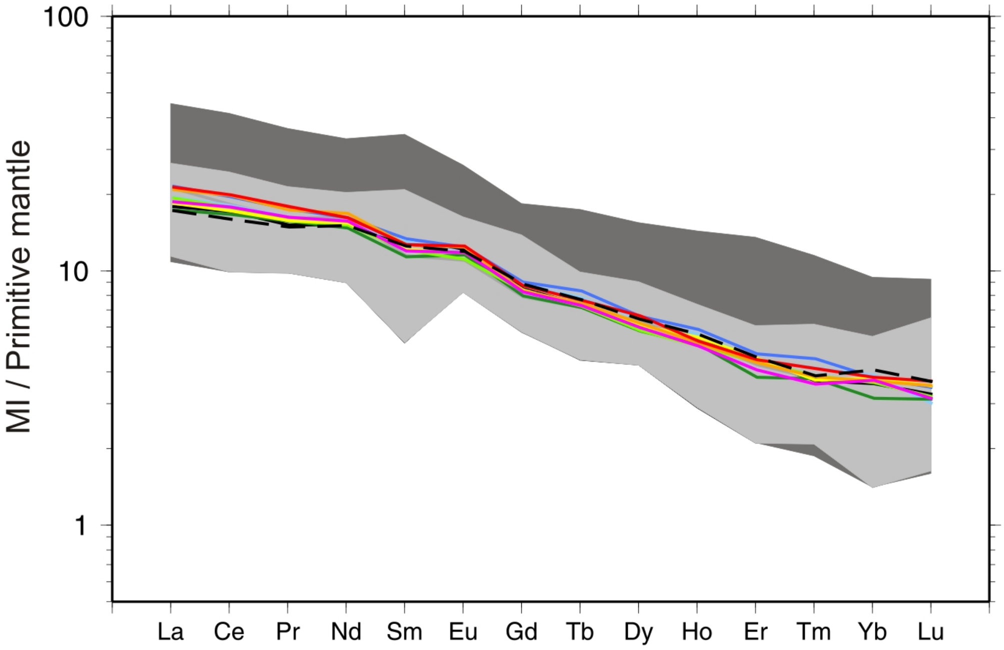

Figure 5.20: Primitive mantle-normalised (*McDonough and Sun*, 1995) REE diagram for the 1959 and 1960 samples. Profiles are the average normalised REE concentrations for each eruptive episode. The maximum range of REE concentrations for the 1959 eruption are shown in the light grey field, together with the maximum range for all pre-historic and historic Kīlauea eruptions sampled in this study (dark grey field).

enrichments within any of the 1959-60 samples.

5.3.4 Volatile chemistry

H_2O and CO_2 concentrations in the 1959 melt inclusions range from 0.09 to 0.64 wt% and from 31 to 656 ppm respectively. These values span almost the entire range of concentrations observed in melts erupted from Kīlauea over the past 500 years (0.07–0.91 wt% H_2O and 0–829 ppm CO_2; Chapter 4) and the maximum H_2O concentration is close to the estimate for undegassed Kīlauea summit magmas ($\sim$0.72 wt%; (*Wallace*, 1998)). Matrix glass compositions vary between 0.04–0.11 wt% H_2O, with all CO_2 concentrations below detection limits.

Volatile concentrations for all episodes of the summit eruption are shown in H_2O-CO_2 space in Figure 5.22. Isobars showing the concentration of saturated melts at constant pressures, were calculated using the H_2O-CO_2 saturation model, VolatileCalc *Newman and*

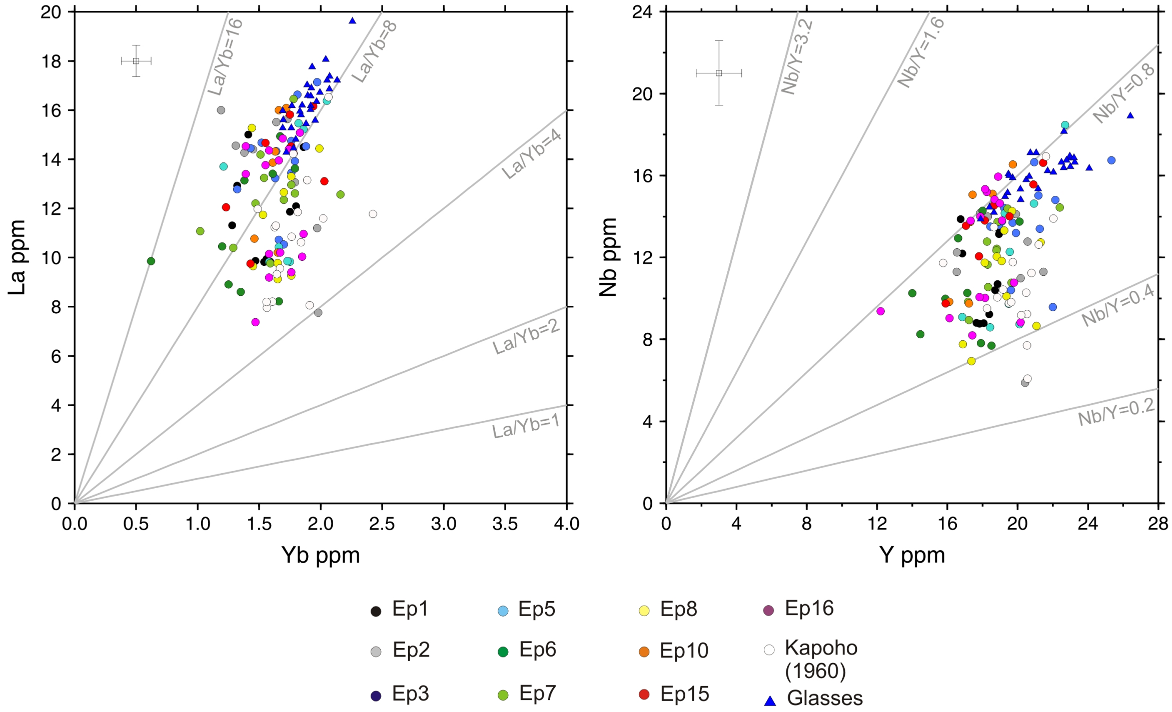

Figure 5.21: (a) La versus Yb and (b) Nb versus Y concentrations in the 1959 and 1960 melt inclusions and matrix glasses. Grey lines denote constant ratios of La/Y and Nb/Y respectively. If fractionation was the dominant control on melt concentrations, compositions would be expected to define a constant ratio.

Lowenstern (2002). The composition of the measured inclusions suggest that their pressures of formation during crystallisation were shallow, with all forming at pressures < 150 MPa, consistent with the estimates of *Anderson and Brown* (1993). However, for those melts which may be undersaturated with respect to H_2O, these represent minimum estimates of pressure.

A striking feature of Figure 5.22 is the apparent temporal trend in volatile concentrations from episode to episode. Episode 1 has the largest range in CO_2 values, with the highest H_2O and CO_2 values. The final episodes of the eruption, 15 and 16 are clearly the most volatile poor melts, with most concentrations grouping at significantly lower H_2O-CO_2 values. The H_2O contents of the Kapoho 1960 eruption inclusions are less variable than those of the summit melts, ranging between 0.41–0.54 wt%. By contrast, CO_2 concentrations are considerably lower in the Kapoho samples, from 25 to 283 ppm. Residual matrix glasses contain no CO_2 above detection limits, and have a H_2O value of 0.07 wt%.

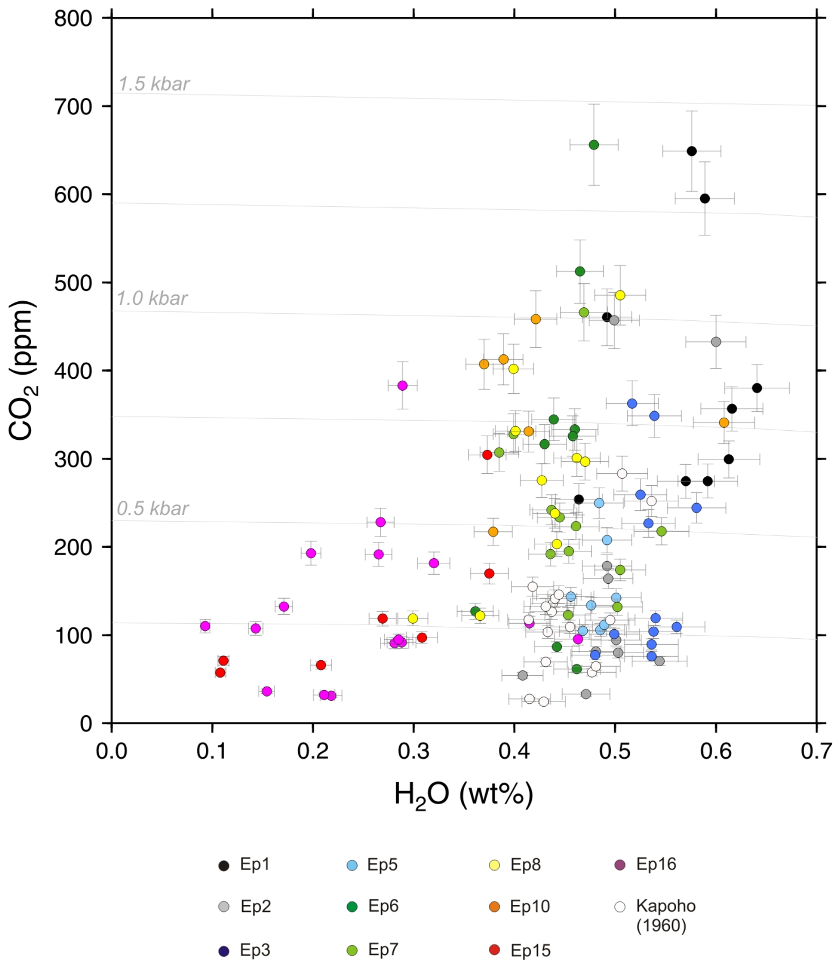

Figure 5.22: H_2O-CO_2 concentrations in melt inclusions of the 1959-60 eruption. Isobars are shown in grey, and were calculated using VolatileCalc (*Newman and Lowenstern*, 2002). Calculations were performed for melts at 49 wt% SiO_2 at 1150 °C. Errors shown are 1σ precision on standard repeats.

Sulphur (S) values in the summit melt inclusions are highly variable and range from 175 to 1530 ppm and between 35–171 ppm in the glasses (Figure 5.23). The considerably lower concentrations of S in the matrix glasses is consistent with extensive, but not complete, syn-eruptive degassing. S does not display any correlation with non-volatile incompatible trace elements indicating that processes other than fractionation are exerting a dominant control over melt concentrations. The inclusion S–CO_2 data display a similar distribution to the H_2O–CO_2 trends of Figure 5.22, but do not display the same temporal trends observed in the H_2O–CO_2 dataset.

Chlorine and fluorine concentrations in the summit and flank eruption inclusions range

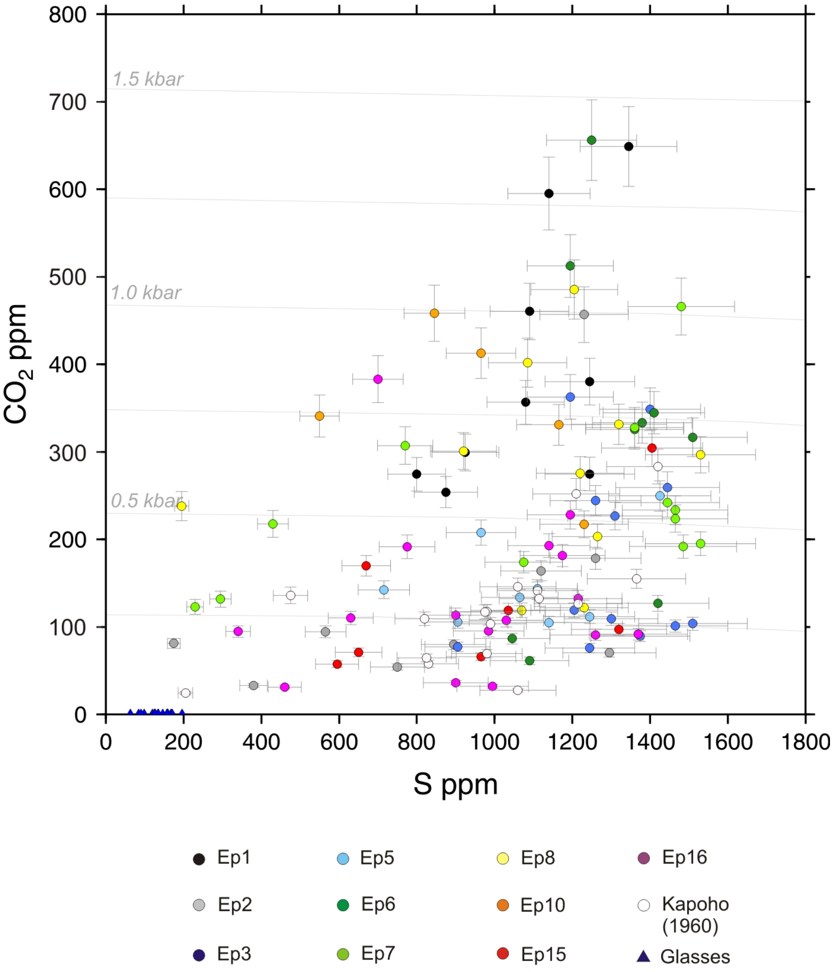

Figure 5.23: CO_2–S concentrations in melt inclusions of the 1959–60 eruption. Isobars shown in grey were calculated as in the previous figure and are shown for comparison. Errors shown are 1σ precision on standard repeats.

from 90–410 ppm and 180–810 ppm repsectively. Both elements have higher solubilities in basaltic melts than other volatile species and are highly incompatible (*Sigvaldason and Oskarsson*, 1975). However, neither element analysed in the 1959-60 eruptions correlate with any non-volatile incompatible elements (Figure 5.24a and b), in contrast with the behaviour of Cl and F observed in other Hawaiian lavas (*Dixon and Clague*, 2001). Matrix glasses contain between 111-268 ppm Cl and 541–714 ppm F. There is no clear relationship between either of these elements and other volatile elements such as H_2O in the 1959-60 melts (Figure 5.24c and d).

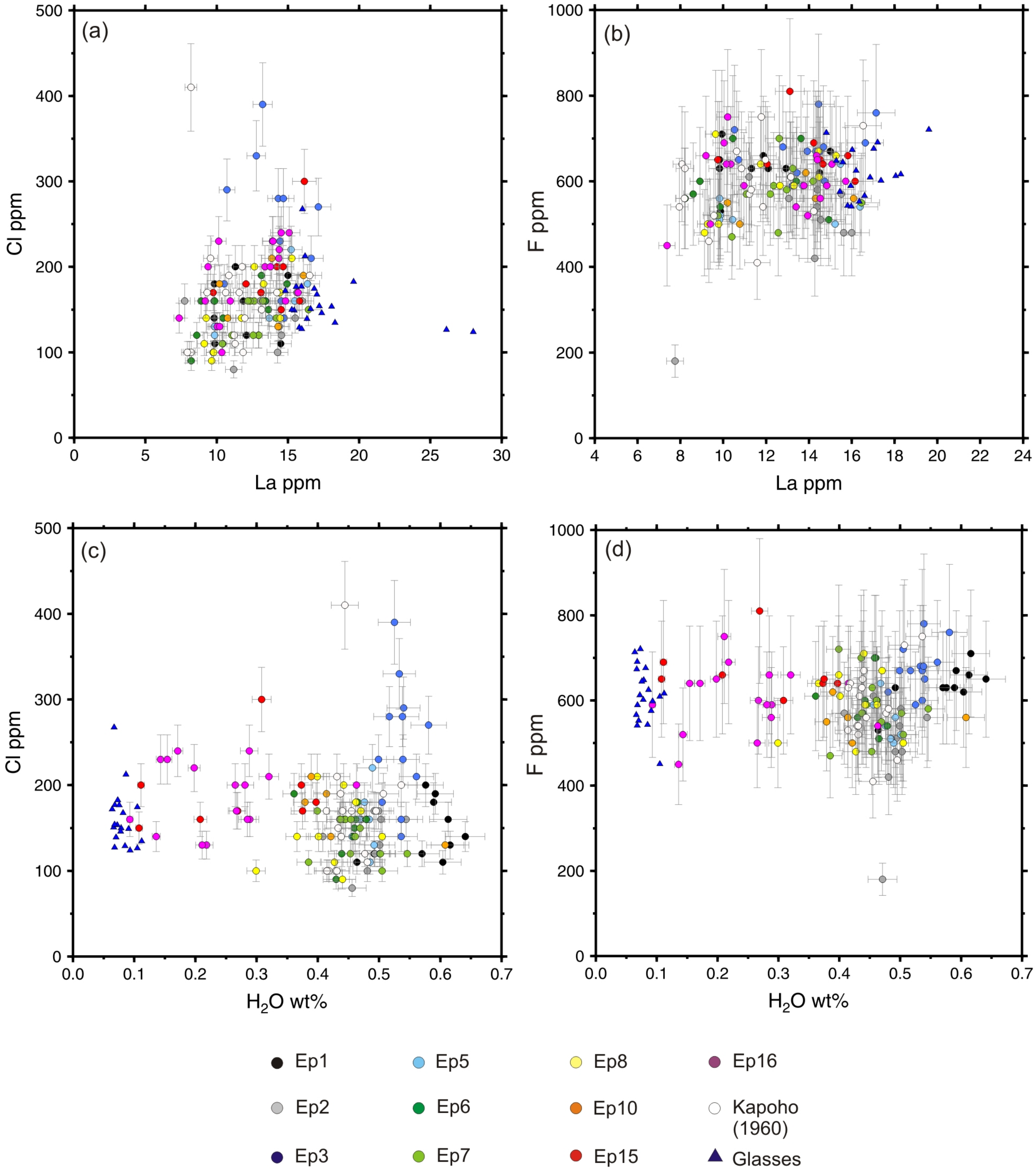

Figure 5.24: Halogen versus La and H_2O concentrations in the 1959-60 melts. (a) Cl versus La; (b) F versus La; (c) Cl versus H_2O. Cl concentrations within the melt inclusions remain within a constant range for all episodes, except for phase 3 of the eruption which is notably Cl-rich. There is little difference between the Cl concentration in the glasses and inclusions; (d) F versus H_2O.

5.3.4.1 Variations in volatile concentrations

Figure 5.25 show average and total volatile concentrations for each episode versus the date of eruption. H_2O concentrations display a very clear negative correlation with time. Regression of the full dataset yields an r^2 correlation coefficient of 0.77 with the date of eruption, or an r^2 equal to 0.87 in the population averages. CO_2 also displays an overall negative correlation such that the earliest episodes were more CO_2-rich and the final phases were CO_2-poor. However, the relationship between CO_2 and eruption date is more complex in the intermediate episodes and there appears to be a trend reversal and linear increase in CO_2 concentrations between episodes 5–6 and 7–10. Temporal variations in other volatiles are less clear: S concentrations are variable between episodes, and only displays a progressive decrease in the melts in later episodes (6–16). Cl increase in concentrations between episodes 7 to 16, whilst F does not vary significantly with time.

CO_2 and H_2O concentrations of the melt inclusions are compared with the maximum fountain heights attained in each eruptive episode and are shown in Figure 5.26. Fountain heights used in the comparison are those from *MacDonald* (1962), shown in Table 5.1. The full range of CO_2 and H_2O concentrations for each eruptive episode are represented on the figures in gray and display similar values between many episodes. However, the range of concentrations represents only the minimum and maximum values and not the distribution of data within each population. For this reason, the average values are taken for each eruptive phase and the errors represent the standard error of the estimate of the mean, (calculated as in Equation 1). Figure 5.26a reveals a distinctive decrease in range of CO_2 concentrations with increasing fountain heights. This negative correlation persists in average CO_2 values for each eruptive phase with an r^2 coefficient of 0.67. Pre-eruptive melt H_2O concentrations exhibit an overall negative correlation with fountain heights although the correlation is much weaker (r^2 coefficient of 0.28) than CO_2. S, Cl and F show no relationship with height and are therefore not included.

Errors in fountain height estimates are difficult to constrain. The estimates themselves were made by *MacDonald* (1962) using three different methods during the eruption, and were corroborated between different observers during the events. They are therefore considered to be robust estimates of the maximum values. However, it is impossible to determine

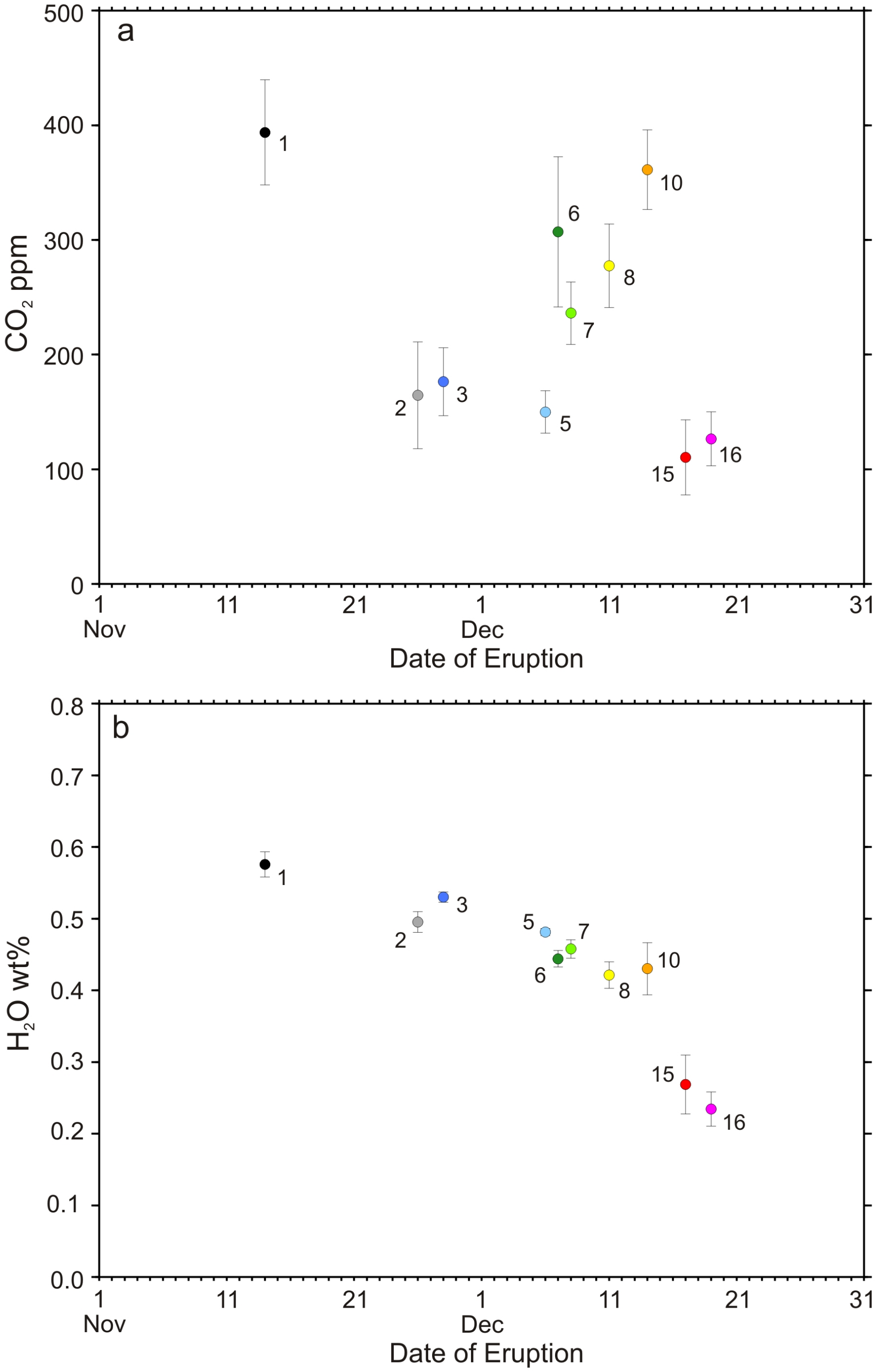

Figure 5.25: Temporal variations in the average pre-eruptive volatile concentrations for each episode during the 1959 summit eruption (a) H_2O versus time; (b) CO_2 versus time

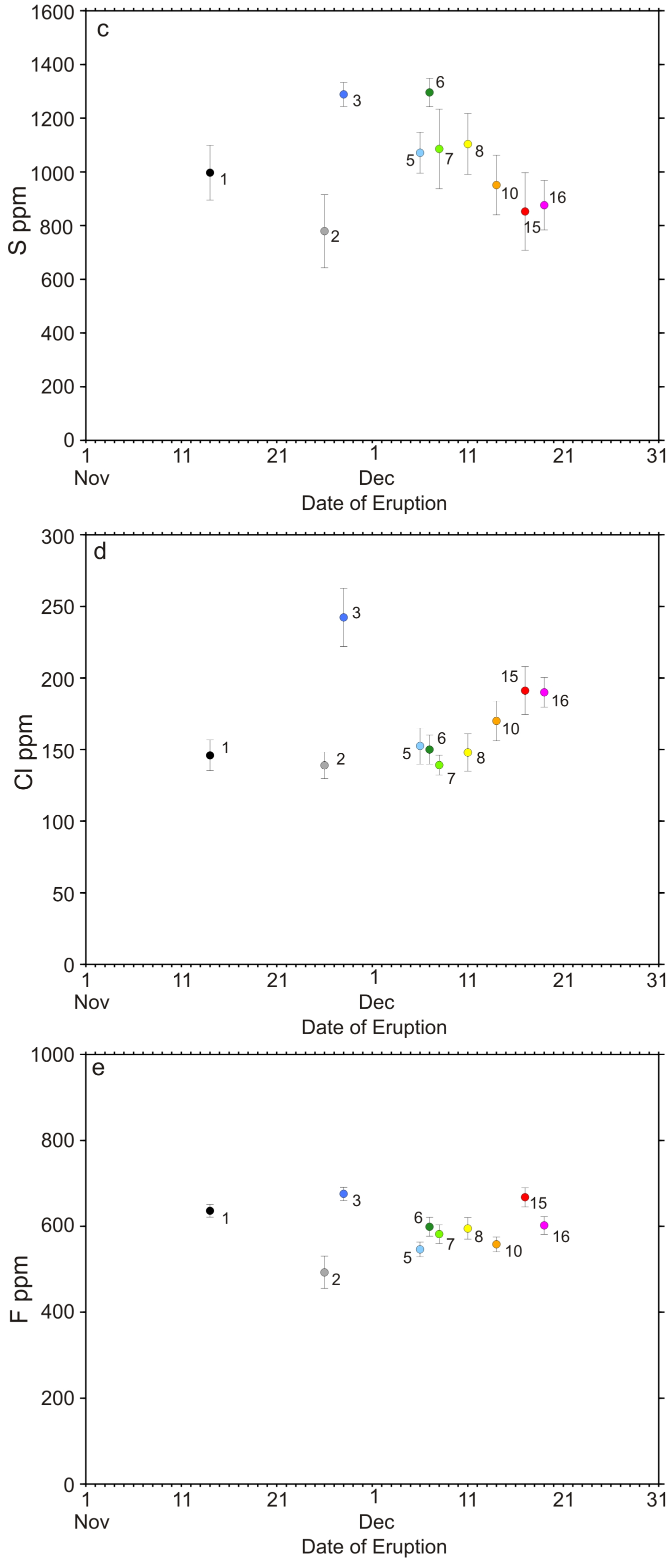

Figure 5.25: Temporal variations in the average pre-eruptive volatile concentrations for each episode during the 1959 summit eruption (cont'd): (c) S; (d) Cl and (e) F. Errors shown are calculated as the standard error of the mean for each episode population.

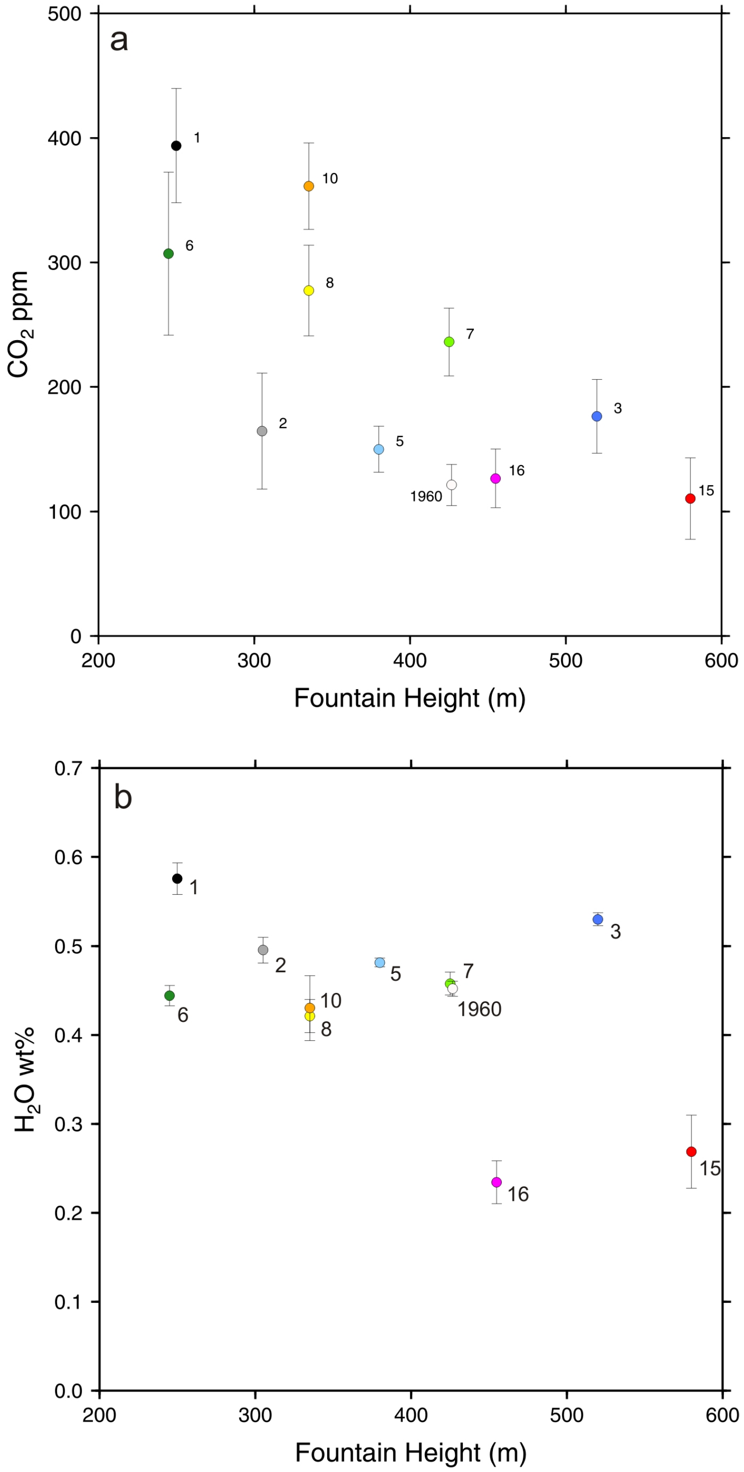

Figure 5.26: (a) CO_2 and (b) H_2O concentrations versus fountain heights for the 1959 and 1960 eruptions. Coloured symbols are the average melt inclusion concentrations for each episode, with error bars representing the standard error on the estimate of the mean. Heights are those recorded by *MacDonald* (1962) and are the maximum values for each phase with the exception of episode 1, for which an average height of 250 m is used (see text for explanation).

whether the tephras sampled in this study were produced from fountains during attainment of their maximum eruptive heights. This is a more significant problem for earlier eruptive phases such as episode 1 which lasted for seven days, but from which only one sample was analysed. For this reason, maximum fountain heights for episode 1 were taken as 250 m, a more representative estimate for the entire phase according to *Stovall et al.* (2011).

5.4 Discussion

5.4.1 Provenance of the melt inclusions

In order to use the melt inclusion compositions for constraining pre- and syn–eruptive processes during the 1959 eruption, it is necessary to consider whether the olivine-hosted inclusions are genetically related to their host-carrier melts. It is seldom possible to distinguish olivine provenance (xenocryst versus phenocryst) on the basis of optical inspection (*Maclennan*, 2008b), and despite the broad range of different crystal sizes and morphologies, no compositional relationships between olivine or melt inclusion chemistry and crystal morphology were apparent.

The extensive variety of olivine morphologies within the Kīlauea Iki tephra has been used in previous studies to suggest that many of the crystals were in fact xenocrysts extracted from a pre-existing deforming cumulate mush within the summit magma reservoir (e.g. *Murata and Richter*, 1966a; *Schwindinger and Anderson Jr*, 1989). Many of the olivines are macrocrysts of multiple grains, with euhedral habits and undulose extinction that have been interpreted as forming through a complex combination of paired nucleation, and crystal aggregation or synneusis (*Schwindinger and Anderson Jr*, 1989). In addition to this *Mangan* (1990) estimated the crystallisation rates required to produce these olivines, by applying growth rates for plagioclase and ilmenite from Makaopuhi lava lake to the 1959 lavas, and concluded a residence time of 10 years prior to eruption. If these interpretations were correct, the melt inclusions analysed in this study would be completely unrelated to the eruption. However, a recent study of olivine growth forms by *Welsch et al.*, has revealed that crystallisation by dendritic growth and ripening, rather than complex aggregation, can account for almost all olivine morphologies, including aggregates, dislocation lamellae and apparent deformation features. They propose that the macrocryst clusters are not cumulate xenocrysts but phenocrysts which develop under a high degree of undercooling (> -60° C) and in suspension within the liquid. Depending on the melt crystallisation history and assuming an initial stage of rapid growth at a rate of $10^{-6}\,\mathrm{m\,s^{-1}}$, a typical macrocryst (0.5–5.0 mm) can crystallise in 8 minutes to 58 days (*Welsch et al.*). Thus it is very plausible to assume the Kīlauea Iki phenocrysts formed over the pre- and syn-eruption timescales.

The poor correlation between the olivine and matrix glass compositions (Figure 5.12) implies strong disequilibrium between the crystals and melt. Disequilibrium may be induced if crystallisation occurred prior to and during extensive magma mixing within the summit reservoir, or if the high-Fo olivines were xenocrysts formed within the mantle. However, the latter explanation is discounted owing to the moderate CaO contents of the crystals (0.25–0.35 wt %) (e.g. *Garcia et al.*, 2003; *Jurewicz and Watson*, 1988). This implies that the olivines may therefore be antecrysts – crystals which formed within the plumbing system of the eruption but are not in chemical equilibrium with the carrier melts at the time of eruption (*Maclennan*, 2008b).

Trace elements provide a further means for testing the genetic relationship between the inclusions and melts. The trace element compositions of the melt inclusions are always more variable than those of the matrix glasses, but the multi-element profiles of the average inclusion compositions are similar to those of the glasses for each episode (Figure 5.19). If parental melts entering a reservoir have slightly variable trace element compositions and are trapped by the inclusions, and each melt inclusion represents a sample of an equal volume of melt then mixing of these melt volumes should produce a final melt (glass) with a composition equal to the average of the inclusions (*Maclennan*, 2008b). This is tested using the average melt inclusion ratios of La/Yb for each episode (calculated as $\sum\mathrm{La}/\sum\mathrm{Yb}$) versus the average La/Yb of the matrix glasses, shown in Figure 5.27. If the glass compositions were the result of mixing melts with compositions represented by the inclusions, the La/Yb ratios should lie within error of the 1:1 correspondance line in Figure 5.27. However, this is only true for episodes 2, 3, 6, 10 and 15. Episodes 1, 5, 7, 8 and 16 lie at lower $\mathrm{La/Yb}_{MI}$ values and the Kapoho 1960 inclusions appear the furthest from equilibrium. At face value Figure 5.27 indicates that 50% of the 1959 episodes may not be related to their carrier melts, however there are a number of possible explanations for this apparent disequilibrium. The

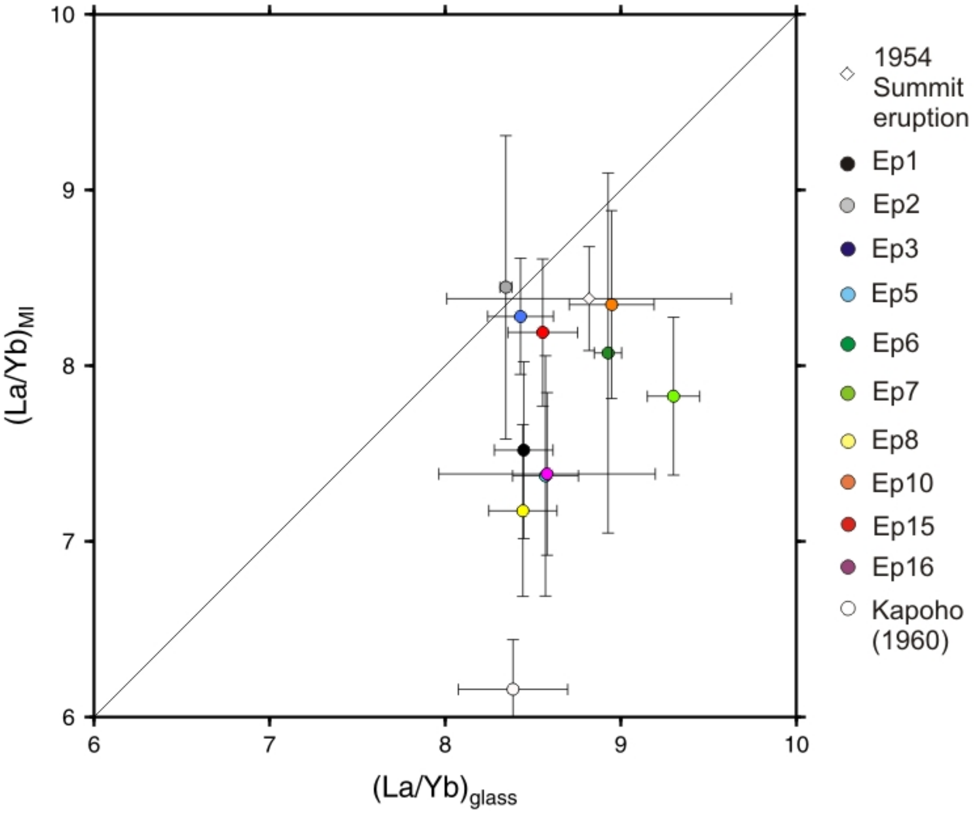

Figure 5.27: Compositional relationship between melt inclusions and host glasses for each episode of the 1959 and 1960 eruptions. Mean La/Yb for melt inclusions (mi) versus mean La/Yb of the host matrix glass (mg). Bars represent the 1σ standard error of estimate of the means (see text for explanation).

La/Yb test assumes pre-eruptive mixing of variable melt compositions (represented by the trapped inclusions of each episode), but if inclusions were trapped prior to the carrier melt encountering a second stored magma with a higher La/Yb ratio, this may produce relatively high La/Yb ratios in the average matrix glasses. Syn-eruptive mixing during drainback, or the arrival of new melts from depth with different La/Yb ratios may also account for some of the variation and will be explored in greater detail below. If matrix glasses are also heterogeneous, undersampling of their composition might affect the 1:1 correlation.

Despite the variation in melt compositions, the distribution of olivine compositions is roughly the same between episodes (Figure 5.12), and there may be some retention of olivines between episodes. However, the distinctive temporal trends in melt inclusion volatile compositions, particularly those of H_2O and CO_2 imply that despite the disequilibrium observed between the olivines and host melts, the melt inclusions are recording syn-eruptive processes.

Another important consideration is whether the inclusions are representative of bulk melt compositions. Crystallisation can lead to the development of a crystal-melt boundary layer enriched in elements that are incompatible in the crystallising phase (*Faure and Schiano*, 2005; *Kent*, 2008; *Baker*, 2008). Melt inclusion formation occurs rapidly and under non-equilibrium conditions, and may trap these boundary melts, rich in slow-diffusing elements, resulting in unusual inclusion compositions. For example, P_2O_5 diffuses more slowly through melts than TiO_2 and may explain why some of the 1959 inclusions have unusually high P concentrations (Figure 5.15a). However, if olivine is the major crystallising phase, boundary layer entrapment predicts that the inclusions would also be enriched in Al_2O_3 relative to CaO (both are incompatible, but Ca diffuses more rapidly) (*Faure and Schiano*, 2005). The 1959 and 1960 inclusions display the opposite trend and are instead enriched in CaO (Figure 5.15b), which led to the previous interpretation that 1959 inclusions reflect entrapment of bulk melt compositions that show an affinity with the CaO-rich S1 endmember (*Anderson and Brown*, 1993; *Loewen*, 2011).

5.4.2 Constraints on magma mixing and fractionation from major and trace elements

Although mixing and fractionation of the Kīlauea Iki melts have been investigated previously with whole rock analyses, melt inclusions and glasses reflect the pre- and syn-eruptive compositions of the melt, and are more sensitive to the processes of magma mixing and mantle source variations, in addition to being unaffected by abundant olivine accumulation. The high MgO content of the most primitive melt inclusions is comparable with the highest MgO concentrations measured for Kīlauea (15 wt%; *Clague et al.* 1995) in submarine glasses from the East Rift Zone, and may therefore be a close representation of the primary melt compositions supplied from depth. Though olivine fractionation trends between the glasses and inclusions are present in Figures 5.14, 5.17 and 5.18, the heterogeneity within inclusion concentrations of minor and trace elements at the same MgO values likely reflects melt compositional variability existing within the summit magma reservoir during olivine crystallisation and provides constraint against single-batch fractionation of a primitive basalt.

The observed variation in olivine-incompatible elements may be the result of magma mixing, varying degrees of partial melting, or variation in the mantle source composition. Magma mixing in the 1959 melts has been investigated in a recent study by *Loewen* (2011). They used incompatible element ratios in matrix glasses to constrain mixing relationships between the S1 and S2 endmember compositions. Sr/Y versus Zr/Nb or Nd/Zr ratios from glasses analysed in this study are shown in Figure 5.28a and b, together with values from *Loewen* (2011) for comparison. The data form an apparent two component mixing trend between the inferred S1 and S2 endmember compositions as determined by *Loewen* (2011). The ratios however may be affected by degree of partial melting or source composition as a garnet-bearing source would retain Y and Zr to a greater extent. Also shown on Figure 5.28a and b, are conceptual vectors for batch partial melting of a garnet lherzolite source showing the trend and magnitude of ratio variations, with partial melting percentages between 8–22% (*Loewen*, 2011). The partial melting trends may explain the approximate shape of variation of Zr/Nb, but a single partial melting model does not fit the Nd/Zr trend. *Loewen* (2011) interpreted these, and other trends, as evidence that glass compositions in the 1959 eruption are controlled by two magma batches with distinct sources. The glasses analysed in this study lie close to or parallel with the trends observed by *Loewen* (2011) and appear to corroborate their interpretation.

However, melt inclusion compositions do not comform to the two-component mixing observed in the glasses (Figure 5.28c and d) and produce no distinct trends. This, together with the observed broad range of inclusion La/Yb and Nb/Y ratios in Figure 5.21, implies that the origin of the variation is likely to be a more complex and suggests greater variation in degree of partial melting.

In volcanic systems in Iceland it has been demonstrated that when primitive melts that are variable in their trace element compositions are supplied to a magma reservoir, crystallisation and mixing occur simultaneously and olivines may trap melt inclusions with a wide range of trace element compositions, whilst mixing homogenises the composition of the host melt (*Maclennan*, 2008b). If the host melt then encountered a second body of melt with a different composition then a second stage of mixing could occur. Mixing of a cooler stored magma with a hotter, more primitive melt would promote rapid olivine crystallisation and further entrapment of inclusions with variable melt compositions. At Kīlauea Iki, *Helz*

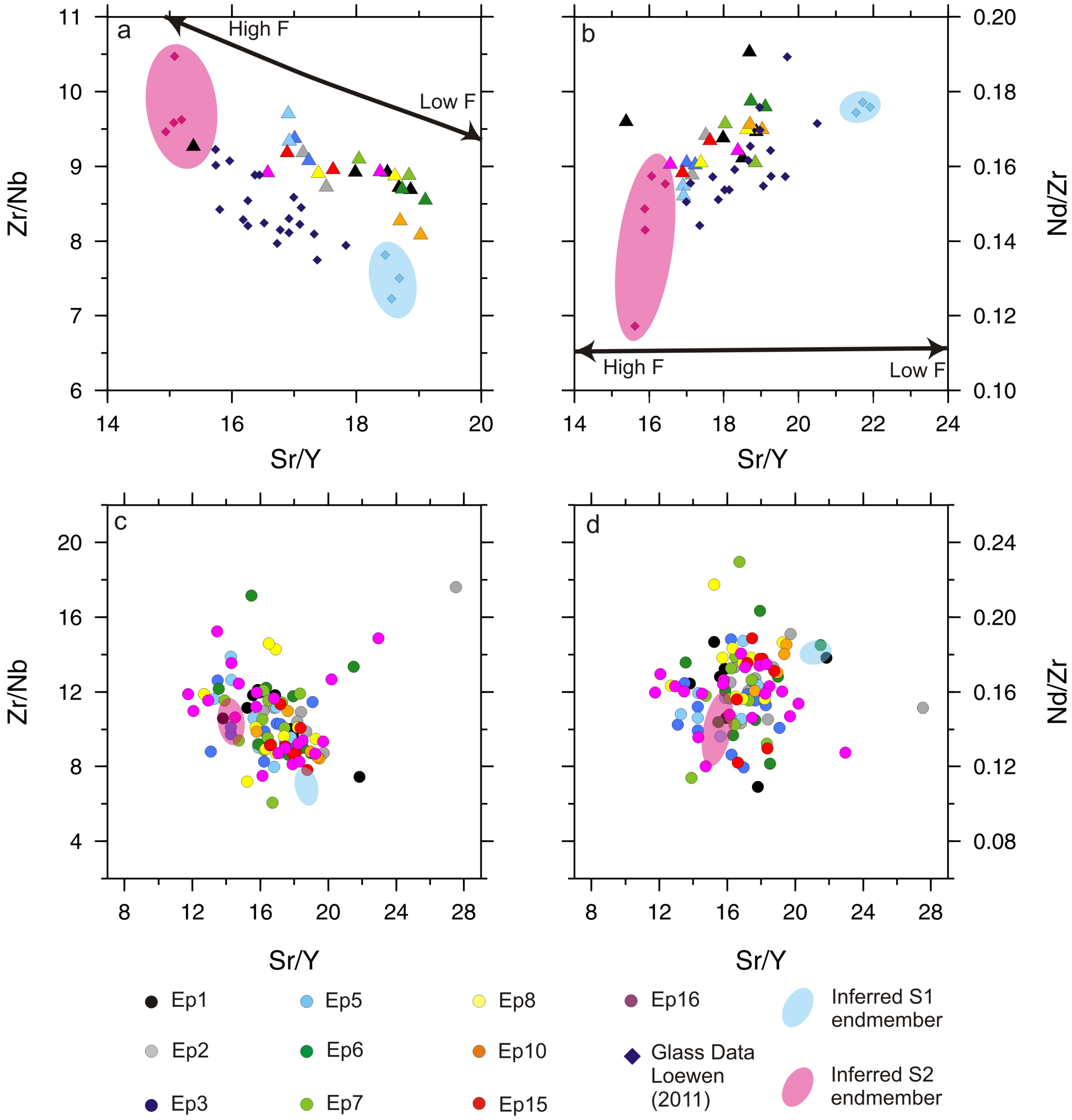

Figure 5.28: (a) Sr/Y versus Zr/Nb and (b) Sr/Y versus Nd/Zr in matrix glasses from the 1959 eruption. Glass compositions from this study are represented by triangles coloured by episode number. Also shown are glass compositions analysed by *Loewen* (2011). S1 and S2 endmember compositions were inferred by comparing glass compositions with whole rock models of *Wright* (1973). Conceptual vectors for batch partial melting of a garnet lherzolite source between 8–22% are also shown (modified from *Loewen* (2011); see text for further explanation).(c) Sr/Y versus Zr/Nb and (b) Sr/Y versus Nd/Zr in melt inclusions of the 1959 eruption (all melt inclusion compositions are from this study).

(1987) suggested that the S1 endmember was primitive melt supplied from mantle depths prior to the eruption, which mixed with an older melt stored in the summit region: the S2 component. The mixing models of *Loewen* (2011), *Helz* (1987) and *Wright* (1973) address only pre-eruptive mixing of the two compositions, however the volume data of *Eaton et al.* (1987) shown in Table 5.2 demonstrates that magma reservoir volumes were constantly changing throughout the eruption due to both the continued arrival of new melt input from mantle depths and drainback of erupted lavas back into the reservoir. The geophysical data imply that the process of mixing was therefore not restricted to pre-eruptive melts, and it is likely that the interaction of drainback melts with new input from depth produced the non-equilibrium conditions necessary for rapid olivine growth and melt entrapment. The inclusions therefore may record incomplete mixing of both the S1-S2 components but also incomplete mixing of new S1 melts from depth. This is supported by the positive correlation between the volume of reservoir inflation (column 4 of Table 5.2) associated with each episode and the variation in melt inclusion Nb/Y for each episode (Figure 5.29). Inflation volumes were calculated for each episode by calibrating the changes in tilt measurements during the eruption (*Eaton et al.*, 1987). The % variation of Nb/Y of melt inclusions in each episode was calculated and normalised to the number of inclusions analysed so as to remove any sampling bias. The correlation is best fitted by a logarithmic regression and has an r^2 value of 0.71. Although there is considerable scatter in the relationship between the two parameters Figure 5.29 clearly shows that the greater the volume of reservoir inflation (including inflation from new melt input and drainback), the greater the degree of compositional variation in the melt inclusion populations. The process of repeated replenishment and drainback, with the accompanying turbulence, may have been a very effective means of homogenising the contents of the reservoir (*Eaton et al.*, 1987) and may explain the limited glass heterogeneity and the dominance of the S1-S2 mixing trend in the host glass compositions.

5.4.3 Volatile systematics

Volatile elements in the Kīlauea Iki melts will also be affected by magma mixing, fractionation and source variability as described above, but their high diffusivity in basaltic melts, and low solubility at shallow summit reservoir pressures can result in an effective decoupling of

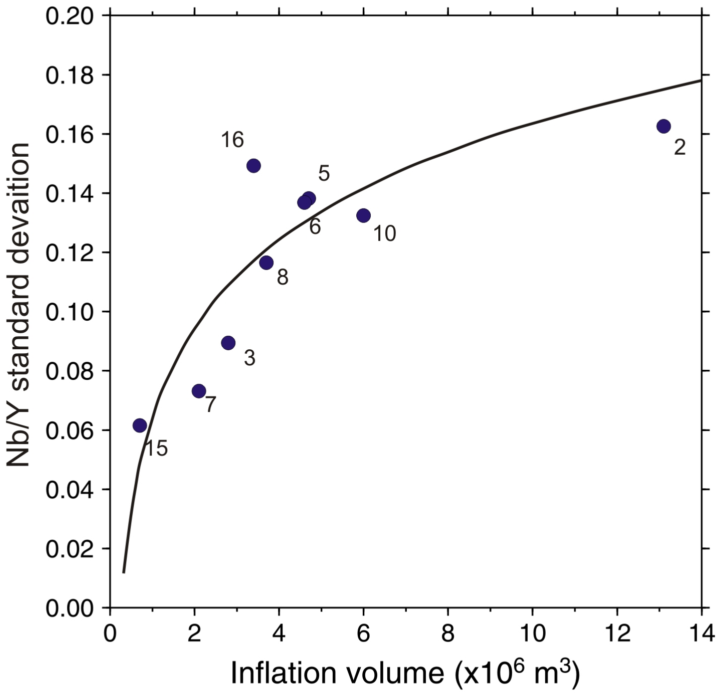

Figure 5.29: Compositional variability of the 1959 melt inclusions relative to magma reservoir inflation volumes throughout the eruption. Inflation volumes reflect new magma input into the reservoir from depth and the return of drainback magmas from the 1959 lava lake. Volumes were calculated from tilt measurements by *Eaton et al.* (1987). Nb/Y standard deviation represents the compositional variation within the inclusion population for each episode. Inflation volumes for episode 1 are not determined and therefore it is excluded from the Figure.

their concentrations from their parental magmas. Volatile elements are highly incompatible during crystallisation and as such, fractionation of an undersaturated melt should result in a constant ratio between the volatile element and another element with a similar partition coefficient. This has been demonstrated in undersaturated MORB melts, which have been shown to retain constant CO_2/Nb and H_2O/Ce ratios of 239±46 and 168±8 respectively during crystallisation (*Saal et al.*, 2002). The 1959 melt inclusions show no correlation between the volatile and trace element concentrations (Figure 5.30). The ratios of CO_2/Nb vary between 3–68 (Figure 5.30). Though the value of the CO_2/Nb ratio has been shown to vary depending on tectonic setting and source composition, and ranges in ocean island melts to values much greater than 300 (*Hauri*, 2010), the lack of correlation between the CO_2 and Nb concentrations in the Kīlauea Iki samples, together with the low value range of the ratio suggests that at reservoir pressures the melts are CO_2-saturated and have undergone considerable CO_2-loss by degassing prior to and during reservoir storage. The H_2O/Ce ratios

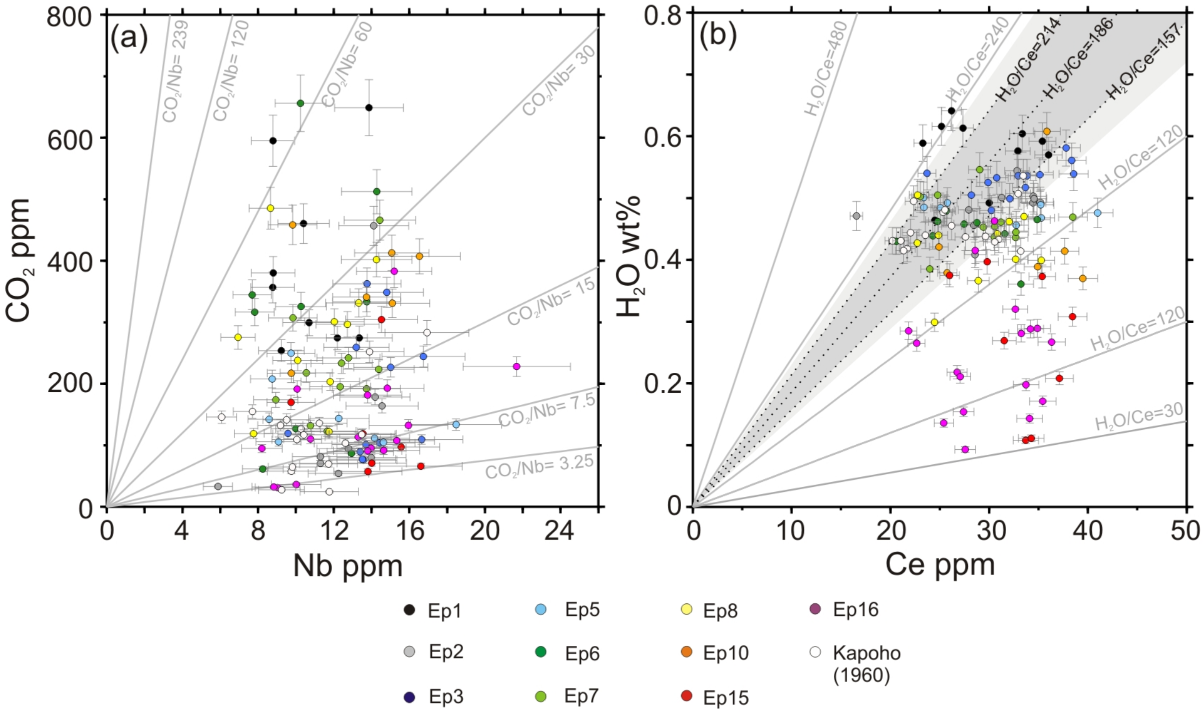

Figure 5.30: (a) CO_2 versus Nb concentrations in 1959 and 1960 melt inclusions. Grey lines represent constant ratios of CO_2/Nb; the value of 239 is that of undersaturated MORB glasses of the EPR (*Saal et al.*, 2002). All Iki and Kapoho inclusions lie at low CO_2/Nb ratios owing to significant loss of CO_2 from the melt; (b) H_2O versus Ce concentrations in 1959-60 melt inclusions, with grey lines of constant H_2O/Ce ratios. The dark grey shaded region within black dotted lines represents ratios previously determined for undegassed submarine Hawaiian glasses from *Dixon and Clague* (2001). Ratios of 214, 186 and 157 were determined from analysis of Loihi, Kīlauea and North Arch Volcanics glasses. Light grey envelopes denote the errors on the previously published ratios (8%).

span a much greater range in values, from 32–284. H_2O/Ce ratios for undegassed high-MgO tholeiites from submarine Kīlauea glasses are reported as 182–196 (*Dixon and Clague*, 2001). The maximum range of H_2O/Ce ratios reported from the same study on a suite of Hawaiian glasses, including samples from Loihi seamount and the North Arch volcanics was 157–214 (*Dixon and Clague*, 2001). Inclusions erupted from many of the 1959 episodes lie within the range of H_2O/Ce ratios previously determined by *Dixon and Clague* (2001), with some from episode 1 exceeding those values, and indicating that some of the pre-eruptive 1959-60 melts may have been inherently H_2O-rich, and undersaturated with respect to H_2O. The low H_2O/Ce ratios at < 150, including phase 15 and 16 of the summit eruption, suggests that some melts have also lost significant amounts of H_2O prior to or during entrapment within the olivine-host.

Melt sulphur concentrations are a complex function of melt composition, temperature and oxygen fugacity (*Wallace and Carmichael*, 1992). In basaltic melts FeO and S correlations may display a positive correlation owing to the formation of an FeS complex. The total FeO concentrations of the 1959-60 melt inclusions and glasses are shown in Figure 5.31a together with data from sulphide-saturated MORB melts (*Mathez*, 1976) and 1959 inclusion compositions of *Anderson and Brown* (1993) for comparison. The uncorrected inclusion compositions of this study, together with those of *Anderson and Brown* (1993) display a broad range, with the majority of inclusions distributed around the sulphide-saturated MORB samples of *Mathez* (1976). This is consistent with calculations by *Wallace* (1998) that the Kīlauea Iki inclusions are largely sulphide-saturated. The corrected concentrations lie at almost constant values of FeO, owing to the assumption in the PEC and FeO-loss correction procedure that primary Kīlauea melts contain near-uniform values of FeO (see Chapter 2), but the corrected inclusions appear to record melts compositions with variable amounts of S loss. Figure 5.31b shows the S concentrations against H_2O for the summit inclusions and glasses. H_2O and S have been shown, in previous studies of basaltic volcanism to behave similarly, such that both volatiles have moderate melt solubilities and only begin to degas from the melt after reaching saturation at relatively low pressures ($< 0.05\,\mathrm{kbar}$; *Gerlach* 1986). Figure 5.31 shows loss of both H_2O and S simultaneously, however the loss of S without a decrease in H_2O concentration may be indicative of S loss by formation of an immiscible sulphide phase (*Collins*, 2010). Development of an immiscible Fe-S-O melt within basaltic magmas of high S concentration is well documented (*Wallace and Carmichael*, 1992). Sulphide globules form at the expense of S dissolved within the silicate melts. After precipitation of the globules within the magma, they may be removed by gravitational settling along with olivine phenocrysts, into the cumulate crystal pile at the base of a magma reservoir, owing to the high density difference between the silicate and sulphide melts, from where they may be re-entrained with magmas on ascent. If the sulphides are re-entrained by a magma which subsequently undergoes degassing, they may become unstable and dissolve back into the melt. An increase in the dissolved melt S concentrations may not be observed if resorption of the Fe-S-O phase is coupled with S degassing from the melt. The production of an immiscible sulphide phase in the 1959 eruption is consistent with the presence of rare sulphides within both the summit and flank samples found in this study (Figure 5.11), and

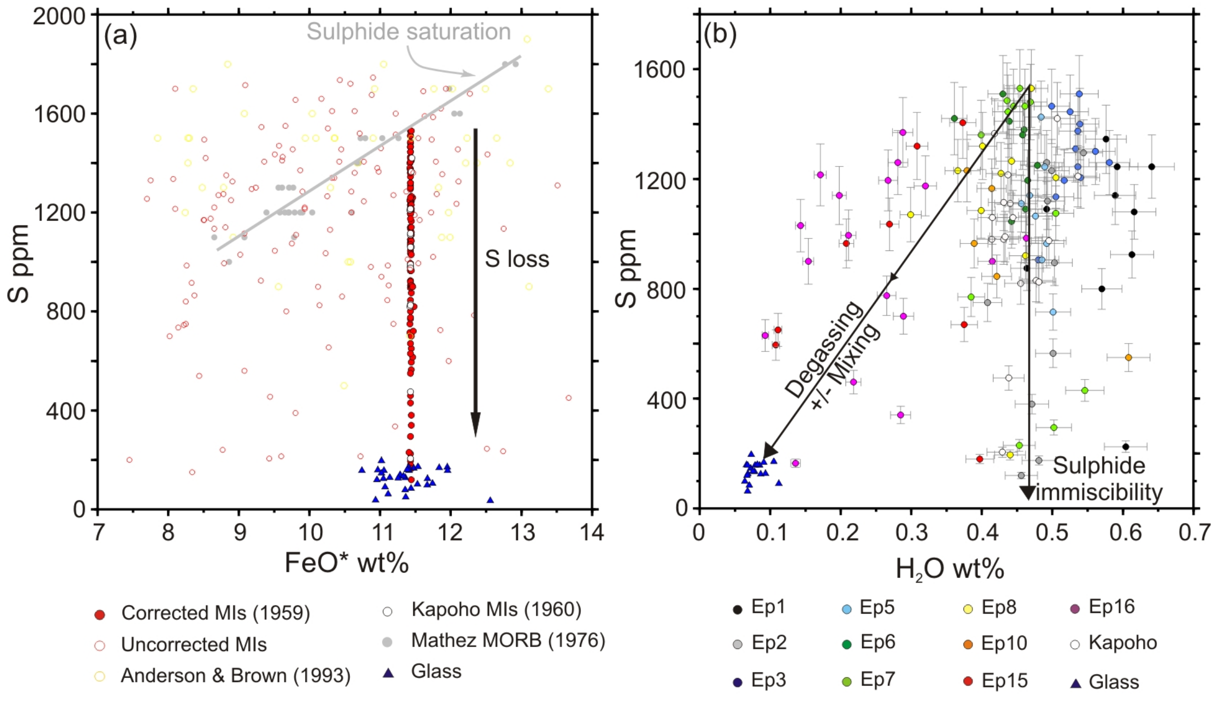

Figure 5.31: (a) S versus total FeO in 1959-60 melt inclusions and glasses. Concentrations in both PEC corrected and uncorrected melt inclusions are shown for comparison, together with 1959 inclusions analysed by *Anderson and Brown* (1993). Sulphide-saturated MORB glasses from *Mathez* (1976) are shown in grey as an indication of saturation concentrations. (b) S versus H_2O concentrations in the 1959-60 melt inclusions and glasses. Coupled degassing of both S and H_2O would produce a trend as shown with the black arrow (a similar trend might expected from mixing of degassed and undegassed melts). However, a decrease in S concentrations with no loss of H_2O cannot be the result of simple degassing systematics and suggests S loss by sulphide formation in the melt.

with previous observations of sulphides within the Kīlauea Iki products (*Helz*, 1987; *Stone*, 1991). It may also account for the lack of any clear correlation with trace element proxies of fractionation, or relationship with other volatile elements.

Cl and F have a much greater solubility in basaltic melts than H_2O, CO_2 or S and the considerable overlap between the dissolved concentrations in the residual glasses and inclusions is consistent with observations that Cl only degasses appreciably from basalts at pressures of < 1 MPa, equivalent to < 35 m in the conduit, and F at pressures < 0.1 MPa (*Edmonds et al.*, 2009; *Sigvaldason and Oskarsson*, 1975). Inclusion concentrations strongly exceed expected Cl and F contents of basaltic melts and suggests significant enrichment due to fractionation. Although there is no direct correlation between F and La in Figure 5.24b, in general the pre-eruptive Kīlauea Iki melts exhibit a 100% increase in F and La concentrations between the minimum and maximum values analysed. The equal range in variation is consistent with fractionation ± mixing as a dominant control on F concentrations. Conversely, Cl values exhibit a 300% variation versus the 100% variation in La concentrations, suggesting that the 1959 melts had experienced some loss of Cl due to degassing. Halogen degassing at conduit pressures is a complicated function of eruption kinetics and the quench rate of magmas (e.g. *Edmonds et al.*, 2009), and as such, they are less effective at recording pre- and syn-eruptive processes and will not be considered further.

5.4.4 The effects of magma mixing, drainback and gas flushing on melt H_2O-CO_2 concentrations during the 1959 eruption

The temporal decrease in the dissolved H_2O concentrations of the melt inclusions in Figure 5.25a not only match the trend observed in the four episodes analysed by *Wallace* (1998), but demonstrate a continuous decrease throughout the entire eruption. *Wallace* (1998) attributed this decrease to progressive mixing of drainback lavas with undegassed melts in the reservoir, although a number of other possible explanations may also be explored, including pre-eruptive mixing of melts with a magma that is inherently H_2O-poor, or the loss of H_2O from the inclusions via post-entrapment diffusive re-equilibration with the external melt.

The relationship between H_2O and Ce in Figure 5.30b provides constraint against pre-eruptive magma mixing as a cause for the H_2O trend. As discussed above, the variable and high H_2O/Ce ($> \sim 150$) ratios in a number of the inclusions indicate that some pre-eruptive melts may have been inherently more enriched in H_2O, but progressive mixing of two melt compositions at reservoir depths, with no degassing, should result in H_2O exhibiting incompatible behaviour, and produce a detectable trend in H_2O–Ce space. Examination of the non-volatile trace elements of the 1959 inclusions does not reveal any temporal changes in composition as a result of S1-S2 mixing. Loss of H_2O from the inclusion melts, whether via pre or post-entrapment routes, could therefore only have occurred if the carrier melts had been exposed to low pressure conditions allowing for some gas loss via exsolution.

The effects of lava drainback on melt volatile concentrations may be explored by adaptation and extension of the *Wallace* (1998) model. The model is an iterative mass balance calculation, based on the magma volume estimates of *Eaton et al.* (1987) (Table 5.2). Using the estimate of reservoir volume at the start of each episode, the volume erupted into the lake and the volume drained back into the vent at the end of the episode, it is possible to calculate the volume of new melt added to the reservoir between episodes. The volume estimates were used to calculate the maximum and minimum limits on the H_2O contents predicted in the reservoir melts during the eruption, and was extended to investigate additional volatile elements. The model results are shown for H_2O and S values in Figure 5.32.

The model relies on a number of key assumptions: (i) that new magma input into the reservoir from the mantle has 0.64 wt% H_2O (or 1530 ppm S) based on the maximum analysed values; (ii) that drainback lavas entering the reservoir have almost entirely degassed and contain only 0.1 wt% H_2O or 100 ppm S, and (c) that mixing of magma in the reservoir is homogeneous (*Wallace*, 1998) (although trace element compositions show this to be an oversimplification). The range of volatile concentrations at the start of episode 1 is defined by the minimum and maximum melt inclusion values. At the end of the first eruptive phase, 30.6×10^6 m^3 magma had erupted but drainback into the reservoir was limited to 1.1×10^6 m^3 of magma until the reservoir was progressively refilled between the end of phase 1 and start of episode 2. Reservoir volumes immediately following the end of episode 1 were the lowest throughout the entire eruption and result in extremely low minimum volatile concentrations, until this is overprinted by new undegassed magma input (*Wallace*, 1998). The minimum melt volatile contents throughout the eruption were calculated as the expected concentrations for degassed melts drained back to the reservoir, mixing completely with whatever magma remained. Upper bounds were estimated based on concentrations of new undegassed melts entering the reservoir and mixing with the hybrid (drainback + residual). In some later episodes *Eaton et al.* (1987) recorded a net loss of melt from the summit reservoir, possibly due to intrusion of melts into the upper east rift zone. During these periods there was no recorded new magma input into the reservoir and consequently only a minimum volatile concentration could be estimated for those episodes. Figure 5.32a demonstrates a remarkable similarity between the predicted H_2O trends and those observed in the melt inclusions. Correlation of the expected versus measured values produce an r^2 value of 0.84. Throughout the eruption the volume of new melt supplied from depth decreased more or less continuously, such that increased cumulative drainback with little or no new input in later episodes resulted in the decrease in volatile concentrations observed. Mixing of

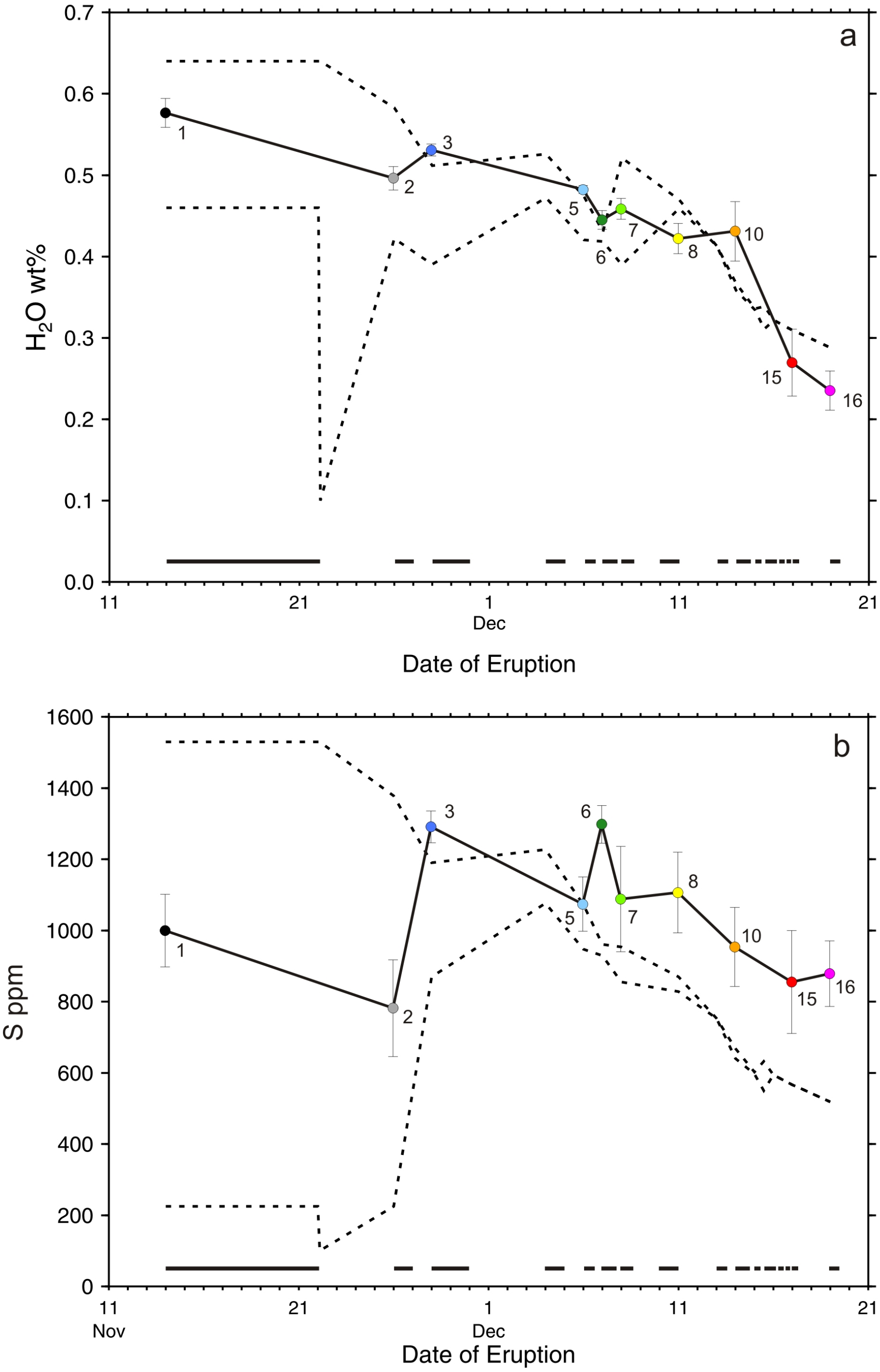

Figure 5.32: Comparison of melt inclusion (a) H_2O and (b) S concentrations and mass balance calculations for the effects of drainback of surface degassed magma on the dissolved H_2O and S of basaltic magma in the subvent reservoir. Average melt inclusion concentrations, together with their calculated standard error of estimate of the mean, are shown as coloured circles with whiskers and continuous black lines through each episode sampled. Maximum and minimum limits on the calculated volatile contents of reservoir magmas are represented by dashed lines (see text for description of calculation). Solid black lines at the base of each plot area denote the duration of each of the 17 episodes. Model is adapted from *Wallace* (1998).

hot, undegassed mantle melts within the reservoir, with degassed, drainback magmas would have encouraged rapid vesiculation and olivine crystal growth within the new melt batches, providing the ideal conditions for melt inclusion formation and entrapment between eruptive episodes. The predicted S and observed S trends in Figure 5.32b do not display as strong a relationship as H_2O, although episodes 1-2 fall within the expected range and episodes 8–16 display the same temporal decrease but at higher than expected concentrations consistent with potential buffering of melt S concentrations during degassing due to sulphide reaction in the melts.

One other possible cause of the temporal decrease in water concentration is diffusive re-equilibration. Recent studies have shown that olivine-hosted inclusions are susceptible to H_2O-loss or gain by exchange with the external melt via H^+ diffusion through the host-olivine structure (e.g.*Hauri*, 2002; *Portnyagin et al.*, 2008). Diffusion would have been possible on the timescales of the Kīlauea Iki eruption as experimental studies have revealed the process is rapid and can occur in a matter of hours if there is a concentration gradient between the external and trapped melt (*Portnyagin et al.*, 2008) and the process could account for the observed decoupling of H_2O and Ce in Figure 5.30. Distinguishing the effects of diffusion from drainback is challenging. Ideally covariance between H_2O and a volatile element which cannot undergo diffusion through olivine, such as S, would provide a robust test (*Collins*, 2010). However, the S concentrations in the Kīlauea Iki melts are influenced by sulphide formation and reaction and the lack of correlation between H_2O and S cannot be clearly interpreted as evidence for diffusive loss. However, as shown in Figure 5.32, S does show some similarity with the predicted composition from drainback which could be used to suggest that the inclusions reflect syn-eruptive compositions. H_2O shows no correlation with other elements which are subject to rapid re-equilibration, such as FeO or Li (*Dohmen et al.*, 2010). However, if the temporal variations are the result of progressive loss by diffusion, the inclusions are still revealing information about syn-eruptive processes, and demonstrate that the carrier melts must have been experiencing progressive H_2O-loss by drainback mixing throughout the eruption, in order for diffusive re-equilibration to occur.

Interpreting magmatic processes from melt CO_2 concentrations is more challenging owing to its extremely low solubility in basaltic melts. Saturation of Kīlauea melts may occur at depths >30 km (*Gerlach and Graeber*, 1985), and melts are thought to enter the summit reservoir with as much as 0.5 wt% CO_2 already exsolved into a separate vapour phase (*Gerlach*, 1986; *Gerlach et al.*, 2002). The CO_2 saturation and extensive pre-eruptive loss from the Kīlauea Iki melts is illustrated by the extremely low CO_2/Nb ratios in Figure 5.30a. As a result CO_2 appears to be effectively decoupled from magmatic processes and does not exhibit any fractionation or mixing signatures.

The drainback model of *Wallace* (1998) was extended to investigate the effects of drainback on melt CO_2 concentrations and is shown in Figure 5.33. The initial upper and lower bounds on CO_2 concentrations were the maximum and minimum values from episode 1, 649 and 254 ppm respectively. Degassed drainback melts were modeled with 50 ppm CO_2 and new melt input into the reservoir was assumed to contain 656 ppm, the maximum concentration analysed in the Kīlauea Iki melts. This maximum may be an underestimate of new melt CO_2 concentrations, since parental melts supplied to Kīlauea are estimated to contain ~0.6 wt% CO_2 (*Gerlach and Graeber*, 1985; *Gerlach*, 1986), but this value was chosen to reflect the melt concentrations at reservoir pressures. Measured CO_2 concentrations bear no resemblance to those predicted by the drainback model (Figure 5.33) with measured values at generally lower concentrations than predicted, consistent with CO_2 concentrations being decoupled from melt processes. Concentrations may also reflect some degassing of residual melts in the reservoir during eruptive phases. The lack of correlation could lend support to the diffusion model of H_2O loss if the CO_2 concentrations do not exhibit any clear temporal trends, suggesting the inclusions are not directly related to eruption melts.

However, Figure 5.34a compares the temporal variation of melt CO_2 with changes in the volume of new melt supplied to the reservoir prior to each eruptive episode. The CO_2 displays a striking similarity to the profile of melt volumes for episodes 1, 2 and 3 and appears to directly reflect the arrival of new melts during the early eruption phases. A sharp decline in melt input prior to episode 5 is accompanied by a significant increase in melt CO_2 concentration and a switch from a positive correlation with magma input (r^2=0.97 episodes 1–3,15–16) to a negative correlation (r^2=0.93) between episodes 5 to 10. Temporal variations in the matrix glass Mg# are also compared with new magma input in Figure 5.34b. The glass Mg#s show a positive correlation with melt input between episodes 1 and 3 and an overall small increase in the proportion of MgO between episodes 5–10, similar to the CO_2 profile. The increase in both CO_2 and Mg# in episodes 5–10 imply that there may have been input of

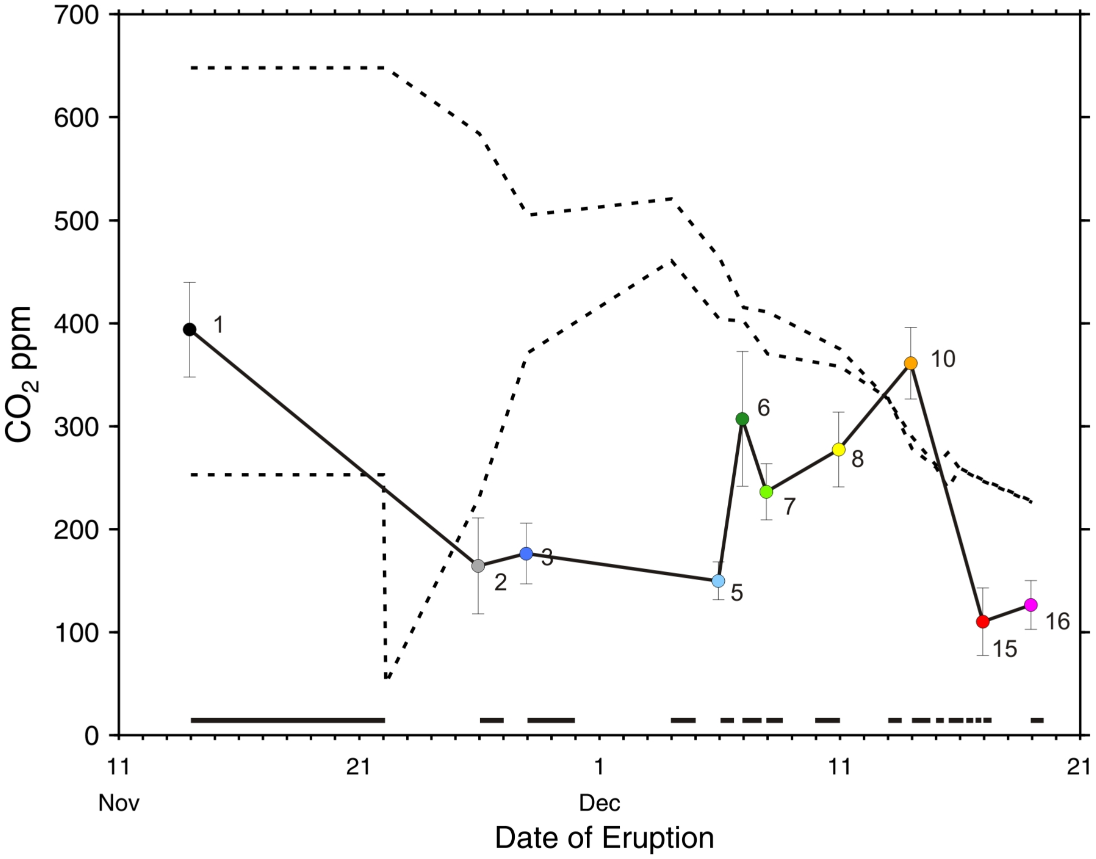

Figure 5.33: Comparison of melt inclusion CO_2 concentrations and mass balance calculations for the effects of drainback of surface degassed magma on the dissolved CO_2 content of basaltic magma in the subvent reservoir. Average melt inclusion concentrations, together with their calculated standard error of estimate of the mean, are shown as coloured circles with whiskers and continuous black lines through each episode sampled. Maximum and minimum limits on the calculated volatile contents of reservoir magmas are represented by dashed lines (see text for description of calculation). Solid black lines at the base of each plot area denote the duration of each of the 17 episodes. Model is adapted from *Wallace* (1998).

small volumes of new melts which were not recorded in input signatures. However Mg# and CO_2 are not always perfectly correlated, for example the decrease in reservoir input between episodes 5 and 6 is reflected in the glass compositions by a decrease in Mg# but coincides with a significant increase in melt CO_2. The CO_2 signatures may therefore be reflecting the arrival of CO_2-rich vapour independent of parental melts from depth. Interaction or ‘flushing’ of reservoir melts with a CO_2-rich vapour would also further decrease the H_2O content of the magmas as increasing the proportion of CO_2 causes a dilution of H_2O by CO_2 in the gas phase, (*Holloway and Blank*, 1994; *Papale and Polacci*, 1999) and effectively results in isobaric dehydration of the melt (*Collins*, 2010; *Spilliaert et al.*, 2006).

The correlation of melt CO_2 with magma input, matrix glass composition and fountain heights (Figure 5.26) suggest that the melt inclusions do largely reflect syn-eruptive volatile compositions and are not unrelated to the 1959 melts. It also provides additional constraint against a diffusion-only model for H_2O variation. The results of drainback modeling and comparison of melt chemistry with magma volumes suggest that H_2O (and to some extent S) concentrations are largely controlled by mixing of degassed drainback melts with continuously decreasing volumes of new undegassed melts in the subvent reservoir. CO_2 concentrations are effectively decoupled from magma mixing of drainback melts and instead reflect the input of CO_2-rich vapour ± new melt input from depth.

5.4.5 Volatile controls on fountain height

Models of fountain dynamics suggest the most important factors influencing fountain height are magma gas content, volume flux and the amount of lava re-entrainment, whereby higher fountains occur after minimum lava re-entrainment and when magma gas content and volume flux is high (*Parfitt and Wilson*, 1995). Episodes 3, 15 and 16 produced the highest fountains observed during the eruption (Figure 5.2). Volatile data presented in this chapter show that the pre-eruptive melts of episodes 15 and 16 were the most volatile-poor (H_2O and CO_2), were associated with the lowest volume of new magma input and the maximum cumulative volume of drainback melts. These observations appear to contradict those predicted by (*Parfitt and Wilson*, 1995), with the exception that greater fountain heights were associated with the highest volume eruption rates (Table 5.1).

A detailed study of fountain dynamics is beyond the scope of this chapter but it is interesting to consider the trend in pre-eruptive melt CO_2 concentrations in relation to fountain heights for the 1959-60 eruptions. In general, the higher the melt CO_2 concentration, the lower the maximum fountain heights (Figure 5.26), suggesting that melt CO_2 content might exert some control on fountain dynamics. Previous numerical models of fountain dynamics were summarised earlier in this chapter. The models assume that either H_2O or CO_2 are the 'driving' gas compositions for fountains but neither the models of *Wilson* (1980) and co workers nor *Jaupart and Vergniolle* (1988) and others, consider the effects of H_2O

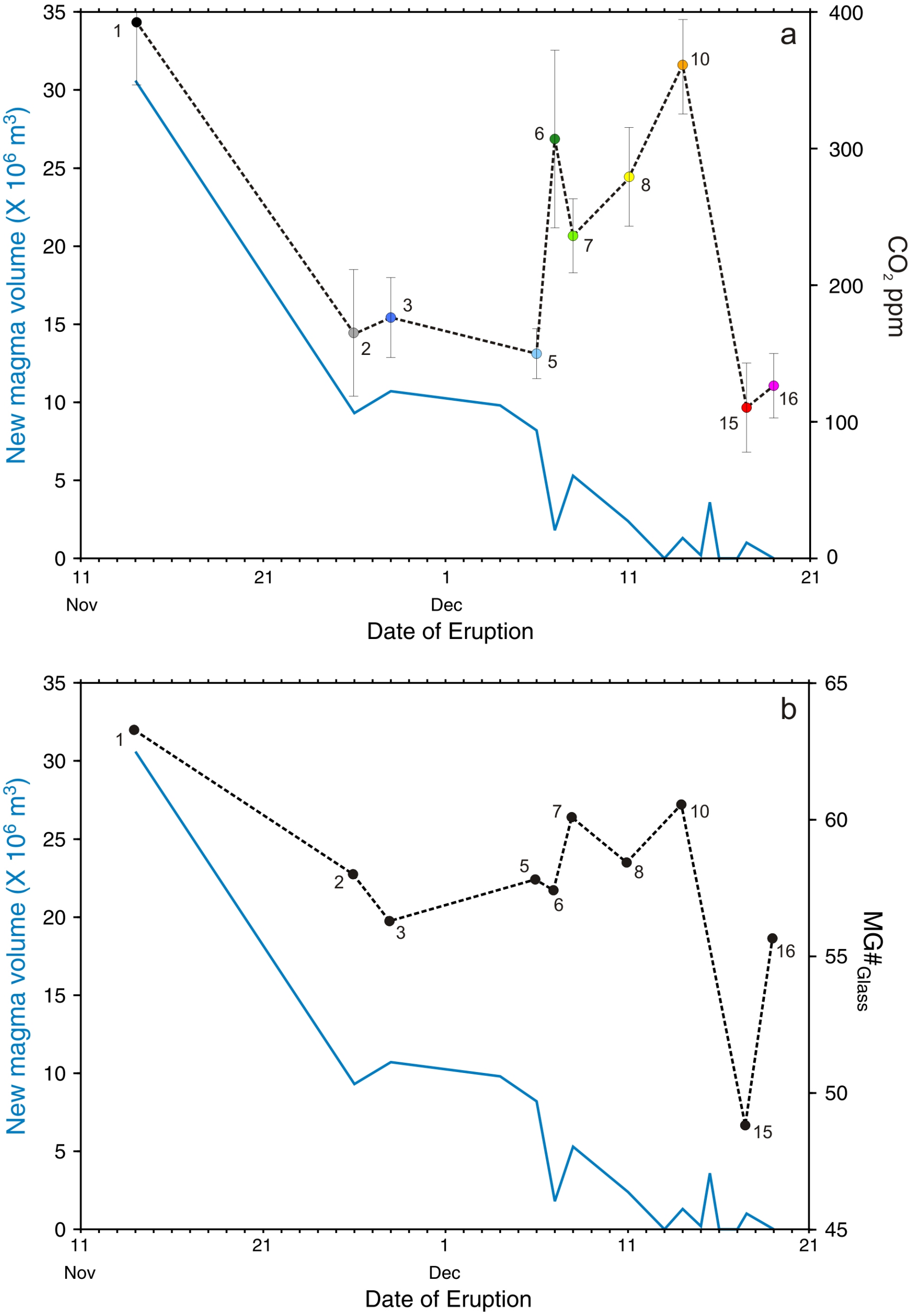

Figure 5.34: Comparison of temporal changes in melt composition versus changes in the volume of new melt supplied to the reservoir prior to each episode during the 1959 eruption. (a) Changes in the average CO_2 concentration of inclusions with time are indicated by labelled coloured circles for each episode together with the standard error estimate of the mean. Dashed lines mark the temporal variation between analysed episodes.(b) Changes in the average Mg# of the matrix glasses for each eruptive episode are represented as labelled black circles and dashed lines. Blue lines on both plots indicate the changes in the volume of new magma supplied to the reservoir from depth, calculated as the difference between reservoir volumes at the end of each episode (after eruption and drainback) and the start of the next episode. Volumes calculated using the data of *Eaton et al.* (1987).

and CO_2.

A more recent study of *Papale and Polacci* (1999) has demonstrated the role of CO_2 on the dynamics of explosive eruptions in a two component system using numerical models. The *Papale and Polacci* (1999) model studied the effect of the presence of a two component gas phase by varying the $CO_2/(CO_2 + H_2O)$ ratio from 0 to 0.5 at either constant total volatile or constant water contents. Magma properties were calculated on the basis of magma composition and crystal content, which were allowed to vary along the conduit due to decreasing pressure and exsolution of gas. The results demonstrated that an increase in the proportion of CO_2 produces a decrease in mass flow rate and an increase in the depth of the fragmentation level. The simulations were run for silicic magma compositions only and consequently caution must be exercised when comparing the results to a basaltic system. The model included a fragmentation criterion based on the transition from ductile to brittle behaviour but basaltic systems are not expected to undergo brittle fragmentation if the crystal content of the magma is low (*Houghton and Gonnerman*, 2008). However, *Papale and Polacci* (1999) state that the same results could equally be obtained by imposing a critical gas volume fraction at fragmentation. The model predicts a gas volume fraction of 0.7–0.8 during simulations, a value that is consistent with the critical volume fractions for fragmentation determined by *Sparks* (1978). Fragmentation as a result of attaining critical gas volume fraction has been an underlying assumption of the basaltic fountaining model of *Wilson and Head* (1981) and other workers, and if the *Papale and Polacci* (1999) model results hold true for basaltic systems, a decrease in the mass flow rate and increase in depth of fragmentation as a result of a greater proportion of CO_2 would result in an observed decrease in fountain height. It should be noted though that basaltic fragmentation mechanisms remains somewhat controversial and are a function not only of gas volume fraction but also decompression rates and viscosity.

Interpretations of the CO_2 and fountain height trend remain tentative. There is little doubt that exsolution of CO_2 plays a crucial role in magma bouyancy at basaltic volcanoes (*Anderson and Brown*, 1993). *Anderson and Brown* (1993) and *Anderson* (1995) suggest that new primitive, dense basaltic melts would pond at the base of a magma reservoir and would never erupt were it not for the CO_2 content of the parental melts. Basaltic melts with > 0.3 wt% CO_2 undergoing exsolution are suggested to be buoyant enough to rise through existing stored magmas, and erupt at the surface (*Anderson and Brown*, 1993). This is further supported by the results in Chapter 4, which demonstrated that pre-eruptive melts of fountain eruptions (relative to other eruption styles) have retained higher concentrations of their initial CO_2 contents by undergoing rapid ascent, most likely due to deep exsolution of CO_2. The results of this Kīlauea Iki case study suggest however that at conduit pressures melt CO_2 might be dictating the depths at which fragmentation occurs.

The results highlight the need for extension of numerical models to investigate the impact of CO_2 on fragmentation and eruption dynamics in basaltic systems and for careful consideration of both the CO_2 and H_2O concentrations in the study of Hawaiian fountains.

5.4.6 Summit versus flank eruption: the 1960 Kapoho melts

Geophysical evidence suggest that the 1960 ERZ Kapoho and the Kīlauea Iki eruptions were related, as the Kapoho eruption (which occurred some 20 km down rift of the summit) and the preceding seismic activity coincided with draining of the summit magma reservoir that had refilled after the 1959 eruption. Previous chemical studies of the Kapoho lavas have suggested that the early erupted material was dominated by melt of the same composition as the 1955 ERZ eruption, which had most likely been stored in the rift zone (*Murata and Richter*, 1966a). As the Kapoho activity progressed, lavas became more similar in composition to the 1959 summit melt (*Murata and Richter*, 1966a). The Kapoho sample analysed in this chapter is thought to have been erupted around January 29 1960, approximately mid-way through the eruption. As well as being similarly olivine-phyric and containing many of the same olivine morphologies as the 1959 tephra, the 1960 sample was compositionally similar to the Kīlauea Iki melts. Glass and melt inclusion major and trace elements follow the fractionation trend defined by the 1959 melts (Figures 5.14, 5.17, 5.18), lying at the lower end of the MgO range. Trace element variability in the 1960 melts spans the range for all of the 1959 products and multi-element and REE profiles for Kapoho display the same patterns of enrichment and depletion as the Kīlauea Iki inclusions (Figure 5.19, 5.20). No samples of the 1955 ERZ eruption were analysed in this study to compare with those of the Kapoho eruption, but the 1960 melts are interpreted as reflecting compositions similar in source to the 1959 eruption. Inclusion S compositions are variable at restricted H_2O concentrations

(Figure 5.31) and indicate S depletion by formation of sulphides, consistent with sulphide globules found in the samples. H_2O/Ce ratios of all but one inclusion lie within the range previously defined for H_2O-undersaturated Hawaiian melts (*Dixon and Clague*, 2001) (Figure 5.30b) and are comparable with the undegassed Kīlauea Iki magmas of episode 1. However pre-eruptive CO_2 concentrations in the Kapoho melts are much more limited and significantly less than those of the summit eruption. The H_2O-CO_2 data are consistent with models of degassing at Kīlauea volcano which suggest that melts erupted in the ERZ are depleted in CO_2 owing to CO_2 loss during residence or transport through the shallow summit magma reservoir, but retain their H_2O and S contents during transport along the ERZ to the site of eruption (*Gerlach and Graeber*, 1985). The occurrence of high fountaining, up to 427 m high during the Kapoho eruption, with pre-eruptive melts at low CO_2 concentrations could lend support to suggestions that exsolution of H_2O-rich gas at shallow conduit depths is the dominant driving gas for fountain production (e.g. *Wilson and Head*, 1981; *Gerlach*, 1986; *Parfitt*, 2004) if pre-eruptive melts were supplied from the same source as the summit eruption and not from a source beneath the ERZ.

5.4.7 Summary

This chapter presents a detailed study of the major, trace and volatile element composition of pre- and syn-eruptive melts from a single high fountain-producing eruption. The results demonstrate the relative effects of olivine-fractionation, magma mixing, drainback and CO_2-gas flushing on the melt compositions of the 1959 eruption.

- Major element compositions were largely dictated by extensive olivine-only fractionation with minor, late-stage crystallisation of clinopyroxene in groundmass glasses.

- Minor and trace element compositions of glasses and melt inclusions reveal extensive pre- and syn-eruptive magma mixing. Glasses record mixing between S1 and S2 magma compositions previously identified by *Murata and Richter* (1966a), *Wright* (1973), *Helz* (1987) and *Loewen* (2011).

- Melt inclusion compositions are much more variable than their carrier melts and indicate that new melts arriving to the reservoir as the S1 component were more variable in their trace element compositions.

- Volatile elements are largely decoupled from trace element compositions owing to their low solubility in basaltic melts at reservoir and conduit pressures. Temporal variations in melt H_2O (and to a lesser extent S) concentrations are effectively explained by a model of lava drainback and the mixing of degassed lavas with increasingly limited volumes of undegassed melt supplied throughout the eruption. S concentrations indicate that the 1959 melts were sulphide-saturated and that breakdown of immiscible sulphide globules in the melt may have buffered sulphur concentrations during degassing and drainback.

- Melt CO_2 concentrations directly reflect volumes of new magma input into the reservoir during early phases of the eruption, but increases in CO_2 concentrations during later episodes do not correlate with new magma input and indicate that residual reservoir melts may have been flushed by input of CO_2-rich gas from depth.

- An increase in melt CO_2 appears to correlate with decreasing fountain heights and suggests CO_2 may exert controls on fountain dynamics, possibly by causing a decrease in mass flow rates and increasing the depth of fragmentation in the conduit.

- High fountains produced during the 1960 ERZ eruption were compositionally similar to the 1959 melts but were H_2O-rich and CO_2-poor, supporting previous models of Kīlauea degassing and suggestions that fountain production may be driven by exsolution of an H_2O-rich gas phase.

This study illustrates the importance and benefit of utilising a wide range of both geochemical and geophysical datasets to deconvolve magmatic processes during an eruption. It also highlights the need for both development of further models of fountaining which would incorporate variations in $CO_2/(CO_2+H_2O)$, and more comprehensive temporal CO_2 and H_2O datasets for other fountain eruptions, in order to further our understanding of the role of CO_2-H_2O degassing during explosive basaltic volcanoes.

Chapter 6

Conclusions and Further Work

The motivation for this project was to examine the relationships between parental melt chemistry, shallow eruption processes and eruption dynamics at Kīlauea volcano, over time scales of days to centuries. Like many hotspot volcanoes including Piton de la Fournaise, Réunion and Fernandina, in the Galapagos islands, Kīlauea displays a broad range of eruptive activity and produces basaltic lavas which display temporal variations in major element and isotopic chemistry. While many studies have been conducted on the volatile compositions of melts erupted from these locations (e.g. *Harris and Anderson*, 1983; *Bureau et al.*, 1998; *Koleszar et al.*, 2009), few if any, have examined the relationship between parental melt heterogeneity and variations in eruptive behaviour at a single ocean island volcano. This project consisted of two major studies: the first examined the changing compositions of pre-eruptive melts supplied to Kīlauea over a 500 year period, to assess the roles of melt heterogeneity inherited from the mantle source, fractionation, magma mixing and degassing on observed variations in eruptive activity; the second study investigated variations in melt volatile geochemistry during a single high-fountaining eruption in order to determine the influence of lava drainback, magma mixing, and gas-flushing on short-term eruption dynamics and fountain heights. This chapter provides a summary of the two studies, a discussion of the broader implications of this work and detailed plans for further work.

6.1 Long-term controls on eruptive behaviour at Kīlauea volcano

Geochemical analyses on 43 prehistoric and historical eruption deposits collected from the summit, east and southwest rift zones of Kīlauea were presented. 374 melt inclusions and 165 matrix glasses were analysed for major, trace and volatile elements. The data have been categorised by both the eruption date and the eruption styles which produced them. These were distinguished as effusive lava flows, fissure and high-Hawaiian fountains, phreatomagmatic and transient subplinian explosions; determined on the basis of eruption observations and/or stratigraphy of the deposits and morphology of individual clasts.

Melt inclusion compositions reveal that parental melts supplying Kīlauea over the past 500 years are heterogeneous with respect to their major, trace and volatile concentrations, and that these heterogeneous melt signatures are overprinted at shallow crustal depths by the effects of concurrent crystallisation, mixing and degassing within the summit magma reservoir. Division of the geochemical dataset into eruption style categories enabled use of the Kolmogorov-Smirnov statistical test to determine that robust and significant differences exist between the pre-eruptive chemistry of melts supplying different eruption types at Kīlauea. High-Hawaiian fountains and fissure melts are inherently more primitive, and enriched in incompatible trace and volatile elements. Effusive and transient explosive events are consistently more evolved and volatile-poor. Melts supplying different eruption types also undergo shallow pre-eruptive processes to different extents such that effusive and subplinian melts are stored for longer periods within the summit reservoir prior to eruption, where they experience extensive fractionation, homogenisation by mixing, degassing and gas flushing with a CO_2-rich vapour. Owing to their inherently more volatile-enriched composition, high-fountaining and to a lesser extent fissure melts undergo more rapid ascent through the plumbing system. Early exsolution of CO_2-rich bubbles enable these melts to become buoyant enough to overcome density stratification within the convecting reservoir, facilitating rapid passage to the surface with less extensive pre-eruptive degassing, homogenisation and fractionation. Progressive changes in pre-eruptive melt chemistry over the past 500 years reflect temporal changes in the source composition and degree of melting, with a decrease in the extent of partial melting of the source region between the 19th–mid-20th century and an abrupt reversal of the trend after 1959.

The results indicate that eruption behaviour at Kīlauea is strongly influenced by the composition of the melts supplied from depth, which are dictated by temporal changes in composition of the mantle source region and/or the extent of partial melting. Whether a primary melt is inherently volatile-enriched or -depleted most likely influences the extent to which the ascending melts are subjected to shallow magmatic processes within the summit reservoir, which in turn exert controls on eruption dynamics, in addition to large-scale structural features within the plumbing system.

Of key consideration is the extent to which the results of this study may be applicable to other basaltic volcanoes. Whether eruption behaviour at other localities is determined by the composition of the melts supplied from depth, may be dependent on the mantle source volatile composition, the temperature of upwelling material, the distribution of heterogeneities within the source region, and configuration of the shallow magmatic system, all of which are highly variable between both oceanic islands and other active basaltic volcanoes.

The volatile compositions measured in this study are comparable to other hotspot basaltic volcanoes. Figure 6.1 compares the H_2O-CO_2 concentrations of Kīlauea melts with those recorded for other geological settings and OIB-producing volcanoes. The Kīlauea compositions define a range almost identical to the composition of melts from Piton de la Fournaise, Réunion. Melt inclusions erupted from Piton de la Fournaise also preserve major and trace element concentrations resembling those of Kīlauea (*Bureau et al.* 1998; *Collins* 2010), along with a very similar range of CO_2/Nb and H_2O/Ce ratios to those observed in this study (9–115 and 22–224 respectively; *Collins* 2010). As in Hawai`i, Réunion island consists of multiple volcanic centres, and Piton de la Fournaise is characterised by a summit caldera and three radiating rift zones (*Albarede and Tamagnan*, 1988). The summit reservoir is stratified with shallow and deep sections which are tapped during cycles of summit and flank eruptions (*Bureau et al.* 1998; *Collins* 2010). The similarity of the shallow volcanic systems, and melt compositions, together with previously identified heterogeneity in the Piton lavas (*Albarede and Tamagnan*, 1988) suggests that a similar relationship between parental melt compositions, shallow magmatic processes and eruptive behaviour at other hotspot volcanoes are likely to exist. Ideally this would be tested by collation and comparison of geochemical datasets. While ocean islands have been the focus of a great many geochemi-

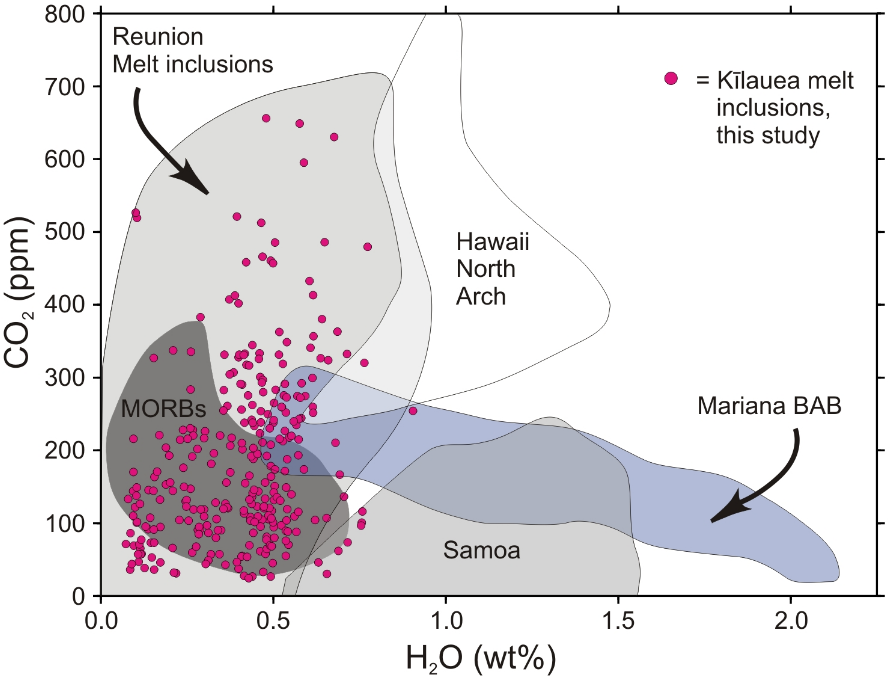

Figure 6.1: Comparison of melt H_2O-CO_2 contents from this study, to magma compositions from other geological settings. Melt from Kīlauea span an almost identical range of concentrations as those observed at Piton de la Fournaise, Réunion (data from *Bureau et al.* 1998; *Collins* 2010. However, the plot also demonstrates that while Kīlauea is a type example of hotspot volcanism, considerable heterogeneity exists between oceanic islands, and melts sampled from Samoa define a different compositional range in H_2O-CO_2 space). Figure modified from *Workman et al.* (2006).

cal studies, comprehensive melt inclusion analyses of major, minor and volatile (especially CO_2) elements for multiple eruptions at one oceanic volcano are rare. Collating time-series datasets for variable eruption styles has also proved difficult because of the paucity of information on the date of eruption and type of activity that produced the analysed materials, and because many ocean island studies have analysed only submarine glasses.

However a number of new studies are now emerging that use complementary geophysical, petrological and geochemical datasets to investigate the links between source and surface processes at other basaltic volcanoes. In particular, recent studies of volcanics from Mount Etna, in Italy have investigated long and short term changes in magma chemistry and eruption styles (*Viccaro and Cristofolini*, 2008; *Nicotra and Viccaro*, 2012). Etna is a basaltic stratovolcano, situated at the destructive plate margin of the African and European plates (*Gvirtzman and Nur*, 1999). A geochemical and isotopic study of historical whole rocks from Etna reveal that recently erupted lavas (post-1971) display short-term compositional variations that reflect partial melting of a mantle source region enriched by metasomatic influxes

(*Viccaro and Cristofolini*, 2008). These volatile-rich magmas are then discharged by more explosive strombolian–plinian activity at the surface (*Viccaro and Cristofolini*, 2008; *Metrich et al.*, 2004; *Kamenetsky et al.*, 2007). While melts may inherit variable amounts of volatiles from the mantle region, the plumbing and volcano tectonics will control the differentiation of the magmas, which subsequently affects eruption style (*Viccaro and Cristofolini*, 2008). At Etna, effusive eruptions are suggested to occur if the magmas steadily degas from an open conduit system, while strombolian/plinian eruptions occur if magmas are stored and evolve in closed reservoirs. While the composition of magmas and plumbing systems at Etna differ from those of an oceanic volcano such as Kīlauea, the results of this thesis are consistent with those of *Viccaro and Cristofolini* (2008), and provide further evidence which may improve our understanding of the influence that compositional heterogeneity in the mantle, and shallow magmatic processes, exert on the volatile geochemistry and eruption behaviour at basaltic volcanoes.

6.2 Degassing and eruption dynamics at Kīlauea

In addition to the examination of large-scale inter-eruption variations in magmatic chemistry, the second study in this thesis explored the short-term variations within a single eruption. Geochemical data for pre- and syn-eruptive melts from the 1959 Kīlauea Iki eruption were presented in Chapter 5. The results demonstrate the importance of olivine fractionation, magma mixing, lava drainback and CO_2 gas flushing on the melt compositions of the 1959 eruption. Major element compositions are largely controlled by extensive olivine-only fractionation with minor, late stage crystallisation of clinopyroxene in groundmass glasses, whilst minor and trace element compositions of glasses and melt inclusions reveal extensive pre- and syn-eruptive magma mixing. Melt inclusion trace element compositions are much more variable than their carrier melts and correlate with the volume of injected magma between episodes as derived from geophysical data. Volatile elements are largely decoupled from trace element compositions owing to their low solubility in basaltic melts at reservoir and conduit pressures. Temporal variations in melt H_2O (and to a lesser extent S) concentrations are effectively explained by a model of lava drain back and the mixing of degassed lavas with increasingly limited volumes of undegassed melt supplied throughout the eruption. Melt inclusion CO_2 concentrations correlate with the Mg number of the glasses and directly reflect volumes of new magma and CO_2-rich vapour input into the reservoir. The results suggest that CO_2 gas is important for triggering lava fountaining, whilst H_2O remains the dominant control on driving fountains, although CO_2 exerts a control on fountain dynamics. Melt inclusion CO_2 correlates inversely with fountain height and we propose that CO_2 decreases mass flow rates and exit velocities, caused by the higher density of CO_2 than H_2O at a fixed pressure and temperature. H_2O remains the primary volatile driving the expansion of the magma during ascent however. High fountains produced during the 1960 ERZ eruption were compositionally similar to the 1959 melts but were H_2O-rich and CO_2-poor, supporting previous models of Kīlauea plumbing and degassing.

The dynamics of basaltic eruptions and the production of lava fountains in particular, have been the focus of numerous investigations over the past 30 years, with studies that have largely concentrated on the physical volcanology of erupted products (e.g. *Mangan and Cashman*, 1996; *Polacci et al.*, 2006) and analogue models of gas-melt separation and magma rise speed (e.g. *Parfitt* 2004) which make significant assumptions about the composition of the melt volatile and gas-phase composition. A review of fountain literature however, does not yield another time-series dataset for a fountain eruption that is comparable with this study, with the exception of the previous Kīlauea Iki study discussed in Chapter 5 (*Anderson and Brown*, 1993; *Wallace*, 1998). This investigation provides new constraints on melt volatile concentrations during a fountain eruption, which could be used to complement and constrain previous analogue models for fountain dynamics. It is also the first study to demonstrate a relationship between melt CO_2 concentration and fountain height and the results call for development of numerical models, similar to those for rhyolitic systems (*Papale and Polacci*, 1999) to examine the effects of a two-component exsolving gas phase on magma ascent and fragmentation for basaltic compositions.

It is only in the last 10 years or so that advances in microanalytical techniques have enabled more accurate and reliable measurements of CO_2 at low concentrations in basaltic melts (*Hauri*, 2002). There are increasing numbers of studies that suggest that CO_2 may play a significant role in determining eruption dynamics. An investigation of eruptions from Mt. Etna in 2006 by *Nicotra and Viccaro* (2012) combined textural, whole rock and real-time gas data to suggest that the onset of variable and explosive activity which included strombolian eruptions and fountaining was associated with transient, rapid ascent of CO_2 vapour and/or CO_2-rich melts.

The results of the Kīlauea Iki case study presented here contribute to the understanding of pre- and syn-eruptive controls on magma compositions and eruption dynamics during high-fountaining eruptions at basaltic volcanoes and may hopefully lead to further research on this topic.

6.3 Suggestions for further work

The rich melt inclusion dataset for Kīlauea amassed during this project facilitates a multitude of additional further research projects, which are discussed briefly below.

6.3.1 Investigation of magma storage, transport and degassing during the 2008-10 summit eruption at Klauea Volcano, Hawai‘i

An extension of this research project, currently in preparation, involves the 47 melt inclusions analysed from the ongoing Kīlauea summit eruption within Halema`uma`u crater. This is the first summit eruption to have occurred at the volcano since 1982 and the first explosive summit eruption since 1924 (*Wilson et al.*, 2008), and has provided an unprecedented opportunity to use a combination of direct gas measurements and petrological datasets to test and validate models of magma storage, degassing and eruption from the upper regions of the magma reservoir at Kīlauea. The 4 samples collected as part of this PhD project preserve a time series of pre- and syn-eruptive melt compositions between 2008 and 2010. The melt inclusion data are used to complement measurements of CO_2 and SO_2 in the gas plume from the summit eruption, which were analysed by using electrochemical and non-dispersive infrared sensors during the first fieldwork campaign in April 2009. Gas measurements were carried out by M. Edmonds, R. Martin, G. Sawyer and R. Herd, with assistance from J. Sutton and T. Elias at the Hawaiian Volcano Observatory. Past studies of degassing at Kīlauea have only rarely related gas emissions to pre-eruptive volatile concentrations from the same eruption. The combination of gas flux and time-series melt inclusion data can be used to estimate magma fluxes to the summit and examine convection processes within the magma column exposed within the Halema`uma`u vent (Chapter 3; Figure 3.6b). This collaborative study seeks to broaden our understanding of the 2008-present summit eruption, and enables a more comprehensive estimate of the total CO_2 and S content of the melt and vapour system.

6.3.2 Raman spectroscopic study of CO_2-vapour bubbles

As described in Chapter 4, a large proportion of the Kīlauea inclusions (116 of 374) contain vapour bubbles, with most occupying > 7 vol% of the inclusion, though some larger bubbles occupying up to 73% were observed in a number of olivines. Vapour bubbles in melt inclusions may form in a number of ways, depending on the melt composition and post-entrapment processes which occur inside the inclusion. It is generally accepted that a shrinkage bubble forms as a result of differential contraction between the melt and the host olivine during cooling (*Roedder*, 1979; *Lowenstern*, 2003; *Metrich and Wallace*, 2008). Alternatively bubbles may form as a result of extensive post-entrapment crystallisation, leading to supersaturation of the inclusion with respect to its volatile species, or as a consquence of diffusive H-loss, leading to internal decompression of the inclusion and exsolution of CO_2 (*Gaetani et al.*, 2012). Some of the larger bubbles however, are unlikely to have formed by exsolution from the small volume of melt in which they are trapped and may represent bubbles trapped with the external melt. Vapour bubbles are often ignored in melt inclusion studies and it was not until some way through the preparation and analyses of samples for this study, that the prevalence of the bubbles was recognised and their significance to constraining the original pre-eruptive volatile concentrations were considered in more detail.

A number of studies have attempted to reconstruct the CO_2 content of the melt inclusions at the time of entrapment by mass balance calculations estimated from the bubble and melt inclusion volumes as well as constraints on the density and composition of the fluid in the bubble (*Anderson and Brown*, 1993; *Shaw et al.*, 2010). *Shaw et al.* (2010) used the measured CO_2 content of the inclusions to estimate a pressure of bubble equilibration, the equilibrium fluid composition and density. The authors found that over half of the original CO_2 present in the inclusion had been exsolved into the vapour bubble and consequently estimates of entrapment pressure based on melt inclusion compositions may be a factor of 3 too low. Other studies have heated melt inclusions to homogenise the vapour back into the melt and observed a similar two-fold increase in the dissolved CO_2 concentrations (*Cervantes et al.*, 2002).

Homogenisation through heating is a problematic method owing to the high temperatures required to dissolve the vapour bubble, which may adversely affect the major and volatile composition of the inclusion. An alternative method for constraining the CO_2 concentrations of the bubbles, and one which will be used in a further study of these Kīlauean melt inclusions, is confocal Raman spectroscopy. If the vapour bubble contains a relatively dense fluid phase at room temperature, Raman analysis of an olivine-hosted inclusion will produce a spectra with peaks characteristic of CO_2 (Figure 6.2a). The distance between the two peaks of the Fermi diad can be used to calculate the density of the fluid in the bubble, using a calibrated equation of *Fall et al.* (2011). Assuming the fluid is pure CO_2, the internal pressure of the bubble can be estimated and mass balance calculations performed to determine the CO_2 concentration originally dissolved in the trapped melt. This method has rarely been applied to bubbles within melt inclusions, but analyses of CO_2 in vapour bubbles within olivine-hosted melt inclusions from a variety of magmatic settings have been reported previously by *Kamenetsky et al.* (2002) and has recently been successfully completed for a suite of Icelandic basaltic melt inclusions (M. Hartley, pers. comm.). Preliminary spectra have already been obtained for bubbles within some of the Kīlauean melt inclusions from this dataset using the Raman spectrometer at the University of Cambridge and are shown in Figure 6.2b. None of the spectra display any peaks for H_2O, and therefore the assumption of a pure CO_2 vapour phase is valid for this study. Spectra will be obtained for every available, intact bubble within the Kīlauea inclusion set analysed in this study and used to provide estimates of undegassed melt CO_2 values that can then be compared with values from surface gas measurements and the CO_2/Nb estimates of this study to develop a comprehensive model for CO_2 degassing at Kīlauea. Spectra from large-volume bubbles identified in this study may also provide information about the composition of the vapour phases associated with the carrier melts at the time of crystallisation in the summit reservoir.

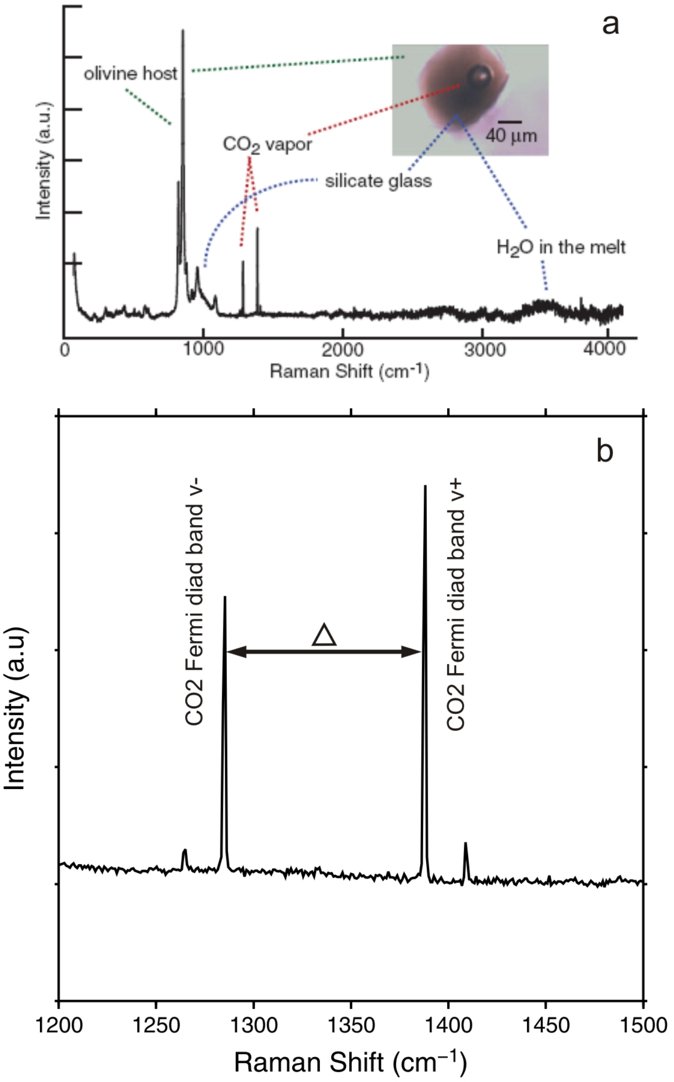

Figure 6.2: Raman spectra for CO_2-rich vapour (shrinkage) bubbles within olivine-hosted melt inclusions. (a) Raman spectrum for a bubble contained within an olivine from Solchiaro volcano, Procida, southern Italy. Peaks labelled 'CO_2 vapour' correspond to the Fermi diad for CO_2, and the distance between these peaks varies as a function of the density of the CO_2 phase (Kawakami et al., 2003). Also shown on the spectrum are peaks corresponding to the host (Fo-rich olivine), the silicate glass, and H_2O dissolved in the glass (melt); figure reproduced from *Steele-Macinnis et al.* (2011); (b) Raw data raman spectrum for a vapour bubble within a Kīlauean melt inclusion. The spectrum obtained during a preliminary study, demonstrates that the Fermi diad peaks are clearly detectable in the samples from this study, and that further reseach using this technique would certainly be viable with this dataset.

6.3.3 D/H isotopic study of Kīlauean melt inclusions

As discussed in Chapters 4 and 5, the greatest uncertainty involved in constraining pre-eruptive melt H_2O concentrations from melt inclusions is the potential for rapid diffusive loss or gain of H^+ through the host olivine. Recent results from hydration-dehydration experiments on olivine-hosted melt inclusions demonstrate that H_2O loss or gain in inclusions is possible on very short time scales (*Gaetani et al.*, 2012). Distinguishing post-entrapment diffusive H-loss from pre-entrapment magmatic processes (such as the mixing of undegassed and degassed drainback melts, or dehydration of pre-eruptive melts by CO_2-rich gas flushing; discussed in Chapter 5), is of great importance for modelling magmatic processes and eruption dynamics in basaltic systems, and while this has been partially achieved here through examining the correlation of inclusion H_2O-concentrations with olivine-incompatible volatile elements such as S, an alternative method would be to analyse the D/H isotopic composition of the inclusions (*Hauri*, 2002). Whilst H^+ diffuses rapidly through olivine, D is relatively immobile and diffusive loss of H^+ results in an increase in the inclusion D/H ratio at low melt H_2O values. This method has been successfully developed and trialed by *Hauri* (2002) in a study of melt inclusions from multiple Hawaiian volcanoes, and further research analysing D/H ratios in the Kīlauea Iki melt inclusions reported here would robustly constrain the drainback model proposed in Chapter 5, and/or enable examination of the effects of syn-eruptive mixing on H-diffusion in silicate melt inclusions.

Bibliography

Albarede, F., and V. Tamagnan (1988), Modelling the recent geochemical evolution of the Piton de la Fournaise volcano, Reunion Island, 1931-1986, *Journal of Petrology*, *29*(5), 997–1030.

Allard, P., M. Burton, and F. Mure (2005), Spectroscopic evidence for a lava fountain driven by previously accumulated magmatic gas, *Nature*, *433*, 407–410.

Anderson, A. (1995), CO_2 and the eruptibility of picrite and komatiite, *Lithos*, *34*(1-3), 19–25.

Anderson, A., and G. Brown (1993), CO_2 contents and formation pressures of some Kilauean melt inclusions, *American Mineralogist*, *78*, 794–803.

Aramaki, S., Y. Hayakawi, T. Fujii, K. Nakamura, and T. Fukuoka (1986), The October 1983 eruption of Miyakejima volcano, *Journal of Volcanology and Geothermal Research*, *29*, 203–229.

Aubaud, C., E. Hauri, and M. Hirschmann (2004), Hydrogen partition coefficients between nominally anhydrous minerals and basaltic melts, *Geophysical Research Letters*, *31*, doi: 10.1029/2004GL021341.

Aubaud, C., F. Pineau, R. Hekinian, and M. Javoy (2005), Degassing of CO_2 and H_2O in submarine lavas from the Society hotspot, *Earth and Planetary Science Letters*, *235*, 511–527.

Ault, W., J. Eaton, and D. Richter (1961), Lava temperatures in the 1959 Kilauea eruption and cooling lake, *Geological Society of America Bulletin*, *72*, 791–794.

Baker, D. (2008), The fidelity of melt inclusions as records of melt composition, *Contributions to Mineralogy and Petrology*, *156*, 377–395.

Barsanti, M., P. Papale, D. Barbato, R. Moretti, E. Boschi, E. Hauri, and A. Longo (2009), Heterogeneous large total CO_2 abundance in the shallow magmatic system of Kilauea volcano, Hawai‘i, *Journal of Geophysical Research*, *114*(B12201), doi:10.1029/2008JB006187.

Bertagnini, A., S. Calvari, M. Coltelli, P. Landi, M. Pompilio, and V. Scribano (1990), *The 1989 eruptive sequence*, pp. 10–22, Mt. Etna: the 1989 eruption, Giardini, Pisa.

Blundy, J., and K. Cashman (2008), Petrologic reconstruction of magmatic system variables and processes, *Reviews in Mineralogy and Geochemistry*, *69*, 179–239.

Brigham, W. (1909), The Volcanoes of Kilauea and Mauna Loa on the Island of Hawai'i, in *Memoirs of the Bernice Pauahi Bishop Museum*, Bishop Museum Press.

Brooker, R., S. Kohn, J. Holloway, P. McMillan, and M. Carroll (1999), Solubility, speciation and dissolution mechanisms for CO_2 in melts on the $NaAlO_2$-SiO_2 join, *Geochimica et Cosmochimica Acta*, *63*(21), 3549–3565.

Bureau, H., F. Pineau, N. Metrich, M. Semet, and M. Javoy (1998), A melt and fluid inclusion study of the gas phase at Piton de la Fournaise volcano (Reunion Island), *Chemical Geology*, *147*, 115–130.

Campbell, I. (2003), Constraints on continental growth models from Nb/U ratios in the 3.5 Ga barberton and other archaean basalt-komatiite suites, *American Journal of Science*, *303*(4), 319–351.

Cartigny, P., F. Pineau, C. Aubaud, and M. Javoy (2007), Towards a consistent mantle carbon flux estimate: Insights from volatile systematics (H_2O/Ce, dD, CO_2/Nb) in the North Atlantic mantle (14^{o}N and 34^{o}N), *Earth and Planetary Science Letters*, *265*, 672–685.

Cashman, K., M. Mangan, and S. Newman (1994), Surface degassing and modifications to vesicle size distributions in active basalt flows, *Journal of Volcanology and Geothermal Research*, *61*(1-2), 45–68.

Cervantes, P., V. Kamenetsky, and P. Wallace (2002), Melt inclusion volatile contents, pressure of crystallization for Hawaiian picrites, and the problem of shrinkage bubbles, *EOS Transactions, American Geophysical Union*, *83*(F1495-F1496), 1.

Cherniak, D. (2010), REE diffusion in olivine, *JAmerican Mineralogist*, *95*, 362–368.

Clague, D., and G. Dalrymple (1987), The Hawaiian-Emperor volcanic chain. Part 1. Geologic evolution, in *Volcanism in Hawai'i*, U.S. Geological Survey Professional Paper, pp. 5–54.

Clague, D., J. Moore, J. Dixon, and W. Friesen (1995), Petrology of submarine lavas from Kilauea's Puna Ridge, Hawai'i, *Journal of Petrology*, *36*(2), 299–349.

Clague, D., J. Hagstrum, D. Champion, and M. Beeson (1999), Kilauea summit overflows: their ages and distribution in the Puna District, Hawai'i, *Bulletin of Volcanology*, *61*, 363–381.

Clague, D., A. Davis, and J. Dixon (2003), Submarine strombolian eruptions along the Gorda mid-ocean ridge, in *Explosive Subaqueous Volcanism*, *AGU Monograph*, vol. 140, edited by J. White, J. Smellie, and D. Clague, pp. 111–128.

Collins, S. (2010), Degassing of volatiles and semi-volatile trace elements at basaltic volcanoes, Ph.D. thesis, University of Cambridge.

Collins, S., D. Pyle, and J. Maclennan (2009), Melt inclusions track pre-eruptive storage and dehydration of magmas at Etna, *Geology*, *37*, 571–574.

Coltelli, M., P. Del Carlo, and L. Vezzoli (2000), Stratigraphic constraints for exlposive activity in the past 100ka at Etna volcano, Italy, *International Journal of Earth Sciences*, *89*, 665–677.

Cottrell, E., M. Spiegelman, and C. Langmuir (2002), Consequences of diffusive re-equilibration for the interpretation of melt inclusions, *Geochemistry, Geophysics, Geosystems*, doi: 000175371900001.

Craven, J. (2007), A beginners guide to Cameca SIMS instruments, University of Edinburgh.

Danyushevsky, L., and P. Plechov (2011), Petrolog v.3.

Danyushevsky, L., F. Della-Pasqua, and S. Sokolov (2000), Re-equilibration of melt inclusions trapped by magnesian olivine phenocrysts from subduction-related magmas: petrological implications, *Contributions to Mineralogy and Petrology*, *138*, 68–83.

Davidson, J., D. Morgan, B. Charlier, R. Harlou, and J. Hora (2007), Microsampling and isotopic analysis of igneous rocks:implications for the study of magmatic systems, *Annual Review of Earth and Planetary Sciences*, *35*, 273–311.

Decker, R., and R. Christiansen (1984), Explosive eruptions of Kilauea volcano, Hawai'i, in *Explosive Volcanism: Inception, Evolution and Hazards*, Studies in Geophysics, pp. 122–132, National Academy Press, Washington, D.C.

Dibble, S. (1843), *History of the Sandwich Islands*, Lahainaluna: Press of the Mission Seminary.

Dixon, J. (1997), Degassing of alkalic basalts, *American Mineralogist*, *82*, 368–378.

Dixon, J., and D. Clague (2001), Volatiles in basaltic glasses from Loihi Seamount, Hawai'i: evidence for a relatively dry plume component, *Journal of Petrology*, *42*(3), 627–654.

Dixon, J., and E. Stolper (1995), An experimental study of water and carbon dioxide solubilities in mid-ocean ridge basaltic liquids. Part II: Applications to degassing, *Journal of Petrology*, *36*(6), 1633–1646.

Dixon, J., D. Clague, and E. Stolper (1991), Degassing history of water, sulfur and carbon in submarine lavas from Kilauea volcano, Hawai‘i, *Journal of Geology*, *99*(3), 371–394.

Dixon, J., E. Stolper, and J. Holloway (1995), An experimental study of water and carbon dioxide solubilities in mid-ocean ridge basaltic liquids. Part I: Calibration and solubility models, *Journal of Petrology*, *36*(6), 1607–1641.

Dixon, J., L. Leist, C. Langmuir, and J. Schilling (2002), Recycled dehydrated lithosphere in plume-influenced mid-ocean-ridge basalt, *Nature*, *420*, 385–389.

Dohmen, R., S. Kaseman, L. Coogan, and S. Chakraborty (2010), Diffusion of Li in olivine. Part I: Experimental observations and a multi species diffusion model, *Geochimica et Cosmochimica Acta*, *74*, 274–292.

Duffield, W., R. Christiansen, R. Koyanagi, and D. Peterson (1982), Storage, migration, and eruption of magma at Kilauea volcano, Hawai‘i, 1971-1972, *Journal of Volcanology and Geothermal Research*, *13*, 273–307.

Dvorak, J. (1990), Geometry of the September 1971 eruptive fissure at Kilauea volcano, Hawai‘i, *Bulletin of Volcanology*, *52*(7), 507–514.

Dvorak, J. (1992), Mechanism of explosive eruptions of Kilauea Volcano, Hawaii, *Bulletin of Volcanology*, *54*, 638–645.

Dzurisin, D., R. Koyanagi, and T. English (1984), Magma supply and storage at Kilauea volcano, hawaii, 1956-1983, *Journal of Volcanology and Geothermal Research*, *21*, 177–206.

Easton, R. (1987), Stratigraphy of Kilauea volcano, in *Volcanism in Hawai‘i*, *U.S. Geological Survey Professional Paper*, vol. 1, edited by R. Decker, T. Wright, and P. Stauffer, pp. 243–260.

Easton, R., and M. Garcia (1980), Petrology of the Hilina Formation, Kilauea Volcano, Hawaii, *Bulletin of Volcanology*, *43-4*, 657–673.

Eaton, J., and K. Murata (1960), How volcanoes grow, *Science*, *132*, 925–938.

Eaton, J., D. Richter, and H. Krivoy (1987), Cycling of magma between the summit reservoir and Kilauea Iki lava lake during the 1959 eruption of Kilauea volcano, *U.S. Geological Survey Professional Papers*, *1350*, 1307–1334.

Edmonds, M., and T. Gerlach (2006), The airborne lava-seawater interaction plume at Kilauea volcano, Hawai'i, *Earth and Planetary Science Letters*, *244*, 83–96.

Edmonds, M., T. Gerlach, and R. Herd (2009), Halogen degassing durning ascent and eruption of water-poor basaltic magma, *Chemical Geology*, *263*(1–4), 122–130.

Elias, T., and A. Sutton (2007), Sulphur dioxide rates from Kilauea Volcano, Hawai'i, an update:2002-2006, *USGS Open File Report 2007-1114*.

Elias, T., A. Sutton, J. Stokes, and T. Casadevall (1998), Sulphur dioxide emission rates of Kilauea Volcano, 1979-1997, *USGS Open File Report 98–462*.

Ellis, W. (1826), *A Narrative of an 1823 Tour Through Hawai'i*, 4th ed., Mutual Publishing.

Emerson, N. (1915), *Pele and Hiiaka: a myth from Hawai'i*, p. 250, Honolulu Star-Bulletin Ltd, revised edition by 'Ai Pohaku Press, Honolulu, 1993.

Engwell, S., and M. Hall (2008), Epoxy resins.

Epp, D., R. Decker, and A. Okamura (1983), Relation of summit deformation to east rift zone eruptions of Kilauea volcano, Hawai'i, *Geophysical Research Letters*, *10*, 493–496.

Fagents, S., and L. Wilson (1993), Explosive volcanic eruptions: VII. the range of pyroclasts ejected in transient exlosions, *Geophysical Journal International*, *113*, 359–370.

Fall, A., B. Tattitch, and R. Bodnar (2011), Combined microthermometric and Raman spectroscopic technique to determine the salinity of h_2o-co_2-nacl fluid inclusions based on clathrate melting, *Geochimica et Cosmochimica Acta*, *75*, 951–964.

Faure, F., and P. Schiano (2005), Experimental investigation of equilibration conditions during fosterite growth and melt inclusion formation, *Earth and Planetary Science Letters*, *236*, 882–898.

Fedotov, S., A. Chirkov, N. Gusev, G. Kovalev, and Y. Slezin (1980), The large fissure eruption in the region of Plosky Tolbachik volcano in Kamchatka, 1975-1976, *Bulletin of Volcanology*, *43*, 47–60.

Finch, R. (1940), Engulfment at Kilauea volcano, in *The Volcano Letter*, vol. 470, edited by R. Fiske, T. Simkin, and E. Nielsen, pp. 1–4, Smithsonian Institution Press, Washington, DC.

Fiske, R., and E. Jackson (1972), Orientation and growth of Hawaiian volcanic rifts: The effect of regional structure and gravitational stresses, *Proceedings of the Royal Society*, *329*(1578), 299–326.

Fiske, R., and W. Kinoshita (1969), Inflation of Kilauea volcano prior to its 1967–1968 eruption, *Science*, *165*, 341–349.

Fiske, R., T. rose rose rose rose, D. Swanson, D. Champion, and J. McGeehin (2009), Kulanaokuaiki Tephra (ca. A.D. 400-1000): Newly recognised evidence for highly explosive eruptions at Kilauea Volcano, Hawai'i, *Geological Society of America Bulletin*, *121*, 712–728.

Ford, C., D. Russell, J. Craven, and M. Fisk (1983), Olivine-liquid equilibria: temperature, pressure and composition dependence of the crystal/liquid cation partition coefficients for Mg, Fe^{2+}, Ca and Mn, *Journal of Petrology*, *24*(3), 256–265.

Fryer, B., S. Jackson, and H. Longerich (1995), Design, operation and role of the laser-ablation microprobe coupled with an inductively-coupled plasma-mass-spectrometer (LA-ICP-MS) in Earth Sciences, *Canadian Mineralogist*, *33*, 303–312.

Gaetani, G., and E. Watson (2000), Open-system behaviour of olivine-hosted melt inclusions, *Earth and Planetary Science Letters*, *183*, 27–41.

Gaetani, G., and E. Watson (2002), Modeling the major-element evolution of olivine-hosted melt inclusions, *Chemical Geology*, *183*, 25–41.

Gaetani, G., J. O'Leary, N. Schimizu, C. Bucholz, and M. Newville (2012), Rapid reequilibration of H_2O and oxygen fugacity in olivine-hosted melt inclusions, *Geology*, *40*(10), 915–918, doi: 10.1130/G32992.1.

Garcia, M., D. Muenow, K. Aggrey, and J. O'Neil (1989), Major element, volatile, and stable isotope geochemistry of Hawaiian submarine tholeiitic glasses, *Journal of Geophysical Research*, *94*(B8), 10,525–10,538.

Garcia, M., J. Rhodes, F. Trusdell, and A. Pietruszka (1996), Petrology of lavas from the Pu'u 'O'o eruption of Kilauea Volcano: Iii. The Kupaianaha episode (1986-1992), *Bulletin of Volcanology*, *58*, 359–379.

Garcia, M., E. Ito, I. Eiler, and A. Pietruszka (1998), Crystal contamination of Kilauea volcano magmas revealed by oxygen isotope analyses of glass and olivine from Pu‘u‘O‘o eruption lavas, *Journal of Petrology*, *39*, 803–817.

Garcia, M., A. Pietruszka, J. Rhodes, and K. Swanson (2000), Magmatic processes during the prolonged Pu'u 'O'o eruption of Kilauea Volcano, Hawai'i, *Journal of Petrology*, *41*(7), 967–990.

Garcia, M., A. Pietruszka, and J. Rhodes (2003), A petrologic perspective of Kilauea Volcano's summit magma reservoir, *Journal of Petrology*, *44*(12), 2313–2339.

Geist, D. (1992), An appraisal of melting processes and the galapagos hotspot: Major- and trace-element evidence, *Journal of Volcanology and Geothermal Research*, *52*, 65–82.

Gerlach, T. (1986), Exsolution of H_2O, CO_2, S during Eruptive Episodes at Kilauea volcano, Hawaii, *Journal of Geophysical Research*, *91*(B12), 12,177–12,185.

Gerlach, T., and E. Graeber (1985), Volatile budget of Kilauea volcano, *Nature*, *313*, 273–277.

Gerlach, T., K. McGee, T. Elias, A. Sutton, and M. Doukas (2002), Carbon dioxide emission rate of Kilauea Volcano: Implications for primary magma and the summit reservoir, *Journal of Geophysical Research*, *107*(B9), 2189.

Giordano, D., and D. Dingwell (2003), Viscosity of hydrous Etna basalt: Implications for Plinian-style basaltic eruptions, *Bulletin of Volcanology*, *65*(1), 8–14.

Gunn, B. (1971), Trace element partition during olivine fractionation of Hawaiian basalts, *Chemical Geology*, *8*, 1–13.

Gvirtzman, Z., and A. Nur (1999), The formation of Mount Etna as the consequence of slab rollback, *Nature*, *401*, 782–785.

Hager, S., T. Gerlach, and P. Wallace (2008), Summit CO_2 emission rates by the CO_2/SO_2 ratio method at Kilauea Volcano, Hawai'i, during a period of sustained inflation, *Journal of Volcanology and Geothermal Research*, *177*, 875–882.

Hall, L. (1999), The effect of water on mantle melting, Ph.D. thesis, University of Bristol.

Halmer, M., H. Schmincke, and H. Graf (2002), The annual volcanic gas input into the atmosphere, in particular into the stratosphere: a global dataset for the past 100 years, *Journal of Volcanology and Geothermal Research*, *115*(3-4), 511–528.

Halter, W., T. Pettke, C. Heinrich, and B. Rothen-Rutishauser (2002), Major to trace element analysis of melt inclusions by laser-ablation ICP-MS: methods of quantification, *Chemical Geology*, *183*, 63–86.

Harris, D., and A. Anderson (1983), Concentrations, sources and losses of H_2O, CO_2, and S in Kilauean basalt, *Geochimica et Cosmochimica Acta*, *47*, 1139–1150.

Hauri, E. (2002), SIMS analyses of volatiles in silicate glasses, 2: isotopes and abundances in Hawaiian melt inclusions, *Chemical Geology*, *282*, 115–141.

Hauri, E. (2010), Water and carbon heterogeneity in morb mantle sources.

Hauri, E., J. Wang, J. Dixon, P. King, C. Mandeville, and S. Newman (2002a), SIMS analysis of volatiles in silicate glasses 1: Calibration, matrix effects and comparisons with FTIR, *Chemical Geology*, *183*, 99–114.

Hauri, E., K. Gronvold, N. Oskarsson, and D. McKenzie (2002b), Abundance of carbon in the Icelandic Mantle: Constraints from melt inclusions, *American Geophysical Union Spring Meeting*, (abstract#V51D-03), 1.

Hauri, E., G. Gaetani, and T. Green (2006), Partitioning of water during melting of the earth's upper mantle at H_2O-undersaturated conditions, *Earth and Planetary Science Letters*, *248*, 715–734.

Head, J., and L. Wilson (1987), Lava Fountain Heights at Pu'u 'O'o, Kilauea, Hawai'i: Indicators of Amount and Variations of Exsolved Magma Volatiles, *Journal of Geophysical Research*, *92*(B13), 13,715–13,719.

Heinrich, C., T. Pettke, W. Halter, M. Aigner-Torres, A. Audetat, D. Gunther, B. Hattendorf, D. Bleiner, M. Guillong, and I. Horn (2003), Quantitative multi-element analysis of minerals, fluid and melt inclusions by laser-ablation inductively-coupled-plasma mass-spectrometry, *Geochimica et Cosmochimica Acta*, *67*(18), 3473–3496.

Heliker, C., and T. Mattox (2003), The first two decades of the Pu'u 'O'o-Kupaianaha eruption: chronology and selected bibliography, *U.S. Geological Survey Professional Paper*, *1676*, 1–27.

Helz, R. (1987), Diverse olivine types in lava of the 1959 eruption of Kilauea volcano and their bearing on eruption dynamics, in *Volcanism in Hawai'i*, *U.S. Geological Survey Professional Paper*, vol. 1, pp. 691–722.

Helz, R. (2009), Processes active in mafic magma chambers: the example of Kilauea Iki Lava Lake, Hawai'i, *Lithos*, *111*, 37–46.

Helz, R., and C. Thornber (1987), Geothermometry of Kilauea Iki lava lake, Hawai'i, *Bulletin of Volcanology*, *49*, 651–668.

Hervig, R., F. Mazdab, P. Williams, Y. Guan, G. Huss, and L. Leshin (2006), Useful ion yields for Cameca IMS 3f and 6f SIMS: Limits on quantitative analysis, *Chemical Geology*, *227*, 83–99.

Hinton, R. (1990), Ion microprobe trace-element analysis of silicates - measurements of multi-element glasses, *Chemical Geology*, *83*, 11–25.

Hinton, R. (1995), *Ion microprobe analysis in geology*, chap. 6, pp. 235–291, Microprobe Techniques in the Earth Sciences, first ed., Chapman & Hall.

Hitchcock, C. (1911), *Hawai'i and its volcanoes*, The Hawaiian Gazette Co.

Holcomb, R. (1987), Eruptive history and long-term behavior of Kilauea volcano, in *Volcanism in Hawai'i*, *U.S. Geological Survey Professional Paper*, vol. 1, edited by R. Decker, T. Wright, and P. Stauffer, pp. 261–350.

Holloway, J., and J. Blank (1994), Application of experimental results to C-O-H species in natural melts, *Reviews in Mineralogy and Geochemistry*, *30*, 187–230.

Houghton, B., and H. Gonnerman (2008), Basaltic explosive volcanism: Constraints from deposits and models, *Chemie der Erde*, *68*, 117–140.

Houghton, B., D. Swanson, R. Carey, J. Rausch, and A. Sutton (2011), Pigeonholing pyroclasts: Insights from the 19 march 2008 explosive eruption of Kilauea volcano, *Geology*, *39*, 263–266.

Humphreys, M., S. Kearns, and J. Blundy (2006), SIMS investigation of electron-beam damage to hydrous, rhyolitic glasses: Implications for melt inclusion analysis, *American Mineralogist*, *91*, 667–679.

Hurwitz, S., F. Goff, C. Janki, W. Evans, D. Counce, M. Sorey, and S. Ingebritsen (2003), Mixing of magmatic volatiles with groundwater and interaction with basalt on the summit of Kilauea volcano, Hawai'i, *Journal of Geophysical Research*, *108*(B1), doi:10.1029/2001JB001594.

Jaggar, T. (1947), Origin and evolution of craters, *Geological Society of America Memoirs*, *121*, 508.

Jaggar, T., and R. Finch (1924), The explosive eruption of Kilauea in Hawai'i, 1924, *American Journal of Science*, *8*(4), 354–374.

Jaupart, C., and S. Vergniolle (1988), Laboratory models of Hawaiian and Strombolian eruptions, *Nature*, *331*, 58–60.

Jaupart, C., and S. Vergniolle (1989), The generation and collapse of foam layer at the roof of a basaltic magma chamber, *Journal of Fluid Mechanics*, *203*, 347–380.

Jellinek, A., and R. Kerr (2001), Magma dynamics, crystallization and chemical differentiation of the 1959 Kilauea Iki lava lake, Hawai'i, revisited, *Journal of Volcanology and Geothermal Research*, *110*, 235–263.

Johnson, E., P. Wallace, K. Cashman, H. Granados, and A. Kent (2008), Magmatic volatile contents and degassing-induced crystallization at Volcan Jorullo, Mexico: Implications for melt evolution and the plumbing systems of monogenetic volcanoes, *Earth and Planetary Science Letters*, *269*, 478–487.

Jurewicz, A., and E. Watson (1988), Cations in olivine, Part 1, Calcium, *Contributions to Mineralogy and Petrology*, *99*, 176–185.

Kamenetsky, V., P. Davidson, T. Mernagh, A. Crawford, J. Gemmell, M. Portnyagin, and R. Shinjo (2002), Fluid bubbles in melt inclusions and pillow–rim glasses: high–temperature precursors to hydrothermal fluids?, *Chemical Geology*, *183*, 349–364.

Kamenetsky, V., M. Pompilio, N. Metrich, A. Sobolev, D. Kuzmin, and R. Thomas (2007), Arrival of extremely volatile-rich high-mg magmas changes explosivity of Mount Etna, *Geology*, *35*, 255–258.

Keiding, J., R. Trumball, I. Veksler, and D. Jerram (2011), On the significance of ultra-magnesian olivines in basaltic rocks, *Geology*, *39*(12), 1095–1098.

Kent, A. (2008), Melt inclusions in basaltic and related volcanic rocks, *Reviews in Mineralogy and Geochemistry*, *69*, 273–331.

Koleszar, A., A. Saal, E. Hauri, A. Nagle, Y. Liang, and M. Kurz (2009), Melt inclusions, the volatile contents of the Galapagos plume and evidence of open system behavior, *Earth and Planetary Science Letters*.

Koyanagi, R., J. Unger, E. Endo, and A. Okamura (1976), Shallow earthquakes associated with inflation episodes at the summit of Kilauea volcano, Hawai'i, *Bulletin of Volcanology*, *39*, 621–631.

Lautze, N., and B. Houghton (2007), Linking variable explosion style and magma textures during 2002 at Stromboli volcano, Italy, *Bulletin of Volcanology*, *69*(4), 445–460.

Le Roux, P., S. Shirey, E. Hauri, M. Perfitt, and J. Bender (2006), The effects of variable sources, processes and contaminants on the composition of norther EPR MORB (8-10^{o}N and 12-14^{o}N): Evidence from volatiles (H_2O, CO_2, S) and halogens (F, Cl), *Earth and Planetary Science Letters*, *251*, 209–231.

Liang, Y., F. Richter, A. Davis, and E. Watson (1996), Diffusion in silicate melts. 1. Self diffusion in Cao-Al_2o_3-Sio_2 at 1500 degrees C and 1 GPa., *Geochimica et Cosmochimica Acta*, *60*, 4353–4367.

Lloyd, A., T. Plank, P. Ruprecht, E. Hauri, and W. Rose (2012), Volatile loss from melt inclusions in pyroclasts of differing sizes, *Contributions to Mineralogy and Petrology*, doi:10.1007/s00410-012-0800-2.

Lockwood, J., R. Tilling, R. Holcomb, F. Klein, A. Okamura, and D. Peterson (1999), Magma migration and resupply during the 1974 summit eruptions of Kilauea Volcano, Hawai'i, *U.S. Geological Survey Professional Paper*, *1613*, 1–37.

Loewen, M. (2011), Analysis of semi-volatile trace metals in basaltic glass by LA-ICP-MS, Master's thesis, Oregon State University.

Lowenstern, J. (2003), *Melt inclusions come of age; volatiles, volcanoes, and Sorby's legacy*, pp. 1–21, Melt Inclusions in Volcanic Systems: Methods, Applications and Problems.

MacDonald, G. (1959), The activity of Hawaiian volcanoes during the years 1951-1956, *Bulletin Volcanologique*, *22*, 3–70.

MacDonald, G. (1962), The 1959 and 1960 eruptions of Kilauea volcano, Hawai'i, and the construction of walls to restrict the spread of the lava flows, *Bulletin of Volcanology*, *24*(1), 249–294.

MacDonald, G., and J. Eaton (1954), Hawaiian volcanoes during 1954, *Geological Survey Bulletin*, *1061-B*, 1–70.

MacDonald, G., and T. Katsura (1961), Variations in the lava of the 1959 eruption in Kilauea Iki, *Pacific Science*, *XV*, 358–369.

MacDonald, G., and T. Katsura (1964), Chemical composition of Hawaiian lavas, *Journal of Petrology*, *5*(1), 82–133.

MacDonald, G., A. Abbott, and F. Peterson (1983), *Volcanoes in the Sea: the geology of Hawai'i*, 2nd ed., University of Hawai'i Press, Honolulu, HI.

Mackwell, S., and D. Kohlstedt (1990), Diffusion of hydrogen in olivine: Implications for water in the mantle, *Journal of Geophysical Research*, *95*(B4), 5079–5088.

Maclennan, J. (2008a), Lead isotope variability in olivine-hosted melt inclusions from Iceland, *Geochimica et Cosmochimica Acta*, *72*, 4159–4176.

Maclennan, J. (2008b), Concurrent mixing and cooling of melts under Iceland, *Journal of Petrology*, *49*(11), 1931–1953.

Mangan, M. (1990), Crystal size distribution systematics and the determination of magma storage times: The 1959 eruption of Kilauea Volcano, Hawaii, *Journal of Volcanology and Geothermal Research*, *44*, 295–302.

Mangan, M., and K. Cashman (1996), The structure of basaltic scoria and reticulite and inferences for vesiculation, foam formation, and fragmentation in lava fountains, *Journal of Volcanology and Geothermal Research*, *73*, 1–18.

Mangan, M., and T. Sisson (2000), Delayed, disequilibrium degassing in rhyolite magma: decompression experiments and implications for explosive volcanism, *Earth and Planetary Science Letters*, *183*, 441–455.

Mangan, M., K. Cashman, and S. Newman (1993), Vesiculation of basaltic magma during eruption, *Journal of Geology*, *21*, 157–160.

Marske, J., A. Pietruszka, D. Weis, M. Garcia, and J. Rhodes (2007), Rapid passage of a small-scale mantle heterogeneity through the melting regions of Kilauea and Mauna Loa Volcanoes, *Earth and Planetary Science Letters*, *259*, 34–50.

Marske, J., M. Garcia, A. Pietruszka, J. Rhodes, and M. Norman (2008), Geochemical variations during Kilauea's Pu'u 'O'o eruption reveal a fine-scale mixture of mantle heterogeneities within the Hawaiian Plume, *Journal of Petrology*, *49*(7), 1297–1318.

Mastin, L. (1997), Evidence for water influx from a caldera lake during the explosive hydromagmatic eruption of 1790, Kilauea volcano, Hawai'i, *Journal of Geophysical Research*, *102*(B9), 20,093–20,109.

Mathez, E. (1976), Sulfur solubility and magmatic sulphides in submarine basalt glass, *Journal of Geophysical Research*, *81*(23), 4269–4276.

May, M. (2008), Keanakakoi reticulite density and dispersal: Implications for erutpion intensity, mechanisms, and chronology, Master's thesis, University of Hawai'i.

McDonough, W., and S. Sun (1995), The composition of the Earth, *Chemical Geology*, *120*, 223–253.

McPhie, J., G. Walker, and R. Christiansen (1990), Phreatomagmatic and phreatic fall and surge deposits from explosions at Kilauea volcano, Hawaii, 1790 AD: Keanakako'i Ash Member, *Bulletin of Volcanology*, *52*, 334–354.

Metrich, N., and P. Wallace (2008), Volatile abundances in basaltic magmas and their degassing paths tracked by melt inclusions.

Metrich, N., P. Allard, N. Spilliaert, D. Andronico, and M. Burton (2004), 2001 flank eruption of the alkali- and volatile-rich primitive basalt responsible for Mount Etna's evolution in the last three decades, *Earth and Planetary Science Letters*, *228*, 1–17.

MGDS (2012), Geomapapp.

Montelli, R., G. Nolet, F. Dahlen, G. Masters, E. Engdahl, and S. Hung (2004), Finite-frequency tomography reveals a variety of plumes in the mantle, *Science*, *303*, 338–343.

Murata, K. (1966), An acid fumarolic gas from Kilauea Iki, *U.S. Geological Survey Professional Paper*, *537-C*, 1–6.

Murata, K., and D. Richter (1966a), Chemistry of the lavas of the 1959-60 eruption of Kilauea volcano, Hawai'i, *U.S. Geological Survey Professional Paper*, *537-A*, 1–25.

Murata, K., and D. Richter (1966b), The settling of olivine in Kilauean magma as shown by lavas of the 1959 eruption, *American Journal of Science*, *264*, 194–203.

Namiki, A., and M. Manga (2008), Transition between fragmentation and permeable outgassing of low viscosity magmas, *Journal of Volcanology and Geothermal Research*, *169*(1-2), 48–60.

Neal, C., and J. Lockwood (2003), Geologic Map of the Summit Region of Kilauea Volcano, Hawai'i, *U.S. Geological Survey, Geologic Investigations Series*, *1–2759*, 1–14.

Newman, S., and J. Lowenstern (2002), Volatilecalc: a silicate melt-H_2O-CO_2 solution model written in Visual Basic for excel, *Computers and Geosciences*, *28*, 597–604.

Nicotra, E., and M. Viccaro (2012), Transient uprise of gas and gas-rich magma batches fed the pulsating behavior of the 2006 eruptive episodes at Mt. Etna volcano, *Journal of Volcanology and Geothermal Research*, *227-228*, 102–118.

Okubo, P., H. Benz, and B. Chouet (1997), Imaging the crustal magma source beneath Mauna Loa and Kilauea volcanoes, Hawai'i, *Geology*, *25*, 867–870.

Papale, P. (1997), Modeling of the solubility of a two-component H_2O + CO_2 fluid in silicate liquids, *American Mineralogist*, *84*, 477–492.

Papale, P. (2005), Determination of total H_2O and CO_2 budgets in evolving magmas from melt inclusion data, *Journal of Geophysical Research*, *110*(B03208), 1–13, doi:10.1029/2004JB003033.

Papale, P., and M. Polacci (1999), Role of carbon dioxide in the dynamics of magma ascent in explosive eruptions, *Bulletin of Volcanology*, *60*, 583–594.

Papale, P., R. Moretti, and D. Barbato (2006), The compositional dependence of the saturation surface of H_2O + CO_2 fluids in silicate melts, *Chemical Geology*, *229*, 78–95.

Parfitt, E. (1998), A study of clast size distribution, ash deposition and fragmention in a Hawaiian-style volcanic eruption, *Journal of Volcanology and Geothermal Research*, *84*, 197–208.

Parfitt, E. (2004), A discussion of the mechanisms of explosive basaltic eruptions, *Journal of Volcanology and Geothermal Research*, *134*, 77–107.

Parfitt, E., and L. Wilson (1994), The 1983-86 Pu'u 'O'o eruption of Kilauea volcano, Hawai'i: a study of dike geometry and eruption mechanisms for a long-derived eruption, *Journal of Volcanology and Geothermal Research*, *59*, 179–205.

Parfitt, E., and L. Wilson (1995), Explosive volcanic eruptions–IX. The transition between Hawaiian-style lava fountaining and Strombolian explosive activity, *Geophysical Journal International*, *121*, 226–232.

Parfitt, E., and L. Wilson (1999), A plinian treatment of fallout from Hawaiian lava fountains, *Journal of Volcanology and Geothermal Research*, *88*, 67–75.

Parfitt, E., L. Wilson, and C. Neal (1995), Factors influencing the height of Hawaiian lava fountains: implications for the use of fountain height as an indicator of magma gas content, *Bulletin of Volcanology*, *57*, 440–450.

Pearce, N., W. Perkins, J. Westgate, M. Gorton, S. Jackson, C. Neal, and S. Chenery (1997), A compilation of new and published major and trace element data for NIST SRM 610 and NIST SRM 612 glass reference materials, *Geostandards Newsletter - Journal of Geostandards and Geoanalysis*, *21*(1), 115–144.

Pichavant, M., and R. Macdonald (2007), Crystallization of primitive basaltic magmas at crustal pressures and genesis of the calc-alkaline igneous suite: experimental evidence from St. Vincent, Lesser Antilles arc, *Contributions to Mineralogy and Petrology*, doi:10.1007/s00410-007-0208-6.

Pietruszka, A., and M. Garcia (1999a), A rapid fluctuation in the mantle source and melting history of Kilauea Volcano inferred from the geochemistry of its historical summit lavas (1790-1982), *Journal of Petrology*, *40*, 1321–1342.

Pietruszka, A., and M. Garcia (1999b), The size and shape of Kilauea Volcano's summit magma storage reservoir: a geochemical probe, *Earth and Planetary Science Letters*, *167*, 311–320.

Pietruszka, A., M. Rubin, and M. Garcia (2001), ^{226}Ra-^{230}Th-^{238}U disequilibria of historical Kilauea lavas (1790-1982) and the dynamics of mantle melting within the Hawaiian plume, *Earth and Planetary Science Letters*, *186*(1), 15–31.

Pioli, L., E. Erlund, E. Johnson, K. Cashman, P. Wallace, M. Rosi, and H. Delgado Granados (2008), Explosive dynamics of violent strombolian eruptions: The eruption of Paricutin volcano 1943-1952 (mexico), *Earth and Planetary Science Letters*, *271*(1–4), 359–368.

Polacci, M., R. Corsaro, and D. Andronico (2006), Coupled textural and compotional characterization of basaltic scoria: Insights into the transition from Strombolian to fire fountain activity at Mount Etna, Italy, *Geology*, *34*(3), 201–204.

Polacci, M., D. Baker, L. Bai, and L. Mancini (2008), Large vesicles record pathways of degassing at basaltic volcanoes, *Bulletin of Volcanology*, *70*(9), 1023–1029.

Poland, M., A. Sutton, and T. Gerlach (2009), Magma degassing triggered by static decompression at Kilauea Volcano, Hawai'i, *Geophysical Research Letters*, *36*, doi:10.1029/2009GL039214.

Poland, M., A. Miklius, A. Sutton, and C. Thornber (2012), A mantle-driven surge in magma supply to Kilauea volcano during 2003-2007, *Nature Geoscience*, *5*, 295–300.

Portnyagin, M., R. Almeev, S. Matveev, and F. Holtz (2008), Experimental evidence for rapid water exchange between melt inclusions in olivine and host magmas, *Earth and Planetary Science Letters*, *272*, 541–552.

Powers, H. (1948), A chronology of explosive eruptions of Kilauea, *Pacific Science*, *2*, 278–292.

Putirka, K. (2005), Mantle potential temperatures at Hawai'i, Iceland and the mid-ocean ridge system, as inferred from olivine phenocrysts: Evidence for thermally driven mantle plumes, *Geochemistry, Geophysics, Geosystems*, *6*(5), doi:10.1029/2005GC000915.

Putirka, K., M. Perfitt, F. Ryerson, and M. Jackson (2007), Ambient and excess mantle temperatures, olivine thermometry, and active vs. passive upwelling, *Chemical Geology*, *241*, 177–206.

Reed, S. (2005), *Electron Microprobe Analysis and Scanning Electron Microscopy in Geology*, second ed., Cambridge University Press.

Rhodes, J., and M. Vollinger (2005), Ferric/ferrous ratios in 1984 Mauna Loa lavas: a contribution to understanding the oxidation state of Hawaiian magmas, *Contributions to Mineralogy and Petrology*, *149*, 666–674.

Richter, D. (1970), Chronological narrative of the 1959-60 eruption of Kilauea volcano, Hawai'i, *U.S. Geological Survey Professional Paper*, *537-E*, 1–73.

Richter, D., and J. Eaton (1960), The 1959-60 eruption of Kilauea volcano, *The New Scientist*, *7*, 994–997.

Richter, D., and J. Moore (1966), Petrology of the Kilauea Iki lava lake, Hawai'i, in *The 1959-60 Eruption of Kilauea Volcano, Hawai'i*, *U.S. Geological Survey Professional Paper*, vol. 537-B, pp. B1–B26.

Richter, D., and K. Murata (1966), Petrography of the lavas of the 1959-60 eruption of Kilauea volcano, Hawai'i, *U.S. Geological Survey Professional Paper*, *537-B*, 1–12.

Richter, D., W. Ault, J. Eaton, and J. Moore (1964), The 1961 eruption of Kilauea volcano, *U.S. Geological Survey Professional Paper*, *474-D*, 1–34.

Roedder, E. (1979), Origin and significance of magmatic inclusions, *Bulletin de Mineralogie*, *102*, 487–510.

Roedder, E. (1984), Fluid inclusions, *Reviews in Mineralogy and Geochemistry*, *12*, 1–644.

Roedder, E., and R. Emslie (1970), Olivine-liquid equilibrium, *Contributions to Mineralogy and Petrology*, *29*, 275–289.

Ryan, M., R. Koyanagi, and R. Fiske (1981), Modeling the three-dimensional structure of macroscopic magma transport systems: Application to Kilauea volcano, Hawai'i, *Journal of Geophysical Research*, *86*(B8), 7111, doi:10.1029/JB086iB08p07111.

Saal, A., E. Hauri, C. Langmuir, and M. Perfitt (2002), Vapour undersaturation in primitive mid-ocean-ridge basalt and the volatile content of Earth's upper mantle, *Nature*, *419*, 451–455.

Schwindinger, K., and A. Anderson Jr (1989), Synneusis of Kilauea Iki olivines, *Contributions to Mineralogy and Petrology*, *103*, 187–198.

Sen, G., and R. Jones (1990), Cumulate xenolith in Oahu, Hawai'i: Implications for deep magma chambers and Hawaiian volcanism, *Science*, *249*, 1154–1157.

Sharp, R., D. Dzurisin, and M. Malin (1987), An early 19th century reticulite pumice from Kilauea volcano, in *Volcanism in Hawai'i*, *U.S. Geological Survey Professional Paper*, vol. 1, pp. 395–404.

Shaw, A., M. Behn, S. Humphris, R. Sohn, and P. Gregg (2010), Deep pooling of low degree melts and volatile fluxes at the 85^oe segment of the Gakkel Ridge: Evidence from olivine-hosted melt inclusions and glasses, *Earth and Planetary Science Letters*, *289*, 311–322.

Shimizu, N., M. Semet, and C. Allegre (1978), Geochemical applications of quantitative ion-microprobe analysis, *Geochimica et Cosmochimica Acta*, *42*, 1321–1334.

Shishkina, T., Botcharnikov, H. R.E., R. F. Almeev, and M. Portnyagin (2010), Solubility of H_2O and CO_2-bearing fluids in tholeiitic basalts at pressures up to 500 MPa, *Chemical Geology*, *277*, 115–125.

Sigvaldason, G., and N. Oskarsson (1975), Chlorine in basalts from Iceland, *Geochimica et Cosmochimica Acta*, *40*, 777–789.

Sims, K., S. Goldstein, J. Blichert-Toft, M. Perfit, P. Kelemen, D. Fornari, P. Michael, M. Murrell, S. Hart, D. DePaolo, G. Layne, L. Ball, M. Jull, and J. Bender (2002), Chemical and isotopic constraints on the generation and transport of magma beneath the East Pacific Rise, *Geochimica et Cosmochimica Acta*, *66*(19), 3481–3504.

Sims, K., J. Blichert-Toft, D. Fornari, M. Perfit, S. Goldstein, P. Johnson, D. DePaolo, S. Hart, M. Murrell, P. Michael, and G. Layne (2003), Aberrant youth: Chemical and isotopic constraints on the origin of off-axis lavas from the East Pacific Rise, 9^o-10^on, *Geochemistry, Geocphysics, Geosystems*, *4*(10), doi:10.1029/2002GC000443.

Sisson, T., and G. Layne (1993), H_2O in basalt and basaltic andesite glass inclusions from four subduction-related volcanoes, *Earth and Planetary Science Letters*, *117*(3-4), 619–635.

Slezin, Y. (2003), The mechanism of volcanic eruptions (a steady-state approach), *Journal of Volcanology and Geothermal Research*, *122*, 7–50.

Sobolev, A., and M. Chaussidon (1996), H_2O concentrations in primary melts from supra-subduction zones and mid-ocean ridges: Implications for H_2O storage and recycling in the mantle, *Earth and Planetary Science Letters*, *137*, 45–55.

Sobolev, A., and N. Shimizu (1993), Ultra-depleted primary melt included in an olivine from the Mid-Atlantic Ridge, *Nature*, *363*, 151–154.

Spandler, C., H. O'Neill, and V. Kamenetsky (2007), Survival times of anomalous melt inclusions from element diffusion in olivine and chromite, *Nature*, *447*, 303–306.

Sparks, R. (1978), The dynamics of bubble formation and growth in magmas: a review and analysis, *Journal of Volcanology and Geothermal Research*, *3*, 1–37.

Sparks, R. (2003), Dynamics of magma degassing, in *Volcanic Degassing*, *Geological Society, London, Special Publications*, vol. 213, edited by C. Oppenheimer, D. Pyle, and J. Barclay, pp. 5–22.

Spilliaert, N., P. Allard, N. Metrich, and A. Sobolev (2006), Melt inclusion record of the conditions of ascent, degassing, and extrusion of volatile-rich alkali during the powerful 2002 flank eruption of Mount Etna (Italy), *Journal of Geophysical Research*, *111*(B04203), doi: 10.1029/2005JB003934.

Steele-Macinnis, M., R. Esposito, and R. Bodnar (2011), Thermodynamic model for the effect of post-entrapment crystallization on the h_2o–co_2 systematics of vapor-saturated, silicate melt inclusions, *Journal of Petrology*, *52*(12), 2451–2482.

Stone, W. (1991), Nickel-copper sulfides from the 1959 eruption of Kilauea volcano, Hawai'i: Contrasting compositions and phase relations in eruption pumice and Kilauea Iki lava lake, *American Mineralogist*, *76*, 1363–1372.

Stovall, W., B. Houghton, H. Gonnerman, S. Fagents, and D. Swanson (2011), Eruption dynamics of Hawaiian-style fountains: the case study of episode 1 of the Kilauea Iki 1959 eruption, *Bulletin of Volcanology*, *73*, 511–529.

Stovall, W., B. Houghton, J. Hammer, S. Fagents, and D. Swanson (2012), Vesiculation of high fountaining Hawaiian eruptions: episodes 15 and 16 of 1959 Kilauea Iki, *Bulletin of Volcanology*, *74*, 441–455.

Stroncik, N., and K. Haase (2004), Chlorine in oceanic intraplate basalts: Constraints on mantle sources and recycling processes, *Geology*, *32*(11), 945–948.

Sutton, A., T. Elias, T. Gerlach, and J. Stokes (2001), Implications for eruptive processes as indicated bu sulphur dioxide emissions from Kilauea Volcano, Hawai'i, 1979-1997, *Journal of Volcanology and Geothermal Research*, *108*(1-4), 283–302.

Sutton, J. E. T., and J. Kauahikaua (2003), Lava-effusion rates for the Pu'u'O'o-Kupaianaha eruption derived from SO_2 emissions and Very Low frequency (vlf) measurements, *Chapter 8 of Heliker, C., Swanson, D.A., and Takahashi, T.J., eds., The Pu'u'O'o-Kupaianaha eruption of Kilauea volcano, Hawai'i: The first 20 years. U.S. Geological Survey Professional Paper 1676*, *1*, 137–148.

Swanson, D. (2008), Hawaiian oral tradition describes 400 years of volcanic activity at Kilauea, *Journal of Volcanology and Geothermal Research*, *176*, 427–431.

Swanson, D., and R. Christiansen (1973), Tragic base surge in 1790 at Kilauea Volcano, *Geology*, pp. 83–87.

Swanson, D., W. Duffield, and R. Fiske (1976), Displacement of the south flank of Kilauea volcano: The result of forceful intrusion of magma into the rift zones.

Swanson, D., W. Duffield, D. Jackson, and D. Peterson (1979), Chronological narrative of the 1969-71 Mauna Ulu eruption of Kilauea volcano, Hawai'i, *U.S. Geological Survey Professional Paper*, *1056*, 1–55.

Swanson, D., T. R. Rose, R. Fiske, and J. McGeehin (2012a), Keanakako'i tephra produced by 300 years of explosive eruptions following collapse of Kilauea's caldera in about 1500 CE, *Journal of Volcanology and Geothermal Research*, *215-216*, 8–25.

Swanson, D., S. Zolkos, and B. Haravitch (2012b), Ballistic blocks around Kilauea caldera: Their vent locations and number of eruptions in the late 18th century, *Journal of Volcanology and Geothermal Research*, *231-232*, 1–11.

Thordarson, T., S. Self, N. Oskarsson, and T. Hulsebosch (1996), Sulfur, chlorine and fluorine degassing and atmospheric loading by the 1783-1784 AD Laki (Skaftar Fires) eruption in Iceland, *Bulletin of Volcanology*, *58*, 205–225.

Tilling, R., and J. Dvorak (1993), Anatomy of a basaltic volcano, *Nature*, *363*, 125–133.

Tilling, R., T. Wright, and H. Millard Jr. (1987), Trace-element chemistry of Kilauea and Mauna Loa lava in space and time: A reconnaissance, in *Volcanism in Hawai'i*, *U.S. Geological Survey Professional Paper*, vol. 1, edited by R. Decker, T. Wright, and NewEditor3, pp. 641–689.

Vergniolle, S. (2008), From sound waves to bubbling within a magma reservoir: a comparison between eruptions at Etna (2001, italy) and Kilauea (Hawai'i), in *Fluid motions in volcanic conduits: A source of seismic and acoustic signals*, *Geological Society, London, Special Publications*, vol. 307, edited by S. Lane and J. Gilbert, pp. 125–146.

Vergniolle, S., and C. Jaupart (1986), Separated two-phase flow and basaltic eruptions, *Journal of Geophysical Research*, *91*(B12), 12,842–12,860.

Vergniolle, S., and C. Jaupart (1990), Dynamics of degassing at Kilauea volcano, Hawai'i, *Journal of Geophysical Research*, *95*(B3), 2793–2809.

Vergniolle, S., and M. Mangan (2000), *Hawaiian and Strombolian eruptions*, pp. 447–461, Encyclopedia of Volcanoes, Academic Press, San Diego, CA.

Viccaro, M., and R. Cristofolini (2008), Nature of mantle heterogeneity and its role in the short-term geochemical and volcanological evolution of Mt. Etna (Italy), *Lithos*, *105*, 272–288.

Vinet, N., and M. Higgins (2011), What can crystal size distributions and olivine compositions tell us about magma solidification processes inside Kilauea Iki lava lake, Hawai'i?, *Journal of Volcanology and Geothermal Research*, *208*, 136–162, doi:10.1016/j.jvolgeores.2011.09.006.

Walker, G. (1973), Explosive volcanic eruptions - a new classification scheme, *Geologische Rundschau*, *62*, 431–446.

Walker, G., and R. Croasdale (1972), Characteristics of some basaltic pyroclasts, *Bulletin of Volcanology*, *35*, 303–317.

Wallace, P. (1998), Water and partial melting in mantle plumes: Inferences from the dissolved H_2O concentrations of Hawaiian basaltic magmas, *Geophysical Research Letters*, *25*(19), 3639–3642.

Wallace, P., and S. Carmichael (1992), Sulfur in basaltic magmas, *Geochimica et Cosmochimica Acta*, *56*, 1863–1874.

Weaver, S., B. Houghton, and D. Swanson (2010), Kilauea's explosive past: Understandin violent explosions at Hawai'i's most active volcano, *American Geophysical Union Fall Meeting*, *V21C-2348*.

Welsch, B., F. Faure, V. Famin, A. Baronnet, and P. Bachelery (), Dendritic crystallization: A single process for all the textures of olivines in basalts?, *Journal of Petrology*, *54*(3), 539–574.

Wilson, D., T. Elias, T. Orr, M. Patrick, J. Sutton, and D. Swanson (2008), Small explosion from new vent at Kilauea's summit, *Eos*, *89*(22), 203.

Wilson, L. (1980), Relationships between pressure, volatile content and ejecta velocity in three types of volcanic explosion, *Journal of Volcanology and Geothermal Research*, *8*, 297–313.

Wilson, L., and J. Head (1981), Ascent and eruption of basaltic magma on the Earth and Moon, *Journal of Geophysical Research*, *86*(B4), 2971–3001.

Wilson, L., and J. Head (1988), Nature of local magma storage zones and geometry of conduit systems below basaltic eruption sites: Pu‘u ‘O‘o, Kilauea East Rift, Hawaii, example, *Journal of Geophysical Research*, *93*(B12), 14,785–14,792.

Woods, A., and H. Huppert (2003), On magma chamber evolution during slow effusive eruptions, *Journal of Geophysical Research*, *108*(2403), doi:10.1029/2002JB002019.

Workman, R., E. Hauri, S. Hart, J. Wang, and J. Blusztajn (2006), Volatile and trace elements in basaltic glasses from Samoa: Implications for water distribution in the mantle, *Earth and Planetary Science Letters*, *241*, 932–951.

Wright, T. (1971), Chemistry of Kilauea and Mauna Loa lavas in space and time, *U.S. Geological Survey Professional Papers*, *735*, 1–45.

Wright, T. (1973), Magma mixing as illustrated by the 1959 eruption, Kilauea volcano, Hawai‘i, *Geological Society of America Bulletin*, *84*, 849–858.

Wright, T., and R. Fiske (1971), Origin of differentiated and hybrid lavas of Kilauea volcano, Hawaii, *Journal of Petrology*, *12*(1), 1–65.

Wright, T., D. Swanson, and W. Duffield (1975), Chemical composition of Kilauea east-rift lava, 1968-1971, *Journal of Petrology*, *16*, 110–133.

Wyss, M., and R. Koyanagi (2006), Isoseismal maps, macroseismic epicenters and estimated magnitudes of historic earthquakes in the Hawaiian islands, *US. Geological Survey Bulletin*, p. 93.

Data Tables

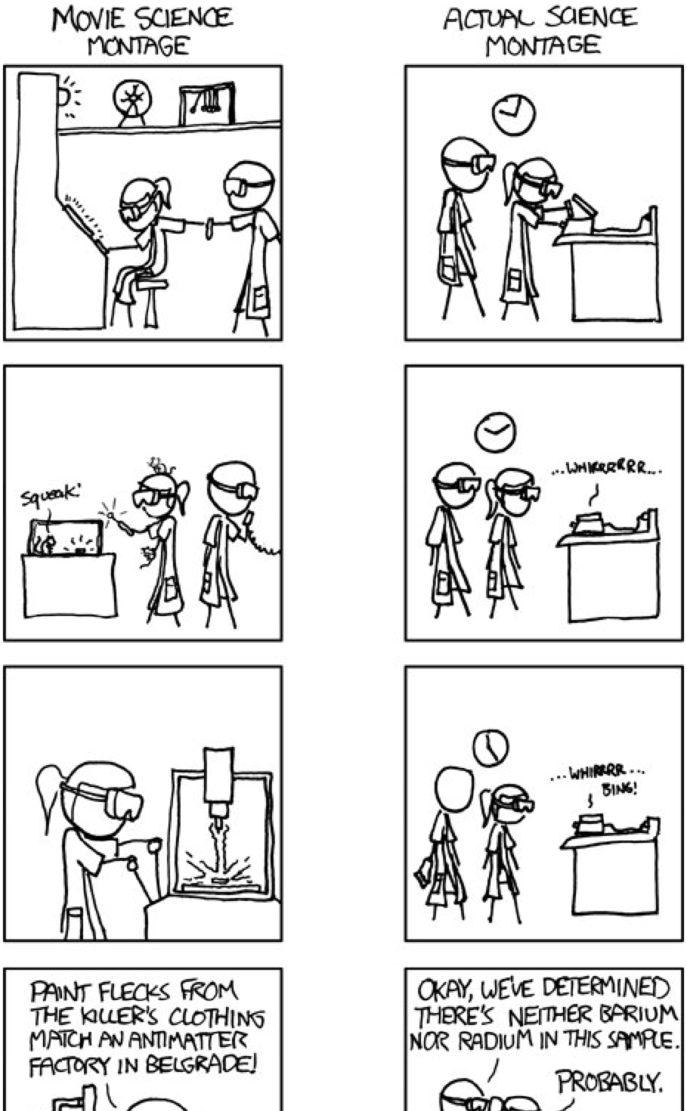

Figure 3: The reality of data acquisition (Science Montage by xkcd.com)

Data tables are presented in the following section. Sample preparation and acquisition of this data set are described fully in Chapter 2; sampling methods and descriptions are detailed in Chapters 4 and 5. Sections are divided into eruptions, olivine, glass and melt inclusion chemistry.

.1 Eruptions and Samples

Table 1 Date, duration and erupted volumes of all historical eruptions at Kīlauea volcano from 1790–2013.

Table 2 Sample details including latitude and longitude for all analysed Kīlauea material in this study.

.2 Olivine Chemistry

Table 3 Major and minor element compositions of olivines hosting Kīlauea and Lō`ihi melt inclusions, as determined by electron microprobe analysis.

.3 Glass Chemistry

Table 4 Major, minor, volatile and trace element compositions of matrix glasses produced during prehistoric and historical eruptions (1400–2010 AD). Major and minor elements, S, Cl and F were determined by electron microprobe; H_2O data presented in this table were acquired using SIMS; CO_2 data is not included as all glass samples were below instrument detection limits. Trace element concentrations were determined by LA-ICP-MS. Volatile and trace elements concentrations are given in ppm, major and minor element oxides are reported in wt%.

Temperatures were calculated using the MgO-glass geothermometry model of *Helz* (1987): $T^{o}C = 20.1MgO + 1014^{o} \pm 10^{o}$.

Glass Mg# were calculated as: Mg# = ((XMg/XFe+2+ + XMg) × 100), with the Fe+2+ set to 90 % of total iron (*Garcia et al.*, 2003)

Table 5 Major, minor, volatile and trace element compositions of matrix glasses produced during the 1959 Kīlauea Iki and 1960 Kapoho eruptions. Table details are as described above. This data was used as part of the historical eruption data analysed in Chapter 4 and was also described more fully in Chapter 5.

Table 6 Major, minor, volatile and trace element compositions of matrix glasses from Lō`ihi seamount. This data is discussed in comparison with Kīlauea historical melt inclusions in Chapter 4.

.4 Melt Inclusion Chemistry

The inclusion concentrations presented have all been corrected for post-entrapment crystallisation of olivine (as described in Chapter 2). Unfortunately owing to the large size of this dataset it is not feasible to include the uncorrected concentrations in this section, but the percentage of olivine addition required to correct each of the inclusions has been included in all of the following tables (Ol %), together with the fosterite composition (Fo mol %) of the host olivine.

Table 7 Major, minor and volatile element compositions of melt inclusions erupted from Kīlauea between 1400–1885 AD. Details of analyses are as described above.

Tables 8, **9**, and **10** Major, minor and volatile element compositions of melt inclusions erupted from Kīlauea between 1920–1969 AD, 1971–1982 AD and 2008–2010 AD respectively.

Table 11 Major, minor and volatile element compositions of melt inclusions erupted during the 1959 Kīlauea Iki, and 1960 Kapoho eruptions. These data were included in the historical dataset discussed in Chapter 4, and were also the basis for Chapter 5's investigation of magmatic processes during a single eruption.

Table 12 Major, minor and volatile element compositions of melt inclusions erupted from Lō`ihi seamount. This dataset are discussed in tandem with the total Kīlauea melt inclusion dataset in Chapter 4.

Table 1: Summary of historical eruptions at Kīlauea volcano

Year	Start Date	Duration (days)	Altitude (m)	Location	Approximate repose period since last eruption (months[a])	Area (km^2)	Volume (km^3)
1790[c]	November(?)	–	–	Caldera	–	No lava flow	No lava flow
1823	Feb–July	Short	510–250	Southwest Rift Zone	–	10.0[d]	11,000,000
1832	Jan. 14	Short	1,100	East rim of caldera	–	(?)	(?)
1840	May 30	26	930–250	East rift	–	17.2[d]	205,000,000
1868	April 2	Short	1,000	Kīlauea Iki	–	0.2	(?)
1868	April 2 (?)	Short	770	Southwest rift	–	0.1	183,000
1877	May 4	1 (?)	1,050	Caldera wall	–	(?)	(?)
1877	May 21 (?)	–	1,040	Keanakakoi	–	0.1	(?)
1884	Jan 22[e]	1	-20	East rift	–	(?)	(?)
1885	March	80	1,090	Caldera	14	(?)	(?)
1894	Mar. 21	6+	1,110	Caldera	108	(?)	(?)
1894	July 7	4(?)	1,110	Caldera	3.5	(?)	(?)
1918	Feb. 23	14	1,110	Caldera	283	0.1	183,000
1919	Feb. 7	294[f]	1,110	Caldera	11	4.2	25,200,000
1919	Dec. 21	221	900	Southwest rift	1	13.0	45,300,000
1921	Mar. 18	7 1,110	Caldera	7.5	2.0	6,400,000	
1922	May 28	2	800–720	Makaopuhi and Napau	14	0.1	(?)
1923	Aug. 25	1	900	East rift	15	0.5	73,000
1924[g]	May 10	17	–	Caldera	8	No lava	No lava
1924	July 19	11	710	Halema`uma`u	2.5	0.1	234,000
1927	July 7	13	720	Halema`uma`u	35	0.1	2,300,000
1929	Feb. 20	2	750	Halema`uma`u	19	0.2	1,400,000

Table 1: Summary of historical eruptions at Kīlauea volcano (cont'd)

Year	Start Date	Duration (days)	Altitude (m)	Location	Approximate repose period since last eruption (months[a])	Area (km^2)	Volume (km^3)
1929	July 25	4	770	Halema`uma`u	5	0.2	2,600,000
1930	Nov.19	19	780	Halema`uma`u	15.5	0.2	6,200,000
1931	Dec. 23	14	810	Halema`uma`u	12.5	0.3	7,000,000
1934	Sept. 6	33	840	Halema`uma`u	44	0.4	6,900,000
1952	June 27	136	860	Halema`uma`u	212.5	0.6	46,700,000
1954	May 31	3	950	Halema`uma`u and caldera	18.5	1.1	6,200,000
1955	Feb. 28	88	390-50	East rift	8.9	15.9	87,600,000
1959	Nov. 14	36	1,050	Kīlauea Iki	53.5	0.6	37,200,000
1960	Jan. 13	36	35	East rift	0.8	10.7	113,200,000
1961	Feb. 24	1	940	Halema`uma`u	12.2	0.1	22,000[h]
1961	Mar. 3	22	940	Halema`uma`u	0.2	0.3	260,000
1961	July 10	7	940	Halema`uma`u	3.5	1.0	12,000.000
1961	Sept. 22	3	780–390	East rift[i]	2.2	0.8	2,200,000
1962	Dec. 7	2	980–930	East rift	14.4	0.1	310,000
1963	Aug. 21	2	940–810	East rift	8.4	0.2	800,000
1963	Oct. 5	1	830–690	East rift	1.4	3.4	6,600,000
1965	Mar. 5	10	900–690	East rift	17.0	7.8	16,800,000
1965	Dec. 24	<1	940–900	East rift	9.5	0.6	850,000
1967	Nov. 5	251	940	Halema`uma`u	23.3	0.7	80,300,000
1968	Aug. 22	5	870–570	East rift	1.3	0.1	130,000
1968	Oct. 7	15 900–720	East rift	1.3	2.1	6,600,000	

Table 1: Summary of historical eruptions at Kīlauea volcano (cont'd)

Year	Start Date	Duration (days)	Altitude (m)	Location	Approximate repose period since last eruption (months[a])	Area (km^2)	Volume (km^3)
1969	Feb. 22	6	930–870	East rift	4.0	6.0	16,100,000
1969	May 24	867	940	East rift	2.0	12.5	176,700,000
1971	Aug. 24	<1	1,100–1,080	Caldera	0	3.1	9,100,000
1971	Sept. 24	5	1,120–820	Caldera and southwest rift	0	3.9	7,700,000
1972	Feb. 4	455	940	East rift	4	35.1	119,600,000
1973	May 5	<1	1,000–980	East rift	0	0.3	1,200,000[j]
1973	Nov. 10	30	980–870	East rift	0	1.0	2,700,000
1973	Dec. 12	203	940	East rift	1	8.1	28,700,000
1974	July 19	3	1,080–980	Caldera and east rift	0	3.1	6,600,000
1974	Sept. 19	<1	1,100	Caldera	2	1.0	10,200,000[k]
1974	Dec. 31	<1	1,080	Southwest rift	3	7.5	14,300,000
1975	Nov. 29[l]	<1	1,080–1,060	Caldera	11	0.3	220,000
1977	Sept. 13	18	620–480	East rift	21.5	7.8	32,900,000
1979	Nov. 16	1	980–960	East rift	26.3	0.3	580,000
1982	Apr. 31	<1	1,080	Caldera	29.5	0.3	500,000
1982	Sept. 25	<1	1,080	Caldera	4.8	>1.0	3,300,000
1983	Jan. 3	$>$9,937[m]	980	East rift	3	119.4	3,300,000,000
2008	Mar. 19	$>$1,826[n]	1,080	Halema`uma`u	0	$<$1,000	$<$1,000

Table 1: Summary of historical eruptions at Kīlauea volcano (cont’d)

Source: Modified after *MacDonald et al.*, 1983. Data for eruptions since 1960 from Hawaiian Volcano Observatory reports.

[a] Written records begin in July-August 1823, when the first European visited the summit of Kilauea. Thereafter until 1924, lava-lake eruptive activity was almost continuous in the caldera. Before the mid-1800s, however, records of the many overflows from the lava lake are sparse. The table lists the periods of major overflows only.

[b] Since 1960 all areas and volimes are based on mapping estimates by the Hawaiian Volcano Observatory

[c] Violent phreatic explosion

[d] Area above sea level. The volume below sea level is unknown, but estimates give the following orders of magnitude: 1823 – 2,200,000 m^3; 1840 – 146,000,000 m^3. These are included in the volumes given in the table.

[e] Pacific Commercial Advertiser, Feb. 2, 1884: “A column of water, like a dome, shot several hundred feet up into the air, accompanied with clouds of smoke and steam.” No further eruption was observed next day.

[f] Several separate flows, with short intervals without extrusion.

[g] Violent phreatic explosions, possibly accompanied by a submarine lava flow on the east rift.

[h] About 230,000 m^3 of lava poured into Halema`uma`u, but most of it drained back into the vents.

[i] 14 outbreaks along a 21 km stretch east of Napau Crater.

[j] Of this, about 220,000 m^3 drained down into fissures in the floors of the craters.

[k] Of this, about 4,400,000 m^3 drained down into cracks in the floor of Halema`uma`u.

[l] Directly following the most severe local earthquake since 1868 (M 7.2).

[m] Activity in the Pu‘u ‘O‘o-Kupaianaha area is continuing and in its 30th year at the time of writing.

[n] In addition to the long-term activity in the east rift zone, this summit eruption within Halema`uma`u has been continuous throughout the past five years and is ongoing at the time of writing.

Table 2: Summary of Kīlauea samples and localities

Eruption Date	Sample	Eruption style	Locality	Latitude	Longitude	Map^{*1} & Lit. Reference^{*1}
$\sim$1400	1400-K	Fissure	Summit	19.434167	-155.272233	A; *Neal and Lockwood* (2003)
$\sim$1445	1445-A	Effusive	Summit	19.415867	-155.238967	A; *Clague et al.* (1999)
$\sim$1500	1500-1	Hawaiian fountain	Summit	19.420550	-155.288250	A; *Swanson et al.* (2012a)
$\sim$1500	1500-BR	Hawaiian fountain	Summit	19.420550	-155.288250	A; *Swanson et al.* (2012a)
$\sim$1550	1550	Phreatomagmatic	Summit	19.401033	-155.293633	A; *Swanson et al.* (2012a)
$\sim$1600	1600-6	Transient explosive	Summit	19.405167	-155.253017	A; *McPhie et al.* (1990)
$\sim$1700	1700	Fissure	SWRZ	19.383150	-155.291067	A/B; *Swanson et al.* (2012a)
$\sim$1790	1790-1	Transient explosive	Summit	19.398450	-155.271567	A; *Swanson et al.* (2012b)
$\sim$1790	1790-w	Transient explosive	Summit	n/a	n/a	A; *Weaver et al.* (2010)
1820-1823	1823	Hawaiian fountain	Summit	19.405583	-155.292600	A; *Sharp et al.* (1987)
Jan. 1832	1832	Fissure	Summit	19.412417	-155.257867	A; *Brigham* (1909)
May 05, 1877	1877	Fissure	Summit	19.407250	-155.259883	A; *Brigham* (1909)
1882-1885	1885-A	Effusive	Summit	19.406600	-155.270750	A; *Brigham* (1909)
1882-1885	1885-B	Effusive	Summit	19.408067	-155.266833	A; *Brigham* (1909)
1919-1920	1920	Effusive	SWRZ	19.353833	-155.398200	A; *Holcomb* (1987)
May 31, 1954	1954	Fissure	Summit	19.408967	-155.277917	A; *MacDonald and Eaton* (1954)
Nov.14, 1959	(1959)-E1	Hawaiian fountain	Summit	19.412250	-155.255600	A; *Richter* (1970)
Nov.26, 1959	(1959)-E2	Hawaiian fountain	Summit	19.408150	-155.257133	A; *Richter* (1970)
Nov.28, 1959	(1959)-E3	Hawaiian fountain	Summit	19.407817	-155.254200	A; *Richter* (1970)
Dec.06, 1959	(1959)-E5	Hawaiian fountain	Summit	19.408150	-155.257133	A; *Richter* (1970)
Dec.07, 1959	(1959)-E6	Hawaiian fountain	Summit	19.408150	-155.257133	A; *Richter* (1970)
Dec.08, 1959	(1959)-E7	Hawaiian fountain	Summit	19.408150	-155.257133	A; *Richter* (1970)
Dec.10, 1959	(1959)-E8	Hawaiian fountain	Summit	19.408150	-155.257133	A; *Richter* (1970)
Dec.14, 1959	(1959)-E10	Hawaiian fountain	Summit	19.408150	-155.257133	A; *Richter* (1970)

Table 2: Summary of Kīlauea samples and localities (cont'd)

Eruption Date	Sample	Eruption style	Locality	Latitude	Longitude	Map*¹ & Lit. Reference*²
Dec.17, 1959	(1959)-E15	Hawaiian fountain	Summit	19.407817	-155.254200	A; *Richter* (1970)
Dec.19, 1959	(1959)-E16	Hawaiian fountain	Summit	19.407817	-155.254200	A; *Richter* (1970)
Jan.17, 1960	(1960)-KO	Hawaiian fountain	ERZ	19.517550	-154.838817	D; *Richter* (1970)
Feb. 1961	1961	Hawaiian fountain	Summit	19.402767	-155.286550	A; *Richter et al.* (1964)
May 24, 1969	1969-mu	Fissure	ERZ	19.363767	-155.214617	C; *Swanson et al.* (1979)
Sep.06, 1969	1969-7	Hawaiian fountain	ERZ	19.348883	-155.208633	C; *Swanson et al.* (1979)
Dec.30, 1969	1969-8	Hawaiian fountain	ERZ	19.348983	-155.208633	C *Swanson et al.* (1979)
Aug.14, 1971	1971	Fissure	Summit	19.402283	-155.277400	A; *Duffield et al.* (1982)
Nov.10, 1973	1973	Fissure	ERZ	19.371883	-155.225167	C; *Holcomb* (1987)
Jul.19, 1974	1974-J1	Fissure	ERZ	19.398917	-155.255617	A; *Lockwood et al.* (1999)
Jul.19, 1974	1974-J2	Fissure	Summit	19.402367	-155.281600	A; *Lockwood et al.* (1999)
Sep.19, 1974	1974-S	Fissure	Summit	19.403350	-155.291700	A; *Lockwood et al.* (1999)
Apr.30, 1982	1982-1	Fissure	Summit	19.409217	-155.276850	A; *Neal and Lockwood* (2003)
Sep. 1982	1982-2	Fissure	Summit	19.393617	-155.283600	A; *Neal and Lockwood* (2003)
Apr.09, 2008	(2008)-S1	Transient explosive	Summit	19.40586	-155.27797	A; *Houghton et al.* (2011)
Aug.27, 2008	(2008)-S2	Transient explosive	Summit	19.40586	-155.27797	A; *Houghton et al.* (2011)
Sep.2, 2008	(2008)-18	Transient explosive	Summit	19.400600	-155.278533	A; *Houghton et al.* (2011)
Apr.26, 2010	(2010)-S3	Transient explosive	Summit	19.40586	-155.27797	A; *Houghton et al.* (2011)

---

*
(1) Reference to Map A, B, C or D in Figure 4.1 of Chapter 3
(2) Example literature reference for eruption

Table 3: Major and minor element core compositions for Kīlauea olivines

Sample	SiO_2	Al_2O_3	FeO	MnO	MgO	CaO	Na_2O	Cr_2O_3	NiO	Total	Fo mol%
1400-K-ol04	39.57	0.04	16.04	0.21	44.58	0.28	0.003	0.02	0.27	101.00	83.21
1400-K-ol32	39.70	0.04	16.58	0.21	44.55	0.28	0.004	0.04	0.25	101.65	82.73
1400-K-ol36	39.71	0.04	15.52	0.19	45.10	0.27	0.007	0.05	0.29	101.16	83.83
1400-K-ol51	39.59	0.03	16.35	0.24	44.34	0.27	0.004	0.06	0.25	101.14	82.86
1445-A-ol17	39.28	0.05	18.26	0.24	42.57	0.29	0.005	0.06	0.24	100.99	80.61
1445-A-ol19	39.17	0.04	18.62	0.23	42.74	0.30	0.008	0.06	0.24	101.40	80.37
1445-A-ol26	39.39	0.03	18.48	0.24	42.64	0.30	0.002	0.04	0.23	101.36	80.45
1445-A-ol29	39.62	0.04	18.41	0.23	42.72	0.29	0.006	0.05	0.24	101.60	80.54
1445-A-ol32	39.22	0.04	18.02	0.23	42.57	0.29	0.002	0.05	0.26	100.68	80.81
1445-A-ol34	39.31	0.03	18.15	0.22	42.68	0.30	0.003	0.04	0.24	100.98	80.74
1445-A-ol41	39.57	0.05	17.41	0.22	43.28	0.30	0.006	0.06	0.25	101.15	81.59
1500-1-ol01	39.74	0.04	16.64	0.24	43.67	0.28	0.007	n.d	0.23	100.84	82.39
1500-1-ol04	39.77	0.04	16.24	0.21	43.31	0.28	0.004	0.05	0.23	100.13	82.62
1500-1-ol08	40.89	0.05	10.65	0.16	48.25	0.24	0.006	n.d	0.48	100.73	88.98
1500-1-ol08b	39.70	0.03	16.07	0.22	43.55	0.27	0.003	0.05	0.24	100.12	82.85
1500-1-ol17	39.41	0.03	16.06	0.22	44.20	0.28	0.005	n.d	0.25	100.45	83.07
1500-1-ol24	39.67	0.04	16.05	0.21	43.96	0.26	0.003	0.03	0.25	100.47	83.00
1500-BR-ol01	40.15	0.05	11.33	0.15	47.68	0.24	0.006	0.11	0.48	100.20	88.24
1500-BR-ol02	40.46	0.05	10.45	0.15	48.52	0.24	0.006	0.11	0.47	100.46	89.23
1500-BR-ol21	38.96	0.03	17.23	0.20	43.38	0.28	0.008	0.04	0.20	100.32	81.79
1500-BR-ol22	40.12	0.06	10.52	0.13	48.50	0.23	0.007	0.09	0.48	100.12	89.16
1550-ol01	40.77	0.06	10.42	0.15	48.02	0.25	0.010	n.d	0.47	100.14	89.15
1550-ol02	40.60	0.06	10.88	0.13	48.13	0.24	0.007	n.d	0.47	100.53	88.74
1550-ol06	40.12	0.06	12.72	0.19	46.67	0.25	0.006	0.07	0.33	100.41	86.74
1550-ol08	39.08	0.03	18.71	0.24	42.02	0.33	0.012	0.05	0.26	100.73	80.02
1550-ol08b	40.03	0.05	12.16	0.17	47.08	0.25	0.006	n.d	0.43	100.17	87.35
1550-ol13	40.43	0.06	10.87	0.15	48.40	0.23	0.007	n.d	0.48	100.63	88.82
1550-ol16	38.77	0.03	19.68	0.27	41.31	0.24	0.003	0.03	0.31	100.64	78.92
1600-6-ol23	38.37	0.04	17.99	0.23	42.31	0.28	0.005	0.04	0.24	99.49	80.74
1600-6-ol31	38.81	0.04	18.06	0.24	42.39	0.28	0.003	0.06	0.25	100.12	80.71
1700-ol02	40.18	0.04	15.11	0.21	44.63	0.29	0.007	n.d	0.28	100.75	84.04
1700-ol07	40.15	0.04	14.95	0.19	45.03	0.27	0.004	n.d	0.36	100.99	84.30
1700-ol13	40.60	0.04	13.58	0.17	45.57	0.24	0.008	n.d	0.31	100.52	85.68
1700-ol14	40.31	0.05	13.99	0.19	45.65	0.24	0.006	n.d	0.38	100.82	85.33
1700-ol22	38.93	0.04	15.24	0.21	45.40	0.26	0.005	0.04	0.36	100.48	84.16
1700-ol25	38.78	0.04	15.73	0.19	45.15	0.26	0.005	0.05	0.31	100.52	83.66
1790-1-ol13	40.19	0.04	12.57	0.16	47.14	0.23	0.006	0.09	0.38	100.82	86.99
1790-1-ol17	39.69	0.05	12.99	0.18	46.85	0.26	0.006	0.06	0.35	100.44	86.54
1790-1-ol20	39.64	0.04	13.48	0.19	46.53	0.27	0.004	0.05	0.34	100.56	86.02
1790-1-ol40	40.45	0.05	12.48	0.19	47.65	0.22	0.006	0.09	0.42	101.55	87.20
1790-w-ol01	39.97	0.06	10.41	0.15	48.35	0.22	0.005	0.13	0.47	99.77	89.23
1790-w-ol04	38.75	0.03	16.70	0.22	43.37	0.27	0.006	0.04	0.21	99.60	82.24
1823-ol05	39.74	0.06	16.66	0.20	43.59	0.22	0.003	0.07	0.34	100.90	82.35
1823-ol07	40.44	0.05	13.16	0.17	46.05	0.24	0.006	0.08	0.37	100.57	86.18
1823-ol12	40.72	0.04	11.55	0.15	47.62	0.23	0.005	0.10	0.46	100.87	88.03
1832-ol13	40.75	0.06	11.27	0.15	48.72	0.26	0.007	0.08	0.47	101.77	88.52
1832-ol14	41.01	0.05	10.99	0.14	48.63	0.26	0.009	0.10	0.47	101.67	88.75
1832-ol16	40.67	0.05	12.57	0.17	47.73	0.25	0.007	0.07	0.40	101.92	87.13
1832-ol26	40.69	0.06	11.40	0.16	48.59	0.26	0.009	0.10	0.45	101.73	88.37
1832-ol28	40.90	0.05	11.47	0.15	48.54	0.23	0.010	0.10	0.43	101.88	88.30
1832-ol31	40.49	0.04	12.42	0.17	47.45	0.24	0.008	0.08	0.40	101.30	87.20
1832-ol34	39.54	0.05	14.26	0.18	46.00	0.28	0.007	0.06	0.45	100.83	85.19
1877-ol03	39.95	0.04	13.87	0.19	46.37	0.29	0.008	0.05	0.36	101.12	85.63
1877-ol23	39.21	0.03	18.49	0.26	42.93	0.29	0.005	0.03	0.21	101.46	80.55
1877-ol40	40.65	0.04	12.52	0.17	47.46	0.27	0.008	0.08	0.38	101.58	87.12
1885-A-ol08	38.72	0.04	20.30	0.26	40.65	0.31	0.005	0.02	0.22	100.54	78.12
1885-A-ol15	38.85	0.03	18.73	0.25	41.98	0.30	0.006	0.03	0.24	100.42	79.99
1885-A-ol16	38.56	0.04	19.74	0.23	41.14	0.29	0.003	0.04	0.25	100.28	78.80
1885-A-ol19	38.53	0.03	19.85	0.25	40.23	0.31	0.004	0.02	0.20	99.41	78.33
1885-A-ol20	39.55	0.04	14.77	0.18	45.38	0.26	0.006	0.05	0.33	100.56	84.57
1885-A-ol21	38.51	0.02	20.45	0.24	40.79	0.30	0.003	0.02	0.24	100.58	78.05
1885-B-ol02	38.45	0.04	20.54	0.25	40.62	0.33	0.003	0.03	0.22	100.49	77.91

Table 3: Major and minor element core compositions for Kīlauea olivines (cont'd)

Sample	SiO_2	Al_2O_3	FeO	MnO	MgO	CaO	Na_2O	Cr_2O_3	NiO	Total	Fo mol%
1885-B-ol05	40.08	0.05	12.36	0.17	46.64	0.26	0.009	0.07	0.40	100.04	87.06
1885-B-ol12	39.17	0.04	16.37	0.21	43.98	0.29	0.005	0.05	0.34	100.45	82.72
1885-B-ol14	38.55	0.03	20.85	0.30	40.52	0.32	0.004	0.05	0.22	100.84	77.60
1885-B-ol16	38.34	0.02	20.12	0.24	40.75	0.32	0.003	0.02	0.22	100.03	78.32
1885-B-ol18	39.23	0.05	16.73	0.22	43.59	0.29	0.005	0.04	0.31	100.46	82.29
1885-A-ol26	38.46	0.03	20.96	0.24	40.45	0.31	0.006	0.04	0.23	100.72	77.48
1920-ol02	40.60	0.05	11.74	0.16	47.27	0.28	0.007	0.08	0.41	100.60	87.77
1920-ol08	40.25	0.04	14.19	0.18	45.89	0.29	0.005	0.07	0.37	101.28	85.22
1920-ol09	39.98	0.04	13.01	0.17	47.08	0.27	0.008	0.08	0.38	101.01	86.58
1954-ol01	39.77	0.03	17.32	0.24	43.68	0.29	0.007	n.d	0.26	101.60	81.80
1954-ol03	39.58	0.04	16.72	0.25	43.51	0.28	0.007	0.04	0.28	100.71	82.27
1954-ol05	39.32	0.04	16.83	0.24	43.47	0.29	0.002	0.03	0.27	100.49	82.16
1954-ol06	39.99	0.04	14.17	0.21	45.54	0.27	0.006	n.d	0.38	100.62	85.14
1954-ol07	39.87	0.03	16.79	0.23	43.51	0.30	0.005	n.d	0.23	100.96	82.21
1954-ol19	39.60	0.04	16.85	0.23	43.60	0.28	0.003	0.03	0.27	100.91	82.19
1959-E1-ol07	40.37	0.05	12.40	0.17	47.83	0.29	0.006	0.08	0.37	101.57	87.30
1959-E1-ol09	40.67	0.04	12.22	0.17	47.93	0.28	0.008	0.07	0.39	101.77	87.49
1959-E1-ol12	40.20	0.05	12.36	0.17	48.26	0.29	0.005	0.10	0.36	101.80	87.44
1959-E1-ol21	40.26	0.04	13.34	0.21	46.29	0.30	0.007	0.07	0.28	100.81	86.08
1959-E1-ol22	40.40	0.06	11.31	0.14	48.85	0.24	0.005	0.09	0.40	101.51	88.51
1959-E1-ol26	40.32	0.06	11.81	0.17	47.98	0.29	0.005	0.10	0.46	101.20	87.87
1959-E1-ol27	40.44	0.05	11.93	0.15	47.80	0.27	0.008	0.09	0.42	101.16	87.72
1959-E2-ol05	39.59	0.04	14.75	0.19	45.50	0.32	0.005	0.06	0.30	100.77	84.62
1959-E2-ol15	40.23	0.06	12.35	0.14	47.41	0.27	0.006	0.10	0.41	100.96	87.25
1959-E2-ol16	40.00	0.06	12.22	0.17	47.23	0.24	0.006	0.07	0.46	100.45	87.33
1959-E2-ol17	40.65	0.04	12.57	0.16	47.22	0.34	0.006	0.05	0.33	101.38	87.01
1959-E2-ol21	40.29	0.04	12.46	0.17	47.64	0.29	0.009	0.07	0.36	101.32	87.21
1959-E2-ol22	39.70	0.04	14.21	0.18	45.97	0.30	0.008	0.06	0.32	100.79	85.22
1959-E2-ol23	39.94	0.05	11.52	0.15	47.89	0.27	0.008	0.10	0.41	100.34	88.11
1959-E3-ol03	39.94	0.03	12.59	0.16	46.80	0.28	0.011	0.08	0.38	100.27	86.89
1959-E3-ol05	40.22	0.05	12.31	0.17	46.92	0.29	0.010	0.10	0.41	100.48	87.18
1959-E3-ol06	40.64	0.04	11.78	0.15	47.89	0.28	0.011	0.07	0.39	101.24	87.87
1959-E3-ol13	40.36	0.05	11.54	0.15	47.92	0.28	0.007	0.09	0.40	100.80	88.10
1959-E3-ol14	40.28	0.03	12.71	0.17	47.16	0.33	0.005	0.06	0.33	101.07	86.87
1959-E3-ol15	39.36	0.03	17.86	0.25	43.70	0.30	0.002	0.03	0.22	101.76	81.35
1959-E3-ol19	39.98	0.04	12.79	0.16	47.07	0.28	0.011	0.06	0.28	100.68	86.78
1959-E3-ol25	40.20	0.03	12.57	0.17	47.51	0.28	0.009	0.09	0.36	101.22	87.08
1959-E5-ol09	40.22	0.05	11.58	0.14	47.88	0.26	0.006	0.10	0.44	100.67	88.06
1959-E5-ol10	39.98	0.04	12.77	0.17	47.02	0.29	0.008	0.08	0.36	100.72	86.78
1959-E5-ol14	40.15	0.04	12.31	0.16	47.31	0.30	0.009	0.07	0.40	100.75	87.26
1959-E5-ol18	40.06	0.05	12.41	0.16	48.00	0.28	0.003	0.08	0.41	101.46	87.34
1959-E6-ol08	39.96	0.05	12.33	0.16	47.26	0.28	0.006	0.07	0.36	100.49	87.24
1959-E6-ol09	40.12	0.06	11.89	0.14	47.57	0.24	0.006	0.11	0.46	100.60	87.70
1959-E6-ol10	40.12	0.05	12.73	0.17	47.35	0.28	0.007	0.08	0.40	101.20	86.90
1959-E6-ol12	39.95	0.05	12.37	0.15	47.09	0.28	0.007	0.08	0.37	100.33	87.16
1959-E6-ol13	39.92	0.04	13.23	0.19	46.35	0.28	0.008	0.06	0.36	100.44	86.20
1959-E6-ol14	40.50	0.05	12.03	0.15	47.71	0.27	0.004	0.09	0.45	101.26	87.61
1959-E7-ol03	40.09	0.05	11.68	0.17	47.72	0.27	0.011	0.07	0.45	100.51	87.93
1959-E7-ol04	39.61	0.04	14.11	0.18	45.72	0.31	0.008	0.05	0.38	100.42	85.25
1959-E7-ol08	39.58	0.04	12.94	0.17	46.58	0.28	0.007	0.07	0.39	100.05	86.52
1959-E7-ol09	39.65	0.05	12.65	0.17	46.82	0.29	0.004	0.07	0.39	100.09	86.84
1959-E7-ol18	39.50	0.04	15.06	0.21	44.67	0.34	0.003	0.05	0.32	100.18	84.10
1959-E7-ol19	39.62	0.05	13.18	0.19	46.23	0.31	0.005	0.06	0.35	100.01	86.21
1959-E8-ol03	39.64	0.04	14.51	0.21	45.47	0.29	0.009	0.07	0.37	100.61	84.82
1959-E8-ol05	39.67	0.05	13.28	0.17	46.64	0.28	0.009	0.06	0.39	100.56	86.23
1959-E8-ol07	39.94	0.05	12.06	0.15	47.34	0.30	0.008	0.07	0.41	100.35	87.50
1959-E8-ol09	40.03	0.04	12.43	0.16	46.63	0.27	0.007	0.07	0.45	100.09	87.00
1959-E8-ol11	40.09	0.04	13.78	0.19	45.78	0.29	0.005	0.05	0.33	100.56	85.56
1959-E8-ol12	40.06	0.04	12.46	0.17	47.44	0.26	0.006	0.06	0.39	100.89	87.16
1959-E8-ol14	39.87	0.05	12.56	0.17	47.08	0.28	0.009	0.09	0.36	100.48	86.98
1959-E8-ol15	40.38	0.06	11.01	0.15	48.23	0.29	0.007	0.10	0.45	100.67	88.65
1959-E8-ol24	40.23	0.05	11.52	0.18	47.11	0.31	0.012	0.09	0.43	99.93	87.94

Table 3: Major and minor element core compositions for Kīlauea olivines (cont'd)

Sample	SiO_2	Al_2O_3	FeO	MnO	MgO	CaO	Na_2O	Cr_2O_3	NiO	Total	Fo mol%
1959-E10-ol05	39.78	0.03	13.88	0.16	45.97	0.29	0.005	0.05	0.35	100.52	85.52
1959-E10-ol06	40.40	0.05	12.01	0.17	47.59	0.28	0.007	0.08	0.39	100.97	87.60
1959-E10-ol09	40.04	0.05	12.97	0.20	46.57	0.28	0.003	0.08	0.37	100.56	86.49
1959-E10-ol12	40.42	0.06	11.67	0.14	48.26	0.26	0.011	0.10	0.43	101.34	88.05
1959-E15-ol01	40.10	0.04	12.94	0.18	47.81	0.28	0.004	0.06	0.39	101.80	86.82
1959-E15-ol10	40.69	0.05	11.78	0.16	48.21	0.29	0.007	0.09	0.43	101.70	87.94
1959-E15-ol16	40.14	0.03	13.64	0.20	47.01	0.31	0.007	0.06	0.33	101.72	86.01
1959-E15-ol19	40.30	0.05	12.86	0.16	47.48	0.28	0.004	0.06	0.39	101.59	86.81
1959-E15-ol30	39.67	0.03	15.16	0.22	45.22	0.29	0.004	0.05	0.31	100.95	84.17
1959-E16-ol02	40.03	0.04	13.86	0.21	46.63	0.29	0.015	0.04	0.36	101.47	85.71
1959-E16-ol04	39.96	0.04	12.55	0.15	47.02	0.32	0.006	0.07	0.37	100.49	86.98
1959-E16-ol06	40.00	0.04	12.78	0.17	47.17	0.28	0.006	0.07	0.41	100.91	86.81
1959-E16-ol08	40.02	0.05	14.02	0.18	46.11	0.27	0.005	0.07	0.39	101.12	85.43
1959-E16-ol07	40.60	0.04	13.38	0.17	46.95	0.29	0.005	0.05	0.36	101.85	86.22
1959-E16-ol10	40.15	0.04	14.08	0.22	45.82	0.29	0.008	0.08	0.36	101.05	85.30
1959-E16-ol11	40.42	0.05	13.07	0.19	47.01	0.27	0.006	0.08	0.38	101.48	86.51
1959-E16-ol14	40.43	0.04	14.58	0.21	45.88	0.31	0.007	0.05	0.34	101.84	84.87
1959-E16-ol17	40.57	0.04	12.81	0.19	46.88	0.34	0.007	0.06	0.33	101.22	86.71
1959-E16-ol18	40.40	0.05	12.78	0.17	46.97	0.29	0.004	0.07	0.38	101.10	86.76
1959-E16-ol26	39.75	0.04	14.33	0.18	46.06	0.26	0.000	0.06	0.38	101.05	85.14
1959-11-ol01	40.86	0.06	12.04	0.18	47.43	0.29	0.010	n.d	0.38	101.24	87.54
1959-11-ol02	40.38	0.04	15.33	0.21	44.16	0.32	0.007	n.d	0.30	100.73	83.70
1959-11-ol04	39.44	0.04	13.88	0.20	45.77	0.28	0.004	0.06	0.34	100.02	85.46
1959-11-ol07	40.69	0.05	12.39	0.18	46.66	0.26	0.004	n.d	0.40	100.63	87.04
1959-12-ol01	39.86	0.06	11.31	0.13	47.50	0.25	0.010	0.09	0.42	99.62	88.22
1959-12-ol05	40.68	0.04	12.46	0.18	46.28	0.27	0.008	n.d	0.37	100.29	86.89
1959-12-ol06	38.72	0.04	15.16	0.21	44.75	0.28	0.006	0.05	0.31	99.52	84.03
1959-12-ol08	39.76	0.04	13.90	0.19	46.22	0.27	0.010	0.06	0.36	100.82	85.57
1959-12-ol08b	40.66	0.04	12.58	0.17	46.58	0.28	0.008	n.d	0.38	100.69	86.85
1959-12-ol10	40.35	0.04	15.31	0.20	45.06	0.30	0.005	n.d	0.30	101.56	83.99
1960-KO-ol03	39.95	0.04	13.05	0.14	47.53	0.29	0.006	0.07	0.39	101.46	86.66
1960-KO-ol04	40.31	0.04	14.21	0.21	45.68	0.34	0.005	0.06	0.34	101.20	85.15
1960-KO-ol09	40.34	0.05	13.19	0.19	46.62	0.31	0.005	0.04	0.36	101.10	86.31
1960-KO-ol11	39.23	0.03	19.82	0.26	41.65	0.29	0.004	0.04	0.25	101.58	78.94
1960-KO-ol14	40.06	0.04	15.25	0.22	45.17	0.30	0.003	0.05	0.32	101.39	84.08
1960-KO-ol15	40.28	0.05	11.74	0.17	48.50	0.30	0.010	0.09	0.41	101.56	88.05
1960-KO-ol18	40.26	0.04	13.35	0.17	46.70	0.30	0.006	0.06	0.37	101.26	86.18
1960-KO-ol20	40.42	0.05	12.84	0.16	47.21	0.27	0.003	0.07	0.42	101.45	86.77
1960-KO-ol21	40.44	0.04	13.77	0.21	46.19	0.34	0.008	0.06	0.35	101.41	85.68
1960-KO-ol26	40.81	0.05	11.42	0.14	48.39	0.25	0.008	0.10	0.43	101.60	88.31
1961-ol05	39.36	0.03	16.45	0.22	43.73	0.29	0.007	0.04	0.22	100.34	82.58
1961-ol08	39.64	0.03	16.48	0.20	44.00	0.28	0.005	0.03	0.28	100.94	82.64
1961-ol12	39.50	0.03	16.55	0.21	43.44	0.23	0.007	0.02	0.28	100.28	82.40
1961-ol22	39.55	0.04	16.78	0.20	44.07	0.29	0.008	0.04	0.26	101.24	82.40
1969-mu-ol01	40.13	0.05	11.78	0.17	47.45	0.29	0.008	0.11	0.42	100.42	87.78
1969-mu-ol06	39.95	0.05	13.09	0.20	46.70	0.28	0.009	0.07	0.39	100.73	86.41
1969-mu-ol14	40.07	0.04	13.11	0.19	46.82	0.31	0.009	0.05	0.37	100.96	86.43
1969-7-ol03	39.92	0.04	11.90	0.16	47.66	0.25	0.006	0.09	0.41	100.43	87.71
1969-7-ol04	39.88	0.04	11.84	0.16	47.82	0.26	0.006	0.09	0.41	100.50	87.81
1969-7-ol07	40.13	0.05	11.68	0.14	48.19	0.27	0.003	n.d	0.41	100.88	88.03
1969-7-ol08	40.00	0.04	12.02	0.18	47.33	0.25	0.007	0.08	0.40	100.30	87.53
1969-7-ol11	40.30	0.04	12.69	0.18	47.58	0.27	0.009	n.d	0.42	101.49	86.99
1969-7-ol12	40.62	0.06	11.73	0.14	47.90	0.25	0.006	n.d	0.41	101.12	87.92
1969-7-ol14	39.84	0.04	11.78	0.15	47.98	0.26	0.006	0.09	0.41	100.56	87.90
1969-8-ol09	39.81	0.03	11.58	0.13	48.14	0.24	0.007	0.09	0.41	100.44	88.11
1969-8-ol12	39.20	0.05	13.05	0.19	47.65	0.28	0.008	0.08	0.35	100.86	86.69
1969-8-ol11	40.71	0.05	11.72	0.16	47.15	0.28	0.007	n.d	0.40	100.50	87.76
1969-8-ol14	40.89	0.05	12.35	0.15	47.18	0.25	0.006	n.d	0.40	101.29	87.20
1969-8-ol16	39.67	0.05	11.56	0.17	47.78	0.25	0.002	0.07	0.42	99.97	88.05
1971-ol05	39.77	0.03	16.84	0.23	43.47	0.29	0.005	n.d	0.22	100.85	82.16
1971-ol06	39.61	0.03	16.70	0.22	43.88	0.30	0.009	n.d	0.23	101.00	82.41
1971-ol10	39.99	0.03	16.78	0.22	43.34	0.29	0.003	n.d	0.22	100.88	82.16
1971-ol14	39.22	0.03	16.97	0.24	43.59	0.31	0.009	n.d	0.21	100.58	82.07

Table 3: Major and minor element core compositions for Kīlauea olivines (cont'd)

Sample	SiO_2	Al_2O_3	FeO	MnO	MgO	CaO	Na_2O	Cr_2O_3	NiO	Total	Fo mol%
1971-ol17	39.81	0.04	17.11	0.24	43.23	0.29	0.004	n.d	0.21	100.93	81.83
1971-ol22	39.70	0.03	17.05	0.23	43.72	0.29	0.003	0.03	0.22	101.27	82.05
1971-ol26	39.86	0.03	16.78	0.22	43.46	0.29	0.004	n.d	0.23	100.87	82.20
1973-ol01	39.77	0.05	12.77	0.19	46.86	0.25	0.001	0.09	0.39	100.36	86.74
1973-ol02	39.90	0.04	11.37	0.16	48.27	0.25	0.011	0.08	0.43	100.51	88.33
1973-ol03	39.79	0.04	11.59	0.15	48.18	0.25	0.002	0.10	0.42	100.53	88.11
1973-ol07	40.12	0.04	11.35	0.15	48.29	0.25	0.007	0.10	0.44	100.75	88.35
1973-ol09	40.10	0.06	12.36	0.18	48.14	0.25	0.003	n.d	0.40	101.50	87.41
1973-ol11	39.77	0.04	13.34	0.17	47.11	0.24	0.008	0.06	0.37	101.11	86.30
1973-ol11b	40.34	0.04	12.23	0.16	47.64	0.27	0.004	n.d	0.39	101.07	87.42
1973-ol13	39.85	0.05	12.38	0.15	47.80	0.24	0.007	0.09	0.44	101.00	87.32
1973-ol17	38.93	0.04	14.72	0.18	45.29	0.26	0.006	0.05	0.34	99.80	84.58
1974-J1-ol10	38.51	0.04	18.04	0.23	42.84	0.27	0.013	0.03	0.23	100.21	80.90
1974-J1-ol17	38.45	0.03	18.00	0.24	42.06	0.27	0.003	0.03	0.21	99.29	80.65
1974-J1-ol19	38.84	0.03	18.31	0.24	42.05	0.27	0.009	0.03	0.21	99.99	80.37
1974-J1-ol35	38.48	0.03	17.86	0.22	42.38	0.27	0.005	0.04	0.22	99.52	80.88
1974-J2-ol02	40.42	0.04	14.00	0.19	46.04	0.27	0.008	n.d	0.34	101.29	85.43
1974-J2-ol08	39.24	0.04	14.03	0.20	45.94	0.28	0.009	0.06	0.30	100.10	85.38
1974-J2-ol08b	39.96	0.04	13.99	0.19	45.79	0.27	0.005	n.d	0.31	100.55	85.38
1974-J2-ol19	40.12	0.03	14.06	0.20	45.64	0.28	0.005	n.d	0.30	100.64	85.27
1974-S-ol08	38.88	0.03	16.85	0.24	44.20	0.28	0.005	0.05	0.25	100.78	82.39
1974-S-ol13	38.60	0.03	16.77	0.24	43.85	0.28	0.007	0.05	0.24	100.07	82.34
1982-1-ol01	39.40	0.03	16.92	0.23	43.60	0.27	0.004	n.d	0.25	100.71	82.13
1982-1-ol04	38.97	0.03	16.90	0.23	43.44	0.28	0.008	0.03	0.24	100.11	82.09
1982-1-ol04b	39.40	0.03	16.99	0.22	43.53	0.29	0.005	n.d	0.23	100.70	82.04
1982-1-ol12	39.55	0.03	17.02	0.23	43.53	0.29	0.003	n.d	0.24	100.89	82.01
1982-1-ol13	38.86	0.03	17.09	0.23	43.81	0.28	0.004	0.03	0.26	100.60	82.05
1982-2-ol10	40.28	0.04	14.55	0.20	44.96	0.27	0.007	n.d	0.33	100.62	84.64
1982-2-ol11	40.17	0.04	15.29	0.22	45.02	0.28	0.004	n.d	0.31	101.32	84.00
1982-2-ol12	39.94	0.03	16.72	0.21	43.85	0.26	0.005	n.d	0.24	101.27	82.38
1982-2-ol22	39.75	0.03	16.52	0.21	44.19	0.28	0.005	n.d	0.26	101.25	82.67
2008-S1-ol06	39.81	0.03	16.43	0.22	44.53	0.27	0.006	0.05	0.22	101.56	82.86
2008-S1-ol13	39.70	0.04	16.82	0.20	44.37	0.26	0.004	0.03	0.23	101.66	82.47
2008-S1-ol17	40.19	0.04	16.73	0.21	44.29	0.26	0.003	0.04	0.20	101.97	82.52
2008-S1-ol21	39.71	0.03	16.98	0.22	43.54	0.26	0.006	0.03	0.21	100.98	82.05
2008-S1-ol24	40.04	0.04	16.64	0.24	44.30	0.27	0.008	0.05	0.24	101.81	82.60
2008-S1-ol26	39.93	0.04	16.48	0.23	44.32	0.28	0.015	0.05	0.19	101.54	82.75
2008-S1-ol41	39.58	0.04	16.79	0.23	44.21	0.27	0.006	0.05	0.21	101.38	82.44
2008-S1-ol46	39.82	0.03	16.92	0.24	44.08	0.27	0.011	0.03	0.21	101.63	82.28
2008-S1-ol47	39.97	0.03	16.30	0.23	44.25	0.26	0.009	0.04	0.22	101.32	82.88
2008-S1-ol53	39.67	0.03	16.40	0.20	43.85	0.26	0.004	0.04	0.20	100.66	82.66
2008-S1-ol55	40.06	0.03	16.73	0.21	44.23	0.26	0.004	0.03	0.19	101.74	82.50
2008-18-ol01	39.29	0.04	17.05	0.22	44.01	0.28	0.006	n.d	0.21	101.11	82.15
2008-18-ol02	38.71	0.03	17.14	0.24	43.98	0.28	0.004	0.02	0.19	100.59	82.06
2008-18-ol02b	40.18	0.04	10.67	0.16	48.64	0.23	0.008	n.d	0.45	100.39	89.04
2008-18-ol07	39.50	0.03	17.27	0.22	43.66	0.28	0.003	n.d	0.19	101.16	81.84
2008-18-ol10	39.38	0.05	16.62	0.24	43.41	0.30	0.006	n.d	0.21	100.21	82.32
2008-18-ol12	39.00	0.03	16.50	0.21	42.98	0.26	0.002	0.04	0.23	99.25	82.28
2008-18-ol13	39.46	0.04	16.51	0.22	43.46	0.29	0.004	n.d	0.22	100.20	82.44
2008-18-ol19	40.34	0.04	12.69	0.17	46.91	0.25	0.007	n.d	0.39	100.81	86.83
2008-18-ol20	38.93	0.03	16.55	0.22	43.09	0.26	0.004	0.04	0.21	99.34	82.28
2008-18-ol22	39.45	0.03	16.73	0.23	43.75	0.28	0.008	n.d	0.20	100.67	82.34
2008-18-ol23	39.69	0.04	16.50	0.22	43.49	0.27	0.004	n.d	0.23	100.44	82.46
2008-18-ol25	39.63	0.04	16.70	0.23	43.59	0.27	0.004	n.d	0.22	100.67	82.32
2008-18-ol29	39.52	0.03	16.91	0.25	43.36	0.27	0.002	0.05	0.22	100.62	82.05
2008-18-ol40	40.20	0.04	17.25	0.22	43.15	0.25	0.005	0.07	0.23	101.41	81.69
2008-S2-ol18	39.69	0.04	16.84	0.21	43.76	0.27	0.003	0.05	0.22	101.07	82.25
2008-S2-ol11	39.74	0.05	17.05	0.21	43.82	0.27	0.009	0.05	0.22	101.41	82.09
2008-S2-ol30	39.63	0.04	17.22	0.23	44.11	0.28	0.005	0.05	0.21	101.79	82.04
2008-S2-ol38	39.67	0.05	16.48	0.21	44.25	0.26	0.008	0.04	0.21	101.19	82.72
2008-S2-ol41	39.69	0.04	17.18	0.24	43.72	0.27	0.007	0.07	0.22	101.44	81.94
2008-S2-ol44i	39.67	0.03	16.75	0.22	43.87	0.28	0.005	0.04	0.19	101.05	82.36

Table 3: Major and minor element core compositions for Kīlauea olivines (cont'd)

Sample	SiO_2	Al_2O_3	FeO	MnO	MgO	CaO	Na_2O	Cr_2O_3	NiO	Total	Fo mol%
2010-S3-ol06	39.47	0.04	16.99	0.23	43.07	0.27	0.007	0.04	0.19	100.32	81.88
2010-S3-ol08	39.22	0.04	17.04	0.23	43.30	0.27	0.005	0.05	0.21	100.37	81.92
2010-S3-ol14	39.57	0.04	17.30	0.24	43.41	0.28	0.002	0.06	0.20	101.09	81.73
2010-S3-ol23	39.48	0.05	17.32	0.23	43.28	0.28	0.002	0.04	0.19	100.89	81.67
2010-S3-ol24	39.64	0.06	17.45	0.21	43.08	0.27	0.002	0.06	0.21	100.98	81.49
2010-S3-ol33	39.55	0.04	17.07	0.21	43.39	0.27	0.003	0.06	0.20	100.81	81.92
2010-S3-ol56	39.52	0.03	17.14	0.23	43.51	0.28	0.007	0.05	0.21	100.95	81.91
2010-S3-ol57	39.65	0.04	17.66	0.22	43.08	0.27	0.005	0.05	0.18	101.15	81.31
2010-S3-ol62	39.40	0.05	17.73	0.22	43.50	0.28	0.002	0.06	0.23	101.45	81.39
L-ol02	40.96	0.06	11.13	0.14	48.64	0.23	0.011	0.12	0.40	101.70	88.63
L-ol12	40.65	0.09	10.96	0.16	48.29	0.26	0.005	0.10	0.33	100.83	88.71
L-ol13	40.41	0.05	10.47	0.16	48.03	0.25	0.006	0.09	0.42	99.89	89.11
L-ol24	40.49	0.05	11.85	0.13	47.79	0.25	0.006	0.10	0.38	101.04	87.80
L-ol28	40.40	0.05	10.57	0.15	48.00	0.25	0.006	0.09	0.41	99.93	89.01
L-ol37	40.32	0.05	10.93	0.15	48.90	0.24	0.003	0.10	0.39	101.08	88.86
L-ol39	40.37	0.05	11.34	0.14	47.69	0.29	0.007	0.09	0.42	100.39	88.24
L-ol41	40.39	0.06	11.22	0.15	48.12	0.24	0.005	0.10	0.36	100.64	88.43
L-ol42	40.36	0.06	11.01	0.16	48.14	0.24	0.004	0.09	0.38	100.45	88.63

Table 4: Prehistoric and historical Kīlauea matrix glass compositions

Sample	1400-g01	1400-g02	1445-A-g03	1445-A-g19	1500-1-g02	1500-1-g03	1500-1-g05	1500-1-g22	1500-1-g24	1500-1-g01	1500-1-g02b	1500-BR-g01
SiO_2	51.61	51.61	52.35	52.34	50.79	51.31	51.19	50.99	50.36	50.67	51.15	50.23
TiO_2	2.71	2.71	2.62	2.70	2.47	2.44	2.43	2.44	2.53	2.48	2.55	2.51
Al_2O_3	13.59	13.59	13.54	13.87	13.41	13.55	13.48	13.31	13.24	13.28	13.29	13.55
Cr_2O_3	0.02	0.02	0.03	0.04	0.05	0.06	0.05	0.03	0.03	0.03	0.04	0.05
FeO	11.42	11.42	10.86	11.47	11.18	11.15	11.20	11.05	11.44	11.24	11.02	10.76
MnO	0.17	0.17	0.17	0.16	0.17	0.17	0.16	0.19	0.18	0.18	0.17	0.17
MgO	6.58	6.58	6.88	6.72	7.70	7.62	7.45	7.58	7.53	7.55	7.64	7.61
CaO	10.87	10.87	11.07	11.19	10.90	10.90	11.25	11.14	11.19	11.16	11.11	10.96
Na_2O	2.50	2.50	2.43	2.41	2.36	2.34	2.34	2.34	2.38	2.36	2.36	2.41
NiO	0.02	0.02	0.02	0.03	0.02	0.01	0.02	0.01	0.02	0.02	0.01	0.01
K_2O	0.47	0.47	0.42	0.43	0.40	0.42	0.42	0.42	0.43	0.43	0.43	0.44
P_2O_5	0.27	0.27	0.25	0.25	0.22	0.22	0.18	0.19	0.19	0.19	0.24	0.25
F ppm	471	471	497	380	402	389	409	382	335	359	320	333
Cl ppm	95	95	85	109	60	96	76	87	101	94	68	108
S ppm	126	126	157	185	133	63	181	150	1298	724	78	78
Total	100.32	100.32	100.73	101.70	99.75	100.25	100.25	99.77	99.83	99.80	100.06	99.00
H_2O wt%	0.11	0.11	0.09	0.09	0.08	0.08	n.d	0.07	n.d	0.06	0.06	n.d
Sc	25.23	26.13	31.44	31.36	31.89	29.59	30.16	25.58	28.05	31.39	30.51	29.70
V	318.09	312.79	284.46	294.26	355.52	317.12	304.03	284.78	292.89	302.67	297.43	297.96
Rb	9.22	8.57	6.29	6.79	9.87	8.69	8.03	6.90	6.69	7.84	7.38	7.02
Sr	367.44	351.51	303.88	303.66	480.18	393.85	357.31	313.78	300.58	343.54	326.86	312.21
Y	22.55	22.21	23.60	24.87	33.32	28.28	27.07	19.85	20.07	24.47	23.57	21.81
Zr	141.02	132.58	130.67	143.36	216.53	177.89	202.91	117.65	138.98	162.58	117.10	134.61
Nb	13.44	12.66	10.01	10.32	20.60	17.02	15.25	11.27	10.70	12.29	10.32	10.41
Ba	118.36	117.39	83.28	82.84	189.80	136.99	113.76	93.72	89.59	106.93	91.14	91.17
La	14.40	13.68	10.30	10.53	21.69	15.35	12.54	12.26	11.33	13.11	11.74	11.45
Ce	36.50	35.02	25.80	25.63	56.39	39.25	32.81	29.07	29.18	31.72	28.05	27.58
Pr	5.53	4.80	3.63	3.57	8.88	5.90	4.90	4.35	4.04	5.07	4.08	3.90
Nd	24.82	23.49	18.36	17.50	41.94	28.17	23.93	20.24	20.27	21.79	20.66	19.46
Sm	6.61	6.23	4.75	5.24	11.41	7.33	6.26	5.64	4.85	6.24	5.80	5.14
Eu	2.79	2.44	1.91	1.82	3.96	2.76	2.21	1.96	2.01	2.10	2.05	1.88
Gd	6.10	6.02	5.27	4.98	11.34	7.60	5.96	5.43	4.85	6.84	4.93	5.26
Tb	1.05	0.95	0.87	0.85	1.75	1.16	1.00	0.86	0.80	1.08	0.90	0.90
Dy	5.88	5.42	4.92	4.95	9.95	6.85	6.73	5.17	4.47	5.86	5.08	4.71
Ho	1.19	1.00	0.99	1.00	2.07	1.35	1.08	0.95	0.87	1.21	0.98	0.92
Er	3.03	2.41	2.23	2.30	5.07	3.52	2.74	2.44	2.25	2.84	2.59	2.31
Tm	0.41	0.35	0.33	0.36	0.71	0.44	0.36	0.30	0.28	0.33	0.34	0.31
Yb	2.64	2.31	2.03	2.24	4.36	2.77	2.33	2.13	2.22	2.18	2.02	2.06
Lu	0.35	0.31	0.30	0.26	0.60	0.41	0.29	0.27	0.24	0.30	0.29	0.28
Hf	4.20	3.88	3.53	3.68	8.43	5.29	5.07	3.28	3.58	3.64	3.82	3.55
Ta	0.79	0.77	0.58	0.60	1.98	1.18	1.01	0.81	0.61	0.70	0.66	0.62
Pb	1.28	0.96	0.81	0.61	2.26	1.32	0.84	1.18	0.90	0.88	1.03	0.75
U	0.39	0.38	0.25	0.26	0.67	0.44	0.36	0.37	0.29	0.33	0.34	0.27
Temp(°C)	1146	1146	1152	1149	1169	1167	1164	1166	1165	1166	1168	1167
Mg#	53	53	56	54	58	58	57	58	57	57	58	58

Table 4: Prehistoric and historical Kīlauea matrix glass compositions (cont'd)

Sample	1500-BR-g22	1550-g02	1550-g01	1600-6-g01	1600-6-g02	1600-6-g14	1600-6-g44	1700-g01	1700-g02	1700-g22	1700-g01b	1700-g02b
SiO_2	50.18	50.44	50.04	50.68	50.66	50.90	51.58	49.70	50.00	49.98	50.98	50.46
TiO_2	2.50	2.49	2.47	3.19	2.59	2.43	2.58	2.43	2.43	2.47	2.43	2.42
Al_2O_3	13.46	13.06	13.15	12.85	13.36	12.92	13.59	12.44	12.40	12.46	12.71	12.57
Cr_2O_3	0.04	0.06	0.04	0.02	0.05	0.06	0.04	0.09	0.08	0.09	0.07	0.07
FeO	11.17	11.16	11.31	12.28	10.98	11.07	11.42	11.47	11.61	11.81	11.89	12.00
MnO	0.17	0.18	0.18	0.17	0.17	0.17	0.18	0.17	0.18	0.17	0.20	0.17
MgO	7.35	8.14	8.25	5.65	6.98	8.55	6.77	9.09	9.12	9.01	8.81	8.89
CaO	11.32	10.45	10.87	10.23	11.18	10.72	11.35	10.48	10.62	10.47	10.60	10.51
Na_2O	2.34	2.38	2.31	2.63	2.36	2.31	2.25	2.22	2.21	2.21	2.22	2.18
NiO	0.02	0.02	0.04	0.01	0.01	0.02	0.00	0.02	0.02	0.01	b.d	b.d
K_2O	0.41	0.45	0.41	0.59	0.46	0.44	0.41	0.35	0.36	0.37	0.40	0.40
P_2O_5	0.24	0.21	0.24	0.33	0.25	0.23	0.20	0.23	0.23	0.23	0.22	0.24
F ppm	438	514	402	614	490	435	486	324	372	389	350	404
Cl ppm	138	90	115	143	95	108	93	84	93	90	84	51
S ppm	634	126	259	144	315	405	347	206	172	185	134	171
Total	99.40	99.12	99.40	98.73	99.16	99.95	100.50	98.77	99.34	99.37	100.60	99.98
H_2O wt%	n.d	0.15	n.d	n.d	0.17	n.d	n.d	n.d	0.12	n.d	n.d	n.d
Sc	29.57	28.96	30.01	26.79	35.18	31.41	27.80	29.94	29.82	30.83	29.28	31.08
V	299.89	340.12	292.09	317.20	367.92	304.70	291.17	289.93	329.60	295.09	278.61	274.02
Rb	6.73	11.81	7.69	9.84	10.40	7.62	7.15	6.12	8.95	7.45	6.27	6.06
Sr	315.50	479.69	307.82	347.46	374.82	347.51	316.91	287.80	423.55	356.41	284.63	273.09
Y	23.95	31.14	22.13	25.84	31.26	24.12	21.66	23.50	32.75	27.15	21.43	21.55
Zr	140.11	201.22	125.76	160.58	209.28	154.10	138.20	131.07	183.36	162.37	123.47	119.67
Nb	10.24	21.55	10.88	16.20	17.70	12.66	13.34	12.06	18.05	15.06	9.77	9.93
Ba	89.48	214.56	91.82	125.67	132.44	102.08	100.33	79.04	149.46	111.27	74.42	73.56
La	11.43	23.29	11.66	12.45	14.24	10.90	10.86	9.48	17.70	13.93	9.76	10.12
Ce	28.06	58.89	28.10	32.44	34.55	27.09	27.59	23.57	45.76	36.55	24.50	24.30
Pr	3.96	9.19	3.77	4.84	5.30	4.09	4.25	3.61	6.82	5.37	3.38	3.22
Nd	19.01	43.28	20.02	22.37	25.57	19.25	19.28	18.77	34.63	26.18	17.32	17.31
Sm	5.29	10.29	4.92	5.86	6.88	5.19	4.97	4.83	9.24	7.31	5.05	4.60
Eu	1.95	3.75	1.83	2.00	2.53	1.85	1.75	1.68	3.47	2.58	1.84	1.69
Gd	5.25	10.63	5.44	6.09	6.55	5.52	4.68	5.50	9.97	7.50	4.65	4.91
Tb	0.89	1.72	0.82	0.83	0.93	0.78	0.90	0.83	1.53	1.10	0.77	0.84
Dy	5.31	9.93	5.02	5.23	5.59	4.81	4.67	4.67	9.47	6.74	4.68	4.66
Ho	0.90	1.86	0.90	0.96	1.14	0.93	0.91	0.90	1.74	1.35	0.93	0.90
Er	2.39	4.84	2.39	2.65	2.87	2.32	2.18	2.33	4.35	3.23	2.22	2.35
Tm	0.34	0.61	0.31	0.30	0.40	0.30	0.33	0.29	0.56	0.44	0.30	0.29
Yb	1.98	4.04	1.99	2.17	2.18	2.18	1.83	2.05	3.83	2.89	1.93	1.99
Lu	0.31	0.55	0.28	0.32	0.34	0.25	0.27	0.27	0.55	0.41	0.28	0.25
Hf	3.45	7.74	3.41	3.96	5.35	4.23	3.34	3.67	6.76	5.09	3.49	3.38
Ta	0.61	1.87	0.67	1.01	0.96	0.99	0.85	0.78	1.63	1.15	0.56	0.60
Pb	0.58	2.61	0.78	1.56	0.98	1.69	1.07	0.62	1.81	1.21	0.79	0.79
U	0.25	0.79	0.34	0.30	0.41	0.26	0.35	0.26	0.55	0.44	0.24	0.26
Temp(^{o}C)	1162	1178	1180	1128	1154	1186	1150	1197	1197	1195	1191	1193
Mg#	57	59	59	48	56	60	54	61	61	60	59	59

Table 4: Prehistoric and historical Kīlauea matrix glass compositions (cont'd)

Sample	1790-1-g07	1790-1-g09	1790-w-g01	1790-w-g02	1823-g01	1823-g02	1823-g05	1832-g02	1832-og08	1832-og25	1832-og34	1877-g01
SiO_2	50.54	50.33	50.90	50.50	51.18	51.56	51.18	51.00	50.39	51.09	51.33	51.64
TiO_2	5.23	5.27	2.50	2.60	2.40	2.50	2.27	2.63	2.63	2.73	2.63	2.68
Al_2O_3	11.71	11.61	13.45	13.52	12.86	12.92	12.55	13.83	14.22	13.89	13.92	13.63
Cr_2O_3	0.01	0.01	0.05	0.04	0.06	0.07	0.07	0.05	0.05	0.04	0.05	0.03
FeO	15.00	15.00	11.04	10.98	11.50	11.28	11.15	10.83	10.64	10.74	10.59	12.62
MnO	0.20	0.17	0.15	0.17	0.17	0.18	0.16	0.16	0.16	0.17	0.18	0.20
MgO	4.42	4.37	6.99	6.83	8.91	9.03	8.87	7.38	7.43	6.95	7.23	6.48
CaO	8.78	8.78	10.82	10.80	10.33	10.62	10.75	11.14	11.24	11.27	11.31	10.86
Na_2O	2.73	2.85	2.43	2.45	2.25	2.23	2.19	2.49	2.41	2.43	2.53	2.29
NiO	0.01	0.01	b.d	0.01	0.01	0.01	0.02	0.02	0.01	0.02	0.00	0.00
K_2O	0.90	0.90	0.43	0.45	0.39	0.42	0.46	0.50	0.53	0.52	0.51	0.23
P_2O_5	0.54	0.54	0.25	0.26	0.23	0.23	0.18	0.25	0.27	0.26	0.26	0.25
F ppm	1012	990	493	489	397	449	413	529	390	555	487	531
Cl ppm	214	220	113	122	83	100	119	87	118	108	109	104
S ppm	98	116	1082	1114	85	171	166	69	83	85	490	99
Total	100.21	99.98	99.30	98.90	100.33	101.15	99.93	100.34	100.05	100.20	100.69	101.00
H_2O wt%	0.14	0.13	0.52	0.50	0.09	0.09	n.d	0.10	0.09	0.10	n.d	0.02
Sc	28.53	27.42	29.41	28.69	28.69	30.09	30.89	30.45	30.28	30.62	29.75	30.08
V	424.04	428.12	300.10	296.58	284.89	301.84	311.97	289.62	285.36	289.83	290.82	288.07
Rb	16.52	16.79	7.17	7.64	6.82	7.56	7.31	7.90	7.82	7.73	8.35	5.91
Sr	357.61	346.96	318.38	329.88	329.94	363.87	359.86	360.43	360.16	354.69	365.34	310.60
Y	45.80	42.34	22.75	22.73	24.40	26.64	24.54	23.87	23.99	22.31	22.87	24.81
Zr	301.19	289.57	134.94	134.05	155.62	158.49	142.61	153.89	161.82	143.55	152.88	143.88
Nb	25.02	24.90	10.99	11.01	13.24	14.10	12.06	15.15	14.29	15.09	16.21	12.04
Ba	208.69	207.89	99.82	99.65	98.54	112.37	99.61	110.81	109.23	110.71	112.99	87.19
La	26.43	26.05	11.60	11.93	10.83	12.73	12.65	11.91	11.77	11.48	11.85	10.21
Ce	64.05	64.03	28.54	29.02	26.83	31.70	26.05	28.86	28.35	28.92	28.85	25.05
Pr	9.04	9.07	4.11	4.10	4.16	4.84	3.73	4.39	4.48	4.55	4.72	4.16
Nd	44.40	43.40	20.02	18.82	19.26	22.43	18.61	21.82	21.94	21.16	23.08	19.39
Sm	11.71	11.59	5.46	5.33	5.02	6.31	4.93	5.29	5.67	5.72	5.45	6.00
Eu	3.89	3.94	1.98	1.97	1.75	2.13	2.09	1.92	1.90	2.13	2.07	1.96
Gd	11.05	10.91	5.19	5.41	5.17	6.35	5.09	5.53	5.38	5.31	5.48	5.74
Tb	1.85	1.73	0.86	0.90	0.75	0.99	0.97	0.83	0.78	0.80	0.80	0.86
Dy	10.01	9.63	4.89	5.01	4.58	6.16	5.55	4.76	5.04	4.64	4.66	5.22
Ho	1.94	1.92	0.98	0.95	0.92	1.11	0.88	0.89	0.94	0.91	0.90	1.03
Er	4.79	4.58	2.35	2.24	2.23	2.83	2.05	2.21	2.20	2.04	2.20	2.41
Tm	0.62	0.64	0.31	0.33	0.28	0.37	0.29	0.31	0.28	0.28	0.29	0.34
Yb	4.08	3.97	1.97	2.18	2.02	2.46	1.97	1.80	1.82	1.82	1.98	2.21
Lu	0.55	0.53	0.27	0.28	0.29	0.31	0.29	0.25	0.26	0.23	0.28	0.31
Hf	8.15	7.81	3.56	3.52	3.69	4.46	3.08	3.73	3.63	3.66	3.48	3.77
Ta	1.52	1.52	0.59	0.65	0.78	0.88	0.81	0.84	0.91	0.89	0.83	0.70
Pb	1.74	2.05	0.78	0.85	1.01	1.59	1.16	0.73	0.76	0.79	0.94	0.74
U	0.63	0.68	0.27	0.28	0.32	0.31	0.33	0.30	0.31	0.28	0.34	0.27
Temp(^oC)	1103	1102	1154	1151	1193	1195	1192	1162	1163	1154	1159	1144
Mg#	37	37	56	55	61	61	61	57	58	56	57	50

Table 4: Prehistoric and historical Kīlauea matrix glass compositions (cont'd)

Sample	1877-g04	1885B-g02	1885A-g03	1885B-og02	1885A-og21	1885B-og12	1920-g01	1920-g02	1920-og02	1920-og05	1920-og08	1954-g01b
SiO_2	51.82	50.23	50.51	50.75	51.02	50.41	50.97	51.15	50.13	50.77	50.44	50.29
TiO_2	2.66	3.06	3.11	3.04	3.05	3.05	2.97	2.90	2.91	2.89	2.79	2.86
Al_2O_3	13.85	13.44	13.22	13.32	13.20	13.35	13.76	13.75	13.47	13.82	13.79	13.52
Cr_2O_3	0.03	0.03	0.02	0.03	0.03	0.02	0.04	0.05	0.05	0.04	0.03	0.02
FeO	11.47	12.15	11.78	12.21	12.21	11.35	10.57	11.09	11.25	10.39	10.79	11.44
MnO	0.18	0.18	0.18	0.17	0.18	0.18	0.18	0.17	0.16	0.15	0.17	0.17
MgO	6.64	6.46	6.35	6.38	6.25	6.32	6.93	6.99	7.12	6.94	6.98	6.76
CaO	10.84	10.92	10.88	10.92	10.89	11.09	11.39	11.45	11.50	11.59	11.44	11.10
Na_2O	2.64	2.59	2.59	2.65	2.60	2.60	2.38	2.42	2.30	2.29	2.39	2.76
NiO	0.01	0.01	0.02	0.00	0.01	0.00	0.01	0.01	0.02	0.03	0.01	0.01
K_2O	0.14	0.58	0.60	0.59	0.62	0.57	0.55	0.54	0.53	0.53	0.49	0.64
P_2O_5	0.25	0.30	0.31	0.31	0.31	0.30	0.27	0.26	0.24	0.24	0.23	0.28
F ppm	472	618	579	581	616	540	544	580	438	508	515	451
Cl ppm	93	123	153	152	134	145	100	110	138	94	105	127
S ppm	82	130	165	135	157	139	136	141	156	140	136	86
Total	100.58	100.05	99.67	100.49	100.48	99.32	100.10	100.89	99.77	99.77	99.64	99.92
H_2O wt%	0.02	n.d	0.13	0.09	0.14	0.11	0.08	n.d	n.d	n.d	n.d	0.11
Sc	30.65	31.43	29.84	28.89	30.42	31.26	30.63	28.65	28.65	27.40	31.06	29.17
V	293.96	329.65	324.17	311.48	326.04	320.87	321.89	315.93	315.93	306.78	325.33	340.96
Rb	4.72	11.29	11.11	10.73	10.85	10.77	10.01	9.79	9.79	11.07	9.91	14.14
Sr	322.07	388.29	379.21	377.79	370.39	393.45	416.15	402.02	402.02	378.33	419.39	530.13
Y	24.66	27.97	26.83	25.82	27.05	27.04	24.31	24.74	24.74	23.20	25.79	31.10
Zr	146.60	183.25	167.78	156.52	172.89	180.57	172.25	170.12	170.12	155.14	174.34	205.58
Nb	12.28	16.73	16.79	16.26	16.52	16.96	20.29	19.06	19.06	16.39	18.94	28.88
Ba	88.96	149.85	145.89	155.03	143.73	150.26	135.53	129.98	129.98	135.13	123.86	238.85
La	10.68	17.20	17.09	16.64	16.48	17.28	15.07	15.06	15.06	17.15	14.95	26.12
Ce	25.45	40.05	40.84	42.79	39.75	42.05	37.44	36.58	36.58	43.82	36.66	63.54
Pr	4.23	5.34	5.67	6.01	5.53	5.38	5.54	5.30	5.30	5.72	5.43	9.19
Nd	20.16	26.68	26.44	26.42	25.99	27.99	25.72	25.05	25.05	28.37	24.78	40.56
Sm	5.35	6.75	6.74	7.02	6.85	6.67	5.67	5.84	5.84	6.83	5.70	10.05
Eu	2.04	2.35	2.40	2.49	2.32	2.28	2.10	1.99	1.99	2.49	1.99	3.22
Gd	5.34	6.66	6.24	6.77	6.33	7.08	6.07	5.64	5.64	6.58	6.27	8.97
Tb	0.87	1.06	1.04	1.06	1.07	1.07	0.89	0.76	0.76	0.96	0.88	1.35
Dy	5.18	5.97	5.90	6.10	5.71	6.54	5.21	4.83	4.83	5.83	5.52	8.46
Ho	1.00	1.13	1.12	1.23	1.12	1.15	0.95	0.94	0.94	1.11	0.96	1.50
Er	2.40	2.89	2.75	2.84	2.67	2.96	2.44	2.48	2.48	2.44	2.70	3.58
Tm	0.32	0.37	0.37	0.38	0.35	0.43	0.29	0.29	0.29	0.34	0.34	0.51
Yb	2.23	2.39	2.43	2.71	2.29	2.45	1.87	1.97	1.97	2.21	2.10	3.08
Lu	0.32	0.33	0.32	0.35	0.30	0.31	0.26	0.28	0.28	0.31	0.28	0.44
Hf	3.56	4.99	4.91	5.13	4.41	4.81	4.34	4.27	4.27	4.94	4.44	7.22
Ta	0.75	1.00	0.97	1.15	0.99	1.00	1.25	1.16	1.16	1.21	1.31	2.25
Pb	0.94	1.11	1.04	1.33	0.92	1.32	0.92	1.02	1.02	1.24	0.91	2.22
U	0.26	0.44	0.42	0.51	0.44	0.57	0.42	0.40	0.40	0.60	0.46	0.92
Temp(^{o}C)	1147	1144	1142	1142	1140	1141	1153	1155	1157	1154	1154	1150
Mg#	53	51	52	51	50	52	56	56	56	57	56	54

Table 4: Prehistoric and historical Kīlauea matrix glass compositions (cont'd)

Sample	1954-g01	1954-g03	1961-g01	1961-g02	1961-og41	1969-mu-g01	1969-mu-g02	1969-7-g01	1969-7-g02	1969-8-g01	1969-8-g02	1969-8-og01
SiO_2	50.00	49.71	50.66	50.83	51.06	50.47	50.21	50.15	50.10	50.49	49.85	49.98
TiO_2	3.01	2.98	2.86	2.89	2.91	2.64	2.65	2.66	2.65	2.66	2.50	2.50
Al_2O_3	13.80	13.73	13.69	13.50	13.56	13.11	13.00	12.83	12.93	12.84	12.36	12.43
Cr_2O_3	-0.01	0.00	0.04	0.05	0.04	0.05	0.05	0.06	0.07	0.07	0.09	0.09
FeO	11.05	11.18	11.45	10.89	10.97	11.31	11.22	11.26	11.86	10.97	11.27	11.84
MnO	0.17	0.18	0.17	0.18	0.16	0.17	0.19	0.18	0.17	0.16	0.15	0.18
MgO	6.67	6.61	7.17	7.09	6.96	8.40	8.39	8.76	9.01	8.78	9.79	10.07
CaO	11.17	11.28	11.09	11.19	11.17	11.03	11.08	10.79	10.60	10.96	10.53	10.62
Na_2O	2.47	2.43	2.46	2.55	2.57	2.39	2.42	2.34	2.28	1.59	2.19	2.18
NiO	0.04	0.02	0.01	0.01	0.02	0.03	0.01	0.02	0.03	0.02	0.03	0.04
K_2O	0.61	0.67	0.58	0.58	0.60	0.53	0.55	0.52	0.52	0.53	0.50	0.49
P_2O_5	0.30	0.31	0.30	0.29	0.29	0.27	0.27	0.27	0.27	0.24	0.22	0.22
F ppm	429	516	556	525	516	559	594	519	498	487	425	454
Cl ppm	166	164	160	153	168	141	131	108	94	92	112	100
S ppm	118	80	132	127	206	139	124	90	99	174	200	207
Total	99.37	99.20	100.59	100.14	100.41	100.48	100.15	99.91	100.55	99.40	99.58	100.72
H_2O wt%	n.d	n.d	0.10	0.09	n.d	0.08	0.07	0.08	0.09	n.d	0.11	n.d
Sc	29.68	27.42	28.45	26.98	28.76	29.26	29.59	28.47	28.46	26.82	26.15	30.42
V	323.79	321.49	298.64	300.76	297.40	302.97	306.05	299.30	293.44	306.48	298.04	304.05
Rb	12.32	11.69	9.99	10.31	9.87	9.72	9.99	10.04	9.18	10.61	9.44	9.41
Sr	386.27	393.88	389.18	393.18	394.12	370.38	373.30	413.35	380.42	433.23	397.09	387.12
Y	24.54	24.10	22.66	21.65	23.60	22.73	23.49	24.66	23.68	24.60	22.70	24.25
Zr	170.40	156.80	166.68	160.72	166.44	142.83	145.10	177.10	164.91	178.39	151.00	175.30
Nb	17.51	19.14	20.61	20.02	20.04	13.24	13.14	18.38	16.67	20.13	17.77	16.55
Ba	151.48	143.08	143.15	147.19	144.37	126.01	127.25	143.40	135.19	166.41	140.40	130.91
La	16.66	18.28	15.79	14.91	15.20	14.52	14.84	16.18	14.90	17.86	14.86	14.43
Ce	40.44	38.73	36.99	36.59	36.32	34.59	34.28	40.08	36.62	44.64	37.60	34.91
Pr	5.42	5.23	5.60	5.59	5.41	4.63	4.74	6.05	5.56	6.60	5.52	5.11
Nd	24.79	25.57	24.05	24.63	23.92	22.21	22.42	28.36	25.88	30.22	24.52	24.08
Sm	6.56	5.97	5.73	5.98	5.95	6.00	5.63	6.88	6.29	7.25	5.89	5.97
Eu	2.17	2.27	2.07	2.14	2.13	2.04	1.98	2.51	2.13	2.57	2.03	2.07
Gd	5.09	5.33	5.73	5.28	5.83	5.72	5.24	7.11	6.11	7.70	5.94	6.15
Tb	0.79	0.91	0.82	0.77	0.88	0.89	0.88	1.07	0.93	1.05	0.86	0.91
Dy	4.61	4.57	4.99	4.86	5.21	4.84	4.92	6.16	5.63	6.06	5.21	4.98
Ho	0.89	0.98	0.92	0.87	0.98	0.94	0.95	1.12	1.03	1.20	1.00	1.00
Er	2.28	2.27	2.13	2.20	2.51	2.28	2.40	2.80	2.61	2.96	2.47	2.48
Tm	0.29	0.28	0.29	0.29	0.31	0.30	0.30	0.37	0.36	0.37	0.32	0.35
Yb	2.11	1.73	1.95	1.89	2.07	2.07	1.79	2.43	2.31	2.44	2.23	2.09
Lu	0.28	0.31	0.25	0.24	0.29	0.26	0.26	0.31	0.30	0.34	0.30	0.29
Hf	3.87	3.57	4.03	3.82	4.35	3.95	4.08	5.14	4.37	5.18	4.24	4.25
Ta	1.00	1.02	1.14	1.12	1.39	0.81	0.84	1.35	1.24	1.38	1.19	1.12
Pb	1.02	0.87	0.95	1.07	1.02	0.97	0.95	1.30	1.46	1.64	1.42	1.23
U	0.46	0.43	0.45	0.42	0.44	0.37	0.37	0.51	0.44	0.58	0.43	0.41
Temp(^{o}C)	1148	1147	1158	1157	1154	1183	1183	1190	1195	1190	1211	1216
Mg#	54	54	55	56	56	60	60	61	60	61	63	63

Table 4: Prehistoric and historical Kīlauea matrix glass compositions (cont'd)

Sample	1969-8-og01	1971-g02	1971-g03	16b_o_22_g	1971-og01	1971-og05	1973-g01	1973-g03	1973-og01	1973-og17	1973-g02	1973-og11
SiO_2	49.79	50.99	51.21	50.68	51.26	51.48	51.16	50.98	50.12	49.82	51.27	51.20
TiO_2	2.44	2.95	2.77	2.77	2.84	2.90	2.54	2.49	2.54	2.48	2.57	2.55
Al_2O_3	12.57	13.64	14.01	13.67	13.66	13.92	13.43	13.61	13.02	12.72	13.30	13.67
Cr_2O_3	0.08	0.01	0.03	0.02	0.03	0.03	0.06	0.05	0.05	0.07	0.06	0.06
FeO	12.07	11.92	11.50	11.09	11.48	11.21	11.45	11.38	10.93	11.11	11.34	11.60
MnO	0.16	0.17	0.18	0.18	0.18	0.17	0.18	0.16	0.18	0.17	0.17	0.18
MgO	9.71	6.49	6.47	6.59	6.88	6.25	7.79	7.77	7.73	7.79	7.69	7.92
CaO	10.38	10.77	10.84	11.16	11.03	11.01	11.19	11.09	11.11	10.98	11.07	10.95
Na_2O	2.23	2.48	2.53	2.46	2.47	2.51	2.37	2.36	2.32	2.25	2.33	2.25
NiO	0.02	0.01	0.01	0.02	0.00	0.02	0.03	0.00	0.01	0.01	0.00	0.02
K_2O	0.47	0.56	0.52	0.56	0.55	0.55	0.47	0.47	0.48	0.46	0.48	0.44
P_2O_5	0.27	0.31	0.29	0.24	0.29	0.29	0.25	0.25	0.25	0.26	0.24	0.25
F ppm	364	565	468	575	373	298	504	482	362	442	307	259
Cl ppm	115	118	136	127	127	127	114	95	137	112	87	105
S ppm	55	115	120	124	101	171	167	160	190	142	110	78
Total	100.25	100.37	100.45	99.55	100.74	100.39	101.00	100.70	98.84	98.22	100.59	101.15
H_2O wt%	n.d	0.09	0.09	0.09	n.d	n.d	0.09	0.10	n.d	n.d	0.09	n.d
Sc	29.05	28.32	28.99	31.29	25.86	28.47	29.25	28.68	37.31	29.82	29.70	29.25
V	268.98	342.55	325.65	331.63	293.39	320.85	293.99	295.37	292.24	299.22	297.40	289.90
Rb	8.42	13.38	11.95	11.38	9.49	10.89	8.17	7.65	7.68	8.04	7.35	7.59
Sr	324.71	565.79	479.84	471.49	344.73	357.86	360.55	347.03	383.18	347.95	340.76	335.30
Y	19.48	34.64	30.03	30.17	22.58	21.83	24.87	23.66	27.53	22.58	22.98	21.55
Zr	122.83	248.04	205.92	220.79	141.98	154.04	153.52	144.75	182.97	150.90	135.07	128.04
Nb	11.45	26.54	21.89	21.29	14.10	12.90	14.98	14.08	15.53	14.68	11.81	11.10
Ba	100.77	252.79	185.41	168.29	123.17	127.42	112.91	111.52	105.97	107.72	105.47	99.31
La	13.14	28.19	20.45	19.17	14.33	14.80	12.45	11.82	14.87	11.59	12.63	12.46
Ce	28.71	70.18	50.92	45.93	34.08	37.74	30.04	29.45	30.93	29.15	30.57	27.94
Pr	4.02	10.59	7.46	7.10	4.46	5.09	4.42	4.39	4.67	4.38	4.33	3.82
Nd	18.95	49.41	33.93	33.34	22.74	26.98	21.68	19.71	23.37	20.04	19.74	20.75
Sm	4.40	12.64	8.73	8.68	5.43	6.42	5.16	5.39	7.26	5.49	5.18	5.55
Eu	1.57	4.28	2.81	2.54	1.90	2.10	2.09	1.81	2.05	1.85	1.84	1.80
Gd	4.55	12.03	8.74	7.98	5.87	5.54	5.66	5.56	5.78	4.94	5.39	5.14
Tb	0.73	1.84	1.32	1.27	0.83	0.96	0.76	0.85	0.80	0.81	0.91	0.80
Dy	3.90	10.79	7.56	6.81	5.10	5.12	5.10	4.68	6.47	4.91	4.46	4.93
Ho	0.70	1.98	1.48	1.36	0.95	0.93	0.95	0.91	1.20	0.86	0.98	0.85
Er	1.79	5.24	3.81	3.20	2.25	2.19	2.50	2.31	2.80	2.34	2.26	2.31
Tm	0.26	0.64	0.49	0.42	0.31	0.30	0.31	0.30	0.51	0.29	0.31	0.30
Yb	1.68	4.13	3.05	2.71	1.96	1.66	2.10	1.96	2.17	1.74	2.07	1.95
Lu	0.19	0.60	0.39	0.40	0.27	0.32	0.27	0.28	0.21	0.27	0.27	0.27
Hf	3.11	8.96	6.39	5.33	3.71	3.53	4.13	4.09	5.23	3.69	3.86	3.93
Ta	0.65	2.18	1.72	1.54	0.88	1.05	0.92	0.90	0.72	0.84	0.54	0.74
Pb	0.75	2.41	1.76	1.30	0.72	0.87	0.91	0.84	2.34	0.88	0.66	0.75
U	0.31	0.92	0.67	0.53	0.40	0.49	0.34	0.31	0.17	0.29	0.33	0.27
Temp(^{o}C)	1209	1144	1144	1146	1152	1140	1171	1170	1169	1171	1169	1173
Mg#	61	52	53	54	54	52	58	58	58	58	57	57

Table 4: Prehistoric and historical Kīlauea matrix glass compositions (cont'd)

Sample	1974-J1-g01	1974-J1-og10	1974-J1-og35	1974-J1-og19	1974-J2-g01	1974-J2-g02	1974-S-g02	1974-S-g03	1982-1-g03	1982-1-og14	1982-1-g02
SiO_2	50.11	50.52	51.61	51.25	50.38	50.56	50.11	49.82	51.39	50.76	50.60
TiO_2	2.80	2.77	2.78	2.75	2.58	2.58	2.74	2.84	2.41	2.84	2.92
Al_2O_3	13.61	13.92	13.69	13.80	13.24	13.24	13.36	13.20	13.61	13.78	13.57
Cr_2O_3	0.03	0.03	0.02	0.02	0.06	0.09	0.03	0.02	0.04	0.02	0.01
FeO	11.75	11.73	11.84	11.30	11.34	11.62	11.59	11.49	11.11	11.35	12.07
MnO	0.18	0.18	0.19	0.17	0.18	0.21	0.18	0.18	0.18	0.19	0.13
MgO	6.56	6.42	6.49	6.42	7.21	7.28	6.37	6.49	7.40	6.10	6.32
CaO	10.96	10.72	10.94	10.77	11.13	11.10	10.82	10.89	10.79	10.83	10.65
Na_2O	2.46	2.63	2.54	2.36	2.33	2.30	2.51	2.50	2.35	2.55	2.53
NiO	0.01	0.00	0.01	0.03	b.d	0.00	0.01	0.01	0.01	0.01	0.02
K_2O	0.51	0.49	0.51	0.57	0.44	0.46	0.54	0.53	0.41	0.55	0.59
P_2O_5	0.27	0.25	0.24	0.24	0.25	0.23	0.29	0.30	0.23	0.27	0.31
F ppm	499	474	470	579	280	97	567	566	432	572	382
Cl ppm	140	137	134	118	129	104	123	136	78	124	133
S ppm	173	174	209	186	36	149	127	175	163	231	114
Total	99.34	99.77	100.96	99.78	99.18	99.71	98.64	98.38	100.03	99.37	99.79
H_2O wt%	0.09	n.d	n.d	n.d	n.d	0.09	n.d	0.10	n.d	n.d	n.d
Sc	29.37	28.29	28.22	27.41	30.68	30.49	29.08	26.86	30.87	27.85	27.26
V	335.98	302.63	331.76	306.61	308.34	306.42	336.34	329.37	306.21	326.10	314.25
Rb	9.56	8.62	9.41	7.94	8.06	8.41	13.31	12.06	7.87	10.02	8.78
Sr	398.15	358.77	370.26	372.43	378.82	368.66	543.83	482.31	352.62	395.65	339.85
Y	25.81	22.51	25.14	25.78	22.37	23.29	34.02	31.94	26.17	26.44	24.00
Zr	171.34	149.58	160.79	155.75	130.26	131.23	221.62	210.83	153.86	168.71	150.55
Nb	17.87	15.77	16.31	15.77	15.06	15.32	24.68	23.36	15.39	18.39	13.19
Ba	136.84	120.94	125.60	119.92	119.34	117.04	228.98	188.38	114.52	137.98	115.61
La	14.66	12.52	13.59	12.52	12.93	12.30	24.40	20.28	12.66	14.90	14.18
Ce	36.72	31.59	32.66	31.79	31.41	31.49	61.25	51.98	32.35	36.59	32.15
Pr	5.55	4.76	5.03	5.19	4.58	4.76	9.27	7.76	5.08	5.65	4.46
Nd	26.32	21.88	21.76	20.90	21.14	21.74	42.62	35.70	24.47	25.25	22.58
Sm	6.27	4.97	5.80	5.62	5.80	5.60	9.79	8.59	5.57	6.47	5.63
Eu	2.19	1.99	2.12	1.89	2.15	1.96	3.89	3.02	2.18	2.24	2.12
Gd	6.26	5.76	5.73	5.56	5.28	5.22	10.61	8.84	6.43	6.59	5.16
Tb	0.89	0.87	0.76	0.74	0.81	0.79	1.63	1.22	0.99	1.06	0.87
Dy	5.54	4.87	4.85	5.59	4.85	4.85	9.88	8.04	5.69	5.67	5.10
Ho	1.12	0.94	0.96	1.10	0.98	0.93	1.80	1.43	1.12	1.14	0.96
Er	2.83	2.25	2.52	2.61	2.45	2.31	4.62	3.78	2.96	2.81	2.32
Tm	0.36	0.30	0.31	0.37	0.33	0.30	0.64	0.46	0.38	0.37	0.35
Yb	2.37	1.92	2.04	2.16	1.93	1.96	4.17	3.04	2.16	2.25	1.96
Lu	0.32	0.30	0.32	0.34	0.28	0.30	0.55	0.46	0.38	0.35	0.30
Hf	4.50	3.54	4.00	4.22	3.79	3.66	8.03	6.63	4.47	4.79	3.71
Ta	1.06	1.02	1.02	1.10	0.98	0.92	2.11	1.65	1.04	1.18	0.75
Pb	1.04	1.05	1.17	1.00	1.18	0.92	2.29	1.68	1.01	1.30	1.05
U	0.43	0.35	0.35	0.31	0.42	0.38	0.81	0.61	0.32	0.43	0.33
Temp(°C)	1146	1143	1144	1143	1159	1160	1142	1144	1163	1137	1141
Mg#	53	52	52	53	56	55	52	53	57	52	51

Table 4: Prehistoric and historical Kīlauea matrix glass compositions (cont'd)

Sample	1982-2-g02	1982-2-g03	2008-S1-g06	2008-S1-g17	2008-S1-g24	2008-S1-g26	2008-S1-g46	2008-S1-g47	2008-S1-g53	2008-S1-g55	2008-S2-g03
SiO_2	51.63	51.48	51.79	51.76	51.83	51.55	52.06	51.79	51.97	52.12	51.90
TiO_2	2.66	2.74	2.37	2.42	2.39	2.46	2.33	2.47	2.47	2.39	2.39
Al_2O_3	13.61	13.55	13.08	13.53	13.93	13.47	13.37	13.30	13.41	13.63	13.54
Cr_2O_3	0.03	0.03	0.05	0.04	0.04	0.05	0.03	0.04	0.05	0.04	0.04
FeO	10.92	10.93	11.52	11.04	11.34	11.18	11.48	11.29	11.11	11.60	11.18
MnO	0.18	0.18	0.19	0.18	0.16	0.17	0.16	0.16	0.17	0.17	0.17
MgO	6.37	6.34	7.48	7.41	7.55	7.42	7.56	7.48	7.48	7.66	7.48
CaO	11.21	11.33	11.05	10.84	10.87	10.93	10.71	10.79	10.81	10.82	10.81
Na_2O	2.45	2.41	2.33	2.31	2.31	2.30	2.27	2.31	2.27	2.31	2.33
NiO	0.02	0.01	0.00	0.02	0.02	0.01	b.d	0.01	0.02	0.01	0.01
K_2O	0.58	0.53	0.41	0.41	0.41	0.41	0.38	0.42	0.42	0.41	0.43
P_2O_5	0.28	0.28	0.24	0.22	0.22	0.23	0.23	0.23	0.23	0.23	0.23
F ppm	500	471	442	387	421	391	361	395	338	396	371
Cl ppm	136	116	99	92	72	87	66	77	88	71	77
S ppm	137	147	157	178	177	209	128	173	171	169	180
Total	100.02	99.90	100.58	100.24	101.15	100.26	100.65	100.37	100.48	101.47	100.58
H_2O wt%	n.d	n.d	n.d	n.d	n.d	0.09	n.d	0.08	0.09	0.09	0.10
Sc	32.01	32.57	28.90	28.17	26.80	31.40	28.17	28.65	29.78	29.11	28.19
V	300.19	317.23	291.62	278.91	291.34	283.82	270.19	280.49	275.84	290.00	284.02
Rb	8.11	9.49	6.13	6.13	6.36	6.19	6.46	6.61	6.24	7.05	6.26
Sr	365.99	383.14	284.15	273.67	296.20	320.02	315.18	321.82	288.75	291.93	329.22
Y	25.48	27.37	20.27	19.76	21.76	23.68	23.16	22.82	21.09	20.86	23.04
Zr	161.49	166.90	104.01	115.34	126.90	134.58	131.59	127.03	113.46	114.30	138.07
Nb	16.01	16.76	10.30	9.48	9.86	12.33	11.97	12.57	9.84	10.14	12.41
Ba	119.38	124.02	84.88	82.39	87.54	92.60	88.22	93.04	87.18	88.56	88.83
La	13.42	13.87	10.34	9.90	11.31	10.25	9.81	9.76	9.71	11.03	9.92
Ce	32.33	32.79	26.50	24.68	26.22	24.88	24.35	25.43	25.00	27.20	25.11
Pr	5.10	4.87	3.44	3.51	3.65	4.11	3.61	3.82	3.40	3.44	3.90
Nd	23.38	22.67	17.17	17.85	16.67	19.26	17.87	17.92	18.25	17.23	17.86
Sm	6.15	6.01	4.53	4.80	4.44	4.73	4.84	4.73	5.30	4.83	4.72
Eu	2.18	1.95	1.66	1.68	1.97	1.72	1.66	1.58	1.70	1.73	1.72
Gd	6.37	5.90	4.27	4.66	4.94	4.95	4.99	5.16	4.92	4.19	4.52
Tb	0.96	0.94	0.76	0.64	0.80	0.69	0.73	0.74	0.75	0.87	0.72
Dy	5.37	5.37	4.66	4.35	4.63	4.98	4.46	4.73	4.45	4.82	4.48
Ho	1.04	1.07	0.78	0.80	0.94	0.98	0.92	0.96	0.93	0.84	0.96
Er	2.55	2.53	2.07	2.03	2.23	2.21	2.33	2.06	2.14	2.15	2.14
Tm	0.32	0.38	0.26	0.23	0.26	0.30	0.33	0.31	0.28	0.28	0.31
Yb	2.31	2.28	1.73	1.60	2.01	2.04	1.94	2.08	1.76	1.70	1.92
Lu	0.31	0.28	0.26	0.24	0.28	0.29	0.28	0.29	0.25	0.19	0.26
Hf	4.03	4.26	2.96	2.99	3.29	3.27	3.61	3.28	2.96	3.34	3.33
Ta	1.01	1.06	0.57	0.54	0.56	0.76	0.72	0.77	0.60	0.58	0.79
Pb	0.95	1.10	0.76	0.78	0.73	0.81	0.76	0.70	0.62	0.65	0.75
U	0.39	0.35	0.22	0.23	0.32	0.28	0.27	0.30	0.25	0.21	0.29
Temp(^{o}C)	1142	1141	1164	1163	1166	1163	1166	1164	1164	1168	1164
Mg#	54	53	56	57	57	57	57	57	57	57	57

Table 4: Prehistoric and historical Kīlauea matrix glass compositions (cont'd)

Sample	2008-S2-g11	2008-S2-g18	2008-S2-g30	2008-S2-g38	2008-S2-g41	2008-S2-g42	2008-S2-g44	2008-18-g01	2008-18-g02	2008-18-og02	2008-18-og12
SiO_2	51.69	51.72	51.64	51.75	51.52	51.65	52.06	51.56	51.45	51.54	51.45
TiO_2	2.39	2.33	2.42	2.42	2.39	2.41	2.41	2.41	2.41	2.47	2.47
Al_2O_3	13.30	13.49	13.48	13.42	13.56	13.59	13.63	13.38	13.49	13.50	13.30
Cr_2O_3	0.05	0.04	0.05	0.06	0.06	0.04	0.04	0.04	0.06	0.05	0.05
FeO	10.84	10.96	11.06	10.89	11.15	11.42	10.95	11.29	10.97	10.82	11.19
MnO	0.18	0.14	0.17	0.17	0.15	0.17	0.16	0.17	0.18	0.16	0.18
MgO	7.48	7.37	7.45	7.50	7.62	7.55	7.55	7.72	7.42	7.46	7.42
CaO	10.82	10.94	10.79	10.74	10.84	10.78	10.83	10.82	10.77	10.85	10.93
Na_2O	2.30	2.29	2.33	2.28	2.27	2.36	2.35	2.37	2.39	2.44	2.49
NiO	0.02	b.d	0.01	0.02	0.01	0.01	0.01	0.02	0.01	0.01	0.01
K_2O	0.44	0.41	0.42	0.42	0.41	0.43	0.42	0.41	0.40	0.38	0.33
P_2O_5	0.23	0.22	0.22	0.22	0.22	0.23	0.23	0.21	0.24	0.23	0.23
F ppm	361	367	336	377	436	341	344	349	306	349	308
Cl ppm	73	90	77	74	79	92	75	80	122	115	120
S ppm	234	181	182	167	596	308	234	159	290	233	250
Total	99.81	100.00	100.12	99.98	100.36	100.74	100.72	100.49	99.89	100.00	100.14
H_2O wt%	n.d	n.d	n.d	0.09	n.d	n.d	0.11	0.16	n.d	n.d	n.d
Sc	30.20	28.28	27.79	27.77	30.02	27.50	30.90	28.27	27.51	31.06	27.43
V	285.02	279.81	279.58	270.00	272.60	280.03	299.76	314.44	300.65	287.87	272.46
Rb	5.53	5.79	6.64	5.56	5.62	6.75	5.90	8.27	7.52	6.57	6.28
Sr	280.23	304.67	315.01	259.11	275.45	312.92	280.49	400.12	366.04	314.98	281.81
Y	20.73	20.61	21.89	19.79	21.41	21.16	20.96	25.41	24.79	22.17	22.71
Zr	113.27	131.47	133.24	111.21	117.60	122.35	112.20	156.98	147.89	121.49	126.13
Nb	9.45	9.34	12.22	9.52	9.59	12.38	9.49	16.04	15.21	10.13	10.55
Ba	75.92	78.12	92.78	79.72	77.08	90.79	82.99	140.65	118.31	93.87	83.00
La	10.12	11.31	9.95	9.73	10.43	9.58	9.17	15.47	12.82	10.83	11.48
Ce	21.47	22.93	25.61	24.73	22.77	25.25	23.67	39.46	33.59	26.24	28.47
Pr	3.41	3.29	3.76	3.78	3.22	3.57	3.26	6.10	5.14	4.13	3.89
Nd	16.40	16.62	16.12	20.17	16.73	18.33	16.92	29.90	24.06	19.26	19.82
Sm	5.11	3.97	5.02	4.99	4.21	4.55	4.45	7.17	6.87	5.34	5.26
Eu	1.87	1.89	1.70	1.61	1.55	1.62	1.69	2.83	2.41	1.69	1.82
Gd	4.30	5.63	4.98	4.28	5.43	5.08	4.45	6.98	7.00	5.36	4.97
Tb	0.77	0.75	0.76	0.74	0.75	0.72	0.79	1.09	0.91	0.91	0.86
Dy	4.63	4.92	4.31	5.21	4.49	4.46	4.27	7.58	6.19	5.40	5.47
Ho	0.77	0.90	0.84	1.01	0.71	0.83	0.81	1.32	1.22	1.13	1.01
Er	2.22	2.06	2.26	2.04	2.23	2.14	2.12	3.42	3.07	2.56	2.49
Tm	0.30	0.29	0.27	0.33	0.22	0.27	0.28	0.46	0.42	0.34	0.36
Yb	1.65	1.93	2.04	1.69	1.60	1.76	1.93	3.12	2.44	2.44	2.06
Lu	0.26	0.28	0.25	0.27	0.27	0.27	0.27	0.44	0.35	0.36	0.24
Hf	3.02	2.78	3.14	3.16	3.33	3.45	2.71	5.30	4.76	4.57	3.48
Ta	0.51	0.46	0.71	0.64	0.60	0.69	0.53	1.30	1.09	0.73	0.62
Pb	1.07	1.07	0.91	0.71	0.85	0.87	0.61	1.71	1.57	0.66	0.82
U	0.24	0.27	0.30	0.27	0.28	0.26	0.24	0.55	0.42	0.33	0.26
Temp(^oC)	1164	1162	1164	1165	1167	1166	1166	1169	1161	1164	1163
Mg#	58	57	57	58	58	57	58	57	56	58	57

Table 4: Prehistoric and historical Kīlauea matrix glass compositions (cont'd)

Sample	2008-18-og04	2008-18-og07	2008-18-og13	2008-18-og14	2008-18-og19	2008-18-og25	2010-S3-g04	2010-S3-g08	2010-S3-g56	2010-S3-g57
SiO_2	51.62	51.70	50.22	50.84	51.71	51.69	51.76	51.71	51.16	51.57
TiO_2	2.46	2.41	2.42	2.39	2.42	2.45	2.39	2.38	2.35	2.41
Al_2O_3	13.41	13.42	13.69	13.87	13.70	13.62	13.53	13.49	13.68	13.59
Cr_2O_3	0.05	0.05	0.04	0.05	0.08	0.04	0.04	0.03	0.05	0.06
FeO	10.56	11.02	10.67	11.59	11.33	11.07	11.20	11.04	11.02	11.59
MnO	0.18	0.17	0.17	0.18	0.20	0.18	0.17	0.17	0.17	0.18
MgO	7.54	7.43	7.64	7.41	7.46	7.39	7.34	7.22	7.52	7.45
CaO	10.92	10.83	11.01	10.95	10.93	10.86	10.94	10.84	10.79	10.87
Na_2O	2.23	2.37	2.25	2.33	2.34	2.32	2.30	2.37	2.31	2.32
NiO	0.01	0.01	b.d	0.02	0.02	0.02	0.00	0.00	0.02	0.02
K_2O	0.41	0.41	0.42	0.43	0.40	0.39	0.41	0.39	0.39	0.41
P_2O_5	0.24	0.23	0.24	0.23	0.22	0.24	0.23	0.23	0.22	0.23
F ppm	371	298	231	282	302	293	420	382	298	385
Cl ppm	91	72	111	101	78	86	83	89	110	90
S ppm	248	144	301	495	218	201	231	406	184	174
Total	99.71	100.11	98.84	100.39	100.88	100.32	100.42	100.01	99.76	100.77
H_2O wt%	0.08	0.11	0.13	0.16	n.d	n.d	0.09	0.16	0.11	0.08
Sc	30.98	30.06	25.78	29.75	27.02	28.67	28.59	29.66	29.68	29.99
V	296.93	285.88	298.04	284.97	291.63	297.50	278.72	275.98	274.45	280.92
Rb	7.31	6.69	6.53	6.76	7.49	6.31	6.26	6.15	6.20	6.12
Sr	315.28	300.20	319.93	288.18	309.01	305.37	312.80	309.74	305.24	321.06
Y	24.69	22.88	20.88	20.50	21.97	22.58	21.38	22.16	21.46	22.11
Zr	141.55	111.92	115.60	134.11	118.75	117.82	122.58	132.65	126.24	131.00
Nb	10.26	9.51	10.27	9.91	9.57	10.02	12.59	13.14	12.29	13.22
Ba	90.04	84.35	94.81	91.53	88.14	87.75	95.47	89.42	85.70	96.24
La	11.87	10.24	12.01	10.44	10.60	10.99	10.12	10.20	9.95	10.18
Ce	27.31	25.50	26.94	26.77	26.46	26.76	24.28	24.66	24.17	25.41
Pr	3.70	3.73	4.07	3.76	3.60	3.48	3.77	3.92	3.75	3.97
Nd	20.00	18.15	18.76	18.48	18.57	18.81	18.59	18.80	18.30	19.56
Sm	5.49	4.87	5.58	4.84	4.54	4.88	4.89	4.92	4.70	5.17
Eu	1.95	1.82	1.83	1.91	1.97	1.96	1.69	1.74	1.76	1.86
Gd	4.91	5.12	4.83	4.79	5.05	5.03	4.58	5.26	4.59	5.46
Tb	0.84	0.80	0.75	0.85	0.84	0.81	0.77	0.77	0.75	0.77
Dy	4.75	4.77	4.61	4.88	4.74	4.53	4.48	4.61	4.62	4.67
Ho	0.98	0.91	0.82	0.93	0.86	0.89	0.87	0.85	0.85	0.87
Er	2.45	2.10	2.30	2.35	2.24	2.26	2.17	2.25	2.09	2.08
Tm	0.30	0.35	0.25	0.28	0.30	0.32	0.29	0.31	0.31	0.31
Yb	2.02	2.12	2.13	2.26	1.83	2.01	1.84	1.78	1.93	1.87
Lu	0.31	0.24	0.26	0.30	0.24	0.25	0.23	0.26	0.27	0.25
Hf	3.93	3.37	3.15	2.88	3.38	3.53	3.14	3.40	3.35	3.04
Ta	0.63	0.54	0.55	0.61	0.54	0.59	0.76	0.76	0.73	0.76
Pb	0.56	0.44	0.55	0.87	0.76	0.76	0.68	0.76	0.68	0.65
U	0.30	0.17	0.26	0.30	0.22	0.26	0.30	0.28	0.26	0.24
Temp(^{o}C)	1166	1163	1167	1163	1164	1162	1162	1159	1165	1164
Mg#	59	57	59	56	57	57	57	56	57	56

Table 5: 1959-60 Kīlauea Iki and Kapoho eruption matrix glass compositions

Sample	E1-g02	E1-g04	E1-g09	E1-og07	E1-og09	E2-g02	E2-g03	E3-g01	E3-g03	E5-g01	E5-g03	E6-g02	E6-g03	E7-g01	E7-g02
SiO_2	49.80	49.54	49.36	50.01	49.84	50.14	49.41	50.29	49.74	49.56	49.90	49.63	49.89	49.25	49.56
TiO_2	2.54	2.57	2.60	2.54	2.58	2.93	2.74	2.94	2.97	2.86	2.87	2.81	2.90	2.80	2.80
Al_2O_3	12.29	12.30	12.11	12.36	12.26	13.36	12.91	13.14	13.19	13.17	13.23	13.30	13.25	12.79	12.92
Cr_2O_3	0.09	0.09	0.09	0.09	0.09	0.04	0.07	0.03	0.02	0.05	0.05	0.04	0.04	0.05	0.07
FeO	11.84	11.95	11.47	11.05	11.96	11.28	11.44	11.41	11.41	10.97	11.53	11.02	11.38	11.28	11.11
MnO	0.18	0.15	0.18	0.18	0.17	0.17	0.16	0.16	0.16	0.17	0.17	0.18	0.18	0.17	0.17
MgO	10.12	10.14	10.28	9.93	10.11	7.17	8.72	7.45	7.36	7.87	7.68	7.55	7.67	8.53	8.46
CaO	11.17	11.10	11.39	11.42	11.20	11.36	11.25	11.48	11.44	11.22	11.46	11.45	11.34	11.28	11.24
Na_2O	2.22	2.16	2.28	2.23	2.28	2.39	2.35	2.47	2.53	2.39	2.42	2.41	2.47	2.38	2.32
NiO	0.03	0.03	0.03	0.02	0.04	0.01	0.02	0.02	0.02	0.03	0.03	0.02	0.00	0.03	0.02
K_2O	0.54	0.57	0.60	0.55	0.49	0.61	0.63	0.60	0.59	0.61	0.60	0.59	0.62	0.58	0.55
P_2O_5	0.26	0.27	0.26	0.26	0.25	0.29	0.27	0.30	0.29	0.29	0.29	0.28	0.29	0.29	0.29
F ppm	576	638	594	543	648	602	553	609	662	566	654	613	676	578	541
Cl ppm	149	168	142	129	150	146	139	175	216	151	141	154	168	156	127
S ppm	168	171	166	157	157	134	84	170	157	159	101	147	160	140	63
Total	101.18	100.98	100.77	100.75	101.38	99.85	100.04	100.40	99.83	99.28	100.31	99.37	100.15	99.53	99.58
H_2O wt%	0.09	n.d	n.d	0.08	0.08	0.08	0.07	0.11	n.d	0.07	n.d	0.07	0.08	n.d	0.07
Sc	29.03	28.43	29.78	30.53	27.95	30.14	29.64	29.97	30.24	30.97	30.83	26.97	29.15	27.96	27.48
V	300.07	285.62	274.68	304.09	299.51	325.27	314.49	321.01	319.06	316.06	322.82	311.14	324.63	305.67	308.67
Rb	9.64	9.76	9.53	10.15	9.90	11.44	11.13	11.70	10.96	10.76	11.05	11.27	11.49	10.13	10.52
Sr	363.88	343.77	325.45	362.36	359.38	394.79	380.14	395.35	395.69	372.45	392.52	394.35	395.94	369.56	371.49
Y	19.29	18.40	21.16	20.15	19.43	23.03	21.71	23.25	22.96	22.03	23.20	21.05	20.72	20.49	19.72
Zr	130.02	125.96	142.28	136.81	135.25	154.79	141.53	156.07	153.87	156.89	157.52	148.72	146.22	143.69	141.04
Nb	14.96	14.45	15.35	15.33	15.16	16.86	16.23	16.65	16.95	16.16	16.87	17.11	17.11	15.80	15.89
Ba	128.45	116.85	122.88	126.73	126.53	147.51	139.72	147.05	144.24	142.40	144.93	151.36	149.68	132.45	137.88
La	15.45	15.27	16.18	15.81	15.28	17.37	16.35	16.85	16.90	16.59	16.72	18.06	17.03	16.17	15.98
Ce	36.75	35.23	36.57	36.44	35.80	39.98	38.82	39.59	39.17	37.83	39.70	41.93	40.89	37.23	37.76
Pr	4.93	4.62	4.66	4.94	4.92	5.36	5.17	5.35	5.33	5.11	5.23	5.74	5.47	5.02	5.16
Nd	22.01	24.00	24.47	22.92	21.93	24.41	23.81	25.12	24.67	24.28	23.95	26.38	25.73	24.63	22.71
Sm	5.39	5.02	5.43	5.61	5.35	5.99	5.92	5.96	6.35	5.93	6.08	6.35	6.08	5.60	5.72
Eu	2.07	1.90	1.76	1.98	1.84	2.20	2.05	2.18	2.11	2.10	2.19	2.37	2.18	1.98	2.02
Gd	5.07	4.71	5.57	5.19	4.96	5.49	5.37	5.68	5.58	5.55	5.39	5.97	5.38	5.20	4.77
Tb	0.81	0.81	0.88	0.84	0.75	0.88	0.84	0.92	0.92	0.90	0.93	0.95	0.90	0.80	0.84
Dy	4.47	4.44	4.45	4.53	4.48	5.06	4.84	5.18	4.99	5.01	5.00	5.11	4.91	4.41	4.68
Ho	0.88	0.79	0.78	0.90	0.80	0.94	0.90	0.99	0.97	0.94	0.97	0.99	0.93	0.83	0.88
Er	2.08	2.10	2.19	2.09	1.92	2.23	2.34	2.37	2.30	2.33	2.34	2.41	2.33	2.04	1.98
Tm	0.27	0.26	0.25	0.30	0.26	0.32	0.30	0.31	0.28	0.29	0.31	0.31	0.29	0.27	0.26
Yb	1.88	1.76	1.92	1.84	1.69	2.07	1.97	2.07	1.92	1.89	1.99	2.04	1.89	1.77	1.69
Lu	0.25	0.25	0.29	0.24	0.23	0.27	0.27	0.28	0.27	0.26	0.27	0.30	0.26	0.26	0.24
Hf	3.59	3.61	3.67	3.93	3.38	4.04	4.04	4.24	4.20	4.11	4.25	4.47	3.99	3.42	3.59
Ta	0.94	0.81	0.86	0.95	0.90	1.00	0.99	1.04	1.03	0.96	1.05	1.09	1.03	0.92	0.95
Pb	0.91	1.17	1.31	1.15	1.01	1.05	1.80	1.15	1.03	1.25	1.01	1.33	1.13	1.19	1.48
U	0.46	0.39	0.46	0.41	0.40	0.44	0.42	0.44	0.44	0.43	0.45	0.51	0.48	0.44	0.44
Temp(^{o}C)	1217	1218	1221	1214	1217	1158	1189	1164	1162	1172	1168	1166	1168	1185	1184
Mg#	63	63	64	64	63	56	60	56	56	59	57	58	57	60	60

Table 5: 1959-60 Kīlauea Iki and Kapoho eruption matrix glass compositions (cont'd)

Sample	E8-g02	E8-g03	E10-g01	E10-g02	E15-g01	E15-g04	11-g01	E16-g01	E16-g02	12-g01	12-g02	12-g05	KO-g01	KO-g02
SiO_2	49.29	49.67	49.56	49.87	50.13	50.00	50.28	48.49	50.14	49.72	49.37	50.34	50.88	51.13
TiO_2	2.77	2.79	2.78	2.80	2.79	2.80	2.86	2.98	2.87	2.90	2.92	2.81	3.17	3.24
Al_2O_3	12.98	13.12	12.85	12.75	12.87	12.81	13.37	13.12	13.39	13.07	13.17	12.76	13.82	13.68
Cr_2O_3	0.05	0.05	0.06	0.05	0.06	0.05	0.04	0.05	0.04	0.05	0.04	0.06	0.03	0.03
FeO	11.67	11.36	11.26	11.14	10.96	11.05	11.36	12.56	11.33	11.07	11.54	11.77	10.74	11.02
MnO	0.17	0.16	0.17	0.16	0.18	0.17	0.18	0.20	0.16	0.17	0.17	0.19	0.18	0.15
MgO	8.38	7.94	8.62	8.70	8.64	8.67	7.31	7.86	7.25	7.33	7.25	8.22	6.27	6.31
CaO	10.99	11.35	11.17	11.09	11.50	11.30	11.25	12.14	11.50	11.23	11.27	11.27	10.06	10.28
Na_2O	2.35	2.38	2.29	2.32	2.44	2.38	2.24	2.18	2.47	2.42	2.49	2.15	3.09	2.87
NiO	0.02	0.01	0.01	0.04	0.03	0.04	0.01	0.03	0.00	0.02	0.03	0.03	0.00	0.02
K_2O	0.59	0.62	0.57	0.59	0.59	0.59	0.59	0.46	0.63	0.62	0.61	0.59	0.71	0.70
P_2O_5	0.29	0.29	0.28	0.28	0.28	0.28	0.29	0.29	0.30	0.29	0.30	0.27	0.36	0.36
F ppm	714	630	589	577	674	625	599	558	645	617	627	364	691	721
Cl ppm	172	142	177	158	268	213	124	111	177	135	148	101	154	183
S ppm	99	79	126	129	120	125	127	35	135	90	173	-5000	157	196
Total	99.64	99.81	99.71	99.92	100.58	100.25	99.87	100.43	100.18	98.98	99.25	100.51	99.43	99.92
H_2O wt%	0.06	n.d	0.07	n.d	0.07	0.09	0.09	n.d	0.08	0.11	n.d	n.d	0.07	0.07
Sc	29.82	29.29	28.38	27.02	30.67	29.50	30.13	30.94	28.82	30.52	31.09	28.64	24.33	27.16
V	303.15	311.08	305.71	311.24	319.67	316.56	349.20	352.86	322.59	323.23	331.64	299.49	302.73	341.62
Rb	9.75	10.85	10.55	10.41	10.80	11.23	14.85	11.68	10.75	11.48	11.73	8.92	11.04	12.63
Sr	350.83	384.45	364.15	371.40	398.65	384.67	562.81	415.93	372.84	414.43	441.11	356.14	363.38	375.51
Y	20.17	20.66	19.48	19.52	22.62	22.78	30.34	22.64	22.50	24.66	25.70	19.72	24.06	26.42
Zr	131.97	141.56	133.02	129.38	146.66	153.81	214.25	162.15	148.52	173.41	172.07	140.55	161.27	184.64
Nb	14.81	15.95	16.08	16.00	16.37	16.75	30.71	18.16	16.66	21.86	22.48	14.80	16.35	18.90
Ba	128.81	144.43	131.55	132.20	139.90	143.17	264.06	154.66	142.43	167.99	165.12	129.73	141.47	154.46
La	14.81	16.57	15.95	15.61	16.02	16.20	28.01	17.76	15.58	18.30	17.59	15.72	17.21	19.61
Ce	35.18	38.19	37.37	36.90	38.55	38.50	68.23	41.74	37.86	43.98	42.58	35.43	39.58	44.21
Pr	4.74	5.02	4.94	4.96	5.25	5.21	9.80	5.68	5.13	6.46	6.19	4.47	5.53	5.95
Nd	21.23	24.04	22.78	21.98	24.48	24.35	44.24	26.63	23.84	29.87	27.04	24.23	24.25	28.19
Sm	5.23	5.69	5.77	5.71	6.11	6.14	10.96	6.36	5.75	6.83	6.61	5.31	6.41	7.04
Eu	1.92	2.18	2.08	2.03	2.15	2.04	3.68	2.30	2.10	2.17	2.15	1.84	2.29	2.40
Gd	4.70	4.91	4.89	4.84	5.26	5.52	10.44	5.56	5.38	6.06	6.01	5.12	5.54	6.14
Tb	0.80	0.89	0.83	0.75	0.93	0.87	1.55	0.88	0.83	0.93	0.93	0.78	0.93	0.99
Dy	4.59	4.62	4.26	4.32	4.65	5.10	8.02	4.96	4.59	5.14	5.62	4.38	5.22	5.93
Ho	0.81	0.92	0.85	0.81	0.94	0.96	1.68	0.96	0.89	1.07	1.05	0.80	0.94	1.08
Er	2.01	2.07	2.05	2.05	2.18	2.29	4.27	2.38	2.04	2.57	2.45	1.88	2.43	2.65
Tm	0.27	0.26	0.27	0.29	0.30	0.30	0.53	0.30	0.31	0.37	0.34	0.29	0.37	0.33
Yb	1.80	1.92	1.83	1.70	1.92	1.85	3.64	1.93	1.96	2.15	2.04	1.93	2.13	2.26
Lu	0.24	0.25	0.24	0.21	0.28	0.27	0.46	0.26	0.24	0.31	0.26	0.25	0.29	0.31
Hf	3.62	3.80	3.73	3.46	4.08	4.16	7.59	4.06	3.92	4.51	4.97	3.81	4.10	4.79
Ta	0.90	1.00	0.91	0.91	1.00	1.04	2.50	1.08	1.01	1.42	1.34	0.95	0.91	1.15
Pb	1.05	0.97	1.10	1.12	1.10	0.88	2.81	1.13	0.98	1.48	1.71	0.82	2.00	1.66
U	0.40	0.41	0.42	0.40	0.41	0.42	1.00	0.43	0.40	0.50	0.59	0.31	0.46	0.50
Temp(^{o}C)	1182	1174	1187	1189	1188	1188	1161	1172	1160	1161	1160	1179	1140	1141
Mg#	59	58	60	61	61	61	56	55	56	57	55	58	54	53

Table 6: Lō`ihi seamount matrix glass compositions

Sample	L-g01	L-g02	L-g09	L-g12	L-g13	L-og24	L-og28	L-og37	L-og39	L-og41	L-og42
SiO_2	48.56	48.61	49.02	48.32	48.87	48.71	48.18	48.33	49.12	48.73	48.83
TiO_2	2.86	2.91	2.91	2.84	2.84	2.90	2.82	2.87	2.87	2.88	2.92
Al_2O_3	12.23	12.16	11.83	12.16	12.15	12.46	12.39	12.06	12.22	11.99	12.00
Cr_2O_3	0.06	0.06	0.05	0.05	0.06	0.07	0.07	0.04	0.07	0.06	0.06
FeO	11.95	11.70	12.12	11.78	12.16	12.17	11.88	11.32	12.37	12.08	11.81
MnO	0.19	0.19	0.17	0.17	0.19	0.18	0.19	0.17	0.18	0.18	0.18
MgO	8.40	8.17	8.45	8.20	8.44	8.23	8.18	8.32	8.42	8.44	8.35
CaO	11.44	11.42	11.64	11.31	11.46	11.24	11.29	11.61	11.38	11.26	11.50
Na_2O	2.34	2.29	2.30	2.25	2.30	2.25	2.24	2.31	2.31	2.33	2.36
NiO	0.02	0.01	0.01	0.02	0.01	0.00	0.03	0.01	0.02	b.d	b.d
K_2O	0.76	0.75	0.75	0.77	0.75	0.76	0.78	0.72	0.74	0.76	0.79
P_2O_5	0.28	0.28	0.27	0.29	0.28	0.29	0.29	0.28	0.29	0.28	0.27
F ppm	954	839	942	938	865	945	1003	907	909	930	902
Cl ppm	468	444	456	464	451	459	445	452	464	480	459
S ppm	886	840	833	913	892	928	898	881	913	860	853
Total	99.42	98.86	99.83	98.48	99.81	99.59	98.65	98.36	100.32	99.33	99.37
H_2O wt%	0.70	0.71	0.69	0.70	0.67	0.71	0.67	0.69	0.66	0.64	0.68
Sc	28.81	31.96	31.13	29.89	32.31	29.18	28.75	30.00	32.08	29.78	29.86
V	317.94	325.85	339.26	329.82	339.36	323.95	334.48	326.35	331.45	317.48	316.87
Rb	15.78	16.07	16.63	16.30	17.36	16.45	15.96	16.10	16.44	15.97	15.35
Sr	467.13	505.16	522.69	503.60	542.46	509.44	501.83	518.27	502.49	496.04	483.85
Y	17.83	19.23	21.99	20.33	21.81	19.30	19.02	18.91	21.02	20.75	20.05
Zr	160.40	165.37	194.98	177.67	207.87	184.73	172.25	166.08	202.45	188.99	184.88
Nb	33.98	34.61	35.94	34.35	36.71	34.61	34.41	34.08	34.98	33.10	32.95
Ba	226.74	235.37	247.95	235.72	246.45	231.25	244.23	234.44	246.75	221.47	218.52
La	31.93	32.93	35.57	33.63	35.60	33.69	34.73	32.40	35.61	33.07	32.83
Ce	73.86	73.57	79.26	76.57	78.94	76.29	78.73	72.33	79.48	73.05	70.91
Pr	9.26	9.45	10.31	9.60	10.15	9.46	9.66	9.44	9.91	9.30	8.95
Nd	33.15	36.23	38.91	36.64	37.83	35.78	36.27	34.58	36.89	35.60	33.76
Sm	5.94	5.61	6.60	6.11	6.39	6.59	6.68	5.89	5.80	5.86	5.65
Eu	1.76	1.87	2.22	1.93	2.06	1.94	2.05	1.81	2.06	1.92	1.90
Gd	4.86	5.11	5.17	5.29	5.09	4.47	5.14	5.33	5.55	5.23	5.03
Tb	0.62	0.71	0.80	0.81	0.80	0.72	0.76	0.62	0.65	0.74	0.70
Dy	3.72	3.97	4.61	4.59	4.56	4.21	4.41	3.64	4.56	4.41	3.94
Ho	0.69	0.73	0.85	0.80	0.96	0.82	0.76	0.70	0.91	0.73	0.78
Er	1.80	1.98	2.13	2.07	2.27	1.92	1.99	1.70	2.07	1.98	2.04
Tm	0.23	0.25	0.31	0.27	0.29	0.26	0.27	0.23	0.30	0.27	0.25
Yb	1.47	1.55	1.76	1.78	1.69	1.72	1.62	1.36	1.59	1.66	1.62
Lu	0.19	0.22	0.26	0.26	0.26	0.23	0.24	0.21	0.25	0.24	0.23
Hf	3.58	3.92	4.80	4.61	4.83	4.65	4.57	3.67	4.90	4.82	4.26
Ta	1.78	1.90	2.33	2.12	2.16	2.07	2.22	1.84	2.15	1.98	1.92
Pb	2.28	2.42	2.59	2.81	2.71	2.49	2.63	2.41	2.90	2.50	2.42
U	0.73	0.75	0.75	0.74	0.79	0.81	0.77	0.72	0.75	0.77	0.70
Temp(^{o}C)	1183	1178	1184	1179	1184	1179	1178	1181	1183	1184	1182
Mg#	58	58	58	58	58	57	58	59	57	58	58

Table 7: Prehistoric and historical (1400–1885 AD) Kīlauea melt inclusion compositions

Sample	1400-02m1	1400-04m1	1400-32m1	1400-36m1	1400-51m1	1445-A17m1	1445-A17m2	1445-A19m1	1445-A26m1	1445-A26m2	1445-A29m1
SiO_2	50.13	50.01	50.03	49.50	50.24	51.19	50.33	51.22	51.14	50.91	51.40
TiO_2	2.38	2.35	2.39	2.45	2.37	2.41	2.41	2.44	2.51	2.37	2.40
Al_2O_3	12.86	12.70	12.72	12.81	12.72	12.89	13.37	13.15	13.05	13.24	13.05
Cr_2O_3	0.05	0.06	0.04	0.09	0.05	0.07	0.05	0.04	0.04	0.05	0.05
Fe_2O_3	0.83	0.85	0.85	0.86	0.86	0.89	0.87	0.89	0.90	0.87	0.88
FeO	10.59	10.60	10.58	10.56	10.57	10.54	10.62	10.54	10.56	10.55	10.55
MnO	0.20	0.18	0.20	0.19	0.18	0.19	0.20	0.18	0.19	0.20	0.18
MgO	8.99	9.27	8.96	9.59	9.04	7.89	7.94	7.82	7.86	7.91	7.93
CaO	10.65	10.67	11.02	10.82	10.70	11.09	11.53	10.75	10.74	10.95	10.64
Na_2O	2.18	2.24	2.15	2.13	2.26	2.14	2.05	2.25	2.24	2.26	2.19
NiO	b.d	0.001	b.d	0.016	0.028	0.016	b.d	0.007	0.016	0.013	0.005
K_2O	0.44	0.40	0.45	0.40	0.42	0.39	0.32	0.39	0.44	0.35	0.39
P_2O_5	0.25	0.23	0.24	0.24	0.24	0.23	0.22	0.23	0.23	0.25	0.23
F ppm	465	559	411	486	422	484	616	470	454	519	395
Cl ppm	113	117	138	104	119	91	83	82	105	65	104
S ppm	1280	1209	1253	1434	1146	196	357	223	196	325	212
Total	98.85	99.88	98.93	99.99	99.95	100.02	99.05	100.01	100.01	100.02	99.99
CO_2 ppm	238	165	n.d	261	283	b.d	144	69	101	65	138
H_2O wt%	0.46	0.43	0.37	0.37	0.36	0.09	0.09	0.10	0.10	0.11	0.10
Sc	24.63	28.42	26.87	29.13	28.44	27.58	26.87	29.02	31.39	30.19	31.03
V	287.92	274.37	276.66	291.47	267.66	296.17	269.88	275.83	265.56	301.77	301.78
Rb	6.55	5.31	6.40	4.72	6.91	6.92	5.68	4.87	6.27	6.32	7.42
Sr	322.23	289.41	283.33	327.82	319.81	296.43	272.93	272.07	309.97	329.39	286.04
Y	19.71	19.72	20.77	18.93	21.69	24.24	23.72	22.98	22.08	22.90	21.84
Zr	126.01	116.33	114.76	108.95	135.15	122.29	119.37	128.44	127.34	127.63	112.65
Nb	11.85	9.91	10.74	9.89	10.96	9.37	9.68	8.77	10.55	9.03	10.29
Ba	69.02	70.51	49.77	62.32	70.35	75.05	66.47	74.08	84.11	83.97	78.34
La	11.57	10.74	10.32	8.57	11.00	9.91	8.65	9.37	8.92	10.53	10.25
Ce	29.74	27.41	26.57	25.84	26.45	23.31	24.31	23.28	23.52	24.20	24.63
Pr	4.12	3.77	3.54	4.25	3.71	2.96	4.14	3.32	3.28	3.74	4.07
Nd	21.36	18.77	20.31	27.94	19.71	16.78	14.21	15.59	19.91	15.48	16.77
Sm	5.34	4.22	4.48	6.14	4.78	5.13	4.16	5.12	4.38	4.44	5.22
Eu	1.90	2.06	1.70	2.78	1.88	1.94	1.27	1.53	1.46	1.61	1.65
Gd	4.28	4.59	5.28	5.99	4.64	3.93	4.41	4.26	4.98	4.77	5.47
Tb	0.58	0.82	0.89	0.76	0.74	0.89	0.74	0.82	0.79	0.79	0.84
Dy	4.65	4.91	4.42	4.10	4.50	4.73	4.29	4.71	4.96	4.60	5.08
Ho	0.88	0.90	0.78	0.79	0.84	0.96	0.77	0.95	0.83	1.01	0.98
Er	1.73	1.74	2.14	2.82	2.06	2.93	1.73	2.13	2.15	2.34	2.34
Tm	0.32	0.33	0.24	0.17	0.26	0.20	0.13	0.30	0.30	0.32	0.31
Yb	1.81	1.50	2.20	1.51	1.90	1.88	1.83	1.51	1.81	1.80	2.07
Lu	0.23	0.27	0.20	0.28	0.23	0.20	0.26	0.26	0.26	0.29	0.24
Hf	3.90	3.02	3.29	2.23	3.66	3.53	3.28	3.65	3.84	3.49	4.57
Ta	0.47	0.59	0.71	0.53	0.64	0.79	0.45	0.61	0.57	0.62	0.47
Pb	b.d	0.99	0.82	b.d	0.62	0.52	0.79	1.06	1.20	0.78	0.83
U	0.29	0.23	0.30	0.26	0.31	0.19	0.24	0.26	0.24	0.23	0.08
Fo mol%	82.7	83.2	82.7	83.8	82.9	80.5	80.6	80.4	80.5	80.6	80.5
Ol %	8.02	7.75	14.86	12.95	8.01	4.64	6.62	4.07	4.94	4.65	5.26

Table 7: Prehistoric and historical (1400–1885 AD) Kīlauea melt inclusion compositions (cont'd)

Sample	1445-A29m2	1445-A32m1	1445-A34m1	1445-A41m1	1445-A44m1	1445-A45m1	1500-101m1	1500-104m1	1500-105m1	1500-108m1	1500-1b8m1
SiO_2	50.94	50.94	51.15	50.97	51.03	51.20	50.43	50.25	50.29	50.41	49.10
TiO_2	2.45	2.46	2.44	2.65	2.45	2.48	2.46	2.45	2.37	2.25	2.14
Al_2O_3	13.22	13.07	12.99	12.83	13.17	13.41	12.71	12.95	12.82	12.72	10.99
Cr_2O_3	0.07	0.04	0.04	0.05	0.05	0.04	0.05	0.05	0.05	0.04	0.16
Fe_2O_3	0.88	0.89	0.91	0.93	0.89	0.90	0.84	0.83	0.83	0.83	1.39
FeO	10.54	10.53	10.59	10.50	10.61	10.53	10.58	10.59	10.59	10.60	10.08
MnO	0.19	0.16	0.19	0.20	0.19	0.19	0.20	0.18	0.19	0.19	0.18
MgO	7.88	7.99	8.04	8.35	7.81	7.91	8.83	8.68	9.00	9.39	14.20
CaO	10.86	10.96	10.71	10.49	10.90	10.20	10.69	10.69	10.64	10.44	9.28
Na_2O	2.29	2.22	2.23	2.31	2.22	2.38	2.17	2.26	2.21	2.19	1.87
NiO	0.020	0.011	0.009	b.d	0.017	0.005	0.014	0.014	0.015	0.025	0.033
K_2O	0.36	0.41	0.41	0.41	0.37	0.43	0.41	0.42	0.38	0.33	0.39
P_2O_5	0.23	0.23	0.22	0.23	0.23	0.25	0.23	0.23	0.21	0.21	0.24
F ppm	401	495	369	451	525	415	296	402	426	383	303
Cl ppm	99	99	94	85	77	107	94	133	101	93	104
S ppm	269	199	221	187	238	476	1024	1495	1393	1414	720
Total	100.02	100.01	100.02	99.00	100.03	100.07	99.85	99.94	99.93	99.95	100.22
CO_2 ppm	102	149	b.d	b.d	b.d	133	256	317	333	290	b.d
H_2O wt%	0.11	0.10	0.08	0.09	0.09	0.08	0.41	0.42	0.42	0.41	n.d
Sc	32.14	27.67	28.38	27.96	31.25	37.65	25.28	27.90	30.67	30.13	23.76
V	404.08	278.66	287.68	291.32	289.37	283.43	251.93	293.28	270.54	298.82	254.40
Rb	7.50	5.56	6.45	6.30	7.65	5.62	5.67	7.57	8.27	7.06	7.61
Sr	286.66	272.49	296.34	296.01	310.40	289.05	252.44	368.87	236.42	323.29	271.51
Y	25.75	23.32	24.13	24.60	23.27	26.77	19.41	26.64	19.65	21.49	19.66
Zr	141.36	135.36	137.07	124.83	129.56	144.36	102.80	150.97	113.70	150.11	114.23
Nb	9.64	9.26	9.53	9.58	10.61	11.41	10.02	13.93	14.54	13.98	10.28
Ba	97.30	90.62	84.29	83.89	84.46	107.30	79.78	105.26	67.47	69.63	48.53
La	12.57	9.50	10.79	10.97	10.65	11.89	10.12	13.93	11.50	11.61	10.80
Ce	26.96	27.93	22.23	24.79	27.63	26.63	26.39	36.96	27.36	27.50	26.67
Pr	3.60	2.88	3.37	3.80	3.99	4.20	4.00	5.53	4.64	3.96	3.57
Nd	16.71	19.61	17.79	18.71	20.33	17.24	19.62	25.47	23.93	17.30	17.64
Sm	5.88	4.35	4.85	5.49	5.91	6.33	5.47	6.81	4.14	3.81	4.12
Eu	1.96	1.69	1.79	1.82	1.89	2.38	1.71	2.51	1.44	1.78	1.89
Gd	6.73	4.51	5.39	5.77	5.47	4.27	4.31	6.73	5.63	3.95	4.94
Tb	0.87	0.83	0.89	0.83	0.83	0.81	1.06	1.18	0.58	0.57	0.86
Dy	4.99	5.08	5.20	4.74	5.26	4.15	4.83	8.24	3.83	4.22	5.35
Ho	0.95	0.87	0.91	0.99	1.00	1.08	0.97	1.12	0.92	0.84	0.84
Er	2.49	2.22	1.92	2.37	2.39	2.24	2.57	3.48	2.12	2.12	2.07
Tm	0.44	0.29	0.33	0.34	0.40	0.31	0.25	0.67	0.26	0.22	0.32
Yb	2.10	2.06	1.98	2.05	2.15	1.92	1.70	2.58	1.08	2.00	1.97
Lu	0.32	0.21	0.29	0.27	0.28	0.28	0.26	0.43	0.15	0.28	0.27
Hf	3.40	3.80	3.03	4.04	3.75	4.47	3.84	6.01	2.93	3.39	3.85
Ta	0.61	0.57	0.42	0.58	0.59	0.65	0.74	1.13	0.55	0.69	0.56
Pb	b.d	1.16	0.58	0.79	0.37	0.96	0.46	1.21	0.28	0.62	0.66
U	0.28	0.23	0.27	0.31	0.24	0.09	0.34	0.64	0.33	0.23	0.28
Fo mol%	80.5	80.8	80.7	81.6	80.2	80.6	82.4	82.2	82.7	83.3	89.0
Ol %	4.34	4.1	6.08	5.59	4.85	11.7	5.59	3.79	5.72	7.15	18.98

Table 7: Prehistoric and historical (1400–1885 AD) Kīlauea melt inclusion compositions (cont'd)

Sample	1500-117m1	1500-122m1	1500-122m2	1500-124m1	1500-BR01m1	1500-BR02m1	1500-BR21m1	1500-BR22m2	1500-BR22m1	1550-06m1	1550-01m1
SiO_2	50.08	50.42	50.07	50.33	49.13	48.48	50.08	48.34	48.67	49.37	48.72
TiO_2	2.41	2.37	2.44	2.38	2.22	1.98	2.47	1.99	2.14	2.21	2.12
Al_2O_3	12.69	12.97	13.07	12.79	11.97	11.03	13.03	11.35	11.41	11.86	11.04
Cr_2O_3	0.05	0.04	0.05	0.04	0.06	0.07	0.03	0.09	0.07	0.10	0.17
Fe_2O_3	0.85	0.83	0.84	0.87	1.23	1.10	0.82	1.08	1.05	0.91	1.41
FeO	10.62	10.59	10.59	10.62	10.23	10.34	10.60	10.36	10.39	10.51	10.07
MnO	0.19	0.19	0.18	0.21	0.18	0.15	0.20	0.17	0.16	0.19	0.17
MgO	9.23	8.80	8.66	8.89	11.96	14.73	8.45	14.39	13.67	11.93	14.30
CaO	10.72	10.40	10.71	10.41	10.35	9.57	11.03	9.47	9.51	9.67	9.49
Na_2O	2.16	2.30	2.38	2.45	2.12	1.73	2.18	1.92	1.94	2.08	1.90
NiO	0.026	0.006	0.019	0.028	0.015	0.035	0.010	0.038	0.026	0.026	0.037
K_2O	0.39	0.45	0.39	0.42	0.34	0.31	0.42	0.30	0.40	0.40	0.37
P_2O_5	0.24	0.22	0.22	0.23	0.22	0.19	0.24	0.22	0.28	0.22	0.26
F ppm	313	385	376	419	358	310	429	331	329	388	371
Cl ppm	111	87	81	93	116	97	158	159	128	111	127
S ppm	951	1488	1444	1015	1260	830	1485	1077	1124	1438	761
Total	99.87	99.93	99.95	99.91	100.31	99.93	99.93	99.97	99.98	99.82	100.24
CO_2 ppm	n.d	238	291	207	n.d	87	262	106	58	n.d	n.d
H_2O wt%	0.39	0.42	0.41	0.38	n.d	0.31	0.44	0.34	0.32	0.54	n.d
Sc	27.91	21.29	27.65	24.48	26.30	20.82	26.41	17.31	22.58	21.96	25.58
V	276.92	305.66	294.25	270.04	260.07	248.18	290.32	236.91	262.66	255.77	262.99
Rb	7.83	7.44	7.87	7.26	6.46	5.36	6.21	3.56	8.15	5.27	5.33
Sr	315.19	347.81	380.51	257.48	287.05	260.45	281.12	235.35	296.71	276.08	229.13
Y	22.55	26.13	25.14	19.62	21.74	21.28	22.49	19.05	19.33	20.07	17.61
Zr	129.62	160.25	151.59	156.26	124.91	122.90	119.07	96.71	127.10	119.08	103.29
Nb	9.35	13.85	14.44	11.43	9.01	8.72	10.19	9.43	10.84	9.97	7.55
Ba	80.82	100.82	101.40	66.93	54.53	22.25	73.55	24.93	40.89	71.31	73.47
La	11.68	11.56	13.99	7.81	10.56	9.61	10.40	8.91	12.27	10.60	9.64
Ce	25.63	32.09	33.83	22.52	27.00	23.33	24.19	24.45	28.48	21.73	20.21
Pr	3.98	5.41	5.07	2.73	3.81	3.44	3.51	2.72	3.97	3.82	2.79
Nd	21.44	26.37	22.14	16.26	19.96	15.79	18.49	15.28	20.03	11.98	15.64
Sm	5.39	8.25	5.88	3.37	5.23	4.49	5.72	3.66	5.08	4.28	4.18
Eu	2.02	2.00	1.94	1.18	2.04	1.54	2.03	1.70	1.83	1.69	1.43
Gd	5.07	5.92	6.64	4.58	5.47	4.52	4.93	3.93	4.90	3.79	4.56
Tb	0.95	0.93	0.93	0.70	0.92	0.81	0.79	0.71	0.87	0.64	0.56
Dy	5.03	5.71	5.54	4.58	5.61	4.17	4.44	3.37	4.53	4.37	3.79
Ho	1.00	1.13	1.28	0.97	1.01	0.76	0.91	0.66	0.94	0.87	0.92
Er	2.25	2.38	2.78	1.86	2.18	2.05	2.25	2.21	2.07	2.41	1.87
Tm	0.30	0.39	0.37	0.31	0.34	0.30	0.23	0.29	0.29	0.25	0.20
Yb	2.00	1.74	2.89	1.90	2.21	1.60	1.85	1.36	1.85	1.21	1.95
Lu	0.28	0.36	0.38	0.19	0.29	0.27	0.25	0.19	0.24	0.22	0.22
Hf	3.56	4.37	5.53	3.37	3.58	2.82	4.01	2.69	3.34	3.63	2.77
Ta	0.62	0.70	1.12	0.26	0.64	0.65	0.45	0.39	0.77	0.83	0.51
Pb	0.59	1.07	1.61	b.d	0.76	0.67	0.52	0.54	1.09	1.00	0.86
U	0.28	0.46	0.47	0.16	0.35	0.20	0.25	0.18	0.35	0.48	0.27
Fo mol%	83.1	82.4	82.3	82.6	87.1	89.2	81.8	89.0	88.4	86.7	89.2
Ol %	5.3	4.11	3.59	9.49	12.53	33.74	3.78	29.6	24.49	10.33	18.28

Table 7: Prehistoric and historical (1400–1885 AD) Kīlauea melt inclusion compositions (cont'd)

Sample	1550-02m1	1550-08m1	1550-08m2	1550-b8m1	1550-13m1	1550-16m1	1550-16m2	1550-26m1	1600-614m1	1600-623m1	1600-631m1
SiO_2	49.00	49.39	49.65	49.75	48.85	52.38	51.83	50.24	50.53	50.48	50.26
TiO_2	2.14	2.11	2.13	2.32	2.23	3.25	3.40	2.31	2.29	2.55	2.58
Al_2O_3	10.78	11.91	11.51	11.63	11.03	12.32	12.07	12.69	13.01	13.54	13.36
Cr_2O_3	0.09	0.08	0.09	0.06	0.10	0.04	0.04	0.05	0.05	0.05	0.06
Fe_2O_3	1.37	1.25	1.26	1.04	1.39	0.89	0.91	0.82	0.80	1.03	0.89
FeO	10.09	10.21	10.20	10.40	10.08	10.52	10.50	10.63	10.61	10.41	10.53
MnO	0.20	0.15	0.15	0.20	0.21	0.19	0.19	0.19	0.15	0.18	0.19
MgO	13.79	12.25	12.44	11.98	13.79	7.26	7.94	9.05	8.24	7.72	7.84
CaO	10.19	9.91	9.97	9.75	9.72	8.99	8.93	10.63	10.78	10.84	11.13
Na_2O	1.76	2.14	1.99	2.09	1.98	2.71	2.77	2.21	2.33	2.44	2.35
NiO	0.029	0.021	0.046	b.d	0.037	0.034	0.035	0.024	0.036	0.031	0.014
K_2O	0.36	0.38	0.40	0.42	0.42	0.52	0.52	0.43	0.42	0.49	0.43
P_2O_5	0.23	0.21	0.22	0.22	0.20	0.31	0.30	0.22	0.26	0.26	0.25
F ppm	281	305	384	348	365	700	756	356	481	527	492
Cl ppm	99	97	89	65	82	117	112	105	122	141	141
S ppm	731	828	758	181	898	139	350	1516	1175	1129	1214
Total	100.21	100.23	100.25	98.94	100.26	99.51	99.57	99.85	99.80	100.32	100.17
CO_2 ppm	n.d	n.d	n.d	145	n.d	46	413	97	275	839	145
H_2O wt%	n.d	n.d	n.d	0.14	n.d	0.63	0.62	0.52	0.53	n.d	0.15
Sc	23.69	25.07	25.14	27.54	25.30	34.13	32.06	30.27	27.14	32.31	29.69
V	248.54	279.49	266.81	272.60	270.03	383.48	374.00	285.86	307.96	295.89	313.97
Rb	4.50	5.95	5.98	7.62	7.03	8.07	8.05	7.15	7.43	9.99	9.92
Sr	281.37	249.50	273.23	331.18	296.06	334.46	346.15	306.59	345.54	372.43	401.79
Y	18.14	19.09	19.92	28.38	22.77	34.84	33.78	24.61	20.32	25.60	28.66
Zr	101.29	88.94	116.60	164.69	122.05	189.76	141.49	153.17	150.52	142.41	150.57
Nb	10.40	8.22	8.52	15.18	9.17	13.97	10.94	13.43	13.37	13.73	18.63
Ba	89.83	78.85	80.25	68.45	90.94	109.77	105.86	89.87	90.51	97.41	122.87
La	10.78	8.30	8.86	14.08	11.24	14.07	12.01	12.22	11.81	12.28	15.79
Ce	23.69	20.96	21.58	32.32	26.07	34.34	33.86	29.51	30.00	28.86	39.09
Pr	3.29	2.89	3.21	5.06	3.70	4.84	4.36	4.38	3.95	4.53	5.98
Nd	17.79	15.27	15.32	24.24	17.07	25.06	21.20	20.26	20.80	17.89	27.77
Sm	4.95	4.07	4.58	5.93	4.89	6.74	6.68	5.67	4.21	3.81	6.56
Eu	1.87	1.60	1.65	2.36	1.63	2.11	2.25	1.98	1.84	1.78	3.38
Gd	3.77	3.85	4.09	6.79	4.49	6.29	7.90	5.05	5.81	4.70	6.95
Tb	0.81	0.63	0.71	1.02	0.70	1.07	1.20	0.88	0.66	0.76	0.97
Dy	4.69	3.74	4.00	5.72	4.78	6.91	6.94	5.66	4.34	4.51	6.26
Ho	0.87	0.79	0.76	1.10	0.91	1.48	1.40	1.09	0.90	0.81	0.99
Er	1.55	2.06	2.03	3.19	2.22	3.21	3.07	2.80	2.60	1.95	3.03
Tm	0.23	0.28	0.24	0.40	0.30	0.50	0.48	0.38	0.38	0.32	0.36
Yb	1.75	1.57	1.67	2.53	2.10	2.97	3.50	2.29	2.03	2.19	2.06
Lu	0.24	0.20	0.21	0.33	0.25	0.46	0.39	0.32	0.25	0.35	0.33
Hf	2.65	2.38	2.57	4.63	3.40	3.94	4.26	4.28	2.75	3.24	4.66
Ta	0.71	0.51	0.56	1.15	0.62	0.79	0.76	0.88	1.06	0.53	0.86
Pb	0.56	0.59	0.68	0.98	0.66	1.06	0.89	1.16	1.16	1.57	2.16
U	0.27	0.21	0.21	0.38	0.28	0.37	0.34	0.34	0.26	0.35	0.40
Fo mol%	88.7	87.4	87.5	86.8	88.8	79.1	80.8	82.7	81.3	80.6	80.7
Ol %	24.76	16.32	18.25	15.84	17.37	12.89	8.13	3.25	1.49	2.8	5.42

Table 7: Prehistoric and historical (1400–1885 AD) Kīlauea melt inclusion compositions (cont'd)

Sample	1600-641m1	1600-644m1	1700-02m1	1700-07m1	1700-13m1	1700-14m1	1700-22m1	1700-22m2	1700-25m1	1700-25m2	1700-27m1
SiO_2	50.44	50.02	50.57	50.39	50.13	51.04	49.18	49.53	49.67	49.26	50.10
TiO_2	2.34	2.42	2.29	2.63	2.43	2.14	2.28	2.39	2.26	2.27	2.20
Al_2O_3	12.87	12.88	12.38	12.02	11.83	11.85	12.81	12.44	12.41	12.71	12.59
Cr_2O_3	0.06	0.04	0.05	0.03	0.04	0.11	0.08	0.09	0.09	0.07	0.07
Fe_2O_3	0.81	0.91	1.09	1.12	1.15	1.15	0.83	0.85	0.84	0.84	0.81
FeO	10.61	10.52	10.35	10.33	10.30	10.32	10.63	10.57	10.58	10.61	10.60
MnO	0.19	0.19	0.20	0.24	0.20	0.17	0.19	0.19	0.20	0.20	0.21
MgO	8.24	9.18	9.74	9.90	10.94	10.85	9.88	10.04	10.01	9.66	9.37
CaO	11.06	10.81	10.65	10.65	10.51	9.65	10.96	10.93	10.76	10.75	10.25
Na_2O	2.25	2.21	2.04	2.07	1.94	2.04	1.99	1.97	2.07	2.23	2.28
NiO	0.032	0.013	0.039	0.005	b.d	0.061	0.022	0.009	0.010	0.015	0.020
K_2O	0.41	0.43	0.43	0.37	0.32	0.39	0.42	0.34	0.35	0.46	0.47
P_2O_5	0.23	0.25	0.22	0.26	0.21	0.30	0.26	0.23	0.27	0.38	0.37
F ppm	389	459	352	358	420	305	348	380	472	452	450
Cl ppm	110	111	100	103	101	121	104	100	75	110	142
S ppm	1562	932	843	829	602	1122	1619	1373	1586	1254	1753
Total	99.90	100.11	100.25	100.22	99.17	100.33	99.89	99.89	99.88	99.75	99.75
CO_2 ppm	238	53	n.d	n.d	n.d	n.d	151	188	242	n.d	210
H_2O wt%	0.50	0.15	n.d	n.d	n.d	n.d	0.50	0.44	0.50	0.57	0.68
Sc	26.54	28.21	28.27	29.48	28.89	22.71	28.00	28.33	26.54	27.10	30.85
V	305.70	242.01	250.28	242.24	245.13	187.30	312.64	281.86	304.56	295.94	346.82
Rb	7.17	10.21	6.72	4.60	5.49	6.96	6.57	4.62	6.06	7.52	9.54
Sr	298.04	396.11	290.85	264.62	270.84	309.43	319.71	308.05	343.40	293.82	404.54
Y	20.09	31.23	20.90	19.12	22.75	21.55	22.85	22.83	22.98	21.34	31.92
Zr	137.14	201.85	121.11	125.60	70.97	132.01	127.55	75.80	156.60	109.13	189.27
Nb	14.94	19.21	10.47	8.97	10.33	9.02	14.07	12.26	14.19	9.47	18.51
Ba	83.04	114.32	87.87	52.92	79.91	77.51	102.71	83.03	67.52	75.25	94.95
La	11.69	17.68	11.44	9.76	11.53	10.39	10.06	8.45	9.32	9.42	15.25
Ce	30.48	41.24	26.48	25.59	24.11	22.92	23.18	24.38	25.38	21.91	37.83
Pr	4.22	6.32	3.57	3.20	3.56	3.24	4.01	3.68	3.71	3.45	5.81
Nd	21.86	33.76	15.65	19.89	12.78	16.32	21.00	18.82	13.43	16.22	22.60
Sm	5.16	8.66	4.30	5.00	5.30	3.71	3.72	3.33	4.30	4.55	7.65
Eu	1.91	2.58	1.66	1.80	2.42	1.67	1.98	2.04	1.43	1.60	2.28
Gd	5.62	7.65	4.85	3.98	3.11	4.53	5.78	4.48	4.61	5.13	6.83
Tb	0.65	1.34	0.69	0.85	0.48	0.87	0.58	0.55	0.86	0.80	1.17
Dy	5.67	8.48	4.37	3.94	4.58	3.93	4.27	5.40	5.02	4.35	6.40
Ho	0.91	1.57	0.84	0.74	0.81	0.78	0.97	0.86	1.01	0.76	1.22
Er	2.40	3.86	2.04	2.13	2.16	1.62	1.85	2.35	2.39	1.90	3.35
Tm	0.21	0.54	0.28	0.25	0.30	0.23	0.25	0.36	0.34	0.30	0.48
Yb	1.84	3.78	1.84	1.25	2.09	1.49	2.01	1.86	2.07	1.54	2.66
Lu	0.28	0.37	0.22	0.23	0.29	0.16	0.28	0.32	0.30	0.21	0.39
Hf	3.71	5.42	2.98	2.65	3.25	3.46	2.86	3.08	3.87	3.22	4.56
Ta	0.92	1.87	0.61	0.33	0.57	0.56	0.61	0.61	0.80	0.58	1.03
Pb	2.30	1.80	0.69	b.d	1.71	0.86	b.d	1.67	0.84	0.61	0.90
U	0.35	0.51	0.29	0.19	0.08	0.32	0.32	0.23	0.14	0.32	0.33
Fo mol%	81.3	83.2	84.0	84.4	85.7	85.3	84.2	84.4	84.3	83.9	83.3
Ol %	3.68	8.4	8.25	4.59	11.99	9.29	3.32	5.02	8.86	7.09	6.95

Table 7: Prehistoric and historical (1400–1885 AD) Kīlauea melt inclusion compositions (cont'd)

Sample	1790-113m1	1790-114m1	1790-117m1	1790-117m2	1790-120m1	1790-140m1	1790-w01m1	1790-w01m2	1790-w04m1	1790-w04m2	1823-05m1
SiO_2	49.30	48.60	49.63	49.67	49.71	49.45	49.10	49.30	50.77	50.40	50.20
TiO_2	2.24	2.09	2.16	2.23	2.11	2.12	1.87	1.92	2.31	2.45	2.54
Al_2O_3	12.23	11.42	12.11	12.27	12.32	12.38	10.99	11.29	12.65	12.96	12.12
Cr_2O_3	0.07	0.15	0.04	0.05	0.05	0.05	0.07	0.07	0.04	0.04	0.07
Fe_2O_3	1.03	1.00	1.01	1.01	1.00	1.02	1.07	1.36	0.87	0.83	0.84
FeO	10.41	10.44	10.42	10.43	10.44	10.42	10.38	10.11	10.59	10.59	10.57
MnO	0.16	0.20	0.17	0.16	0.18	0.16	0.17	0.15	0.20	0.20	0.18
MgO	11.73	13.62	11.70	11.20	11.21	11.74	14.24	13.80	8.61	8.63	8.85
CaO	9.91	9.67	9.99	10.04	10.07	9.78	9.39	9.56	10.58	10.48	11.28
Na_2O	2.19	1.85	2.11	2.25	2.22	2.18	1.86	1.94	2.37	2.31	1.98
NiO	b.d	0.054	0.003	0.014	0.015	0.018	0.011	0.033	0.021	0.016	0.023
K_2O	0.41	0.32	0.34	0.38	0.38	0.38	0.31	0.30	0.46	0.44	0.39
P_2O_5	0.22	0.21	0.22	0.22	0.21	0.21	0.20	0.21	0.24	0.24	0.57
F ppm	496	363	533	459	517	406	351	358	499	510	616
Cl ppm	134	111	158	121	126	124	88	76	121	128	99
S ppm	351	1010	387	394	351	333	975	899	1335	1097	1379
Total	99.02	99.87	100.04	100.04	100.03	100.04	99.89	100.26	100.05	99.86	99.96
CO_2 ppm	b.d	108	b.d	47	b.d	122	43	n.d	226	27	55
H_2O wt%	0.11	0.43	0.11	0.11	0.12	0.10	0.36	n.d	0.30	0.44	0.41
Sc	21.59	24.74	21.49	22.34	21.85	20.06	21.63	27.87	28.16	26.08	27.90
V	211.34	242.93	230.84	228.87	205.90	182.54	236.17	251.91	275.39	285.41	297.16
Rb	6.44	4.69	7.72	7.22	7.34	6.41	4.99	6.90	8.03	6.84	5.42
Sr	300.29	263.44	286.87	294.73	286.45	277.68	237.74	204.40	306.44	299.57	328.08
Y	19.83	17.33	20.87	18.80	18.47	18.19	20.17	19.18	21.72	22.55	24.75
Zr	119.95	101.83	124.13	111.04	130.58	106.89	108.47	60.00	135.44	139.32	178.48
Nb	9.73	8.23	8.46	9.98	9.56	8.17	8.77	8.65	10.82	10.69	9.71
Ba	35.49	72.71	37.66	34.62	31.94	30.99	26.97	23.60	69.95	76.03	90.70
La	9.94	9.52	10.41	10.57	9.35	9.67	8.35	7.11	12.05	10.51	14.96
Ce	23.49	21.67	23.98	24.61	23.75	24.12	23.00	21.84	25.43	25.72	43.16
Pr	3.19	3.23	3.49	3.32	3.29	3.80	3.12	2.85	3.36	3.77	6.55
Nd	14.83	14.47	19.62	17.14	16.13	16.85	15.89	15.76	16.83	17.29	31.83
Sm	4.58	4.14	4.61	4.84	5.86	4.35	4.41	4.60	6.00	5.06	5.90
Eu	1.86	1.54	1.63	1.73	1.70	1.87	1.51	1.67	1.67	1.84	2.23
Gd	4.57	4.36	4.54	4.05	4.37	5.14	4.76	4.80	5.84	5.90	5.31
Tb	0.74	0.74	0.72	0.69	0.70	0.81	0.67	0.48	0.83	0.87	0.92
Dy	4.10	3.95	4.18	4.29	4.50	3.99	4.23	3.94	4.86	5.02	4.81
Ho	0.79	0.81	0.59	0.85	0.65	0.90	0.72	0.78	1.04	0.94	1.02
Er	1.98	1.75	1.96	1.86	1.75	2.13	2.00	2.48	2.32	2.03	2.15
Tm	0.26	0.28	0.18	0.26	0.28	0.25	0.33	0.27	0.29	0.33	0.33
Yb	1.64	1.66	1.74	1.71	1.60	1.56	1.52	1.85	2.05	2.06	2.27
Lu	0.26	0.24	0.21	0.27	0.33	0.33	0.19	0.30	0.30	0.31	0.29
Hf	2.90	2.37	3.63	3.20	3.22	3.37	2.30	2.07	3.13	3.35	4.91
Ta	0.61	0.46	0.54	0.54	0.61	0.56	0.47	0.30	0.58	0.57	0.66
Pb	0.43	0.79	0.69	0.72	0.65	0.59	0.70	0.36	0.50	0.88	1.47
U	0.22	0.19	0.23	0.19	0.21	0.28	0.28	0.09	0.21	0.28	0.29
Fo mol%	86.7	88.3	86.5	86.1	86.0	86.6	88.8	88.7	82.0	82.1	82.4
Ol %	28.1	1.09	28.32	25.79	26.5	27.95	30.61	30.02	6.08	5.23	1.64

Table 7: Prehistoric and historical (1400–1885 AD) Kīlauea melt inclusion compositions (cont'd)

Sample	1823-07m1	1823-07m2	1823-12m1	1832-13m1	1832-14m1	1832-16m1	1832-26m1	1832-28m1	1832-31m1	1832-34m1	1832-34m2
SiO_2	49.85	49.70	49.36	48.72	48.45	49.30	48.96	48.93	49.08	49.86	50.10
TiO_2	2.21	2.33	2.24	2.10	2.29	2.31	2.17	2.04	2.15	2.58	2.59
Al_2O_3	11.84	11.79	11.15	11.59	11.29	11.88	10.94	11.49	11.59	13.24	13.17
Cr_2O_3	0.08	0.11	0.13	0.08	0.08	0.08	0.07	0.06	0.08	0.06	0.04
Fe_2O_3	0.91	0.91	1.01	1.13	1.15	0.93	1.04	1.02	1.00	0.90	0.88
FeO	10.51	10.51	10.43	10.32	10.30	10.50	10.40	10.42	10.44	10.54	10.55
MnO	0.19	0.19	0.18	0.15	0.16	0.18	0.18	0.18	0.18	0.17	0.19
MgO	11.58	11.49	13.39	13.64	13.92	11.48	13.76	13.53	12.60	8.47	8.45
CaO	9.99	10.11	9.39	9.45	9.63	10.32	9.81	9.38	9.90	10.91	10.71
Na_2O	1.95	1.92	1.85	2.09	1.93	2.00	1.75	2.02	2.02	2.36	2.30
NiO	0.027	0.034	0.013	0.022	0.018	0.014	0.013	0.017	0.034	0.026	0.017
K_2O	0.29	0.33	0.33	0.38	0.44	0.38	0.34	0.34	0.38	0.48	0.52
P_2O_5	0.22	0.24	0.19	0.22	0.25	0.30	0.22	0.21	0.28	0.26	0.26
F ppm	361	404	433	456	416	474	466	560	485	488	561
Cl ppm	85	100	87	123	139	108	84	96	116	177	188
S ppm	1045	1323	1472	614	679	419	210	613	964	875	373
Total	99.91	99.99	100.00	100.06	100.07	99.79	99.75	99.80	99.98	100.08	99.91
CO_2 ppm	121	331	255	73	92	b.d	b.d	38	49	153	104
H_2O wt%	0.37	0.36	0.36	0.15	0.14	0.36	0.36	0.40	0.31	0.19	0.25
Sc	25.87	23.19	22.13	18.68	20.86	26.37	24.21	21.59	20.30	21.17	30.22
V	231.77	253.30	298.41	170.15	225.06	242.99	217.77	205.63	228.18	223.71	278.43
Rb	4.77	4.97	9.32	4.97	6.41	7.38	6.01	6.09	5.94	7.80	8.22
Sr	267.93	315.97	397.41	288.78	308.09	304.82	274.25	261.80	292.20	389.46	353.38
Y	19.59	20.53	33.48	19.84	18.75	21.94	19.15	19.24	20.62	21.71	20.17
Zr	108.77	133.78	155.91	125.50	124.99	133.88	125.37	124.38	108.13	154.98	142.82
Nb	10.73	11.46	14.81	12.01	14.12	13.50	11.16	11.53	12.45	13.52	14.00
Ba	77.68	84.15	55.56	31.22	30.32	43.46	27.18	30.20	36.44	82.72	85.40
La	8.75	10.42	11.45	9.03	10.63	11.35	9.44	8.85	9.62	10.93	11.55
Ce	21.07	24.47	33.94	22.37	25.30	24.20	24.61	22.41	22.34	27.73	29.01
Pr	3.75	4.19	5.31	3.54	4.03	3.89	3.96	4.13	3.74	4.37	4.64
Nd	14.19	19.25	29.78	18.12	18.93	20.06	19.80	16.82	16.31	26.06	19.27
Sm	5.61	4.34	8.03	5.11	4.74	5.00	4.13	5.92	4.39	6.75	5.08
Eu	1.77	1.93	2.45	1.54	1.43	1.58	1.53	1.86	1.75	1.98	1.68
Gd	6.40	4.98	7.19	4.56	3.89	4.25	4.37	4.06	5.17	5.87	6.18
Tb	0.57	0.68	1.08	0.70	0.67	0.86	0.72	0.65	0.70	0.99	0.78
Dy	4.83	5.09	4.83	4.25	4.27	4.88	3.97	5.36	4.21	4.38	5.00
Ho	0.87	0.91	1.05	0.79	0.70	0.94	0.82	0.72	0.64	0.90	0.92
Er	2.27	2.52	3.90	1.91	1.94	1.88	1.84	1.94	1.96	2.49	1.91
Tm	0.27	0.32	0.44	0.28	0.23	0.30	0.25	0.29	0.30	0.31	0.24
Yb	1.70	1.95	2.03	1.37	1.51	1.82	1.49	1.82	1.46	1.92	1.41
Lu	0.30	0.30	0.41	0.19	0.21	0.23	0.20	0.21	0.20	0.39	0.25
Hf	3.23	3.29	4.55	2.60	2.51	3.28	3.27	3.65	2.98	3.21	3.06
Ta	0.52	0.77	1.28	0.75	0.76	0.79	0.69	0.62	0.87	0.75	0.83
Pb	0.56	0.86	1.56	0.60	0.75	0.67	0.74	0.61	0.63	0.85	0.93
U	0.26	0.25	0.22	0.23	0.33	0.21	0.31	0.28	0.29	0.26	0.24
Fo mol%	86.2	86.1	88.0	88.5	88.8	86.3	88.4	88.3	87.5	82.1	81.9
Ol %	13.14	11.1	25.28	27.51	34.87	19.5	31.71	25.04	23.69	9.8	6.2

Table 7: Prehistoric and historical (1400–1885 AD) Kīlauea melt inclusion compositions (cont'd)

Sample	1832-34m3	1877-03m1	1877-23m1	1877-40m1	1877-40m2	1885B-02m1	1885B-05m1	1885B-05m2	1885B-12m1	1885B-12m2	1885B-14m1
SiO_2	50.43	48.98	51.13	48.30	48.56	50.47	48.46	48.71	49.60	49.34	50.42
TiO_2	2.44	2.37	2.36	2.60	2.52	2.72	2.38	2.32	2.49	2.65	2.85
Al_2O_3	13.01	11.78	13.41	11.94	11.86	13.64	12.01	11.88	12.75	13.48	13.57
Cr_2O_3	0.05	0.08	0.05	0.12	0.11	0.03	0.06	0.06	0.06	0.05	0.03
Fe_2O_3	0.86	0.90	0.98	1.23	1.24	0.92	1.24	1.24	0.96	0.93	0.92
FeO	10.57	10.53	10.46	10.22	10.22	10.63	10.22	10.22	10.47	10.50	10.52
MnO	0.19	0.19	0.20	0.17	0.20	0.19	0.17	0.18	0.18	0.18	0.20
MgO	8.58	11.10	7.96	11.70	11.74	6.75	11.80	11.98	9.99	7.75	6.54
CaO	10.52	10.76	10.75	10.88	10.78	11.39	10.77	10.72	10.40	11.78	11.53
Na_2O	2.24	2.04	1.60	2.06	2.05	2.37	2.12	2.07	2.21	2.40	2.43
NiO	0.014	0.023	0.023	0.035	0.028	0.013	0.030	0.014	0.027	0.022	0.005
K_2O	0.53	0.46	0.88	0.50	0.50	0.51	0.47	0.39	0.51	0.53	0.56
P_2O_5	0.29	0.25	0.23	0.29	0.25	0.29	0.28	0.23	0.27	0.32	0.29
F ppm	470	557	392	613	583	511	566	507	555	537	566
Cl ppm	148	160	104	160	140	135	181	135	157	162	119
S ppm	1193	1409	192	1133	1123	187	615	706	599	893	225
Total	100.01	99.81	100.11	100.34	100.33	100.02	100.23	100.22	100.11	100.18	99.99
CO_2 ppm	44	235	114	n.d	n.d	b.d	n.d	n.d	519	170	95
H_2O wt%	0.30	0.57	n.d	n.d	n.d	0.09	n.d	n.d	0.11	0.09	0.13
Sc	28.53	31.07	27.91	28.49	27.75	29.45	24.65	24.84	24.05	26.99	29.48
V	306.84	269.88	264.52	259.17	257.85	331.99	249.23	257.17	192.98	282.94	322.26
Rb	8.86	8.78	5.87	8.16	7.13	11.73	9.68	7.56	9.95	10.80	10.05
Sr	345.25	328.57	275.82	355.31	321.00	405.02	325.59	297.34	352.67	384.44	380.74
Y	21.07	22.59	25.03	21.06	20.79	23.79	19.75	20.26	22.51	21.12	25.02
Zr	124.13	141.54	151.51	152.22	142.98	148.91	117.45	121.27	144.95	134.83	153.59
Nb	11.80	20.04	11.69	18.86	18.09	18.37	12.75	11.85	13.58	14.41	14.37
Ba	94.48	90.38	56.22	90.00	89.88	168.05	59.33	48.62	73.47	104.96	120.15
La	11.43	13.67	9.11	14.32	13.16	20.47	14.07	12.32	15.58	13.64	14.89
Ce	28.21	32.51	21.68	30.57	32.34	48.39	32.02	29.87	34.37	33.91	35.09
Pr	4.06	4.85	3.64	5.15	4.86	7.54	4.47	4.24	4.70	4.37	4.76
Nd	19.69	21.85	18.21	20.29	21.63	31.18	22.01	20.31	23.55	20.72	22.86
Sm	6.94	4.80	5.32	5.41	4.50	7.79	5.61	5.39	6.00	5.34	5.76
Eu	2.40	1.80	1.75	1.69	1.57	3.17	2.10	2.16	2.10	2.01	2.14
Gd	5.47	4.18	5.50	5.84	5.00	7.98	5.19	5.03	5.51	5.46	5.34
Tb	0.92	0.69	0.89	0.77	0.67	1.14	0.90	0.96	0.88	0.81	0.89
Dy	4.82	4.98	5.28	4.10	4.31	6.88	4.94	4.98	5.33	4.79	5.53
Ho	0.90	0.94	0.99	0.85	0.77	1.30	0.94	0.95	0.88	0.87	1.02
Er	2.22	1.98	2.03	2.20	2.07	3.34	2.37	2.41	1.97	2.01	2.54
Tm	0.25	0.31	0.31	0.31	0.24	0.43	0.30	0.31	0.26	0.26	0.37
Yb	1.64	1.62	1.70	1.55	1.38	3.04	2.12	1.93	1.98	1.68	2.04
Lu	0.24	0.33	0.31	0.29	0.24	0.44	0.27	0.23	0.23	0.26	0.31
Hf	3.66	3.27	3.47	3.54	3.09	5.56	3.69	3.40	3.56	3.45	4.13
Ta	1.23	1.18	0.47	1.26	1.03	1.38	0.87	0.69	0.90	0.93	0.94
Pb	0.98	1.09	0.49	0.68	0.71	1.63	1.06	0.80	0.84	0.70	0.93
U	0.32	0.28	0.23	0.37	0.28	0.65	0.38	0.37	0.33	0.40	0.33
Fo mol%	82.0	86.0	80.6	87.1	87.1	77.9	87.2	87.3	84.6	80.9	77.6
Ol %	5.41	6.01	4.9	8.64	8.09	1.57	21.29	21.1	13.66	5.61	0.39

Table 7: Prehistoric and historical (1400–1885 AD) Kīlauea melt inclusion compositions (cont'd)

Sample	1885B-14m2	1885B-16m1	1885B-18m1	1885B-18m2	1885A-08m1	1885A-15m1	1885A-16m1	1885A-19m1	1885A-20m1	1885A-21m1	1885A-26m1
SiO_2	50.57	50.85	50.10	50.19	50.59	49.75	50.44	50.84	49.23	50.72	50.41
TiO_2	2.76	2.92	2.49	2.59	2.85	2.76	2.96	3.19	2.35	3.08	3.26
Al_2O_3	13.47	13.17	13.08	12.97	13.33	13.84	13.14	12.81	12.52	13.21	13.14
Cr_2O_3	0.04	0.02	0.03	0.03	0.03	0.03	0.03	0.04	0.05	0.03	0.03
Fe_2O_3	0.91	0.97	0.92	0.93	0.93	0.91	0.93	1.00	0.97	0.95	1.00
FeO	10.52	10.52	10.52	10.56	10.52	10.52	10.50	10.53	10.46	10.48	10.44
MnO	0.20	0.21	0.18	0.21	0.21	0.20	0.19	0.19	0.16	0.18	0.20
MgO	6.57	6.81	8.48	8.51	6.75	6.93	6.96	6.82	9.92	6.70	6.41
CaO	11.70	10.95	11.12	10.83	11.46	11.85	11.66	11.09	11.32	11.28	11.51
Na_2O	2.30	2.63	2.29	2.32	2.40	2.37	2.31	2.53	2.13	2.41	2.56
NiO	0.004	0.004	0.014	0.005	0.009	0.004	0.016	0.017	0.018	0.013	0.014
K_2O	0.56	0.56	0.40	0.49	0.53	0.45	0.49	0.57	0.48	0.55	0.61
P_2O_5	0.29	0.31	0.29	0.27	0.29	0.29	0.29	0.31	0.32	0.31	0.33
F ppm	542	678	494	446	619	575	651	726	648	672	646
Cl ppm	106	150	112	124	155	108	119	160	166	126	124
S ppm	205	173	822	186	211	171	167	152	654	138	164
Total	99.99	100.03	100.14	99.98	100.01	100.01	100.01	100.04	100.14	100.01	100.03
CO_2 ppm	58	n.d	526	b.d	57	b.d	b.d	b.d	b.d	b.d	b.d
H_2O wt%	0.12	0.09	0.10	0.12	0.12	0.10	0.11	0.10	0.10	0.11	0.10
Sc	28.68	30.75	27.35	27.59	29.28	33.70	28.13	29.95	23.37	31.92	28.02
V	324.97	315.43	257.64	229.18	305.89	265.17	290.94	321.01	199.38	331.04	325.19
Rb	9.97	9.63	8.00	10.51	9.18	9.19	10.36	10.79	7.98	11.08	10.15
Sr	367.82	357.24	301.54	338.15	367.02	347.34	378.86	369.11	328.96	361.65	329.87
Y	25.44	27.02	21.75	23.11	24.74	24.51	25.86	27.22	20.81	28.91	27.96
Zr	170.78	151.91	150.72	150.37	162.93	127.00	163.63	172.54	134.84	157.97	221.83
Nb	14.68	15.24	10.32	12.21	14.85	13.94	15.09	17.25	13.07	15.70	15.04
Ba	117.90	115.70	68.66	84.61	106.89	99.48	110.32	118.53	67.19	126.69	131.23
La	15.02	15.97	12.25	14.53	17.06	12.85	15.31	15.78	12.91	15.05	16.35
Ce	35.95	36.60	28.42	34.97	36.34	29.72	35.03	38.49	30.39	39.57	41.55
Pr	4.94	5.24	3.45	4.50	5.10	4.09	5.11	5.43	4.67	5.30	4.62
Nd	23.71	24.65	18.55	23.37	24.75	20.07	22.06	24.64	22.40	23.49	23.94
Sm	5.37	5.91	4.63	6.10	6.40	4.71	6.58	6.25	5.03	6.67	5.99
Eu	2.14	2.35	1.92	2.26	2.49	2.13	2.23	2.14	2.03	2.75	2.58
Gd	6.53	6.20	4.87	5.81	5.44	4.48	6.18	6.57	5.46	5.99	5.04
Tb	1.00	0.93	0.83	0.88	0.89	0.65	1.01	1.07	0.84	1.21	1.20
Dy	5.58	5.12	4.51	4.62	4.76	4.21	5.36	6.09	4.78	6.02	4.77
Ho	1.05	1.13	0.86	0.96	0.92	0.93	0.93	1.07	0.95	1.19	1.37
Er	2.73	2.63	1.85	2.16	2.70	1.98	2.42	2.88	2.10	2.67	3.75
Tm	0.39	0.33	0.26	0.36	0.38	0.24	0.35	0.37	0.31	0.36	0.39
Yb	2.25	2.41	2.25	1.71	2.45	2.37	2.13	2.62	1.98	2.01	2.42
Lu	0.23	0.29	0.19	0.28	0.30	0.29	0.31	0.33	0.26	0.41	0.44
Hf	4.31	4.66	3.55	4.66	4.36	3.70	4.19	4.74	3.44	4.64	6.68
Ta	1.00	1.00	0.57	0.90	1.06	0.78	0.95	0.95	0.74	1.11	0.87
Pb	0.75	1.11	0.59	0.70	1.19	0.43	0.95	0.97	0.67	1.32	0.26
U	0.40	0.34	0.36	0.32	0.39	0.27	0.44	0.47	0.32	0.32	0.38
Fo mol%	77.6	78.3	82.0	82.0	78.1	78.8	78.7	78.3	84.6	78.1	77.5
Ol %	1.93	1.79	9.18	9.65	4.41	3.12	4.88	4.03	14.35	1.9	3.92

Table 8: Historical (1920–1969 AD) Kīlauea melt inclusion compositions

Sample	1920-02m1	1920-08m1	1920-08m2	1920-09m1	1920-09m3	1920-10m1	1954-03m1	1954-05m1	1954-19m1	1954-01m1	1954-06m1	1954-07m1
SiO_2	48.46	49.06	48.97	49.66	49.11	48.54	49.47	49.45	49.44	49.40	49.43	49.77
TiO_2	2.41	2.46	2.56	2.45	2.42	2.55	2.73	2.70	2.70	2.83	2.61	2.67
Al_2O_3	11.59	12.07	12.15	12.41	12.11	11.75	12.79	12.70	12.33	13.16	12.19	12.78
Cr_2O_3	0.07	0.07	0.07	0.07	0.06	0.06	0.04	0.04	0.05	0.05	0.04	0.06
Fe_2O_3	1.12	1.00	1.03	1.01	1.01	1.09	0.84	0.83	0.87	1.09	1.16	1.06
FeO	10.33	10.44	10.41	10.44	10.42	10.36	10.61	10.59	10.56	10.36	10.29	10.38
MnO	0.16	0.18	0.17	0.17	0.18	0.16	0.19	0.21	0.20	0.22	0.20	0.17
MgO	12.35	10.99	10.92	10.61	10.70	12.11	8.54	8.63	8.80	8.10	10.22	8.46
CaO	10.72	10.87	10.81	10.09	11.16	10.53	11.20	11.34	11.56	11.50	10.88	11.84
Na_2O	2.03	2.04	2.09	2.29	2.06	2.07	2.16	2.14	2.17	2.43	2.13	2.07
NiO	0.026	0.021	0.027	0.030	0.014	0.026	0.007	0.011	0.006	0.004	0.028	0.004
K_2O	0.46	0.46	0.49	0.48	0.45	0.46	0.55	0.49	0.55	0.57	0.60	0.46
P_2O_5	0.24	0.25	0.26	0.25	0.24	0.23	0.27	0.27	0.25	0.30	0.25	0.27
F ppm	601	455	508	544	596	488	525	513	419	730	556	524
Cl ppm	114	122	110	86	149	91	164	166	157	164	196	102
S ppm	712	656	482	248	803	328	1385	1344	1247	819	1017	909
Total	100.17	100.08	100.10	100.05	100.16	100.06	99.74	99.73	99.79	100.26	100.31	100.25
CO_2 ppm	71	n.d	36	216	86	44	260	252	319	n.d	n.d	n.d
H_2O wt%	0.07	0.13	0.09	0.09	0.09	0.09	0.61	0.62	0.53	n.d	n.d	n.d
Sc	25.77	21.95	22.47	23.39	23.62	22.36	26.26	31.53	22.99	36.31	n.d	31.77
V	249.22	197.06	251.56	197.06	238.55	258.64	316.68	334.16	296.17	348.00	n.d	329.64
Rb	7.23	8.52	7.58	9.28	7.40	9.22	11.90	10.94	9.11	7.75	n.d	12.11
Sr	300.02	319.55	331.46	338.01	327.98	376.68	408.70	386.33	349.77	388.26	n.d	356.75
Y	19.64	18.55	18.57	18.44	19.09	21.94	26.68	27.46	20.82	21.09	n.d	22.61
Zr	124.74	131.04	120.25	151.40	89.48	148.81	193.04	141.31	149.97	92.88	n.d	138.13
Nb	12.16	13.84	12.94	14.13	14.01	16.85	22.22	23.29	15.19	13.85	n.d	15.99
Ba	101.53	102.56	96.50	118.94	130.16	65.74	127.38	133.00	127.92	93.13	n.d	133.16
La	12.12	13.79	12.80	12.80	15.99	15.75	19.13	19.15	13.77	13.56	n.d	16.67
Ce	28.15	30.08	30.69	31.39	23.90	38.55	42.67	43.61	34.62	36.61	n.d	37.88
Pr	3.82	4.33	4.09	4.66	4.25	5.62	5.46	6.13	4.29	5.14	n.d	5.10
Nd	19.09	19.48	18.43	21.53	18.34	28.12	23.79	30.17	19.00	23.40	n.d	26.87
Sm	4.52	5.26	4.92	4.93	5.34	5.93	7.97	6.12	6.39	7.96	n.d	5.83
Eu	1.53	1.55	1.75	1.69	1.76	1.97	2.93	2.46	1.89	1.72	n.d	2.09
Gd	5.29	3.76	4.48	4.94	3.92	5.18	6.99	6.01	4.55	7.24	n.d	5.68
Tb	0.73	0.64	0.68	0.72	0.67	0.75	0.64	0.87	0.73	0.94	n.d	0.92
Dy	4.40	4.30	4.37	4.51	4.66	5.57	5.26	5.21	4.65	5.03	n.d	5.02
Ho	0.76	0.80	0.78	0.73	0.88	0.99	0.98	0.99	0.89	1.14	n.d	0.80
Er	1.81	1.74	2.06	2.31	2.09	2.25	2.59	2.66	2.09	2.19	n.d	2.31
Tm	0.26	0.26	0.22	0.25	0.29	0.33	0.42	0.31	0.30	0.35	n.d	0.30
Yb	1.53	1.44	1.53	1.65	1.75	2.20	2.31	2.23	2.00	1.32	n.d	1.96
Lu	0.21	0.23	0.21	0.22	0.11	0.27	0.33	0.25	0.22	0.25	n.d	0.29
Hf	3.08	3.51	2.91	4.12	2.59	4.19	4.82	4.20	3.35	5.16	n.d	4.11
Ta	0.72	0.81	0.78	0.81	0.75	1.16	1.31	1.58	0.85	0.92	n.d	0.77
Pb	0.78	1.50	0.86	0.86	b.d	1.20	1.91	2.07	1.52	0.67	n.d	0.83
U	0.41	0.34	0.36	0.41	0.44	0.48	0.58	0.43	0.43	0.35	n.d	0.58
Fo mol%	87.6	85.9	85.9	85.4	85.6	87.3	82.1	82.3	82.7	81.8	85.1	82.2
Ol %	21.35	17.22	16.62	15.35	14.93	20.03	6.55	6.92	10.3	5.55	20.24	8.59

Table 8: Historical (1920–1969 AD) Kīlauea melt inclusion compositions (cont'd)

Sample	11-03m1	11-04m1	11-01m1	11-02m1	11-02m2	11-07m1	12-01m1	12-06m1	12-b8m1	12-b8m2	12-05m1	12-08m1	12-08m2
SiO_2	49.22	48.71	47.74	49.82	49.94	49.40	48.59	49.41	48.94	49.24	48.54	48.32	48.78
TiO_2	2.24	2.61	2.86	1.96	2.11	2.17	2.16	2.42	2.51	2.48	2.60	2.79	2.47
Al_2O_3	11.50	12.63	11.43	12.11	11.58	11.69	11.02	12.38	12.06	11.55	11.73	12.17	11.86
Cr_2O_3	0.09	0.07	0.07	0.05	0.07	0.07	0.09	0.07	0.09	0.09	0.08	0.10	0.06
Fe_2O_3	0.92	0.94	1.29	1.07	1.11	1.24	1.06	0.97	0.94	0.94	1.25	1.18	1.24
FeO	10.52	10.49	10.18	10.38	10.37	10.22	10.38	10.47	10.50	10.48	10.20	10.28	10.22
MnO	0.20	0.18	0.14	0.23	0.18	0.17	0.18	0.17	0.19	0.19	0.17	0.20	0.18
MgO	11.02	10.41	12.25	9.43	9.85	12.05	13.43	9.66	11.02	11.01	11.48	11.62	11.89
CaO	11.17	10.75	11.09	12.71	12.60	10.28	10.14	11.43	10.46	10.75	10.89	10.81	10.54
Na_2O	1.97	2.20	2.14	1.71	1.67	2.04	1.98	2.16	2.16	2.06	2.18	1.81	1.96
NiO	0.019	0.017	0.001	b.d	0.025	0.018	0.025	0.018	0.035	0.027	b.d	0.028	0.063
K_2O	0.37	0.50	0.36	0.31	0.29	0.40	0.33	0.48	0.50	0.49	0.55	0.47	0.58
P_2O_5	0.37	0.26	0.45	0.22	0.23	0.28	0.28	0.29	0.23	0.29	0.32	0.26	0.23
F ppm	644	596	675	435	346	474	503	579	508	592	556	733	258
Cl ppm	102	167	111	138	104	146	81	152	129	155	139	197	1108
S ppm	899	1196	722	906	819	616	1188	1146	914	1559	679	705	759
Total	99.86	100.06	100.22	99.24	100.24	100.20	99.98	100.21	99.89	100.00	99.21	100.26	100.35
CO_2 ppm	114	228	n.d	n.d	n.d	n.d	58	126	521	202	n.d	n.d	n.d
H_2O wt%	0.42	0.27	n.d	n.d	n.d	n.d	0.34	0.11	0.39	0.41	n.d	n.d	n.d
Sc	25.21	24.74	26.11	27.93	29.35	20.30	20.89	24.49	28.03	27.29	27.16	31.51	24.21
V	282.60	293.18	290.76	274.41	271.64	233.70	257.08	304.41	275.31	244.01	289.90	319.08	259.97
Rb	7.05	9.52	5.44	4.11	6.69	7.08	6.60	9.49	8.66	8.81	8.88	8.97	8.72
Sr	282.81	383.42	222.47	206.01	245.94	230.50	307.04	405.25	324.57	290.60	332.62	295.53	353.97
Y	23.45	23.77	18.94	15.93	15.57	16.12	24.44	26.51	19.72	18.35	17.87	22.78	18.65
Zr	145.94	162.79	123.28	105.52	103.70	112.80	155.20	185.01	124.43	119.77	119.44	170.41	146.53
Nb	13.29	21.68	10.37	9.15	8.66	8.33	13.02	18.04	14.40	14.57	14.40	17.00	14.21
Ba	68.64	89.87	72.79	70.69	68.09	87.13	50.08	110.76	121.18	112.41	122.57	144.62	110.96
La	10.36	15.72	11.77	9.17	9.01	11.16	11.08	15.75	14.77	14.55	14.49	14.32	14.41
Ce	28.60	36.33	24.95	22.82	21.61	22.40	27.48	36.31	34.37	30.64	33.71	31.44	30.69
Pr	4.91	5.37	3.71	2.51	2.49	3.15	4.71	5.31	4.59	4.65	4.49	5.23	3.85
Nd	24.72	24.06	19.66	17.20	17.22	15.29	23.57	25.38	21.60	19.90	20.78	24.76	19.42
Sm	5.96	8.45	4.47	4.49	4.30	3.92	6.23	7.24	5.10	3.98	5.18	6.06	4.42
Eu	1.93	1.81	1.72	1.51	1.56	1.47	2.47	2.19	1.86	1.73	1.75	2.45	1.50
Gd	5.42	4.85	4.44	5.29	4.22	4.11	6.09	5.05	5.30	4.29	4.16	7.53	5.37
Tb	0.81	0.80	0.67	0.50	0.45	0.70	0.98	0.88	0.79	0.73	0.69	0.95	0.67
Dy	4.03	4.30	3.87	3.68	3.37	3.57	6.10	5.83	4.37	4.24	3.80	4.42	4.26
Ho	0.85	1.10	0.76	0.98	0.77	0.85	1.09	0.98	0.83	0.93	0.80	0.86	0.62
Er	2.27	2.19	1.96	1.52	1.83	2.24	2.61	2.47	2.00	1.87	1.80	2.47	2.34
Tm	0.34	0.29	0.29	0.29	0.35	0.14	0.33	0.40	0.27	0.24	0.22	0.21	0.19
Yb	1.58	2.25	1.21	1.08	1.35	1.35	2.14	2.26	1.82	1.35	1.69	2.15	1.40
Lu	0.18	0.44	0.23	0.17	0.23	0.21	0.29	0.31	0.23	0.20	0.22	0.36	0.18
Hf	4.23	4.32	2.84	2.45	3.47	3.24	4.60	4.45	4.07	3.65	3.50	2.24	3.14
Ta	0.68	1.22	0.65	0.38	0.53	0.59	0.96	1.03	0.90	0.79	0.84	0.57	0.75
Pb	1.29	1.43	b.d	0.50	0.79	1.22	0.90	0.86	0.73	0.80	0.57	1.21	1.21
U	0.21	0.52	0.25	0.21	0.44	0.25	0.33	0.42	0.46	0.41	0.42	0.51	0.47
Fo mol%	85.8	85.3	87.8	83.7	84.3	87.1	88.3	84.2	85.9	85.9	86.9	86.9	87.2
Ol %	10.64	11.91	20.08	8.57	9.94	20.82	19.33	6.67	6.24	7.43	6.91	19.38	20.57

Table 8: Historical (1920–1969 AD) Kīlauea melt inclusion compositions (cont'd)

Sample	12-10m1	1961-05m1	1961-08m1	1961-08m2	1961-12m1	1961-22m1	1961-41m1	1961-41m2	1961-41m3	1961-45m1	1969-mu01m1
SiO_2	49.97	49.87	50.20	49.79	50.42	49.69	49.08	48.79	49.41	49.72	48.46
TiO_2	2.48	2.71	2.75	2.69	3.01	2.76	2.72	3.26	2.96	2.75	2.08
Al_2O_3	12.01	12.63	12.72	12.84	12.83	12.76	12.90	12.68	12.57	12.71	11.37
Cr_2O_3	0.07	0.04	0.05	0.04	0.04	0.04	0.06	0.05	0.05	0.05	0.08
Fe_2O_3	1.13	0.86	0.93	0.87	0.88	0.86	0.87	0.90	0.87	0.91	0.98
FeO	10.36	10.56	10.50	10.59	10.54	10.56	10.57	10.54	10.56	10.52	10.45
MnO	0.25	0.19	0.19	0.21	0.19	0.20	0.19	0.18	0.18	0.19	0.18
MgO	9.59	8.79	8.64	8.43	8.69	8.81	8.59	8.52	8.64	8.59	12.78
CaO	11.27	10.72	10.70	10.88	9.40	10.59	11.52	11.67	11.38	10.89	10.64
Na_2O	2.07	2.30	2.31	2.32	2.69	2.29	2.26	2.16	2.14	2.43	1.94
NiO	0.049	0.022	0.026	0.023	0.021	0.018	0.026	0.019	0.017	0.027	0.026
K_2O	0.50	0.55	0.55	0.59	0.46	0.62	0.52	0.52	0.50	0.63	0.36
P_2O_5	0.32	0.28	0.30	0.29	0.31	0.29	0.26	0.27	0.28	0.28	0.20
F ppm	637	570	493	522	553	494	560	542	513	504	526
Cl ppm	197	154	184	159	138	200	177	217	219	772	97
S ppm	1096	800	949	512	1177	919	1375	1343	1382	1211	1039
Total	100.35	99.75	100.12	99.72	99.80	99.73	99.90	99.89	99.89	100.06	99.81
CO_2 ppm	n.d	265	b.d	211	259	188	120	156	192	128	111
H_2O wt%	n.d	0.50	0.16	0.47	0.52	0.54	0.47	0.48	0.48	0.33	0.49
Sc	38.01	27.64	31.78	26.62	26.23	29.13	25.94	31.03	31.85	29.73	27.80
V	329.76	281.24	321.71	282.62	245.54	279.73	283.36	301.58	296.34	291.56	290.11
Rb	8.29	8.68	9.05	11.69	6.61	8.97	7.66	8.14	8.96	10.20	6.30
Sr	451.95	327.33	376.97	365.13	287.15	364.81	334.55	363.04	354.34	387.21	263.33
Y	22.84	21.45	27.06	27.29	22.57	23.12	22.30	22.90	23.82	24.82	17.65
Zr	208.74	139.14	173.48	188.94	122.97	181.47	155.04	147.16	178.01	169.21	101.67
Nb	19.55	19.81	25.06	22.84	13.82	22.57	20.26	17.45	20.85	13.90	8.75
Ba	125.19	94.36	113.18	94.30	70.58	108.48	88.44	94.24	95.95	143.89	49.68
La	15.55	14.84	17.92	20.61	10.76	16.72	13.81	14.40	15.91	14.53	9.05
Ce	30.34	32.53	39.67	36.58	23.98	35.21	33.65	31.00	33.17	35.96	22.87
Pr	4.80	5.10	5.84	3.66	4.10	5.23	4.83	4.80	4.59	4.77	3.23
Nd	21.31	23.61	27.88	26.79	19.63	25.11	23.04	21.17	23.40	24.14	17.23
Sm	6.69	5.13	5.32	3.23	4.87	6.53	6.20	5.23	6.20	4.69	4.33
Eu	1.43	1.79	2.26	1.68	1.94	1.81	2.35	1.83	1.64	2.40	1.64
Gd	6.25	4.73	6.96	5.21	5.72	6.44	3.72	5.72	6.31	5.78	4.22
Tb	0.73	0.70	1.01	0.96	0.81	0.93	0.77	0.78	0.85	0.84	0.73
Dy	4.42	3.88	5.56	5.41	4.67	4.34	4.63	4.96	5.62	5.30	4.01
Ho	1.21	0.76	0.86	1.27	0.90	0.86	0.74	0.98	0.97	0.87	0.77
Er	5.05	2.09	2.07	1.39	2.34	1.72	1.87	2.40	2.59	2.42	1.88
Tm	0.21	0.26	0.34	0.40	0.31	0.33	0.31	0.28	0.41	0.32	0.25
Yb	1.02	1.58	2.36	1.48	2.00	1.37	1.96	1.93	1.85	2.30	1.65
Lu	0.15	0.20	0.30	0.37	0.22	0.40	0.23	0.25	0.25	0.33	0.25
Hf	3.55	3.01	3.37	3.11	2.85	3.28	3.67	3.65	3.88	3.81	3.03
Ta	0.66	1.13	1.08	0.45	0.74	0.92	1.31	1.31	1.30	0.82	0.51
Pb	b.d	0.88	1.35	1.87	0.87	1.50	1.04	0.82	1.15	0.63	0.69
U	0.57	0.37	0.39	0.33	0.12	0.55	0.40	0.37	0.36	0.35	0.22
Fo mol%	84.0	82.6	82.3	81.9	82.4	82.7	82.4	82.4	82.4	82.4	87.8
Ol %	3.8	7.28	6.53	6.03	6.75	6.92	6.11	5.21	6.26	6.66	12.71

Table 8: Historical (1920–1969 AD) Kīlauea melt inclusion compositions (cont'd)

Sample	1969-mu06m1	1969-mu14m1	1969-708m1	1969-708m2	1969-714m1	1969-703m1	1969-704m1	1969-707m1	1969-711m1	1969-712m1
SiO_2	48.68	48.20	48.53	48.81	48.55	48.93	48.53	48.80	49.00	48.14
TiO_2	2.21	2.19	2.59	2.60	1.97	2.43	2.32	2.68	2.26	2.36
Al_2O_3	11.65	11.34	11.25	11.36	11.43	12.09	11.34	10.74	11.46	11.63
Cr_2O_3	0.09	0.12	0.09	0.09	0.08	0.07	0.11	0.09	0.10	0.09
Fe_2O_3	0.90	0.93	0.96	0.93	0.98	0.93	0.96	1.00	0.94	0.96
FeO	10.52	10.50	10.47	10.50	10.45	10.50	10.47	10.44	10.49	10.47
MnO	0.18	0.20	0.19	0.18	0.17	0.17	0.19	0.16	0.20	0.18
MgO	11.40	11.79	12.39	12.26	13.07	11.67	12.69	13.20	12.13	12.95
CaO	11.50	11.90	10.11	9.98	10.25	9.91	10.20	9.76	10.24	9.69
Na_2O	1.80	1.69	1.97	1.96	1.87	2.11	1.94	1.88	1.93	1.93
NiO	0.006	0.024	0.027	0.027	0.025	0.042	0.021	0.001	0.023	0.042
K_2O	0.34	0.36	0.48	0.46	0.30	0.49	0.46	0.43	0.45	0.56
P_2O_5	0.24	0.28	0.40	0.27	0.46	0.25	0.23	0.29	0.27	0.45
F ppm	570	607	502	471	558	420	333	438	393	351
Cl ppm	122	96	138	149	89	166	133	150	138	164
S ppm	627	298	1270	1430	943	732	907	946	824	910
Total	99.71	99.66	99.77	99.75	99.85	99.80	99.67	99.72	99.73	99.69
CO_2 ppm	69	68	116	104	54	101	272	213	135	174
H_2O wt%	0.49	0.50	0.57	0.62	0.42	0.45	0.58	0.53	0.51	0.59
Sc	32.73	33.27	24.72	25.31	22.73	26.36	27.43	21.47	26.39	23.80
V	316.31	335.17	279.18	278.72	273.02	268.30	278.08	236.62	260.04	254.93
Rb	6.46	7.17	10.83	7.67	5.97	8.94	8.39	6.94	7.08	10.87
Sr	262.83	265.79	439.94	303.88	277.27	327.55	300.06	300.08	313.44	333.77
Y	22.46	18.25	25.70	19.76	26.75	20.23	19.21	20.17	19.93	19.84
Zr	133.31	96.27	168.03	113.33	125.17	130.52	113.31	144.00	151.73	121.78
Nb	10.06	9.80	23.35	14.73	11.15	14.62	13.30	13.62	12.04	16.28
Ba	35.43	54.32	97.42	100.76	47.96	115.92	101.84	100.10	95.96	136.49
La	11.30	11.23	21.39	15.00	9.86	14.08	13.09	13.42	11.02	16.95
Ce	27.09	27.20	48.07	32.08	25.72	33.27	30.85	31.34	26.82	36.21
Pr	3.74	3.39	6.80	4.24	4.49	4.42	4.16	4.22	3.02	4.64
Nd	18.08	18.71	30.00	22.11	20.94	22.58	19.04	18.29	16.42	19.12
Sm	5.22	4.05	7.63	5.39	4.65	4.90	4.79	4.82	4.46	4.64
Eu	1.89	1.68	2.41	1.96	1.66	1.83	1.68	1.72	1.37	1.55
Gd	4.82	4.19	6.04	5.51	6.71	4.82	4.98	4.65	3.46	4.27
Tb	0.69	0.69	1.08	0.70	1.32	0.82	0.68	0.76	0.72	0.71
Dy	4.21	4.16	6.71	4.73	6.40	4.50	4.41	4.28	3.54	4.37
Ho	0.82	0.75	1.17	0.78	1.28	0.88	0.77	0.76	0.75	0.84
Er	2.10	2.04	2.95	2.10	3.03	2.22	2.14	2.11	2.36	1.70
Tm	0.30	0.29	0.39	0.23	0.42	0.26	0.31	0.26	0.24	0.27
Yb	1.80	1.61	2.48	2.13	2.58	1.76	1.71	1.52	1.26	1.69
Lu	0.26	0.29	0.35	0.25	0.32	0.25	0.23	0.19	0.27	0.21
Hf	3.42	2.86	5.41	2.84	3.92	3.49	3.05	3.48	3.54	3.33
Ta	0.69	0.62	1.64	0.83	0.90	0.84	0.75	0.80	0.62	0.96
Pb	0.63	0.70	1.36	0.84	0.95	1.27	0.94	1.14	0.69	1.35
U	0.36	0.28	0.75	0.32	0.34	0.37	0.36	0.42	0.34	0.37
Fo mol%	86.3	86.8	87.3	87.2	87.9	86.6	87.7	88.0	87.0	87.9
Ol %	21.06	15.58	15.81	12.57	17.08	11.09	11.95	18.14	13.38	12.79

Table 8: Historical (1920–1969 AD) Kīlauea melt inclusion compositions (cont'd)

Sample	1969-809m1	1969-812m1	1969-816m1	1969-816m2	1969-819m1	1969-821m1	1969-811m1	1969-814m1	1969-814m2
SiO_2	48.70	48.18	48.30	48.48	48.37	47.72	48.88	49.43	49.32
TiO_2	2.29	2.37	2.34	2.32	2.44	2.33	2.39	2.43	2.38
Al_2O_3	11.28	11.29	11.31	11.18	11.18	11.36	11.52	11.67	11.51
Cr_2O_3	0.10	0.10	0.12	0.11	0.11	0.14	0.10	0.12	0.13
Fe_2O_3	0.96	0.92	0.93	0.95	0.95	0.95	1.27	1.23	1.26
FeO	10.47	10.51	10.50	10.48	10.47	10.48	10.20	10.23	10.20
MnO	0.20	0.21	0.19	0.17	0.19	0.18	0.19	0.20	0.21
MgO	12.93	11.85	12.64	12.59	12.66	13.09	12.63	12.07	12.39
CaO	9.79	11.35	10.47	10.39	10.35	10.61	10.33	9.96	9.84
Na_2O	1.99	2.02	1.82	1.96	1.94	1.79	1.89	1.94	1.97
NiO	0.031	0.032	0.031	0.033	0.017	0.031	0.016	0.051	0.036
K_2O	0.44	0.19	0.42	0.45	0.40	0.38	0.37	0.47	0.49
P_2O_5	0.21	0.34	0.28	0.25	0.31	0.30	0.24	0.25	0.30
F ppm	437	476	485	525	553	466	440	347	412
Cl ppm	125	372	120	160	152	100	85	95	153
S ppm	1310	521	896	1302	1252	797	1356	107	958
Total	99.71	99.54	99.58	99.69	99.69	99.59	100.34	100.12	100.28
CO_2 ppm	327	n.d	363	631	486	324	n.d	n.d	n.d
H_2O wt%	0.64	0.68	0.69	0.68	0.65	0.66	n.d	n.d	n.d
Sc	23.50	30.97	30.22	27.78	26.82	28.07	27.77	29.05	25.88
V	282.40	312.91	293.39	333.59	290.68	321.35	282.65	246.03	262.02
Rb	9.10	2.06	7.69	9.93	7.99	6.58	5.40	6.91	8.37
Sr	387.55	355.44	400.29	350.59	354.37	316.45	245.57	263.66	339.42
Y	21.87	18.52	22.13	22.62	24.13	24.16	16.01	19.44	19.20
Zr	154.10	121.07	114.45	138.01	162.49	163.18	105.65	100.71	145.00
Nb	18.51	10.98	12.83	16.35	17.36	12.63	7.65	10.83	11.31
Ba	107.96	97.52	81.03	82.18	123.07	64.18	69.23	100.22	110.79
La	14.45	11.72	10.71	12.64	13.87	10.65	8.25	9.83	12.28
Ce	36.67	27.87	28.19	30.22	31.56	24.63	22.07	24.44	29.54
Pr	5.25	3.76	4.21	4.50	4.62	4.14	3.16	3.20	3.92
Nd	24.01	17.66	21.98	23.36	19.71	19.03	15.32	17.25	17.23
Sm	5.63	4.89	5.87	5.33	6.71	4.96	4.62	4.21	4.95
Eu	2.03	1.68	2.06	2.24	1.83	2.27	1.50	1.54	1.80
Gd	5.92	4.54	5.28	5.06	5.86	5.15	3.80	5.08	4.83
Tb	0.75	0.67	0.83	1.09	0.92	0.71	0.54	0.79	0.79
Dy	5.21	3.91	4.13	4.87	5.38	4.70	3.29	4.34	3.93
Ho	0.97	0.84	0.76	0.91	0.88	0.89	0.72	0.70	0.92
Er	2.25	2.02	2.02	1.96	2.62	2.15	1.73	1.85	2.08
Tm	0.30	0.21	0.30	0.24	0.30	0.29	0.21	0.28	0.22
Yb	2.03	1.76	2.09	2.05	1.56	1.69	1.39	1.92	1.80
Lu	0.29	0.20	0.29	0.30	0.34	0.27	0.21	0.13	0.21
Hf	3.76	3.05	3.78	4.36	4.03	3.46	2.64	3.41	3.33
Ta	1.18	0.69	0.79	0.94	1.14	0.74	0.36	0.49	0.79
Pb	1.04	1.93	1.57	1.27	1.24	0.64	0.69	0.63	0.69
U	0.48	0.34	0.43	0.30	0.40	0.35	0.21	0.15	0.41
Fo mol%	87.8	86.9	87.6	87.6	87.6	88.1	87.8	87.1	87.5
Ol %	6.94	2.05	8.43	8.71	13.53	8.82	6.49	14.85	7.27

Table 9: Historical (1971–1982 AD) Kīlauea melt inclusion compositions

Sample	1971-b10m1	1971-22m1	1971-24m1	1971-24m2	1971-05m1	1971-06m1	1971-10m1	1971-10m2	1971-14m1	1971-14m2	1971-17m1	1971-26m1
SiO_2	49.91	49.32	49.79	49.66	49.50	51.48	49.96	50.29	49.93	49.98	50.05	50.37
TiO_2	2.70	2.73	2.53	2.70	2.68	2.58	2.53	2.51	2.62	2.60	2.54	2.62
Al_2O_3	12.55	13.08	12.76	12.69	12.68	13.08	12.85	12.64	12.36	12.58	12.48	12.67
Cr_2O_3	0.05	0.04	0.05	0.05	0.05	0.04	0.04	0.04	0.05	0.05	0.05	0.04
Fe_2O_3	0.93	0.83	0.82	0.83	0.84	0.81	0.83	0.84	0.85	0.90	0.80	0.79
FeO	10.50	10.58	10.59	10.58	10.58	10.60	10.59	10.59	10.58	10.53	10.62	10.62
MnO	0.20	0.21	0.20	0.21	0.22	0.21	0.18	0.20	0.20	0.20	0.18	0.20
MgO	8.60	8.35	8.72	8.68	8.72	8.99	8.58	8.74	8.55	8.45	8.47	8.92
CaO	11.29	11.26	11.08	11.17	11.33	8.57	10.89	10.57	11.49	11.59	10.83	11.31
Na_2O	2.35	2.26	2.17	2.13	2.17	2.31	2.23	2.27	2.12	2.15	2.28	1.39
NiO	0.006	b.d	0.011	0.018	b.d	0.027	0.004	0.007	0.013	0.011	0.005	0.001
K_2O	0.48	0.48	0.46	0.46	0.43	0.53	0.51	0.49	0.47	0.49	0.52	0.44
P_2O_5	0.27	0.29	0.27	0.28	0.27	0.24	0.27	0.27	0.27	0.27	0.28	0.26
F ppm	508	531	555	563	380	484	401	390	428	359	340	430
Cl ppm	162	144	134	128	208	138	141	144	146	128	147	137
S ppm	1273	1097	1366	1393	1360	1149	1296	1373	1193	1056	1203	366
Total	100.14	98.71	99.78	99.81	98.79	99.77	99.79	99.80	99.79	100.04	99.39	99.76
CO_2 ppm	204	243	193	240	149	220	172	1348	216	214	254	n.d
H_2O wt%	0.19	0.57	0.57	0.56	0.54	0.55	0.53	0.54	0.52	0.23	0.91	0.37
Sc	33.18	25.17	29.52	26.06	27.93	19.96	29.61	30.37	32.70	28.13	29.31	30.19
V	303.99	267.78	294.93	294.11	286.87	229.14	277.13	265.06	297.69	308.92	280.34	313.44
Rb	8.76	8.18	7.84	8.84	9.01	6.67	7.29	9.05	8.24	9.64	8.30	7.32
Sr	367.63	385.69	364.60	351.13	320.20	276.21	338.99	301.73	346.88	310.78	293.54	329.96
Y	23.35	22.59	24.01	21.88	16.85	16.08	20.28	17.99	22.36	21.74	20.36	21.20
Zr	125.43	166.00	190.23	149.15	126.42	101.44	147.27	119.71	145.55	161.33	144.88	135.58
Nb	17.83	14.48	18.56	14.97	11.43	10.02	12.78	11.02	13.31	13.56	11.20	11.90
Ba	74.90	86.57	90.46	79.55	83.95	48.02	85.19	72.71	115.45	100.79	105.98	103.54
La	14.29	13.43	14.17	12.15	14.24	11.10	14.59	12.74	13.88	12.89	12.59	13.08
Ce	32.17	35.10	36.65	28.69	31.98	24.95	28.42	30.21	33.78	32.41	28.77	31.54
Pr	5.35	4.78	5.90	4.42	4.27	3.70	4.25	3.52	4.15	3.99	3.33	3.87
Nd	14.78	23.86	29.73	19.56	19.35	16.98	19.71	17.36	19.30	19.98	15.14	21.08
Sm	4.61	7.41	7.02	5.34	4.29	3.98	4.13	5.36	5.75	4.67	3.71	5.02
Eu	2.36	1.92	2.29	1.75	2.24	1.50	1.89	1.85	1.94	1.73	1.97	1.84
Gd	6.20	3.95	4.66	4.14	5.33	3.70	5.35	4.24	5.60	5.61	4.72	5.15
Tb	1.14	0.89	0.98	0.90	0.66	0.68	0.69	0.61	0.78	0.71	0.72	0.71
Dy	4.19	6.21	4.84	4.08	3.69	3.33	4.53	4.45	4.68	4.86	4.65	4.51
Ho	0.88	1.05	1.08	0.82	0.66	0.68	0.93	0.84	0.72	1.09	0.90	0.79
Er	2.90	2.45	2.50	2.19	1.70	1.55	2.65	2.12	2.05	1.91	2.04	1.79
Tm	0.26	0.23	0.32	0.15	0.30	0.23	0.29	0.21	0.30	0.21	0.30	0.25
Yb	1.64	2.04	2.42	1.61	1.14	1.51	2.14	1.15	1.86	1.54	1.72	1.71
Lu	0.24	0.27	0.21	0.26	0.26	0.19	0.24	0.24	0.26	0.20	0.18	0.18
Hf	4.85	4.50	4.56	3.46	2.61	2.87	3.58	3.86	3.26	3.63	3.44	3.39
Ta	0.78	1.13	1.21	0.83	0.63	0.62	0.76	0.38	0.87	0.58	0.67	0.81
Pb	0.72	0.98	0.99	0.86	0.83	0.59	0.74	1.72	0.86	0.69	1.23	0.97
U	0.29	0.41	0.52	0.31	0.45	0.33	0.28	0.28	0.29	0.43	0.27	0.33
Fo mol%	82.4	81.9	82.4	82.3	82.5	82.4	82.1	82.3	82.1	82.0	81.8	82.2
Ol %	10.52	9.74	8.11	7.77	10.27	17.75	6.45	7.37	9.16	8.13	6.25	8.99

Table 9: Historical (1971–1982 AD) Kīlauea melt inclusion compositions (cont'd)

Sample	1973-01m1	1973-02m1	1973-03m1	1973-03m2	1973-07m1	1973-07m2	1973-11m1	1973-13m1	1973-17m1	1973-09m1	1973-11m1
SiO_2	49.62	48.49	48.45	48.85	48.62	48.29	49.41	48.75	49.58	48.78	48.67
TiO_2	2.25	2.19	2.29	2.21	2.46	2.42	2.57	2.31	2.33	2.50	2.44
Al_2O_3	11.35	11.40	11.22	11.10	11.42	11.55	12.08	11.46	11.90	11.62	11.65
Cr_2O_3	0.08	0.08	0.07	0.07	0.07	0.08	0.06	0.07	0.10	0.08	0.06
Fe_2O_3	0.90	0.98	1.02	1.05	0.97	0.99	1.19	0.95	0.87	0.96	0.95
FeO	10.53	10.45	10.42	10.39	10.46	10.45	10.27	10.48	10.55	10.47	10.48
MnO	0.19	0.17	0.17	0.20	0.18	0.18	0.17	0.17	0.22	0.18	0.17
MgO	11.55	13.50	13.72	13.63	12.95	12.94	11.29	12.71	10.66	12.52	12.51
CaO	10.61	9.55	9.54	9.40	9.81	9.97	10.10	9.88	10.66	9.77	10.05
Na_2O	1.84	1.86	1.90	2.04	1.91	1.98	2.11	1.90	2.04	1.92	1.87
NiO	0.008	0.022	0.023	0.023	0.024	0.019	0.030	0.025	0.029	0.008	0.024
K_2O	0.31	0.46	0.44	0.42	0.41	0.44	0.50	0.46	0.36	0.50	0.45
P_2O_5	0.28	0.31	0.27	0.26	0.25	0.23	0.26	0.32	0.22	0.25	0.24
F ppm	474	440	379	371	492	426	385	517	498	227	311
Cl ppm	106	105	136	136	150	164	155	300	124	155	150
S ppm	1209	1212	838	921	1226	1049	1241	1116	1254	785	753
Total	99.81	99.78	99.75	99.86	99.84	99.80	100.33	99.79	99.83	99.73	99.75
CO_2 ppm	45	88	26	46	107	121	504	55	331	123	n.d
H_2O wt%	0.50	0.54	0.49	0.39	0.49	0.49	n.d	0.54	0.52	0.47	0.47
Sc	21.87	22.85	26.82	26.19	23.72	24.52	24.62	21.65	26.36	26.43	25.66
V	212.39	269.51	230.56	249.28	255.29	256.59	253.91	260.35	264.77	264.52	277.15
Rb	5.15	8.99	8.42	5.28	7.67	8.04	9.29	10.70	8.35	7.58	7.64
Sr	281.61	369.78	320.36	339.21	294.64	286.04	312.41	391.95	296.94	345.79	342.55
Y	20.74	21.91	18.07	18.34	19.37	20.73	20.50	22.90	16.76	20.44	18.66
Zr	105.58	148.42	141.16	131.73	109.39	125.18	129.13	151.60	123.99	145.79	123.05
Nb	9.12	16.76	12.54	10.43	13.38	12.33	15.16	22.55	11.26	13.22	13.73
Ba	75.24	63.91	108.13	98.62	103.27	94.96	115.61	76.45	100.79	99.31	116.03
La	11.33	14.43	13.02	11.09	12.30	12.53	14.68	19.39	11.54	14.87	14.56
Ce	24.80	31.08	30.40	28.62	29.84	28.01	34.70	44.36	25.48	33.66	31.82
Pr	3.40	4.76	4.07	3.60	3.67	3.77	4.36	6.26	3.79	4.30	4.30
Nd	18.45	22.40	19.04	15.53	18.41	19.78	18.96	28.41	22.38	24.13	20.33
Sm	4.37	5.85	5.04	4.86	4.62	4.28	4.63	6.48	4.24	4.86	5.23
Eu	1.92	1.98	1.73	1.86	1.58	1.69	1.68	2.18	1.90	1.82	1.82
Gd	5.15	6.55	3.46	3.58	4.50	4.45	5.20	6.37	3.98	4.59	4.36
Tb	0.76	0.84	0.78	0.68	0.67	0.69	0.70	0.99	0.76	0.71	0.73
Dy	4.24	4.95	4.04	3.63	3.89	4.30	4.23	6.02	3.65	4.05	4.10
Ho	0.90	0.93	0.81	0.59	0.80	0.78	0.80	1.14	0.80	0.75	0.80
Er	1.99	2.17	1.83	1.43	2.22	1.95	2.01	2.64	1.78	2.17	1.83
Tm	0.31	0.37	0.29	0.33	0.27	0.24	0.27	0.36	0.27	0.27	0.26
Yb	1.82	1.98	1.52	1.53	1.47	1.81	1.71	2.29	1.57	1.47	1.61
Lu	0.24	0.23	0.17	0.28	0.20	0.21	0.24	0.33	0.21	0.22	0.22
Hf	2.82	3.84	3.33	2.41	3.65	2.91	3.26	5.09	2.33	3.24	3.44
Ta	0.55	1.27	0.75	0.79	0.82	0.72	0.95	1.67	0.67	0.91	0.85
Pb	1.07	1.04	1.32	0.80	0.93	0.73	0.93	1.30	2.35	0.55	1.02
U	0.25	0.37	0.27	0.21	0.33	0.30	0.39	0.60	0.40	0.36	0.34
Fo mol%	86.2	88.3	88.5	88.4	87.8	87.9	86.4	87.6	85.3	87.4	87.4
Ol %	21.07	20.42	21.66	24.3	18.68	17.34	13.18	21.11	12.66	16.74	18.35

Table 9: Historical (1971–1982 AD) Kīlauea melt inclusion compositions (cont'd)

Sample	1974-J110m1	1971-J117m1	1974-J119m1	1974-J122m1	1974-J135m1	1974-J208m1	1974-J220m1	1974-J227m1	1974-J227m2
SiO_2	50.22	49.87	49.87	50.35	50.05	49.37	49.20	49.58	49.52
TiO_2	2.44	2.69	2.60	2.44	2.47	2.35	2.50	2.32	2.27
Al_2O_3	13.15	13.27	13.27	12.68	13.27	12.04	12.42	11.71	12.01
Cr_2O_3	0.04	0.03	0.04	0.04	0.06	0.08	0.08	0.07	0.07
Fe_2O_3	0.82	0.84	0.89	0.82	0.80	0.88	0.87	1.02	0.95
FeO	10.61	10.61	10.55	10.59	10.62	10.54	10.55	10.42	10.48
MnO	0.21	0.21	0.21	0.18	0.19	0.22	0.20	0.18	0.20
MgO	8.30	7.80	7.79	8.58	7.87	10.77	10.31	11.13	10.91
CaO	10.60	11.02	11.28	10.81	11.02	10.65	10.59	10.79	10.70
Na_2O	2.34	2.43	2.50	2.26	2.33	1.97	2.10	2.08	2.08
NiO	0.012	0.012	0.010	0.005	0.032	0.008	0.026	0.028	0.018
K_2O	0.50	0.47	0.49	0.45	0.47	0.42	0.46	0.38	0.39
P_2O_5	0.25	0.27	0.27	0.26	0.29	0.24	0.25	0.20	0.20
F ppm	492	553	486	421	463	376	436	466	432
Cl ppm	138	145	149	124	144	133	146	128	124
S ppm	1433	1558	1568	1278	1409	1429	1791	403	530
Total	99.82	99.90	100.13	99.76	99.79	99.88	99.97	100.05	99.95
CO_2 ppm	273	230	284	139	292	293	280	77	b.d
H_2O wt%	0.54	0.49	0.26	0.55	0.58	0.47	0.47	0.12	0.23
Sc	28.72	25.72	28.64	28.71	28.27	32.14	52.36	27.47	23.95
V	314.87	332.43	320.08	318.05	314.08	272.95	309.66	297.15	266.96
Rb	9.56	9.19	7.97	10.90	9.10	6.43	6.02	5.83	7.36
Sr	348.58	369.86	341.36	516.77	409.73	307.86	336.67	337.26	333.76
Y	22.75	25.11	23.17	29.07	30.24	22.94	18.29	19.40	15.71
Zr	167.30	175.52	167.64	200.95	169.37	111.82	52.37	101.07	116.14
Nb	17.84	18.50	17.79	21.87	18.86	13.25	13.72	13.78	13.61
Ba	98.71	101.77	87.30	146.15	137.08	100.54	121.30	105.71	101.00
La	14.73	14.76	12.20	21.24	17.73	10.90	7.49	10.79	9.89
Ce	33.18	35.51	32.85	53.94	44.75	25.71	20.72	27.65	25.23
Pr	4.81	5.71	4.45	7.98	6.27	4.07	5.38	4.23	3.56
Nd	22.18	23.76	20.06	36.89	28.73	20.32	18.57	20.06	18.27
Sm	6.16	7.14	4.77	9.54	9.58	4.92	3.27	4.05	4.63
Eu	1.99	1.68	1.80	3.48	2.74	1.80	1.60	2.29	1.66
Gd	5.25	6.54	5.06	9.47	8.04	4.48	5.43	4.24	4.68
Tb	0.74	0.68	0.86	1.33	1.37	0.74	0.57	0.63	0.53
Dy	4.40	5.56	4.93	7.90	7.73	3.99	4.17	4.39	2.99
Ho	0.84	0.93	0.85	1.81	1.53	0.77	0.38	0.64	0.77
Er	2.23	2.14	2.15	4.48	3.79	2.34	1.78	1.73	1.70
Tm	0.21	0.29	0.28	0.60	0.38	0.29	b.d	0.20	0.25
Yb	1.96	2.01	2.34	3.48	3.17	1.95	4.23	1.29	1.65
Lu	0.24	0.20	0.31	0.53	0.38	0.26	b.d	0.27	0.20
Hf	3.46	3.30	3.85	7.52	5.89	3.64	3.81	2.82	2.34
Ta	0.76	0.94	0.76	1.76	1.56	0.87	0.37	0.73	0.89
Pb	0.92	0.91	0.72	4.86	1.86	0.76	4.63	0.63	0.81
U	0.27	0.29	0.33	0.61	0.58	0.26	0.26	0.12	0.30
Fo mol%	81.5	80.6	80.8	82.0	80.6	85.4	84.9	86.0	85.7
Ol %	6.74	4.96	5.16	9.5	4.22	9.35	3.9	11.99	10.88

Table 9: Historical (1971–1982 AD) Kīlauea melt inclusion compositions (cont'd)

Sample	1974-J202m1	1974-J208m1	1974-J219m1	1974-J219m2	1974-S08m1	1974-S13m1	1981-104m3	1982-113m1	1981-101m1	1982-101m2
SiO_2	49.46	49.34	48.88	48.63	49.93	49.58	50.40	49.90	50.64	50.34
TiO_2	2.31	2.43	2.52	2.75	2.59	2.52	2.35	2.50	2.31	2.58
Al_2O_3	12.39	12.36	11.74	12.09	12.59	12.72	12.76	12.90	12.68	12.89
Cr_2O_3	0.05	0.08	0.10	0.07	0.05	0.05	0.03	0.05	0.06	0.05
Fe_2O_3	1.12	1.15	0.93	1.15	0.85	0.84	0.81	0.83	1.05	1.06
FeO	10.33	10.30	10.50	10.30	10.58	10.60	10.62	10.59	10.39	10.38
MnO	0.17	0.18	0.21	0.18	0.20	0.18	0.20	0.21	0.23	0.18
MgO	10.60	10.43	10.09	10.09	8.49	8.58	8.74	8.64	8.58	8.53
CaO	11.04	10.90	11.68	11.93	11.06	11.46	10.70	10.98	11.14	11.03
Na_2O	1.91	2.18	2.19	1.94	2.34	2.24	2.19	2.22	2.17	2.26
NiO	0.017	b.d	0.001	0.033	0.018	0.012	0.012	0.008	0.004	0.026
K_2O	0.39	0.43	0.48	0.53	0.49	0.44	0.43	0.45	0.42	0.47
P_2O_5	0.23	0.23	0.29	0.33	0.27	0.27	0.21	0.22	0.32	0.24
F ppm	467	418	431	303	477	464	523	464	273	367
Cl ppm	141	155	135	165	137	127	130	126	68	102
S ppm	857	928	1321	844	1397	1347	1176	1284	767	869
Total	100.25	100.24	99.91	100.25	99.79	99.81	99.75	99.80	100.19	100.25
CO_2 ppm	n.d	n.d	210	n.d	215	291	88	131	n.d	n.d
H_2O wt%	n.d	n.d	0.41	n.d	0.57	0.53	0.57	0.52	n.d	n.d
Sc	30.30	28.24	29.34	47.90	78.90	31.34	37.10	36.84	30.37	63.09
V	277.12	260.90	294.32	443.14	285.75	284.06	348.91	326.09	278.93	298.47
Rb	5.58	6.69	7.12	9.69	7.12	7.36	13.19	12.11	6.63	5.21
Sr	306.77	267.85	332.79	358.34	387.52	383.63	527.29	502.12	293.92	212.57
Y	21.66	20.07	20.83	25.48	28.00	22.42	35.87	30.37	18.94	26.72
Zr	123.12	107.02	126.96	268.74	167.34	132.10	258.84	236.72	119.49	128.43
Nb	13.76	10.38	11.93	16.17	11.17	15.12	18.99	21.29	10.36	12.14
Ba	107.85	92.57	108.67	157.07	76.43	118.16	163.96	163.16	104.50	101.53
La	10.47	11.25	13.69	20.90	11.92	12.30	23.48	22.28	12.09	10.93
Ce	32.31	28.86	32.46	32.24	27.70	29.71	54.51	55.12	28.85	32.33
Pr	3.81	3.84	4.87	5.21	3.72	4.64	9.19	9.12	4.05	3.44
Nd	15.41	14.39	20.89	30.33	12.63	23.51	36.62	41.34	22.60	14.96
Sm	4.84	4.33	5.35	5.43	3.22	5.28	13.93	10.51	4.33	1.88
Eu	1.99	1.98	2.04	1.28	1.82	1.82	4.00	3.95	1.73	2.51
Gd	5.22	4.99	5.36	7.71	8.10	6.33	8.73	9.28	5.35	1.77
Tb	0.95	0.90	0.75	1.08	0.63	0.64	1.63	1.29	0.82	0.74
Dy	5.24	4.52	5.08	5.19	3.53	5.36	9.07	9.64	4.16	6.54
Ho	0.90	0.91	0.80	1.07	1.16	0.85	1.81	1.81	0.88	1.73
Er	1.77	1.70	1.86	4.23	1.65	2.22	5.92	4.10	1.98	2.72
Tm	0.28	0.21	0.26	0.56	0.32	0.29	0.76	0.52	0.34	0.67
Yb	1.71	1.48	2.25	1.43	3.87	1.94	2.95	4.16	2.38	4.27
Lu	0.36	0.24	0.21	b.d	b.d	0.27	0.43	0.52	0.28	0.44
Hf	3.58	2.58	3.06	7.20	4.24	4.40	8.12	6.89	3.37	5.75
Ta	0.81	0.72	0.81	0.63	0.54	0.72	2.19	2.06	0.58	0.47
Pb	0.80	1.27	0.93	8.67	b.d	0.97	1.41	2.20	0.75	2.26
U	0.45	0.37	0.30	0.72	0.76	0.33	0.85	0.82	0.24	b.d
Fo mol%	85.4	85.4	84.9	85.1	82.0	82.2	82.2	82.2	82.1	82.2
Ol %	9.23	7.55	11.86	12.07	6.19	7.65	8.19	7.3	9.44	6.43

Table 9: Historical (1971–1982 AD) Kīlauea melt inclusion compositions (cont'd)

Sample	1982-104m1	1982-104m2	1982-104m3	1982-104m4	1982-112m1	1982-210m1	1982-211m1	1982-211m2	1982-212m1	1982-222m1
SiO_2	49.91	50.60	50.61	50.27	50.47	50.28	49.78	49.89	50.24	50.04
TiO_2	2.62	2.50	2.45	2.52	2.56	2.21	2.50	2.58	2.59	2.50
Al_2O_3	13.36	12.52	12.99	12.98	13.23	12.51	12.73	12.96	12.92	12.85
Cr_2O_3	0.04	0.06	0.05	0.06	0.03	0.03	0.06	0.06	0.06	0.06
Fe_2O_3	1.04	1.07	1.06	1.06	1.06	1.12	1.08	1.06	1.06	1.06
FeO	10.41	10.43	10.38	10.38	10.45	10.34	10.39	10.38	10.38	10.38
MnO	0.18	0.19	0.17	0.16	0.20	0.15	0.21	0.19	0.20	0.19
MgO	8.41	8.73	8.62	8.56	8.50	10.15	9.23	8.92	8.61	8.77
CaO	11.11	11.10	10.69	10.99	10.42	10.35	11.22	11.15	10.96	11.28
Na_2O	2.19	2.10	2.26	2.28	2.36	2.20	2.13	2.15	2.26	2.13
NiO	0.015	0.029	b.d	0.024	0.007	b.d	0.061	0.038	0.014	0.002
K_2O	0.47	0.44	0.52	0.50	0.46	0.42	0.43	0.40	0.47	0.48
P_2O_5	0.25	0.26	0.24	0.24	0.26	0.26	0.25	0.26	0.26	0.25
F ppm	343	544	533	594	293	343	370	431	433	538
Cl ppm	190	112	161	92	155	113	114	85	145	103
S ppm	870	754	900	839	731	942	834	834	727	959
Total	100.24	100.24	99.25	100.26	100.20	99.23	100.27	100.26	100.22	100.26
CO_2 ppm	n.d	n.d	n.d	n.d	n.d	n.d	n.d	n.d	n.d	n.d
H_2O wt%	n.d	n.d	n.d	n.d	n.d	n.d	n.d	n.d	n.d	n.d
Sc	31.25	33.21	29.44	28.54	n.d	40.28	45.12	48.67	26.94	33.29
V	284.81	221.23	286.00	289.10	n.d	271.73	314.77	328.17	283.82	289.53
Rb	4.90	5.33	7.16	7.29	n.d	5.37	11.05	8.43	8.40	7.68
Sr	390.07	284.08	309.98	343.60	n.d	309.43	340.96	425.80	295.16	331.98
Y	20.04	22.93	23.69	22.41	n.d	26.99	23.59	30.46	21.43	23.81
Zr	152.23	69.92	133.89	142.85	n.d	154.79	85.66	161.71	118.71	131.05
Nb	13.84	11.50	10.64	10.78	n.d	11.82	14.34	19.63	11.25	11.52
Ba	97.93	116.70	105.39	101.56	n.d	107.80	104.65	163.34	102.41	104.44
La	15.06	9.92	12.44	12.65	n.d	13.18	14.58	10.32	11.76	13.40
Ce	35.95	24.09	26.78	28.62	n.d	28.35	30.02	23.11	28.35	29.90
Pr	3.96	3.87	3.92	3.63	n.d	4.35	3.98	4.68	3.98	4.02
Nd	17.73	19.01	18.11	19.21	n.d	20.61	19.95	21.98	20.20	21.30
Sm	5.42	6.14	5.05	4.58	n.d	3.86	7.51	4.22	5.37	5.57
Eu	1.36	1.85	1.81	1.93	n.d	2.00	2.04	1.58	1.76	1.82
Gd	4.17	3.84	4.80	4.82	n.d	5.99	5.88	3.49	5.69	6.07
Tb	0.71	0.41	0.80	0.64	n.d	0.96	0.73	0.56	0.81	0.78
Dy	5.54	6.27	4.42	4.67	n.d	4.21	4.54	5.43	4.74	4.82
Ho	0.99	0.94	0.85	0.84	n.d	1.05	0.85	0.93	1.07	1.11
Er	2.35	1.49	2.17	2.03	n.d	1.41	1.74	1.97	2.20	2.33
Tm	0.30	b.d	0.31	0.27	n.d	0.49	0.24	0.28	0.26	0.27
Yb	1.45	b.d	1.39	2.23	n.d	1.79	1.55	3.36	2.03	2.03
Lu	0.21	0.60	0.24	0.28	n.d	0.14	0.18	0.28	0.28	0.29
Hf	3.16	3.73	3.53	3.47	n.d	3.40	5.23	6.84	3.80	4.27
Ta	0.78	0.52	0.59	0.80	n.d	0.61	0.77	1.06	0.56	0.64
Pb	0.61	1.24	0.74	0.47	n.d	1.46	1.38	4.28	0.93	0.51
U	0.23	b.d	0.27	0.26	n.d	0.37	b.d	0.68	0.28	0.36
Fo mol%	82.0	82.4	82.3	82.3	82.0	84.7	83.5	83.0	82.4	82.7
Ol %	5.86	8.39	7.47	7.34	6.84	12.78	11.71	11.33	7.62	6.84

Table 10: Historical (2008–2010 AD) Kīlauea melt inclusion compositions

Sample	S1-06m1	S1-17m1	S1-21m1	S1-24m1	S1-26m1	S1-46m1	S1-47m1	S1-53m1	S1-55m1	S2-11m1	S2-18m1	S2-30m1
SiO_2	50.54	50.52	50.67	50.67	50.42	50.69	50.58	50.82	50.81	50.89	50.61	50.86
TiO_2	2.33	2.33	2.35	2.34	2.38	2.27	2.29	2.31	2.37	2.23	2.36	2.32
Al_2O_3	12.76	12.76	13.10	12.75	12.81	12.83	12.58	12.74	12.72	12.85	12.91	12.80
Cr_2O_3	0.05	0.05	0.05	0.04	0.04	0.05	0.05	0.07	0.05	0.06	0.05	0.04
Fe_2O_3	0.84	0.83	0.88	0.84	0.84	0.87	0.85	0.83	0.81	0.85	0.84	0.86
FeO	10.58	10.59	10.54	10.58	10.64	10.55	10.58	10.60	10.61	10.58	10.59	10.57
MnO	0.18	0.18	0.19	0.20	0.19	0.18	0.20	0.19	0.20	0.20	0.18	0.20
MgO	9.16	9.16	8.91	8.92	9.16	8.72	9.15	8.71	9.11	8.88	8.63	8.70
CaO	10.52	10.51	10.41	10.55	10.50	10.90	10.67	10.70	10.77	10.48	10.88	10.55
Na_2O	2.11	2.11	2.16	2.16	2.05	2.18	2.13	2.13	1.64	2.13	2.11	2.26
NiO	0.032	0.032	0.011	0.014	0.013	0.015	0.008	0.022	0.006	0.014	0.010	0.023
K_2O	0.37	0.37	0.40	0.38	0.38	0.37	0.38	0.36	0.39	0.40	0.35	0.38
P_2O_5	0.23	0.23	0.22	0.23	0.24	0.22	0.22	0.22	0.23	0.22	0.24	0.22
F ppm	388	388	416	378	417	338	345	406	402	435	357	355
Cl ppm	91	90	97	96	87	96	93	97	84	86	90	73
S ppm	1334	1333	1091	1086	1119	800	1057	1062	1080	1111	1148	1062
Total	100.00	99.98	100.15	99.93	99.93	100.05	99.93	99.95	99.99	100.04	100.02	100.03
CO_2 ppm	220	156	39	90	120	46	196	90	85	130	59	132
H_2O wt%	0.35	0.36	0.13	0.35	0.36	0.17	0.33	0.34	0.28	0.25	0.27	0.25
Sc	30.38	28.89	27.69	29.13	28.98	26.78	27.21	29.64	25.80	31.02	29.80	27.39
V	268.76	269.80	264.82	274.90	273.84	274.60	265.77	265.18	260.94	273.93	269.30	265.36
Rb	6.91	5.58	7.12	6.19	7.34	6.26	6.07	6.37	5.39	6.41	6.87	6.51
Sr	309.78	309.69	300.11	280.12	302.20	322.57	292.50	269.86	263.23	277.24	257.13	325.08
Y	22.83	22.37	21.55	18.68	22.84	21.83	22.01	20.48	19.61	23.68	21.51	22.25
Zr	145.28	134.49	133.60	100.99	152.84	109.33	115.29	123.31	113.34	119.34	111.33	148.30
Nb	12.44	12.07	11.04	9.76	12.14	11.90	11.26	9.74	9.10	8.38	8.17	12.08
Ba	74.67	67.21	57.39	85.56	60.75	72.09	63.15	75.65	82.42	75.54	85.70	73.69
La	10.05	9.74	10.03	10.49	10.25	10.28	9.27	10.04	10.80	8.35	8.78	10.29
Ce	22.90	23.90	23.88	25.50	23.78	23.17	24.29	24.58	24.63	21.97	26.95	22.55
Pr	4.09	3.60	3.64	3.36	3.99	3.90	3.54	3.19	3.35	3.39	3.44	3.79
Nd	16.31	16.89	16.92	17.27	17.89	17.02	18.80	18.41	17.26	17.65	14.81	18.36
Sm	4.65	4.56	4.69	4.46	4.56	4.50	4.58	4.26	4.61	4.03	4.99	4.46
Eu	1.63	1.49	1.64	1.77	1.47	1.63	1.60	1.67	1.76	1.63	1.36	1.84
Gd	4.93	4.86	4.28	4.35	5.77	4.70	5.14	4.39	4.66	5.40	4.43	4.29
Tb	0.66	0.86	0.77	0.75	0.60	0.82	0.85	0.65	0.74	0.73	0.78	0.55
Dy	3.98	4.61	4.40	4.24	5.15	4.98	5.56	4.36	4.12	4.49	4.08	3.25
Ho	0.93	0.91	0.86	0.83	0.89	0.93	0.99	0.84	0.81	0.78	0.78	0.74
Er	2.47	2.39	2.13	1.97	2.46	2.50	2.08	1.81	1.95	2.13	2.32	2.02
Tm	0.27	0.31	0.24	0.30	0.29	0.28	0.34	0.34	0.26	0.29	0.23	0.25
Yb	1.90	1.56	1.63	1.77	1.74	2.05	1.63	1.91	1.56	1.42	1.81	1.86
Lu	0.32	0.24	0.28	0.26	0.25	0.27	0.24	0.28	0.21	0.26	0.22	0.32
Hf	3.56	2.95	3.29	3.10	3.04	3.09	3.31	3.81	2.80	3.14	2.79	3.05
Ta	0.70	0.53	0.58	0.62	0.62	0.66	0.65	0.51	0.49	0.45	0.59	0.53
Pb	0.59	0.63	0.76	0.62	0.70	1.02	0.67	0.94	1.11	0.74	0.84	0.73
U	0.29	0.27	0.27	0.28	0.31	0.23	0.26	0.20	0.21	0.21	0.15	0.26
Fo mol%	82.9	82.9	82.5	82.5	82.8	82.2	82.9	82.0	82.5	82.3	81.9	82.1
Ol %	6.04	6.09	9.49	4.96	7.16	4.77	9.63	6.04	8.96	5.21	5.75	3.45

Table 10: Historical (2008–2010 AD) Kīlauea melt inclusion compositions (cont'd)

Sample	S2-38m1	S2-41m1	S2-42m1	S2-44m1	18-b2m1	18-02m2	18-12m1	18-20m1	18-29m1	18-40m1	18-01m2	18-02m1
SiO_2	50.78	50.66	51.40	50.91	50.51	50.59	50.36	50.61	50.78	50.54	50.14	48.68
TiO_2	2.18	2.37	2.17	2.29	2.49	2.39	2.37	2.36	2.29	2.36	2.38	2.06
Al_2O_3	13.20	13.09	12.68	12.83	12.88	12.90	13.04	12.92	13.03	12.86	13.12	11.58
Cr_2O_3	0.04	0.04	0.06	0.05	0.06	0.04	0.05	0.04	0.05	0.06	0.06	0.07
Fe_2O_3	0.84	0.85	0.85	0.86	0.84	0.84	0.84	0.85	0.84	0.85	0.88	1.08
FeO	10.58	10.57	10.57	10.60	10.58	10.57	10.59	10.58	10.59	10.58	10.54	10.36
MnO	0.18	0.19	0.18	0.18	0.19	0.20	0.20	0.19	0.19	0.19	0.20	0.18
MgO	8.89	8.84	8.87	8.98	8.64	8.64	8.58	8.53	8.55	8.49	8.42	14.01
CaO	10.12	10.37	10.09	10.40	10.78	10.78	10.89	10.76	10.61	10.84	10.74	9.21
Na_2O	2.30	2.18	2.26	2.11	2.10	2.15	2.17	2.27	2.25	2.26	2.60	1.97
NiO	0.022	0.024	0.027	0.008	0.005	b.d	0.013	0.008	b.d	0.018	0.030	0.036
K_2O	0.39	0.39	0.37	0.38	0.41	0.40	0.37	0.37	0.34	0.42	0.41	0.36
P_2O_5	0.22	0.23	0.24	0.22	0.24	0.22	0.26	0.22	0.21	0.23	0.23	0.19
F ppm	399	401	365	405	444	315	378	408	452	380	431	272
Cl ppm	90	86	107	78	108	76	95	133	103	92	76	70
S ppm	1181	1052	878	736	1168	1134	1195	1141	943	1133	674	836
Total	100.03	100.04	99.98	99.98	100.00	98.98	100.00	99.99	98.96	99.96	99.94	99.98
CO_2 ppm	68	176	b.d	104	217	119	b.d	109	202	80	n.d	147
H_2O wt%	0.28	0.24	0.27	0.23	0.30	0.29	0.30	0.30	0.28	0.33	0.28	0.26
Sc	26.41	26.13	19.96	30.45	32.21	26.54	26.98	32.83	33.59	24.77	29.87	22.72
V	250.04	271.33	224.45	261.84	270.68	291.31	299.11	350.07	286.89	264.32	273.38	236.46
Rb	6.79	6.43	5.56	6.31	5.90	6.38	7.23	10.49	6.21	7.07	6.49	6.65
Sr	297.65	313.30	290.80	280.54	299.36	339.61	376.83	480.80	294.00	323.78	277.18	251.48
Y	18.97	20.19	20.98	21.94	21.73	27.00	26.34	34.19	28.37	22.50	20.63	18.83
Zr	99.24	119.24	114.12	120.40	147.09	150.62	170.51	199.70	175.43	160.34	126.55	102.26
Nb	12.08	12.17	9.71	11.84	12.05	13.11	15.97	19.87	13.18	13.15	9.22	8.04
Ba	67.60	77.53	50.93	67.69	67.72	86.70	101.15	164.07	92.31	96.71	77.09	74.44
La	10.11	9.51	7.42	9.98	9.50	11.52	14.94	21.77	10.50	11.61	9.71	9.15
Ce	22.47	25.17	19.96	22.48	23.58	28.08	36.99	52.94	27.77	28.65	23.59	21.82
Pr	3.65	3.52	3.20	3.45	3.30	4.09	5.52	8.74	3.86	4.23	3.23	2.81
Nd	15.23	17.04	16.82	15.88	15.76	20.96	29.00	41.06	19.58	21.16	15.11	14.26
Sm	4.56	5.43	4.16	5.32	4.89	5.91	6.38	12.14	4.59	3.55	4.27	3.97
Eu	1.49	1.49	1.43	1.65	1.91	2.07	2.57	3.32	1.73	2.22	1.62	1.43
Gd	4.04	4.23	4.14	5.68	4.33	5.31	6.94	9.99	4.26	5.24	4.53	4.08
Tb	0.58	0.69	0.73	0.63	0.79	0.93	1.09	1.72	0.79	0.93	0.74	0.71
Dy	3.86	4.44	5.27	3.67	4.91	5.48	7.38	10.43	5.08	5.21	4.60	4.19
Ho	0.77	0.75	0.90	1.02	0.88	1.03	1.30	2.14	1.09	1.05	0.83	0.73
Er	1.71	2.45	1.91	1.90	2.37	2.62	3.43	5.57	2.63	2.79	2.00	1.71
Tm	0.25	0.28	0.30	0.22	0.27	0.29	0.38	0.78	0.22	0.38	0.29	0.26
Yb	1.53	1.99	1.31	1.44	1.87	2.07	2.37	4.11	1.74	2.08	1.90	1.72
Lu	0.22	0.25	0.25	0.19	0.21	0.36	0.27	0.62	0.41	0.38	0.24	0.24
Hf	2.94	2.65	2.59	3.44	4.06	4.20	5.29	7.68	3.48	3.62	2.50	2.96
Ta	0.67	0.76	0.43	0.89	0.81	0.82	1.22	1.84	0.75	0.90	0.56	0.45
Pb	0.95	0.90	0.98	0.61	0.76	0.84	1.32	2.11	1.05	1.10	0.34	0.74
U	0.30	0.28	0.28	0.25	0.14	0.27	0.46	0.53	0.42	0.28	b.d	0.22
Fo mol%	82.4	82.3	82.2	82.5	82.0	82.0	81.9	81.9	81.8	81.8	82.0	88.7
Ol %	4.58	3.53	8.31	5.37	4.3	4.24	4.51	3.8	3.51	2.81	2.73	24.86

Table 10: Historical (2008–2010 AD) Kīlauea melt inclusion compositions (cont'd)

Sample	18-07m1	18-10m1	18-10m2	18-10m3	18-10m4	18-13m1	18-13m2	18-19m1	18-19m2	18-22m1	18-22m2	18-23m1
SiO_2	50.55	50.34	50.51	50.09	50.69	50.47	50.61	49.21	49.63	50.36	50.17	50.59
TiO_2	2.34	2.43	2.19	2.41	2.25	2.42	2.43	2.13	2.05	2.32	2.38	2.36
Al_2O_3	13.16	13.03	13.16	13.11	13.02	12.96	13.17	12.11	12.19	12.96	13.14	12.87
Cr_2O_3	0.04	0.06	0.07	0.07	0.06	0.06	0.05	0.06	0.06	0.04	0.04	0.05
Fe_2O_3	0.84	0.84	0.83	0.84	0.85	0.87	1.03	1.00	1.21	0.86	0.86	0.89
FeO	10.58	10.58	10.59	10.59	10.58	10.55	10.41	10.43	10.24	10.57	10.58	10.53
MnO	0.19	0.19	0.19	0.20	0.17	0.17	0.20	0.17	0.16	0.20	0.17	0.21
MgO	8.51	8.81	8.78	8.75	8.64	8.78	8.54	11.84	12.10	8.76	8.61	8.71
CaO	10.52	10.67	10.72	11.01	10.68	10.56	10.75	9.89	9.70	10.85	10.96	10.71
Na_2O	2.32	2.11	2.15	2.04	2.24	2.32	2.19	2.32	2.11	2.24	2.30	2.36
NiO	0.019	0.019	0.032	0.016	0.010	0.006	0.024	0.018	0.038	0.014	0.025	0.010
K_2O	0.42	0.39	0.35	0.38	0.37	0.38	0.36	0.38	0.32	0.37	0.34	0.34
P_2O_5	0.23	0.28	0.22	0.25	0.22	0.22	0.27	0.23	0.23	0.22	0.23	0.21
F ppm	403	377	327	352	364	418	442	263	380	390	337	373
Cl ppm	80	91	87	89	91	89	80	83	90	101	72	86
S ppm	931	1358	739	1156	651	801	1525	810	837	380	370	567
Total	99.95	100.07	99.96	100.03	99.93	99.98	100.38	99.99	100.25	99.89	99.91	100.00
CO_2 ppm	b.d	220	231	336	216	150	n.d	b.d	n.d	123	b.d	221
H_2O wt%	0.30	0.27	0.26	0.26	0.25	0.24	n.d	0.23	n.d	0.25	0.23	0.17
Sc	28.60	26.61	26.91	31.77	26.90	27.73	23.16	19.14	24.88	30.15	26.28	26.24
V	279.61	271.08	271.53	292.22	300.92	271.51	273.99	220.53	263.49	302.55	273.51	271.70
Rb	5.36	7.16	5.88	5.54	5.47	6.27	6.82	7.58	5.86	7.35	7.50	6.65
Sr	306.23	284.32	315.50	317.31	326.16	291.70	314.94	262.07	270.13	308.60	305.01	270.63
Y	24.26	22.23	22.64	22.57	24.65	21.72	22.08	18.22	20.94	22.64	21.72	20.57
Zr	133.49	124.62	132.35	153.17	134.59	116.33	100.11	108.67	126.85	125.12	109.16	109.61
Nb	9.06	10.04	8.22	9.52	11.59	9.75	9.08	8.13	9.07	10.16	9.19	9.55
Ba	88.05	83.50	86.07	69.89	91.47	87.09	94.32	80.43	70.49	93.93	86.59	81.84
La	9.69	10.28	10.21	10.40	10.85	9.45	11.23	9.15	7.05	11.25	10.73	9.75
Ce	23.53	23.92	23.76	22.40	30.97	24.89	23.76	23.38	22.36	25.66	25.99	22.51
Pr	3.57	3.30	3.45	3.76	2.84	3.57	3.06	2.97	3.24	3.81	3.27	3.51
Nd	16.62	16.88	19.46	17.94	21.46	17.61	16.60	12.03	18.63	18.13	14.75	17.41
Sm	5.23	4.45	5.20	5.85	3.64	4.38	7.46	3.73	3.87	5.09	4.41	4.66
Eu	1.68	1.57	1.80	1.80	2.05	1.73	1.53	1.75	1.71	2.01	1.86	1.97
Gd	5.19	4.17	4.65	4.29	4.30	4.90	6.15	4.51	5.22	5.25	4.36	5.04
Tb	0.72	0.67	0.80	0.75	0.78	0.73	0.79	0.70	0.57	0.69	0.82	0.70
Dy	4.78	4.33	4.32	5.00	5.40	3.90	4.02	3.18	4.39	5.17	4.33	3.94
Ho	0.92	0.80	0.99	0.91	1.13	0.85	0.74	0.63	0.95	0.86	0.94	0.92
Er	2.34	2.09	2.24	2.64	2.60	2.01	2.37	1.56	2.07	2.13	2.08	2.06
Tm	0.29	0.26	0.29	0.28	0.37	0.29	0.28	0.29	0.27	0.26	0.28	0.28
Yb	1.78	1.44	1.88	1.40	2.24	2.00	2.34	1.89	1.99	2.03	1.80	1.85
Lu	0.24	0.29	0.30	0.28	0.40	0.27	0.29	0.16	0.27	0.29	0.26	0.27
Hf	2.65	2.98	3.43	2.94	3.56	2.52	3.66	2.57	3.24	3.66	3.29	2.62
Ta	0.55	0.44	0.59	0.58	0.31	0.51	0.56	0.45	0.27	0.45	0.59	0.46
Pb	0.42	0.93	0.65	0.42	b.d	0.78	1.13	0.57	0.88	1.35	0.46	1.05
U	0.34	0.20	0.27	0.16	0.18	0.15	0.51	0.18	0.17	0.26	0.15	0.38
Fo mol%	81.8	82.3	82.2	82.3	82.0	82.4	82.0	86.8	87.1	82.3	82.1	82.3
Ol %	2.2	4.68	4.47	3.61	3.84	3.34	2.87	18.05	18.38	5.71	4.16	5.71

Table 10: Historical (2008–2010 AD) Kīlauea melt inclusion compositions (cont'd)

Sample	18-25m1	18-25m2	S3-06m1	S3-08m1	S3-14m1	S3-23m1	S3-24m1	S3-33m1	S3-56m1	S3-57m1	S3-62m1	S3-62m2
SiO_2	50.35	50.73	50.77	50.85	51.20	51.12	51.29	51.07	50.70	50.85	50.94	50.74
TiO_2	2.31	2.34	2.34	2.27	2.24	2.24	2.23	2.23	2.28	2.30	2.25	2.29
Al_2O_3	12.91	12.89	12.93	13.07	12.88	12.91	12.91	13.03	13.24	13.16	12.99	13.24
Cr_2O_3	0.06	0.05	0.06	0.05	0.05	0.05	0.06	0.04	0.05	0.05	0.05	0.06
Fe_2O_3	0.87	0.87	0.86	0.88	0.87	0.88	0.86	0.85	0.87	0.88	0.87	0.85
FeO	10.55	10.55	10.56	10.57	10.56	10.56	10.62	10.57	10.55	10.62	10.56	10.57
MnO	0.20	0.18	0.19	0.19	0.18	0.19	0.19	0.19	0.18	0.19	0.19	0.18
MgO	8.81	8.73	8.63	8.60	8.54	8.49	8.47	8.65	8.47	8.33	8.33	8.32
CaO	10.82	10.57	10.69	10.47	10.48	10.57	10.23	10.34	10.61	10.63	10.85	10.78
Na_2O	2.31	2.27	2.14	2.26	2.23	2.25	2.27	2.20	2.25	2.25	2.21	2.17
NiO	0.018	0.008	0.003	0.012	0.014	0.028	0.036	0.019	0.015	0.013	0.014	0.015
K_2O	0.36	0.38	0.42	0.41	0.40	0.39	0.43	0.40	0.41	0.38	0.37	0.39
P_2O_5	0.21	0.22	0.22	0.22	0.22	0.22	0.24	0.22	0.24	0.23	0.23	0.24
F ppm	420	319	466	351	369	357	365	362	392	460	369	391
Cl ppm	111	80	95	64	62	73	68	85	104	90	95	96
S ppm	1241	627	672	656	448	502	672	698	942	488	597	649
Total	100.08	99.96	99.98	100.03	99.97	100.02	100.00	100.00	100.10	100.02	100.02	100.03
CO_2 ppm	228	b.d	337	327	95	91	145	156	73	b.d	163	171
H_2O wt%	0.24	0.22	0.21	0.15	0.17	0.15	0.21	0.20	0.15	0.14	0.16	0.16
Sc	28.78	27.40	28.21	27.09	27.03	24.16	26.90	27.49	29.50	20.99	26.69	26.71
V	283.30	280.91	267.80	277.95	275.95	263.93	269.14	272.63	298.52	272.45	262.14	268.89
Rb	7.13	6.13	6.28	5.50	6.00	5.37	7.30	6.10	5.32	6.21	6.80	7.01
Sr	297.62	305.32	281.82	279.91	292.96	273.66	297.18	303.09	270.76	295.92	298.53	298.37
Y	21.30	20.55	21.92	20.19	21.89	19.48	19.72	21.71	21.65	16.18	21.13	21.98
Zr	106.30	112.73	144.96	106.64	117.14	108.09	121.55	104.99	110.74	88.06	100.02	120.07
Nb	8.60	b.d	7.86	8.71	13.41	10.15	10.78	12.02	8.95	9.02	11.60	10.99
Ba	90.99	88.35	85.52	88.31	74.10	65.72	77.79	79.08	86.16	68.14	83.99	73.62
La	11.40	10.40	10.17	10.98	9.63	8.46	9.73	8.86	11.67	12.21	8.80	9.37
Ce	26.29	24.48	26.23	24.33	24.89	21.13	24.14	24.00	25.13	26.62	20.45	23.84
Pr	3.44	3.41	3.15	3.65	3.81	3.24	3.37	3.91	3.40	3.49	3.65	3.28
Nd	17.07	18.04	15.38	16.58	18.13	13.28	15.51	16.47	18.24	17.48	15.33	17.38
Sm	4.89	4.88	5.08	4.56	3.79	4.08	4.26	4.58	5.03	3.95	3.71	3.89
Eu	2.04	1.79	1.90	1.75	1.38	1.45	1.49	1.50	1.60	1.64	1.46	1.78
Gd	4.48	4.54	4.58	4.54	5.17	3.95	4.39	4.28	5.84	4.34	3.93	4.23
Tb	0.75	0.68	0.80	0.75	0.64	0.68	0.58	0.75	0.83	0.73	0.72	0.73
Dy	4.74	4.23	4.25	4.48	3.70	4.35	4.54	3.92	5.21	4.30	4.05	4.10
Ho	0.79	0.88	0.87	0.86	0.89	0.78	0.88	0.85	1.03	0.85	0.81	0.73
Er	2.06	1.95	1.81	2.36	2.12	1.81	2.01	2.36	2.63	2.75	2.20	2.03
Tm	0.30	0.27	0.29	0.25	0.28	0.24	0.25	0.28	0.27	0.24	0.28	0.29
Yb	1.94	1.79	1.82	1.59	2.25	1.25	1.41	1.84	2.04	1.58	1.42	1.74
Lu	0.16	0.27	0.31	0.27	0.24	0.22	0.26	0.26	0.26	0.35	0.32	0.21
Hf	3.92	3.02	3.11	3.32	3.66	2.84	2.93	2.57	2.88	2.00	3.67	3.13
Ta	0.57	0.57	0.64	0.63	0.65	0.84	0.79	0.80	0.55	0.80	0.49	0.78
Pb	1.38	0.75	0.99	0.65	0.95	0.49	0.93	0.74	0.83	0.60	0.39	0.81
U	0.18	0.24	0.31	0.25	0.32	0.22	0.25	0.27	0.27	0.21	0.18	0.26
Fo mol%	82.5	82.2	82.0	81.9	81.7	81.7	81.5	81.9	81.7	81.3	81.4	81.4
Ol %	4.96	6.31	4.66	3.72	4.31	4.09	4.6	4.11	3.51	4.16	3.9	4.05

Table 11: 1959-60 Kīlauea Iki and Kapoho eruption melt inclusion compositions

Sample	E1-05m1	E1-05m2	E1-07m1	E1-09m1	E1-10m1	E1-12m1	E1-27m1	E1-21m1	E1-22m1	E1-26m1	E2-05m1	E2-15m1	E2-16m1	E2-17m1
SiO_2	48.09	48.15	48.36	48.19	48.95	48.40	47.74	48.17	48.70	48.38	49.21	48.31	49.27	48.74
TiO_2	2.10	2.17	2.32	2.40	2.33	2.45	2.25	2.65	2.06	2.24	2.32	2.45	2.35	2.27
Al_2O_3	11.14	11.04	11.44	11.44	11.61	11.35	11.77	11.54	10.94	11.05	11.92	11.65	11.97	10.75
Cr_2O_3	0.14	0.14	0.11	0.13	0.11	0.11	0.09	0.11	0.14	0.14	0.07	0.06	0.08	0.07
Fe_2O_3	1.00	0.99	0.94	0.97	0.94	0.95	0.95	0.92	1.04	0.97	0.87	0.97	0.87	0.97
FeO	10.43	10.44	10.49	10.46	10.49	10.48	10.48	10.51	10.40	10.47	10.55	10.47	10.56	10.47
MnO	0.20	0.18	0.17	0.18	0.19	0.18	0.18	0.22	0.18	0.19	0.19	0.18	0.17	0.15
MgO	13.14	13.41	12.01	12.37	11.33	12.47	12.58	10.99	13.92	12.91	10.27	12.15	10.61	12.13
CaO	10.33	10.17	10.85	10.55	10.69	10.46	10.78	11.63	9.60	10.55	11.68	10.51	10.78	11.50
Na_2O	2.11	1.95	1.99	2.05	2.13	1.77	1.96	1.91	1.93	1.92	1.74	2.01	2.00	1.71
NiO	0.029	0.048	0.034	0.022	0.018	0.027	0.040	0.030	0.028	0.024	0.014	0.032	0.015	0.030
K_2O	0.38	0.38	0.43	0.45	0.46	0.55	0.42	0.51	0.34	0.34	0.45	0.51	0.44	0.42
P_2O_5	0.33	0.37	0.29	0.24	0.30	0.27	0.22	0.25	0.29	0.22	0.32	0.25	0.37	0.33
F ppm	665	708	621	627	631	628	632	674	531	650	570	481	557	576
Cl ppm	162	130	107	199	125	120	177	194	108	140	140	173	164	129
S ppm	924	1081	225	1344	1089	798	1140	1245	874	1244	750	1259	1294	567
Total	99.68	99.73	99.55	99.80	99.82	99.69	99.76	99.77	99.80	99.71	99.83	99.86	99.80	99.71
CO_2 ppm	299	357	b.d	649	460	274	595	275	254	380	54	178	70	94
H_2O wt%	0.61	0.62	0.60	0.58	0.49	0.57	0.59	0.59	0.46	0.64	0.41	0.49	0.54	0.50
Sc	28.63	25.50	28.38	29.03	28.10	27.24	26.96	32.15	25.82	24.15	36.69	25.87	23.34	23.15
V	259.87	253.18	266.72	253.61	272.19	247.89	291.01	346.79	237.53	256.36	263.77	282.94	263.96	294.26
Rb	7.07	6.72	8.82	7.70	7.61	9.38	6.97	9.35	6.21	6.38	7.41	9.39	9.04	7.95
Sr	300.89	277.80	336.02	365.58	315.79	300.02	275.19	339.55	253.42	279.95	309.34	352.44	347.54	345.60
Y	18.86	17.83	18.93	16.75	18.72	16.85	18.07	18.95	18.38	17.65	16.54	17.87	21.47	20.56
Zr	127.87	103.63	126.52	103.12	122.96	121.95	98.06	130.33	97.74	106.42	121.00	123.84	123.97	142.25
Nb	10.70	8.77	13.14	13.87	10.41	12.19	8.79	13.36	9.23	8.80	12.25	14.19	11.30	12.78
Ba	62.32	65.21	82.96	79.42	77.75	63.15	58.89	93.87	41.98	59.36	68.60	63.76	62.58	65.06
La	11.87	9.94	14.50	11.31	12.09	12.93	9.83	15.00	9.87	9.82	15.51	15.63	13.06	14.40
Ce	27.36	25.18	33.37	32.90	30.01	36.01	23.28	35.39	24.49	26.18	28.57	34.43	32.82	31.27
Pr	3.94	3.55	4.30	4.07	4.05	3.07	3.64	4.04	3.20	3.73	4.26	4.50	4.04	3.63
Nd	18.69	17.42	20.56	18.38	21.77	13.32	18.31	21.11	16.06	18.33	20.94	23.64	20.47	20.36
Sm	4.13	4.78	5.42	4.38	6.62	7.28	4.70	6.10	5.20	5.19	2.11	4.86	6.14	3.71
Eu	1.74	1.84	1.79	1.75	2.10	2.34	1.70	2.51	1.57	1.79	1.28	1.79	2.08	1.48
Gd	4.79	4.46	4.25	5.05	5.74	4.00	4.34	4.82	3.84	4.18	3.12	4.59	3.90	3.94
Tb	0.79	0.77	0.70	0.44	0.83	0.89	0.74	0.70	0.84	0.74	0.72	0.76	0.81	0.76
Dy	4.15	4.15	4.21	3.67	4.39	3.10	3.82	4.39	4.39	4.30	4.82	3.86	4.55	3.80
Ho	0.82	0.83	0.76	0.78	0.87	1.15	0.77	0.79	0.79	0.81	0.82	0.71	0.87	0.61
Er	1.84	1.80	2.03	1.72	2.29	1.39	1.85	2.09	2.14	1.81	1.62	1.88	2.46	1.77
Tm	0.27	0.27	0.22	0.22	0.30	0.25	0.27	0.20	0.27	0.24	0.28	0.20	0.27	0.21
Yb	1.75	1.56	1.86	1.28	1.80	1.32	1.59	1.41	1.47	1.54	1.64	1.73	1.79	1.45
Lu	0.23	0.21	0.23	0.22	0.21	0.19	0.23	0.20	0.26	0.19	0.13	0.22	0.26	0.21
Hf	3.16	2.86	3.84	3.50	3.89	3.47	3.20	4.16	3.21	3.10	3.69	3.56	3.64	2.76
Ta	0.70	0.50	0.78	0.80	0.69	1.11	0.55	0.99	0.74	0.56	0.87	0.93	0.62	0.66
Pb	0.58	0.73	0.73	0.33	0.74	b.d	0.67	0.65	1.07	0.76	2.06	1.04	1.23	0.87
U	0.27	0.23	0.32	0.45	0.34	0.44	0.27	0.17	0.22	0.28	0.23	0.42	0.32	0.45
Fo mol%	88.2	88.3	87.1	87.5	86.3	87.4	87.7	86.1	88.6	87.9	84.8	87.3	85.2	87.1
Ol %	9.52	9.98	8.11	11.2	7.24	17.6	11.61	5.12	18.58	8.95	14.5	18.66	13.59	15.54

Table 11: 1959-60 Kīlauea Iki and Kapoho eruption melt inclusion compositions (cont'd)

Sample	E2-17m2	E2-17m3	E2-21m1	E2-21m2	E2-22m1	E2-23m1	E3-03m1	E3-05m1	E3-05m2	E3-06m1	E3-13m1	E3-14m1	E3-15m1	E3-15m2
SiO_2	48.75	48.60	47.87	48.28	49.30	48.49	48.16	48.39	48.20	48.29	47.79	48.30	49.07	49.38
TiO_2	2.03	2.15	2.72	2.45	2.47	2.16	2.44	2.24	2.35	2.43	2.53	2.43	2.87	2.74
Al_2O_3	10.86	10.88	11.55	11.47	11.90	10.94	11.46	11.50	11.47	11.13	11.42	11.97	13.21	12.21
Cr_2O_3	0.07	0.07	0.07	0.05	0.06	0.08	0.12	0.08	0.08	0.07	0.08	0.07	0.03	0.05
Fe_2O_3	0.94	0.95	0.98	0.97	0.91	1.04	0.94	0.96	0.96	1.00	1.02	0.95	0.87	0.88
FeO	10.49	10.49	10.46	10.46	10.52	10.40	10.49	10.48	10.47	10.43	10.42	10.48	10.59	10.54
MnO	0.18	0.42	0.16	0.19	0.19	0.18	0.17	0.17	0.18	0.19	0.16	0.19	0.20	0.20
MgO	12.08	12.00	11.93	12.07	10.46	13.11	11.78	12.08	12.04	12.78	12.89	11.75	8.00	8.00
CaO	12.03	12.02	10.99	10.78	10.73	10.32	11.40	10.92	11.07	10.42	10.45	10.41	11.21	12.51
Na_2O	1.45	1.63	2.05	2.00	2.19	2.09	1.85	2.05	1.98	2.00	2.11	2.13	2.50	2.24
NiO	0.019	0.180	0.037	0.038	0.028	0.005	0.041	0.049	0.059	0.027	0.022	0.031	0.017	0.023
K_2O	0.42	0.24	0.48	0.51	0.53	0.41	0.42	0.38	0.42	0.47	0.41	0.55	0.59	0.46
P_2O_5	0.24	0.10	0.26	0.27	0.24	0.33	0.26	0.22	0.25	0.24	0.25	0.25	0.29	0.27
F ppm	422	176	506	482	540	611	593	651	676	598	623	673	762	777
Cl ppm	105	160	124	162	170	83	389	287	328	137	160	277	275	227
S ppm	174	380	1119	894	1232	118	1446	1207	1311	1243	906	1193	1258	1400
Total	99.62	99.82	99.83	99.78	99.85	99.64	99.90	99.84	99.89	99.81	99.80	99.85	99.79	99.86
CO_2 ppm	81	33	164	80	457	b.d	259	119	227	76	77	363	244	349
H_2O wt%	0.48	0.47	0.49	0.50	0.50	0.46	0.53	0.54	0.53	0.54	0.48	0.52	0.58	0.54
Sc	29.50	29.99	26.22	23.24	29.83	26.73	27.96	28.06	32.01	25.99	25.13	27.52	27.64	34.80
V	293.17	300.30	287.17	276.06	305.10	239.60	274.72	288.60	303.11	271.28	283.91	285.27	305.12	310.87
Rb	8.02	2.13	12.15	8.91	10.15	7.26	7.72	6.21	9.76	9.47	7.88	11.96	10.49	10.02
Sr	284.93	561.75	341.57	332.44	351.15	331.52	283.55	296.69	359.40	330.73	299.44	364.09	411.43	380.09
Y	16.53	20.42	18.58	18.30	19.90	20.17	19.89	22.00	21.18	18.94	18.45	19.10	25.33	22.14
Zr	98.71	103.54	158.99	145.81	130.72	103.56	128.36	120.95	154.65	125.76	111.64	157.42	165.49	152.24
Nb	11.30	5.88	14.56	13.99	14.12	10.98	13.20	9.58	15.02	13.57	13.51	13.76	16.75	14.81
Ba	59.00	27.26	62.38	59.37	82.85	39.12	54.18	49.98	61.50	62.60	46.35	72.78	117.00	119.78
La	14.27	7.75	14.55	16.00	14.38	11.20	13.23	10.72	12.78	14.74	13.44	14.32	17.14	14.45
Ce	27.94	16.56	35.16	34.45	34.54	28.44	29.88	23.72	30.76	33.84	30.23	33.66	37.78	38.55
Pr	3.68	2.74	4.97	3.95	4.31	4.68	3.99	3.69	4.13	4.62	4.10	4.85	5.29	5.21
Nd	15.83	15.67	23.08	22.63	21.85	17.94	17.89	19.91	18.48	20.87	20.99	22.15	20.91	24.19
Sm	4.32	5.07	6.17	3.81	5.08	5.09	5.12	5.58	6.26	5.30	5.90	4.96	5.88	5.41
Eu	1.49	1.51	1.99	1.57	1.88	1.83	1.87	1.88	1.88	1.92	1.83	2.05	2.12	1.97
Gd	4.00	4.63	5.13	4.14	4.94	4.49	4.28	4.73	3.91	4.95	5.42	5.01	5.57	5.32
Tb	0.61	0.49	0.69	0.79	0.76	0.70	0.75	0.82	0.76	0.78	0.87	0.84	0.88	0.84
Dy	4.58	4.66	4.08	3.85	4.43	3.94	4.42	3.73	4.64	4.14	4.65	4.79	4.74	4.82
Ho	0.82	0.79	0.89	0.83	0.83	0.81	0.78	0.81	1.01	0.86	0.85	1.02	0.95	0.87
Er	1.30	1.57	1.88	1.74	2.15	2.36	2.03	2.13	2.18	1.95	2.05	1.80	1.81	2.33
Tm	0.24	0.26	0.28	0.25	0.30	0.27	0.35	0.26	0.42	0.28	0.34	0.22	0.39	0.28
Yb	1.38	1.98	1.31	1.19	1.75	1.97	1.63	1.66	1.32	1.76	1.76	1.64	1.97	1.43
Lu	0.18	0.27	0.21	0.19	0.26	0.19	0.26	0.18	0.11	0.22	0.17	0.26	0.31	0.30
Hf	2.91	1.44	2.95	3.52	3.88	3.41	3.74	3.19	3.37	3.35	3.58	3.94	3.99	4.31
Ta	0.74	0.32	0.69	0.63	0.89	0.64	0.89	0.48	0.62	0.90	0.97	0.97	1.05	1.01
Pb	0.61	0.52	3.27	1.37	0.82	0.50	1.21	0.84	1.91	0.97	0.81	1.20	1.24	0.78
U	0.36	0.05	0.28	0.51	0.39	0.30	0.28	0.25	0.33	0.39	0.19	0.35	0.41	0.38
Fo mol%	87.0	87.0	87.2	87.2	85.2	88.1	86.9	87.2	87.2	87.9	88.1	86.9	81.4	81.4
Ol %	16.48	20.2	13.74	17.11	11.38	26.82	18.45	16.75	17.99	17.13	25.27	13.75	5.47	3.93

Table 11: 1959-60 Kīlauea Iki and Kapoho eruption melt inclusion compositions (cont'd)

Sample	E3-19m1	E3-19m2	E3-19m3	E3-25m1	E3-28m1	E5-09m1	E5-05m2	E5-10m1	E5-10m2	E5-10m3	E5-10m4	E5-14m1	E5-18m1	E6-08m1
SiO_2	48.41	48.69	48.71	48.34	48.78	48.51	48.39	49.05	48.37	48.19	48.25	48.63	48.65	48.24
TiO_2	2.41	2.45	2.32	2.41	2.74	2.12	2.11	2.16	2.60	2.59	2.45	2.47	2.19	2.41
Al_2O_3	11.31	11.23	11.20	11.57	12.20	11.30	11.33	11.32	11.57	11.64	11.64	11.13	11.39	11.45
Cr_2O_3	0.07	0.07	0.06	0.07	0.04	0.07	0.07	0.07	0.07	0.07	0.07	0.06	0.08	0.07
Fe_2O_3	0.96	0.97	0.97	0.95	0.91	1.00	1.01	0.94	0.96	0.96	0.96	0.97	0.97	0.97
FeO	10.47	10.46	10.46	10.48	10.52	10.43	10.42	10.48	10.47	10.48	10.47	10.46	10.46	10.46
MnO	0.19	0.20	0.20	0.16	0.18	0.18	0.18	0.18	0.19	0.18	0.20	0.19	0.17	0.21
MgO	11.84	11.66	12.19	11.97	9.91	12.76	13.04	11.95	11.63	11.84	11.52	12.24	12.33	12.15
CaO	11.10	10.91	10.72	10.95	10.95	10.42	10.25	10.77	10.88	10.96	11.16	10.74	10.58	11.00
Na_2O	2.03	2.12	2.00	2.01	2.32	2.07	2.06	1.99	2.03	1.97	2.08	1.88	2.07	1.98
NiO	0.002	0.024	0.026	0.033	0.014	0.019	0.025	0.019	0.026	0.029	0.026	0.028	0.031	0.025
K_2O	0.43	0.47	0.44	0.36	0.59	0.41	0.43	0.33	0.52	0.44	0.49	0.47	0.35	0.29
P_2O_5	0.24	0.23	0.24	0.22	0.31	0.22	0.22	0.24	0.25	0.24	0.24	0.26	0.29	0.33
F ppm	666	677	668	724	694	560	515	523	645	587	541	503	514	563
Cl ppm	159	282	231	182	209	126	106	123	159	142	181	219	161	85
S ppm	1375	1511	1467	1137	1298	964	905	715	1138	1112	1064	1246	1425	1511
Total	99.83	99.88	99.91	99.84	99.80	99.79	99.78	99.73	99.87	99.87	99.83	99.86	99.90	99.96
CO_2 ppm	89	104	101	b.d	109	208	106	142	105	144	134	112	250	316
H_2O wt%	0.54	0.54	0.50	0.51	0.56	0.49	0.49	0.50	0.47	0.46	0.48	0.49	0.48	0.43
Sc	27.82	29.37	30.16	26.55	28.90	26.24	26.34	29.25	29.66	28.14	30.91	27.05	26.11	28.61
V	277.93	271.75	277.99	259.91	302.37	258.06	240.75	259.90	310.55	285.65	301.34	275.04	253.58	282.83
Rb	8.25	8.73	8.56	7.06	11.12	7.67	6.76	6.25	9.66	9.52	9.12	9.10	6.46	5.06
Sr	303.51	346.41	347.80	256.58	382.87	286.58	285.36	263.19	332.35	305.21	381.38	343.05	258.51	242.77
Y	21.26	19.24	19.71	19.62	20.94	20.11	16.84	18.43	20.93	19.55	22.69	19.26	19.49	17.91
Zr	135.23	128.86	128.62	91.51	151.90	121.26	101.67	108.56	131.94	129.68	147.49	135.36	113.16	95.04
Nb	13.40	14.42	13.70	10.41	16.65	8.74	9.09	8.59	14.63	12.27	18.47	14.16	9.74	7.82
Ba	62.82	66.75	59.96	49.24	105.23	46.10	43.55	48.77	76.45	64.68	92.33	66.43	46.20	33.06
La	14.53	14.68	13.92	10.53	16.63	9.83	10.43	9.86	15.47	13.70	16.38	15.22	9.82	8.22
Ce	32.93	35.15	32.10	28.20	38.35	25.76	23.39	23.36	35.29	32.73	40.98	35.22	25.05	20.61
Pr	4.35	4.50	4.16	3.59	5.16	3.58	3.58	3.29	4.77	4.19	5.45	4.68	3.37	3.19
Nd	20.54	20.58	19.98	13.02	23.20	17.72	19.03	17.30	20.70	17.66	21.45	22.14	16.76	16.69
Sm	5.03	5.45	5.46	4.43	5.85	4.95	4.53	5.18	5.44	4.85	7.28	5.44	4.51	4.75
Eu	1.63	1.95	1.76	1.81	2.10	1.89	1.78	1.66	1.87	1.77	2.11	1.81	1.67	1.81
Gd	4.43	4.81	4.65	4.96	5.65	4.52	5.26	4.64	4.71	4.09	5.28	5.10	4.71	4.33
Tb	0.84	0.81	0.82	0.81	0.91	0.72	0.77	0.81	0.82	0.72	0.82	0.78	0.76	0.73
Dy	4.16	4.34	4.29	4.47	4.90	4.18	4.11	4.22	4.59	4.70	4.63	4.32	4.07	4.39
Ho	0.87	0.85	0.82	0.77	0.90	0.75	0.78	0.88	0.87	0.80	0.89	0.83	0.90	0.81
Er	2.23	1.98	2.01	2.09	2.23	2.02	1.82	2.12	2.13	1.72	1.87	1.96	2.01	1.96
Tm	0.29	0.28	0.25	0.32	0.30	0.28	0.26	0.28	0.25	0.31	0.32	0.27	0.28	0.26
Yb	1.88	1.52	1.79	1.70	1.81	1.75	1.66	1.73	1.82	1.21	2.05	1.86	1.58	1.66
Lu	0.29	0.26	0.22	0.21	0.26	0.21	0.23	0.23	0.19	0.15	0.13	0.25	0.23	0.22
Hf	3.56	3.56	2.88	2.55	4.06	3.33	3.37	3.26	3.55	3.10	4.92	3.76	2.59	2.58
Ta	0.82	0.81	0.79	0.68	0.97	0.55	0.66	0.53	0.93	0.71	0.68	0.80	0.56	0.44
Pb	0.83	0.92	0.95	0.71	1.21	0.62	0.59	0.77	1.09	1.03	0.73	0.99	0.83	0.90
U	0.42	0.34	0.33	0.27	0.36	0.24	0.19	0.24	0.42	0.38	0.31	0.40	0.25	0.21
Fo mol%	87.0	86.8	87.2	87.1	84.7	87.8	88.1	86.9	86.8	87.0	86.7	87.3	87.3	87.2
Ol %	16.99	15.62	18.14	18.78	8.31	17.28	18.84	15.35	12.75	15.5	12.97	16.64	16.28	13.9

Table 11: 1959-60 Kīlauea Iki and Kapoho eruption melt inclusion compositions (cont'd)

Sample	E6-09m1	E6-09m2	E6-10m1	E6-10m2	E6-10m3	E6-12m1	E6-13m1	E6-14m1	E7-03m1	E7-04m1	E7-05m1	E7-08m1	E7-09m1	E7-18m1
SiO_2	48.56	48.21	48.10	48.86	48.16	48.28	48.49	48.52	48.75	48.35	48.71	48.67	48.79	49.49
TiO_2	2.29	2.41	2.48	2.39	2.66	2.43	2.39	2.37	2.26	2.36	2.50	2.57	2.08	2.19
Al_2O_3	11.45	11.38	11.84	12.16	11.85	11.65	12.19	11.42	11.31	11.95	11.13	11.66	11.19	12.12
Cr_2O_3	0.08	0.06	0.11	0.12	0.15	0.11	0.07	0.10	0.06	0.13	0.13	0.12	0.14	0.08
Fe_2O_3	0.99	1.01	0.94	0.98	0.96	0.97	0.93	0.97	0.97	0.89	0.97	0.94	0.94	0.87
FeO	10.44	10.43	10.48	10.44	10.47	10.46	10.50	10.46	10.46	10.54	10.46	10.49	10.49	10.56
MnO	0.19	0.18	0.20	0.16	0.20	0.17	0.19	0.17	0.16	0.19	0.19	0.19	0.21	0.19
MgO	12.71	12.66	11.92	11.87	11.72	12.00	10.94	12.54	12.26	10.64	11.64	11.53	11.90	9.78
CaO	10.08	10.46	10.75	9.16	10.49	10.61	10.97	10.71	10.61	11.79	11.27	10.61	11.35	11.79
Na_2O	2.06	2.17	1.98	2.49	2.19	2.08	2.13	1.70	2.03	1.89	1.91	1.99	1.81	1.94
NiO	0.009	0.022	0.040	0.065	0.011	0.026	0.008	0.033	0.042	0.028	0.015	0.035	0.037	0.032
K_2O	0.43	0.33	0.41	0.63	0.44	0.53	0.53	0.40	0.37	0.46	0.41	0.50	0.37	0.40
P_2O_5	0.26	0.26	0.32	0.26	0.24	0.25	0.24	0.30	0.25	0.27	0.28	0.29	0.25	0.21
F ppm	595	574	702	541	704	510	598	609	524	581	724	553	571	468
Cl ppm	155	117	147	163	136	181	160	191	99	124	166	152	120	112
S ppm	1089	1409	1379	1251	1362	1193	1044	1422	1073	431	1362	1480	293	770
Total	99.84	99.94	99.94	99.91	99.91	99.87	99.85	100.04	99.81	99.64	99.98	99.93	99.66	99.86
CO_2 ppm	61	345	333	656	326	512	87	127	174	218	328	466	132	307
H_2O wt%	0.46	0.44	0.46	0.48	0.46	0.47	0.44	0.36	0.51	0.55	0.40	0.47	0.50	0.39
Sc	22.46	24.75	28.85	22.86	28.06	26.09	20.92	20.17	26.36	31.70	n.d	35.32	22.61	34.31
V	246.34	282.60	301.09	253.73	441.45	281.15	283.03	257.24	257.46	302.22	n.d	340.85	295.01	294.28
Rb	8.69	5.35	8.37	8.85	7.66	9.57	7.87	9.23	6.90	8.96	n.d	9.90	8.70	6.86
Sr	259.19	286.56	319.45	259.26	279.83	341.49	293.30	341.41	283.39	316.07	n.d	374.16	289.32	278.06
Y	14.46	18.50	20.10	14.01	17.13	18.00	16.61	15.89	17.22	18.31	n.d	22.40	19.64	17.18
Zr	97.01	131.93	126.38	92.15	125.47	124.63	111.63	133.20	103.26	120.59	n.d	87.49	101.05	118.94
Nb	8.25	7.69	13.75	10.25	10.27	14.28	12.94	9.99	8.94	10.55	n.d	14.44	10.77	9.84
Ba	40.00	42.60	76.97	109.94	67.58	94.50	58.82	64.53	50.04	85.01	n.d	84.02	70.54	87.01
La	8.91	8.60	13.63	9.86	10.45	14.93	13.41	13.14	9.76	12.96	n.d	16.45	11.08	10.40
Ce	24.79	24.31	28.76	25.64	27.45	34.86	31.59	33.21	24.78	29.03	n.d	38.48	23.02	24.00
Pr	3.24	3.54	4.03	3.45	4.14	4.71	4.52	4.91	3.54	3.62	n.d	3.98	3.13	3.53
Nd	19.72	18.96	20.28	11.20	17.17	20.95	16.19	24.63	18.45	18.75	n.d	20.10	15.95	17.40
Sm	4.26	5.00	5.26	4.44	4.57	5.23	4.81	3.19	4.89	5.08	n.d	5.72	4.16	4.34
Eu	1.44	1.82	1.98	1.37	2.02	1.87	1.49	2.19	1.68	1.66	n.d	1.30	1.87	1.70
Gd	4.61	4.64	5.18	3.48	4.16	4.34	4.41	3.82	4.41	5.03	n.d	5.44	3.27	4.17
Tb	0.59	0.68	0.86	0.62	0.85	0.69	0.69	0.68	0.67	0.75	n.d	0.73	0.65	0.69
Dy	3.26	4.46	4.58	3.48	4.06	4.19	3.53	3.27	3.71	3.98	n.d	4.70	2.87	3.72
Ho	0.68	0.86	0.89	0.55	0.89	0.77	0.78	0.64	0.68	0.76	n.d	0.73	0.81	0.69
Er	1.54	1.76	2.04	1.04	1.08	1.72	1.78	2.12	1.77	2.02	n.d	2.66	1.78	1.81
Tm	0.21	0.28	0.32	0.16	0.23	0.24	0.30	0.30	0.22	0.27	n.d	0.19	0.37	0.25
Yb	1.25	1.35	1.79	0.62	1.20	1.67	1.61	1.38	1.59	1.76	n.d	1.78	1.02	1.29
Lu	0.18	0.26	0.24	0.14	0.18	0.20	0.19	0.29	0.19	0.19	n.d	0.34	0.20	0.18
Hf	2.48	3.04	3.11	1.48	2.63	3.26	3.36	3.78	2.87	3.00	n.d	3.27	2.55	2.74
Ta	0.49	0.45	0.93	1.12	0.76	0.86	0.87	0.83	0.53	0.58	n.d	0.60	0.63	0.55
Pb	0.37	0.72	1.12	0.90	2.06	0.87	0.95	1.13	0.81	0.99	n.d	0.74	1.07	0.82
U	0.23	0.27	0.38	0.06	0.17	0.42	0.25	0.18	0.26	0.30	n.d	0.20	0.33	0.22
Fo mol%	87.7	87.8	87.0	87.0	86.9	87.2	86.0	87.5	87.3	85.6	86.7	86.5	86.8	84.1
Ol %	19.24	17.59	8.85	0.59	11.12	6.9	16.59	13.37	13.94	4.84	11.61	13.45	13.8	1.81

Table 11: 1959-60 Kīlauea Iki and Kapoho eruption melt inclusion compositions (cont'd)

Sample	E7-18m2	E7-19m1	E7-19m2	E7-19m3	E7-19m4	E7-19m5	E8-03m1	E8-05m1	E8-05m2	E8-07m1	E8-09m1	E8-11m1	E8-12m1	E8-14m1
SiO_2	48.74	48.10	48.35	48.47	48.48	48.38	49.70	48.33	48.87	48.64	49.18	48.58	48.63	49.12
TiO_2	2.28	2.54	2.59	2.56	2.42	2.61	2.35	2.44	2.49	2.22	2.18	2.55	2.36	2.14
Al_2O_3	12.17	11.79	11.55	11.66	11.76	11.65	12.09	11.41	11.67	11.30	11.43	11.63	11.53	11.47
Cr_2O_3	0.08	0.10	0.11	0.08	0.09	0.09	0.07	0.13	0.08	0.08	0.11	0.10	0.06	0.06
Fe_2O_3	0.86	0.93	0.95	0.93	0.93	0.93	0.91	0.97	0.95	0.99	0.95	0.93	0.99	0.94
FeO	10.55	10.50	10.48	10.50	10.50	10.50	10.52	10.46	10.49	10.45	10.48	10.51	10.44	10.49
MnO	0.19	0.16	0.21	0.20	0.18	0.19	0.19	0.20	0.19	0.19	0.18	0.22	0.20	0.19
MgO	9.71	10.97	10.97	10.82	10.77	10.95	10.21	11.54	11.26	12.26	12.17	10.59	12.07	11.79
CaO	12.05	11.89	11.64	11.65	11.74	11.68	10.38	11.41	10.84	10.74	10.22	11.68	10.59	10.82
Na_2O	1.89	1.94	2.01	2.02	2.04	1.99	2.31	2.00	2.02	2.08	1.97	2.05	2.06	1.96
NiO	0.045	0.034	0.029	0.019	0.038	0.024	0.048	0.030	0.034	0.034	0.023	0.027	0.036	0.039
K_2O	0.51	0.38	0.44	0.42	0.40	0.36	0.59	0.43	0.51	0.40	0.40	0.44	0.46	0.37
P_2O_5	0.51	0.27	0.25	0.24	0.25	0.22	0.23	0.28	0.25	0.22	0.30	0.24	0.25	0.22
F ppm	483	704	594	600	568	625	590	611	665	588	478	670	643	714
Cl ppm	116	156	157	137	160	163	178	141	207	203	111	170	141	94
S ppm	229	1484	1463	1464	1447	1528	922	1322	1085	1266	1219	1529	1228	197
Total	99.70	99.98	99.95	99.92	99.96	99.95	99.85	99.97	99.94	99.93	99.90	99.95	99.99	99.72
CO_2 ppm	123	192	233	224	242	195	301	331	402	203	275	297	122	238
H_2O wt%	0.45	0.44	0.45	0.46	0.44	0.45	0.46	0.40	0.40	0.44	0.43	0.47	0.37	0.44
Sc	33.29	30.80	28.91	30.36	30.91	32.12	27.51	25.07	26.69	28.69	24.31	28.89	26.53	25.78
V	315.96	335.90	322.68	342.64	328.68	329.39	280.34	287.06	288.09	258.71	244.44	295.96	271.51	265.81
Rb	8.52	6.29	7.02	7.12	7.63	6.19	11.84	8.06	10.11	8.30	5.73	7.85	7.50	7.21
Sr	254.08	305.82	327.81	319.18	334.48	302.97	362.16	334.73	358.14	323.07	293.36	324.50	295.66	304.18
Y	18.28	18.85	18.81	19.43	18.25	18.79	18.81	19.23	19.68	19.09	17.37	21.30	18.13	19.36
Zr	134.30	121.99	125.07	137.12	152.09	129.93	114.01	128.15	144.10	103.11	99.09	91.42	105.19	102.08
Nb	11.65	13.73	12.42	14.38	12.78	12.34	12.04	13.32	14.27	11.82	6.94	12.73	11.75	10.10
Ba	105.58	64.19	69.46	68.27	66.62	63.89	105.38	77.81	91.14	71.42	48.86	81.07	66.74	61.57
La	12.57	12.61	12.35	14.19	12.20	13.24	13.30	14.46	15.27	12.65	9.12	14.44	11.74	9.65
Ce	29.41	32.68	32.72	31.19	30.51	30.57	32.04	32.68	35.28	30.82	22.73	33.52	28.90	24.86
Pr	3.55	4.56	4.47	4.70	4.40	4.49	4.37	4.10	4.73	4.07	3.48	5.06	4.10	3.48
Nd	15.31	21.07	20.81	19.51	20.11	20.32	21.26	22.85	22.50	18.10	15.48	19.88	19.27	18.21
Sm	4.25	5.63	4.92	5.02	5.18	4.72	4.95	5.38	5.33	5.09	4.10	4.62	4.82	5.60
Eu	1.46	1.88	1.80	1.86	1.81	1.74	1.96	1.90	2.03	1.88	1.54	1.78	1.74	1.86
Gd	4.73	4.83	4.47	4.58	4.53	4.45	4.77	4.57	5.12	4.08	4.41	6.25	4.15	3.92
Tb	0.75	0.75	0.77	0.77	0.74	0.64	0.76	0.78	0.72	0.67	0.66	0.76	0.71	0.72
Dy	3.82	3.80	4.14	4.31	4.18	3.87	4.12	4.09	4.23	4.01	3.74	4.35	3.80	3.99
Ho	0.78	0.78	0.75	0.76	0.84	0.70	0.80	0.81	0.82	0.94	0.69	0.84	0.80	0.78
Er	1.52	1.93	1.98	1.68	1.92	2.00	2.11	2.11	2.02	1.93	1.84	2.17	1.77	1.88
Tm	0.30	0.24	0.28	0.27	0.24	0.26	0.27	0.25	0.28	0.25	0.24	0.26	0.24	0.25
Yb	2.16	1.79	1.70	1.51	1.47	1.54	1.76	1.75	1.44	1.70	1.65	1.99	1.53	1.45
Lu	0.19	0.24	0.24	0.22	0.19	0.19	0.21	0.20	0.25	0.24	0.22	0.25	0.21	0.29
Hf	3.60	3.49	3.74	3.72	3.50	3.05	3.14	3.10	3.66	3.44	3.13	3.33	2.99	3.13
Ta	0.66	0.75	0.74	0.58	0.69	0.78	0.70	0.77	0.86	0.74	0.40	0.81	0.67	0.44
Pb	0.71	0.81	0.96	0.88	0.98	1.17	1.02	1.02	0.81	0.94	0.88	1.12	0.83	0.55
U	0.27	0.29	0.34	0.49	0.44	0.34	0.30	0.33	0.49	0.32	0.18	0.23	0.28	0.26
Fo mol%	84.1	86.1	86.1	85.9	85.8	86.0	84.8	86.7	86.2	87.3	87.0	85.6	87.2	86.7
Ol %	1.76	9.21	8.62	9.4	9.67	10.71	6.16	10.48	8.03	11.14	11.33	11.25	12.38	9.22

Table 11: 1959-60 Kīlauea Iki and Kapoho eruption melt inclusion compositions (cont'd)

Sample	E8-15m1	E8-24m1	E10-05m1	E10-06m1	E10-09m1	E10-12m1	E10-15m1	E15-01m1	E15-01m2	E15-01m3	E15-10m1	E15-16m1	E15-19m2
SiO_2	49.07	49.11	48.87	48.40	49.48	48.76	48.71	48.54	48.60	48.34	48.29	48.75	48.95
TiO_2	2.09	2.22	2.51	2.39	2.18	2.17	2.54	2.51	2.59	2.63	2.33	2.30	2.31
Al_2O_3	10.87	11.17	11.94	11.10	11.29	11.30	12.01	11.81	12.23	11.86	11.54	11.85	11.48
Cr_2O_3	0.07	0.11	0.08	0.14	0.11	0.09	0.09	0.06	0.06	0.07	0.06	0.07	0.07
Fe_2O_3	1.06	0.99	0.94	0.97	0.96	1.03	0.94	1.07	1.03	1.01	1.06	0.95	0.96
FeO	10.37	10.44	10.50	10.46	10.47	10.41	10.49	10.37	10.41	10.43	10.37	10.48	10.47
MnO	0.15	0.18	0.19	0.18	0.17	0.18	0.16	0.17	0.17	0.17	0.17	0.18	0.20
MgO	13.36	13.17	10.60	12.56	11.61	13.21	10.66	11.55	10.64	11.21	12.75	11.00	11.93
CaO	10.17	9.43	10.95	10.52	10.58	9.83	11.11	10.86	11.10	11.18	10.29	11.13	10.67
Na_2O	1.92	2.04	2.23	1.97	2.09	2.03	2.14	2.19	2.28	2.11	2.17	2.13	1.99
NiO	0.029	0.020	0.037	0.015	0.039	0.025	0.038	0.024	0.015	0.038	0.031	0.010	0.016
K_2O	0.34	0.40	0.52	0.47	0.42	0.38	0.52	0.50	0.52	0.51	0.46	0.50	0.34
P_2O_5	0.23	0.24	0.27	0.24	0.22	0.23	0.26	0.26	0.27	0.28	0.23	0.29	0.25
F ppm	498	501	564	556	497	547	620	654	691	655	806	641	651
Cl ppm	104	139	190	135	138	185	207	153	196	164	175	202	172
S ppm	1070	1207	1167	549	843	1229	964	594	652	965	1036	1404	670
Total	100.00	99.82	99.93	99.59	99.85	99.97	99.92	100.12	100.12	100.11	100.07	100.00	99.86
CO_2 ppm	119	485	331	341	458	217	413	58	71	66	119	305	170
H_2O wt%	0.30	0.51	0.41	0.61	0.42	0.38	0.39	0.11	0.11	0.21	0.27	0.37	0.38
Sc	25.17	24.29	26.71	25.06	24.35	22.33	25.29	23.29	22.66	25.92	21.08	27.04	22.67
V	239.91	208.41	300.08	277.13	240.41	220.68	300.57	255.25	255.84	285.35	243.97	337.27	256.98
Rb	5.54	5.85	9.85	9.05	7.06	7.25	10.99	9.20	8.89	9.49	6.08	8.68	7.03
Sr	278.48	266.98	361.90	335.26	283.94	271.80	330.24	327.79	323.79	356.29	320.00	342.58	273.11
Y	16.88	21.06	18.57	17.31	16.11	17.23	17.43	18.13	19.54	21.44	17.06	18.65	15.90
Zr	113.20	102.98	127.26	116.93	107.91	96.26	132.59	120.44	128.25	152.47	105.88	146.32	110.47
Nb	7.76	8.66	15.10	13.74	9.83	9.76	15.07	13.81	14.01	16.62	13.54	14.53	9.75
Ba	37.12	49.38	121.83	87.25	68.52	51.27	96.13	59.18	66.71	69.70	58.63	84.92	46.08
La	9.78	9.27	16.09	14.31	10.77	10.20	13.86	14.53	14.23	15.82	13.11	14.66	9.75
Ce	24.47	22.76	37.65	35.84	24.91	25.75	34.90	33.70	34.26	37.12	31.53	35.37	26.00
Pr	3.37	3.11	5.05	4.69	3.55	3.37	4.54	4.65	4.53	4.75	4.54	4.60	3.37
Nd	17.81	16.82	23.58	21.09	17.33	16.02	22.57	21.40	20.00	18.60	18.14	18.98	19.39
Sm	4.97	4.35	5.28	4.95	4.96	4.00	5.25	5.07	5.10	5.72	5.11	4.99	4.04
Eu	1.73	1.77	2.20	1.85	1.59	1.71	1.83	1.87	1.84	2.13	2.10	1.73	1.74
Gd	3.93	4.56	4.93	4.64	3.75	4.08	4.59	4.65	4.87	4.92	4.89	4.77	4.16
Tb	0.65	0.78	0.84	0.69	0.68	0.65	0.70	0.75	0.72	0.82	0.82	0.78	0.59
Dy	4.15	4.50	4.50	4.08	3.77	3.91	4.48	4.16	4.17	5.27	4.91	4.47	4.10
Ho	0.80	0.86	0.87	0.75	0.65	0.68	0.79	0.78	0.78	0.73	0.67	0.89	0.76
Er	1.76	2.23	2.15	1.84	1.69	1.78	1.92	1.89	1.91	2.37	1.75	2.04	1.93
Tm	0.22	0.26	0.29	0.25	0.24	0.23	0.24	0.26	0.25	0.33	0.27	0.24	0.25
Yb	1.65	1.76	1.72	1.63	1.46	1.65	1.61	1.76	1.78	1.75	2.03	1.55	1.43
Lu	0.24	0.27	0.24	0.22	0.23	0.21	0.30	0.22	0.21	0.35	0.22	0.27	0.26
Hf	2.77	2.91	3.43	3.51	2.90	2.80	4.32	3.57	3.56	3.78	3.25	3.91	3.16
Ta	0.49	0.47	0.92	0.92	0.59	0.60	0.97	0.86	0.84	1.09	0.93	1.08	0.57
Pb	0.72	0.61	1.17	0.94	0.74	0.65	1.18	1.02	1.06	1.08	1.01	1.60	0.74
U	0.21	0.17	0.47	0.42	0.28	0.26	0.33	0.43	0.44	0.62	0.56	0.39	0.29
Fo mol%	88.2	87.9	85.5	87.6	86.5	88.1	85.6	86.8	85.8	86.4	87.9	86.0	86.9
Ol %	18.8	12.99	2.9	9.22	7.59	16	5.68	18.19	14.9	17.93	20.66	9.67	19.12

Table 11: 1959-60 Kīlauea Iki and Kapoho eruption melt inclusion compositions (cont'd)

Sample	E15-19m1	E15-30m1	E16-02m1	E16-04m1	E16-04m2	E16-06m1	E16-07m1	E16-08m1	E16-08m2	E16-10m1	E16-11m1	E16-14m1	E16-14m2
SiO_2	49.10	48.86	49.13	49.05	49.66	48.57	48.41	49.50	48.87	49.64	48.57	48.91	49.01
TiO_2	2.29	2.68	2.60	2.55	2.28	2.49	2.34	2.36	2.42	2.26	2.44	2.63	2.55
Al_2O_3	11.35	12.48	11.78	11.01	10.88	11.71	11.25	12.01	12.29	11.99	11.70	12.39	12.38
Cr_2O_3	0.07	0.06	0.07	0.07	0.07	0.06	0.06	0.06	0.05	0.09	0.08	0.06	0.06
Fe_2O_3	0.98	0.93	0.98	1.07	1.08	1.01	0.99	0.99	0.94	0.94	0.97	0.98	0.97
FeO	10.45	10.50	10.46	10.37	10.36	10.42	10.44	10.47	10.49	10.49	10.46	10.46	10.47
MnO	0.16	0.20	0.19	0.17	0.17	0.20	0.17	0.18	0.17	0.18	0.19	0.18	0.19
MgO	11.76	9.55	10.75	11.15	11.38	11.68	12.32	10.63	10.39	10.59	11.42	10.04	10.26
CaO	10.60	11.32	10.79	11.47	10.99	10.85	10.82	10.86	11.00	10.77	11.13	11.09	10.90
Na_2O	2.08	2.30	2.20	2.12	2.27	2.06	1.98	2.24	2.19	2.19	2.03	2.25	2.23
NiO	0.024	0.032	0.013	0.031	0.034	0.032	0.022	0.044	0.010	0.029	0.034	0.020	0.021
K_2O	0.46	0.55	0.53	0.53	0.40	0.45	0.51	0.33	0.37	0.38	0.43	0.56	0.52
P_2O_5	0.30	0.28	0.25	0.30	0.32	0.29	0.25	0.21	0.61	0.22	0.25	0.29	0.28
F ppm	645	605	592	524	453	688	535	638	753	504	659	636	648
Cl ppm	180	302	161	225	143	127	198	232	134	201	212	242	219
S ppm	182	1319	699	1028	163	460	983	898	995	775	1177	1217	1140
Total	99.75	100.08	99.94	100.17	99.99	99.99	99.83	100.16	100.09	99.99	100.04	100.18	100.14
CO_2 ppm	b.d	97	383	107	b.d	31	95	36	32	192	182	132	193
H_2O wt%	0.40	0.31	0.29	0.14	0.14	0.22	0.46	0.15	0.21	0.27	0.32	0.17	0.20
Sc	25.94	30.27	26.99	30.43	33.73	25.12	25.36	25.83	23.20	24.84	29.07	27.91	26.25
V	250.37	317.88	291.71	288.85	254.68	297.73	276.37	251.96	268.01	262.47	297.52	305.56	298.61
Rb	7.35	11.00	9.46	11.04	5.55	7.32	9.46	6.25	6.33	6.19	7.92	10.90	10.14
Sr	310.82	374.61	350.72	357.45	280.05	271.04	311.88	285.70	271.57	262.57	325.78	338.08	341.90
Y	17.80	20.89	18.24	18.15	12.20	16.12	17.87	18.15	20.17	17.83	19.10	18.88	18.68
Zr	109.39	135.36	131.93	143.19	139.49	105.28	125.53	112.29	134.62	125.21	120.21	129.62	122.59
Nb	12.06	15.57	15.20	15.33	9.38	9.03	13.99	10.02	8.83	10.07	13.80	15.95	14.83
Ba	57.12	104.97	97.25	68.44	33.01	48.26	53.57	44.67	50.53	59.26	82.87	86.93	78.98
La	12.05	16.16	14.84	13.95	7.37	10.04	13.40	10.15	10.21	9.40	14.36	15.08	14.40
Ce	29.79	38.45	34.89	34.10	25.41	26.76	30.55	27.41	27.07	22.65	32.64	35.43	33.73
Pr	4.40	5.42	4.73	4.39	3.84	3.49	4.25	3.54	4.21	3.42	4.52	4.73	4.57
Nd	20.63	24.05	21.15	21.02	17.76	18.99	18.33	18.44	21.55	15.03	20.80	22.56	21.45
Sm	5.26	5.76	5.45	5.27	4.51	3.76	4.74	4.75	5.38	4.19	5.02	5.22	5.20
Eu	1.79	2.18	1.81	1.82	2.05	1.88	1.61	1.92	1.83	1.47	1.84	1.91	1.96
Gd	4.21	5.52	4.60	4.28	3.93	4.13	4.56	4.55	4.88	4.85	4.65	4.73	4.48
Tb	0.66	0.92	0.74	0.73	0.54	0.78	0.66	0.72	0.88	0.71	0.68	0.73	0.80
Dy	3.80	4.93	3.92	4.17	3.22	4.00	4.16	4.21	4.10	3.92	4.18	4.00	3.82
Ho	0.78	0.91	0.75	0.82	0.43	0.73	0.66	0.90	0.86	0.82	0.81	0.79	0.81
Er	1.68	2.08	1.90	1.74	0.92	1.62	1.83	1.92	1.81	1.88	1.84	1.95	2.01
Tm	0.38	0.26	0.25	0.22	0.26	0.19	0.24	0.25	0.21	0.29	0.26	0.28	0.25
Yb	1.23	1.94	1.69	1.66	1.47	1.85	1.39	1.58	1.67	1.76	1.58	1.83	1.74
Lu	0.21	0.25	0.19	0.21	0.26	0.24	0.23	0.17	0.18	0.17	0.22	0.24	0.20
Hf	3.17	3.66	3.28	3.33	3.22	3.17	3.34	2.62	3.38	2.93	3.09	3.19	3.25
Ta	0.90	0.95	0.85	0.95	0.34	0.71	0.84	0.59	0.42	0.59	0.78	0.85	0.85
Pb	0.82	1.08	1.16	1.11	2.02	0.75	1.16	0.98	0.73	0.40	0.78	1.03	0.82
U	0.31	0.43	0.43	0.39	0.17	0.34	0.36	0.29	0.21	0.19	0.36	0.36	0.38
Fo mol%	86.7	84.2	85.7	86.3	86.4	86.8	87.4	85.4	85.1	85.3	86.5	84.9	85.1
Ol %	16.96	6.59	6.88	18.1	22.17	17.55	18.98	14.83	12.28	8.79	9.17	9.87	10.8

Table 11: 1959-60 Kīlauea Iki and Kapoho eruption melt inclusion compositions (cont'd)

Sample	E16-17m1	E16-17m2	E16-18m1	E16-26m1	KO-03m1	KO-04m1	KO-09m1	KO-11m1	KO-11m2	KO-14m1	KO-15m1	KO-15m3
SiO_2	49.17	48.84	49.28	50.08	49.12	49.31	48.82	51.43	50.66	50.61	48.15	48.25
TiO_2	2.35	2.33	2.10	2.07	2.25	2.00	2.25	2.32	2.48	2.19	2.40	2.32
Al_2O_3	11.00	11.02	11.50	12.67	11.56	11.69	11.79	12.85	12.74	11.82	10.92	10.96
Cr_2O_3	0.08	0.06	0.08	0.05	0.06	0.06	0.06	0.03	0.04	0.05	0.09	0.07
Fe_2O_3	1.00	1.01	0.99	0.97	0.96	0.90	0.93	0.77	0.81	0.87	1.05	1.03
FeO	10.43	10.42	10.45	10.46	10.47	10.53	10.50	10.65	10.64	10.55	10.39	10.41
MnO	0.19	0.17	0.19	0.17	0.17	0.20	0.17	0.19	0.20	0.18	0.16	0.14
MgO	11.22	11.35	11.82	10.56	11.70	10.51	11.37	7.33	7.21	9.93	13.12	13.04
CaO	11.62	11.81	10.66	9.93	10.49	11.55	11.04	11.24	11.89	10.58	10.67	10.57
Na_2O	1.93	1.97	2.07	2.26	2.08	1.84	1.96	1.94	2.12	2.07	2.02	1.97
NiO	0.013	0.038	0.009	0.012	0.016	0.028	0.024	0.029	0.008	0.017	0.026	0.027
K_2O	0.48	0.47	0.37	0.42	0.49	0.64	0.43	0.46	0.44	0.44	0.34	0.36
P_2O_5	0.25	0.25	0.21	0.26	0.25	0.35	0.26	0.26	0.26	0.26	0.27	0.47
F ppm	594	564	659	592	533	525	606	750	731	415	644	633
Cl ppm	201	239	156	158	173	209	145	196	187	174	103	100
S ppm	1261	1370	341	632	982	979	991	1211	1419	818	1365	1062
Total	100.06	100.10	99.87	100.12	99.87	99.87	99.86	99.83	99.88	99.79	99.96	99.90
CO_2 ppm	91	91	95	110	117	69	103	252	283	109	155	27
H_2O wt%	0.28	0.29	0.29	0.09	0.41	0.43	0.43	0.54	0.51	0.46	0.42	0.42
Sc	29.13	31.23	26.98	24.67	24.91	31.83	26.79	24.82	29.62	32.59	24.64	25.84
V	294.15	310.34	274.43	267.78	252.43	287.11	308.71	275.78	329.65	314.41	269.30	290.27
Rb	9.35	9.06	6.02	7.02	8.79	12.32	8.58	7.23	9.76	7.30	6.43	6.37
Sr	320.03	346.15	351.64	286.80	321.08	258.19	296.98	314.06	300.74	290.80	247.64	275.32
Y	17.32	18.98	17.41	19.78	18.65	15.75	21.20	22.04	21.60	18.83	20.54	20.53
Zr	129.50	135.00	103.99	114.59	128.74	88.16	113.48	116.56	136.09	103.72	107.97	79.67
Nb	13.79	14.64	8.20	10.77	13.48	11.73	12.62	13.90	16.94	10.05	7.70	9.24
Ba	69.60	75.93	43.17	51.67	57.67	93.38	54.21	100.84	115.67	58.15	29.92	34.29
La	13.76	14.53	9.19	10.96	14.23	9.56	13.16	11.78	16.53	11.59	8.07	8.21
Ce	33.25	34.19	21.84	27.57	33.19	20.21	30.97	33.43	32.93	26.18	21.70	21.33
Pr	4.61	4.49	3.19	3.77	4.89	2.68	4.35	4.40	4.92	3.76	3.27	3.30
Nd	21.11	21.49	15.99	18.22	22.94	15.94	19.13	18.85	19.43	16.57	15.83	17.37
Sm	4.63	5.71	4.26	4.82	5.69	4.81	4.80	5.47	5.59	4.85	5.10	4.88
Eu	1.63	1.95	1.83	1.79	1.91	1.70	1.77	1.89	2.19	1.69	1.72	1.93
Gd	4.28	4.44	4.55	4.36	5.20	4.14	5.05	5.52	4.36	3.89	4.58	5.89
Tb	0.72	0.72	0.66	0.75	0.81	0.68	0.75	0.72	0.74	0.76	0.79	0.86
Dy	3.82	4.41	4.03	4.40	4.55	3.77	4.00	4.79	4.68	3.93	4.77	4.52
Ho	0.72	0.71	0.72	0.77	0.88	0.79	0.80	0.82	0.92	0.77	0.81	0.90
Er	1.80	1.80	1.70	2.08	2.13	2.14	1.92	1.85	2.01	2.03	1.89	2.28
Tm	0.23	0.23	0.24	0.25	0.27	0.17	0.29	0.33	0.32	0.25	0.26	0.27
Yb	1.55	1.39	1.58	1.86	1.78	1.67	1.89	2.43	2.06	2.02	1.91	1.61
Lu	0.22	0.24	0.20	0.21	0.25	0.23	0.24	0.26	0.26	0.23	0.27	0.25
Hf	3.03	3.28	2.39	2.94	3.77	2.38	2.84	3.08	2.93	2.71	2.92	3.47
Ta	0.70	0.78	0.50	0.62	0.84	0.73	0.80	0.73	0.74	0.69	0.44	0.60
Pb	0.77	0.66	0.68	0.76	0.93	0.93	0.98	1.40	1.11	0.81	0.73	0.76
U	0.33	0.40	0.20	0.28	0.41	0.32	0.28	0.34	0.36	0.27	0.15	0.31
Fo mol%	86.2	86.5	86.8	85.1	86.7	85.2	86.3	78.9	78.9	84.1	88.2	88.1
Ol %	13.63	13.19	14.43	16.02	19.33	13.25	18.51	1.82	1.24	13.3	24.61	25.1

Table 11: 1959-60 Kīlauea Iki and Kapoho eruption melt inclusion compositions (cont'd)

Sample	KO-18m1	KO-18m3	KO-18m4	KO-20m1	KO-21m1	KO-21m2	KO-26m1	KO-26m2	KO-20m1
SiO_2	49.05	49.24	48.82	49.32	48.93	49.61	48.95	48.73	49.16
TiO_2	2.26	2.22	2.60	2.25	2.39	2.14	2.07	2.06	2.24
Al_2O_3	11.71	11.45	11.76	11.39	11.84	11.72	11.13	11.20	11.56
Cr_2O_3	0.06	0.06	0.06	0.05	0.06	0.05	0.06	0.06	0.05
Fe_2O_3	0.94	0.94	0.94	0.95	0.91	0.91	1.01	1.00	0.94
FeO	10.49	10.49	10.49	10.48	10.52	10.52	10.42	10.43	10.49
MnO	0.17	0.19	0.17	0.18	0.18	0.18	0.17	0.17	0.19
MgO	11.17	11.43	11.11	11.86	10.85	11.07	13.33	13.63	11.69
CaO	10.82	10.81	10.77	10.31	11.06	10.70	9.85	9.74	10.40
Na_2O	2.17	2.09	2.09	2.07	2.07	2.09	2.00	1.86	2.11
NiO	0.020	0.015	0.030	0.010	0.035	0.022	0.031	0.032	0.013
K_2O	0.45	0.36	0.47	0.41	0.40	0.34	0.29	0.38	0.43
P_2O_5	0.29	0.29	0.28	0.26	0.38	0.24	0.28	0.26	0.26
F ppm	538	648	665	573	626	543	557	462	578
Cl ppm	104	139	175	119	185	105	407	170	115
S ppm	205	475	1109	831	1213	1113	1061	976	824
Total	99.70	99.75	99.90	99.77	99.92	99.88	99.89	99.79	99.77
CO_2 ppm	25	136	141	58	127	132	146	117	64
H_2O wt%	0.43	0.44	0.44	0.48	0.44	0.43	0.44	0.50	0.48
Sc	27.20	28.26	26.01	23.32	29.16	31.32	21.21	20.17	23.46
V	279.32	311.57	269.49	251.08	301.83	291.11	249.13	209.87	252.62
Rb	8.67	8.07	6.80	7.26	7.46	5.01	8.18	7.04	7.31
Sr	321.56	298.90	264.86	283.99	307.37	254.47	152.20	223.13	285.73
Y	19.73	20.79	18.25	19.50	20.48	20.20	20.56	19.17	19.62
Zr	139.02	126.58	118.32	123.79	122.19	101.15	97.67	109.72	124.54
Nb	11.77	11.24	9.51	9.76	10.28	9.18	6.08	10.42	9.82
Ba	58.71	51.99	45.62	44.02	52.58	33.99	32.17	29.54	45.38
La	11.86	11.97	10.63	11.23	10.85	7.95	8.19	9.33	11.30
Ce	30.57	29.63	23.54	25.34	27.60	21.05	22.05	22.36	25.50
Pr	4.22	4.01	3.33	3.60	3.72	3.32	2.94	3.46	3.62
Nd	22.39	24.00	17.24	18.84	17.94	15.69	15.02	20.04	18.95
Sm	5.13	5.41	4.42	5.05	4.84	4.07	5.45	4.50	5.08
Eu	2.15	1.98	1.86	1.72	1.96	2.06	1.48	1.59	1.74
Gd	5.78	4.48	4.96	4.56	5.07	4.68	4.97	4.06	4.59
Tb	0.82	0.81	0.72	0.72	0.82	0.72	0.82	0.65	0.72
Dy	4.55	3.80	4.70	4.49	4.36	4.87	4.09	3.94	4.52
Ho	0.94	0.93	0.80	0.78	0.84	0.96	0.86	0.79	0.78
Er	2.01	1.89	2.00	1.87	2.23	2.02	1.85	1.99	1.88
Tm	0.24	0.22	0.26	0.25	0.30	0.27	0.21	0.31	0.25
Yb	1.81	1.49	1.84	1.62	1.76	1.56	1.56	1.64	1.63
Lu	0.28	0.30	0.18	0.25	0.23	0.29	0.23	0.24	0.25
Hf	4.25	3.52	3.58	3.32	3.01	2.54	2.29	2.93	3.34
Ta	0.74	0.69	0.59	0.59	0.62	0.29	0.36	0.65	0.59
Pb	0.48	1.17	0.40	0.78	0.81	b.d	0.41	0.87	0.79
U	0.29	0.33	0.32	0.23	0.28	0.21	0.29	0.27	0.23
Fo mol%	86.1	86.3	86.1	86.7	85.7	85.8	88.1	88.3	86.6
Ol %	17.48	17.68	16.78	20.03	15.69	19.05	25.72	28.45	19.3

Table 12: Lō`ihi seamount melt inclusion compositions

Sample	L-02m1	L-02m2	L-09m1	L-12m1	L-13m1	L-24m1	L-28m1	L-37m1	L-37m2	L-39m1	L-39m2	L-41m1	L-41m2	L-42m1
SiO_2	48.36	48.24	48.00	47.63	48.03	49.84	48.48	48.60	48.80	47.30	47.27	48.31	48.33	48.33
TiO_2	1.95	2.05	2.72	2.15	2.16	1.31	1.96	1.80	1.88	2.05	2.35	1.97	1.96	1.97
Al_2O_3	10.07	10.15	11.56	10.27	9.54	10.04	9.49	9.78	10.05	10.14	10.23	9.92	10.27	10.10
Cr_2O_3	0.08	0.09	0.07	0.13	0.11	0.09	0.11	0.11	0.10	0.09	0.09	0.10	0.08	0.09
Fe_2O_3	1.11	1.09	1.00	1.10	1.16	1.04	1.17	1.12	1.06	1.13	1.06	1.16	1.10	1.12
FeO	10.95	10.96	11.04	10.95	10.91	11.01	10.89	10.94	10.99	10.93	10.99	10.90	10.96	10.94
MnO	0.20	0.19	0.19	0.18	0.17	0.19	0.18	0.18	0.17	0.20	0.19	0.18	0.18	0.18
MgO	15.23	15.28	10.94	14.78	14.91	14.38	15.21	15.18	14.38	15.07	13.89	14.98	14.48	14.69
CaO	9.09	9.08	10.63	9.79	9.80	9.27	9.65	9.42	9.67	10.21	11.25	9.43	9.52	9.48
Na_2O	1.75	1.64	2.21	1.66	1.78	1.72	1.74	1.65	1.66	1.45	1.33	1.83	1.85	1.84
NiO	0.021	0.027	0.033	0.029	0.025	0.018	0.026	b.d	0.020	0.043	0.025	0.023	0.030	0.027
K_2O	0.29	0.28	0.72	0.39	0.39	0.21	0.28	0.29	0.32	0.49	0.43	0.33	0.32	0.32
P_2O_5	0.18	0.21	0.26	0.26	0.34	0.13	0.21	0.18	0.17	0.23	0.24	0.28	0.26	0.27
F ppm	302	406	803	572	872	368	910	306	356	623	697	584	446	517
Cl ppm	269	175	440	250	394	53	116	121	95	398	533	303	317	310
S ppm	1240	1187	850	1329	1040	789	1274	1159	1083	1276	1278	1022	1068	1046
Total	99.57	99.57	99.68	99.66	99.64	99.45	99.73	98.51	99.52	99.69	99.71	99.70	99.63	99.66
CO_2 ppm	100.78	96.59	n.d	332.33	73.67	479.37	106.86	319.95	115.93	136.37	166.77	n.d	61.91	30.32
H_2O wt%	0.76	0.75	0.64	0.71	0.72	0.77	0.65	0.76	0.76	0.71	0.69	0.62	0.69	0.66
Sc	23.12	23.55	28.02	25.91	16.91	21.65	19.60	27.77	26.82	25.96	27.41	24.17	22.37	24.52
V	231.59	262.57	311.04	264.43	215.75	223.39	188.65	233.80	231.34	287.46	321.09	241.59	234.78	233.90
Rb	3.54	4.15	15.40	5.46	6.94	2.50	4.90	4.24	4.29	10.28	7.69	6.04	5.17	4.86
Sr	252.22	250.19	461.74	292.77	242.16	150.29	255.84	312.24	290.74	315.90	316.16	265.87	304.03	257.38
Y	13.96	14.29	17.58	15.53	13.97	14.97	11.58	15.62	13.39	17.35	16.76	15.91	17.47	18.01
Zr	79.21	84.31	152.42	117.96	92.55	51.24	65.44	107.07	136.38	90.50	83.44	85.05	84.81	89.06
Nb	8.32	7.04	24.54	9.06	12.28	3.37	8.79	9.52	11.12	12.99	13.23	8.57	12.81	12.11
Ba	58.82	49.67	207.59	76.45	88.74	31.92	65.34	71.18	84.58	120.53	110.00	67.37	67.71	81.96
La	8.02	7.56	34.88	9.92	9.24	4.01	8.53	9.56	10.61	12.38	13.17	9.12	9.89	8.93
Ce	18.51	18.95	71.52	24.89	19.75	9.26	21.88	20.20	24.03	26.81	28.57	20.87	20.91	21.03
Pr	3.20	2.83	8.31	3.45	2.52	1.49	3.44	3.21	3.42	3.28	3.48	3.30	3.57	3.17
Nd	13.70	14.19	33.13	15.66	11.79	8.21	12.25	15.68	17.22	16.63	16.60	14.02	13.57	12.94
Sm	4.17	3.86	5.42	4.34	3.03	2.29	3.77	3.78	3.07	3.06	3.43	3.72	4.39	4.00
Eu	1.59	1.40	1.86	1.37	1.41	1.04	1.21	1.27	1.37	1.11	1.10	1.44	1.27	1.21
Gd	3.19	3.23	4.52	3.43	3.36	2.98	3.13	3.82	4.99	3.39	3.07	3.56	4.42	4.09
Tb	0.52	0.52	0.70	0.65	0.54	0.49	0.84	0.52	0.61	0.55	0.66	0.62	0.61	0.63
Dy	3.49	3.02	3.84	3.33	3.34	3.10	3.16	3.77	2.85	3.65	3.56	3.57	2.93	3.41
Ho	0.56	0.63	0.68	0.69	0.55	0.60	0.49	0.67	0.61	0.65	0.62	0.75	0.75	0.67
Er	1.48	1.66	1.84	1.64	1.47	1.49	1.44	1.77	1.64	1.58	1.72	1.77	1.54	1.61
Tm	0.18	0.21	0.19	0.26	0.22	0.20	0.12	0.24	0.26	0.23	0.23	0.21	0.23	0.24
Yb	1.24	1.38	1.49	1.49	0.73	1.39	0.71	1.32	1.60	1.61	1.82	1.29	1.44	1.47
Lu	0.22	0.16	0.20	0.24	0.18	0.19	0.16	0.18	0.20	0.26	0.25	0.25	0.26	0.16
Hf	1.97	2.14	4.17	2.47	2.18	1.65	2.38	2.48	2.59	2.51	2.91	2.30	2.66	2.47
Ta	0.51	0.40	1.32	0.50	0.53	0.22	0.37	0.62	0.73	0.80	0.84	0.51	0.74	0.78
Pb	0.62	0.63	2.37	0.88	0.80	0.30	0.75	0.63	1.28	0.79	0.60	0.56	0.87	0.64
U	0.17	0.14	0.66	0.25	0.16	0.06	0.18	0.18	0.19	0.25	0.27	0.14	0.26	0.20
Fo mol%	88.9	88.9	85.5	88.8	88.9	88.0	89.0	88.9	88.2	89.1	88.2	88.9	88.5	88.6
Ol %	23.98	24.35	7.24	24.81	35.12	25.42	30.19	27.84	27.20	22.71	18.70	24.04	21.97	22.86